

Engineering Materials

Felipe de Almeida La Porta
Carlton A. Taft *Editors*

Emerging Research in Science and Engineering Based on Advanced Experimental and Computational Strategies

 Springer

Engineering Materials

This series provides topical information on innovative, structural and functional materials and composites with applications in optical, electrical, mechanical, civil, aeronautical, medical, bio- and nano-engineering. The individual volumes are complete, comprehensive monographs covering the structure, properties, manufacturing process and applications of these materials. This multidisciplinary series is devoted to professionals, students and all those interested in the latest developments in the Materials Science field.


More information about this series at <http://www.springer.com/series/4288>

Felipe de Almeida La Porta · Carlton A. Taft
Editors

Emerging Research
in Science and Engineering
Based on Advanced
Experimental
and Computational Strategies

 Springer

Editors

Felipe de Almeida La Porta 
Departamento de Química
Universidade Tecnológica Federal do Paraná
Londrina, Brazil

Carlton A. Taft
Centro Brasileiro de Pesquisas Físicas
Rio de Janeiro, Brazil

ISSN 1612-1317

Engineering Materials

ISBN 978-3-030-31402-6

<https://doi.org/10.1007/978-3-030-31403-3>

ISSN 1868-1212 (electronic)

ISBN 978-3-030-31403-3 (eBook)

© Springer Nature Switzerland AG 2020

This work is subject to copyright. All rights are reserved by the Publisher, whether the whole or part of the material is concerned, specifically the rights of translation, reprinting, reuse of illustrations, recitation, broadcasting, reproduction on microfilms or in any other physical way, and transmission or information storage and retrieval, electronic adaptation, computer software, or by similar or dissimilar methodology now known or hereafter developed.

The use of general descriptive names, registered names, trademarks, service marks, etc. in this publication does not imply, even in the absence of a specific statement, that such names are exempt from the relevant protective laws and regulations and therefore free for general use.

The publisher, the authors and the editors are safe to assume that the advice and information in this book are believed to be true and accurate at the date of publication. Neither the publisher nor the authors or the editors give a warranty, expressed or implied, with respect to the material contained herein or for any errors or omissions that may have been made. The publisher remains neutral with regard to jurisdictional claims in published maps and institutional affiliations.

This Springer imprint is published by the registered company Springer Nature Switzerland AG
The registered company address is: Gewerbestrasse 11, 6330 Cham, Switzerland

Preface

Our Society depends on numerous biomolecules and materials for even our most basic needs such as housing, transportation, energy, defense, communication, clothing, agriculture, environment, health care and entertainment.

Some of the bio/materials addressed in this book includes plasmonics, excitonics, hybrid nanostructures, imprinted polymers, semiconductor oxides, biomass, xanthan gum, starch, nanocellulose, inorganic nanotubes, core-shell colloidal quantum dots, antimicrobial nanocrystals, chitosan, biomolecules/proteins for disease inhibition and citrus canker control, natural products in medicine, polymers, zeolites, graphitic carbon nitride related compounds and ferrite nanoparticles.

For all these materials we introduce some level of review, basic theory for beginners, actual state of the art, emerging research fields, insights for future perspectives and in some cases an actual research project is developed.

In spite of the large/wide range of materials presented we show that a small tool box of experimental techniques (synthesis, characterization, fabrication, properties), physical/chemistry/biological concepts as well as quantum and classical mechanics/statistical methods can be used to understand explain and even predict technological applications of these systems.

Theoretical-computational methods include Hartree-Fock (HF), Post HF, Density Functional Theory (DFT), Time-dependent-DFT, Semi Empirical Methods, Molecular Mechanics, Molecular Dynamics, Periodic Models, Band Theory, Quantum Mechanics (QM), Molecular Mechanics (MM), QM/MM, Quantitative Structure Activity Relationships (QSAR), Docking, Pharmacophore Modeling and Homology Modeling.

A detailed survey of methods of synthesis including epitaxial growth, substrate and solution based wet chemistry, hydro/solvo thermal, continuous flow, hot-injection, sol-gel, co-precipitation and microwave-assisted methods are addressed. There is an in-depth discussion of modern fabrication methods including top down and bottom up techniques whereas it is possible to fabricate nanoparticles with a wide variety of shapes, sizes, properties and functionalities. Characterization methods including structural, surface, optical and electrical techniques are also thoroughly discussed.

Theoretical/computational methods are mini reviewed whereas experimental methods are enumerated, classified and described in order to show advantages and provide an overall picture for beginners as well as workers in the field. The interplay between theory, computation, experiment and technological/engineering applications are also emphasized underlining advantages and importance of emerging future trends.

The book seeks to help readers understand the basic physical chemical and biological properties of the systems discussed and how these properties translate into innovative technological and engineering gain.

This book is divided into three parts consisting mostly of reviews, description of methodologies, insights, perspectives and a few research oriented chapters. The first section of the book consists of 7 chapters addressing experimental methods for synthesis/fabrication, characterization, properties, technological and engineering applications of materials as well as theoretical computational methods. The first chapter is an intensive/extensive review on plasmon enhanced hybrid photovoltaics. Another chapter reviews chitosan nanoparticles. The readers will also be walked through research projects that investigate photocatalytic photoluminescent and gas interaction with oxides, adsorption of quinoline, degradation of coconut shells and optoelectronic applications of core-shell colloidal quantum dots.

The second part is dedicated to biomolecular and antimicrobial systems. Experimental and computational models used are discussed. The readers are walked through projects to design/build/screen and inhibit three dimensional proteins against diseases (metabolic syndrome, obesity, metastasis, angiogenesis) using theoretical computational methods. Experimental methods to investigate antimicrobial nanocrystals are reviewed and described.

The third part comprises short reviews of theoretical/computational and experimental methods to investigate selected materials including polymers, zeolites and graphitic carbon nitride related-compounds. The readers are walked through computational simulation of polymers and evaluation of selected theoretical/computational parameters.

It is our expectation, that this book could help readers acquire an overview of the research areas, knowledge of fundamental concepts and perhaps even stimulation for involvement in research projects with applications in exciting and promising technologies.

The editors would like to thank authors, scientists, educators, students, colleagues and collaborators that participated in this project making this book possible. Please enjoy!

Londrina, Brazil
Rio de Janeiro, Brazil

Felipe de Almeida La Porta
Carlton A. Taft

Contents

Strategies and Research with Advanced Engineering Materials

- Plasmon Enhanced Hybrid Photovoltaics** 3
Swayandipta Dey
- Photocatalytic and Photoluminescent Properties of TiO₂ Nanocrystals
Obtained by the Microwave Solvothermal Method** 67
Kleber Figueiredo de Moura, Laís Chantelle,
Márcia Rejane Santos da Silva, Elson Longo, Máximo Siu-Li,
Maria Gardênia Fonseca, Ary da Silva Maia
and Iêda Maria Garcia dos Santos
- Magnetic Molecularly Imprinted Polymers for Selective Adsorption
of Quinoline: Theoretical and Experimental Studies** 85
Liz Nayibe Martinez Saavedra, Ricardo Gonçalves Penido,
Lucas de Azevedo Santos, Teodorico de Castro Ramalho,
Bruno Eduardo Lobo Baeta and Adilson Candido da Silva
- Insights into Novel Antimicrobial Based on Chitosan Nanoparticles:
From a Computational and Experimental Perspective** 107
Letícia C. Assis, Nerilson M. Lima, Teresinha J. A. S. Andrade,
Patricia H. Y. Cordeiro, Carlton A. Taft and Felipe A. La Porta
- Effect of Light Stimulation on a Thermo-Cellulolytic Bacterial
Consortium Used for the Degradation of Cellulose of Green
Coconut Shells** 145
Pedro Jorge Louro Crugeira, F. A. Chinalia, H. N. Brandão,
J. B. T. L. Matos, A. L. B. Pinheiro and P. F. Almeida
- High Coverage of H₂, CH₄, NH₃ and H₂O on (110) SnO₂
Nanotubes** 169
Júnio César Fonseca Silva, José Divino dos Santos,
Jorge Luiz Costa Junior, Carlton Anthony Taft, João Batista Lopes Martins
and Elson Longo

Surface Engineering in Alloyed CdSe/CdSe_xCdS_{1-x}/CdS Core-Shell Colloidal Quantum Dots for Enhanced Optoelectronic Applications	189
Sidney A. Lourenço, Anielle Christine A. Silva, Victor M. Zelaya, Carlos E. Cava, Gabriel D. A. Rocha, Marco A. T. da Silva, José L. Duarte, Flavio Franchello, Felipe de Almeida La Porta and Noelio O. Dantas	
Biomolecular, Antimicrobial Research Insights and Applications	
Antimicrobial Activity of Nanocrystals	209
Marcelly Chue Gonçalves, César Augusto Tischer, Renata Katsuko Takayama Kobayashi and Gerson Nakazato	
Connecting Pathway Errors in the Insulin Signaling Cascade: The Molecular Link to Inflammation, Obesity, Cancer, and Alzheimer's Disease	219
Yessica J. Sosa, Harolin M. Sosa, Victor A. Epiter-Smith, Gemma R. Topaz and Kimberly A. Stieglitz	
Prediction of the Three-Dimensional Structure of Phosphate-6-mannose PMI Present in the Cell Membrane of <i>Xanthomonas citri</i> subsp. <i>citri</i> of Interest for the Citrus Canker Control	259
Mariana Pegrucci Barcelos, Leonardo Bruno Federico, Carlton A. Taft and Carlos H. T. de Paula da Silva	
Design of Inhibitors of the Human Fibroblast Activation Protein α as a Strategy to Hinder Metastasis and Angiogenesis	277
Daniel F. Kawano, Carlos H. T. de Paula da Silva and Carlton A. Taft	
Pharmacophore Mapping of Natural Products for Pancreatic Lipase Inhibition	305
Matheus Gabriel de Oliveira, Waléria Ramos Nogueira de Souza, Ricardo Pereira Rodrigues, Daniel F. Kawano, Leonardo Luiz Borges and Vinicius Barreto da Silva	
Perspectives and Strategies for Zeolites, Graphitic, Polymeric and Ferrite Systems	
Theoretical Insights About the Chemical Dependent Role of Exchange-Correlation Functionals: A Case Study	341
Leonardo Konopaski Andreani, Renan Augusto Pontes Ribeiro, Luis Henrique da Silveira Lacerda and Sérgio Ricardo de Lázaro	
Design and Applications in Catalytic Processes of Zeolites Synthesized by the Hydrothermal Method	359
Patricia H. Y. Cordeiro, Heveline Enzweiler, Luiz Jardel Visioli, Cássio Henrique Zandonai, João Lourenço Castagnari Willimann Pimenta and Gimerson Weigert Subtil	

Design and Applications of Spherical Infinite Coordination Polymers (ICPS)	391
Guilherme Arroyos, Caroline M. da Silva and Regina C. G. Frem	
Current Perspective on Synthesis, Properties, and Application of Graphitic Carbon Nitride Related-Compounds	413
F. M. Pinto and F. A. La Porta	
Chemical Modification of Polysaccharides and Applications in Strategic Areas	433
Nívia do Nascimento Marques, Keila dos Santos Alves, Rosangela Regia Lima Vidal, Ana Maria da Silva Maia, Liszt Yeltsin Coutinho Madruga, Priscila Schroeder Curti and Rosangela de Carvalho Balaban	
A TD-DFT Simulation on Organic Polymer: The Case of PEDOT	473
A. M. Andrade, A. Camilo Jr. and S. R. de Lazaro	
Magnetic Properties of Conducting Polymers	493
A. A. Correa, E. C. Pereira and A. J. A. de Oliveira	
Revised Fundamental Properties and Crystal Engineering of Spinel Ferrite Nanoparticles	511
Rafaella Casado Silva, Walmir Eno Pottker, Alane Stephanye A. Batista, Jefferson Ferraz Damasceno Felix Araujo and Felipe de Almeida La Porta	

Strategies and Research with Advanced Engineering Materials

Plasmon Enhanced Hybrid Photovoltaics



Swayandipta Dey

Abstract Plasmonics is an emerging area concerning in the fields of optics, telecommunications, optoelectronics and photovoltaics. Plasmonic nanostructures in general possess the capability to effectively concentrate and trap the electromagnetic field into the active region of the device covering different spectral regions of the entire solar spectrum. This could be finely tuned by optimizing several parameters such as the type of material, its shape, size and the local dielectric medium surrounding the particles. Excitonics, on the other hand is another independent branch of study primarily involving with the manipulation in generation and recombination of electron-hole pairs in inorganic and organic semiconductors, dyes and polymers. There is a subtle, yet a strong complementarity that exists between Plasmonics and Excitonics which could be exploited to generate several hybrid functional materials and devices to potentially enhance/boost the performance and efficiency of the devices. In this book chapter, I will start by discussing with the background on Plasmonics and Excitonics and how we can combine materials from these individual fields to develop hybrid heterostructures and fabricate all next generation photovoltaic devices. Next, I will give a detailed survey on how these materials could be synthesized using several substrate and solution based wet-chemistry, solvothermal, continuous flow and hot-injection methods. Several surface, optical and electrical characterization techniques will be thoroughly discussed concerning the plasmonic and excitonic nanostructures. The latter half of the chapter will be followed by discussing the underlying design principles and the device physics involving the interfacial exciton generation, recombination and charge carrier extraction processes when these plasmonic and excitonic materials are incorporated/embedded in between other transport layers. Finally, in conclusion, I will briefly discuss certain future prospects and perspectives involving these materials that could potentially open up new opportunities in the fabrication strategies of several high performance hybrid photovoltaic devices.

Keywords Plasmonics • Excitonics • Plasmon-exciton coupling • Metal nanoparticle-quantum dot hybrid nanoheterostructures • Hybrid photovoltaics

S. Dey (✉)

Weizmann Institute of Science, Rehovot, Israel

e-mail: swayandipta.dey@weizmann.ac.il

© Springer Nature Switzerland AG 2020

F. A. La Porta and C. A. Taft (eds.), *Emerging Research in Science and Engineering Based on Advanced Experimental and Computational Strategies*, Engineering Materials, https://doi.org/10.1007/978-3-030-31403-3_1

1 Metal Nanoparticles and Localized Surface Plasmons

Nanoparticles are microscopic particulates which could be in the form of nanopowder, nanocrystal or nanocluster and typically of dimension in the order from a few to >100 nm. With its wide variety of shapes, sizes and the type of materials (metals, semiconductors) that can be now synthesized, nanoparticles have gained a significant research attention over the last few decades. Historically, the existence and usage of nanoparticles date back to appearance of metallic luster decorations of glazed ceramics as early as in Mesopotamia during the 9th century [1–3]. Another finest example of artwork rediscovered in Europe was the Lycurgus cup manufactured by the Romans as early as 5th century A.D. where noble metal nanoparticles such as Ag, Au, Cu was dispersed in ruby glass matrix (Fig. 1a shows the original Lycurgus cup displayed in the British museum). Although, from a scientific standpoint, the next big leap in nanoparticle research was initially taken by Michael Faraday approximately 150 years ago (Fig. 1b shows the first original bottles of MNP samples as prepared by Faraday) [4].

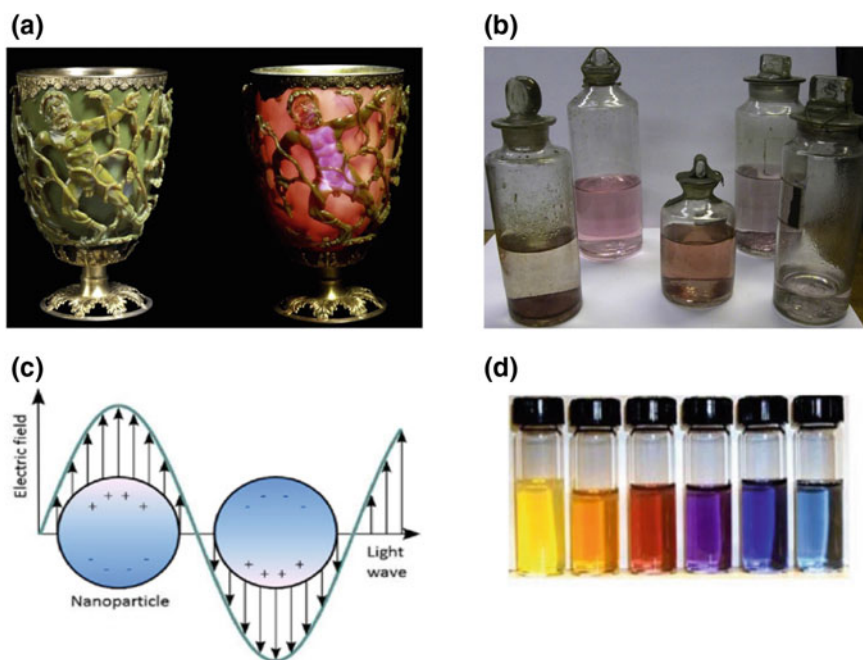


Fig. 1 **a** The Lycurgus Cup in reflected (left) and in transmitted (right) light. © Trustees of the British Museum. **b** Five original bottled samples prepared by Michael Faraday. *Source* <http://aveburybooks.com/faraday/catalog.html>. **c** Coherent oscillation of electrons in the form of localized surface plasmon resonance in metal nanoparticles and its interaction with EM light field. **d** Colored colloidal suspensions of gold nanoparticles. *Source* <http://esciencenews.com/articles/2010/03/12/a.golden.bullet.cancer>. Reproduced with permission from Heiligtag et al., 2013

As a result of his systematic study on the interaction of light with MNPs, it gave birth to a new era of modern colloidal chemistry with the emergence of Nanoscience and Nanotechnology. Some of these man-made works of extraordinary obviously indicate that nanoparticles are not necessarily synthesized in modern scientific laboratories, but have obviously existed in nature for a significantly long period and their usage can be even traced back to ancient times.

Noble metal nanoparticles (MNPs) like Ag, Cu, Au, Fe etc. have long fascinated scientists due to their unique optical properties including large optical field enhancement resulting in the form of strong scattering and absorption of light [5–7]. Due to their intrinsic property of possessing a negative real and small positive imaginary dielectric constant over a range of wavelengths, they are capable of supporting what is known as surface plasmon resonance (SPR) when these MNPs interact with electromagnetic light. SPR in MNPs arise as a result of coherent and collective oscillation of free electrons interacting with the oscillating electromagnetic (EM) light as can be seen from Fig. 1c [6, 8]. This process is resonant at a particular frequency of light and it could be visualized as a coherent motion of conduction band electrons of the metal. The SPR can be either propagating or localized. Propagating surface plasmons are frequent in thin metallic films whereas the localized surface plasmons (LSPR) are observed in metallic nanostructures. Typically, when the dimension of the metallic nanoparticles smaller than the wavelength of interacting electromagnetic radiation field, the plasmons are confined (localized, and therefore the term LSPR).

The classical model states that the electric field component of the incoming light wave induces a polarization of conduction band free electrons with respect to the heavier ionic core in MNP. This in turn acts as a restoring force which initiates a coherent dipolar oscillation (as represented in Fig. 1c). When the frequency of the incoming light matches with the frequency of this electron motion, it creates a resonance condition which is manifested as the strong absorption and the physical origin of the color observed in noble MNPs (as seen in Fig. 1d from the colored colloidal suspensions of Au NPs).

The physical origin of linear optical properties such as extinction and scattering of a spherical MNP was first explained theoretically in the groundbreaking work by Mie in 1908 [9]. By solving the Maxwell's equations, he was able to explain the theory of scattering of an electromagnetic wave induced by a spherical particle. The extinction (absorption plus scattering) of a sphere of radius a with dimensions smaller than the wavelength of light can be expressed as:

$$E(\lambda) = \frac{(1 + \chi)^2 8\pi^2 N a^3 \epsilon_{out}^{3/2}}{3\lambda \ln 10} \left\{ \frac{\epsilon_i(\lambda)}{(\epsilon_r(\lambda) + \chi \epsilon_{out})^2 + \epsilon_i(\lambda)^2} \right\}$$

with ϵ_r and ϵ_i being the real and imaginary parts of the metal dielectric function, respectively, and χ a shape factor whose value is 2. Later on, it was Gans who extended this theoretical model to other Au and Ag spheroidal particles [10, 11]. Apart from the geometry and dimension of the MNPs itself, other significant factors

that influence the frequency and width of LSPR peak are the dielectric constant of the MNPs itself and the local dielectric environment \mathcal{E}_{out} (or refractive index, η of the medium that includes solvent and the surroundings in which the MNPs are dispersed or adsorbed in). For the noble metals like Cu, Ag, Au, the plasmon resonance is strongest in the visible part of the electromagnetic spectrum; whereas for other transition metals, the LSPR absorption peak is broad and only poorly resolved in the ultraviolet region. This difference in optical response could be attributed to the different dielectric constants of the metals as explained adequately in Drude's free-electron model and to the effects of interband excitation of plasmon transition [12, 13].

Elementary excitations such as plasmon when interact with the photon can result in a coupled excited state such as Polaritons. When surface plasmon in MNPs interact with the incoming photon of the electromagnetic wave, it forms surface plasmon polariton (SPP). These SPPs are essentially two-dimensional EM wave which are observed to be propagating at the interfaces between the conductor surface and dielectric [14–16].

In regard to this context, it is worth mentioning that some of the recent advancement in optical technology and the emerging various photonic applications rely vastly on the unique optical properties possessed by the MNPs such as the localized and propagating surface plasmon polaritons. To name a few, where this optical behavior of MNPs are widely exploited are development of near-field optical probes and enhanced optical detection techniques such as Tip-Enhanced Raman Spectroscopy, Surface-Enhanced Raman Spectroscopy and plasmon-based nanophotonic waveguide devices. Some of these techniques will be discussed later on under the topic of characterization tools and techniques of nanoparticles.

2 Excitons in Semiconductor Nanocrystals

With the emergence and improvement of several epitaxial growth techniques like Molecular Beam Epitaxy (MBE), Metal-Organic Chemical-Vapor Deposition (MOVCD) and microscopy based characterization methods like Scanning Electron Microscopy (SEM), Transmission Electron Microscopy (TEM) in the early 1970 s and 80 s, solid state physicists initiated the early investigations of so-called “quantum structures”. The introduction of these early one dimensional spatially confined quantum-well structures had a profound impact on the later development of compound semiconductors in terms varied dimensions and extending the spatial quantum confinement into two dimensions (quantum wires, QWs) and in all three dimensions (quantum dots, QDs) [17, 18]. Under optical or electrical excitation, when a semiconductor absorbs a photon, it promotes an electron to the conduction band leaving behind a positively charged state ‘hole’ in the valence band thereby generating a bound electron-hole pair (known as “exciton”) as can be seen from Fig. 2a. When the size of the semiconductor nanocrystallite is of the same order as the electrostatically bound characteristic length scale of electron-hole pair (“exciton

Bohr radius”, describes the order of spatial extension of excitons and typically denoted in terms of length scale nm or angstrom, Å), the electron and hole are “quantum confined” by the crystallite boundary. In simpler terms, a quantum dot (QD) is a nanometer-sized crystallite composed of several thousand of atoms and usually of the size 1–10 nm. These QDs, often called “artificial atoms” exhibit discrete energy levels and electronic excitations with electron and hole wavefunctions delocalized within and confined by the dot boundary. Due to this particular discretization of density of states (DOS) and spatial confinement of electron and hole wavefunction, unlike the bulk material, these nanocrystals display strong dependence of their optoelectronic properties to their size and shape (Fig. 2b shows the energy band gap and dependence of emission properties on the size of NCs and degree of quantum confinement of excitons).

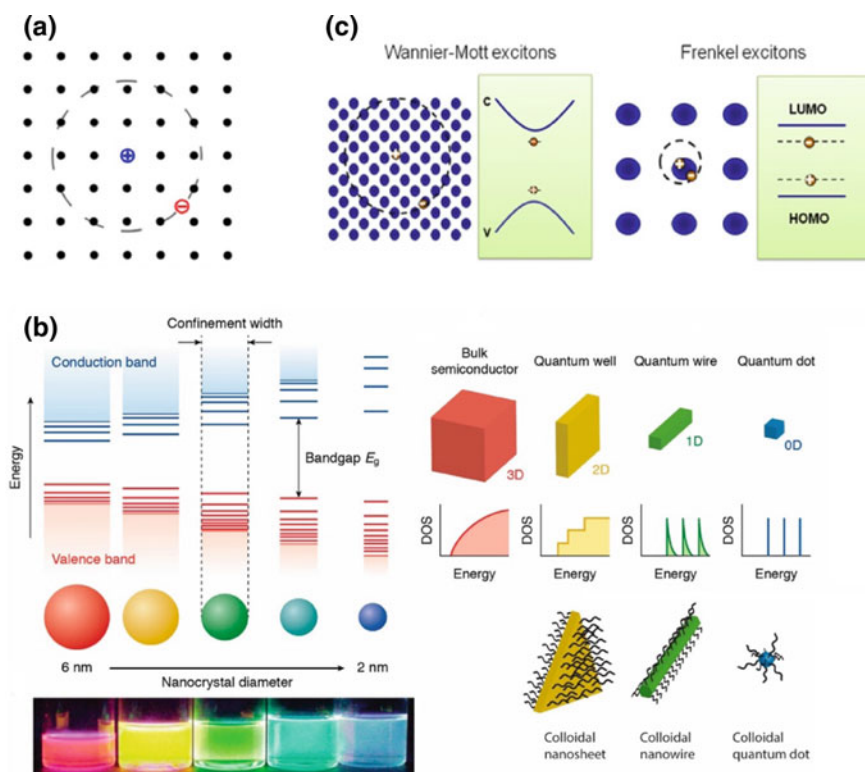


Fig. 2 a Cartoon shows the creation of electron-hole pairs (“exciton”) within the crystal lattice. Source <https://en.wikipedia.org/wiki/Exciton>. b Schematic shows the quantum confinement of excitons in quantum dots and their continuous tuning of energy band-gap levels (emission color) as a function of their size. It also exhibits how the density of states (DOS) gradually change from continuous (bulk semiconductors) to discrete function (quantum confined semiconductors) Reproduced with permission from Donega et al., 2010. c Comparison of Wannier-Mott and Frenkel excitons

Louis Brus, who pioneered the field of “colloidal quantum dots” chemistry and photophysics offered a convenient description for these systems by treating them as particle in a sphere [19–23]. Using an effective mass approximation model, the Hamiltonian of the system could be described as:

$$\hat{H} = -\frac{\hbar}{2m_h}\nabla_h^2 - \frac{\hbar}{2m_e}\nabla_e^2 - \frac{e^2}{\epsilon|r_e-r_h|} + \text{polarization terms}$$

where m_e is the effective mass of the electron, m_h is the effective mass of the hole and ϵ is the bulk dielectric constant of the semiconducting material. This expression comprises of the kinetic energy terms of the confined charge carriers (hole and electron), and a Coulomb interaction. Finally, the polarization terms correct for the form of Coulomb interaction to consider the surface properties. From this Hamiltonian, the approximated energy expression of the lowest electronically excited state can be further derived as:

$$E(r) = E_g + \frac{\hbar^2\pi^2}{2R^2}\left(\frac{1}{m_e} + \frac{1}{m_h}\right)^2 - \frac{1.8e^2}{\epsilon R} + \text{smaller terms}$$

Here, two main contributions are added to the bulk band gap energy (E_g). The first term represents the quantum localization of the electron and hole and scales as $1/R^2$. The second term represents the Coulomb interaction between the electron and the hole, and scales as $-1/R$. Since the Coulomb interaction is not strong, the confinement potential can be treated separately for electrons and holes. From this expression, we can see that for small enough particles the apparent band gap will increase when reducing the QD diameter. This is manifested as a blue-shift of the absorption band that correlates to the lowest-energy excitonic transition, as well as a blue shift of the emission band that correlates to the band-edge transition. Furthermore, the photoluminescence (PL) band in QDs is usually red-shifted compared to the wavelength of the absorption of the first exciton. This red-shift is terms *Stokes shift* [24], and is the result of coupling of the exciton to phonons which allows non-radiative relaxation of the excited charge carriers to the band edges prior to their radiative recombination. This relaxation typically occurs at a time scale of several tens to hundreds of fs (10^{-15} s).

Both electrons and holes can mutually coexist within the nanocrystal provided they are far apart from each other and therefore their mutual interaction could be neglected. In this case, each quasiparticle whether its an electron or hole behaves as an independently existing particle. However, if an electron and hole are located relatively close to each other, then it constitutes an electrically neutral formation. This kind of behavior is typically observed in *Mott exciton*, which although may move within the crystal lattice but doesn't necessarily contribute to charge transport. The *Wannier-Mott* type excitons exist as a result of reduced Coulomb interaction (screened electrostatic interaction) and they typically have radii larger than the lattice spacing [25]. Consequently, this type of excitons possesses much lower binding energy, of the order of 0.01 eV. On the other hand, in materials with a

relatively small dielectric constant, the Coulomb interaction between an electron and a hole may be strong enough such that the exciton radii is of the same order as the size of a unit cell. This type of molecular excitons with a much higher binding energy, of the order 0.1–1 eV is known as *Frenkel exciton*, named after Frenkel [26]. This type of excitons are typically found in alkali halide crystals and in organic molecular crystals composed of aromatic molecules, such as anthracene and tetracene. Besides these, an intermediate type between Frenkel and Wannier excitons, *Charge-transfer (CT) excitons* has been observed when the electron and the hole occupy adjacent molecules [27]. They are primarily observed in ionic crystals. Unlike Frenkel and Wannier excitons (displayed in Fig. 2c) they display a static electric dipole moment. Irrespective of the kind, an exciton in a semiconductor nanocrystal is not infinitely long-lived, instead they possess some finite lifetime (referred to as photoluminescence decay lifetime) and sooner or later they disappear. This typically happens in two ways: either by annihilation (recombination) of electron and hole constituting the exciton or by the dissociative process where an exciton breaks up into a free electron and a free hole.

It has been well recognized at this point that the key to most device development lies in the quality and the properties of the material from which the device is fabricated. As a part of semiconductor device development process and in the interest of performance characteristics, it is therefore essential to have a thorough understanding of the structure-property relationships, including the effect of impurities (intrinsic or extrinsic), nature of defects as well as uniformity of incorporation and position in the host lattice. These are some of the factors that most often determine the efficiency and performance of devices. Intense photoluminescence can be experimentally observed in many semiconductors utilizing most of the standard optical spectroscopy setups. The photoluminescence spectra provides an extensive source on identification of different electronically excited states and the spectral transitions arising either from different impurities, defects, surface or trap state related emission. The peaks and sharp lines appearing in the absorbance and photoluminescence spectra help us identify the bound excitonic states that act as a fingerprint of band-edge emission or bound-to-bound transitions. So, this makes exciton an important probe as far as the photophysical investigation of semiconductors are concerned.

3 Fabrication Techniques of Metal NPs, Semiconductor NCs and Metal-Semiconductor Hybrids

3.1 *Synthesis of Metal NPs*

The development of novel materials with varied functionality is the primary aim for the scientific community involved in materials chemistry research. After several decades of intense research effort and subsequent evolution of modern fabrication

techniques that has now made us possible to synthesize a wide variety of metal nanoparticles. Any researcher entering the nanoscience arena should definitely read Feynman's 1959 "There's Plenty of Room at the Bottom" speech, if only for its historical relevance. Besides just exploring the interesting optical properties of metal nanoparticles (MNPs), in recent times there has been a huge demand in the mass production of these MNPs due to its diverse applications in the field of catalysis, electronics, nanophotonics, photovoltaics (energy production and storage), health monitoring, environmental, biotechnology and so on. Noble MNPs such as Ag, Au and Cu usually exhibit increased photochemical activity because of their high surface/volume ratio and unusual electronic properties. Hollow nanostructures using these metals are a particularly interesting class of materials with unusual chemical and physical properties often determined by their shape and composition holds immense potential in the development of novel bio-sensing and drug-delivery applications [28–33]. Until now, several hollow nanospheres, cubes, rods, tubes, and triangles have been successfully synthesized using the colloidal bottom-up synthetic methods. Furthermore, recent usage of core/shell, alloyed, bi-/tri-metallic nanoparticles have attracted a significant amount of interest since they exhibit improved catalytic performance as compared to monometallic catalysts [34, 35].

Nanoparticles, in general can be broadly prepared by either physical (top down) or chemical (bottom up) methods (Fig. 3a shows the schematic of these fabrication approaches on how metal NPs can be derived from its bulk form). The physical methods which frequently involve vapor deposition of various reaction precursors depend on the principle of subdividing these bulk precursors into the form of nanoparticles. Several other physical methods such as ion-implantation [36–39], RF sputtering [40–42], pulsed laser ablation [43–46], proton beam irradiation, spray pyrolysis [47–49], atom beam co-sputtering, microwave irradiation [50, 51] and electrochemical based multi-pulsed techniques has emerged over the last few decades. These methods provide the possibility of controlling the nanoparticle size by adjusting several reaction parameters such as temperature, pressure, power density, gas flow rate etc. Figure 3b show the experimental schematics of vapor phase and laser assisted method of synthesizing metal NPs.

On the other hand, chemical approaches including solution based liquid phase routes are based on primarily reducing the metal ions to metal atoms in the presence of different colloidal stabilizers or surfactants, followed by controlled growth process and aggregation of atoms. Besides the early developed method of chemical reduction, electrochemical and photochemical reduction are widely used as well to fabricate metal nanoparticles. Wet-chemistry solution based techniques are frequently preferred because they are not only economical/inexpensive with advantages of low reaction temperatures and flexibility, but also they are highly effective in good size and morphology control with near uniform homogeneity of the as prepared nanocrystal samples.

Many of the earliest syntheses of nanoparticles were achieved via co-precipitation technique of sparingly soluble products from aqueous solutions followed by thermal decomposition of those products to oxides. Due to the

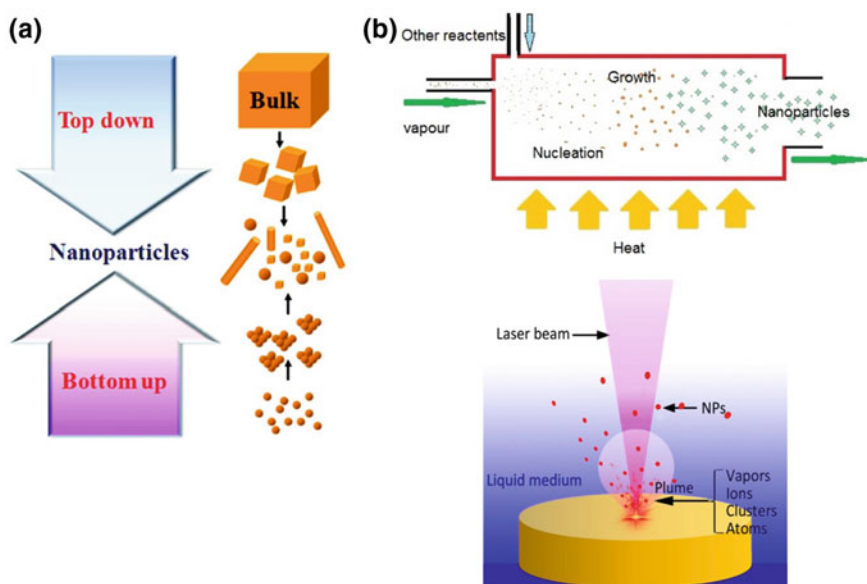


Fig. 3 a Schematic illustration of fabrication techniques of nanoparticles. b Cartoon shows chemical vapor phase (top) and pulsed laser beam-assisted (bottom) modes of syntheses. *Source* <https://niniti.wordpress.com/gas-phase-synthesis/>. Reproduced with permission from Zhang et al., 2017

simultaneous processes of nucleation, crystal growth, coarsening and agglomeration, it is often challenging to isolate these individual stages of reaction which makes even difficult to control the size of the particles. It has still not been very clear on the fundamental growth mechanisms of this co-precipitation technique.

Enormous progress has been made in developing the general architecture method of fabricating multicomponent and multi shaped MNPs using template based methods such as: (a) *hard template* such as anodic alumina oxide (AAO) (b) *soft template* such as cationic surfactant CTAB, CTAC and (c) *sacrificial templates*. Hard templates provide a facile route to grow one-dimensional nanowires. In this method, the template acts as the scaffold where the wire-like nanostructure grow in the voids of the scaffold. Several other porous inorganic scaffold such as polymer membranes carbon nanotubes have been used too.

Using electrochemical deposition of the precursors into porous membrane of the scaffolds, freely standing one dimensional nanowires of different materials could be synthesized using this technique. Nanowires of magnetic materials involving transition metals (Fe, Co, Ni and alloyed forms like Fe–Pt, Co–Pt and others) have been prepared by several research groups using porous AAO templates. These materials are potentially useful in ultra-high density magnetic data storage devices. On the other hand, soft matter templates involve use of surfactant assemblies such as liquid crystals, micelles, vesicles, organic and organometallic ligands, polymers,

and hydrogels to grow metal nanostructures of varied morphologies. In the case of syntheses of Au and Ag nanorods with well controlled diameters and aspect ratios, this has been achieved from the self-assemblies of soft templates like cetyltrimethylammonium bromide (CTAB) or liquid crystalline phases made of sodium bis(2-ethylhexyl) sulfosuccinate (AOT), p-xylene, and water [50–60] (Fig. 4a, b shows the general see-mediated synthetic approach of fabricating Au nanorods of various aspect ratios).

Silver nanodisks have also been synthesized by sonicating AgNO_3 and hydrazine (N_2H_4) in the presence of reverse micelles self-assembled from an AOT/isooctane/water system. Polyol synthesis has proven to be a simple and versatile route to fabricating colloidal particles made of metals and alloys with typical examples including Ag, Au, Cu, Co, Ir, Ni, Pd, Pt, Ru, CoNi, and FeN. Among a few others, Xia's group demonstrated a polyol synthesis method to control silver nanostructures by reduction of silver salt (AgNO_3) with ethylene glycol in the presence of poly-vinylpyrrolidone (PVP) [61–70]. This process involves the reduction of an inorganic salt (silver nitrate) by polyol at an elevated temperature with PVP as the surface stabilizers (also prevent in agglomeration) of as prepared colloidal Ag NPs. The rate of nucleation and growth processes can be ideally controlled with careful monitoring of temperature. It is believed that PVP kinetically control the growth rates of various faces of silver by adsorption and desorption effects, suggesting that there seems to exist a selectivity capping of specific facets for the functional group. Consequently, the growth rates of some surfaces would be greatly decreased, leading to a highly anisotropic growth of these nanostructures. Figure 5 shows the schematic of Ag NP synthesis with various morphologies from nanocubes to nanowires with different edge lengths and aspect ratios.

When it comes to the synthesis of gold nanoparticles, probably the most convenient and widely used synthesis technique so far is the so-called “citrate route” (now more widely known as “Turkevich method”) originally developed by Turkevich et al. more than 60 years ago. The chemistry of this reaction process is very simple which involves reduction of Au^{III} salt (used in the form of $\text{HAuCl}_4 \cdot 3\text{H}_2\text{O}$) to Au NPs in the presence of sodium citrate (reducing agent) and water as the reaction medium (solvent) [71–76]. The obtained gold nanoparticles using this rather simple method exhibit a spherical morphology with a relatively narrow size distribution (20 ± 1.5 nm). Although the citrate route is still very popular for the preparation of aqueous gold nanoparticle sols, many other approaches have been developed, performed in specific organic solvents or in the presence of different types of surfactants like long chain alkylamine or alkyl acids and reducing agents to fine-tune the morphology and develop fascinating architectures from nanocubes to hexagonal shapes, nanorods, nanoprisms, nanoflowers and nanostars [77–79]. Brust et al., however, reported the synthesis of alkanethiol stabilized colloidal Au nanoparticles that are stable almost indefinitely in nonpolar solvents [77–79]. Using the similar reaction, Ag NPs have been prepared by reduction of AgNO_3 or AgClO_4 by N,N-dimethylformamide (DMF), where APTES (3-(aminopropyl)trimethoxysilane) served as the stabilizing agent. With the variation of different synthetic parameters like reaction precursor concentration, type of

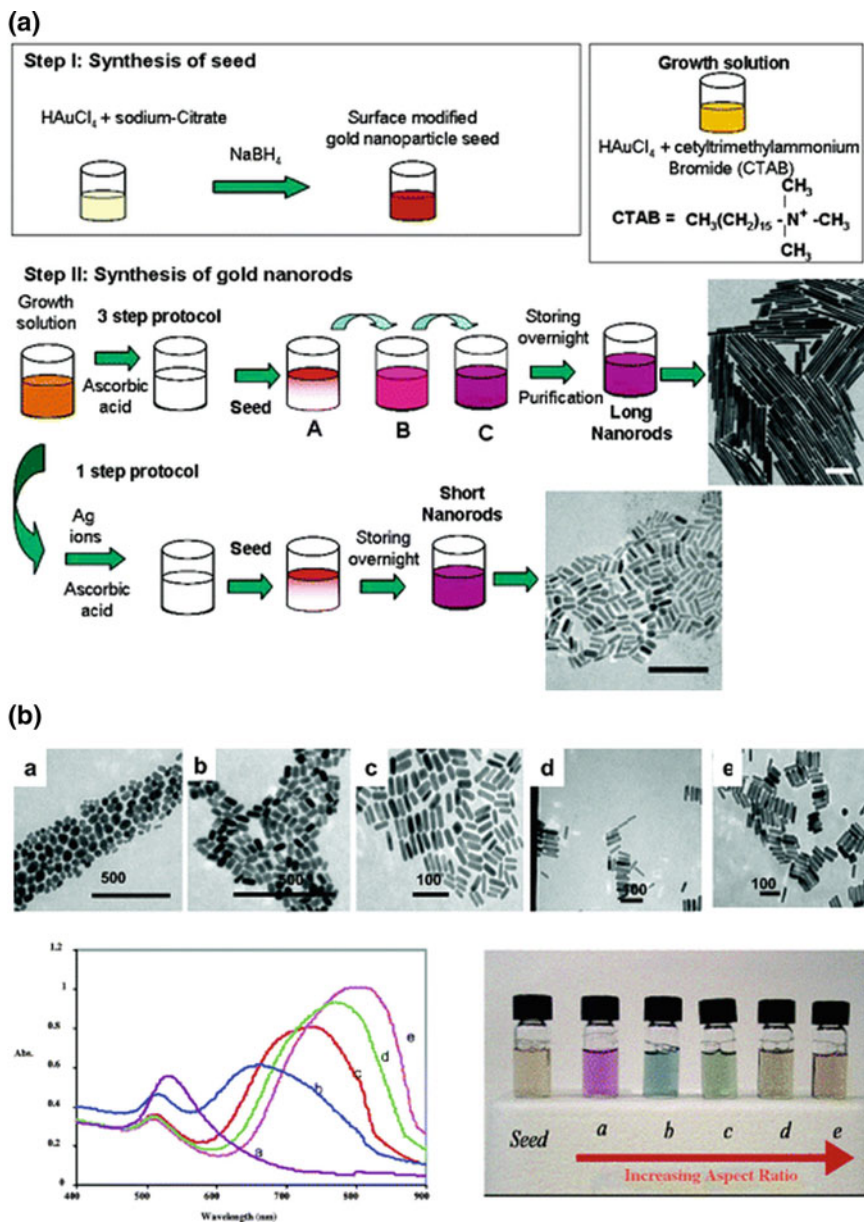


Fig. 4 a Schematic of the seed-mediated synthesis of gold nanorods The seed is modified with citrate (that acts as the reducing agent); ascorbic acid here acts as weak reducing agent A–C are each growth solutions; the seed is added to A, and then after the color changes, an aliquot of solution A is added to B, etc. For short gold nanorods, silver nitrate and ascorbic acid are added to the growth solution, followed by the seed solution. Shown at the right are TEM micrographs of the final purified (centrifuged and washed) gold nanorod products. Scale bars represent 200 nm. Reproduced with permission from Murphy et al., 2006. **b** Transmission electron microscopic images (top), optical extinction spectra (left), and photographs of (right) aqueous solutions of gold nanorods of various aspect ratios prepared via seed-mediated approach. Reproduced with permission from Murphy et al., 2005

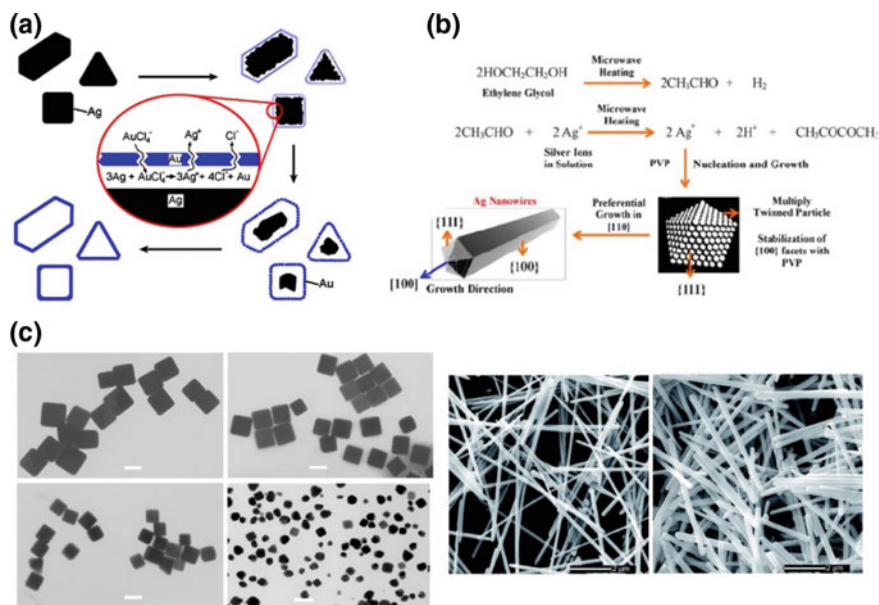


Fig. 5 **a** Schematic illustration of the experimental procedure that generates nanoscale shells of gold from silver templates with various morphologies. Note that the shape of each silver nanoparticle is essentially preserved in this template-engaged reaction. Reproduced with permission from Sun et al., 2002. **b** Schematic shows the microwave-assisted synthetic methodology of polyvinyl pyrrolidone (PVP) capped anisotropic silver nanowires. Reproduced with permission from Melendrez et al., 2015. **c** TEM images of silver nanocubes (left) with different edge lengths; Reproduced with permission from Sun et al., 2002 and silver nanowires (right); Reproduced with permission from Ma et al., 2014

surfactants or co-surfactants temperature and growth time, these solution phase methods can facilitate in fine tuning and shifting the major plasmon resonance peaks of the MNPs as experimentally observed from their optical absorption spectra.

Growth of metal nanostructures with a hollow interior by utilizing the outer shell or surface as the template is the heart of the sacrificial template method. In regard to this, a number of different approaches has been recently developed involving the *Ostwald ripening* and *Kirkendall effect* to synthesize various hollow core-solid/porous shell metal nanostructures [80–84].

The *Kirkendall effect* (as can be seen from Fig. 6a which shows the schematic with its general mechanism which is explained by the difference in diffusion rates of two or more different solids, its origin lies at the field of general metallurgy. Due to the differential rate in the diffusive migration of solids (or reactants), the resultant product often exhibit some alloyed form and a certain degree of porosity. It was later experimentally proven that atomic diffusion occurs between cation exchange vacancies and not by actual interchange of atoms. The sacrificial template has

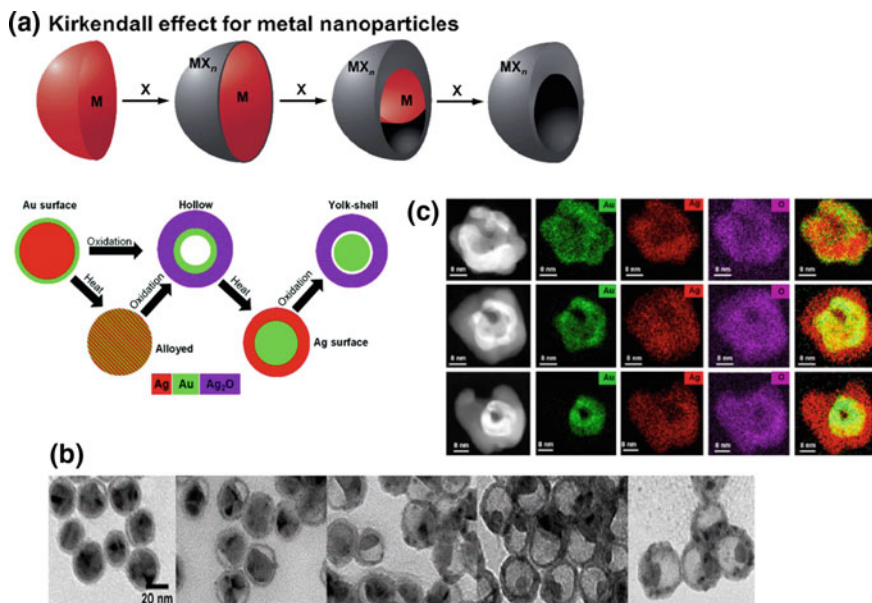


Fig. 6 **a** Graphical depictions of examples of NP conversion chemistry via- Kirkendall effect: during the reaction of the metal (M) with reactive species X to form MX_n , void formation occurs resulting in alloyed, hollow and yolk-shell like structures Reproduced with permission from Tracy et al., 2014. **b** TEM images of single Au NPs and gradual incorporation of Ag resulting in formation of Ag–Au hollow NPs. **c** Real-time imaging and HAADF STEM elemental mapped images showing the transformation of a single nanoparticle, from an Au surface segregated Ag–Au structure to a hollow Au-core Ag_2O -shell structure. Reproduced with permission from Lewis et al., 2014

proven to be an effective method for fabrication of hollow metal nanostructures by consuming the more reactive component (template) exploiting the process of galvanic replacement occurring between the template and the reactant. This process of controlled synthetic methodology using *Galvanic replacement* reaction allows us to design varied structures of hollow (Fig. 6b) and bi, trimetallic MNPs that are extensively desirable towards photocatalytic and electrocatalytic applications. Transforming metal nanostructures into hollow structures improves their performance because doing so reduces their densities with increment in their surface areas above those of their solid counterparts [84–91].

3.2 Synthesis of Semiconductor NCs

Semiconducting nanocrystals (NCs), especially the class of inorganic semiconducting fluorophores which are more popularly known as quantum dots (QDs) have

long proven an excellent track record in the field of electronics, photovoltaics and optoelectronics. In addition to broad range light absorption capability with sharp, spectrally pure tunable emission these materials also possess superior charge carrier mobilities with high thermal and photo stability. Due to their interesting optoelectronic properties and their ever-increasing demand in applications ranging from electronics, biosensing, bioimaging, catalysis to renewable energy, it is becoming more necessary now than ever to fabricate these functional nanostructures in a more inexpensive and versatile fashion [92–104]. Therefore, solution processed colloidal fabrication of these inorganic semiconducting nanostructures is itself developing into a whole new branch of synthetic chemistry. Starting with preparation of simple objects like monodispersed spherical inorganic core particles, over the last few decades the field has evolved into fabricating more sophisticated and complex nano architectures like core/shell, core/(multi) shell, quantum rods, quantum wires, dumbbells, tetrapods, quantum dots in rods, nanoplatelets and so on [105–113]. Figure 7a shows the architecture of semiconducting NCs with various morphologies that can be fabricated using wet-chemistry colloidal method.

These colloidal hetero nanocrystals can be regarded as solution grown hybrid nanoparticles since most frequently it possesses an inorganic component that are overcoated with a layer of organic component. These organic components usually composed of either ligand of different functional groups, polymers or molecular linkers that act as some sort of surfactant or surface stabilizers for the inner inorganic component (Fig. 7b). The interaction between the inorganic component and the outer organic surfactant layer allows us to tune the size and shape of the heteronanocrystals that are manifested by novel optoelectronic properties of these materials [114]. One of the important manifestations of quantum confinement in these semiconducting nanocrystals is the correlation between the particle size and their electronic structure. The degree of discrete spatial delocalization between electron and hole states can be precisely tuned by varying the particle size. In addition to this, the organic layer allows the synthetic chemists another degree of freedom to tailor the material's properties by manipulating its surface chemistry. Typically, these colloidal semiconducting nanocrystals are chemically synthesized using appropriate molecular compounds such as inorganic salts or organometallic precursors. Early attempts based on the wet chemical solvothermal syntheses were successful in fabrication of several type II-VI, III-V classes of chalcogenides like CdSe, CdS, CdTe, PbSe, PbS, InS, ZnTe, InP, InAs and so on. Later on, with further synthetic efforts, compound heterointerface based semiconducting nanocrystals with designs including core/shell, core/multishell, alloyed core/shell etc. by combining different types of materials were also obtained. The most popular method of preparing these nanocrystals in a rather flexible and inexpensive fashion is the *hot-injection method*, which was introduced in a seminal paper published by Murray, Norris and Bawendi in early 90s, which skillfully applied a principle of 'separation of nucleation and growth' to prepare high quality monodispersed quantum dots [115, 116]. In this method, the precursors are rapidly injected into the hot solvent followed by subsequent quenching (cooling down) of the reaction. This method, in general involves several consecutive stages of crystal formation starting

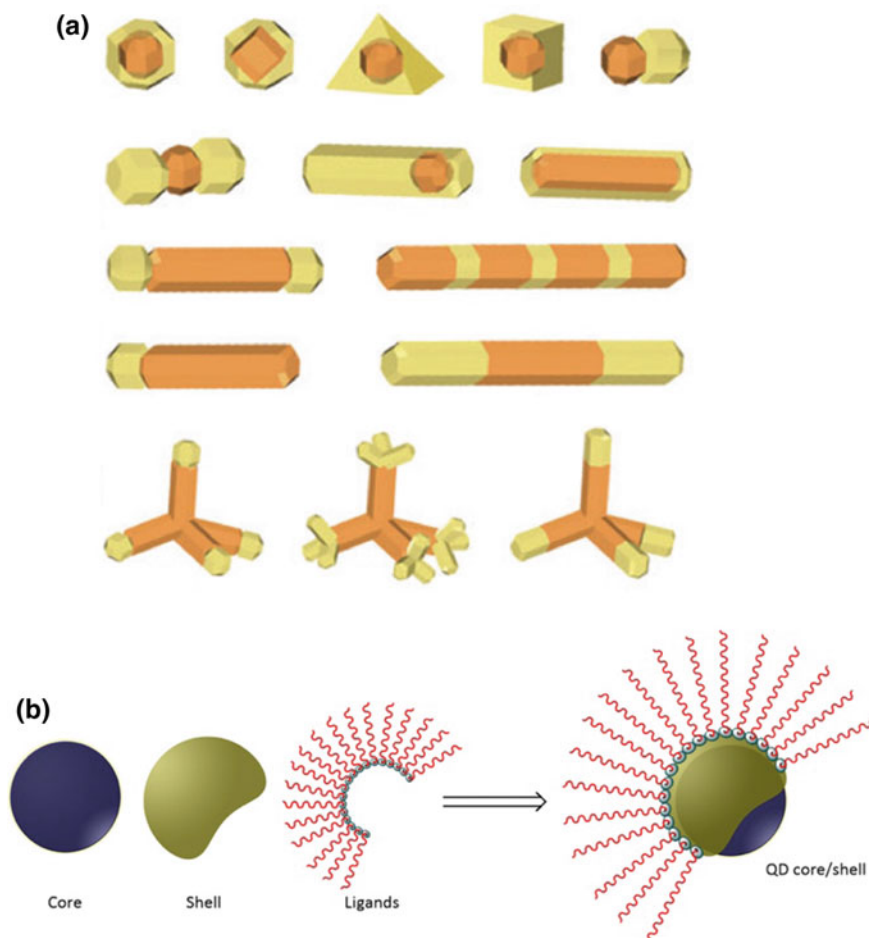


Fig. 7 **a** Schematic survey of colloidal HNC architectures (for clarity the surfactant layer is not represented). The diversity of possible material combinations for each category can be illustrated by a few examples with morphologies ranging widely from core/shell, dot-in-rod, dumbbell, core/shell nanorod, tetrapod and so on. Reproduced with permission from Donega et al., 2011. **b** Cartoon shows the transformative process of core to core/shell overcoated with organic ligands. Source <https://www.intechopen.com/books/green-nanotechnology-overview-and-further-prospects/-green-quantum-dots-basics-green-synthesis-and-nanotechnological-applications>

with nucleation from homogenous solution mixture of molecular salts (precursors), growth of preformed nuclei followed by arresting the growth process and further isolation of the nanocrystals of desired size from the reaction mixture and other post-preparative processing or treatments. Using this method, most often the size and the optoelectronic properties (as a result of quantum confinement of excitons) of the nanocrystals can be finely tuned by variation of precursor and surfactant

concentration, injection and reaction growth temperature, reaction growth time and cooling process. In a colloidal synthesis, the semiconducting nanocrystals grow through a process known as *Ostwald ripening* mechanism wherein the largest particles grow at the expense of dissolving smaller nuclei in the solution. As a result, the average particle size increases with time and the monomer (precursor) concentration decreases. In order to understand the growth mechanism process and the particle size distribution, Peng et al identified two separate regimes involving the growth process that were referred to as “focusing” and “defocusing” [117–123]. *Nano-Ostwald ripening* model was further proposed to describe the evolution of an ensemble of particles in nanoscale form. The nucleation and growth process occurs in the presence of different organic surfactant molecules like long chain carboxylic acids (Oleic acid), phosphonic acids (Tetradecylphosphonic acid, TDPA; Octadecylphosphonic acid, ODPA), amines (Oleylamine, Hexadecylamine), alkanethiols (Dodecanethiol, DDT), alkyl phosphines (Tributylphosphine, TBP; Trioctylphosphine, TOP) or alkyl phosphine oxides (Trioctylphosphine oxide, TOPO) used either as coordinating solvents such as (also acts as ligands) or non-coordinating solvents like 1-octadecene, ODE (act as reaction medium). With a judicious control and manipulation of surface chemistry utilizing these ligands, one can eliminate the mid-gap, shallow or surface trap states that are associated with surface dangling bonds resulting in highly photostable and with better luminescence quantum efficiency of the nanocrystals. Discussion of solution phase semiconducting nanocrystals will be left incomplete without mentioning other methodologies like low temperature aqueous phase or sol-gel synthetic techniques. In comparison to high temperature synthesis taking place in non-polar organic solvents, the aqueous phase follow milder and greener conditions using low temperature and utilizing thiol molecules with polar groups (thioglycolic acid, cysteamine) or amino acids (L-cysteine, Glycine) or even silica or polymer (polyethylene glycol, PEG) capped nanocrystals. Generally, the NCs made in aqueous medium are not as monodisperse or as high quality as those prepared typically in organic solvents, but in other aspects, such as luminescence efficiency, colloidal stability, and, especially, cost per gram, they can be very competitive. The other prominent methodology is the *sol-gel* route which has been widely used for synthesis of oxide based materials. Typically, it involves hydrolysis or polycondensation of metal alkoxides or metal chloride precursors to form a colloid. Traditional sol-gel technique involves a series of hydrolysis and condensation in pH controlled acidic or basic aqueous or alcoholic media resulting in formation of colloidal (sol) which controllably aggregate to form a wet network of agglomerates or nanocomposites (gel). Depending on how the wet gel has been dried, the density and porosity of the extended network can be modified. Post-synthetic treatments including thermal annealing, drying and supercritical extraction of solvent from the gel often results in aerogels and xerogels. Analogous to bulk crystals, the nanoparticles are terminated by crystal facets of different surface energies that expose various crystallographic planes. Site selective attachment of surfactant molecules (ligands) to certain crystal facets and preferential growth along a specific plane or crystalline axis allow us to tune the growth kinetics and morphology of nanocrystals, often resulting in highly

anisotropic materials like dumbbell, arrow shaped, tetrapods, teardrop like architectures. Other growth mechanism techniques like the oriented attachment and solid-liquid-solid are often applied to engineer the shape of the nanocrystals resulting in the formation of nanowires or oriented branched chains [117–123].

Besides the conventional type II–VI, compound semiconducting nanocrystals belonging to category II–V have attracted much attention since they exhibit strong size- and composition—dependent optical and electrical properties capable to incorporating in large-gain low-threshold quantum cascade lasers, light emitting diodes, single electron transistors, avalanche photon detectors and so on. GaAs and InGaAs are one of the most important semiconducting materials with potential applications in developing integrated circuit technology, infrared photodetectors, quantum well lasers, solar cells etc. So far, electrochemical based and laser ablation techniques have been widely used to fabricate GaAs nanocrystals with various sizes and densities. In addition, laser-induced etching method using a Nd:YAG (1060 nm laser) has been also used to synthesize GaAs nanocrystals with high purity. Most importantly, one of the prevalently used top-down fabrication method of *molecular beam epitaxy (MBE)* has been acting as the primary synthetic workhorse in semiconductor based microfabrication industries to prepare InAs and GaAs based devices. *Metal-organic vapor-phase epitaxy (MOVPE)* has also been used earlier to prepare these classes of semiconducting nanocrystals.

The toolbox of wide variety of synthetic techniques is rapidly expanding with many novel structures of wide functionality are getting reported every year. No doubt, the synthetic efforts among the material scientists will further continue, providing both scientists and engineers with potential functional building blocks to design and progress the field of nanoelectronics and nanophotonics.

3.3 Synthesis of Metal-Semiconductor Hybrid Nanostructures

With an advancement in nanoscale optics that led to a major progress in the development of nanoelectronic and nanophotonic devices over the last few decades, it is becoming more obvious to us the necessity of designing novel multifunctional hybrid nanostructures involving disparate building blocks like metal nanoparticles (MNPs) and semiconducting nanocrystals (SNCs). Hybrid nanoassemblies and nanostructures fabricated from plasmonic MNPs and excitonic SNCs often exhibit unconventional optoelectronic properties arising from the mutual synergistic interaction between these individual components. As a result of plasmon-exciton interaction occurring in most of the metal-semiconductor hybrid nanoparticles, it often alters their optical properties like plasmon resonance (spectral linewidth, line shift), scattering, exciton generation and exciton recombination dynamics which lead to particles with entirely new properties that are different from either of the

nanocomponents. This opens up new doors of applications in the fields of optical communication, lasing, biosensing and photovoltaics.

Over the past decade, numerous synthetic strategies have been developed as a result of improving the synthetic efforts involved in nanoscale systems. Until now, several multicomponent hybrid nanostructures utilizing MNPs and SNCs have been fabricated with well controlled morphology and composition both via colloidal bottom-up and top-down methods. Synthetic methods can be broadly categorized as such in two parts: solution-based approaches and substrate-based techniques [124] (Fig. 8 shows the diagrammatic representation of solution and substrate based bottom up strategies to fabricate colloidal quantum dots).

In order to obtain such hybrid heterostructures with desired optoelectronic properties, several factors like shape, size, composition, relative concentration, spatial orientation, geometry & inter-particle distance between the individual nanoconstituents need to be considered while designing them. While perhaps the simplest means of achieving MNP-SNC hybrid assemblies rely on solution based technique, it comes with its own set of limitations, namely, precise control and arrangement of different nanoconstituents is hard to control. This often results in

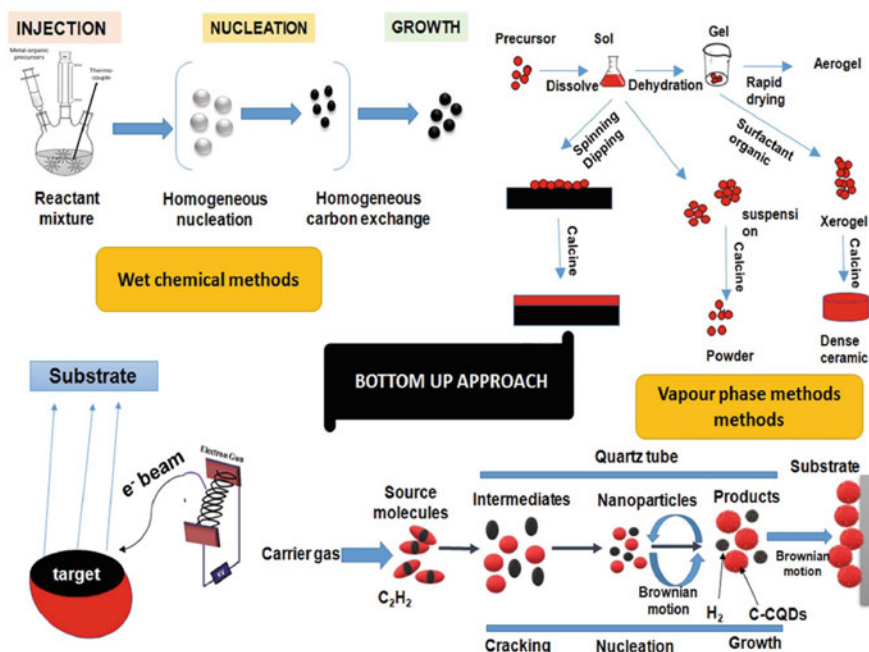


Fig. 8 A diagrammatic representation of different bottom-up approaches for quantum dots synthesis. Bottom-up approaches involves the rearrangement and assembling of small atoms and molecules to achieve large nanostructures which could involve techniques ranging from wet-chemical based to vapor-phase methods (sputtering, substrate based physical and chemical vapor deposition), Reproduced with permission from Singh et al., 2018

low reproducibility and low yield. Nevertheless, a wide variety of other techniques have been introduced and utilized by several research groups to fabricate such hybrid assemblies in solution, including covalent linkage of small molecules, biomolecules, DNA hybridization and self-assembly to build superlattices. Generally speaking, the solution based synthetic methods can be broadly categorized into two categories. The first method involves growing metal (or semiconductor) components onto pre-synthesized semiconductor (or metal) nanocrystals, either growing them at the tips or terminal ends of the nanocrystals. The second approach relies on combining pre-fabricated metal and semiconducting nanoconstituents by means of either wet-chemistry methods or by physical adhesion or adsorption. Some of the solution based approaches on developing these multi-component heterostructures was initiated earlier by Banin's group [107, 112, 125, 126] which involved site-selective deposition of noble metals (Au, Ag) onto the tips of pre-synthesized semiconductor nanocrystals resulting in metal-semiconductor heterointerfaces or segmented heterojunctions (Au-tipped CdS, CdSe nanorods) [127–129] as can be seen from Fig. 9.

This site-selective deposition [130] has been further applied to fabricate other structural variations such as Au, Pt, Pd tipped CdS, Ag₂S and so on as displayed in Fig. 10.

Combining two or more metals on the same semiconductor-metal hybrid system through core/shell structures or by creating interfacial alloys can often lead to enhanced physicochemical properties including electric field enhancement,

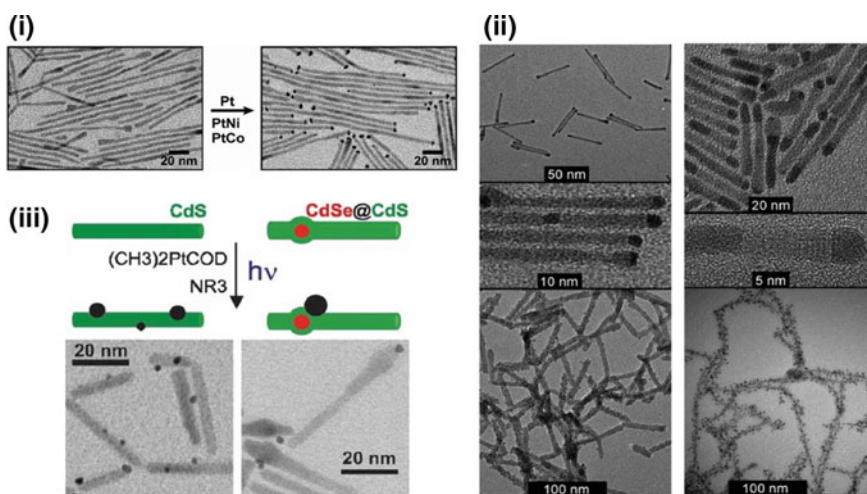


Fig. 9 (i) TEM images showing selective growth of Pt, PtNi and PtCo on the tips of CdS nanorods, Reproduced with permission from Habas et al., 2008 (ii) TEM images showing family of hybrid CdS-PdX ($X = O, S$) nanoparticles, Reproduced with permission from Shemesh et al., 2010 (iii) Diagrammatic representation and resultant TEM images of preferential photochemical deposition of Pt on CdS nanorods and CdSe@CdS core@shell heteronanorods, Reproduced with permission from Dukovic et al., 2008

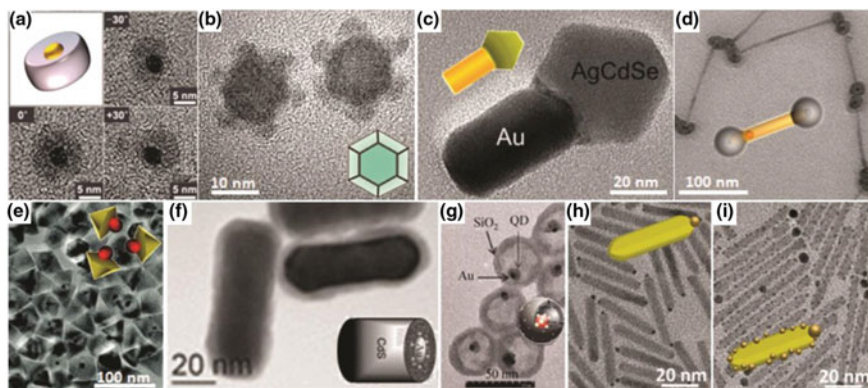


Fig. 10 Various hybrid nanoparticles with their corresponding schematic architectures and TEM images ranging from **a** Cu_2S -Au **b** Ru nanocaged Cu_2S **c** AgCdSe-Au nanorods **d** CoO-tipped CdSe/CdS nanorods **e** ZnO-Au nano-hexagonal pyramid **f** CdS-Au core/shell nanorod **g** CdSe/CdS/ZnS- Au @ hollow SiO_2 yolk/shell nanospheres **h** Au-tipped CdS nanorod **i** CdS-Au body decorated nanorod, Reproduced with permission from Banin et al., 2014

surface plasmon modification. Due to efficient charge separation at the metal-semiconductor interface, these hybrid nanostructures also exhibited enhanced photocatalytic activity upon optical excitation. Another method is seed-mediated growth approach where metal nanocrystals act as seed and help initiate one dimensional growth of different metal chalcogenides (CdS, MnS, ZnS, CdSe) onto specific crystal facets. Other solution based methods via photoinduced heteroepitaxial nucleation, hydrothermal growth and aqueous phase oxidation resulted in different forms of hybrid materials such as metal/semiconductor core@shell heterostructures.

For strategies relying on covalent linkage, the MNPs and SNCs are most often coated with ligands with different reactive functional groups which upon mixing forms a covalent bond such as amide, imine or disulfide linkage between the metal and semiconductor nanocomponents [131–134]. Usage of small molecules (cross-linkers) and activators like EDC (dimethylaminopropyl) carbodiimide and N-hydroxysuccinimide (NHS) via EDC-NHS coupling has been a facile route to link quantum dots (QDs) and small metal NPs through formation of an amide linkage between them. The QDs are initially made water soluble through surface functionalization with certain polymers like polyethylene glycol (PEG) ligand terminated with either carboxylated (-COOH) or carboxy-thiol groups e.g. 3-mercaptopropionic acid (-COOH-SH) so as to bind both the QDs and the MNPs. To this end, EDC-NHS coupling has been successfully used to couple Au, Ag NPs and CdSe/CdS, CdSe/ZnS QDs via a peptide linker (Fig. 11a). Equally as effective was an azo linkage wherein the QDs are functionalized with 4-aminothiophenol and further converting into diazonium group (Fig. 11b). In both these cases of covalent linkage strategy, it was possible to bind two to four MNPs surrounding the QDs

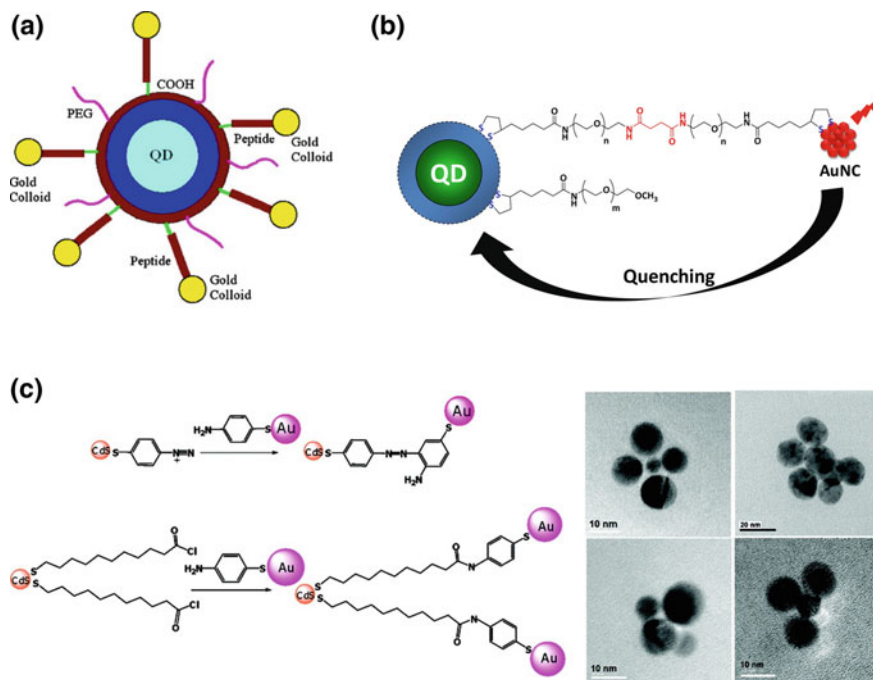


Fig. 11 **a** Schematic shows Au NP linkage to quantum dots (QD) via peptide-bond, Reproduced with permission from Chang et al., 2005. **b** Schematic representation of the QD-PEG-AuNC conjugates; one cluster per conjugate is shown, Reproduced with permission from Aldeek et al., 2013. **c** Schematic shows the amido- and azo-linkage chemistry of nanoparticles alongside with the TEM images of typical assembly of nanoparticles with amido- linkages with dimer, trimer and tetramers of Au dots surrounding the CdS QD, Reproduced with permission from Maneeprakorn et al., 2010

based on the relative concentration of individual constituents or one in excess of other (Fig. 11c).

Compared to linking via small molecules, linking with biomolecules especially DNA offers several advantages. With DNA being such a versatile molecule where the specific lengths can be varied using number of base pairs. In addition, its double helix structure is fairly rigid which allows precise control of inter-particle spacing between the nanoparticles. Until now, DNA hybridization has been used by several researchers to link MNPs to QDs ranging from different inter-particle distance to different conformations forming superlattice self-assembled MNP-QD nanostructures [135–138]. Usually, in order to link the nanoparticles through DNA hybridization, a single-stranded DNA (ssDNA) has been utilized so far to functionalize both the MNPs and QDs. Since linkage of Au NPs is usually strong and stable with thiol- (-SH) group, direct addition of thiol-terminated ssDNA has been used to accomplish successful binding of DNA to Au NPs. On the other hand, in order to link DNA with QDs, they first need to be aqueous soluble which

is done through ligand exchange using carboxylate molecules such as DHLA, 3-mercaptopropionic acid (MPA) or even pre-coating the QDs with water soluble polymers like PEG which can then be further coupled with DNA. The techniques of using DNA origami has been extensively used by Liedl group [135, 137] to achieve better control over the coupling process. Using DNA origami scaffolding methodology, the general shape of the obtained structures varied in different topological forms from triangle, square to even arms with satellites. By altering the DNA origami structure by varying the length and number of arms or even the arrangement of satellites per arm, a remarkable precision could be obtained between the nanoparticles in terms of their relative location, orientation and spatial arrangement as can be observed from Fig. 12.

Similarly, using biomolecules like proteins with affinity for each other have been exploited so far for coupling of MNPs and QDs. The most commonly used is the biotin/streptavidin complex due to its well-known affinity between these two partners as well as easy commercial availability of core/shell QDs functionalized with streptavidin which could be linked to biotin functionalized MNPs. To this end, Kotov's lab has performed extensive work using biotin-streptavidin complex binding to attach MNPs on the surface of QDs and nanowires [139–141]. Bovine serum albumin (BSA) is another functional protein that has also been used to fabricate self-assemblies between MNPs and QDs. This could be done via EDC coupling by attaching MPA-capped QDs to BSA-stabilized MNPs. BSA can also interact with the nanoparticles through charge or electrostatic interactions with the ligands attached to nanoparticles. Self-assembly of similar and disparate nanoparticles occur through electrostatic attraction, ligand exchange or hydrophobic interactions. With no additional chemistry being involved, self-assembly techniques are the most straightforward tools when it comes to fabricating nanoassemblies with usually large area network of interconnected particles. While relying on electrostatic

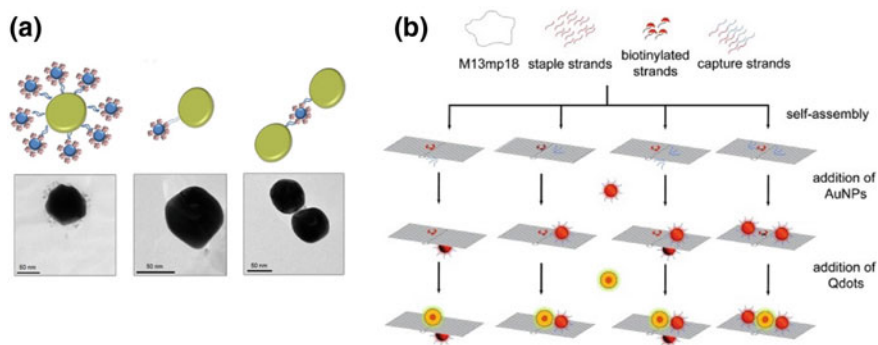


Fig. 12 **a** QD-Au NP hetero-complexes where QDs are surrounded by streptavidin which are intermediately connected to biotin-dsDNA-thiol molecule attached to Au NPs, Reproduced with permission from Cohen-Hoshen et al., 2012. **b** Engineering of QD-Au NP conjugates and their self-assembly using DNA origami constructs, Reproduced with permission from Hyeon Ko et al., 2012

self-assembly, the MNPs and QDs must be functionalized with oppositely charged ligands. With varying molar ratio of individual components, the architecture and particle size distribution could be more or less controlled, though not to a very high degree of precision. A more complex self-assembled organization was previously undertaken by Kotov's group where the positively charged CTAB-stabilized Au nanorods and negatively charged cysteine capped CdTe QDs were mixed resulting in monomeric subunits of Au nanorods surrounded by QDs. Self-assembly can be also achieved by relying on surface manipulation of via ligand exchange which provides a more rugged connection than electrostatic self-assembly and also leading to a better control over the spacing and structure of the assembly. Besides short chain organic molecular linkers, block copolymers such as poly(isoprene)-b-PEG have been also utilized as ligands to facilitate thiol-based self-assembly. In order to control particle spacing between the assembled nanoconstituents, polymer, siloxane and silane shells have been also exploited to instead of using longer linkers like DNA or protein. Using such shells added extra advantage providing rigidity and even preventing such nanoassemblies from aggregation. MNPs coated with silane shells via amine group ligand exchange and then controlling the thickness with addition of tetramethoxysilane (TMOS) have been used earlier to attach QDs pre-functionalized with mercaptopropyltrimethyl- (MPTS) or trimethoxysilane (MPTMS). Specifically, the surface of the MNPs was modified with a layer of dielectric silica spacer via a Stober's reverse microemulsion method followed by specific adsorption of QDs onto these amino functionalized shells. This method resulted in one to two monolayers of QDs surrounding the MNPs. Another similar study was conducted by growing silane shells around Ag nanowires and then attaching CdSe/ZnS QDs. Here, MPTS monolayer was first grown on Ag nanowires, and then tetraethylorthosilicate (TEOS) was further added to grow the silane shell with controllable thickness. Once again, the inter-particle distance was controlled by changing the relative concentration of the silicate precursors. Hybrid nanoarchitectures in the form of a more compact plasmonic/fluorescent system has been realized as metal-core@ semiconductor-shell systems. A couple of studies has been reported where a continuous ultrathin Au-nanoshell has been used to grow around silica-encapsulated QDs [125, 142–145] (Fig. 13c, e).

In comparison to most solution based approaches, the substrate based fabrication of MNP-SNC self-assemblies offer more control. The substrate itself offers an additional degree of freedom to create various design of ordered nanoassemblies which could be created using various state of the art nanopatterning techniques. However, most often these nanopatterning top-down approaches could be rather time consuming and expensive and involve usage of specialized instruments and clean room nanofabrication facilities. Although this substrate based methods possess the capability to fabricate more uniform precise self-assembled structures, they generally involve the use of smaller quantities as compared to solution based techniques and are mostly reserved for single particle studies or synthesis of well-ordered nanoarrays. Two-dimensional binary superlattices using different components like MNPs and SNCs has been created using substrate based self-assembly method on comparatively large micron sized wafer or pre-patterned

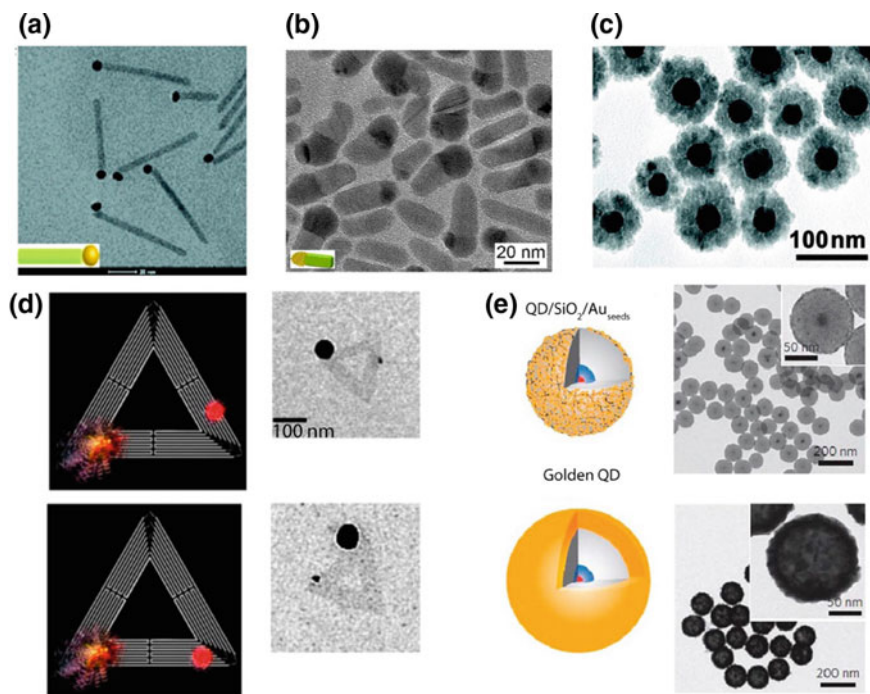


Fig. 13 TEM images of hybrid metal–semiconductor nanostructures. **a** Au-tipped CdS nanorods. **b** Heterogeneous Ag–CdSe nanorod. **c** Au@Cu₂O core@shell nanoparticles. **d** Schemes and corresponding TEM images of Au NP and a QD assembled onto a triangle DNA origami with controlled spacing. **e** Schematic representation and corresponding TEM images of QD/silica/Au seeds and QD/silica/Au nanoshell, Reproduced with permission from Dey et al., 2016

substrates. Several factors are involved while fabricating these nanodimensional superlattices like the solvent evaporation rate, physical properties of the solvent, functionality and steric factors from ligands, interactive forces between the substrate and the nanoparticles like VanderWaals force, electrostatic repulsion/attraction and interfacial cohesive/adhesive forces between the substrate and particles. Constructing such well-ordered nanoarrays require optimal conditions of these aforementioned variables. Using the so-called *Nanosphere Lithography*, it is also possible to use template material such as polystyrene-polyvinyl pyridine micro- or nanosphere beads to form well-ordered polygonal shaped monolayers of nanoarrays made out of MNPs or SNCs. Hybrids of these materials can be created using the *Layer-by-layer (LBL)* method of self-assembly. As the name itself suggest, two or more disparate materials can be successively deposited as layers one on top of other. Nanoparticles can be either immobilized or linked to each other on top of the pre-treated substrate by relying on the simple adsorption or chemistry of conjugation. Many of these coupling techniques has been discussed earlier to link plasmonic and semiconducting nanocrystals onto the substrate by means of

ligand-induced self-assembly, DNA hybridization, covalent bonding via EDC, EDC-NHS coupling, electrostatic attraction or even utilizing dielectric silica shells. Effective binding or immobilization of various NPs require optimal manipulation of surface chemistry and sometimes excess loading or incubation concentration of using different linkers like 4-aminophenol, thiol, carboxylate and so on. Often the thickness of the spacer layer depends of the specific type of molecules being used for linkage. One should be aware of the fact that depending on the size difference and relative concentration (or particle density) between the MNPs and SNCs, it can result in random arrangement of hybrid conjugates with different cross-linking sites or variation in binding sites. Until now, numerous experiments have been carried out several groups on studying the LBL deposition of MNPs and QDs. Almost all of these experiments employed spin casting as the most widely mode of deposition of nanoparticles on the substrate from its colloidal dispersion in certain solvents. The most straightforward way involved sequential deposition followed by subsequent drying. Until now, configurations of noble metal based plasmonic nanostructures in the form of Au nanospheres, Au nanorods, Ag nanocubes, Ag nanoprisms and so on has been deposited in combination with QDs as two separate layers one on top of other in order to study the plasmon-exciton interaction between them in these large-scale hetero-nanoassemblies [146–149] (Fig. 14). Most often, these LBL deposition between MNPs and QDs involve addition of an extra spacer layer (silica, polymer like PMMA, PDDA, PSS etc.) so as to avoid direct photoluminescence quenching of QDs arising from various non-radiative charge transfer phenomena like FRET (Fluorescence Resonance Energy Transfer), Dexter energy transfer, exciton-exciton energy transfer, self-quenching etc.

As reported earlier in few studies, silica spacers can be either grown on individual NPs in the solution or deposited as a separate layer between the sequential deposition steps. Sometimes, *electron beam lithography (EBL)* has been further employed in conjunction with LBL to fabricate well-ordered nanoarrays with specific dimensions and morphology. This allows precise patterning of NPs in specific arrangement. However, lithographically patterned matrices or arrays of NPs are often time consuming in addition to possessing grain boundaries that could potentially act as plasmon damping sites (for MNPs) leading to weaker near-field interactions or non-radiative trap states (for SNCs) reducing their performance capabilities. In addition to photolithography, there are other techniques that have been also developed based on scanning probe microscopy like AFM for precise placement of QDs in close proximity to MNPs and individual manipulation of MNP-QD hybrids.

The thrust behind developing all these different methodologies for fabrication of metal-semiconductor hybrid NPs lies in the fact that a synergistic and judicious combination of MNPs and QDs into a single coupled hybrid system lead to interesting and often new form of optical interactions between plasmons and excitons. As a result of this plasmon-exciton coupling, it results in either increase or decrease of photoluminescence QY, PL emission intensity and lifetime, variation in Purcell factor, change in PL intermittency (blinking) behavior, modification of exciton/biexciton quantum yield and single/multi-photon emitting capabilities of

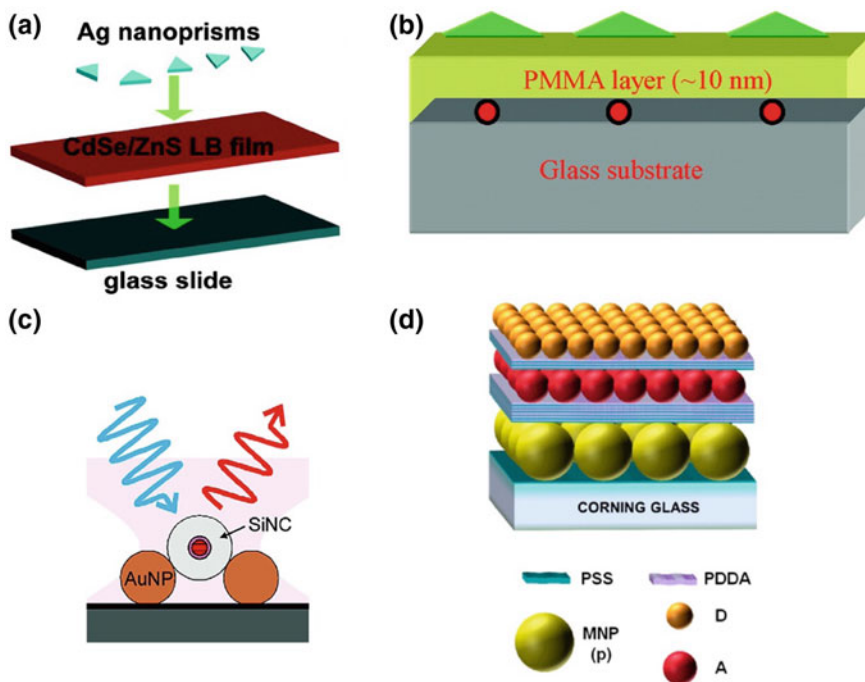


Fig. 14 **a** A schematic illustration of the substrate structure. A monolayer of quantum dots is made by Langmuir–Blodgett deposition. Ag nanoprisms are placed on top by drop casting., Reproduced with permission from Munechika et al., 2010. **b** Substrate sample configuration of Ag nanoprisms coupled CdSe/Zns QDs, Reproduced with permission from Yuan et al., 2009. **c** Sample sketch of silica coated CdSe multishell QDs on top of thin layer of Au NPs, Reproduced with permission from Ma et al., 2010. **d** Schematic showing the layered architecture (prepared via layer-by-layer deposition) of donor Au NPs with the acceptor QDs on top of it with intermediate deposition of polymeric PDDA to control the distance/spacing between the layers, Reproduced with permission from Ozel et al., 2013

single QDs. A combination of various processes are often responsible for this resultant modification of photoluminescence property of QDs like increase in excitation rate of QD, increase in effective absorption cross-section of QDs due to enhancement in plasmon-based local electric field, energy transfer from QD to MNP and subsequent change in radiative and non-radiative decay rates. Figure 15 shows modification of photon emission behavior of single QDs when coupled to various forms of plasmonic metal nanostructures as derived from photo correlation spectroscopic measurements [150–154].

On the other hand, for MNPs, this kind of local coupling effects can lead to modification in scattering properties affecting the primary plasmon peak frequency or depending on the degree of coupling occurrence of Fano resonances and Rabi splitting (Fig. 16) phenomena has been also observed. While designing such hybrid nanosystems, one should take into account different factors that might influence the

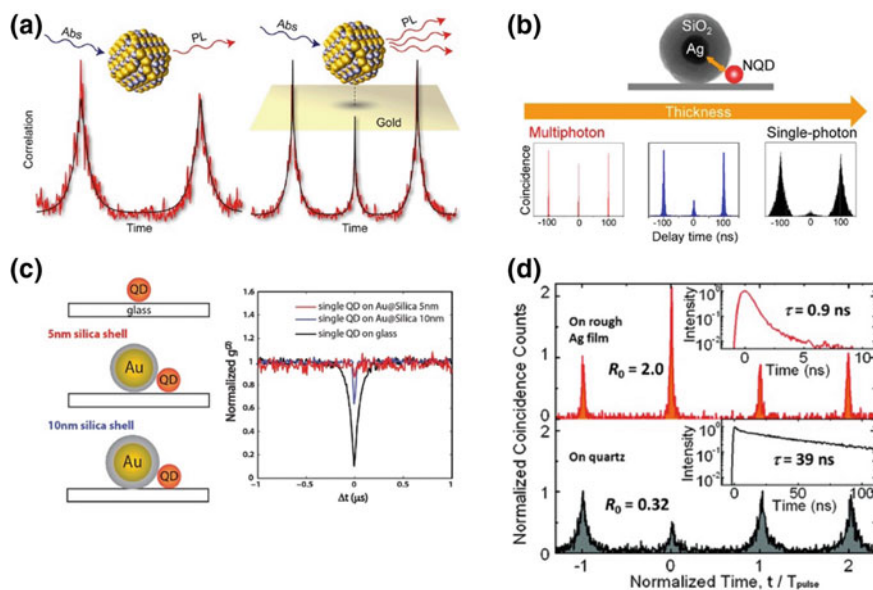


Fig. 15 **a** Photon correlation curves showing enhancement in multiphoton emission from single QDs on Au substrate as compared to bare glass, Reproduced with permission from LeBlanc et al., 2013. **b** Photon correlation curves showing degree of enhancement in multiphoton emission of single QDs in presence of plasmonic silica coated Ag NPs (multiphoton emission capability is investigated as a function of silica shell thickness), Reproduced with permission from Naiki et al., 2017. **c** Photon antibunching measurements under continuous wave excitation on single QDs coupled to variable thickness of silica coated Au NPs, Reproduced with permission from Dey et al., 2015. **d** Photon correlation measurements showing a significant change from photon antibunching to a completely bunching behavior from single QD adsorbed onto plasmonic rough Ag film substrate, Reproduced with permission from Park et al., 2013

plasmon-exciton coupling processes like particle's size, shape, composition, spectral overlap, inter-particle distance, spatial orientation etc. [155, 156].

So far, with the development of new synthetic methodologies in combination with theoretical modeling software (like FDTD, molecular dynamics, DDA, DFT, ab-initio and semi-empirical simulations) and time-resolved optical spectroscopic techniques, plasmonic manipulation of exciton/multiexciton emission of QDs have been successful and optimized in the form of various designs of MNP-QD hybrids. However, further effort is still required to better understand what regulate the mechanisms of plasmon-exciton coupling, how new charge/energy recombination pathways are created and what are the structure-property relationships concerning these hybrid hetero nanostructures.

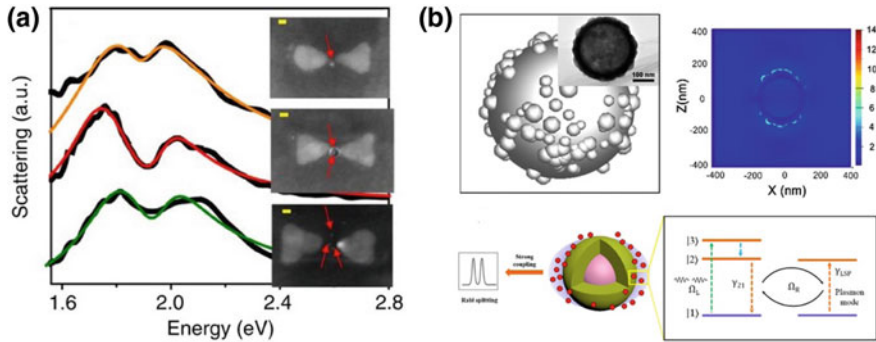


Fig. 16 **a** Scattering spectra of Au NP bowties with (from top to bottom) one, two and three QDs in the gap, respectively. All spectra show a transparency dip due to Rabi splitting as a result of strong plasmon-exciton coupling between the excitons in QDs and plasmons in Au bowties, Reproduced with permission from Santosh et al., 2016. **b** Schematic diagram of a rough SiO₂@Ag nanoshell with Ag NPs. The inset is the TEM image of a single Ag nanoshell, (right) Electric field distribution for a rough SiO₂@Ag nanoshell obtained by means of FDTD (Finite Domain Time Difference) simulation, (bottom) Schematic representation of collective strong coupling of many QDs with the radiative dipole mode of an Ag nanoshell, (bottom right) shows the energy diagram and optical transitions in the hybrid system, and the Rabi oscillation Ω_R describes the transfer of an excitation between the LSP mode of and the QDs emitters at Rabi frequency, Reproduced with permission from Zhou et al., 2016

4 Structural, Electrical and Optical Characterization Techniques

With the advent of modern electronics and hardware equipment, several characterization techniques have been developed so far in order to investigate the grain size, elemental composition, crystal structure and lattice parameters, magnetic properties, phase information and a variety of other physical properties of nanoparticles. With many more different kinds of nanomaterials that are being synthesized every day, it is imperative to develop more precise analytical characterization tools that would allow us to characterize the materials and get reliable information of their properties from all the way bulk to their nano- forms. Based on the different capabilities and limitations of each technique/s and the sort of information it can provide, they are chosen to study the samples. Classification of different techniques are usually based on the theory and concept the technique rely on and the kind of physical properties (structural, electrical, optical, magnetic etc.) they are destined for. Here, some of the structural (SEM, TEM, AFM, XRD); electrical (XPS, SPV, EBIC, EI, DLTS), optical (UV-Vis, PL, TA, TRPL, FTIR, Rayleigh and Raman Scattering, DLS)—the full names of the individual techniques will be provided later on in the text as they will be discussed in further details. Several of these methods are frequently used for characterization of materials involved in optoelectronic and photovoltaic devices.

5 Structural Methods

A *scanning electron microscope (SEM)* uses an electron gun to impinge highly energetic electron beam directed on the sample surface. The typical arrangement of essential components on this microscope based technique consists of an assembly of electro-optical vacuum chambers to which emits electron from a heated filament under some accelerating voltage in a constant beam down the column. The electron beam accelerates as they pass through a series of electromagnetic lens and interacts with the sample focused on a tight spot at the end of the column. Thus, smaller the spot size, the higher is the resolution. As the primary electron beam interacts with the sample, the material emits secondary, backscattered, x-ray and transmitted electrons (Fig. 17a shows the general outline of device components in a typical SEM). The SEM has a good spatial resolution and its depth of field is about 300 times than that of light microscope. The typical working distance using this technique wherein the height of the sample is kept between 10 and 25 mm. The materials that are characterized usually need to be prepared on certain conductive substrates like silicon wafer, Si/SiO₂, ITO etc. Conventional SEM can provide us with high resolution imaging of surfaces of various materials with different modes

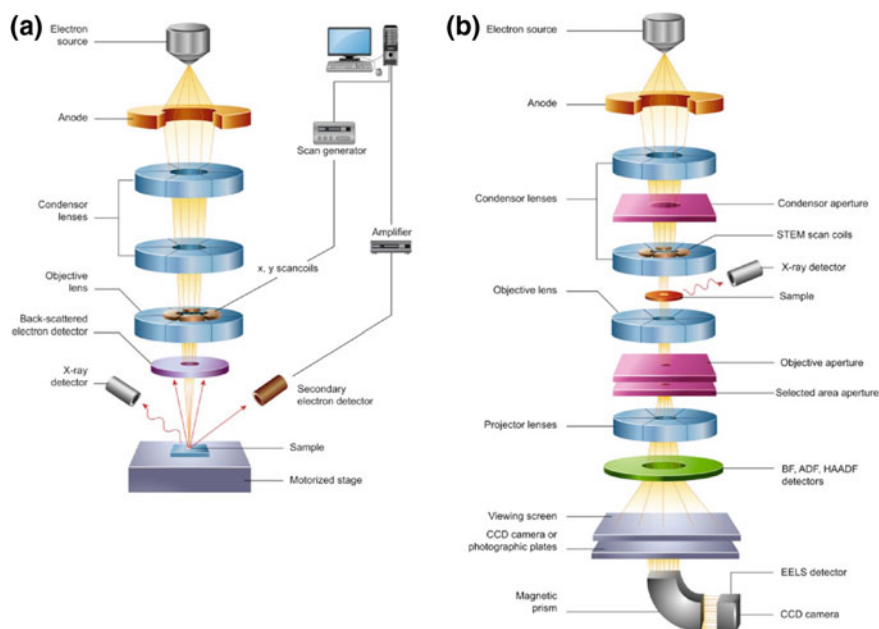


Fig. 17 Schematic illustrations show the various instrument components of **a** Scanning Electron Microscope (SEM) and **b** Transmission Electron Microscope (TEM) with their respective detector systems like secondary electron (SE), backscattered electron (BSE), X-ray, high angle annular diffraction (HAADF), Reproduced with permission from Inkson et al., 2016

of detection using certain kind of specific detectors: In-Lens, Secondary Electron (SE), Electron Back Scattering detector (EBSD) or E-T(Everhart-Thornley) to derive further topographical information about the materials [157].

Transmission Electron Microscopy (TEM) is another microscope (Fig. 17b shows a typical transmission electron microscope with its device parts along with its detectors) based high resolution imaging technique with typically much higher working accelerating voltage (60–200 keV) directed on a thin layer of sample deposited on a carbon grid. Especially because of its high spatial resolution, TEM can resolve objects that are separated by even less than 0.2 nm. It is by far one of the most hands-on characterization technique particularly to the materials scientist who are working on nanostructured materials particularly MNPs and QDs among other various kind of materials and desire to acquire high resolution fine images along with crystalline structural information obtainable from diffraction data. Being such a versatile characterization tool, it not only produces enhanced morphological and structural information of the nanomaterials, but it is also capable of other analytical information such as electronic structure (in *electron-energy loss spectroscopy, EELS*) and chemical composition (*energy dispersive X-ray spectroscopy, EDAX*) of the nanomaterials. *High-resolution TEM (HRTEM)* imaging combines the transmitted and scattered electron signal and forms image using phase contrast method. This method of phase contrast imaging mode by far provides the highest resolution of internal structure detectable down to single arrays of atoms in crystalline nanostructures. HRTEM in its Selected Area Electron Diffraction (SAED) mode can distinguish between amorphous, single and polycrystalline materials and offers opportunity to even further identify structural defects of the materials under investigation [157].

In Scanning Transmission EM (STEM) mode, the electron beam is focused on to a fine spot and the sample is raster scanned; this method of continuous scanning of the beam across the sample makes the STEM method more appropriate to implement Z-contrast annular dark field imaging and spectroscopic elemental mapping by energy-dispersive X-ray (EDX) or EELS spectroscopy. On the other hand, *high-angle annular dark field imaging (HAADF-STEM)* is a method of performing elemental mapping in the samples which help us visually analyze the individual elemental distribution in nanoparticles on the surfaces or interfaces by collecting the scattered electrons in with an annular dark-field detector and by acquiring Z-scan across the individual particles. This is a very informative tool useful particularly in doped and alloyed samples and often help us comprehend the growth mechanism process of colloiddally synthesized NPs occurring via different mechanistic pathways like solid-state diffusion, Galvanic replacement, Kirkendall effect and so on.

Atomic Force Microscopy (AFM) is another scanning microscopy based technique which is capable of producing three-dimensional image of surfaces under certain magnification. The principle of this technique is based on the interaction between the AFM tip (probe) and the molecule on the substrate. The probe is a sharp tip usually coupled to the end of a cantilever made of silicon or silicon nitride. In order to study plasmon-exciton interaction, sometimes the AFM tip has been modified by attaching MNPs; subsequently due to this reason other techniques like

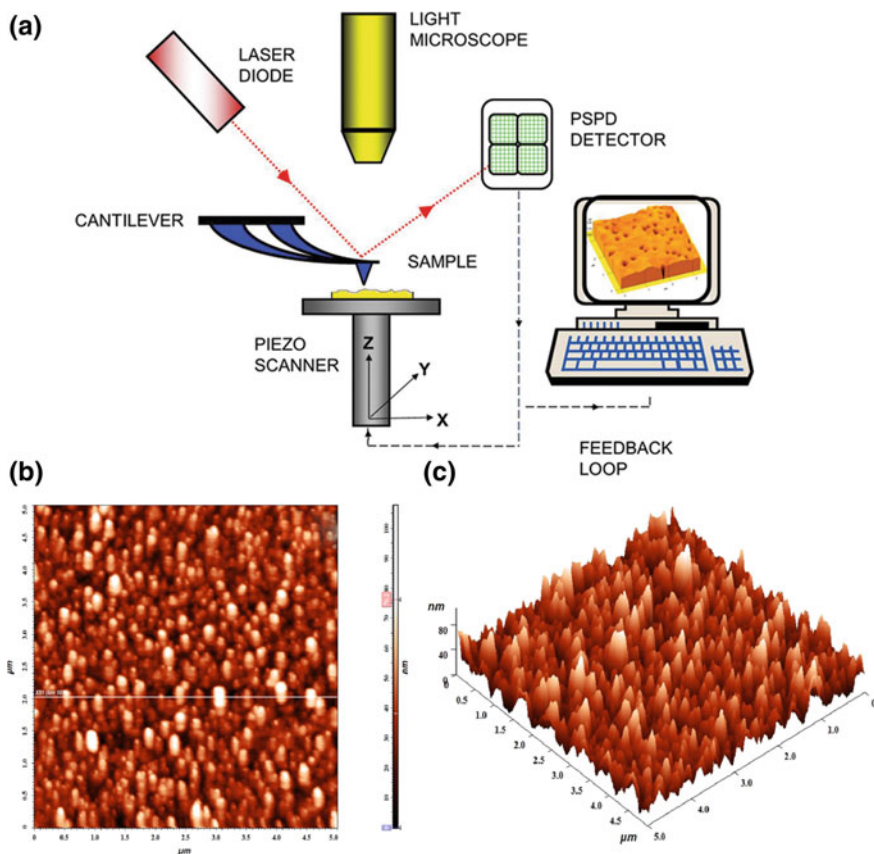


Fig. 18 **a** Schematic illustration of a typical Atomic Force Microscopy (AFM) setup. **b** A typical AFM image of Copper Zinc Tin Sulfide (CZTS) powder on quartz substrate, Reproduced with permission from Shyju et al., 2015

tip-enhanced Raman spectroscopy (TERS) has been developed which made possible to collect enhanced signals from the samples as a result of electric field enhancement from MNPs. AFM can scan the samples in different modes (contact, non-contact or intermediate tapping mode) depending on the degree of proximity between the probe and the sample. Vast topological information regarding the surfaces such as surface roughness, surface height, and grain boundaries in polycrystalline materials etc. can be derived using this technique. Figure 18a shows a typical instrumental configuration of a AFM microscope setup and Fig. 18b exhibit a typical AFM data plot generated which provides us with information like sample roughness, height and topographical features [157].

X-ray diffraction (XRD) is one of the most prevalently used structural characterization technique that provides detailed information on the crystalline structure, nature of the phase, grain size and lattice parameters. The composition

(stoichiometric ratio) of the elements in the particle can be deduced by comparing the position and intensity of the characteristic peaks with the reference patterns available in the database from International Center for Diffraction Data (ICDD) or Joint Committee on Powder Diffraction Standards (JCPDS). The lattice parameters are obtained from the Scherrer equation by observing the broadening of the most intense peak in the spectrum.

6 Electrical Measurement Tools

X-ray photoelectron spectroscopy (XPS) is a charge particle based chemical analysis tool (Fig. 19 shows the general outline of XPS technique and correlation of binding energy with kinetic energy of photoelectron, instrument work function and local electric potential) which is extremely sensitive to electrical potentials developed due to uncompensated electric charges [158]. Its underlying physical principle is based on the photoelectric effect. In addition to chemical composition and identity of elements along with their oxidation (valence states), electronic structure, binding energy of atoms, work function, change in chemical shift in response to local environment can be also determined. The surface depth sensitivity of this technique is between 10 and 15 nm which arises from the band-bending at the surface/vacuum interface. Depending on the mode of data collection, for example under photo-illumination conditions, once can even measure the photoconductivity

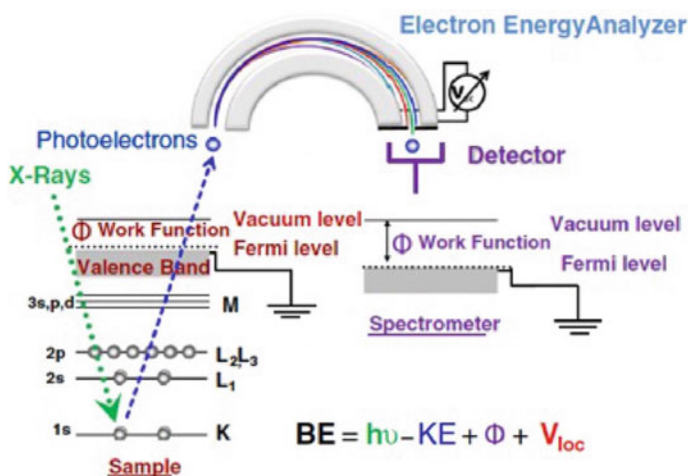


Fig. 19 Schematic diagram of the XPS technique and the equation correlating the binding energy (BE) with the kinetic energy (KE), work function (Φ) and local electric potential (V_{loc}). Note that the measured binding energy (B.E.) of a specific peak is influenced by the local electrical potential (V_{loc}) of the sample, in addition to its elemental nature and chemical state (chemical shift). Reproduced with permission from Sezen et al., 2013

and photo voltage shifts. This technique in general, can give us both qualitative and quantitative information related to nature of dopant, effect of substrate (p-/n-type) on interfacial charge accumulation & band bending, external bias (forward/reverse bias) polarity dependence on p- and n-domains of an operating p-n junction and even dynamics of electron and photoinduced charge accumulation in both bulk and thin films.

Surface Photovoltage (SPV or SPS) spectroscopy is a contactless method for measuring the change in electrochemical potential using a Kelvin probe in space-charge region of semiconductors under illumination of suitable wavelength (energy) and intensity. Figure 20 shows the outline of a typical SPV instrumental setup. It is often used to measure a wide range of material parameters and therefore deduce the quality of the samples determined from surface voltage, surface barrier height, surface charge density, minority carrier diffusion length, recombination lifetimes, doping density etc. Two major types of probes are used in SPV measurements: Kelvin probe, where the electrode vibrates vertically altering the capacitance between the probe and sample; and the Monroe probe where the electrode is fixed and a grounded shutter in front of the electrode is vibrated horizontally thereby modulating the probe to wafer capacitance. The contact potential difference (V_{CPD}) is measured using an AC current and determined from:

$$I = V_{CPD} \cdot \frac{dC}{dt}$$

where C is the capacitance between the probe and sample and CPD (difference between the work function of sample and probe) = $WF_{sample} - WF_{probe}$.

Another major application of SPV is to measure the minority carrier diffusion length and lifetimes thereby providing information regarding the low defect densities. It is a preferred characterization technique to determine diffusion lengths since it is a steady-state, non-destructive, contactless with no complex sample

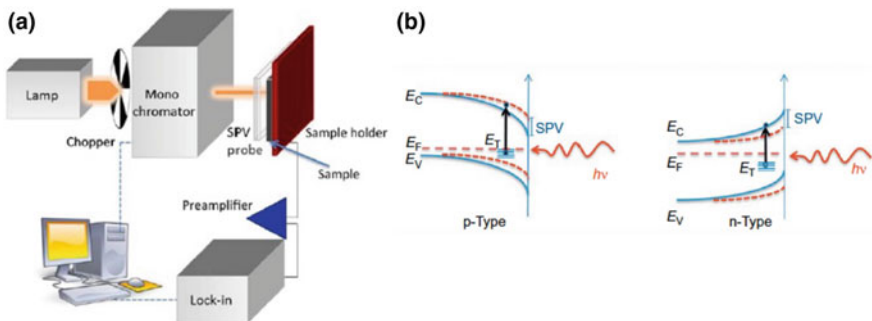


Fig. 20 a Schematic illustration of a Surface Photovoltage (SPV) instrumental setup. b Band diagram of a p-type (left) and n-type (right) semiconductor close to the surface under non-equilibrium/ above bandgap illumination condition. Band edges (E_C , E_V) and Fermi energy (E_F) are indicated in the diagram. Reproduced with permission from Cavalcoli et al., 2015

preparation requirements and the instruments are commercially available. The wafer could be homogenous or in the form of p-n junction or metal-semiconductor junction. In dynamic SPV, the sample wafer is illuminated by a monochromatic light pulse with high intensity. Depending on the excitation pulse width and photon flux, it gives information of surface band-bending, (Fig. 20b) density of interface states, recombination behavior and majority carrier lifetime. Whereas, in static SPV, the sample is illuminated with monochromatic light of tunable wavelength so that the penetration depth of the impinging photons could be varied. This gives information of diffusion length of excess carriers in sample [159].

Electron-Beam Induced Current (EBIC) is a SEM- based microscopic technique for characterizing the electrical properties of semiconducting materials and devices, and study the sub-surface electronic and defect states. The electrical current is typically measured that flows through the sample when it exposed to an electron beam. The principle of operation of EBIC involves creating local electron-hole pairs and subsequently measuring the contribution of each of electron and hole components from the current signals (Fig. 21a shows the schematic illustration of a typical EBIC and CL experimental setup). As the electron beam is scanned across the sample, it forms an image of the response at each point. The signal difference can originate as a result of junctions with electric fields, variation in doping levels/impurities in the device, or from crystalline defect states or surface/interface dangling bonds yielding important information on minority carrier diffusion lengths, relaxation times and microscopic images of width of depletion regions. The incident electron beam generates a large number of e-h pairs within a small interaction volume (considered as a teardrop shape that is dependent on Z contrast, atomic weight of the material, its density and also accelerating voltage of incoming electron beam). These e-h pairs can undergo either radiative relaxation by emitting light (signals measured via *Cathodoluminescence*, CL method), or non-radiatively in the form of heat, or electrical current within the external measurement device circuit (signals measured via *EBIC*). For a standard EBIC measurement, the internal

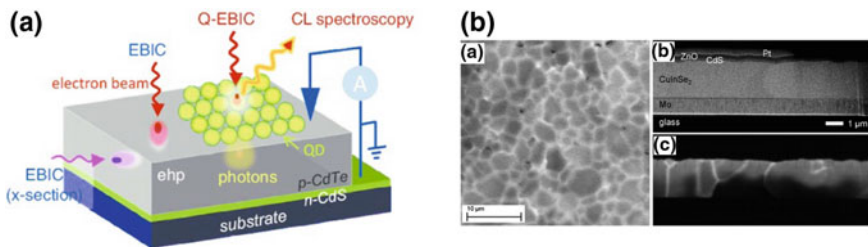


Fig. 21 **a** Schematic illustration of a typical EBIC and Cathodoluminescence (CL) experimental setup. **b** **(a)** EBIC image acquired at 10 keV on a $\text{Cu(In,Ga)Se}_2/\text{CdS}/i\text{-ZnO}/\text{ZnO:Al}$ stack, lifted off the Mo/glass substrate; the Cu(In,Ga)Se_2 was in contact with Ag epoxy glue, leading to Ag diffusion into the Cu(In,Ga)Se_2 layer, assuming a decreased net-doping density in the absorber; grain boundaries exhibit enhanced EBIC signals as compared with the grain interiors. Reproduced with permission from Abou-Ras et al., 2019

electric field gradient associated with p-n junction causes charge separation and hence results in a net current flow. With a proper knowledge on carrier generation, drift, diffusion, recombination and collection, it is possible to estimate the factors that govern the EBIC signals. When characterizing the junctions, EBIC measurements can be performed in different specimen configurations both in planar or cross-sectional positions. The planar view configuration can be used to examine recombination centers such as dislocations, grain boundaries, homogeneity of junctions; whereas the cross-section studies can be used to locate and characterize the depletion regions, and measure diffusion lengths. With recent developments in electronics and optics, the detection levels and resolution of EBIC images have been pushed down to even investigate nano-electronic devices [159].

Impedance Spectroscopy (IS) is another powerful, non-destructive electrical characterization tool that can be implemented coupled with device illumination for in-situ monitoring of charge transport and recombination processes at different points of the solar cells. It has been frequently used to investigate device aging, performance loss mechanisms in response to external stress factors as well as how different protocols of fabrication affect the device performance. Usually, IS is a voltage perturbation method wherein a DC voltage potential establishes a steady-state condition and a small working AC potential is applied at different frequencies to monitor the change in impedance in addition to measuring recombination resistance and geometrical capacitance. In general, IS is applied to systems with electrical Ohmic contacts which involves measurement of AC electrical current $I(\omega)$ at a certain angular frequency ω under the application of an AC voltage, $V(\omega)$; then the impedance is $Z(\omega) = \frac{\widehat{V(\omega)}}{\widehat{I(\omega)}}$.

The impedance data are analyzed using equivalent circuit and capacitance-frequency models wherein the global response data of the sample is quantified from the resistive and capacitive contributions to the impedance spectrum over the full frequency range of measurement. Using these models, the transport and recombination processes are interpreted [160–162].

Deep-level Transient Spectroscopy (DLTS) is another efficient method in understanding the physics and engineering of photo-carrier generation, escape and collection processes in photovoltaic materials and characterizing electrically active deep-level defects/impurities in semiconductors. DLTS is a capacitance thermal scanning transient technique, usually operating at a high frequency (MHz) range. Utilizing the capacitance of a p-n junction or Schottky barrier, it monitors the changes in charge state of deep level traps/defects. It can distinguish between majority and minority carrier traps giving information on concentration, thermal stability, and energy and capture rates for both kind of traps. The transients provide the information regarding an impurity level in the depletion region by monitoring the capacitance transient originating from the initial to thermal equilibration state after a perturbation is applied to the system. DLTS has certain specific advantages over other previously mentioned techniques as it allows us for a complete characterization of a deep center and their correlation with the device properties.

In particular, it can measure effectively the capture cross-section and activation energy of deep level trap states in addition to just distinguishing between traps and recombination centers [160–162].

7 Optical Methods

Basic light-matter interactions are primarily governed by three different processes: absorption, scattering and transmission. The first two processes result in an attenuation of incident light intensity after passing through matter. And the total loss of these two processes is defined as extinction as $Y_{\text{ext}} = Y_{\text{abs}} + Y_{\text{scatt}}$.

UV-Visible (UV-Vis) spectroscopy is a relatively facile and straightforward low-cost optical characterization tool that is frequently used to study these optical parameters of nanomaterials. It measures the intensity of light reflected (transmitted) from a sample in comparison to the intensity of light reflected (transmitted) from the reference material (could be the blank solvent in which the actual sample is dispersed in, or air, or glass if measuring the samples in the form of solid thin films). MNPs in particular have optical properties (localized surface plasmon, LSP discussed earlier), these localized surface plasmon resonance, LSPR peak position and peak width are highly sensitive to size, shape, concentration, agglomeration state (polydispersity index), local dielectric environment or refractive index of the surrounding medium. This makes UV-Vis spectroscopy an important handy tool to rapidly identify and characterize the type and quality of materials as well as evaluate the stability of nanoparticles in different solvents. These LSPR bands could appear anywhere in the electromagnetic spectrum in UV, Visible to even near or far-IR regions. As for the QDs are concerned, the UV-Vis spectroscopy has proven to be an equally important tool to identify the quality and homogeneity of the samples since these colloidal semiconducting NCs often show their characteristic excitonic peaks arising from the different discrete electronic transitions/ energy levels in these so called “atom-like” quantum confined systems.

Photoluminescence Spectroscopy (PL) is another commonly used technique to study the photoluminescence emission behavior of optically active fluorophores such as metal nanoclusters, quantum dots, organic dye molecules and fluorescent proteins, polymers etc. It monitors the light emitted from atoms or molecules that have absorbed photons and results in re-emission of photons by releasing excess energy. Excited states both in single atoms or molecules can undergo optically-allowed transitions following certain sets of selection rules of transitions and give out the electromagnetic radiation in the form of light emission. Depending on the nature and relative timescales of emission from the excited states, PL can be broadly divided into fluorescence and phosphorescence.

Both the above techniques (UV-Vis absorption or PL spectroscopy) as discussed above can be performed under both steady-state and time-resolved conditions. Conventional and easy to perform steady-state measurements provide information of light-matter interaction primarily to and from/ with the ground states; whereas

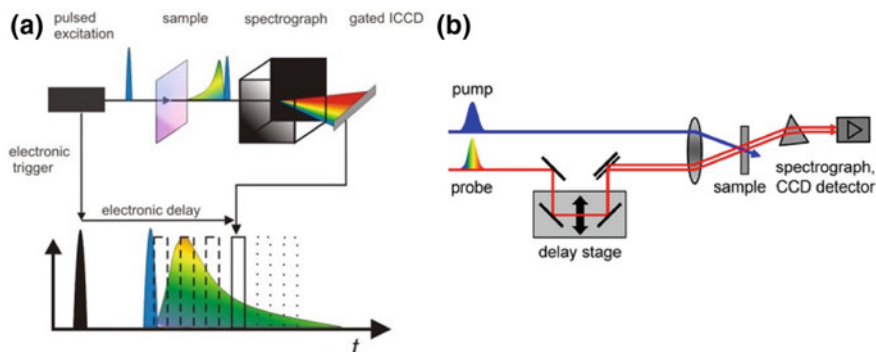


Fig. 22 Schematic illustration of experimental setups of **a** Time-resolved Photoluminescence spectroscopy (TRPL) and **b** pump-probe ultrafast transient absorption spectroscopy (TA). *Source* https://www.mpip-mainz.mpg.de/65134/Time_Resolved_Photoluminescence_Spectroscopy, <https://www.temps.phc.uni-kiel.de/en/research/laboratories-and-instrumentation/fs-transient-absorption>

time resolved spectroscopy gives us vivid information on interaction between different electronically higher order excited states occurring at different timescales (depending on the sensitivity of the technique itself or temporal resolution of the detectors) within the same or between different molecules.

Time-integrated or time-resolved photoluminescence spectroscopy (TRPL or TIPL) simply measures an integrated PL or temporal evolution over a time much longer (this can be well modulated by varying the repetition rate of the incoming excitation pulse) than the normal intrinsic emission lifetime of the materials under study. TRPL can be performed using different methods such as time-correlated single photon counting (TCSPC), phase modulation or by using streak camera detection for high temporal resolution and light sensitivity. Figure 22a shows the experimental scheme of a typical state of the art time-resolved PL setup.

Transient Absorption (TA) spectroscopy, (Fig. 22b shows a typical pump-probe spectroscopic setup) on the other hand measures the light absorption at the transient excited states, the temporal resolution of which could vary from few sub-picoseconds (ps) to even few hundreds to femtoseconds (fs). In order to monitor the transient absorption process at very fast timescales, two beams are used, namely the pump and the probe. The pump beam is usually strong and chirped short laser pulse to generate a population of the excited states; whereas the probe beam maybe continuous wave (CW) white light beam or pulsed which is sent through the sample to probe the perturbation caused by the initial pump beam on the sample. This could be monitored by sending the probe beam at some delayed times and also at other wavelengths with respect to the pump beam. This method gives us valuable information on different excited states and on various physical processes occurring at different timescales such as ground state bleaching, photoinduced absorption and stimulated emission.

Infrared (IR) spectroscopy is another essential and a straightforward characterization technique that is often used to elucidate the structure of matter at a molecular

scale. Information regarding the chemical composition, bonding arrangement, functional groups (or chemical identification of surface ligands) can be obtained from the characteristic fingerprint vibrational frequencies that appear in the spectrum. The Fourier-Transform IR (FTIR) obtain the spectrum by Fourier transformation of the signal in frequency domain that permits us to identify the chemical components or group of atoms that absorb IR at particular frequencies. In addition to chemical identification, this technique can be also used to measure tacticity, crystallinity and molecular strain of different polymers (macromolecules).

Raman Spectroscopy is a well-known optical tool, named after the eminent Indian scientist Dr. C.V. Raman who first observed this inelastic scattering phenomenon. This method is being used to detect vibrations at the molecular level which provides information on the chemical identification and physical forms of the materials. Samples in the form of solid, liquid, vapor or in the form of particles (powder) or surface layers can be studied using this method (Fig. 23a shows a typical Raman spectroscopic setup). Raman scattering might have certain disadvantages including sample degradation or fluorescence since most often signals collected from the sample are weak and thus higher laser excitation powers are used to study the particles. However this problem has been substantially reduced with modern and improved Raman spectroscopic methods like surface-enhanced or tip-enhanced Raman (SERS or TERS) which are being currently used for chemical imaging of surfaces at the nanometer scale.

Dynamic Light Scattering (DLS) is a widely employed optical technique (Fig. 23b) to estimate the size of colloidal NPs in suspensions that are typically in the nano- to sub-micron ranges. The NPs dispersed in a colloidal solution are in some continuous form of random Brownian motion. This method measures light scattering as a function of time which combined with the Stokes-Einstein assumption (Stokes-Einstein equation with Diffusion coefficient terms) in order to

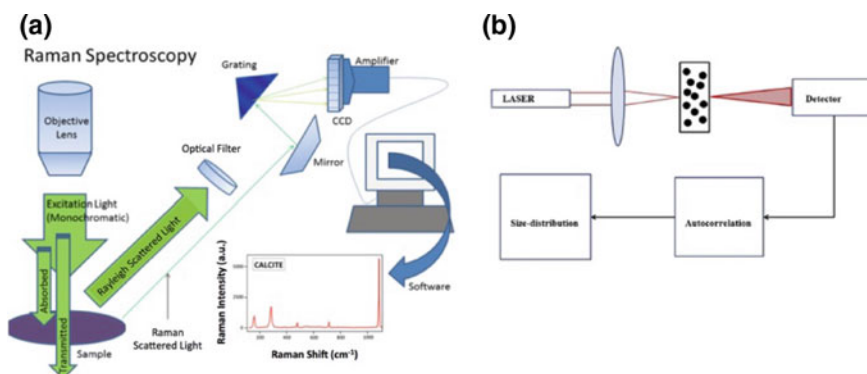


Fig. 23 Schematic illustration of instrumental setups of **a** Raman spectroscopy and **b** Dynamic Light Scattering. *Source* <https://doi.org/10.13140/rg.2.1.3818.0322> MSc Thesis: Raman Spectroscopy Applied to Enhanced Oil Recovery Research, J. Magn. Magn. Mater. 427 (2017) 19e24

calculate the hydrodynamic diameter. Basically, it gives us a size distribution profile based on temporal fluctuations that are analyzed by means of intensity or photon auto-correlation function.

8 Operational Mechanism and Design Principles in Plasmon Enhanced Photovoltaics

The photovoltaic community has been actively studying the light-matter interaction in plasmonic metallic nanostructures in order to understand the plasmon enhancement mechanisms and as well as strive to improve and tune the spectral range of photon absorption (collection) and photon-to-electrical energy conversion efficiency. Surface plasmon, as we introduced earlier are collective oscillations of free electrons in metallic materials which when interact with the electromagnetic light creates a coherent optical response at certain frequency matching condition to generate what is known as the Surface Plasmon Resonance. Plasmonic enhancement could be achieved by judicious design and fabrication of MNPs incorporating within the energy based optoelectronic and photovoltaic devices as well as working through different mechanisms such as far-field scattering, near-field coupling, and charge or resonant energy transfer. Figure 24a shows the diagrammatic representation of various plausible plasmon induced mechanisms typically encountered in all plasmon mediated photovoltaics. It was by Atwater and Polman, who earlier outlined three different approaches that MNPs can be employed to enhance the light absorption properties of solar cells [163–165] (Fig. 24c). In the following paragraphs, different architectures of plasmonic nanoparticles and their role in enhancement mechanisms in photovoltaic devices will be discussed in details.

Firstly, plasmonic nanostructures or nanoarrays can be incorporated as sub-wavelength scattering centers for efficient coupling and trapping of the incoming radiation into the active absorbing layer (dyes, polymers, quantum dots and recently perovskites as individually identified as the different generations of solar cells). Usually within a thin active layer, the light absorption is insufficient, thus in order to improve the light absorption efficiency, plasmonic MNPs introduced as sub-wavelength scattering sites in different geometries and orientations would help increase the angular speed and travelling distance of generated excitons (e-h pairs) in the active layer. The vast array of assembled MNPs would also result in multiple scattering of exciton that will lead to an effective increase in optical path length and absorption and as well as enhancing the probability of charge collection efficiency. Depending on the dimension of NPs, the scattering direction could be manipulated, for e.g. smaller NPs result in forward scattering whereas larger NPs result in backward scattering (reflection) of the incident light. MNPs when placed between the interfaces of dielectric layers, the light gets preferentially scattered into the high index substrate. Since light scattering and the absorption losses in MNPs is highly sensitive to the material composition, size and shape, one needs to be extra

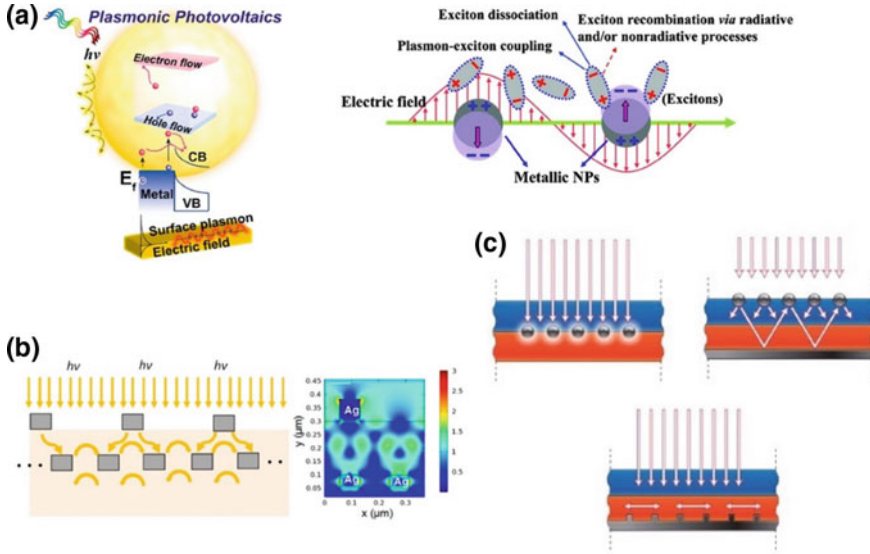


Fig. 24 **a** Schematic illustration show various mechanisms and effects related to plasmon mediated photovoltaics. Reproduced with permission from Jang et al., 2016; Wu et al., 2011. **b** Light trapping effect between the plasmonic nanostructures and simulated electric field profile (FDTD simulation) for scattering. Reproduced with permission from Lin et al., 2013. **c** Plausible light trapping geometries for thin film solar cells. Light trapping by scattering from metal nanoparticles at the surface of the solar cell. (left) Light is preferentially scattered and trapped into the semiconductor thin film by multiple and high-angle scattering, causing an increase in the effective optical path length in the cell. (right) Light trapping by the excitation of localized surface plasmons in metal nanoparticles embedded in the semiconductor. The excited particles' near-field causes the creation of electron-hole pairs in the semiconductor. (bottom) Light trapping by the excitation of surface plasmon polaritons at the metal/semiconductor interface. A corrugated metal back surface couples light to surface plasmon polariton or photonic modes that propagate in the plane of the semiconductor layer. Reproduced with permission from Atwater et al., 2010

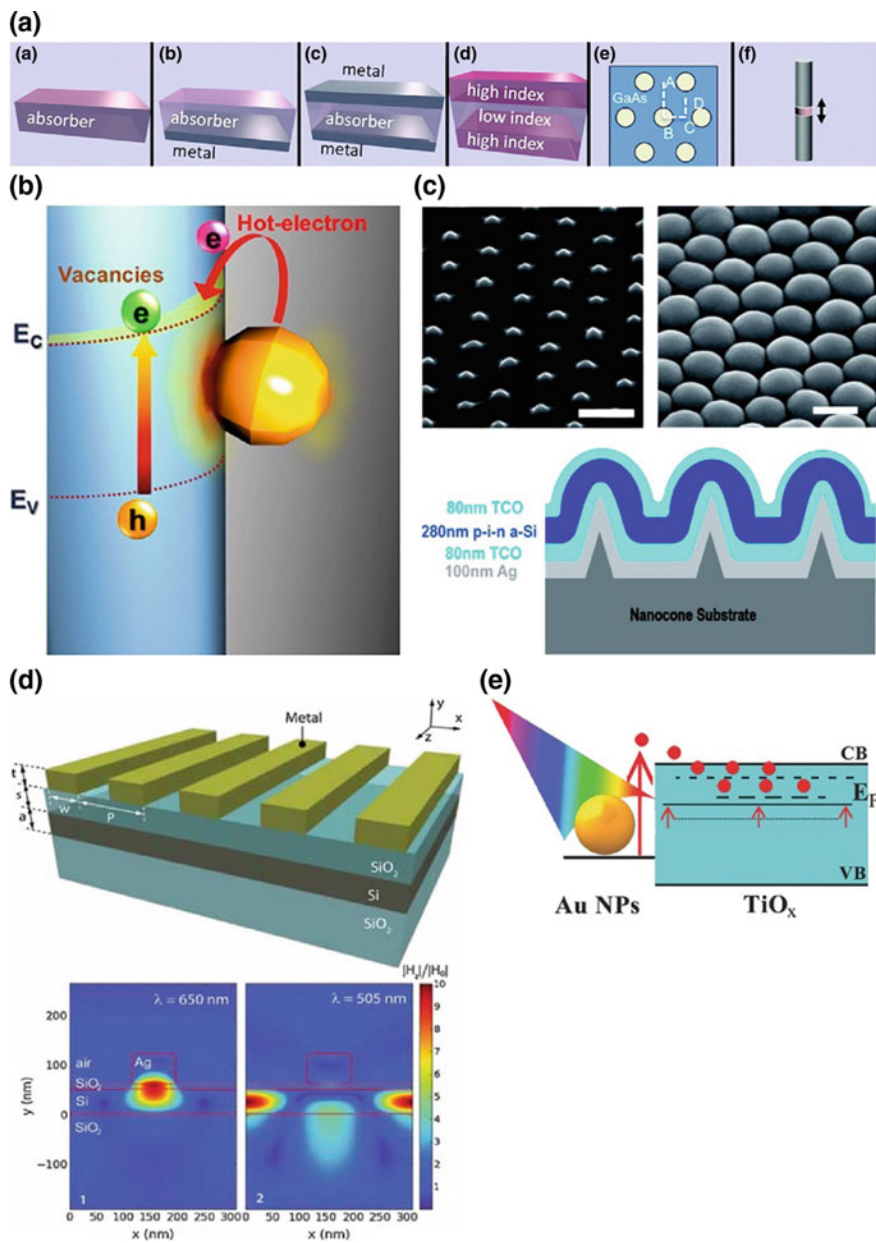
careful while trading off the percentage contribution of scattering versus the percentage of absorption loss when selecting the size and shape of metallic nanoparticles. Ideally, we want to make sure that the plasmonic MNPs absorb little light (reduced parasitic absorption loss) and scatter more light (increased light-trapping via far-field scattering).

Secondly, the near-field coupling effect which results in strongly confined electric field near MNPs can be further exploited to increase the light absorption efficiency in solar cells. In this approach, the MNPs act as sub-wavelength nanoantennae that couple the electromagnetic light into their near-field. However, for relatively larger NPs, contributions from both scattering and near-field coupling effects play a dual role in enhancing the light absorption process. While comparing specific geometries of MNPs, it has been observed both experimentally and theoretically that for similar MNPs with identical volume, the field enhancement vary largely with different shapes in the order pyramidal > cube > cylinder > sphere

(the anisotropic structural effect plays quite a significant role in the extent of plasmonic evanescent field and degree of local electric field enhancement). Additionally, with an appropriate phase matching condition, the EM light could be also coupled with plasmons to generate surface plasmon polariton (SPP) modes at the interface between metal and semiconductor. Efficient excitation of SPP modes can be achieved by incorporating different 2D- or 3D- designs such as grooves, periodic gratings, holes, islands etc. Figure 25a, c, d show different configurations and designs involving metal NPs incorporated within the device. Since the propagation lengths of these SPP modes are quite large extending to even few hundreds of μm , it can contribute to further increase the absorption efficiency of solar cells. The concentrated near-field effect extends into both metal and dielectric layers where the photovoltaic enhancement takes place.

And finally, it is also possible to effectively utilize and harvest the plasmon induced hot charge carriers (hot electrons) to usable form of electricity by energy conversion. Hot carriers are generated by inducing electron excitation above the Fermi energy level either via intraband or interband transitions. The hot carriers with excess energy usually possess very short (ultrafast: of the order of few hundred femtosecond, 10^{-15} s to few picosecond, 10^{-12} s) lifetime resulting in rapid decay and dissipation of energy in the form of heat (Joule heating). However, if these metal nanostructures are located in near proximity or in direct contact to the active semiconducting layer, these hot electrons with sufficient energy and momentum via dephasing of plasmons can non-radiatively transfer or inject themselves into conduction band edge of the active layer thus yielding a usable photocurrent. Figure 25b, e show the general outline of plasmon induced hot carrier transfer mechanism from metal NP to nearby semiconductors. Plasmonically excited electrons with energy higher than the Schottky barrier establish an internal electric field which results in upward or downward band-bending depending on whether the semiconducting layer is n- or p-type that results in electron transport from the metal into the bulk of the active layer; however there is always a competition between the overall charge extraction and thermal relaxation as a consequence of these hot carriers generation [166–170].

The improvement and interpretation of enhancement mechanisms in photovoltaic performance by MNPs could be quite complicated where other energy transfer effects are often involved in addition to light trapping and harvesting. Coupling between plasmon in MNPs and excitons in the active semiconducting layer largely influence the charge transfer processes and facilitating exciton dissociation/ annihilation by modifying the dynamical properties of excited states and carrier relaxation/dissociation pathways of hot carriers. Plasmonic Resonant Energy Transfer (PRET) which is an analogous to Forster Resonance Energy Transfer (FRET) is yet another plausible mechanism that involves a form of non-radiative energy transfer between a coupled dipole-dipole fluorescent donor and acceptor within a certain distance. In PRET, the MNPs act as a donor wherein it transfers energy via charge carriers (electrons or holes) to the active semiconducting layer. This mode of energy transfer is a little different from that of the near-field effect in the sense that this mechanism follows the similar requirements of FRET (spectral



◀**Fig. 25** **a** Schematics for new solar cell designs with an elevated local density of optical states (LDOS) for the absorbers based on metal-absorber-metal or high-low-high index materials. Reproduced with permission from Callahan et al., 2012. **b** Cartoon showing the plasmon induced effect via hot electron transfer mechanism from metal NPs to the semiconducting photoactive layer in solar cell. Reproduced with permission from Chen et al., 2012. **c** Nanodome a-Si:H solar cell structure. SEM images taken at 45° on nanocone quartz substrate (top) and a-Si:H nanodome solar cells after deposition of multilayers of materials on nanocones (right). Scale bar 500 nm. Schematic showing the cross-sectional structure of nanodome solar cells (bottom). Reproduced with permission from Zhu et al., 2010. **d** Noble metal nanostructure designs utilizing high near-field effects surrounding the plasmonic nanostructures and coupling to waveguide modes with realization of broadband absorption enhancement. Reproduced with permission from Pala et al., 2009. **e** A unique sandwiched structure of $\text{TiO}_x/\text{Au-NPs}/\text{TiO}_x$ that has been used to improve the charge transport properties of a TiO_x film via plasmonic-mediated hot carrier injection at the metal-semiconductor Schottky junction. Reproduced with permission from Yuan et al., 2015

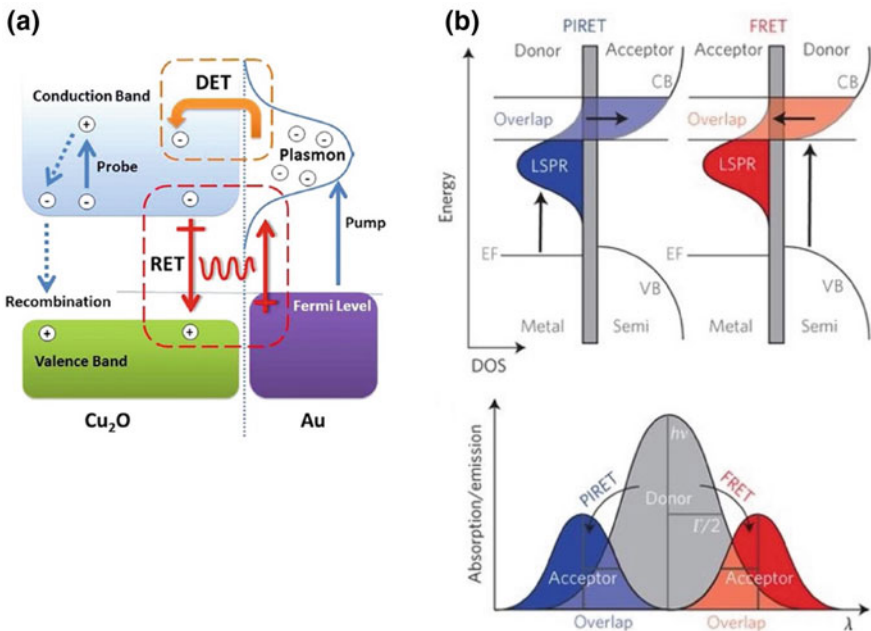


Fig. 26 **a** Plasmonic resonant energy transfer and charge separation mechanisms in hybrid metal NP-semiconductor photovoltaics. Metal@semiconductor structures can increase charge separation by direct electron transfer (DET) of hot electrons contained in LSPR to the semiconductor, local electromagnetic field enhancement (LEMF) of the semiconductor charge separation process, or by resonant energy transfer (RET) from the LSPR dipole to the electron hole pair in the semiconductor shell. Reproduced with permission from Cushing et al., 2012. **b** Complementary energy transfer mechanisms via Plasmon Induced Resonance Energy Transfer (PIRET) and Forster Resonant Energy Transfer (FRET) in $\text{Au}@ \text{SiO}_2\text{-Cu}_2\text{O}$ hybrid systems. Parameters such as spectral overlap and dipole-dipole interaction depend on whether the semiconductor is excited by PIRET or quenched by FRET. Reproduced with permission from Li et al., 2015

overlap, distance between the particles <10 nm). Figure 26 show the outline of various plasmon induced resonant energy transfer mechanisms often encountered in plasmon mediated photovoltaic devices [171, 172].

Before the recent research surge with newly encountered perovskite solar cells, the early 3rd generation of photovoltaic devices were based on dye-sensitized active layer which have gained a significant interest due to their relatively low production cost as compared to traditional indirect band-gap Si solar cells combined with their high power conversion efficiency. Later on, plasmonic nanostructures were further incorporated into these dye-sensitized solar cells (DSSCs) to maximize the charge generation and efficient extraction processes. Figure 27 show incorporation of different plasmonic metal NPs within the DSSC which boosted the overall performance and efficiency of the devices. To date, plasmon-enabled DSSCs with a balanced broadband panchromatic light response yielded a highest efficiency of about 11%, a ~30% improvement in compared to the reference device. In 2000, it was Wen and co-workers who implemented Ag-island films in ruthenium based dye-sensitized photoelectrochemical cells and observed an increment in photore-sponse in the visible region [173]. Hupp et al investigated the distance dependent optical response by adjusting the distance between the photosensitizer and plasmonic particles and correlated the connection between plasmon enhanced electromagnetic field and the enhanced extinction response of the dye sensitizer [173]. Ihara et al introduced modified Ag nanoparticles with block copolymers to increase

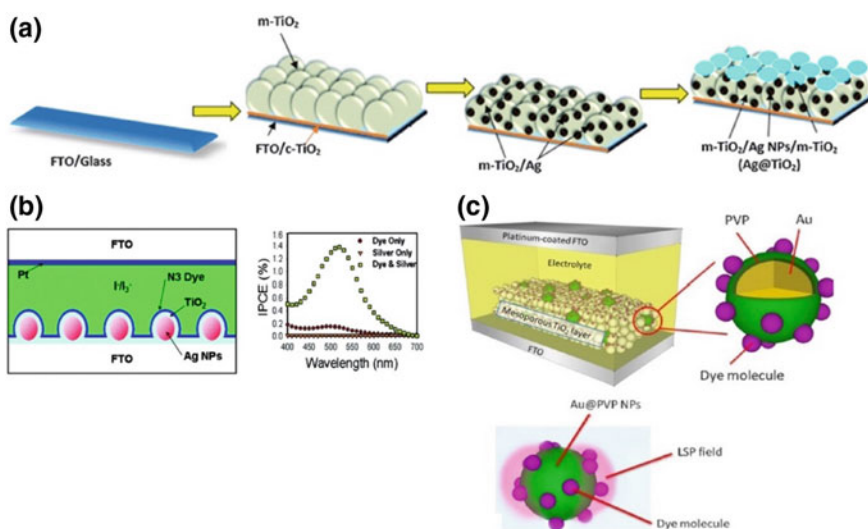


Fig. 27 **a** Schematic of plasmonic photoanode preparation process based on Ag NPs on mesoporous TiO₂. Reproduced with permission from Isah et al., 2016. **b** Configuration of solar cell containing Ag NPs and dye. Reproduced with permission from Standridge et al., 2009. **c** Configuration of core-shell Au@PVP nanoparticles (NPs) into dye-sensitized solar cells. Reproduced with permission from Xu et al., 2012

the stability of electrolyte [174]. Later, it was Liu et al who prepared plasmonic core/shell/metal organic Au/PVP NPs and embedded them within the TiO_2 photoanode [175].

These modified well coated NPs not only exhibited enhanced stability from recombination, or photolytic degradation or electrolyte corrosion but also possessed the ability to adsorb onto the dyes. It was Kamat and co-workers who reported that the photovoltaic performance could be influenced in at least two major ways: plasmonic and electronic charging effects (Fig. 28a). The increased excitation of the photosensitizer (dye) and subsequent increment in photocurrent could be attributed to enhanced EM field from the plasmonic NPs embedded within the device [175]. Hagglund et al demonstrated an enhanced charge carrier generation using photoconductivity measurements when performed on TiO_2 sensitized by a combination of dye molecules and arrays of elliptical Au nanodisks [175] (Fig. 28b). In 2009, Chen et al have implemented vertically aligned ZnO nanorod arrays coated with Au NPs as Schottky barrier solar cells and observed an enhancement in optical absorption in visible range due to the effect of surface plasmon resonance with an increment in PCE (power conversion efficiency) from 0.7% to 1.2% [176]. In 2010, McGehee and coworkers have used 2D arrays of Ag nanodomes as plasmonic back reflectors using nanoimprint lithography [177].

They observed an enhanced absorption through excitation of plasmonic modes and increased external quantum efficiency close to 15% due to light scattering effects in the long wavelength range 600–900 nm. In addition, there are several studies dedicated to numerous designs of plasmonic nanostructures such as Au@SiO_2 , Ag@TiO_2 , $\text{Au@Ag}_2\text{S}$, Au@TiO_2 hollow submicrospheres and so on

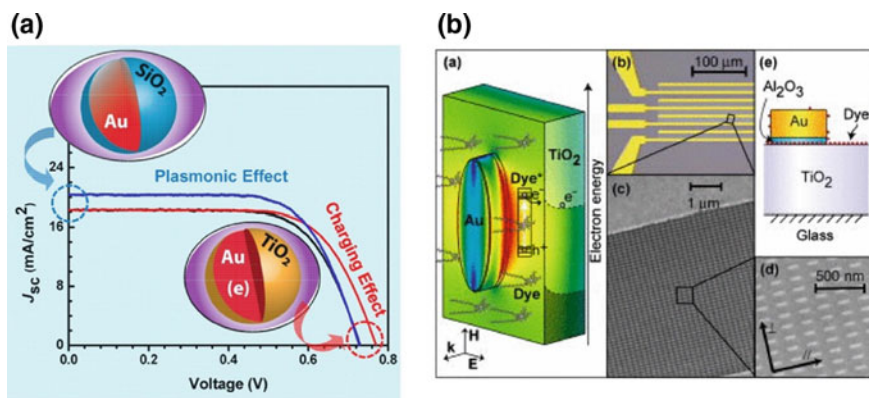


Fig. 28 a Charging effect (Au@TiO_2) versus plasmonic effect (Au@SiO_2) of metal core–oxide shell particles in dye-sensitized solar cells. Reproduced with permission from Choi et al., 2012. b Schematic shows enhanced charge carrier generation in dye sensitized solar cells by nanoparticle plasmons. The field amplifies excitation of dye molecules Dye^* adsorbed on the semiconductor TiO_2 substrate, leading to enhanced electron transfer rate to the TiO_2 conduction band. The SEM images are close-ups of an array of elliptical Au disks, and the schematic picture shows the sample arrangement from the side. Reproduced with permission from Hagglund et al., 2008

which has observed the synergetic effect of enhanced light absorption and accelerated energy transfer in addition to plasmon induced charge excitation and separation [163, 178–181]. As a consequence of all these combined effects, an improvement in PCE parameters (short circuit current density: J_{SC} , open circuit voltage: V_{OC}) has been observed. The light harvesting capability in DSSCs was further demonstrated by incorporating dielectric silica coated Ag, Au nanoparticles with various interesting morphologies ranging from nanostars, nanorods, nanocubes, nanoprisms and taking advantage of their additional anisotropic plasmonic effect on the dye sensitizers (Fig. 29a, b). For example, Bardhan and coworkers observed an enhanced PCE of 7.8% from the reference 5.8% when silica coated ($Au@SiO_2$) nanocubes are embedded within the photoanodes of DSSCs [182] (Fig. 29c). Similarly, a panchromatic response in light harvesting capability of the

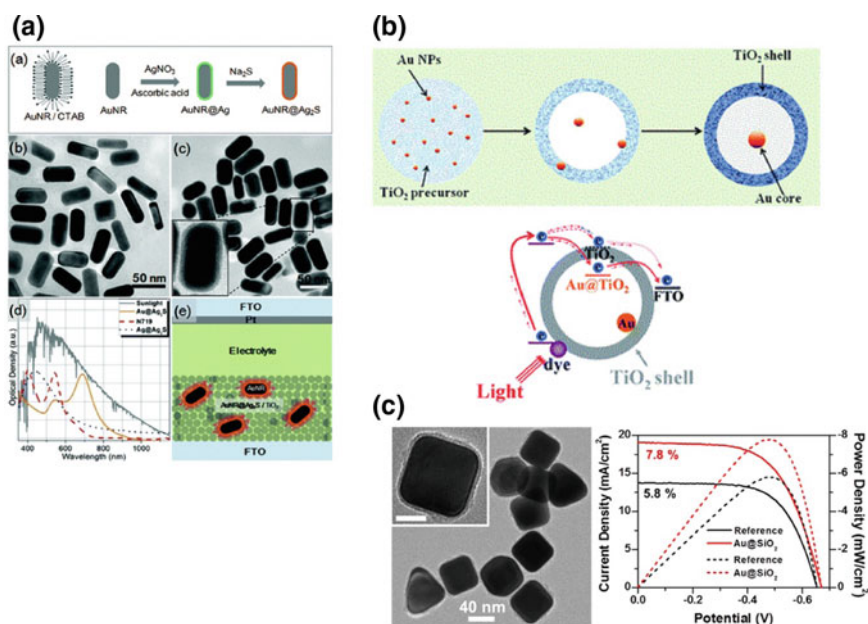


Fig. 29 a Schematic illustration of a Au nanorod stabilized by hexadecyltrimethylammonium bromide (CTAB) and a two-step chemical process towards AuNR@Ag₂S (a) (CTAB is not drawn in the synthesis scheme for clarity); TEM images of as-synthesized Au nanorods (b) and AuNR@Ag₂S with Ag₂S thickness of 2 nm (c); solar irradiance spectrum, absorption of AuNR@Ag₂S (2 nm in shell thickness), N719 dye solution in acetonitrile and t-butanol and Ag₂S-encapsulated Ag nanoparticles, AgNP@Ag₂S (d) and a 2D device configuration of the plasmon-enhanced DSSCs, in which dye molecules were not included for clarity (e). SEM images of the TiO₂/AuNR@Ag₂S anode film. Reproduced with permission from Chang et al., 2012. **b** Illustrations of (top) formation process of Au@TiO₂ hollow microspheres and (bottom) the charge separation process in the DSSCs with the photoanode of Au@TiO₂ hollow microspheres. Reproduced with permission from Du et al., 2012. **c** Enhancement in efficiency of dye sensitized solar cells when silica-coated nanocubes ($Au@SiO_2$) embedded in the photoanodes. Reproduced with permission from Zarick et al., 2014

DSSC was observed when Au@SiO₂ triangular nanoprisms were incorporated within the device resulting in a 15% increase of PCE from 3.9% to 4.4%. In another study by Elbohy et al., when Au nanostars are incorporated into photoanodes, the PCE of the solar cells were increased by $\approx 20\%$ from 7.1% to almost 8.4% along with an improvement in the incident photon-to-current conversion efficiency (IPCE) and the spectral response was broadened in the region between 380 and 1000 nm [183]. Complex architectures involving bimetallic Au/Ag/SiO₂ and alloyed plasmonic nanostructures were also used for improved light trapping and subsequent enhancement in light harvesting capability resulting in increment of 26–30% of PCE with additional enhancement in charge carrier generation and rapid charge transfer to electrodes.

In addition to the above studies, recently solar cells with plasmonic sensitizers were also demonstrated in order to study the plasmon induced charge separation, which is believed to be an essential process for photocurrent generation. Su et al conducted a study on surface plasmon resonance of layer-by-layer Au NPs induced photoelectric current generation in plasmon sensitized solar cells and showed that by depositing multiple layers of Au NPs on surface of solar cells increases the amount of light scattering on its surface, thereby boosting the absorption and improving the device efficiency [184]. Finally, in addition to just merely incorporating plasmonic nanostructures of various forms and morphologies into the photoelectrochemical cells, MNPs has been also used to modify the electrodes (specifically the photoanodes) with different morphologies such as nanowires, nanotubes, sphere, hollow sphere and core-shell types. These metal nanoparticles modified photoanodes offer efficient photon collection as well as exhibit plasmon-enhanced light absorption [185–187].

Not just in DSSCs, plasmonic NPs and effect of surface plasmon resonance has been also observed in organic photovoltaic devices (OPVs). The principal consideration in designing plasmon enhanced OPVs is by trading off between two primary goals: minimizing the active layer or cell thickness down to the carrier diffusion length but at the same time to design cells with sufficient thickness to provide necessary degree of absorption by taking advantage of the enhanced electric field via utilizing the SPR effect. An increase of up to 24% was observed when a blend of Au nanospheres and nanorods were introduced into the hole-transport layer (HTL) [188]. Later on, Ginger, Chen and Jen's groups has independently conducted in-depth study on the multi-scattering effect from the LSPRs of Ag prisms and observed PCE values to increase from 6.55% to 9.02% [189–192]. Most of the studies have interpreted the improvement in device performance is due to enhanced optical absorption via near-field enhancement and light scattering effect resulting from the plasmonic nanostructures. However, these plasmonic NPs can also alter the electrical properties by promoting photocarrier mobility to the generated charge carriers and also the photoconductivity based on their metallic characteristics; largely depending on the morphology and location of these nanoparticles within the device. Recently, the Choy group investigated the mechanism of plasmonic effect in OPVs by embedding Au nanospheres within HTL; instead of enhancement in optical absorption, the IPCE was increased that

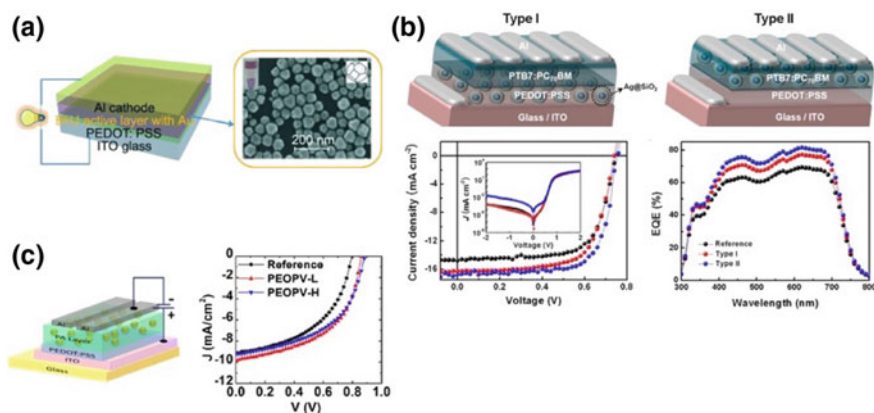


Fig. 30 **a** Addition of truncated octahedral Au nanoparticles (ca. 70 nm diameter) to bulk heterojunction (BHJ) photovoltaic cells fabricated from a variety of donor polymers and PC₇₀BM as acceptor gives a boost in the power conversion efficiency (PCE). Reproduced with permission from Wang et al., 2011. **b** High performance polymer solar cells as a function of different positions of silica coated Ag NPs between the active and hole transport layers. Reproduced with permission from Choi et al., 2013. **c** Schematic device structure used to fabricate Organic Photovoltaics (OPVs), (right) PV characteristic curve of reference (PCDBT:PC70BMPEDOT:PSS:PC70BM) device doped with Au NPs. Reproduced with permission from Tyagi et al., 2016

contributed to the final device performance [193]. In another study by the same group, when a Ag metal grating was integrated onto the top electrode, the SPR effect led to a broadening of light absorption resulting in an increase in PCE and EQE values [194]. Besides investigation of scattering effect of Au or Ag NPs in active layers (Fig. 30a, c), Park and Heeger groups further implemented UPS and XPS to study the electron transfer mechanism in OPVs [195, 196]. The MNPs act as some sort of electron transport barrier and instead acted as hole transporting layer thereby efficient hole extraction was possible in these device configurations. Mathews and Sum groups further utilized Au nanowires in plasmonic OPVs, wherein the thickness of HTL was controlled to allow the evanescent field to extend to photoactive layer [197]. Due to the high aspect ratio and anisotropic properties, the metal nanorods and nanowires like system provided a platform to further investigate the polarization dependent effect on photocurrent and PCE. It was by Kim et al. [195] who later investigated the importance of plasmonic NPs location within the OPV devices and reported that a device with Ag@SiO₂ situated between the HTL and active layer showed a higher efficiency than the device with the nanostructures located between the bottom electrode and HTL (Fig. 30b). The coupling effect was observed to be much stronger between the Ag NPs and active layer when they are in close contact with the maximum PCE value of 8.92%, an improvement in ~19% over the Ag NP free device.

Lately, with such a huge research interest globally in the field of perovskites based solar cells (PSCs), some of the recently developed approaches in efficient

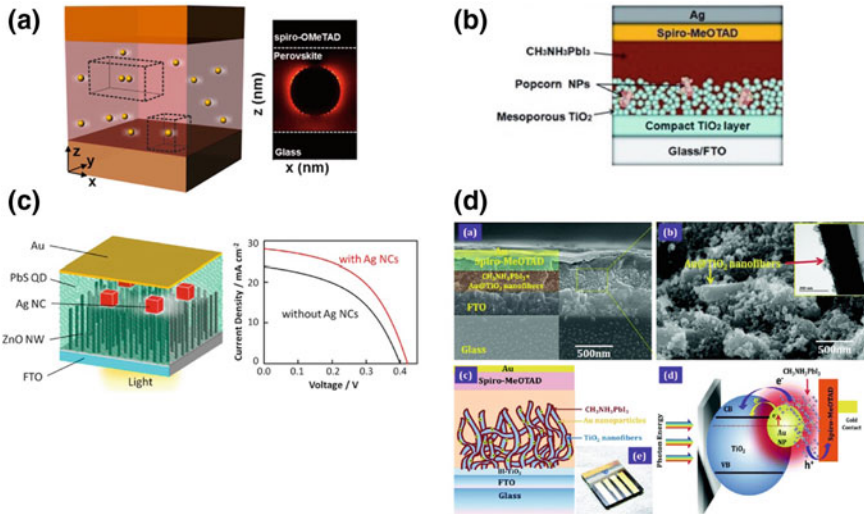


Fig. 31 a Schematics of a unit cell with dimensions $L_x \times L_y \times L_z$, of a glass–perovskite–SpiroOMeTAD system with plasmonic Au NPs embedded within the perovskite films show an absorption enhancement. Reproduced with permission from Palacios et al., 2015. **b** Schematic shows Plasmonic-enhanced perovskite solar cells using Au–Ag alloy popcorn nanoparticles. Reproduced with permission from Lu et al., 2015. **c** Schematic of a PbS QD/ZnO NW solar cell with embedded Ag NCs results in an improvement in PCE in BHJs Reproduced with permission from Kawawaki et al., 2015. **d** In situ processed gold nanoparticle-embedded TiO_2 nanofibers enabling plasmonic perovskite solar cells to exceed 14% conversion efficiency. Reproduced with permission from Mali et al., 2016

optical management have given efforts in exploiting the plasmonic effects in these classes of photovoltaic devices. PSCs are generally constructed based on an n-i-p and p-i-n architecture with the intrinsic active layer (organic/ inorganic lead halide based perovskites) embedded between the ETL and HTL. With an aim for a better optical (photon) management and achieving a higher performance device with improved device parameters (J_{SC} , V_{OC} , FF), it might be an interesting strategy to employ plasmonic NPs and exploit the plasmonic effects especially in semi-transparent solar cells. The improvement in optical absorption due to Au NPs within the PSC have been theoretically demonstrated by Carretero-Palacios et al. [198] wherein the plasmonic near-field enhancement and scattering effects were correlated as a function of NP size using FDTD (Finite Domain Time Difference) simulations (Fig. 31a).

In a recent study, electrospinning has been employed to fabricate in-situ Au-embedded TiO_2 nanofibers for plasmon-enhanced generation in PSCs [199]. The photovoltaic performance was enhanced in Au@ TiO_2 nanofiber based devices with a maximum photocurrent density of 21.63 mA cm^{-2} and PCE of 14.92%. In another report, Au-Ag alloy popcorn-shaped NPs [200] were employed in PSCs which lead to an increased performance resulting in an improvement in broadband

light absorption and efficient charge-transfer (Fig. 31b). Other attempts to improve the performance of plasmon mediated solar cells included Ag nanocubes embedded in a QD/ZnO nanowire [201] based bulk-heterojunction solar cell wherein, the location and stoichiometric amount of Ag nanocubes were controlled to enhance the photocurrent, particularly in the near-IR region (Fig. 31c). Implementation of metal NPs in other kind of CIGS solar cells has effectively improved the carrier transportation across the p-n junction by enhancing the absorption and carrier generation wherein the PCE has increased from 8.31% to 10.36% [202].

Having discussed the already explored numerous designs and architectures of plasmonic metal nanostructures being incorporated within the device active layer, embedded within the ETL or HTL or even used to modify the electrodes; there are still some inherent critical issues that is worth discussing here while rationally designing and fabricating plasmon mediated photovoltaics. Although with the capability of concentrating and trapping light through various mechanisms, there are several limitations when employing plasmonic NPs in the devices such as their physicochemical instability, charge recombination, narrowband absorption, plasmon radiative and non-radiative losses etc. that often hamper the long term performance of the as fabricated devices. In this final section, these currently existing problems will be comprehensively discussed and several points that need to be addressed.

First, the chemical and electrical stability must need to be guaranteed in these plasmon mediated photovoltaic devices. In order to do so, incorporation of various passivating layers such as silica, titania, and organic polymers on the surface of plasmonic nanostructures is an essential strategy to minimize any degradation or loss of plasmonic activity. Often these protective layers could simply resist against corrosion or prevent deterioration of charge separation and current collection capability of these metal NPs. In addition to this, they can also provide thermal and structural stability. However, when these additional protective layers are grown on the surface of plasmonic nanostructures, the crucial point to note is to take into consideration of other parameters like optimal thickness of the passivation layer that is required to maintain electrical or chemical stability, and inter-particle/ separation distance between the MNPs and the active photosensitizing layer and how it influence the electromagnetic field and plasmon-induced field enhancement factor.

Secondly, by now we already know that light harvesting efficiency can be improved by incorporating properly designed metal nanostructures into solar cells. Although taking into careful consideration of spectral overlap factor (between the SPR bands and the absorption spectrum of the photoactive material) and the efficiency of resonant energy transfer, it is equally important to tune the spectral position of the LSPR band (through proper size and shape control of the MNPs) in order to achieve a balanced light absorption. Tuning of LSPR band is not just because of the spectral overlap factor but also to extend the plasmonic response to a broader range by specifically improving the light absorption capability in the weakly absorbing regions of the solar spectrum. In this context, it is yet another feasible strategy to utilize the multiple plasmon modes (transverse, longitudinal) arising from anisotropic MNPs such as rods, nanowires, cubes, prisms etc.

In addition to just merely extending the absorption range all the way from UV-Vis to NIR from the multiple plasmon peaks, utilizing these kind of morphologies with sharp features like corners, edges additionally yield strong plasmonic field resulting in higher enhancement of electric fields, thereby boosting overall PCE of the devices.

Finally, let's discuss some of the future prospective approaches in the field of plasmon enhanced photovoltaics which could potentially open up not only exciting opportunities in all next generation hybrid photovoltaics with possibly new interesting features and capabilities, but at the same time will also allow us to further explore fundamental interaction mechanisms between the plasmon and exciton, therefore guiding us to rationally fabricate high performance plasmon based photovoltaic and optoelectronic devices. By far, most works until now have primarily focused on noble metals like Ag, Au, Cu which no doubt have contributed a significant growth in the field of plasmonic photovoltaics. However, recently there are many other alternative plasmonic materials such as Aluminum (Al), Aluminum Zinc Oxide (AZO), Gallium Zinc Oxide (GZO), Zirconium nitride (ZrN), Hafnium nitride (HfN) as well as non-noble metal based plasmonics like Graphene, alloys, Indium Tin oxide (ITO) etc. that have been recently proposed in addition to these conventional plasmonic NPs which could be potentially used in plasmon enhanced photovoltaics. Furthermore, dielectric NPs with sufficiently high permittivity and

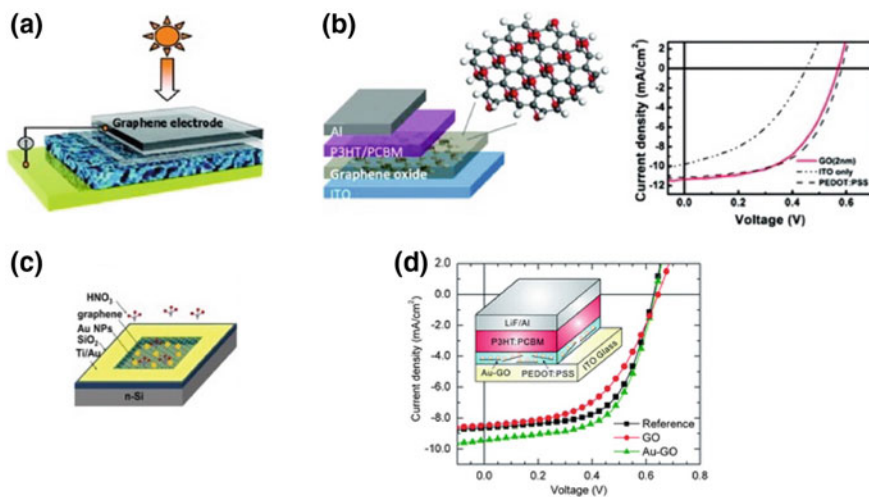


Fig. 32 **a** Illustration of dye-sensitized solar cell using graphene film as electrode, the four layers from bottom to top are Au, dye-sensitized heterojunction, compact TiO₂, and graphene film. Reproduced with permission from Wang et al., 2008. **b** Schematic of the photovoltaic device structure consisting of the following: ITO/GO (graphene oxide)/P3HT:PCBM/Al and PV characteristic curve with enhanced current density when GO being used as HTL. Reproduced with permission from Li et al., 2010. **c** Incorporation of Au-GOs into the anodic buffer layer (PEDOT:PSS) resulted in highly efficient plasmon enhanced solar cells. Reproduced with permission from Fan et al., 2012

low dissipation level can also result in certain degree of improvement in thin film semi-transparent solar cells. In order to achieve higher enhancement and increase PCE in these devices, the dielectric materials should have a low dissipation, low dispersion and high permittivity such as SiO_2 , SiC , TiO_2 etc. Graphene plasmonics is a rapidly emerging field ever since its experimental discovery and because of its immense potential in the field of electronics, photonics, telecommunication and optoelectronics. As such, the light-matter interaction in graphene has a promising prospect in the field of photovoltaics. The PCE of solar cells can be improved by exploiting dual coupling effect from metal as well as graphene plasmons. There are already few reports that are existing where graphene has been implemented as transparent electrodes, as well as component in HTL in OPV or even as interface modifiers in Si solar cells. So far, there has been several efforts in trying to utilize the synergetic effect by incorporating an ensemble/bulk graphene and metal nanostructures in photovoltaics. Figure 32 exhibit incorporation of different graphene, and graphene-oxide materials either in the form of electrodes or embedded within the active layer of the devices [203–206].

In addition to these examples, recently there has been a few reports where plasmon upconversion coupling effect has been implemented to produce photons with a higher energy through sequential absorption of two or more lower energy photons. Incorporating plasmonic nanoparticles within the cells as solar upconverters has been expected to enhance the performance. Lanthanide ion doped oxides whose emission wavelength overlap with the SPR frequency of MNPs will enable an increment in plasmon resonance energy transfer (PRET) process, thereby the resultant EM field could be strengthened, subsequently showing certain degree of improvement in photoconversion efficiency [207].

9 Concluding Remarks (Outlook and Perspective)

In this chapter, a fundamental background on plasmonics and excitonics has been introduced concisely followed by an in-depth discussion on various top-down and bottom-up based fabrication methodologies of metal nanoparticles, semiconducting nanocrystals and metal-semiconductor hybrid nanoheterostructures. Furthermore, some of the most frequently used state of the art structural, electrical and optical characterization tools along with their corresponding working principles that are essential for materials design and device fabrication have been discussed. The latter half of the chapter uncovers some of the most advanced solution and substrate based design strategies for manufacturing hybrid plasmon based metal-semiconductor nanoassemblies which are being currently employed in the form of either electrodes or photosensitive (active) layer in most currently available photovoltaic and optoelectronic devices. Additionally, a comprehensive survey to various operational mechanisms (mode of plasmon-exciton interaction) that are often encountered between the metal NPs and the photoactive fluorophores (dye, quantum dots) when incorporated within the device has been laid out which would

give an overview to the readers who would be interested to rationally design and further explore plasmon mediated/ enhanced energy and storage devices and their operational mechanisms. Although, to enhance the performance of these devices, further research needs to be extensively continued in the following directions. By now, we have realized that plasmonic effect could be an interesting means to improve the solar cell functionality and improve the overall device performance by exploiting their fascinating optical properties derived from the mutual coexistence of electrons and photons upon interaction with electromagnetic light and when confined in nano-dimensional spaces. In this regard, recently there has been active interest to develop inexpensive methods and fabricate viable plasmon mediated hybrid photovoltaic devices using solution processed metal NPs and semiconducting nanocrystals and their self-assemblies and further tailor the patterning to optimally tune the plasmonic functionality when embedded within the devices. However, the degree of improvement in the efficiency gained as a result of active incorporation of these plasmonic metal nanostructures may vary widely and depend critically on several important parameters (dimension, morphology, material composition, processing conditions, photochemical stability, location within the devices etc.) that need to be further optimized every time by taking into consideration all these variables that typically affect the overall performance of the devices.

Finally, to summarize, it is worthwhile mentioning that it is still a challenge to establish a unified approach for designing plasmonic solar cells which would yield the best performance, especially with all the necessary elements of the cell that all researchers working in this area need to consider for building any target-oriented solar cell types. However, with many new alternative plasmonic materials (plasmonic upconverters, graphene and 2D materials) that are frequently emerging, thanks to the material synthetic chemists, it is quite beneficial for most solar cell device engineers to come up with more creative solutions of fabricating next generation hybrid plasmon mediated energy devices. Additionally, in order for successful device fabrication, it is imperative to have a clear theoretical understanding and background on mechanisms (near field effects and electromagnetic field enhancement affecting exciton emission decay dynamics) involving manipulation of exciton and multiexciton efficiency of active layers (quantum dots, dyes, semiconducting polymers) due to various plasmonic nanostructures to be incorporated in these devices. However, much effort is still required to better comprehend the mode of interactions in hybrid plasmonic/excitonic systems and what regulates the strength of plexcitonic interaction and consequences in affecting the optical behavior and in turn the overall performance of the devices. Development of new synthetic methods with advanced material (and device) characterization tools are the key to answer these fundamental questions. With such a thorough understanding of these physical interaction processes, it is surely expected that hybrid metal/semiconductor heterosystems will potentially be the primary materials to be incorporated in all next generation hybrid plasmon mediated photovoltaic and optoelectronic devices and thereby transforming the key areas of renewable energy technologies.

References

1. Leonhardt, U.: Invisibility cup. *Nat. Photonics* **1**, 207–208 (2007). <https://doi.org/10.1038/nphoton.2007.38>
2. Freestone, I., Meeks, N., Sax, M., Higgitt, C.: The Lycurgus cup—a Roman nanotechnology. *Gold Bull.* **40**, 270–277 (2007). <https://doi.org/10.1007/BF03215599>
3. Sciau, P., Mirguet, C., Roucau, C., et al.: Double nanoparticle layer in a 12th century lustreware decoration: accident or technological mastery? *J. Nano Res.* **8**, 133–139 (2009). <https://doi.org/10.4028/www.scientific.net/JNanoR.8.133>
4. Heiligtag, F.J., Niederberger, M.: The fascinating world of nanoparticle research. *Mater. Today* **16**, 262–271 (2013). <https://doi.org/10.1016/j.mattod.2013.07.004>
5. Jana, J., Ganguly, M., Pal, T.: Enlightening surface plasmon resonance effect of metal nanoparticles for practical spectroscopic application. *RSC Adv.* **6**, 86174–86211 (2016). <https://doi.org/10.1039/C6RA14173K>
6. Willets, K.A., Van Duyne, R.P.: Localized surface plasmon resonance spectroscopy and sensing. *Annu. Rev. Phys. Chem.* **58**, 267–297 (2007). <https://doi.org/10.1146/annurev.physchem.58.032806.104607>
7. Petryayeva, E., Krull, U.J.: Localized surface plasmon resonance: nanostructures, bioassays and biosensing—a review. *Anal. Chim. Acta* **706**, 8–24 (2011). <https://doi.org/10.1016/j.aca.2011.08.020>
8. Zhang, J.Z., Noguez, C.: Plasmonic optical properties and applications of metal nanostructures. *Plasmonics* **3**, 127–150 (2008). <https://doi.org/10.1007/s11468-008-9066-y>
9. Mie, G.: Beiträge zur Optik trüber Medien, speziell kolloidaler Metallösungen. *Ann. Phys.* **330**, 377–445 (1908). <https://doi.org/10.1002/andp.19083300302>
10. Gans, R.: Über die Form ultramikroskopischer Goldteilchen. *Ann. Phys.* **342**, 881–900 (1912). <https://doi.org/10.1002/andp.19123420503>
11. Gans, R.: Über die Form ultramikroskopischer Silberteilchen. *Ann. Phys.* **352**, 270–284 (1915). <https://doi.org/10.1002/andp.19153521006>
12. Odom, T.W., Schatz, G.C.: Introduction to plasmonics. *Chem. Rev.* **111**, 3667–3668 (2011). <https://doi.org/10.1021/cr2001349>
13. Johnson, P.B., Christy, R.W.: Optical constants of the noble metals. *Phys. Rev. B* **6**, 4370–4379 (1972). <https://doi.org/10.1103/PhysRevB.6.4370>
14. Litinskaya MBT-RM in MS and ME: Polaritons★. Elsevier (2019)
15. Fukui, M., Okamoto, T., Haraguchi, M.: Chapter 3—linear and nonlinear optical response of concentric metallic nanoshells. In: Kawata, S., Masuhara HBT-HN (eds.) *Nanoplasmonics*, pp. 31–54. Elsevier (2006)
16. Wang, X., Deng, Y., Li, Q., et al.: Excitation and propagation of surface plasmon polaritons on a non-structured surface with a permittivity gradient. *Light Sci. Appl.* **5**, e16179–e16179 (2016). <https://doi.org/10.1038/lsa.2016.179>
17. Ashoori, R.C.: Electrons in artificial atoms. *Nature* **379**, 413–419 (1996). <https://doi.org/10.1038/379413a0>
18. Henini, M.: Quantum dot nanostructures. *Mater. Today* **5**, 48–53 (2002). [https://doi.org/10.1016/S1369-7021\(02\)00639-9](https://doi.org/10.1016/S1369-7021(02)00639-9)
19. Brus, L.E.: Electron–electron and electron-hole interactions in small semiconductor crystallites: the size dependence of the lowest excited electronic state. *J. Chem. Phys.* **80**, 4403–4409 (1984). <https://doi.org/10.1063/1.447218>
20. Brus, L.: Zero-dimensional “excitons” in semiconductor clusters. *IEEE J. Quant. Electron.* **22**, 1909–1914 (1986). <https://doi.org/10.1109/JQE.1986.1073184>
21. Bawendi, M.G., Carroll, P.J., Wilson, W.L., Brus, L.E.: Luminescence properties of CdSe quantum crystallites: resonance between interior and surface localized states. *J. Chem. Phys.* **96**, 946–954 (1992). <https://doi.org/10.1063/1.462114>
22. Brus, L.: Quantum crystallites and nonlinear optics. *Appl. Phys. A* **53**, 465–474 (1991). <https://doi.org/10.1007/BF00331535>

23. Brus, L.: Electronic wave functions in semiconductor clusters: experiment and theory. *J. Phys. Chem.* **90**, 2555–2560 (1986). <https://doi.org/10.1021/j100403a003>
24. Bagga, A., Chattopadhyay, P.K., Ghosh, S.: Stokes shift in quantum dots: origin of dark exciton. In: 2007 International Workshop on Physics of Semiconductor Devices. pp. 876–879 (2007)
25. Wannier, G.H.: The structure of electronic excitation levels in insulating crystals. *Phys. Rev.* **52**, 191–197 (1937). <https://doi.org/10.1103/PhysRev.52.191>
26. Frenkel, J.: On the transformation of light into heat in solids. I. *Phys. Rev.* **37**, 17–44 (1931). <https://doi.org/10.1103/PhysRev.37.17>
27. Knoester, J., Agranovich, V.M.: (2003) Frenkel and charge-transfer excitons in organic solids. In: *Electronic Excitations in Organic Nanostructures*, pp. 1–96. Academic Press
28. Mandal, S., Selvakannan, P.R., Pasricha, R., Sastry, M.: Keggin Ions as UV-switchable reducing agents in the synthesis of Au Core–Ag shell nanoparticles. *J. Am. Chem. Soc.* **125**, 8440–8441 (2003). <https://doi.org/10.1021/ja034972t>
29. Taton, T.A., Mirkin, C.A., Letsinger, R.L.: Scanometric DNA array detection with nanoparticle probes. *Science* (80-) **289**, 1757–1760 (2000). <https://doi.org/10.1126/science.289.5485.1757>
30. Kamat, P.V.: Photophysical, photochemical and photocatalytic aspects of metal nanoparticles. *J. Phys. Chem. B* **106**, 7729–7744 (2002). <https://doi.org/10.1021/jp0209289>
31. Elghanian, R., Storhoff, J.J., Mucic, R.C., et al.: Selective colorimetric detection of polynucleotides based on the distance-dependent optical properties of gold nanoparticles. *Science* (80-) **277**, 1078–1081 (1997). <https://doi.org/10.1126/science.277.5329.1078>
32. Link, S., Burda, C., Nikoobakht, B., El-Sayed, M.A.: How long does it take to melt a gold nanorod?: a femtosecond pump–probe absorption spectroscopy study. *Chem. Phys. Lett.* **315**, 12–18 (1999). [https://doi.org/10.1016/S0009-2614\(99\)01214-2](https://doi.org/10.1016/S0009-2614(99)01214-2)
33. Ahmadi, T.S., Wang, Z.L., Green, T.C., et al.: Shape-controlled synthesis of colloidal platinum nanoparticles. *Science* (80-) **272**, 1924–1925 (1996). <https://doi.org/10.1126/science.272.5270.1924>
34. Chen, H.M., Liu, R.-S.: Architecture of metallic nanostructures: synthesis strategy and specific applications. *J. Phys. Chem. C* **115**, 3513–3527 (2011). <https://doi.org/10.1021/jp108403r>
35. Jeevanandam, J., Barhoum, A., Chan, Y.S., et al.: Review on nanoparticles and nanostructured materials: history, sources, toxicity and regulations. *Beilstein J. Nanotechnol.* **9**, 1050–1074 (2018). <https://doi.org/10.3762/bjnano.9.98>
36. Hunt, E.M., Hampikian, J.M.: Ion implantation-induced nanoscale particle formation in Al₂O₃ and SiO₂ via reduction. *Acta Mater.* **47**, 1497–1511 (1999). [https://doi.org/10.1016/S1359-6454\(99\)00028-2](https://doi.org/10.1016/S1359-6454(99)00028-2)
37. Hunt, E.M., Hampikian, J.M.: Implantation parameters affecting aluminum nano-particle formation in alumina. *J. Mater. Sci.* **36**, 1963–1973 (2001). <https://doi.org/10.1023/A:1017562311310>
38. McHargue, C.J., Ren, S.X., Hunn, J.D.: Nanometer-size dispersions of iron in sapphire prepared by ion implantation and annealing. *Mater. Sci. Eng. A* **253**, 1–7 (1998). [https://doi.org/10.1016/S0921-5093\(98\)00722-9](https://doi.org/10.1016/S0921-5093(98)00722-9)
39. Sharma, S.K., Pujari, P.K.: Embedded Si nanoclusters in α -alumina synthesized by ion implantation: an investigation using depth dependent Doppler broadening spectroscopy. *J. Alloys Compd.* **715**, 247–253 (2017). <https://doi.org/10.1016/j.jallcom.2017.04.285>
40. Sigmund, P.: Mechanisms and theory of physical sputtering by particle impact. *Nucl. Instrum. Methods Phys. Res. Sect. B Beam Interact Mater. Atoms* **27**, 1–20 (1987). [https://doi.org/10.1016/0168-583X\(87\)90004-8](https://doi.org/10.1016/0168-583X(87)90004-8)
41. Thompson, M.W.: II. The energy spectrum of ejected atoms during the high energy sputtering of gold. *Philos. Mag. A J. Theor. Exp. Appl. Phys.* **18**, 377–414 (1968). <https://doi.org/10.1080/14786436808227358>

42. Rashid, J., Barakat, M.A., Salah, N., Habib, S.S.: ZnO-nanoparticles thin films synthesized by RF sputtering for photocatalytic degradation of 2-chlorophenol in synthetic wastewater. *J. Ind. Eng. Chem.* **23**, 134–139 (2015). <https://doi.org/10.1016/j.jiec.2014.08.006>
43. Fumitaka, Mafuné, Kohno, J., Takeda, Y., et al.: Formation and size control of silver nanoparticles by laser ablation in aqueous solution. *J. Phys. Chem. B* **104**, 9111–9117 (2000). <https://doi.org/10.1021/jp001336y>
44. Kudryashov, I.S., Samokhvalov, A.A., Nastulyavichus, A.A., et al.: Nanosecond-laser generation of nanoparticles in liquids: from ablation through bubble dynamics to nanoparticle yield. *Materials* **12** (2019)
45. Ganjali, M., Vahdatkhah, P., Marashi, S.M.B.: Synthesis of Ni nanoparticles by pulsed laser ablation method in liquid phase. *Proc. Mater. Sci.* **11**, 359–363 (2015). <https://doi.org/10.1016/j.mspro.2015.11.127>
46. Matsubara, M., Yamaki, T., Itoh, H., et al.: Preparation of TiO₂ nanoparticles by pulsed laser ablation: ambient pressure dependence of crystallization. *Jpn. J. Appl. Phys.* **42**, L479–L481 (2003). <https://doi.org/10.1143/jjap.42.L479>
47. Tsai, S.C., Song, Y.L., Tsai, C.S., et al.: Ultrasonic spray pyrolysis for nanoparticles synthesis. *J. Mater. Sci.* **39**, 3647–3657 (2004). <https://doi.org/10.1023/B:JMSE.0000030718.76690.11>
48. Gavrilović, T.V., Jovanović, D.J., Dramićanin, M.D.: Chapter 2—synthesis of multifunctional inorganic materials: from micrometer to nanometer dimensions. In: Bhanvase, B.A., Pawade, V.B., Dhoble, S.J., et al. (eds.) *Micro and Nano Technologies*, pp 55–81. Elsevier (2018)
49. Gröhn, A.J., Pratsinis, S.E., Sánchez-Ferrer, A., et al.: Scale-up of nanoparticle synthesis by flame spray pyrolysis: the high-temperature particle residence time. *Ind. Eng. Chem. Res.* **53**, 10734–10742 (2014). <https://doi.org/10.1021/ie501709s>
50. Sunkari, S., Gangapuram, B.R., Dadigala, R., et al.: Microwave-irradiated green synthesis of gold nanoparticles for catalytic and anti-bacterial activity. *J. Anal. Sci. Technol.* **8**, 13 (2017). <https://doi.org/10.1186/s40543-017-0121-1>
51. Milkin, S.S., Starodubov, A.V., Herman, S.V., et al.: On the interaction of electromagnetic microwave radiation with emulsion containing magnetic nanoparticles. In: 2014 24th International Crimean Conference Microwave & Telecommunication Technology, pp. 968–969 (2014)
52. Sander, M.S., Gao, H.: aligned arrays of nanotubes and segmented nanotubes on substrates fabricated by electrodeposition onto nanorods. *J. Am. Chem. Soc.* **127**, 12158–12159 (2005). <https://doi.org/10.1021/ja0522231>
53. Maillard, M., Giorgio, S., Pileni, M.-P.: Silver nanodisks. *Adv. Mater.* **14**, 1084–1086 (2002). [https://doi.org/10.1002/1521-4095\(20020805\)14:15%3c1084:AID-ADMA1084%3e3.0.CO;2-L](https://doi.org/10.1002/1521-4095(20020805)14:15%3c1084:AID-ADMA1084%3e3.0.CO;2-L)
54. Toneguzzo, P., Viau, G., Acher, O., et al.: CoNi and FeCoNi fine particles prepared by the polyol process: physico-chemical characterization and dynamic magnetic properties. *J. Mater. Sci.* **35**, 3767–3784 (2000). <https://doi.org/10.1023/A:1004864927169>
55. Yener, D.O., Sindel, J., Randall, C.A., Adair, J.H.: Synthesis of nanosized silver platelets in octylamine-water bilayer systems. *Langmuir* **18**, 8692–8699 (2002). <https://doi.org/10.1021/la011229a>
56. Murphy, C.J., Sau, T.K., Gole, A.M., et al.: Anisotropic metal nanoparticles: synthesis, assembly, and optical applications. *J. Phys. Chem. B* **109**, 13857–13870 (2005). <https://doi.org/10.1021/jp0516846>
57. Huang, L.M., Wang, H.T., Wang, Z.B., et al.: Nanowire arrays electrodeposited from liquid crystalline phases. *Adv. Mater.* **14**, 61–64 (2002). [https://doi.org/10.1002/1521-4095\(20020104\)14:1%3c61:AID-ADMA61%3e3.0.CO;2-Y](https://doi.org/10.1002/1521-4095(20020104)14:1%3c61:AID-ADMA61%3e3.0.CO;2-Y)
58. Whitney, T.M., Searson, P.C., Jiang, J.S., Chien, C.L.: Fabrication and magnetic properties of arrays of metallic nanowires. *Science (80-)* **261**, 1316–1319 (1993). <https://doi.org/10.1126/science.261.5126.1316>

59. Murphy, C.J., Gole, A.M., Hunyadi, S.E., Orendorff, C.J.: One-dimensional colloidal gold and silver nanostructures. *Inorg. Chem.* **45**, 7544–7554 (2006). <https://doi.org/10.1021/ic0519382>
60. Nicewarner-Peña, S.R., Freeman, R.G., Reiss, B.D., et al.: Submicrometer metallic barcodes. *Science* (80-) **294**, 137–141 (2001). <https://doi.org/10.1126/science.294.5540.137>
61. Wiley, B., Sun, Y., Mayers, B., Xia, Y.: Shape-controlled synthesis of metal nanostructures: the case of silver. *Chem.—Eur. J.* **11**, 454–463 (2005). <https://doi.org/10.1002/chem.200400927>
62. Sun, Y., Xia, Y.: Large-scale synthesis of uniform silver nanowires through a soft, self-seeding, polyol process. *Adv. Mater.* **14**, 833–837 (2002). [https://doi.org/10.1002/1521-4095\(20020605\)14:11%3c833::AID-ADMA833%3e3.0.CO;2-K](https://doi.org/10.1002/1521-4095(20020605)14:11%3c833::AID-ADMA833%3e3.0.CO;2-K)
63. Sun, Y., Xia, Y.: Multiple-walled nanotubes made of metals. *Adv. Mater.* **16**, 264–268 (2004). <https://doi.org/10.1002/adma.200305780>
64. Lee, J.S., Suh, J.S.: Uniform field emission from aligned carbon nanotubes prepared by CO disproportionation. *J. Appl. Phys.* **92**, 7519–7522 (2002). <https://doi.org/10.1063/1.1525063>
65. Sun, Y., Xia, Y.: Triangular nanoplates of silver: synthesis, characterization, and use as sacrificial templates for generating triangular nanorings of gold. *Adv. Mater.* **15**, 695–699 (2003). <https://doi.org/10.1002/adma.200304652>
66. Sun, Y., Xia, Y.: Mechanistic Study on the replacement reaction between silver nanostructures and chloroauric acid in aqueous medium. *J. Am. Chem. Soc.* **126**, 3892–3901 (2004). <https://doi.org/10.1021/ja039734c>
67. Sun, Y., Xia, Y.: Shape-controlled synthesis of gold and silver nanoparticles. *Science* (80-) **298**, 2176–2179 (2002). <https://doi.org/10.1126/science.1077229>
68. Sun, Y., Xia, Y.: Alloying and dealloying processes involved in the preparation of metal nanoshells through a galvanic replacement reaction. *Nano Lett.* **3**, 1569–1572 (2003). <https://doi.org/10.1021/nl034765r>
69. Sun, Y., Mayers, B., Xia, Y.: Metal nanostructures with hollow interiors. *Adv. Mater.* **15**, 641–646 (2003). <https://doi.org/10.1002/adma.200301639>
70. Sun, Y., Mayers, B.T., Xia, Y.: Template-engaged replacement reaction: a one-step approach to the large-scale synthesis of metal nanostructures with hollow interiors. *Nano Lett.* **2**, 481–485 (2002). <https://doi.org/10.1021/nl025531v>
71. Frens, G.: Controlled nucleation for the regulation of the particle size in monodisperse gold suspensions. *Nat. Phys. Sci.* **241**, 20–22 (1973). <https://doi.org/10.1038/physci241020a0>
72. Pong, B.-K., Elim, H.I., Chong, J.-X., et al.: New insights on the nanoparticle growth mechanism in the citrate reduction of Gold(III) salt: formation of the Au nanowire intermediate and its nonlinear optical properties. *J. Phys. Chem. C* **111**, 6281–6287 (2007). <https://doi.org/10.1021/jp068666o>
73. Kimling, J., Maier, M., Okenve, B., et al.: Turkevich method for gold nanoparticle synthesis revisited. *J. Phys. Chem. B* **110**, 15700–15707 (2006). <https://doi.org/10.1021/jp061667w>
74. Frens, G.: Particle size and sol stability in metal colloids. *Kolloid-Zeitschrift und Zeitschrift für Polym* **250**, 736–741 (1972). <https://doi.org/10.1007/BF01498565>
75. Turkevich, J., Stevenson, P.C., Hillier, J.: A study of the nucleation and growth processes in the synthesis of colloidal gold. *Discuss. Faraday Soc.* **11**, 55–75 (1951). <https://doi.org/10.1039/DF9511100055>
76. Larm, N.E., Essner, J.B., Pokpas, K., et al.: Room-temperature Turkevich method: formation of gold nanoparticles at the speed of mixing using cyclic oxocarbon reducing agents. *J. Phys. Chem. C* **122**, 5105–5118 (2018). <https://doi.org/10.1021/acs.jpcc.7b10536>
77. Sajanlal, P.R., Sreeprasad, T.S., Samal, A.K., Pradeep, T.: Anisotropic nanomaterials: structure, growth, assembly, and functions. *Nano Rev.* **2**, 5883 (2011). <https://doi.org/10.3402/nano.v2i0.5883>
78. Wiley, B., Sun, Y., Xia, Y.: Synthesis of Silver nanostructures with controlled shapes and properties. *Acc. Chem. Res.* **40**, 1067–1076 (2007). <https://doi.org/10.1021/ar7000974>

79. Phiri, M.M., Mulder, D.W., Vorster, B.C.: Seedless gold nanostars with seed-like advantages for biosensing applications. *R. Soc. Open Sci.* **6**, 181971 (2019). <https://doi.org/10.1098/rsos.181971>
80. Liu, B., Zeng, H.C.: Fabrication of ZnO “Dandelions” via a modified Kirkendall process. *J. Am. Chem. Soc.* **126**, 16744–16746 (2004). <https://doi.org/10.1021/ja044825a>
81. Yang, H.G., Zeng, H.C.: Preparation of hollow anatase TiO₂ nanospheres via Ostwald ripening. *J. Phys. Chem. B* **108**, 3492–3495 (2004). <https://doi.org/10.1021/jp0377782>
82. Yin, Y., Rioux, R.M., Erdonmez, C.K., et al.: Formation of hollow nanocrystals through the nanoscale Kirkendall effect. *Science* (80-) **304**, 711–714 (2004). <https://doi.org/10.1126/science.1096566>
83. Chang, Y., Lye, M.L., Zeng, H.C.: Large-scale synthesis of high-quality ultralong copper nanowires. *Langmuir* **21**, 3746–3748 (2005). <https://doi.org/10.1021/la050220w>
84. Zeng, H.C.: Synthetic architecture of interior space for inorganic nanostructures. *J. Mater. Chem.* **16**, 649–662 (2006). <https://doi.org/10.1039/B511296F>
85. Brust, M., Fink, J., Bethell, D., et al.: Synthesis and reactions of functionalised gold nanoparticles. *J. Chem. Soc. Chem. Commun.*, 1655–1656 (1995). <https://doi.org/10.1039/C39950001655>
86. da Silva, A.G.M., Rodrigues, T.S., Haigh, S.J., Camargo, P.H.C.: Galvanic replacement reaction: recent developments for engineering metal nanostructures towards catalytic applications. *Chem. Commun.* **53**, 7135–7148 (2017). <https://doi.org/10.1039/C7CC02352A>
87. Bansal, V., O’Mullane, A.P., Bhargava, S.K.: Galvanic replacement mediated synthesis of hollow Pt nanocatalysts: significance of residual Ag for the H₂ evolution reaction. *Electrochem. Commun.* **11**, 1639–1642 (2009). <https://doi.org/10.1016/j.elecom.2009.06.018>
88. Chen, H.M., Liu, R.-S., Lo, M.-Y., et al.: Hollow platinum spheres with nano-channels: synthesis and enhanced catalysis for oxygen reduction. *J. Phys. Chem. C* **112**, 7522–7526 (2008). <https://doi.org/10.1021/jp8017698>
89. Liu, X., Wang, D., Li, Y.: Synthesis and catalytic properties of bimetallic nanomaterials with various architectures. *Nano Today* **7**, 448–466 (2012). <https://doi.org/10.1016/j.nantod.2012.08.003>
90. Teng, X., Wang, Q., Liu, P., et al.: Formation of Pd/Au nanostructures from pd nanowires via galvanic replacement reaction. *J. Am. Chem. Soc.* **130**, 1093–1101 (2008). <https://doi.org/10.1021/ja077303e>
91. Cobby, C.M., Xia, Y.: Engineering the properties of metal nanostructures via galvanic replacement reactions. *Mater. Sci. Eng. R. Rep.* **70**, 44–62 (2010). <https://doi.org/10.1016/j.mser.2010.06.002>
92. Talapin, D.V., Lee, J.-S., Kovalenko, M.V., Shevchenko, E.V.: Prospects of colloidal nanocrystals for electronic and optoelectronic applications. *Chem. Rev.* **110**, 389–458 (2010). <https://doi.org/10.1021/cr900137k>
93. Somers, R.C., Bawendi, M.G., Nocera, D.G.: CdSe nanocrystal based chem-/bio- sensors. *Chem. Soc. Rev.* **36**, 579–591 (2007). <https://doi.org/10.1039/B517613C>
94. Peng, X., Chen, J., Misewich, J.A., Wong, S.S.: Carbon nanotube–nanocrystal heterostructures. *Chem. Soc. Rev.* **38**, 1076–1098 (2009). <https://doi.org/10.1039/B811424M>
95. Rogach, A.L., Klar, T.A., Lupton, J.M., et al.: Energy transfer with semiconductor nanocrystals. *J. Mater. Chem.* **19**, 1208–1221 (2009). <https://doi.org/10.1039/B812884G>
96. Frey, N.A., Peng, S., Cheng, K., Sun, S.: Magnetic nanoparticles: synthesis, functionalization, and applications in bioimaging and magnetic energy storage. *Chem. Soc. Rev.* **38**, 2532–2542 (2009). <https://doi.org/10.1039/B815548H>
97. de Mello, Donegá C., Liljeroth, P., Vanmaekelbergh, D.: physicochemical evaluation of the hot-injection method, a synthesis route for monodisperse nanocrystals. *Small* **1**, 1152–1162 (2005). <https://doi.org/10.1002/sml.200500239>
98. Nie, Z., Petukhova, A., Kumacheva, E.: Properties and emerging applications of self-assembled structures made from inorganic nanoparticles. *Nat. Nanotechnol.* **5**, 15–25 (2010). <https://doi.org/10.1038/nnano.2009.453>

99. Hillhouse, H.W., Beard, M.C.: Solar cells from colloidal nanocrystals: fundamentals, materials, devices, and economics. *Curr. Opin. Colloid Interface Sci.* **14**, 245–259 (2009). <https://doi.org/10.1016/j.cocis.2009.05.002>
100. Konstantatos, G., Sargent, E.H.: Nanostructured materials for photon detection. *Nat. Nanotechnol.* **5**, 391–400 (2010). <https://doi.org/10.1038/nnano.2010.78>
101. van Sark, W.G.J.H.M., Barnham, K.W.J., Slooff, L.H., et al.: Luminescent solar concentrators—a review of recent results. *Opt. Express* **16**, 21773–21792 (2008). <https://doi.org/10.1364/OE.16.021773>
102. Holder, E., Tessler, N., Rogach, A.L.: Hybrid nanocomposite materials with organic and inorganic components for opto-electronic devices. *J. Mater. Chem.* **18**, 1064–1078 (2008). <https://doi.org/10.1039/B712176H>
103. Wood, V., Panzer, M.J., Caruge, J.-M., et al.: Air-stable operation of transparent, colloidal quantum dot based LEDs with a unipolar device architecture. *Nano Lett.* **10**, 24–29 (2010). <https://doi.org/10.1021/nl902425g>
104. Michalet, X., Pinaud, F.F., Bentolila, L.A., et al.: Quantum dots for live cells, in vivo imaging, and diagnostics. *Science (80-)* **307**, 538–544 (2005). <https://doi.org/10.1126/science.1104274>
105. Robinson, R.D., Sadtler, B., Demchenko, D.O., et al.: Spontaneous superlattice formation in nanorods through partial cation exchange. *Science (80-)* **317**, 355–358 (2007). <https://doi.org/10.1126/science.1142593>
106. Milliron, D.J., Hughes, S.M., Cui, Y., et al.: Colloidal nanocrystal heterostructures with linear and branched topology. *Nature* **430**, 190–195 (2004). <https://doi.org/10.1038/nature02695>
107. Mokari, T., Rothenberg, E., Popov, I., et al.: Selective growth of metal tips onto semiconductor quantum rods and tetrapods. *Science (80-)* **304**, 1787–1790 (2004). <https://doi.org/10.1126/science.1097830>
108. Talapin, D.V., Nelson, J.H., Shevchenko, E.V., et al.: Seeded growth of highly luminescent CdSe/CdS nanoheterostructures with rod and tetrapod morphologies. *Nano Lett.* **7**, 2951–2959 (2007). <https://doi.org/10.1021/nl072003g>
109. Steiner, D., Dorfs, D., Banin, U., et al.: Determination of band offsets in heterostructured colloidal nanorods using scanning tunneling spectroscopy. *Nano Lett.* **8**, 2954–2958 (2008). <https://doi.org/10.1021/nl801848x>
110. Reiss, P., Protière, M., Li, L.: Core/Shell semiconductor nanocrystals. *Small* **5**, 154–168 (2009). <https://doi.org/10.1002/sml.200800841>
111. Cozzoli, P.D., Pellegrino, T., Manna, L.: Synthesis, properties and perspectives of hybrid nanocrystal structures. *Chem. Soc. Rev.* **35**, 1195–1208 (2006). <https://doi.org/10.1039/B517790C>
112. Costi, R., Saunders, A.E., Banin, U.: Colloidal hybrid nanostructures: a new type of functional materials. *Angew Chemie Int. Ed.* **49**, 4878–4897 (2010). <https://doi.org/10.1002/anie.200906010>
113. Casavola, M., Buonsanti, R., Caputo, G., Cozzoli, P.D.: Colloidal strategies for preparing oxide-based hybrid nanocrystals. *Eur. J. Inorg. Chem.* **2008**, 837–854 (2008). <https://doi.org/10.1002/ejic.200701047>
114. de Mello Donegá, C.: Synthesis and properties of colloidal heteronanocrystals. *Chem. Soc. Rev.* **40**, 1512–1546 (2011). <https://doi.org/10.1039/C0CS00055H>
115. Koole, R., Luijckes, B., Tachiya, M., et al.: Differences in cross-link chemistry between rigid and flexible dithiol molecules revealed by optical studies of CdTe quantum dots. *J. Phys. Chem. C* **111**, 11208–11215 (2007). <https://doi.org/10.1021/jp072407x>
116. Kairdolf, B.A., Smith, A.M., Nie, S.: One-pot synthesis, encapsulation, and solubilization of size-tuned quantum dots with amphiphilic multidentate ligands. *J. Am. Chem. Soc.* **130**, 12866–12867 (2008). <https://doi.org/10.1021/ja804755q>
117. Yu, W.W., Wang, Y.A., Peng, X.: Formation and stability of size-, shape-, and structure-controlled CdTe nanocrystals: ligand effects on monomers and nanocrystals. *Chem. Mater.* **15**, 4300–4308 (2003). <https://doi.org/10.1021/cm034729t>

118. Qu, L., Peng, X.: Control of photoluminescence properties of CdSe nanocrystals in growth. *J. Am. Chem. Soc.* **124**, 2049–2055 (2002). <https://doi.org/10.1021/ja017002j>
119. Peng, Z.A., Peng, X.: Nearly monodisperse and shape-controlled CdSe nanocrystals via alternative routes: nucleation and growth. *J. Am. Chem. Soc.* **124**, 3343–3353 (2002). <https://doi.org/10.1021/ja0173167>
120. Peng, Z.A., Peng, X.: Mechanisms of the shape evolution of CdSe nanocrystals. *J. Am. Chem. Soc.* **123**, 1389–1395 (2001). <https://doi.org/10.1021/ja0027766>
121. Peng, Z.A., Peng, X.: Formation of high-quality CdTe, CdSe, and CdS nanocrystals using CdO as precursor. *J. Am. Chem. Soc.* **123**, 183–184 (2001). <https://doi.org/10.1021/ja003633m>
122. Peng, X., Wickham, J., Alivisatos, A.P.: Kinetics of II-VI and III-V colloidal semiconductor nanocrystal growth: “focusing” of size distributions. *J. Am. Chem. Soc.* **120**, 5343–5344 (1998). <https://doi.org/10.1021/ja9805425>
123. Peng, X., Manna, L., Yang, W., et al.: Shape control of CdSe nanocrystals. *Nature* **404**, 59–61 (2000). <https://doi.org/10.1038/35003535>
124. Singh, R.D., Shandilya, R., Bhargava, A., et al.: Quantum dot based nano-biosensors for detection of circulating cell free miRNAs in lung carcinogenesis: from biology to clinical translation. *Front. Genet.* **9**, 616 (2018). <https://doi.org/10.3389/fgene.2018.00616>
125. Menagen, G., Macdonald, J.E., Shemesh, Y., et al.: Au growth on semiconductor nanorods: photoinduced versus thermal growth mechanisms. *J. Am. Chem. Soc.* **131**, 17406–17411 (2009). <https://doi.org/10.1021/ja9077733>
126. Mokari, T., Sztrum, C.G., Salant, A., et al.: Formation of asymmetric one-sided metal-tipped semiconductor nanocrystal dots and rods. *Nat. Mater.* **4**, 855 (2005)
127. Shemesh, Y., Macdonald, J.E., Menagen, G., Banin, U.: Synthesis and photocatalytic properties of a family of CdS-PdX hybrid nanoparticles. *Angew Chemie Int. Ed.* **50**, 1185–1189 (2011). <https://doi.org/10.1002/anie.201006407>
128. Habas, S.E., Yang, P., Mokari, T.: Selective growth of metal and binary metal tips on CdS nanorods. *J. Am. Chem. Soc.* **130**, 3294–3295 (2008). <https://doi.org/10.1021/ja800104w>
129. Dukovic, G., Merkle, M.G., Nelson, J.H., et al.: Photodeposition of Pt on colloidal CdS and CdSe/CdS semiconductor nanostructures. *Adv. Mater.* **20**, 4306–4311 (2008). <https://doi.org/10.1002/adma.200800384>
130. Banin, U., Ben-Shahar, Y., Vinokurov, K.: Hybrid semiconductor-metal nanoparticles: from architecture to function. *Chem. Mater.* **26**, 97–110 (2014). <https://doi.org/10.1021/cm402131n>
131. Li, M., Cushing, S.K., Wang, Q., et al.: Size-dependent energy transfer between CdSe/ZnS quantum dots and gold nanoparticles. *J. Phys. Chem. Lett.* **2**, 2125–2129 (2011). <https://doi.org/10.1021/jz201002g>
132. Maneeprakorn, W., Malik, M.A., O’Brien, P.: Developing chemical strategies for the assembly of nanoparticles into mesoscopic objects. *J. Am. Chem. Soc.* **132**, 1780–1781 (2010). <https://doi.org/10.1021/ja910022q>
133. Chang, E., Miller, J.S., Sun, J., et al.: Protease-activated quantum dot probes. *Biochem. Biophys. Res. Commun.* **334**, 1317–1321 (2005). <https://doi.org/10.1016/j.bbrc.2005.07.028>
134. Aldeek, F., Ji, X., Mattoussi, H.: Quenching of quantum dot emission by fluorescent gold clusters: what it does and does not share with the Förster formalism. *J. Phys. Chem. C* **117**, 15429–15437 (2013). <https://doi.org/10.1021/jp404952x>
135. Roller, E.-M., Argyropoulos, C., Högele, A., et al.: Plasmon-exciton coupling using DNA templates. *Nano Lett.* **16**, 5962–5966 (2016). <https://doi.org/10.1021/acs.nanolett.6b03015>
136. Cohen-Hoshen, E., Bryant, G.W., Pinkas, I., et al.: Exciton-Plasmon interactions in quantum dot-gold nanoparticle structures. *Nano Lett.* **12**, 4260–4264 (2012). <https://doi.org/10.1021/nl301917d>
137. Schreiber, R., Do, J., Roller, E.-M., et al.: Hierarchical assembly of metal nanoparticles, quantum dots and organic dyes using DNA origami scaffolds. *Nat. Nanotechnol.* **9**, 74 (2013)

138. Ko, S.H., Du, K., Liddle, J.A.: Quantum-dot fluorescence lifetime engineering with DNA origami constructs. *Angew Chemie Int. Ed.* **52**, 1193–1197 (2013). <https://doi.org/10.1002/anie.201206253>
139. Shevchenko, E.V., Talapin, D.V., Kotov, N.A., et al.: Structural diversity in binary nanoparticle superlattices. *Nature* **439**, 55–59 (2006). <https://doi.org/10.1038/nature04414>
140. Lee, J., Hernandez, P., Lee, J., et al.: Exciton–plasmon interactions in molecular spring assemblies of nanowires and wavelength-based protein detection. *Nat. Mater.* **6**, 291–295 (2007). <https://doi.org/10.1038/nmat1869>
141. Lee, J., Govorov, A.O., Dulka, J., Kotov, N.A.: Bioconjugates of CdTe nanowires and Au nanoparticles: Plasmon–Exciton interactions, luminescence enhancement, and collective effects. *Nano Lett.* **4**, 2323–2330 (2004). <https://doi.org/10.1021/nl048669h>
142. Ji, B., Giovannelli, E., Habert, B., et al.: Non-blinking quantum dot with a plasmonic nanoshell resonator. *Nat. Nanotechnol.* **10**, 170–175 (2015). <https://doi.org/10.1038/nnano.2014.298>
143. Chen, S., Thota, S., Reggiano, G., Zhao, J.: Generalized seeded growth of Ag-based metal chalcogenide nanorods via controlled chalcogenization of the seeds. *J. Mater. Chem. C* **3**, 11842–11849 (2015). <https://doi.org/10.1039/C5TC02904J>
144. Samanta, A., Zhou, Y., Zou, S., et al.: Fluorescence quenching of quantum dots by gold nanoparticles: a potential long range spectroscopic ruler. *Nano Lett.* **14**, 5052–5057 (2014). <https://doi.org/10.1021/nl501709s>
145. Zhang, L., Blom, D.A., Wang, H.: Au–Cu₂O core-shell nanoparticles: a hybrid metal-semiconductor heteronanostructure with geometrically tunable optical properties. *Chem. Mater.* **23**, 4587–4598 (2011). <https://doi.org/10.1021/cm202078t>
146. Ozel, T., Hernandez-Martinez, P.L., Mutlugun, E., et al.: Observation of selective plasmon-exciton coupling in nonradiative energy transfer: donor-selective versus acceptor-selective plexcitons. *Nano Lett.* **13**, 3065–3072 (2013). <https://doi.org/10.1021/nl4009106>
147. Chen, Y., Vela, J., Htoon, H., et al.: “Giant” multishell CdSe nanocrystal quantum dots with suppressed blinking. *J. Am. Chem. Soc.* **130**, 5026–5027 (2008). <https://doi.org/10.1021/ja711379k>
148. Ma, X., Tan, H., Kipp, T., Mews, A.: Fluorescence enhancement, blinking suppression, and gray states of individual semiconductor nanocrystals close to gold nanoparticles. *Nano Lett.* **10**, 4166–4174 (2010). <https://doi.org/10.1021/nl102451c>
149. Munechika, K., Chen, Y., Tillack, A.F., et al.: Spectral control of plasmonic emission enhancement from quantum dots near single silver nanoprisms. *Nano Lett.* **10**, 2598–2603 (2010). <https://doi.org/10.1021/nl101281a>
150. Naiki, H., Uedao, T., Wang, L., et al.: Multiphoton emission enhancement from a single colloidal quantum dot using SiO₂-coated silver nanoparticles. *ACS Omega* **2**, 728–737 (2017). <https://doi.org/10.1021/acsomega.6b00520>
151. LeBlanc, S.J., McClanahan, M.R., Jones, M., Moyer, P.J.: Enhancement of multiphoton emission from single CdSe quantum dots coupled to gold films. *Nano Lett.* **13**, 1662–1669 (2013). <https://doi.org/10.1021/nl400117h>
152. Park, Y.-S., Ghosh, Y., Chen, Y., et al.: Super-Poissonian statistics of photon emission from single CdSe–CdS core-shell nanocrystals coupled to metal nanostructures. *Phys. Rev. Lett.* **110**, 117401 (2013). <https://doi.org/10.1103/PhysRevLett.110.117401>
153. Dey, S., Zhou, Y., Tian, X., et al.: An experimental and theoretical mechanistic study of biexciton quantum yield enhancement in single quantum dots near gold nanoparticles. *Nanoscale* **7** (2015). <https://doi.org/10.1039/c5nr00274e>
154. Wax, T.J., Dey, S., Chen, S., et al.: Excitation wavelength-dependent photoluminescence decay of hybrid gold/quantum dot nanostructures. *ACS Omega* **3** (2018). <https://doi.org/10.1021/acsomega.8b01959>
155. Zhou, N., Yuan, M., Gao, Y., et al.: Silver nanoshell plasmonically controlled emission of semiconductor quantum dots in the strong coupling regime. *ACS Nano* **10**, 4154–4163 (2016). <https://doi.org/10.1021/acsnano.5b07400>

156. Santhosh, K., Bitton, O., Chuntonov, L., Haran, G.: Vacuum Rabi splitting in a plasmonic cavity at the single quantum emitter limit. *Nat. Commun.* **7**, ncomms11823 (2016). <https://doi.org/10.1038/ncomms11823>
157. Inkson, B.J.: 2—Scanning electron microscopy (SEM) and transmission electron microscopy (TEM) for materials characterization. In: Hübschen, G., Altpeter, I., Tschuncky, R., Herrmann H-GBT-MCUNE (NDE) M. (eds.), pp. 17–43. Woodhead Publishing (2016)
158. Sezen, H., Suzer, S.: XPS for chemical- and charge-sensitive analyses. *Thin Solid Films* **534**, 1–11 (2013). <https://doi.org/10.1016/j.tsf.2013.02.002>
159. Cavalcoli, D., Fraboni, B., Cavallini, A.: Chapter Seven—Surface and defect states in semiconductors investigated by surface photovoltage. In: Romano, L., Privitera, V., Jagadish, S. (eds.) *Defects in Semiconductors*, pp. 251–278. Elsevier (2015)
160. Bisquert, J., Bertoluzzi, L., Mora-Sero, I., Garcia-Belmonte, G.: Theory of impedance and capacitance spectroscopy of solar cells with dielectric relaxation, drift-diffusion transport, and recombination. *J. Phys. Chem. C* **118**, 18983–18991 (2014). <https://doi.org/10.1021/jp5062144>
161. Braña, A.F., Forniés, E., López, N., García, B.J.: High efficiency Si solar cells characterization using impedance spectroscopy analysis. *J. Phys: Conf. Ser.* **647**, 12069 (2015). <https://doi.org/10.1088/1742-6596/647/1/012069>
162. Wang, Q., Moser, J.-E., Grätzel, M.: Electrochemical impedance spectroscopic analysis of dye-sensitized solar cells. *J. Phys. Chem. B* **109**, 14945–14953 (2005). <https://doi.org/10.1021/jp052768h>
163. Wu, J.-L., Chen, F.-C., Hsiao, Y.-S., et al.: Surface plasmonic effects of metallic nanoparticles on the performance of polymer bulk heterojunction solar cells. *ACS Nano* **5**, 959–967 (2011). <https://doi.org/10.1021/nn102295p>
164. Atwater, H.A., Polman, A.: Plasmonics for improved photovoltaic devices. *Nat. Mater.* **9**, 205–213 (2010). <https://doi.org/10.1038/nmat2629>
165. Jang, Y.H., Jang, Y.J., Kim, S., et al.: Plasmonic solar cells: from rational design to mechanism overview. *Chem. Rev.* **116**, 14982–15034 (2016). <https://doi.org/10.1021/acs.chemrev.6b00302>
166. Yuan, Z., Wu, Z., Bai, S., et al.: Hot-electron injection in a sandwiched TiO_x–Au–TiO_x structure for high-performance planar Perovskite solar cells. *Adv. Energy Mater.* **5**, 1500038 (2015). <https://doi.org/10.1002/aenm.201500038>
167. Zhu, J., Hsu, C.-M., Yu, Z., et al.: Nanodome solar cells with efficient light management and self-cleaning. *Nano Lett.* **10**, 1979–1984 (2010). <https://doi.org/10.1021/nl9034237>
168. Pala, R.A., White, J., Barnard, E., et al.: Design of plasmonic thin-film solar cells with broadband absorption enhancements. *Adv. Mater.* **21**, 3504–3509 (2009). <https://doi.org/10.1002/adma.200900331>
169. Callahan, D.M., Munday, J.N., Atwater, H.A.: Solar cell light trapping beyond the ray optic limit. *Nano Lett.* **12**, 214–218 (2012). <https://doi.org/10.1021/nl203351k>
170. Chen, H.M., Chen, C.K., Chen, C.-J., et al.: Plasmon inducing effects for enhanced photoelectrochemical water splitting: X-ray absorption approach to electronic structures. *ACS Nano* **6**, 7362–7372 (2012). <https://doi.org/10.1021/nn3024877>
171. Li, J., Cushing, S.K., Meng, F., et al.: Plasmon-induced resonance energy transfer for solar energy conversion. *Nat. Photonics* **9**, 601 (2015)
172. Cushing, S.K., Li, J., Meng, F., et al.: Photocatalytic activity enhanced by plasmonic resonant energy transfer from metal to semiconductor. *J. Am. Chem. Soc.* **134**, 15033–15041 (2012). <https://doi.org/10.1021/ja305603t>
173. Isah, K.U., Jolayemi, B.J., Ahmadu, U., et al.: Plasmonic effect of silver nanoparticles intercalated into mesoporous betalain-sensitized-TiO₂ film electrodes on photovoltaic performance of dye-sensitized solar cells. *Mater. Renew. Sustain. Energy* **5**, 10 (2016). <https://doi.org/10.1007/s40243-016-0075-z>
174. Ihara, M., Kanno, M., Inoue, S.: Photoabsorption-enhanced dye-sensitized solar cell by using localized surface plasmon of silver nanoparticles modified with polymer. *Phys E*

- Low-dimensional Syst. Nanostruct. **42**, 2867–2871 (2010). <https://doi.org/10.1016/j.physe.2010.04.001>
175. Xu, Q., Liu, F., Meng, W., Huang, Y.: Plasmonic core-shell metal-organic nanoparticles enhanced dye-sensitized solar cells. *Opt. Express* **20**, A898–A907 (2012). <https://doi.org/10.1364/OE.20.00A898>
176. Chen, Z.H., Tang, Y.B., Liu, C.P., et al.: Vertically aligned ZnO nanorod arrays sensitized with gold nanoparticles for Schottky barrier photovoltaic cells. *J. Phys. Chem. C* **113**, 13433–13437 (2009). <https://doi.org/10.1021/jp903153w>
177. Ding, I.-K., Zhu, J., Cai, W., et al.: Plasmonic dye-sensitized solar cells. *Adv. Energy Mater.* **1**, 52–57 (2011). <https://doi.org/10.1002/aenm.201000041>
178. Li, Y., Wang, H., Feng, Q., et al.: Gold nanoparticles inlaid TiO₂ photoanodes: a superior candidate for high-efficiency dye-sensitized solar cells. *Energy Environ. Sci.* **6**, 2156–2165 (2013). <https://doi.org/10.1039/C3EE23971C>
179. Du, J., Qi, J., Wang, D., Tang, Z.: Facile synthesis of Au@TiO₂ core-shell hollow spheres for dye-sensitized solar cells with remarkably improved efficiency. *Energy Environ. Sci.* **5**, 6914–6918 (2012). <https://doi.org/10.1039/C2EE21264A>
180. Chang, S., Li, Q., Xiao, X., et al.: Enhancement of low energy sunlight harvesting in dye-sensitized solar cells using plasmonic gold nanorods. *Energy Environ. Sci.* **5**, 9444–9448 (2012). <https://doi.org/10.1039/C2EE22657J>
181. Brown, M.D., Suteewong, T., Kumar, R.S.S., et al.: Plasmonic dye-sensitized solar cells using core-shell metal-insulator nanoparticles. *Nano Lett.* **11**, 438–445 (2011). <https://doi.org/10.1021/nl1031106>
182. Zarick, H.F., Erwin, W.R., Boulesbaa, A., et al.: Improving light harvesting in dye-sensitized solar cells using hybrid bimetallic nanostructures. *ACS Photonics* **3**, 385–394 (2016). <https://doi.org/10.1021/acsphotonics.5b00552>
183. Elbohy, H., Kim, M.R., Dubey, A., et al.: Incorporation of plasmonic Au nanostars into photoanodes for high efficiency dye-sensitized solar cells. *J. Mater. Chem. A* **4**, 545–551 (2016). <https://doi.org/10.1039/C5TA06425B>
184. Su, Y.-H., Ke, Y.-F., Cai, S.-L., Yao, Q.-Y.: Surface plasmon resonance of layer-by-layer gold nanoparticles induced photoelectric current in environmentally-friendly plasmon-sensitized solar cell. *Light Sci. Appl.* **1**, e14–e14 (2012). <https://doi.org/10.1038/lsa.2012.14>
185. Wang, Q., Butburee, T., Wu, X., et al.: Enhanced performance of dye-sensitized solar cells by doping Au nanoparticles into photoanodes: a size effect study. *J. Mater. Chem. A* **1**, 13524–13531 (2013). <https://doi.org/10.1039/C3TA12692G>
186. Sahu, G., Gordon, S.W., Tarr, M.A.: Synthesis and application of core-shell Au-TiO₂ nanowire photoanode materials for dye sensitized solar cells. *RSC Adv.* **2**, 573–582 (2012). <https://doi.org/10.1039/C1RA00762A>
187. Ahn, S.H., Kim, D.J., Chi, W.S., Kim, J.H.: Plasmonic, interior-decorated, one-dimensional hierarchical nanotubes for high-efficiency, solid-state, dye-sensitized solar cells. *J. Mater. Chem. A* **3**, 10439–10447 (2015). <https://doi.org/10.1039/C5TA00801H>
188. Lee, K.-S., El-Sayed, M.A.: Dependence of the enhanced optical scattering efficiency relative to that of absorption for gold metal nanorods on aspect ratio, size, end-cap shape, and medium refractive index. *J. Phys. Chem. B* **109**, 20331–20338 (2005). <https://doi.org/10.1021/jp054385p>
189. Kulkarni, A.P., Noone, K.M., Munchika, K., et al.: Plasmon-enhanced charge carrier generation in organic photovoltaic films using silver nanoprisms. *Nano Lett.* **10**, 1501–1505 (2010). <https://doi.org/10.1021/nl100615e>
190. Salvador, M., MacLeod, B.A., Hess, A., et al.: Electron accumulation on metal nanoparticles in Plasmon-enhanced organic solar cells. *ACS Nano* **6**, 10024–10032 (2012). <https://doi.org/10.1021/nn303725v>
191. Yao, K., Salvador, M., Chueh, C.-C., et al.: A general route to enhance polymer solar cell performance using plasmonic nanoprisms. *Adv. Energy Mater.* **4**, 1400206 (2014). <https://doi.org/10.1002/aenm.201400206>

192. Yang, X., Chueh, C.-C., Li, C.-Z., et al.: High-efficiency polymer solar cells achieved by doping plasmonic metallic nanoparticles into dual charge selecting interfacial layers to enhance light trapping. *Adv. Energy Mater.* **3**, 666–673 (2013). <https://doi.org/10.1002/aenm.201200726>
193. Wang, C.C.D., Choy, W.C.H., Duan, C., et al.: Optical and electrical effects of gold nanoparticles in the active layer of polymer solar cells. *J. Mater. Chem.* **22**, 1206–1211 (2012). <https://doi.org/10.1039/C1JM14150C>
194. You, J., Li, X., Xie, F., et al.: Surface Plasmon and scattering-enhanced low-bandgap polymer solar cell by a metal grating back electrode. *Adv. Energy Mater.* **2**, 1203–1207 (2012). <https://doi.org/10.1002/aenm.201200108>
195. Choi, H., Lee, J.-P., Ko, S.-J., et al.: Multipositional Silica-coated silver nanoparticles for high-performance polymer solar cells. *Nano Lett.* **13**, 2204–2208 (2013). <https://doi.org/10.1021/nl400730z>
196. Wang, D.H., Kim, D.Y., Choi, K.W., et al.: Enhancement of donor-acceptor polymer bulk heterojunction solar cell power conversion efficiencies by addition of Au nanoparticles. *Angew Chemie Int. Ed.* **50**, 5519–5523 (2011). <https://doi.org/10.1002/anie.201101021>
197. Oo, T.Z., Mathews, N., Xing, G., et al.: Ultrafine Gold nanowire networks as plasmonic antennae in organic photovoltaics. *J. Phys. Chem. C* **116**, 6453–6458 (2012). <https://doi.org/10.1021/jp2099637>
198. Carretero-Palacios, S., Calvo, M.E., Míguez, H.: Absorption enhancement in organic-inorganic Halide Perovskite films with embedded plasmonic gold nanoparticles. *J. Phys. Chem. C* **119**, 18635–18640 (2015). <https://doi.org/10.1021/acs.jpcc.5b06473>
199. Mali, S.S., Shim, C.S., Kim, H., et al.: In situ processed gold nanoparticle-embedded TiO₂ nanofibers enabling plasmonic perovskite solar cells to exceed 14% conversion efficiency. *Nanoscale* **8**, 2664–2677 (2016). <https://doi.org/10.1039/C5NR07395B>
200. Lu, Z., Pan, X., Ma, Y., et al.: Plasmonic-enhanced perovskite solar cells using alloy popcorn nanoparticles. *RSC Adv.* **5**, 11175–11179 (2015). <https://doi.org/10.1039/C4RA16385K>
201. Wang, H., Gonzalez-Pedro, V., Kubo, T., et al.: Enhanced carrier transport distance in colloidal PbS quantum-dot-based solar cells using ZnO nanowires. *J. Phys. Chem. C* **119**, 27265–27274 (2015). <https://doi.org/10.1021/acs.jpcc.5b09152>
202. Moroz, P., Liyanage, G., Kholmicheva, N.N., et al.: Infrared emitting PbS nanocrystal solids through matrix encapsulation. *Chem. Mater.* **26**, 4256–4264 (2014). <https://doi.org/10.1021/cm501739h>
203. Liu, X., Zhang, X.W., Meng, J.H., et al.: High efficiency Schottky junction solar cells by co-doping of graphene with gold nanoparticles and nitric acid. *Appl. Phys. Lett.* **106**, 233901 (2015). <https://doi.org/10.1063/1.4922373>
204. Li, S.-S., Tu, K.-H., Lin, C.-C., et al.: Solution-processable graphene oxide as an efficient hole transport layer in polymer solar cells. *ACS Nano* **4**, 3169–3174 (2010). <https://doi.org/10.1021/nn100551j>
205. Fan, G.-Q., Zhuo, Q.-Q., Zhu, J.-J., et al.: Plasmonic-enhanced polymer solar cells incorporating solution-processable Au nanoparticle-adhered graphene oxide. *J. Mater. Chem.* **22**, 15614–15619 (2012). <https://doi.org/10.1039/C2JM31878D>
206. Wang, X., Zhi, L., Müllen, K.: Transparent, conductive graphene electrodes for dye-sensitized solar cells. *Nano Lett.* **8**, 323–327 (2008). <https://doi.org/10.1021/nl072838r>
207. Goldschmidt, J.C., Fischer, S.: Upconversion for photovoltaics—a review of materials, devices and concepts for performance enhancement. *Adv. Opt. Mater.* **3**, 510–535 (2015). <https://doi.org/10.1002/adom.201500024>

Photocatalytic and Photoluminescent Properties of TiO₂ Nanocrystals Obtained by the Microwave Solvothermal Method



Kleber Figueiredo de Moura, Laís Chantelle, Márcia Rejane Santos da Silva, Elson Longo, Máximo Siu–Li, Maria Gardênia Fonseca, Ary da Silva Maia and Iêda Maria Garcia dos Santos

Abstract In the present work, the influence of the short-range disorder on the photocatalytic activity of TiO₂ nanocrystals obtained by a rapid microwave solvothermal method was evaluated. The synthesis of TiO₂ was performed without synthesis additives and with two different capping agents, sodium dodecyl sulfate (SDS) or carboxymethyl cellulose (CMC). Higher short-range disorder was obtained when SDS was used, as indicated by photoluminescence (PL) and also in the Raman spectra. In the second step, TiO₂ samples were used as photocatalysts for the degradation of remazol golden-yellow dye (RNL). High efficiency was observed, with meaningful variations in the percentage efficiency depending on the short-range order of the photocatalyst. Our best results were comparable to those of commercial TiO₂ Degussa P25. Adsorption isotherms were also evaluated as a function of time, indicating that chemisorption appears to take place, with a high adsorption capacity of the RNL by the photocatalysts.

Keywords TiO₂ · Solvothermal method · Template · Photocatalysis · Azo-dye

K. F. de Moura · L. Chantelle · M. R. S. da Silva · M. G. Fonseca · A. da Silva Maia · I. M. G. dos Santos (✉)

Núcleo de Pesquisa e Extensão-Laboratório de Combustíveis e Materiais (NPE/LACOM), Universidade Federal da Paraíba, João Pessoa, PB, Brazil
e-mail: ieda@quimica.ufpb.br

E. Longo

Centro de Desenvolvimento de Materiais Funcionais—CDMF, Laboratório Interdisciplinar de Eletroquímica e Cerâmica—LIEC, Centro de Desenvolvimento de Materiais Funcionais—CDMF, Laboratório Interdisciplinar de Eletroquímica e Cerâmica—LIEC, Universidade Federal de São Carlos, São Carlos, SP, Brazil

M. Siu–Li

IFSC, Universidade de São Paulo, São Carlos, SP, Brazil

© Springer Nature Switzerland AG 2020

F. A. La Porta and C. A. Taft (eds.), *Emerging Research in Science and Engineering Based on Advanced Experimental and Computational Strategies*, Engineering Materials, https://doi.org/10.1007/978-3-030-31403-3_2

1 Introduction

The anatase form of TiO_2 has long been largely studied in heterogeneous photocatalysis [1–5]. In spite of this, however, the synergism between the synthesis conditions and the photocatalytic activity is not completely understood [6–9]. It is well known that photocatalytic efficiency is influenced by different properties like morphology, particle size, presence of other polymorphic phases and also by the disorder at short-, medium- and long-range [6, 7, 10–12]. Different defects have been naturally observed in the anatase TiO_2 structure (e.g., such as oxygen vacancies, reduced Ti^{4+} , interstitial Ti^{4+} , and lattice distortions), which in turn change the behavior of the electron-hole pair, responsible for the photocatalytic processes. As a consequence, some works report the pivotal influence of the defects in the photocatalytic efficiency of the anatase [6, 13, 14].

An interesting technique for the fast evaluation and understanding of structural defects (especially at medium-range) on advanced materials is photoluminescence (PL) spectroscopy. Also, PL investigations are extremely useful in designing new target materials and hence are widely used in optimizing of the synthetic parameters. However, its association with photocatalysis should be carefully done. For instance, Liqiang associated the PL spectra with the photocatalytic activity of pure ZnO and pure anatase, as well [15]. Oxygen vacancies may, in theory, capture photo-induced electrons, avoiding recombination processes. Such defects can also promote O_2 adsorption, which may capture photo-induced electrons, forming $^*\text{O}_2$ radicals that degrade the organic compounds [15]. Dong et al. [16] also emphasize the importance of PL in the investigation of trap states in the structure of TiO_2 . In spite of these, few papers report the association between PL and photocatalysis for undoped TiO_2 obtained by microwave-assisted hydrothermal/solvothermal methods. For instance, Suprabha et al. [17] associated the PL with indirect transitions, which, according to the authors, are the exclusive route for the charge carrier recombination. Very similar PL spectra were observed for the different TiO_2 phases—anatase and rutile. Hu et al. [18] deposited anatase on natural rutile using the microwave-assisted hydrothermal synthesis and associated the lowest PL emission of the composite comparing to P25 TiO_2 to a lower recombination rate, which favors the photocatalytic activity. Su et al. [19] synthesized anatase by the microwave-assisted hydrothermal method with a post-calcination at different temperatures as strategy. According to the authors, samples calcined at higher temperatures showed a higher crystallinity and a lower PL intensity, which was related to a lower rate of electron-hole pair recombination and is associated with higher photocatalytic activity.

The solvothermal/hydrothermal methods stand out among available syntheses methods due to its ability to obtain TiO_2 , in large amounts, with a varying of well-defined morphologies, by the use of different methodologies of precipitation, capping agents or templates [17, 20–31]. Mesoporous TiO_2 has been synthesized by the use of sodium dodecyl sulfate, tetradecyl-phosphate, cetyltrimethylammonium bromide and others as templates [22, 23, 28, 32–34]. The drawback of these materials synthesized from this strategy is the need for further step to the

elimination of the templates used. D'Elia et al. [35] synthesized TiO₂ with different morphologies (e.g., nanoparticles, nanotubes, and aerogels) by the hydrothermal method, with varying synthesis conditions. These engineered advanced materials exhibited different photocatalytic behaviors, being the aerogels of TiO₂ with better performance, which was ascribed to the beneficial interaction of charge separation processes.

In the previous work, our research group obtained nanometric particles of anatase/brookite by the microwave-assisted solvothermal method, with high efficiency in the photodiscoloration of a textile dye [36]. In the present work, TiO₂ photocatalysts were synthesized with and without two different capping agents, are discussed. The PL profile of these materials was correlated with their efficiency in the photodiscoloration of the remazol golden yellow dye (RNL).

2 Materials and Methods

2.1 Synthesis of Photocatalysts

During the synthesis of the photocatalysts, sodium dodecyl sulfate [SDS-CH₃(CH₂)_nOSO₃Na-Kasvi], or carboxymethylcellulose [CMC-(C₆H₇O₂(OH)₂CH₂COONa)_n-Adhes] were used as a capping agent, titanium isopropoxide (IPT-Aldrich, 97%) was used as a precursor. To obtain the TiO₂ particles, the synthesis was then carried out in an ethanol suspension with the respective capping agent (0.2 mol L⁻¹) under stirring for 10 min. After wards, IPT was added to the solution in order to obtain a concentration of about 1.0 mol L⁻¹, with stirring for a further 10 min. The syntheses without a capping agent were also carried out for comparison. All the solvothermal reactions were performed under microwave irradiation in a Teflon reactor at 120 °C for 1 min at a heating rate of 10 °C min⁻¹ and a maximum pressure of approximated 2 kgf/cm². After the solvothermal process was carried out, the white precipitate that formed was washed several times with distilled water and centrifuged at 5000 rpm at room temperature until a neutral pH (approximately 7) was reached. After this process, the precipitate was calcined at 300 °C for a period of 5 h to eliminate the organic material. To end, all prepared samples were denoted as TiP (surfactant-free synthesis), TiSDS (synthesis with SDS) and TiCMC (synthesis with CMC), respectively.

The powders were characterized by X-ray diffraction (XRD) using a Shimadzu 6000 diffractometer with Cu K α radiation. The crystallite sizes were calculated using the Scherrer equation. Raman spectra were collected using a Bruker FT-Raman RFS/100/S spectrophotometer. The spectra were obtained using a 1064 nm and 60 mW Nd:YAG laser. The scan range used was 50 to 750 cm⁻¹, with a resolution of 4 cm⁻¹. Infrared spectra were collected using an IR Prestige Shimadzu-21 spectrometer. The scan range used was 2000 to 450 cm⁻¹. A morphological evaluation was performed by field emission-scanning electron

microscopy using a FEG-VP Zeiss Supra 35 microscope. Surface area analysis was performed by N_2 adsorption using the BET equation. Measurements were taken using a BELSORP II instrument. Also, PL spectra were collected from pellets at room temperature under an air atmosphere using a Monospec 27 monochromator (Thermal Jarrel Ash, USA) coupled to an R446 photomultiplier (Hamamatsu Photonics, Japan). A krypton ion laser (Coherent Innova 90 K, USA) ($h\nu = 350$ nm) was employed as an excitation source. Its maximum power output was maintained at 500 mW, with a maximum power of 40 mW on the sample after passing through an optical chopper.

2.2 Photocatalytic Process

For the photocatalytic test, was used 5.0 mg of the catalyst in about of 15.0 mL of a RNL solution (50 mg L^{-1}) at $\text{pH} \approx 6$. Firstly, the suspensions were magnetically stirred in the dark for 1 h (photolysis). In sequence, the suspensions were then irradiated with a Super Niko UVC lamp (model ZG-30T8, 0.5–1.0 mW) for a period of 4 h. After the photocatalytic reaction, at room temperature, the sample solution was collected in different times and then centrifuged for 30 min at 5000 rpm for the analysis of supernatant. Thus, the collected supernatant was measured by UV-Vis spectroscopy (SHIMADZU UV-2550 spectrometer) at a λ of 411 nm.

2.3 Adsorption Tests

For the adsorption tests (without irradiation), 15.0 mL of the dye solutions at different initial concentrations (5, 15, 25, 50, 75, and 100 mg L^{-1}), and 5.0 mg of the photocatalyst were placed into Petri plates. The plates were then kept in the dark for 0, 20, 40, 60, 80, 100, and 120 min, before being centrifuged and analyzed, as described before.

2.3.1 Adsorption Isotherms

Hence, the Langmuir and Freundlich adsorption isotherms were also evaluated in this work. Firstly, the Langmuir model is typically characterized by the formation of a monolayer on the powder surface [37]. The linearized form of the Langmuir isotherm is represented in Eq. 1.

$$\frac{C_e}{q_e} = \frac{1}{K_L Q_0} + \frac{C_e}{Q_0} \quad (1)$$

where q_e is the adsorbate/adsorbent ratio (mg/g), C_e is the adsorbate equilibrium concentration (mgL⁻¹), Q_o is the amount adsorbed when the surface is covered by a monolayer (mg g⁻¹), and K_L is the Langmuir adsorption constant, which is related to the adsorption energy (L mg⁻¹).

While the Freundlich isotherm [38] was applied using its linearized form (Eq. 2).

$$\ln q_e = \ln K_F + \frac{1}{n} \ln C_e \quad (2)$$

where K_F and $1/n$ are the Freundlich empirical parameters. These parameters depend on several experimental factors and are related to the adsorption capacity and adsorption intensity, respectively [38].

Another important parameter, R_L , known as the separation factor or equilibrium parameter, is determined according to the following relation:

$$R_L = \frac{1}{1 + K_L C_0} \quad (3)$$

where K_L is the Langmuir constant, and C_0 is the initial concentration of RNL. Thus, the value of R_L indicates the isotherm type, which is either unfavorable ($R_L > 1$), linear ($R_L = 1$), favorable ($0 < R_L < 1$), or irreversible ($R_L = 0$) [39].

3 Results and Discussion

3.1 Characterization of Photocatalysts

All of the XRD patterns for the TiO₂ synthesized in the present work are presented in Fig. 1. In spite of the very short irradiation time, the anatase structure (JCPDS# 89-4981) was formed in all samples, however, with a small amount of brookite (JCPDS# 76-1934) as secondary phase, in agreement to our previous results [36]. The average crystallite size of the anatase phase was approximately 5.8 nm. The unit cell volume was approximately 133.5 Å³. This result indicates that a contraction took place when comparing to the theoretical value of 136.0 Å³.

FE-SEM images are presented in Fig. 1b-d. All of the materials presented nearly spherical nanometric particles, which form agglomerates with different formats. For TiP sample (Fig. 1b) nanoparticles of 10-25 nm form an agglomerate with an average diameter of approximately 0.5 μm with no defined shape. For TiSDS sample, (Fig. 1c) nanoparticles with an average diameter of 10-25 nm and plate-like agglomerates were formed. FE-SEM images of the TiCMC samples (Fig. 1d) revealed a spherical morphology with an average diameter of 0.5 μm. Coalescence of the microspheres can also be observed, besides a rougher surface.

The difference in the morphologies is directly related to the effect of the capping agents. SDS is well known by its application in the synthesis of mesoporous

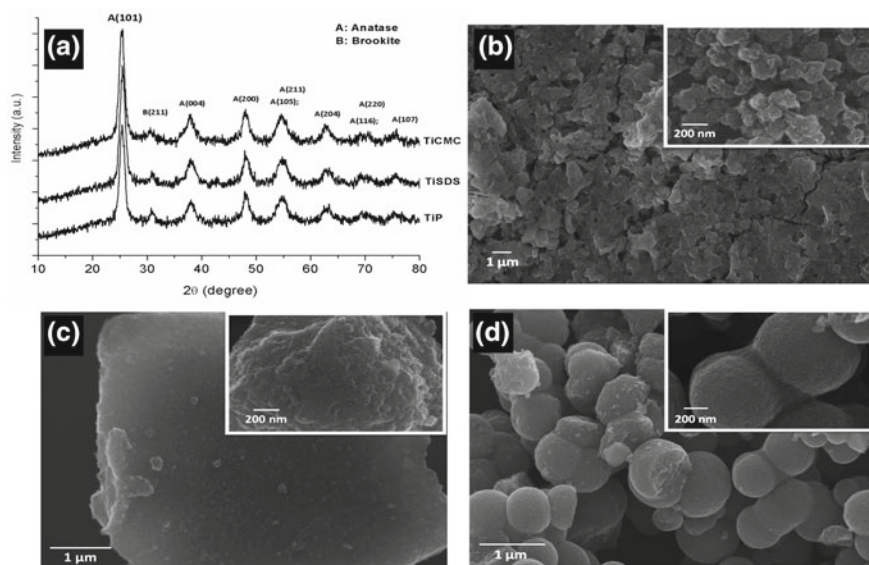


Fig. 1 (a) XRD patterns of TiO_2 samples. FE-SEM images of the TiO_2 samples: (a) TiP, (b) TiSDS and (c) TiCMC

materials, likely due to the formation of micelles in aqueous solutions [32]. According to literature, in alcohol, reverse micelles may be formed for some surfactants [40], while no micelle is formed by SDS when the amount of ethanol in the water:ethanol solutions exceeds 45% for a SDS concentration of $20 \text{ mmol}\cdot\text{L}^{-1}$ [41]. In the present work, we believe that the sulphate group of SDS adsorbs onto the particles, formed when IPT is added into SDS alcoholic solution. This adsorption is due to an attraction force among SDS polar part and the surface and seems to occur in a flat manner, i.e., favoring the formation of the plate-like agglomerates. On the other hand, in particular, CMC is a polymer with different groups which interact with the particle surface by different mechanisms—electrostatic interaction of the carboxylate anions and hydrogen bridging of the hydroxyl groups. The polymeric nature of the capping agent may in principle be responsible for the formation of the spherical agglomerates.

FE-SEM results also indicate that crystal growth process occur by interaction of randomly oriented particles, i.e., coalescence [12]. As a consequence, the orientation of a particular plane for these samples does not seem to take place, which is also consistent with obtained the XRD data.

The particle properties and the bandgap are presented in Table 1. The surface area of the samples obtained in the present work are higher than those of P25. Moreover, the particle size of the sample obtained without capping agent is twice that of the samples synthesized using SDS or CMC. The crystallite size does not vary as much and the amount of crystallites per particle is higher for samples obtained without capping agent indicating that SDS and CMC do not seem to

Table 1 Surface area (S_{BET}), particle size (P_{BET}), and the amount of crystallites per particle (P_{BET}/TC) obtained using the BET method and the *band gap* values for TiP, TiSDS, TiCMC, and also P25, respectively

Samples	S_{BET} (m ² /g)	P_{BET} (nm)	P_{BET}/TC	<i>Band gap</i> (eV)
TiP	65.6	23.2	4.0	3.1
TiSDS	153.1	10.5	1.8	3.1
TiCMC	137.6	11.1	2.1	3.1
P25	50.0	30.6	1.5	3.2

interfere in the nucleation/crystallization process. These results indicate that the capping agent inhibits the growth process of the particles, probably due to its adsorption onto the particle surface. Thus, in this perspective, such results could be made more difficult the coalescence process among particles.

The infrared spectra are shown in Fig. 2a. In relation to the oxygen-metal bonds in the anatase structure, various bands overlap between 450 and 906 cm⁻¹, while one band at approximately 1634 cm⁻¹ is typically assigned to the H–O–H vibrations due to the water adsorbed on the powder surface. The bands at 1384 and 1440 cm⁻¹ are assigned to the symmetric ($\delta_{\text{S}}\text{CH}_3$) and asymmetric ($\delta_{\text{AS}}\text{CH}_3$) vibrations of the C–H methyl groups, respectively, while the band at 1527 cm⁻¹ is caused by the changes in the hydrocarbon, i.e., due to its ramification [42, 43]. Also, the infrared spectra indicate that the heat treatment effectively eliminated the organic material from the samples synthesized using CMC, while the sample synthesized using SDS still presents a small amount of the organic material on the surface.

Raman spectroscopy was used to verify the short-range order, shown in Fig. 2b. According to group theory, the anatase structure has six active modes in Raman: 143 (E_g), 198 (E_g), 395 (B_{1g}), 507/518 (B_{1g}/A_{1g}), and 639 cm⁻¹ (E_g) [36, 44, 45]. The presence of bands at about 149–155 (E_g), 200 (E_g), 401–405 (B_{1g}), 520–525 (B_{1g}/A_{1g}), and 642–646 cm⁻¹ (E_g) were observed in the present work. Weak bands were also observed at 263, 341, and 383 cm⁻¹, which were assigned to the brookite phase. Table 2 shows the full width at half maximum (FWHM) and the Raman shift for the E_g (1), B_{1g} (1), and E_g (3) modes. This analysis was not carried out for the B_{1g} (2) and A_{1g} modes due to overlapping, and for the E_g (2) mode, due to its low intensity.

According to the E_g (1) and E_g (3) modes, the TiP and TiCMC samples have higher short-range order than the TiSDS sample. Early studies show that the E_g mode is related to vibrations in the [100] direction, whereas the E_g (1) mode is mainly assigned to the Ti⁴⁺ vibration inside the [TiO₆] octahedra, and the E_g (3) mode is typically assigned to the O²⁻ anions between octahedra. For the B_{1g} mode, which is related to the Ti–O–Ti stretching in the [001] direction, no significant difference was found for the FWHM values [36, 46].

PL spectroscopy was also carried out, as showed in Fig. 3. PL emission was found for all of the samples in this work, presenting a similar behavior to a multiphonon process. Moreover, no band-band transition was observed, and the PL signals can be classified as excitonic [47].

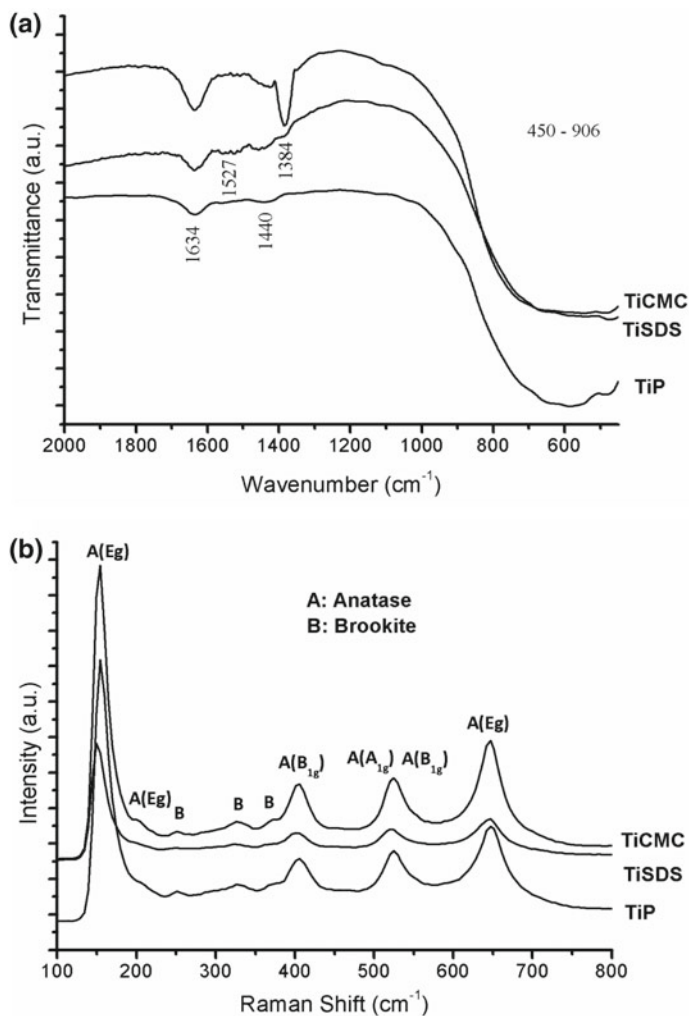


Fig. 2 (a) Infrared and (b) Raman spectra of the TiO₂ samples

Table 2 FWHM and Raman shift values of E_g(1), B_{1g}(1), and E_g(3) modes for TiP, TiSDS and TiCMC

	FWHM E _g	Raman Shift (cm ⁻¹)	FWHM B _{1g}	Raman Shift (cm ⁻¹)	FWHM E _g	Raman Shift (cm ⁻¹)	R ²
[45]	–	143	–	395	–	639	
TiP	15.5	153.91	15.2	405.09	21.9	647.30	0.99
TiSDS	19.0	154.77	14.4	399.83	28.4	646.46	0.99
TiCMC	16.2	154.02	15.5	403.92	21.7	646.13	0.99

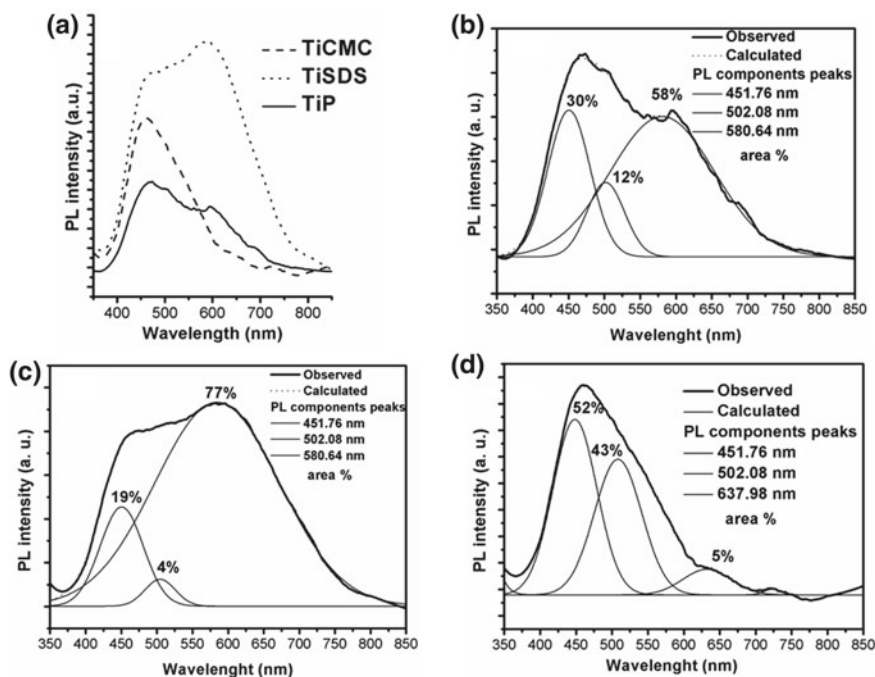


Fig. 3 (a) PL spectra of the TiO₂ samples, (b) TiP, (c) TiSDS and (d) TiCMC

Different interpretations have been given to the PL spectra of TiO₂. Most papers correlate the different regions of excitonic PL signal with self-trapped excitons (STE) and oxygen vacancies or also with Ti³⁺ species when a reducing atmosphere is used during synthesis or during a post-annealing treatment [48–51]. As expected the PL spectra are deeply related to the defects present in the structure, different assignments can be found depending on the method of synthesis and by the alteration of their morphology and particle size of these materials.

Recently, Silva Jr. et al. [12] evaluated the PL emission spectra of TiO₂ nanoparticles synthesized by the sol-gel process followed by the microwave-assisted solvothermal method. From the XPS data, they evaluation showed that Ti³⁺ was not present on the material surface. Three different PL sub-bands were found at 451, 523 and 605 nm, respectively, which were strongly associated with the symmetry breaking process of [TiO₆] octahedral and additional disturbances of the Ti–O bond lengths forming different oxygen vacancies species (V_{O}^x , V_{O}^{\bullet} , $V_{O}^{\bullet\bullet}$). According to the authors, in particular, the oxygen vacancies might be understood as disturbances of the Ti–O bond lengths, leading to a displacement of the oxygen atom position in the TiO₂ lattice.

In the present study, three bands were also observed, as showed in Fig. 3. Comparing to the results of Silva Jr. et al. [12] it is observed that similar band positions were found for TiP and TiSDS, while a dislocation of the third band

(580 nm) to higher wavelengths is observed for TiCMC. As Silva Jr. [12] also used microwave irradiation during synthesis, we believe that similar defects were obtained in the present work. Results presented in Fig. 3 also show that the proportions among the three emission bands are very different for the TiO₂ samples obtained at different conditions. For TiCMC, the band with the highest contribution is located at 450 nm (52%) and 500 nm (43%), with a very small contribution of the band at 640 nm (5%). The opposite behavior is observed for TiSDS, with the highest contribution of the band at 580 nm (77%). TiP has an intermediate behavior, with a high contribution of the band at 580 nm (58%) and 450 nm (31%).

According to Longo et al. [52] emissions at different regions in the photoluminescence spectra can be nominally associated to defects localized at different energy levels inside the band gap. Hence, the drawback of the violet and blue emissions are attributed to shallow defects states, while the green–yellow–red emissions are assigned to deep defects states which occurs in the forbidden gap of TiO₂.

Considering Longo assignments, in particular, the PL emissions observed for these samples, indicate that TiSDS has a higher amount of deep defects, with small amount of shallow defects. For TiP deep defects are also observed, but a higher amount of shallow defects are present. For TiCMC, most-likely shallow defects are predominated in this sample. These complex defects (at short-, medium- and long-range) can in principle trap electrons and holes with a great influence in the photocatalytic activity.

This analysis of the PL results is in agreement with the Raman evaluation, which indicated that TiSDS presented the highest short-range disorder, which can in principle be caused by the smallest particle size (see Fig. 2), i.e., that leads to a higher amount of distorted octahedra nearby the surface [53–58]. This behavior may also be related to the adsorption of the capping agents on the particle surfaces. Sulphate group of the SDS capping agent has a stronger adsorption as indicated by the higher difficulty in its complete elimination (Fig. 2a). As a consequence, during the process of calcination, a higher distortion of the material surface may also occur.

3.2 Adsorption and Photocatalytic Tests

As is well-known, the color of azo-dyes is determined by the interaction between the azo bonds ($-N=N-$) and the aromatic groups. Dyes carry an acceptor group, which is an aromatic group that often contains a chromophore, and a donor group, which can be an alkyl chain or OH groups [36, 59]. The cleavage of the $-N=N-$ bonds leads to the dye discoloration, while the band at 292 nm can be assigned to $\pi-\pi^*$ transition related to aromatic ring linked to the azo group. In this case, the decrease in the absorption intensities at 238 and 293 nm indicates a partially degradation of the dye molecular structure [60].

Initial tests using the TiP sample have indicated a better performance when 5 mg of the catalyst was used. In all tests, the solution pH was not modified (pH = 6), which is below of the zero charge point (zcp) of TiO₂ systems, leading to the

protonation of the TiO₂ surface, whereas the dye is anionic, favors the electrostatic interaction with the surface. The lower activity using 10 mg of catalyst can be related to the higher amount of catalyst under suspension, which decreases the radiation penetration. On the other hand, when 2.5 mg was used, the main problem is likely the low catalyst amount.

The Fig. 4 shows that the photodegradation process using TiO₂ decreased the absorption band intensity as the irradiation time (1, 2, and 4 h) increased.

In this case, the highest discoloration and degradation performance was achieved using TiCMC, followed by TiP, and then TiSDS. The TiSDS sample had a very poor performance after 1 h of irradiation, while the discoloration reached at least 70% for all catalysts after 4 h. However, our results for TiCMC are similar to those of P25. No correlation was observed between the photocatalytic efficiency and the surface area for all samples as the highest surface area of TiSDS did not favor the photocatalysis.

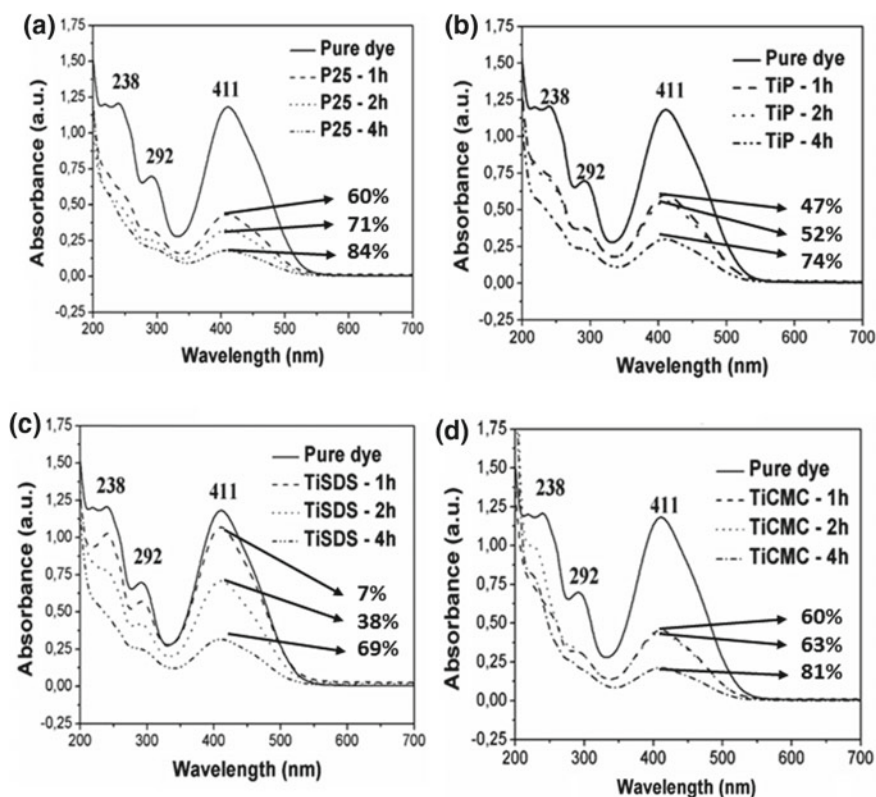


Fig. 4 Results of the photocatalytic test obtained using UV-vis spectroscopy. (a) P25, (b) TiP, (c) TiSDS and (d) TiCMC

PL is widely used to investigate the active sites on the surface of oxide materials. In spite of this, correlation between PL and photocatalytic efficiency is not direct. According to Liqiang et al. [15] if a band-band transition takes place, a high emission usually indicates that a high recombination rate of photo-induced electron-hole pairs takes place, leading to low photocatalytic efficiency. On the other hand, excitonic PL signals mainly result from defects as surface oxygen vacancies. Depending on the properties of the semiconductor, in general, these defects may trap electrons/holes, avoiding its recombination improving the photocatalysis.

In the present work, the excitonic processes depend on the synthesis conditions, as different PL spectra are obtained, indicating a possible different degree of short-range disorder. The TiSDS sample presented the highest short-range disorder, with deep defects, which seems to favor the electron-hole recombination process making their participation in the photocatalytic process more difficult and decreasing its efficiency. The highest photocatalytic efficiency was attained for TiCMC, which presented the highest amount of shallow ones [61–63].

To investigate the retention of dye on solid-liquid interfaces, the sorption isotherms for both TiP and TiCMC catalysts using different initial dye concentrations (as a function of time) were obtained and are present in Fig. 5. The amount of adsorbed dye, q , increased with the contact time for all concentrations and was proportional to the initial concentration of the solution. A sorption/desorption equilibrium was reached at almost the same time for all concentrations. This result indicated that the initial concentration of the dye solutions does not influence the equilibrium time. The maximum adsorption capacity of the dye by the catalysts was reached after 60 min for the TiP (Fig. 5a), and 40 min for the TiCMC (Fig. 5b), which also presented higher adsorption amounts. This behavior may be related to the surface area of TiCMC which is twice that of the TiP.

Regression results for the Langmuir and Freundlich isotherms are presented in Fig. 6, while the calculated parameters are presented in Table 3. Hence, the values

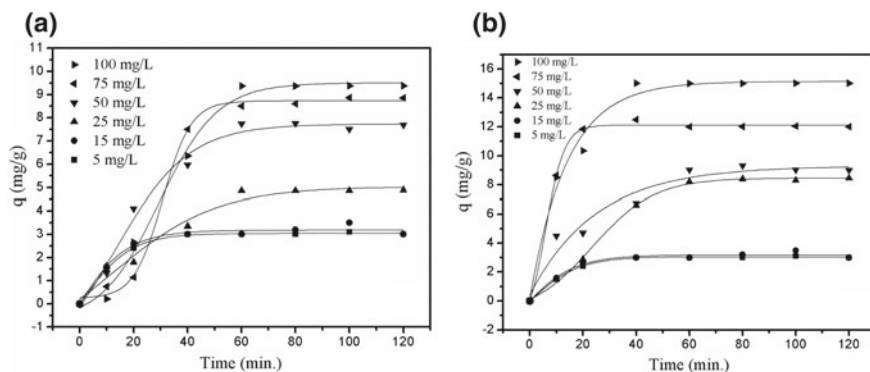


Fig. 5 Adsorption isotherms as a function of time of RNL on TiO_2 for different initial dye concentrations for (a) TiP and (b) TiCMC

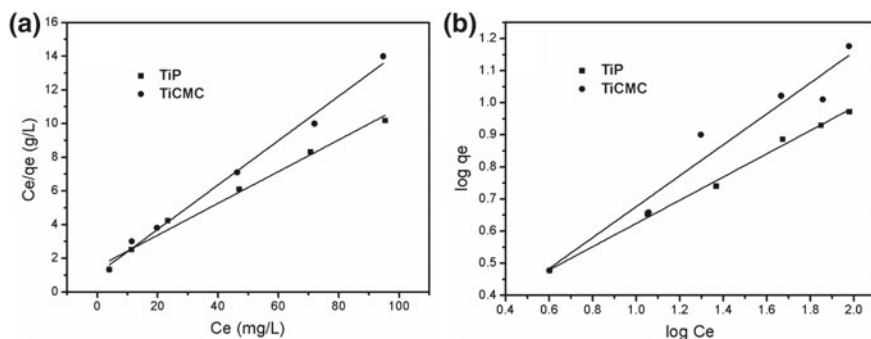


Fig. 6 Linearized isotherms for TiP and TiCMC according to the (a) Langmuir and (b) Freundlich models

Table 3 Langmuir and Freundlich constants obtained for the adsorption of Remazol yellow RNL on the TiP and TiCMC (0.05 g adsorbent, 15.0 mL of a 0–100 mg/L concentration dye at 25 °C)

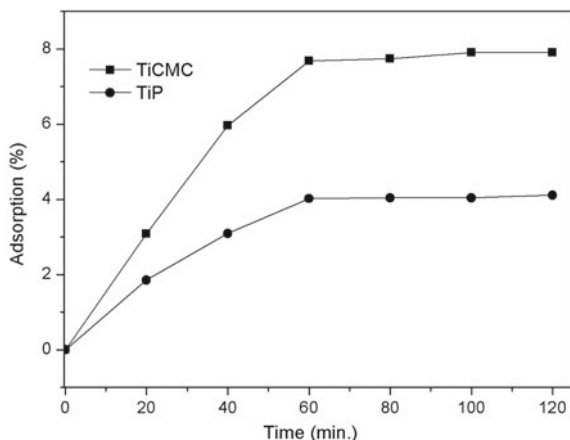
	Photocatalyst	Q ₀ (mg/g)	Q _{0, exp} (mg/g)	K _L (L/mg)	R ²	
Langmuir isotherm	TiP	5.26	7.7	0.10	0.99	
	TiCMC	6.67	12.0	0.10	0.99	
	Photocatalyst	K _F (mg/g)		n (L/g)	R ²	
Freundlich isotherm	TiP	1.3		2.7	0.99	
	TiCMC	1.2		2.0	0.89	
C ₀ (mg/L)	5	15	25	50	75	100
R _L	0.67	0.40	0.28	0.17	0.12	0.09

of correlation coefficient (R^2) were higher for the Langmuir model than the Freundlich one. This indicates that chemisorption is taking place, with the formation of a monolayer on the powder surface.

The calculated R_L values versus initial RNL concentrations are shown in Table 3. R_L values are less than 1, and greater than zero. These results indicate that the adsorption is favorable. Figure 7 presents the discoloration results due to adsorption (tests without radiation) using the TiP and TiCMC catalysts at 50 ppm concentration of the dye.

These results confirm that the discoloration process takes place by the photochemistry mechanism, and not by adsorption only. It also indicates that an indirect mechanism of photodegradation is present, with hole/electron transfer from the semiconductor to the O₂ and/or H₂O molecules, leading to the formation of hydroxyl radicals. Moreover, photocatalysis becomes even more important when higher dye concentrations are present in aqueous media.

Fig. 7 Adsorption test for TiP and TiCMC at different time intervals



4 Conclusions

In summary, TiO_2 particles were prepared in CMC–SDS alcoholic solution under microwave irradiation, facile, rapid, and morphology-controlled synthesis route. The samples in the absence of capping agent promote irregular morphology, compared with capping agent of SDS and CMC favoring the formation of different morphologies. In the process, SDS micelles act as the primary capping agent to mediate the particles with diameter of 10–25 nm and morphology plates according to the micelle templates. CMC supramolecular act as the secondary capping agent to fabricate TiO_2 spheres, this because the CMC is a polymer with different groups which interact with the particle surface by different mechanisms—electrostatic interaction. These results indicate that the capping agent inhibits the growth process of the particles increasing the surface area.

Finally, we show that TiO_2 plates presented the highest amount of deep defects level, which decreases its efficiency in the photocatalytic process. Deep defects levels are also observed for TiP, but a higher amount of shallow defects are present in this sample. The highest photocatalytic efficiency was attained for TiCMC, which presented the lowest amount of deep defects and the highest amount of shallow ones. The photocatalysts also showed a high adsorption capacity and the model was well fitted in terms of the photocatalytic discoloration of RNL.

Acknowledgements This work is supported by Brazilian Funding Agencies FAPESP, CNPq/MCTIC, CT-INFRA/FINEP/MCTIC and Coordenação de Aperfeiçoamento de Pessoal de Nível Superior—Brasil (CAPES)—Finance Code 001.

References

1. Xing, Z., Zhang, J., Cui, J., et al.: Recent advances in floating TiO₂-based photocatalysts for environmental application. *Appl. Catal. B* **225**, 452–467 (2018)
2. Liu, M., Li, H., Wang, W.: Defective TiO₂ with oxygen vacancy and nanocluster modification for efficient visible light environment remediation. *Catal. Today* **264**, 236–242 (2016)
3. Zou, M., Xiong, F., Ganeshraja, A.S., et al.: Visible light photocatalysts (Fe, N):TiO₂ from ammonothermally processed, solvothermal self-assembly derived Fe–TiO₂ mesoporous microspheres. *Mater. Chem. Phys.* **195**, 259–267 (2017)
4. Soni, H., Nirmal, J.I., Patel, K., Kumar, R.N.: Photocatalytic decoloration of three commercial dyes in aqueous phase and industrial effluents using TiO₂ nanoparticles. *Desalin Water Treat* **57**, 6355–6364 (2016)
5. Soutsas, K., Karayannis, V., Poullos, I., et al.: Decolorization and degradation of reactive azo dyes via heterogeneous photocatalytic processes. *Desalination* **250**, 345–350 (2010)
6. Wu, W., Xue, X., Jiang, X., et al.: Lattice distortion mechanism study of TiO₂ nanoparticles during photocatalysis degradation and reactivation. *AIP Adv.* **5**, 057105 (2015)
7. Dufour, F., Pigeot-Remy, S., Durupthy, O., et al.: Morphological control of TiO₂ anatase nanoparticles: what is the good surface property to obtain efficient photocatalysts? *Appl. Catal. B* **174–175**, 350–360 (2015)
8. Kumar, S.M., Deshpande, P.A., Krishna, M., et al.: Photocatalytic activity of microwave plasma-synthesized TiO₂ nanopowder. *Plasma Chem. Plasma Process.* **30**, 461–470 (2010)
9. Zhang, J., Wu, B., Huang, L., et al.: Anatase nano-TiO₂ with exposed curved surface for high photocatalytic activity. *J. Alloys. Compd.* **661**, 441–447 (2016)
10. Naldoni, A., Allieta, M., Santangelo, S., et al.: Effect of nature and location of defects on bandgap narrowing in black TiO₂ nanoparticles. *J. Am. Chem. Soc.* **134**, 7600–7603 (2012)
11. Ding, Y., Zhang, X., Chen, L., et al.: Oxygen vacancies enabled enhancement of catalytic property of Al reduced anatase TiO₂ in the decomposition of high concentration ozone. *J. Solid State Chem.* **250**, 121–127 (2017)
12. Silva Junior, E., La Porta, F.A., Siu-Liu, M., et al.: A relationship between structural and electronic order–disorder effects and optical properties in crystalline TiO₂ nanomaterials. *Dalton Trans.* **44**, 3159–3175 (2015)
13. Valentin, C.D., Selloni, A.: Bulk and surface polarons in photoexcited anatase TiO₂. *J. Phys. Chem. Lett.* **2**, 2223–2228 (2011)
14. Verma, R., Samdarshi, S.K.: Correlating oxygen vacancies and phase ratio/interface with efficient photocatalytic activity in mixed phase TiO₂. *J. Alloys Compd.* **629**, 105–112 (2015)
15. Liqiang, J., Yichun, Q., Baiqi, W., et al.: Review of photoluminescence performance of nano-sized semiconductor materials and its relationships with photocatalytic activity. *Sol. Energy Mater. Sol. Cells* **90**, 1773–1787 (2006)
16. Dong, B., Liu, T., Li, C., Zhang, F.: Species, engineering and characterizations of defects in TiO₂-based photocatalyst. *Chinese Chem. Lett.* **29**, 671–680 (2018)
17. Suprabha, T., Roy, H.G., Thomas, J., et al.: microwave-assisted synthesis of titania nanocubes, nanospheres and nanorods for photocatalytic dye degradation. *Nanoscale Res. Lett.* **4**, 144–152 (2009)
18. Hu, W., Dong, F., Zhang, J., et al.: A high-efficiency photocatalyst, flaky anatase@natural rutile composite using one-step microwave hydrothermal synthesis. *Res. Chem. Intermed.* **44**, 705–720 (2018)
19. Su, C.-H., Hu, C.-C., Sun, Y.-C.C., Hsiao, Y.-C.: Highly active and thermo-stable anatase TiO₂ photocatalysts synthesized by a microwave-assisted hydrothermal method. *J. Taiwan Institute Chem. Eng.* **59**, 229–236 (2016)
20. Cheng, T., Zhang, G., Xia, Y., et al.: Template-free synthesis of titania architectures with controlled morphology evolution. *J. Mater. Sci.* **51**, 3941–3956 (2016)
21. Borkar, S.A., Dharwadkar, S.R.: Effect of microwave processing on polymorphic transformation of TiO₂. *Ceram. Int.* **30**, 509–514 (2004)

22. Jia, X., He, W., Zhang, X., et al.: Microwave-assisted synthesis of anatase TiO₂ nanorods with mesopores. *Nanotechnology* **18**, 75602–75607 (2007)
23. Wang, H.W., Kuo, C.H., Lin, H.C., et al.: Rapid formation of active mesoporous TiO₂ photocatalysts via micelle in a microwave hydrothermal process. *J. Am. Ceram. Soc.* **89**, 3388–3392 (2006)
24. Hart, J.N., Menzies, D., Cheng, Y.B., et al.: A comparison of microwave and conventional heat treatments of nanocrystalline TiO₂. *Sol. Energy Mater. Sol. Cells* **91**, 6–16 (2007)
25. Oh, S.W., Park, S., Sun, Y.: Hydrothermal synthesis of nano-sized anatase TiO₂ powders for lithium secondary anode materials. *J. Power Sources* **161**, 1314–1318 (2006)
26. Chen, Z., Li, W., Zeng, W., et al.: Microwave hydrothermal synthesis of nanocrystalline rutile. *Mater. Lett.* **62**, 4343–4344 (2008)
27. Murugan, A.V., Samuel, V., Ravi, V.: Synthesis of nanocrystalline anatase TiO₂ by microwave hydrothermal method. *Mater. Lett.* **60**, 479–480 (2006)
28. Nešić, J., Manojlović, D.D., Anđelković, I., et al.: Preparation, characterization and photocatalytic activity of lanthanum and vanadium co-doped mesoporous TiO₂ for azo-dye degradation. *J. Mol. Catal. A-Chem.* **378**, 67–75 (2013)
29. Fumin, W., Shi, Z., Gong, F., et al.: Morphology control of anatase TiO₂ by surfactant-assisted hydrothermal method. *Chinese J. Chem. Eng.* **15**, 754–759 (2007)
30. Luo, S., Wang, F., Shi, Z., Xin, F.: Preparation of highly active photocatalyst anatase TiO₂ by mixed template method. *J. Sol-Gel Sci Technol* **52**, 1–7 (2009)
31. Lv, K.L., Yu, J.G., Cui, L.Z.: Preparation of thermally stable anatase TiO₂ photocatalyst from TiOF₂ precursor and its photocatalytic activity. *J. Alloy. Compd.* **509**, 4557–4562 (2011)
32. Chowdhury, I.H., Ghosh, S., Naskar, M.K.: Aqueous-based synthesis of mesoporous TiO₂ and Ag–TiO₂ nanopowders for efficient photodegradation of methylene blue. *Ceram. Int.* **42**, 2488–2496 (2016)
33. Kumaresan, L., Prabhu, A., Palanichamy, M., Murugesan, V.: Synthesis of mesoporous TiO₂ in aqueous alcoholic medium and evaluation of its photocatalytic activity. *Mater. Chem. Phys.* **126**, 445–452 (2011)
34. Li, C.-Y., Jia, Y.-R., Zhang, X.-C., et al.: Photocatalytic degradation of formaldehyde using mesoporous TiO₂ prepared by evaporation-induced self-assembly. *J. Cent. South Univ.* **21**, 4066–4070 (2014)
35. D’Elia, D., Beauger, C., Hochepped, J.F., et al.: Impact of three different TiO₂ morphologies on hydrogen evolution by methanol assisted water splitting: nanoparticles, nanotubes and aerogels. *Int. J. Hydrogen Energy* **36**, 14360–14373 (2011)
36. Moura, K.F., Maul, J., Albuquerque, A.R., et al.: TiO₂ synthesized by microwave assisted solvothermal method: experimental and theoretical evaluation. *J. Solid State Chem.* **210**, 171–177 (2014)
37. Langmuir, I.: The adsorption of gases on plane surfaces of glass, mica and platinum. *J. Am. Chem. Soc.* **40**, 1361–1403 (1918)
38. Freundlich, H.M.F.: Über die adsorption in losungen. *Z Phys. Chem. A* **57**, 385–470 (1906)
39. Webber, T.W., Chakravorti, R.K.: Pore and solid diffusion models for fixed-bed adsorbers. *AIChE J.* **20**, 228–238 (1974)
40. Sjoblom, J., Blokhuis, L.A.M., Sun, W.M., Friberg, S.E.: Surfactants and cosurfactants in lamellar liquid crystals and adsorbed on solid surfaces—I, the model system sodium dodecyl sulfate/butanol or sodium dodecyl sulfate/benzyl alcohol and α -alumina. *J. Colloid Interf. Sci.* **140**, 481–491 (1990)
41. Meguro, K., Shoji, N.: Application of keto-enol tautomerism to the study of micellar property of surfactants. In: Mittal, K.L. (ed.) *Solution chemistry of surfactants*, vol. 1. Plenum Press, New York (1979)
42. El-Roz, M., Bazin, P., Thibault-Starzyk, F.: An operando-IR study of photocatalytic reaction of methanol on new *BEA supported TiO₂ catalyst. *Catal. Today* **205**, 111–119 (2013)
43. Vieira, F.T.G., Melo, D.S., Lima, S.J.G., et al.: The influence of temperature on the color of TiO₂: Cr pigments. *Mater. Res. Bull.* **44**, 1086–1092 (2009)

44. Golubovic, A., Šćepanović, M., Kremenovic, A., et al.: Raman study of the variation in anatase structure of TiO₂ nanopowders due to the changes of sol–gel synthesis conditions. *J. Sol-Gel. Sci. Technol.* **49**, 311–319 (2009)
45. Šćepanovic, M.J., Grujić-Brojčin, M., Dohčević-Mitrović, Z., Popović, Z.: Characterization of anatase TiO₂ nanopowder by variable-temperature Raman spectroscopy. *Sci. Sint.* **41**, 67–73 (2009)
46. Albuquerque, A.R., Garzim, M.L., Santos, I.M., et al.: DFT study with inclusion of the grimme potential on anatase TiO₂: structure, electronic, and vibrational analyses. *J. Phys. Chem. A* **116**, 11731–11735 (2012)
47. Sekiya, T., Kamei, S., Kurita, S.: Luminescence of anatase TiO₂ single crystals annealed in oxygen atmosphere. *J. Lumin.* **89**, 1140–1142 (2000)
48. Iijima, K., Goto, M., Enomoto, S., et al.: Influence of oxygen vacancies on optical properties of anatase TiO₂ thin films. *J. Lumin.* **128**, 911–913 (2008)
49. Toyoda, T., Yindeesuk, W., Okuno, T., et al.: Electronic structures of two types of TiO₂ electrodes: inverse opal and nanoparticulate cases. *RSC Adv* **5**, 49623 (2015)
50. Nishanthi, S.T., Sundarakannan, B., Subramanian, E., et al.: Enhancement in hydrogen generation using bamboo like TiO₂ nanotubes fabricated by a modified two-step anodization technique. *Renew. Energy* **77**, 300–307 (2015)
51. Choudhury, B., Choudhury, A.: Oxygen defect dependent variation of band gap, urbach energy and luminescence property of anatase, anatase–rutile mixed phase and of rutile phases of TiO₂ nanoparticles. *Physica E* **56**, 364–371 (2014)
52. Longo, V.M., Cavalcante, L.S., Erlo, R., et al.: Strong violet–blue light photoluminescence emission at room temperature in SrZrO₃: joint experimental and theoretical study. *Acta Mater.* **56**, 2191–2202 (2008)
53. Ju, T., Lee, H., Kang, M.: The photovoltaic efficiency of dye sensitized solar cell assembled using carbon capsulated TiO₂ electrode. *J. Ind. Eng. Chem.* **20**, 2636–2640 (2014)
54. Shanmugam, M., Durcan, C., Gedrim, R.J., et al.: Oxygenated-graphene-enabled recombination barrier layer for high performance dye-sensitized solar cell. *Carbon* **60**, 523–530 (2013)
55. Tang, B., Hu, G.: Two kinds of graphene-based composites for photoanode applying in dye-sensitized solar cell. *Power Sources* **220**, 95–102 (2012)
56. Kumar, K.S., Song, C.-G., Bak, G.M., et al.: Phase control of yttrium (Y)-doped TiO₂ nanofibers and intensive visible photoluminescence. *J. Alloy. Compd.* **617**, 683–687 (2014)
57. Arier, Ü.Ö.A., Tepehan, F.Z.: Influence of heat treatment on the particle size of nanobrookite TiO₂ thin films produced by sol–gel method. *Surf. Coat. Technol.* **206**, 37–42 (2011)
58. Manassero, A., Satuf, M.L., Alfano, O.M.: Evaluation of UV and visible light activity of TiO₂ catalysts for water remediation. *Chem. Eng. J.* **225**, 378–386 (2013)
59. Moura, K.F., Chantelle, L., Rosendo, D., et al.: Effect of Fe³⁺ doping in the photocatalytic properties of BaSnO₃ Perovskite. *Mater. Res.* **20**, 317–324 (2017)
60. Chen, C.-Y., Cheng, M.-C., Chen, A.-H.: Photocatalytic decolorization of remazol black 5 and remazol brilliant orange 3R by mesoporous TiO₂. *J. Environ. Manage.* **102**, 125–133 (2012)
61. Katoh, R., Murai, M., Furube, A.: A electron–hole recombination in the bulk of a rutile TiO₂ single crystal studied by sub-nanosecond transient absorption spectroscopy. *Chem. Phys. Lett.* **461**, 238–241 (2008)
62. Jie, H., Park, H., Chae, K., et al.: Suppressed recombination of electrons and holes and its role on the improvement of photoreactivity of flame-synthesized TiO₂ nanopowders. *Chem. Phys. Lett.* **470**, 269–274 (2009)
63. Xin, B., Ren, Z., Wang, P., et al.: Study on the mechanisms of photoinduced carriers separation and recombination for Fe³⁺-TiO₂ photocatalysts. *Appl. Surf. Sci.* **253**, 4390–4395 (2007)

Magnetic Molecularly Imprinted Polymers for Selective Adsorption of Quinoline: Theoretical and Experimental Studies



Liz Nayibe Martinez Saavedra, Ricardo Gonçalves Penido, Lucas de Azevedo Santos, Teodorico de Castro Ramalho, Bruno Eduardo Lobo Baeta and Adilson Candido da Silva

Abstract For the synthesis of magnetic molecularly imprinted polymers (MMIPs), quinoline was used as a template molecule, methacrylic acid (MAA) as a functional monomer, ethylene glycol dimethacrylate (EGDMA) as a cross-linking agent and toluene as porogenic solvent, adding magnetic character with nanoparticles of maghemite ($\gamma\text{-Fe}_2\text{O}_3$). The solvents for extraction of the template were cyclohexane (EC) or a mixture of methanol/acetic acid (9:1 v/v) (EM), obtaining the materials MMIP-EC and MMIP-EM nomenclatures corresponding to the respective extractions. The materials were characterized by thermogravimetric analysis (TGA), infrared with Fourier transform (FT-IR), scanning electron microscopy (SEM), X-ray diffraction (XRD) and specific area (BET). The adsorption capacity of the materials was evaluated through kinetic tests and adsorption isotherms at different temperatures. 288.15, 298.15, 308.15 and 318.15 K. The adsorption process was evaluated with thermodynamic parameters $\Delta_{\text{ads}}G^\circ$, $\Delta_{\text{ads}}H^\circ$, and $\Delta_{\text{ads}}S^\circ$. In order to shed some light on the interaction between monomer and template, theoretical calculations were carried out. Results indicate 3-hour balance time. For MMIP-EM, more efficient adsorption was shown with the temperature increase, with an adsorption capacity q_{max} in 318.15 K of 36.66 mg g⁻¹. Negative values of $\Delta_{\text{ads}}G^\circ$ and positives of $\Delta_{\text{ads}}H^\circ$ indicate spontaneous, favorable, endothermic and physical adsorption processes. The printing factor (IF) of quinoline over MMIP-EM was 1.086 indicating better adsorption effectiveness in the selective process.

Keywords MMIP · Quinoline · Adsorption · Selectivity

L. N. M. Saavedra · R. G. Penido · B. E. L. Baeta · A. C. da Silva (✉)
Departamento de Química, Instituto de Ciências Exatas e Biológicas,
Universidade Federal de Ouro Preto, Ouro Preto, Minas Gerais 35400-000, Brazil
e-mail: adilsonqui@iceb.ufop.br; adilsonufla@gmail.com

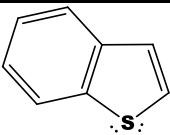
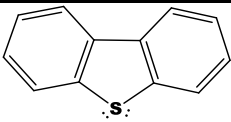
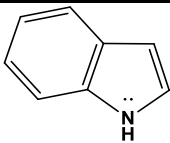
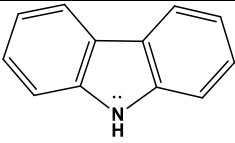
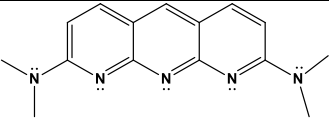
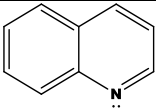
L. de Azevedo Santos · T. de Castro Ramalho
Departamento de Química, Universidade Federal de Lavras, Lavras,
Minas Gerais 37200-000, Brazil

1 Introduction

Adsorption processes have been studied for several years demonstrating really effective results in the removal of toxic compounds, which significantly affect human health. Quinoline is one of them, found mostly compounds from petroleum such gasoline, diesel, kerosene, etc. The environmental repair generated by the burning, combustion of these hydrocarbons is a task that needs a lot of studies. Hydrodesnitration (HDN) and hydrodesulphurization (HDS) processes are currently performed with the aim of ensuring permissible limits. For diesel the maximum sulphur limit in its composition is 50 ppm and for gasoline of 300 ppm, respectively, thus reaching international standards. With all these guidelines to be met, technological innovations appear in order to strengthen and meet environmental requirements, one of them is the use of magnetic molecular imprinted polymers (MMIPs) as selective adsorbents for the removal of specific contaminants, which are in this case the heterocyclic compounds (quinoline, benzothiofene-BTs, dibenzothiophene-DBTs, Indol, Carbazole, Acridine etc.) shown in Table 1, coming from fossil fuels. Previous studies have demonstrated the low effectiveness of removing these with conventional technologies [12].

The low removal of nitrogen or sulfur compounds in conventional treatments is attributed to the presence of nitrogen compounds. Nitrogen compounds strongly inhibit the removal process, this by the competitive adsorption that nitrogen atoms exhibit on the active sites present on the surface of the catalysts, compared to sulfur atoms. This phenomenon happens because of differences in the electronegativity of

Table 1 Some heterocyclic polluting compounds in fuels

POLLUTANT COMPOUNDS IN FUELS		
		
Benzothiophene BT	Dibenzothiophene DBT	Indol
		
Carbazole	Acridine	Quinoline

the two atoms involved (nitrogen and sulfur) producing an acceptance/donation of the free electrons present in the atom [14, 24]. It is then highlighted that, if nitrogen removal in conventional methods is prioritized, most likely the total removal of sulfur atoms will be effective, thus reaching the limits that are required, or better yet by improving concentration below those limits. This is how research focuses mainly on the study of the removal of nitrogenous heterocyclic compounds in this case quinoline, through the development of molecular printing technologies that can be as a continuous process along with HDTs.

2 Materials and Methods

2.1 Chemicals

Quinoline (98%), Dibenzothiophene (98%), Carbazole ($\geq 95\%$), methacrylic acid (MAA), ethylene glycol dimethacrylate (EGDMA), and 2,2'-azobisisobutyronitrile (AIBN) were purchased from Sigma Chemical Company, U.S.A. Toluene (Quimex), cyclohexane (Dinâmica), methanol, NaOH (Synth), and n-Heptane (Neon Ltda) were acquired from Brazilian Chemical Industries. Glacial acetic acid (Merck KGaA) from Germany. All chemicals were used as received from the manufacturer without additional purification.

2.2 Apparatus

Thermogravimetric analyses were performed on an SDT2960 from room temperature to 1000 °C with a rate of 10 °C per minute under an inert atmosphere of N₂. FTIR spectra were scanned in a range of 400–4000 cm⁻¹ using an ABB Bomem FTIR spectrometer equipped with accessories of diffuse attenuated reflectance (DRIFT). The quantification and identification of quinoline, dibenzothiophene, and carbazole were carried out on a spectrophotometer UV–VIS (Hewlett Packard 8453) in the wavelength of 314 nm, and on a Gas Chromatograph BID 2010 Plus SHIMADZU equipped with plasma detector and a column SH-Rtx-5. SEM images were carried out on a JSM-5500 scanning electron microscope. Surface area and porosity were determined from adsorption experiments using an AutosorbIQ surface area and pore size analyzer. X-ray diffraction analyses were performed using a Panalytical Empyrean diffractometer equipped with a graphite monochromator, nickel filter and CuK α radiation ($\lambda = 1.54056 \text{ \AA}$, 40 kV, and 20 mA). For the analysis of the polymers, a scanning (2θ) of 10–80° and step of 0.5° min⁻¹ was applied.

2.3 Preparation of $\gamma\text{-Fe}_2\text{O}_3$

$\gamma\text{-Fe}_2\text{O}_3$ nanoparticles were prepared by dissolving 5.56 g $\text{Fe}(\text{SO}_4)_2(\text{NH}_4)_2 \cdot 6\text{H}_2\text{O}$ in highly purified water. After this stage 100 mL of NaOH (2 mol L^{-1}) were added slowly drop by drop until the formation of a green precipitate. After the formation of a precipitate, 5 mL of H_2O_2 30% (v/v) were immediately added with continuous stirring. The precipitate was washed several times with distilled water and dried in a vacuum desiccator at room temperature [11].

2.4 Preparation of MMIP-EC and MMIP-EM

The magnetic molecularly imprinted polymer was synthesized by the method "Bulk". The polymerization mixture was formed adding the template (Quinoline) in 1 mmol (0.13 mL) and 3 mmol (0.26 mL) of functional monomer (MAA) dissolved in 20 mL of Toluene in a closed amber bottle. The mixture was kept under stirring for 1 h. After the solubilization, 22.5 mmol (4.25 mL) of the cross-linking agent (EGDMA) and 1 g of maghemite $\gamma\text{-Fe}_2\text{O}_3$ previously solubilized in 1 mL of oleic acid were added to the reaction. This mixture was maintained under ultrasonic stirring for 30 min. After this time 1 mL of the radical initiator (AIBN) was added. The reaction medium was purged with the N_2 flow for 8 min to ensure an inert atmosphere. The polymerization was carried out at 70 °C under constant stirring for 72 h. The template was removed by Soxhlet extraction with a solution containing MeOH and glacial acetic acid (90:10 v/v) for MMIP-EM or cyclohexene for MMIP-EC at 80 °C for 48 h until no quinoline was detected in the eluate. Verification was performed using UV-VIS spectrophotometer UV-VIS (Hewlett Packard 8453) wavelengths of 235 and 225 nm, respectively. After guaranteed the removal of the template the polymer was dried at 40 °C for 24 h and stored at room temperature. At the same time, the magnetic non-imprinted polymer (MNIP-EM and MNIP-EC) was prepared as a reference using the same reaction mixture without the addition of the template and being treated by the same procedure used for preparing the MMIP-EM and MMIP-EC. A schematic representation of the process employed for the preparation of MMIP is shown in Fig. 1.

2.5 Adsorption Tests

In the adsorption studies, n-heptane was used as a solvent for simulating the gasoline medium. The quinoline quantification was made in triplicate and the adsorption capacities determined by Eq. (1).

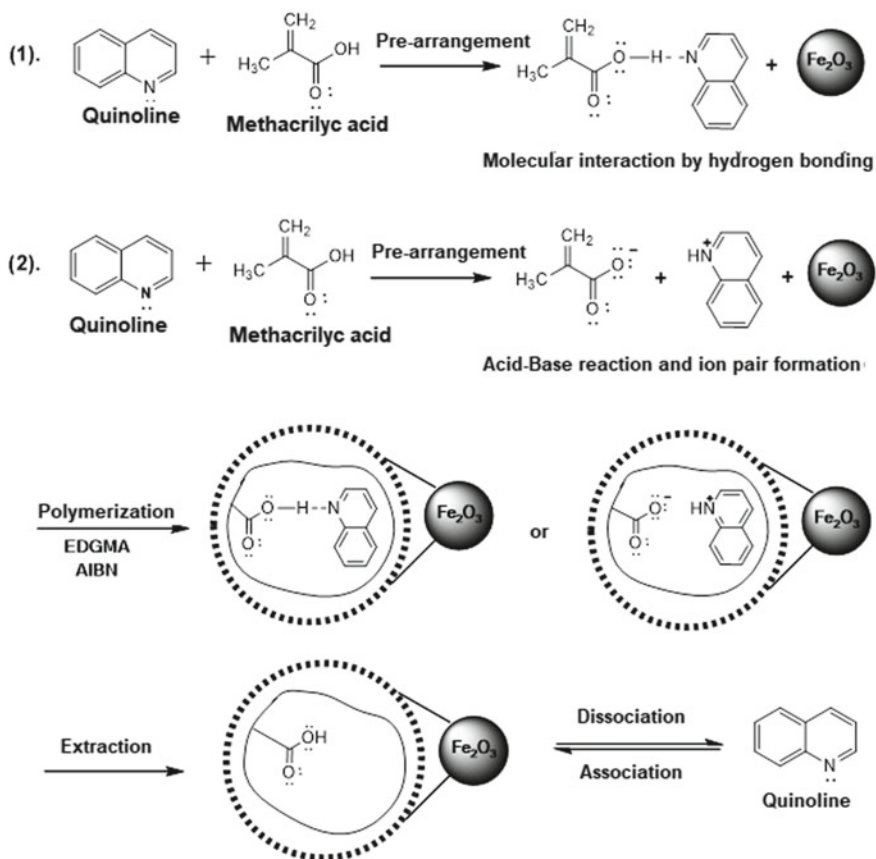


Fig. 1 Schematic illustrations of two possible molecular printing procedures

$$q_e = \frac{(C_i - C_f)\nu}{m} \quad (1)$$

where q_e (mg g^{-1}) is the equilibrium adsorption capacity, C_i and C_f (mg L^{-1}) are the adsorbate concentrations before and after the adsorption, respectively; ν (L) is the volume of the solution, and m (g) is the mass of adsorbent.

The binding percentage (B), the distribution coefficient (K_d), and the printing factor (IF), evaluate the affinity for quinoline that was created in MMIPs. The printing actor (IF) parameter considered the most important, relates the printing ability with the binding, which allows the choice of the best materials [15]. Materials with values of IF > 1.5 are considered adsorbents with an effective binding yield and selectivity by the target molecule.

$$B = \frac{(C_i - C_e)}{C_i} \cdot 100 \quad (2)$$

$$K_d = \frac{C_e}{q_e} \quad (3)$$

$$IF = \frac{K_d(MIPs)}{K_d(NIPs)} \quad (4)$$

2.6 Isotherm Adsorption

Quinoline solutions were prepared at different concentrations 4, 12, 20, 28, 36, 44, 52, 60, 68, 76 and 82 mg L⁻¹ and in each assay were added 10 mg of the polymeric materials in an amber bottle with 5 mL of quinoline solutions previously prepared. All the experiments of isotherms adsorption were carried out in triplicate. Adsorption isotherm studies were carried out in a Shaker Tecnal (TE-421) with temperature control device at 288.15, 298.15, 308.15, and 318.15 K, the samples were kept under stirring at 180 rpm for 4 h. The data were fitted to nonlinear models of Sips and Temkin.

The Sips model is a versatile expression that can simulate behaviors of the Langmuir and Freundlich models. It is a model of three parameters, deduced for the prediction of heterogeneous adsorption systems, and avoids limiting the concentration of adsorbate output in the Freundlich model [16]. Equation 5 represents the mathematical model:

$$q_e = \frac{Q_m b C_e^{1/n}}{1 + b C_e^{1/n}} \quad (5)$$

where b is the affinity constant of adsorption (L mg⁻¹) and n is a heterogeneity index. The Temkin model assumes that the decrease in the adsorption heat is linear in all the adsorbent layers; this is due to possible adsorbate/adsorbent interactions. Thus, the adsorption is characterized as being uniform over the entire contact surface [13]. Equation 6 represents the model:

$$q_e = \left(\frac{RT}{b_T} \right) \ln(A_T C_e) \quad \therefore B = \frac{RT}{b_T} \quad (6)$$

where R is the gas constant, T is the temperature in kelvin, and A_T and b are Temkin constants.

2.7 Kinetic Studies

5 mL of 50 mg L⁻¹ quinoline solution was placed in contact with 10 mg of MMIP-EM or MNIP-EC and kept under stirring at 180 rpm in a Shaker Tecnal incubator (TE-421) at 288.15, 298.15, 308.15, and 318.15 K. Aliquots of 2 mL were taken at predetermined times (5, 15, 30, 60, 90, 120, 180, 240 and 300 min), centrifuged and analyzed. The experimental data were fitted to nonlinear pseudo first PFO, second order PSO, and order n PNO.

The model described by Lagergren may also be manifested for the kinetic model of order n PON, Expressing the adsorption rate according to the nonlinear equation usually represented by the Eq. 7 [22]:

$$\frac{q_t}{q_e} = 1 - \frac{1}{[1 + (n-1)q_e^{n-1}k_n t]^{1/(n-1)}} \quad (7)$$

where n is the order of the reaction and k_n (gⁿ⁻¹ mg¹⁻ⁿ min⁻¹) the adsorption constant of the PON model.

The kinetic model pseudo-first order (PPO) states that each adsorbent molecule is assigned an adsorbent adsorption site and governed by a surface reaction, where in terms of velocity is represented as in the following differential equation [19]:

$$\frac{dq_t}{dt} = k_{1ads}(q_e - q_t) \quad (8)$$

where q_e e q_t (mg g⁻¹) are the adsorption capacities in equilibrium and time t respectively, k_{1ads} (min⁻¹) is the adsorption velocity constant. After integration and application of boundary conditions $t = 0$ a $t = t$, e $q_t = 0$ para $q_t = q_t$, the integrated form of Eq. 8 generates the nonlinear equation [23]:

$$q_t = q_e(1 - e^{-k_{1ads}t}) \quad (9)$$

The kinetic model pseudo-second order (PSO) establishes that for each adsorption molecule two active adsorption sites are assigned, where control of reaction speed is given by chemical reaction. The differential equation [7] most widely used is expressed as:

$$\frac{dq_t}{dt} = k_{2ads}(q_e - q_t)^2 \quad (10)$$

where k_{2ads} (g mg⁻¹ min⁻¹) is the velocity constant.

2.8 Thermodynamic Parameters

The parameters of the changes in Gibbs free energy (ΔG°), enthalpy (ΔH°) and entropy (ΔS°) were determined by the Eqs. 11 and 12.

$$\Delta G^\circ = -RT \ln K_p \quad (11)$$

where K_p (L g^{-1}) is the thermodynamic equilibrium constant, T (K) is the absolute temperature, R ($8.314 \text{ J mol}^{-1} \text{ K}^{-1}$) is the ideal gas constant. The equilibrium thermodynamic constant was obtained from the where K_p is the thermodynamic constant of equilibrium, T (K) is the absolute temperature, and R ($8.314 \text{ J mol}^{-1} \text{ K}^{-1}$) is the universal gas constant.

The equilibrium thermodynamic constant was obtained from the Langmuir equation [1, 17, 26]. The variation of Gibbs free energy also is related to the change in entropy and enthalpy at a constant temperature, thus:

$$\ln K_p = \left(\frac{-\Delta H^\circ}{R} \right) \left(\frac{1}{T} \right) + \frac{\Delta S^\circ}{R} \quad (12)$$

The plot $\ln K_p$ versus $1/T$ follows a straight line, and the slope and intercept coefficient values allow to obtain the values of ΔH° and ΔS° , respectively. The equation of Van't Hoff shows the dependence of the adsorption equilibrium constant and the temperature [3].

2.9 Selectivity Tests for the Quinoline Adsorption

A solution containing 50 mg L^{-1} carbazole, dibenzothiophene, and quinoline in n-heptane was prepared. The experiment was performed by adding 10.00 mg of MIP-EM (the material with better results) to flasks containing 5.00 mL of the simulated mixed solution. The flasks were subjected to constant stirring at 180 rpm and a temperature of 298.15 K for 4 h. After adsorption, the supernatant was separated and analyzed in a GC BID2010 Plus Gas Chromatograph (SHIMADZU) with a plasma detector and SH-Rtx-5 column using the following parameters: detector temperature of 553 K, injection opening temperature of 623 K, furnace temperature of 493 K. Through the parameters outlined in Eqs. (13–14), specific coefficients were determined to evaluate the selectivities of the imprinted adsorbents. The distribution coefficient K_d (L g^{-1}) for each compound was calculated by the Eq. 3.

The selectivity coefficient k of quinoline concerning the analogous molecule (identified as X) was calculated by Eq. 10, as follows:

$$k = \frac{K_d(\text{Quinolina})}{K_d(X)} \quad (13)$$

The relative selectivity coefficient k' in relation to MMIP-EM and MNIP-EM was calculated as follows:

$$k' = \frac{k_{\text{MMIP-EM}}}{k_{\text{MNIP-EM}}} \quad (14)$$

2.10 Recyclability Studies

In this study, after adsorption of the quinoline (50 mg L^{-1}) in the organic phase (10.00 mL) over 10.00 mg of MIPs, the adsorbents were collected and separated from the solution. The polymers were vacuum filtrated and washed with methanol/acetic acid (9:1 v/v). Then, the adsorbents were regenerated in 10.00 mL methanol/acetic acid solution on a thermostatic shaker at $25 \text{ }^\circ\text{C}$ for 1 h, or until quinoline could not be determined in the eluate. The regenerated MIPs were used to adsorb quinoline again (50 mg L^{-1}) at 298.15 K over a contact time of 4 h. In total, five regeneration cycles were performed.

2.11 Computational Details

To understand the interaction between monomer and template (Fig. 3), optimization and frequency calculations were performed at the M06-2X/6-311++g(d, p) level using Gaussian 09 software [5]. The solvation environment was implicitly simulated by the IEFPCM method [6, 9, 21] using toluene at a temperature of 343.15 K . For the dissociation studies, the Gibbs free energy for the reaction $\text{MAA} \cdots \text{Quinoline} \rightarrow \text{Quinoline} + \text{MAA}$ was calculated in methanol and cyclohexane.

3 Results and Discussion

Figure 1 shows schematic illustrations of two possible molecular printing procedures in MMIPs are shown, being a result of molecular interaction through hydrogen bonding between monomer and template and the second by acid-base reaction with formation of an ionic pair.

3.1 Characterization

3.1.1 Thermogravimetric Analysis

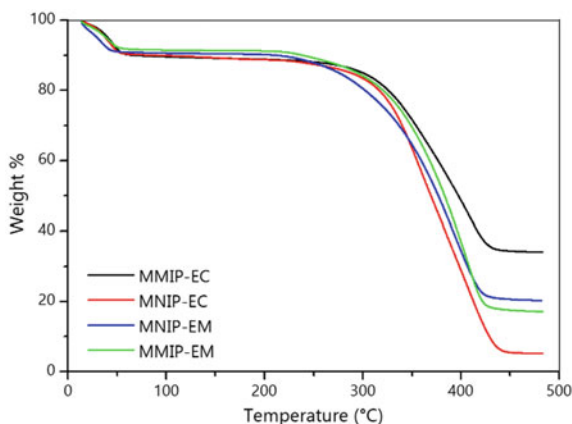
Figure 2 presents the thermogravimetric analyses of the polymeric materials obtained after the extraction of the template.

In all graphs it can be perceived that at the beginning of the decomposition process of all materials, up to an approximate temperature of 50 °C, 10% mass loss was observed, possibly due to traces of volatile compounds trapped inside the cavities of the materials [18]. A major loss of mass is presented for all adsorbents in the temperature range of 250–450 °C, with percentages between 56 and 90%. Mass loss of 55%, 70% and 72%, corresponding to the polymers MMIP-EC, MNIP-EM, MMIP-EM. This decomposition in the material happens by which part of the mass in the magnetic polymers corresponds to a compound that does not decompose thermally. The presence of the maghemite ($\gamma\text{-Fe}_2\text{O}_3$) in the cavities of the polymer printed in connection with some active site decreases the loss of mass [18]. Whereas the melting point of the maghemite ($\gamma\text{-Fe}_2\text{O}_3$) starts at temperatures greater than 1400 °C. It is possible to conclude that the amount of mass of the magnetic compound present in MMIPs is 35%-MMIP-EC, 20%-MNIP-EM and 18%-MMIP-EM and 6%-MNIP-EC.

3.1.2 Scanning Electronic Microscopy (SEM)

Figure 3 shows the images of the surfaces of the materials obtained by SEM. The different micrometric scales of 10–20 μm , the external morphology of each sample with increases from 800 to 1000 times, showing macroporous cavities. It can be perceived that in the images of the MNIPs EC and EM, some white particles are presented, which can be attributed to maghemite, $\gamma\text{-Fe}_2\text{O}_3$.

Fig. 2 TGA profiles for the magnetic molecularly polymers



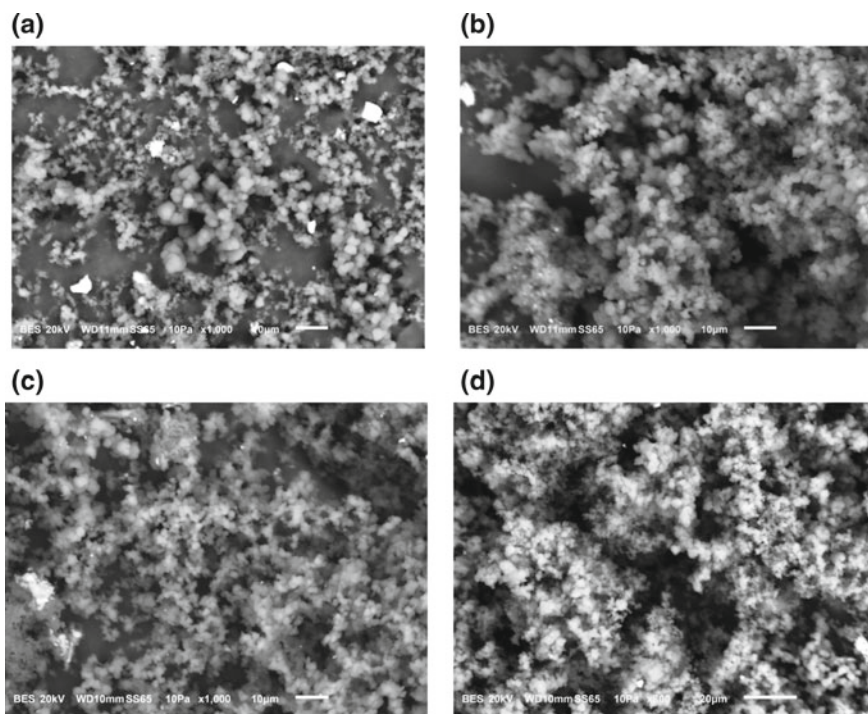


Fig. 3 SEM images of the different synthesized polymers: **a** MNIP-EC, **b** MMIP-EC, **c** MNIP-EM, **d** MMIP-EM

3.1.3 Surface Characterization

Table 2 presents the characterization of the polymers obtained by the adsorption/desorption method of N_2 at a temperature of 77 K, by analyzing the adsorption isotherms and the results of the pore size distribution BJH.

MMIP-EM developed the largest specific area ($263.65 \text{ m}^2 \text{ g}^{-1}$), to syntheses in the presence of maghemite ($\gamma\text{-Fe}_2\text{O}_3$) allows further development in specific areas.

Table 2 Surface characterization of MMIPs and MNIPs

Polymer	Specific area BET ($\text{m}^2 \text{ g}^{-1}$)	Average pore sizes (\AA)		Pore volume DR ($\text{cm}^3 \text{ g}^{-1}$)		
		Micro	Meso	Micro	Meso	Total
MNIP-EC	67.042	17.739	127.146	0.034	1.434	1.467
MMIP-EC	148.288	17.763	128.612	0.073	1.058	1.132
MNIP-EM	86.917	17.754	131.637	0.043	1.317	1.360
MMIP-EM	263.65	17.292	96.132	0.124	0.782	0.905
$\gamma\text{-Fe}_2\text{O}_3$	79.131	13.128	74.278	0.055	1.199	1.254

With respect to pore volume, for all MMIPs, there was a greater development of the amount of mesopores (20–500 Å) than micropores (<20 Å). MMIP-EM obtained a greater amount of micropores ($0.124 \text{ cm}^3 \text{ g}^{-1}$) compared to other materials. The average size of the micropores for all materials was 17 Å, and mesopores of 120–130 Å. Note that the specific areas of the MNIPs are much lower than those of the corresponding MMIPs, this indicates that the porogenic solvent has better developed the porous structure in the presence of the template, this occurs by the formation of specific molecular interactions between the monomer, template and solvent.

These interactions were explored by mean of theoretical calculations to understand the role of solvent in the interactions between monomer and template. Monomer and template are bonded via hydrogen bonding (HB), in which the template acts as HB acceptor via the nitrogen atom as well as weak HB donor through a C–H bonding (see Fig. 4). On the other hand, the monomer also acts as both HB donor and acceptor. These interactions are slightly less stabilizing in methanol than in cyclohexane, around $0.7 \text{ kcal mol}^{-1}$ (see Table 3). The destabilization of HB in methanol due to the competition between the monomer and the solvent for the template, whereas the cyclohexane is a non-polar solvent with no HB accepting or donating sites. Obviously, methanol can also be a strong HB donor to interact with nitrogen of the quinoline. However, the solvent will not be strong enough to dissociate completely the quinoline from the MAA, since the acid can also accept one hydrogen via its carbonyl oxygen.

As consequence of the weakening of the hydrogen bonds, the dissociation of the template from the monomer is more favorable in methanol than in cyclohexane (see Table 3). In methanol, the dissociation is exergonic, giving the Gibbs free energy value of $-3.0 \text{ kcal mol}^{-1}$. In cyclohexane, its value is only $0.1 \text{ kcal mol}^{-1}$. It should be emphasized that dissociation reactions are often entropically favorable. Thus, the hydrogen bonds are so stabilizing in cyclohexane that starts to overcome the gain in entropy. If there are solvents competing by the leading interactions between monomer and template, the entropy factor will prevail over the stabilization through intermolecular interactions, favoring the dissociation process.

Fig. 4 MAA-Quinoline hydrogen bonding interactions

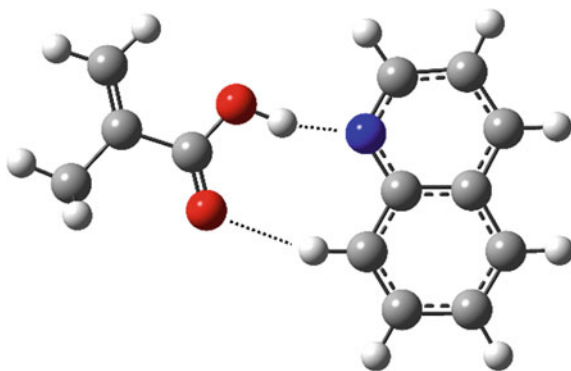


Table 3 MAA and Quinoline interaction energies and Gibbs free energy for the dissociation^[a] in kcal mol⁻¹[^{b]}

Polymer	ΔE	ΔG
MMIP-EC	-12.9	0.1
MMIP-EM	-11.6	-3.0

^[a]Energy for the reaction MAA...Quinoline \rightarrow Quinoline + MAA. Computed at IEFPCM-M06-2X/6-311++g(d, p), 345.15 K and 1 atm

During the template removal, it seems that the solvent has some influence in the availability of micropores. The solvent should have considerable polarity, but, most importantly, must be a hydrogen bonding donor strong enough to break the HB between monomer and template.

3.1.4 Fourier Transform Infrared (FTIR)

Figure 5 shows the spectra corresponding to the printed polymers obtained after template extraction. For all polymers there is similarity in the bands. A broad band at 3170–3672 cm⁻¹ with maximum at 3500 cm⁻¹ is observed, attributed to the stretch mode (O–H) of hydroxyl groups of the functional monomer MAA [10]. The position and asymmetry of the band at lower wavelengths indicate the presence of strong hydrogen bonds of carboxylic acids or alcohols. The band in 2900 cm⁻¹ appears due to stretch vibration (C–H) and its stretch-deformation (CH₂) arises in 1384 cm⁻¹ [25]. In 1480 cm⁻¹ a band appears which is attributed to the stretch (–COO) of MAA, and strong bands in 1750 (C=O), 1230 and 1125 cm⁻¹ (C–O–C) characteristics of ester of EGDMA [4, 8]. The bands in 937, 875 e 750 cm⁻¹ due to deformation outside the plane of (C–H) for different substituted benzene rings. A small band is presented in 1633 cm⁻¹ by the vibrations (C–C) of aromatic rings. The medium broad band in 625–520 cm⁻¹ with maximum on 580 cm⁻¹ is attributed to the bond Fe–O. Spectra indicate that Quinoline extraction was effective, because the spectra of MMIP with the template printing are the same as those of the materials MNIP without the impression of Quinoline, this indicates that in the polymeric materials there is no template residue, indicating that the use of the washing solvents was adequate.

3.2 Adsorption Tests

Table 4 shows the values of the adsorbed quantity (q_e), binding percentage (B), of the distribution coefficient (K_d), and the impression factor (IF), data obtained from the adsorption study performed for each of the materials. The determination of the parameters was made through the Eqs. (2), (3) e (4). Binding percentage values (B) indicate that materials with methanol extraction MMIP-EM/MNIP-EM were

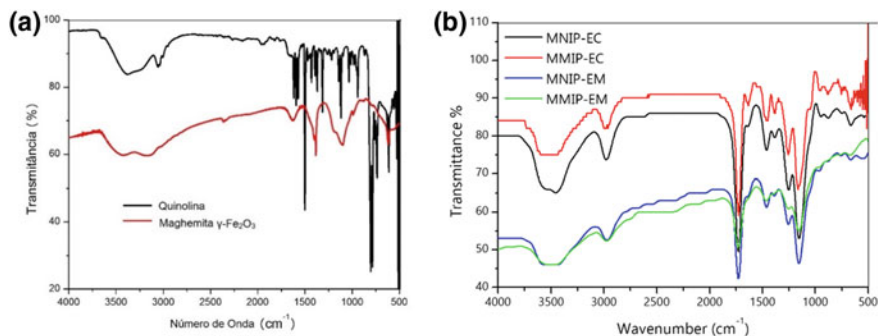


Fig. 5 FTIR spectra **a** Quinoline and maghemita ($\gamma\text{-Fe}_2\text{O}_3$), **b** MMIPs and MNIPs after extraction

those that presented the highest adsorption capacity. The recognition of MMIPs in relation to MNIPs can be confirmed when evaluating the impression factor, demonstrating that specific sites for quinoline were formed more efficiently in the synthesized polymers using methanol as extraction solvent.

3.2.1 Kinetics Studies

Figure 6 presents the corresponding graphs of the kinetic models of pseudo order n -PON, pseudo first order-PPO and pseudo second order-PSO, indicate that for all materials the adsorbed amounts increase over time to steady state, maximum adsorption capacity is reached after a given time (240 min).

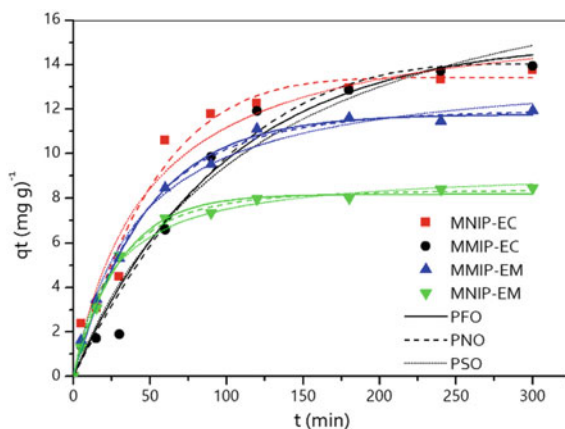
Table 5 shows the parameters determined for each nonlinear model obtained for the materials studied. The model that best fit the materials was the pseudo-order n (PON). This choice was motivated by the fact that the order model n generated lower RMSE values and R^2 values closer to 1, when compared to the other models.

Parameter n is responsible for measuring the order of the reaction, the values of this variable for synthesized polymers were close to 1. Adjustment of this model may indicate that the adsorption process for toluene synthesized materials occurs by occupying a single active site on a solid and energetically homogeneous surface, present in the materials [20].

Table 4 Data obtained from polymer adsorption study

Polymer	q_e (mg g^{-1})	B (%)	K_d (L g^{-1})	IF
MNIP-EC	8.340	33.360	0.250	0.953
MMIP-EC	8.075	32.303	0.238	
MNIP-EM	10.078	42.313	0.366	1.086
MMIP-EM	11.586	44.347	0.398	

*B =Percent binding, K_d = Coefficient of distribution, IF = Print Factor

Fig. 6 Kinetic models **a** and intraparticle diffusion **b** of the polymers**Table 5** Adsorption kinetic parameters of MMIPs and MNIPs

MODEL	POLYMER	MNIP-EC	MMIP-EC	MNIP-EM	MMIP-EM
	$q_{e,exp}$ (mg g^{-1})	13.761	13.940	8.450	11.928
<i>Pseudo first order</i>	$q_{e,calc}$ (mg g^{-1})	–	15.144	8.176	11.768
	K_1 (min^{-1})	–	0.010	0.020	0.033
	X^2	–	0.921	0.063	0.180
	Adj. R^2	–	0.971	0.990	0.993
	R^2	–	0.974	0.995	0.997
	RMSE	–	0.960	0.084	0.141
<i>Pseudo second order</i>	$q_{e,calc}$ (mg g^{-1})	16.570	15.846	9.329	13.970
	K_2 (min^{-1})	1.24E-3	3.97E-4	4.37E-3	1.70E-3
	X^2	1.073	1.251	0.152	0.158
	Adj. R^2	0.962	0.961	0.984	0.987
	R^2	0.983	0.982	0.993	0.994
	RMSE	1.036	1.118	0.130	0.132
<i>Pseudo order n</i>	$q_{e,calc}$ (mg g^{-1})	13.419	14.040	8.364	11.970
	k_n (min^{-1})	0.029	0.024	0.013	0.021
	n	0.817	0.663	1.238	1.138
	X^2	0.744	0.795	0.098	0.149
	Adj. R^2	0.973	0.975	0.992	0.992
	R^2	0.989	0.990	0.997	0.997
	RMSE	0.863	0.892	0.104	0.129

According to the adsorption studies carried out, the MMIP-EM material was selected to develop subsequent studies (isothermal, thermodynamic, selectivity and regeneration) because it developed a better molecular recognition against quinoline printing, demonstrating that specific sites were formed with greater efficiency in the polymers in which the methanol extraction solvent was used.

3.2.2 Adsorption Isotherms

Figure 7 shows an increase in the amount of quinoline adsorbed with increasing temperature. The differences in q_e values of MMIP-MS and MNIP-MS give an idea of the selective recognition ability of MMIP by Quinoline. From the results it can be observed that the most remarkable specific recognition was obtained at the temperature of 298.15 K, with a difference in adsorption capacities of $7.0 \text{ (mg g}^{-1}\text{)}$ between MNIP-EM and MMIP-EM. Remembering that in MMIP-EM was incorporated the compound $\gamma\text{-Fe}_2\text{O}_3$ in the polymeric matrix, conferring magnetic properties on the material. The results are interesting from the application point of view, since the magnetic property of the polymer allows the reuse of the material, facilitating the subsequent steps of separation. Some authors demonstrated that MMIPs with magnetic properties develop a better specific area, more efficient selective recognition and removal, this is thanks to the small particles inserted into the polymers, which contain unique physical and chemical properties.

Table 6 shows the parameter values determined by the models used for the adsorption system. The model that best fit the data was that of Sips., the range of R^2

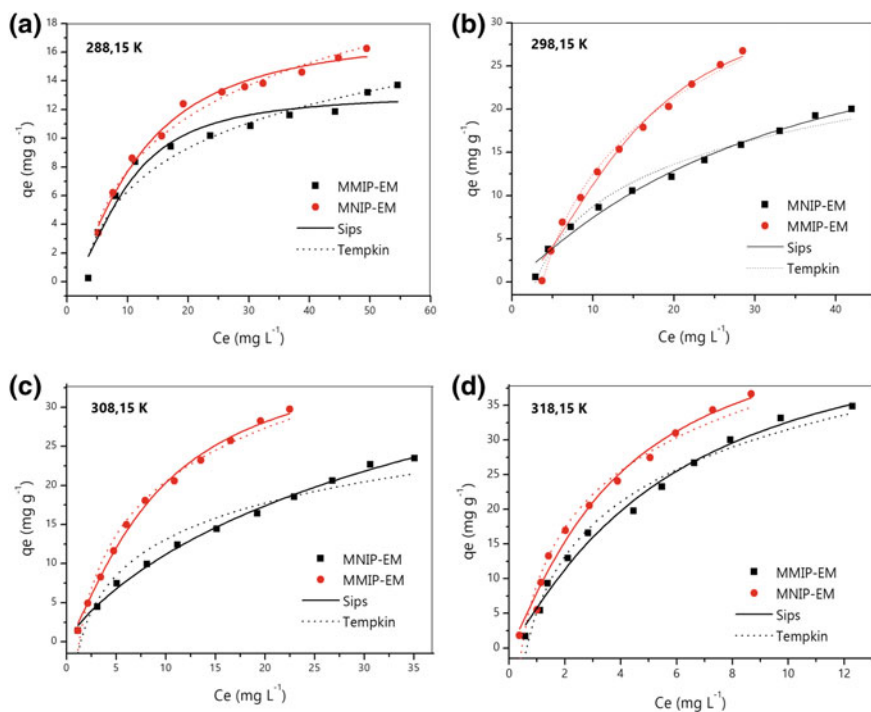


Fig. 7 Non-linear Sips and Temkin models obtained at different temperatures for MMIP-EM adsorption isotherms

correlation coefficient values ranged from 0.994 to 0.997, In addition, the RMSE and X^2 values presented for this model were better when compared to those observed for the other model. The principle of the Sips equation considers that on the adsorbent surface there are active sites with different adsorption forces, where molecules interact with an active site, indicating energetic heterogeneity on the surface. The surface heterogeneity of the adsorbent is described by the parameter (n), where for homogeneous surfaces the value of (n) is equal to or close to 1 thus reducing the isotherm expression to the Langmuir equation, and for values of (n) less than 1 the porous material is said to be energetically heterogeneous. The values of parameter (n) presented in Table 6, obtained for MNIP-EM (0.545; 0.900; 0.669; 0.865) and MMIP-EM (0.562; 0.543; 0.763; 0.821) are less than 1, proposing an energetically heterogeneous surface in the corresponding materials, thus establishing a phenomenon of positive cooperation between adsorbate and surface adsorbent.

The Q_{\max} parameter of the model represents the maximum amount of adsorption that can develop the MMIP. Note that the value of this variable increases with increasing temperature, same behavior as for the experimentally determined q_{\exp} adsorbed quantities discussed at the beginning of this item.

Table 6 Parameters obtained from the non-linear equations for the MNIP-EM and MMIP-EM polymers

Polymer		MNIP-EM				MMIP-EM			
Model	Parameters	Temperature (°K)							
		288.15	298.15	308.15	318.15	288.15	298.15	308.15	318.15
Sips	q_{exp} (mg g ⁻¹)	13.699	20.107	23.462	34.851	16.259	26.747	29.761	36.666
	Q_{\max} (mg g ⁻¹)	13.075	34.561	36.019	49.871	16.591	33.747	37.967	49.572
	b (L mg ⁻¹)	0.103	0.031	0.019	0.173	0.090	0.068	0.111	0.258
	n	0.545	0.900	0.669	0.865	0.562	0.543	0.763	0.821
	X^2	0.745	0.444	0.181	1.168	0.348	0.416	0.347	1.495
	Adj. R^2	0.957	0.985	0.995	0.987	0.987	0.994	0.994	0.985
	R^2	0.980	0.994	0.998	0.994	0.994	0.997	0.997	0.994
	RMSE	0.863	0.666	0.426	1.080	0.590	0.645	0.589	1.222
Temkin	b_T (kJ mol ⁻¹)	0.551	0.338	0.359	0.210	0.426	0.188	0.242	0.202
	A_T (L mg ⁻¹)	0.426	0.343	0.713	1.587	0.382	0.266	0.797	2.173
	X^2	0.880	0.843	2.552	2.070	0.458	0.850	1.383	3.984
	Adj. R^2	0.950	0.979	0.942	0.980	0.983	0.985	0.981	0.964
	R^2	0.979	0.990	0.973	0.990	0.993	0.994	0.991	0.984
	RMSE	0.938	0.918	1.597	1.438	0.677	0.922	1.176	1.995

3.2.3 Thermodynamic Parameters

Table 7 presents the thermodynamic parameters obtained by linear analysis of the van't Hoff equation.

Gibbs free energy results, $\Delta_{\text{ads}}G^\circ$, were negative for all adsorption systems, indicating spontaneity in the process, and more negative values represent a more favorable energy adsorption [13]. For all studied systems, it is possible to observe an increase in spontaneity with increasing temperature. Thus, the adsorption enthalpy values $\Delta_{\text{ads}}H^\circ$ obtained in this study for the MMIP-EM (30,521 kJ mol⁻¹), best material in terms of adsorption capacity and selectivity, is in the range in which the adsorption process occurs by the physisorption phenomenon, indicating presence of electrostatic interactions probably being stronger for materials synthesized with toluene. In addition, the positive value obtained from the parameter $\Delta_{\text{ads}}H^\circ$ states that quinoline adsorption was endothermally directed. Entropy results were positive, which indicates an increase in the degree of freedom in the system, this is a consequence of the dissolution between quinoline and n-heptane after adsorption.

3.2.4 Selectivity Tests for the Quinoline Adsorption

Figure 8 shows the graph corresponding to the selective adsorption study. It is remarkable the adsorption capacity developed by the MMIP-EM with quinoline, q_{exp} of (10,983 mg g⁻¹) compared with DBT adsorption and carbazole, q_{exp} detailed in Table 8. A higher adsorption capacity of Carbazole is observed than by DBT in MMIP-EM, one explanation for such behavior is the presence of the nitrogen group in the carbazole molecule, which allows binding of the compound to similarly created printed sites to the interaction of quinoline. The sulfur group present in the DBT structure, makes the molecule likely to bind at the present sites of the printed polymers, the phenomenon could be explained by the fact that the force, as electrostatic attraction or intermolecular force between the DBT of printed materials, was weaker than the hydrogen bond [2]. For the MNIP-EM and MNIP-EM a higher adsorption capacity is observed for carbazole than for quinoline, this is possible due to the absence of stable and preferable binding sites for a single molecule, facilitating and favoring hydrogen bonding with carbazole.

Table 7 Thermodynamic parameters MMIP-EM and MNIP-EM

Polymer	Temperature (K)				$T\Delta_{\text{ads}}S^\circ$ (kJ mol ⁻¹)	$\Delta_{\text{ads}}H^\circ$ (kJ mol ⁻¹)
	288.15	298.15	308.15	318.15		
	$\Delta_{\text{ads}}G^\circ$ (kJ mol ⁻¹)					
MNIP-EM	-19.051	-21.067	-22.720	-25.499	62.319	41.280
MMIP-EM	-20.765	-22.397	-23.895	-26.215	52.951	30.521

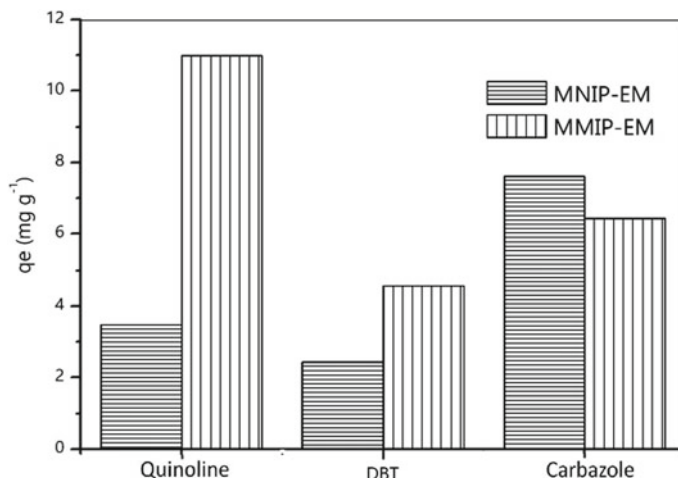


Fig. 8 Adsorption selectivities of quinoline and its analogues on MMIPs

Table 8 Selectivity tests for the quinoline adsorption

Polymer	Selectivity parameters	Template and analog molecule		
		Quinoline	DBT	Carbazole
MNIP-EM	q_{exp} (mg g ⁻¹)	3.475	2.438	7.613
	K_d (L g ⁻¹)	0.080	0.054	0.218
	k	–	1.493	0.368
MMIP-EM	q_{exp} (mg g ⁻¹)	10.983	4.568	6.428
	K_d (L g ⁻¹)	0.391	0.111	0.173
	k	–	3.504	2.263
	k'	–	2.346	6.140

3.2.5 Recyclability Studies

To verify the reusability of the materials studied, material reuse tests were performed. Figure 9 presents the result of the recyclability studies.

After five adsorption/desorption cycles the corresponding adsorption capacities of MNIP-EM and MMIP-EM were maintained. For MMIP-EM the regeneration percentage (70%) decreased in the 3^o cycle and remained practically constant in the other cycles, with final regeneration of 63%. In general, from the results obtained, MMIP-EM synthesized in the present study has a favorable regeneration capacity, with small loss percentages in their initial adsorption capacities. In addition, it is important to highlight the possibility of target molecule recovery and easy separation of magnetic materials.

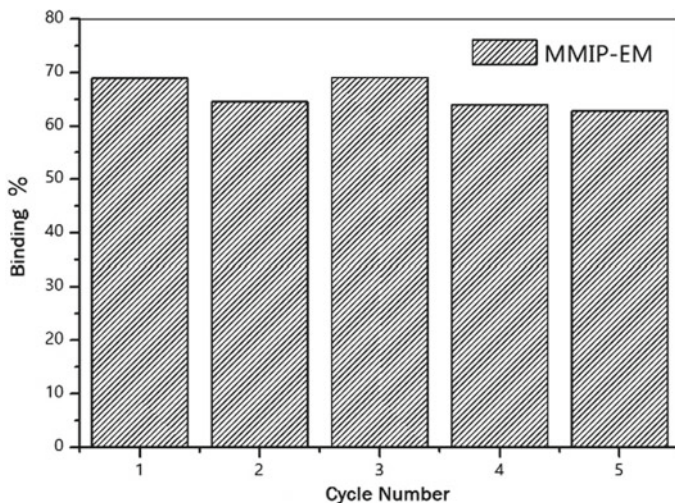


Fig. 9 Reuse of MMIP-EM after five cycles

4 Conclusions

The present work demonstrated that the magnetic polymer synthesis method using methanol/acetic acid (MMIP-EM) may be more suitable for the synthesis of a selective adsorbent for quinoline, developing more efficient specific recognition and high adsorption capacity ($3666.10 \text{ mg g}^{-1}$ at 308.15 K). The methanol/acetic acid favors the interaction compared to cyclohexane because methanol/acetic acid has a higher dielectric constant. Solvents with higher dielectric constants consequently increase the diffusional effect increasing the specificity bond between the template and the monomer.

The computational calculations indicate that hydrogen bonds are predominant between the monomer and the template and methanol/acetic acid favors this interaction. The produced adsorbent materials presented high thermal stability, which enables their use in petrochemical industries. MMIP-EM demonstrated the capability to regenerate itself and to be reused with good efficiency in different cycles, which facilitates the recovery of quinoline after the process.

References

1. Anastopoulos, I., Kyzas, G.Z.: Are the thermodynamic parameters correctly estimated in liquid-phase adsorption phenomena? *J. Mol. Liquids* **218**, 174–185 (2016) (Elsevier B.V.). <https://doi.org/10.1016/j.molliq.2016.02.059>
2. Cao, Y., et al.: Surface molecularly imprinted polymer prepared by reverse atom transfer radical polymerization for selective adsorption indole. *J. Appl. Polym. Sci.* **131**(13), 1–10 (2014). <https://doi.org/10.1002/app.40473>

3. Denderz, N., et al.: Thermodynamic study of molecularly imprinted polymer used as the stationary phase in high performance liquid chromatography. *J. Chromatogr. A* **1235**, 77–83 (2012)
4. Fayazi, M., et al.: Preparation of molecularly imprinted polymer coated magnetic multi-walled carbon nanotubes for selective removal of dibenzothiophene. *Mater. Sci. Semicond. Process.* **40**, 501–507 (2015). (Elsevier)
5. Frisch, M.J., Trucks, G.W., Schlegel, H.B., Scuseria, G.E., Robb, M.A., Cheeseman, J.R., Scalmani, G., Barone, V., Petersson, G.A., Nakatsuji, H., Li, X., Caricato, M., Marenich, A. V., Bloino, J., Janesko, B.G., Gomperts, R., Mennucci, B., Hratchian, H.P., Ortiz, J.V., Izmaylov, A.F., Sonnenberg, J.L., Williams-Young, D., Ding, F., Lipparini, F., Egidi, F., Goings, J., Peng, B., Petrone, A., Henderson, T., Ranasinghe, D., Zakrzewski, V.G., Gao, J., Rega, N., Zheng, G., Liang, W., Hada, M., Ehara, M., Toyota, K., Fukuda, R., Hasegawa, J., Ishida, M., Nakajima, T., Honda, Y., Kitao, O., Nakai, H., Vreven, T., Throssell, K., Montgomery, J.A., Jr., Peralta, J.E., Ogliaro, F., Bearpark, M.J., Heyd, J.J., Brothers, E.N., Kudin, K.N., Staroverov, V.N., Keith, T.A., Kobayashi, R., Normand, J., Raghavachari, K., Rendell, A.P., Burant, J.C., Iyengar, S.S., Tomasi, J., Cossi, M., Millam, J.M., Klene, M., Adamo, C., Cammi, R., Ochterski, J.W., Martin, R.L., Morokuma, K., Farkas, O., Foresman, J.B., Fox, D.J.: Gaussian, Inc., Wallingford CT. Gaussian 09, Revision C.01 (2009)
6. Guimaraes, A.P., et al.: Design of new chemotherapeutics against the deadly anthrax disease. docking and molecular dynamics studies of inhibitors containing pyrrolidine and riboamidrazone rings on nucleoside hydrolase from bacillus anthracis. *J. Biomol. Struct. Dyn.* **28**(4), 455–467 (2011). <https://doi.org/10.1080/07391102.2011.10508588>
7. Ho, Y.S., McKay, G.: The kinetics of sorption of divalent metal ions onto sphagnum moss peat. *Water Res.* **34**(3), 735–742 (2000)
8. Huang, W., et al.: Selective adsorption of dibenzothiophene using magnetic molecularly imprinted polymers. *Adsorpt. Sci. Technol.* **30**(4), 331–344 (2012)
9. La Porta, F.A., et al.: Orbital signatures as a descriptor of regioselectivity and chemical reactivity: the role of the frontier orbitals on 1,3-dipolar cycloadditions. *J. Phys. Chem. A* **115**, 824–833 (2011)
10. Lee, S.H., Doong, R.A.: Adsorption and selective recognition of 17 β -estradiol by molecularly imprinted polymers. *J. Polym. Res.* **19**(8) (2012)
11. Leone, V.O., Pereira, M.C., Aquino, S.F., Oliveira, L.C.A., Correa, S., Ramalho, T.C., Gurgel, L.V., Silva, A.C.: Adsorption of diclofenac on a magnetic adsorbent based on maghemite: experimental and theoretical studies. *New J. Chem.* **42**, 437–449 (2018)
12. Liu, D., Gui, J., Sun, Z.: Adsorption structures of heterocyclic nitrogen compounds over Cu(I) Y zeolite: a first principle study on mechanism of the denitrogenation and the effect of nitrogen compounds on adsorptive desulfurization. *J. Mol. Catal. A: Chem.* **291**(1–2), 17–21 (2008)
13. Liu, K., et al.: Adsorption of Cu(II) ions from aqueous solutions on modified chrysotile: thermodynamic and kinetic studies. *Appl. Clay Sci.* **80–81**, 38–45 (2013) (Elsevier B.V.)
14. Liu, K., Ng, F.T.T.: Effect of the nitrogen heterocyclic compounds on hydrodesulfurization using in situ hydrogen and a dispersed Mo catalyst. *Cataly. Today* **149**(1–2), 28–34 (2010)
15. Liu, L., et al.: Rational design and preparation of magnetic imprinted polymers for removal of indole by molecular simulation and improved atom transfer. *RSC Adv.* **4**, 605–616 (2014)
16. Liu, W., et al.: Selective removal of benzothiophene and dibenzothiophene from gasoline using double-template molecularly imprinted polymers on the surface of carbon microspheres. *Fuel* **117**(PART A), 184–190 (2014) (Elsevier Ltd.)
17. Milonjić, S.K.: A consideration of the correct calculation of thermodynamic parameters of adsorption. *J. Serb. Chem. Soc.* **72**(12), 1363–1367 (2007)
18. Niu, D., et al.: Preparation and characterization of magnetic molecularly imprinted polymers for selective recognition of 3-methylindole. *J. Appl. Polym. Sci.* **130**(4), 2859–2866 (2013)

19. Pinzón-bedoya, M.L., Estella, L.U.Z., Villamizar, V.: Modelamiento de la cinética de Bioadsorción de Cr (III) usando cáscara de naranja. *Dyna* **160**(III), 95–106 (2009)
20. Plazinski, W., Rudzinski, W., Plazinska, A.: Theoretical models of sorption kinetics including a surface reaction mechanism : a review. *Adv. Colloid Interface Sci.* **152**(1–2), 2–13 (2009) (Elsevier B.V.). <https://doi.org/10.1016/j.cis.2009.07.009>
21. Thompson, J.D., et al.: New universal solvation model and comparison of the accuracy of the SM5.42R, SM5.43R, C-PCM, D-PCM, and IEF-PCM continuum solvation models for aqueous and organic solvation free energies and for vapor pressures. *J. Phys. Chem. A* **108**, 6532–6654 (2004). <https://doi.org/10.1021/jp0496295>
22. Tseng, R., et al.: A convenient method to determine kinetic parameters of adsorption processes by nonlinear regression of pseudo- n th-order equation. *Chem. Eng. J.* **237**, 153–161 (2014) (Elsevier B.V.). <https://doi.org/10.1016/j.cej.2013.10.013>
23. Wang, L., et al.: Adsorption of Pb(II) on activated carbon prepared from Polygonum orientale Linn.: kinetics, isotherms, pH, and ionic strength studies. *Bioresour. Technol.* **101**(15), 5808–5814 (2010). (Elsevier Ltd.)
24. Wen, J., et al.: A critical study on the adsorption of heterocyclic sulfur and nitrogen compounds by activated carbon: equilibrium, kinetics and thermodynamics. *Chem. Eng. J.* **164**(1), 29–36 (2010) (Elsevier B.V.)
25. Xu, W., et al.: A molecularly imprinted polymer based on TiO₂ as a sacrificial support for selective recognition of dibenzothiophene. *Chem. Eng. J.* **172**(1), 191–198 (2011) (Elsevier B.V.)
26. Zhou, X., Zhou, X.I.N.: The unit problem in the thermodynamic calculation of adsorption using the langmuir equation. *J. Chem. Eng. Commun.* **201**(22), 1459–1467 (2014). <https://doi.org/10.1080/00986445.2013.818541>

Insights into Novel Antimicrobial Based on Chitosan Nanoparticles: From a Computational and Experimental Perspective



Letícia C. Assis, Nerilson M. Lima, Teresinha J. A. S. Andrade, Patricia H. Y. Cordeiro, Carlton A. Taft and Felipe A. La Porta

Abstract Chitosan-based nanoparticles are interesting bioactive polymers for a variety of emergent applications, due to their excellent physicochemical properties. Diverse strategies have been widely used for preparation and processing of chitosan-related nanoparticles. Notable examples include emulsion, ionic gelation, reverse micellar and self-assembling methods. This chapter endeavors to summarize current progress in the understanding of their synthesis and pharmacological potential, from a computational and experimental perspective in order to afford new chemical insights in the materials design with new/tailored properties. This combined approach could contribute to the development of more efficient materials and stimulate creative innovation in this research field. Critical assessment of selected therapeutic usages of this polymer is also discussed in this chapter.

L. C. Assis

Department of Chemistry, Federal University of Lavras, CEP 37200-000 Lavras, Minas Gerais, Brazil

N. M. Lima

Departamento de Química, Universidade Federal de Juiz de Fora, Juiz de Fora, MG, Brazil

T. J. A. S. Andrade

NIAC-Núcleo de Investigação Aplicado às Ciências-Instituto Federal de Educação, Ciência e Tecnologia do Maranhão, IFMA- Campus, Timon, Brazil

P. H. Y. Cordeiro

Laboratório de Engenharia - Colegiado de Engenharia Química, Universidade Tecnológica Federal do Paraná, PR Estr. dos Pioneiros, 3131 - Jardim Morumbi, 86036-370 Londrina, PR, Brazil

C. A. Taft

Centro Brasileiro de Pesquisas Físicas, Rua Dr. Xavier Sigaud, 150, Urca, 22290-180 Rio de Janeiro, Brazil

F. A. La Porta (✉)

NANOQC - Laboratory of Nanotechnology and Computational Chemistry, Federal Technological University of Paraná UTFPR, 86036-370 Londrina, PR, Brazil
e-mail: felipelaporta@utfpr.edu.br

© Springer Nature Switzerland AG 2020

F. A. La Porta and C. A. Taft (eds.), *Emerging Research in Science and Engineering Based on Advanced Experimental and Computational Strategies*, Engineering Materials, https://doi.org/10.1007/978-3-030-31403-3_4

107

Keywords Chitosan · Functional biopolymer · Nanoparticles synthesis · In-silico methods · Bioactivity studies · Nanoparticles · Theoretical modeling · Polymer synthesis

1 Introduction

Chitosan, which is a natural cationic polysaccharide, can be obtained from the alkaline deacetylation process (partially or fully) of the chitin compound, and have received much attention in recent years [1, 2]. This important polysaccharide, however, is composed of N-acetyl-glucosamine and N-glucosamine units linked through β (1 \rightarrow 4) glycosidic bonds and is properly characterized by its average degree of deacetylation [3, 4]. In general, the chitosan compound must have a degree of deacetylation of more than 50% and is considered to be a partially deacetylated polymer group [4, 5]. The possible characteristics, as well as applications of chitosan, depend on the size of its polymer chain and the degree of deacetylation [4, 5]. In addition, this compound has good biocompatibility, mucoadhesive, miscibility with other polymers, low toxicity, easy biodegradability, as well as a highly reactive chemical structure [2–6]. Consequently, chitosan-based nanomaterials can in principle be used in biomedicine [1–9].

There are numerous advantages regarding applications of chitosan-based materials in drug delivery, including for example: (a) an effective drug release control; (b) the ability to help improve the uptake of nanoparticles, since during the manufacture of these materials, in particular, chitosan can dissolve in an acidic aqueous solution, generated free of toxic organic reagents; (c) act as an electrostatic stabilizer, i.e., providing sufficient charge through the free amino groups that are readily available to bind biomolecules, as well as providing optimal stability [1, 3–9]. However, the fundamental understanding of these physical and chemical characteristics may, in principle, contribute to significantly improved intranasal and intravenous drug administration in the brain for example [3, 7, 8].

In terms of biomedical applications, its low water-solubility can be a large limiting factor that results in poor capacity for encapsulation of hydrophilic and hydrophobic drugs [3, 9]. It is well-known that the rational chemical modification of the chitosan materials, in principle, can be used as a strategy for making this compound highly soluble [3–5, 7]. As such, tailoring these functional properties make chitosan nanoparticles an attractive and versatile material for the development of numerous emergent applications [1–9].

In this context, this work presents an overview of the challenges involved in understanding the chitosan-based nanoparticles, from a computational and experimental perspective. Improving the ‘practical’ control of the fabrication of these chitosan related-compounds can in principle help drive the creative innovation in this line of research.

2 Chitosan and the Importance of Computational Methods

Chitosan-based materials are extremely bioactive (likely due to the presence of reactive functional amino groups along the polymer chain) and hence have long been studied for different proposes [1–10]. This fact suggests promising biological, biomechanical and physicochemical properties [5, 10, 11]. These functional properties could contribute to effective applications in various fields, including biotechnology/biomedical applications [4, 9–13].

A better understanding of the chemical nanoscale phenomena has been important for the development of chitosan-based applications and stimulation of emergent new technologies [3, 5, 9]. Numerous recent studies are based on using molecular modeling (robust “in silico” model) as the primary tool. In molecular modeling design studies (Fig. 1), there are usually two approaches widely used in many areas of research [12, 14–21]. First, the classical approach, which covers the

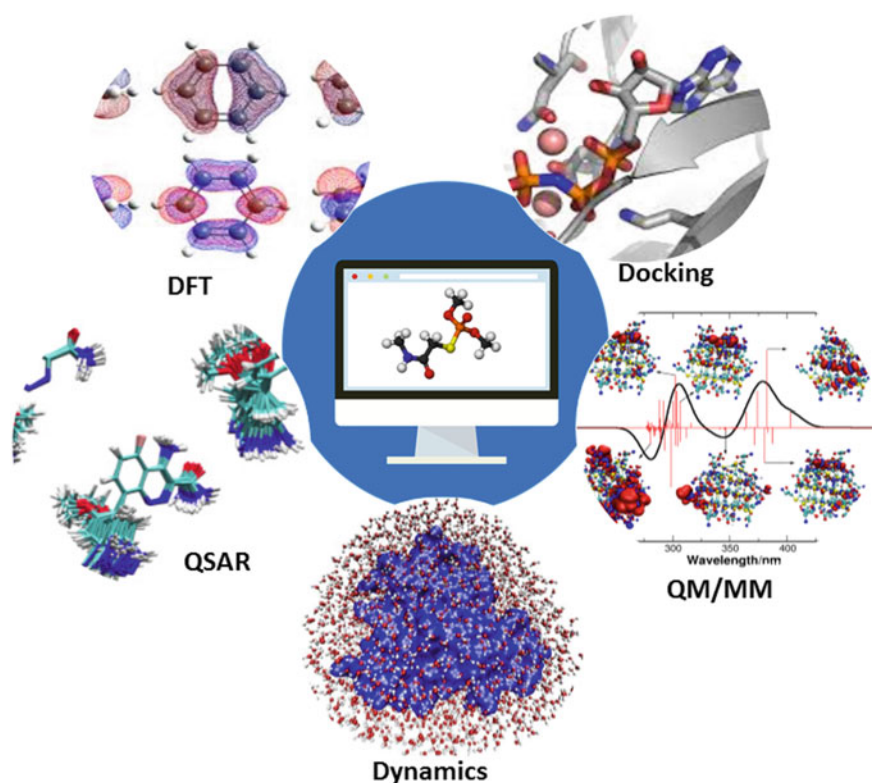


Fig. 1 Computational methodologies derived from the quantum and molecular mechanics-based approaches

methods of molecular mechanics (MM). Second, the quantum approach, which covers the ab initio and semi-empirical methods. Generally, to choose between these two approaches, it is necessary to know which properties to evaluate in the study, as well as the computational capacity available for performing the calculations [12, 14–21].

3 Molecular Mechanics

Obtaining emergent materials with highly tunable properties still represents a major technological challenge. Currently, in order to solve these problems, computational methods have gained considerable attention, especially over the last years. This can also be attributed to the fact that such approaches open the possibility of affording new chemical insights in the materials design [15]. In the field of biomedical applications, in particular, the MM methods are widely used for multiple purposes. Fundamentally, it can be said that in MM calculations, the molecules are described as a set of “connected atoms,” in which each atom is considered as a point mass that is connected by springs, which are chemical bonds [12, 14–21]. Hence, the motion of each atom is determined by the forces acting on it by all other atoms [14]. These forces acting on each particle are, in turn, calculated at each step using parameterized force fields [12, 14–21].

Generally, the force-field parameters involve a complete set of potential interactions between atoms, i.e., linked potential terms (connecting lengths and angles, dihedral angles) and also non-connected atoms (van der Waals and Coulomb interactions) [14–17]. There are different types of force fields, which include other terms, in order to obtain better agreement with vibrational spectra, such as terms that better describe the coupling of oscillations between angles or bonding lengths. The choice of the force field depends, in general, on the properties that will be studied in the system and is a very important step since it directly influences the reliability of the results [15]. There are various methodologies that normally use MM as a strategy whereas those with most usage involve molecular docking, QSAR, and molecular dynamics simulations [15–66].

3.1 Molecular Docking

Molecular docking is a popular methodology employed in predicting the binding mode of the linker within a targeted binding site [15, 31, 32, 66]. This theoretical tool investigates the intermolecular interactions that occur between the ligand and the protein, in cases in which the three-dimensional (3D) structure of the protein is known [33]. Yet, the most commonly used docking programs today are: GLIDE [34]; GOLD[®] [35]; AUTODOCK [36]; and DOCK-6 [37].

In the course of a molecular docking simulation, in particular, innumerable binder positions are generated within the active site of the protein [31–33, 65, 66]. In the design, such poses eventually correspond to the possible positions/orientations acquired by the target binder (in the active site) and its relative stability throughout a simulation. As several poses are generated, in particular, a model is needed to evaluate these solutions, and then we may finally choose the most likely stable structure for the ligand-protein complex [65]. This selection model can, in principle, be represented by the combination of two components: a search algorithm and a score function [15–17, 38, 39, 66].

In this perspective, the search algorithm analyzes the various degrees of freedom of the enzymatic side chains and also the molecular structure of the ligand at the targeted binding site [15–17, 38, 39]. However, in particular, the most used search algorithms in docking programs are: (i) Monte Carlo, (ii) Lamarckian Genetic Algorithm, and (iii) Differential Evolution Algorithm [39, 40, 66]. All docking programs are based fundamentally provided by search algorithms developed in order to obtain a fast computational method and at the same time, capable of identifying the probable modes of connection between two or more molecules.

In addition, the score functions are usually able to classify affinity or intermolecular bonding energy, from the hypothesis that the lowest energy score offers a pathway to determine the best pose from docking [15–17, 31–33, 65, 66]. Currently, docking methods are refined with other computational techniques, such as Molecular Dynamics simulations and calculations using quantitative analysis between chemical structure and biological activity (QSAR), thus providing more accuracy and reliability in the results [65].

3.2 Quantitative Analysis Between Chemical Structure and Biological Activity

The QSAR strategy was developed by Hansch and Fujita in 1964 [41]. This strategy is a popular method that has been widely used for the rational drug development based on target ligands, which predicts the physicochemical and biological properties of new molecules, from the correlation with structural characteristics and properties of the compounds that are codified within descriptors by means of mathematical equations [42–45]. QSAR predicts the properties of new compounds, using mathematical equations, which directly correlates with their structure characteristics (for a large number of similar compounds) [44–48]. Consequently, this tool is less expensive and reduces the time and efforts to find new drug candidates for example [44–48].

Once the structure is known, any molecular descriptor can be calculated, even if the compound of interest is previously synthesized or not [48]. There are several current QSAR methodologies, QSAR-1D to QSAR-7D, each one being characterized by different approaches to calculations, molecular descriptors and statistical algorithms for the construction of highly predictive models [15–22, 49].

3.3 *Molecular Dynamics*

Classical molecular dynamics (MD) simulation is a tool that provides microscopic information about the forces involved in the interaction enzyme-ligand as a function of time and also provides an understanding of the solvent effect on protein dynamics [15–17, 27, 29, 41].

MD calculations, as strategy are in theory based on the numerical solution of Newton's equation of motion and widely used to investigate the structure, dynamics, thermodynamics of biomacromolecules and their complexes [15–17, 28, 29]. In addition, the calculations provide detailed information on the fluctuations and conformational changes of such compounds (i.e., dynamic calculations) [41, 42].

However, it is important to emphasize that the solution of the equation depends on the position, velocity, and also acceleration for each particle. As such, the time interval must be very small so that the acceleration can be considered constant in this interval, allowing simulation of the higher frequency movements of the system, which are often the vibrations of the connections [43, 44]. Normally, the algorithms used in MD calculations to integrate the motion equations are: Verlet's algorithm [45], the Beeman algorithm [46], and the *leap-frog* method [47]. After the definition of the force field, the velocities can be and after integration, the change of coordinates of each particle determined.

Summarizing, the MD equations are solved successively, in a very small space of time generating the "trajectory", which is set of positions and velocities of each particle over time yielding potential and kinetic energies of the system [15–17, 41, 43]. To perform an MD calculation, we can start by identify the initial positions of each particle of the system placed them in the positions of a crystal lattice (box) for example [65]. Thus, in this perspective, the system of interest can be placed inside a box and assume multiple geometries. Subsequently, water molecules can be placed in the box, in cases of biomolecular systems, and a periodic boundary conditions model applied to avoid particles escaping the crystalline network [41, 43].

After the preparation of the initial complex, energy minimization can be done in order to find a set of coordinates that minimize the potential energy of the system [15–17, 43, 48–51]. This is important because there is relaxation of the chemical bonds, the angles between connections and the van der Waals contacts in order to obtain energy close to the local minimum [29, 65]. The most used minimization algorithms are: the steepest descent method that uses the first derivative to determine the direction for the minimum [48, 49]; the conjugate gradient method that uses information from the first derivative prior to determine an optimal search direction [50]; and finally, the Newton-Raphson method, which uses both the first and second derivatives of the function [51].

Then, the system is gradually warmed to the temperature of interest, and the pressure, known as the equilibration, is also adjusted, which is finished when the thermodynamic equilibrium is reached. Frequently used thermostats are: Berendsen thermostat [52], the Nosé-Hoover thermostats [53, 54], and Nosé-Poincaré [53]. Yet, in order to control the pressure, in particular, the most used barostats are those

of Berendsen [49] and Parrinello–Rahaman [55]. Once the equilibration stage has been reached, one can then obtain the MD trajectories [15–17, 65]. Remarkably, MD methods usually work with the energy average. Finally, through the MD calculations, it is possible to analyze the changes of conformation undergone by the enzymes, as well as to investigate and understand the behavior of a chemically active molecule in the active site of a receptor, among other processes [15, 56, 65].

4 Quantum Mechanics

In the first half of the last century, in particular, were established the foundations and the interpretations of quantum mechanics (QM) [15, 18, 57, 58, 66, 67]. Since then, several approximations based on QM methods have widely been developed to solve major problems. In this perspective of design, QM calculations can also be used in combination with MM methods, which in turn provide crucial information towards understanding diverse complex systems. Hence, QM/MM is a hybrid method highly recommended for elucidating the physical and chemical behavior from a fundamental point of view and hence have been widely used in computational medicinal chemistry [15–17, 47–49, 59–61].

4.1 *Mechanical and Molecular Mechanics (QM/MM)*

In recent decades, QM calculations combined with MM calculations have become the method of choice for reactions involving biomolecular systems, solid-state systems, and chemical processes, for example, that occur in explicit solvents [15, 59–61]. Numerous successful applications of these coupled techniques (QM and MM) are addressed in the literature and represent an important computational method that allows the modeling of complex reactions within enzymes, associating the power and accuracy of QM calculations and with the simplicity of MM methods, as well [59–61]. Thus, in this perspective, the QM methods allow the modeling of the electronic processes of interesting complex systems, involved in the breaking or formation of chemical bonds, charge transfer and excitation of electrons in a variety of complex systems of interest [15, 59–61].

In addition, it has the advantage of providing energy information that controls all chemical processes [59, 62]. However, QM calculations only include systems up to a few hundred atoms; therefore, the size and conformational complexity of large molecular structures are a problem for this type of calculation, since these biomolecules require methods capable of analyzing up to hundred thousand atoms and hence allowing simulations along with scales of tens of nanoseconds [59]. One way of investigating the larger systems, in particular, consists of using the MM methods [15–17, 62–64].

Therefore, by associating the two QM and MM techniques, it is possible to study large biomolecules and investigate a small portion of the system, using QM calculations, and the rest of the system by MM methods [59]. For example, in the case of enzymes, the region of the enzyme, which is not directly involved in the reaction, would be treated by calculations of molecular mechanics, which are based on the fields of force, and the region of the active site would be analyzed by QM calculations using an ab initio, semi-empirical, or density functional theory (DFT) [15–17, 62–64, 67–70].

4.2 Density Functional Theory

DFT method describes the energy of the system from the electron probability density ρ [x, y, z] [15, 67–70]. Hence, the electron density and Hamiltonian have a functional relationship that allows the computation of all molecular properties in the ground state without a wave function [15, 58–61, 67, 68]. However, these theorems do not mention how to find ground state energy from ρ or from ψ , so in the 1960s, Kohn and Sham solved this problem by proposing that the purely electronic energy of a molecule with many electrons in the ground state would be represented by Eq. 1 [69, 70]:

$$E_0 = -\frac{1}{2} \sum_{i=1}^n [\Psi_i(1) | \nabla_1^2 | \Psi_i(1)] - \sum_{\alpha} \int \frac{z_{\alpha p}(1)}{r_{1\alpha}} dv_1 + \frac{1}{2} \iint \frac{\rho(1)\rho(2)}{r_{12}} dv_1 dv_2 + E_{xc}[\rho] \quad (1)$$

where $\Psi_i(1)$, $i = 1, 2, \dots, n$ are the Kohn-Sham orbitals, and $E_{xc}[\rho]$ is the exchange and correlation energy. The main problem of the method is the lack of a systematic process to determine $E_{xc}[\rho]$, so several functional types have already been proposed [67–70]. This functional is actually divided into two parts: one of exchange and one of correlation [68].

5 In Silico Studies of Nanoparticles Based on Chitosan and Chitin Derivatives

As mentioned previously, the particular use of polymer nanoparticles as a drug carrier has diverse advantages, for example, in terms of drug protection from degradation, increased biodistribution, increased bioavailability, active targeting by surface functionalization, increased drug efficiency and also reduced levels of toxicity [4, 71–73].

The up-and-coming and remarkable biological properties of chitosan nanoparticles classify this polysaccharide as an essential choice in contributing to the development of more efficient drugs, and this can be proven, due to a large number of research and review articles published in the literature [4, 74, 75]. As noted, several research groups are focused on the development of nanoparticles based on chitosan or derivatives thereof, aiming their potential use (in various forms) in the pharmaceutical area [4, 76, 77]. In light of this, we report some relevant works that used molecular modeling, such as molecular docking, MD simulation, and QSAR, in order to predict the behavior of these chitosan nanoparticles in several therapeutic strategies.

A theoretical investigation on the administration of polymer-based drugs was performed by Mousav and Hashemianzadeh, in 2019, as a function of the radius of the nanoparticles, due to spherically agglomerated PBCA nanoparticles in non-ionic and/or ionic medium [78]. From these characteristics and results, the authors concluded that the comparison of the radius of rotation of the polymer and the equilibrium distance of the donepezil molecules indicated that the chitosan nanoparticles are spherically agglomerated before and after the addition of ions [78]. This finding, however, suggests that the transporter of rivastigmine molecules changed after the addition of ions [78].

In addition, the three-dimensional chitosan nanoparticle lengths and the closest distance to the center of mass of the drug molecules relative to the nanoparticles demonstrate that the entanglement of the polymer chains is decreased [78]. Therefore, this finding suggests that the drug loading capacity in chitosan nanoparticles is reduced in rivastigmine systems compared to donepezil systems. This is likely due to the opening of some polymer chains and the release of some drug molecules [78]. This evaluation showed good agreement between the theoretical results of the MD calculations and other experimental work [78, 79].

Another interesting study was conducted by Dhanasekaran et al. [80], combined *in vitro* and *in silico* approaches to evaluate the drug delivery properties of chitin and chitosan polymers—both in the form of nanoparticles—by using two different therapeutic agents: such as curcumin (a hydrophobic drug) and insulin (a therapeutic protein). Investigation of *in vitro* drug release experiments, in particular, suggests that chitosan nanoparticles exhibited better encapsulation efficiency, drug loading capacity, and also sustained release of drug molecules (both curcumin and insulin) than those of chitin nanoparticles [80]. Meanwhile, *in silico* experiments, using molecular docking and MD methods, were critical in predicting the molecular interactions and binding energy between the nanoparticles and target drug [15–17, 79]. Furthermore, it is well-known that the ability of DNA to capture oligonucleotide molecules from a solution is of great importance in biomedical applications [81–83]. Hence, the DNA hybridization event in which the probe, recognizes the complementary target and forms a stable duplex structure, is the basis of highly specific bio-recognizable devices. The probe is usually a single-stranded DNA covalently immobilized on a functionalized surface [82]. For instance, in 2016, Omar and colleagues applied computational methodologies, such as molecular docking and QSAR, semi-empirical level (PM3), in order to evaluate the interaction

of single-stranded DNA with chitosan-functionalized silicon substrates through binding and the biological activity of the proposed compounds [81].

Recently, there has been a rapid increase in the use of chitosan in applications that require excellent chelation properties. This has substantially promoted interest in experimental and theoretical investigations of metal ion interactions with both native and chemically modified chitosan. The development of novel procedures that improve sorption capabilities and selectivity has also garnered increased attention [84].

In this context, in 2015, Portnyagin and co-workers conducted a theoretical study on the complexation of Ni^{2+} ions with chitosan and its derivatives, (N-(2-pyridylethyl) chitosan (2-PEC), N-(4-pyridylethyl) chitosan (4-PEC), and N-(5-methyl-4-imidazolyl) methyl chitosan (IMC)) [84]. More specifically, the authors employed DFT calculations, B3LYP, and a 6–31 $\text{g}^{**}/\text{SBKJC}$ basis set. Usually, however, this quantum method is robust, reliable, and widely used in theoretical investigations of the complexation of metal ions with chitosan derivatives [85, 86]. Hence, the results showed that the formation of “pendant” structures was more favorable in the case of cross-linked polymers. This is likely due to steric hindrance and the limited number of saccharide units in the vicinity of each other within the polymer network [84]. The ($\text{Ni}^{2+}/2\text{-PEC}$) complexes showed an asymmetric bridge structure, which suggested that the sorption capacity of 2-PEC could be lower than expected from the number of functional groups when adsorption occurs in solutions with a high concentration of Ni^{2+} ions [84]. However, the interactions of Ni^{2+} with nitrogen atoms of the heterocycle in 4-PEC were low for the “pendant” model, suggesting that only “asymmetric bridge” complexes are formed in this case [84]. The $\text{Ni}^{2+}/4\text{-PEC}$ Ni^{2+} complex is predominantly bound to unsubstituted chitosan rings; however, it is possible to form small fractions of “bridge” type complexes with pyridyl-substituted rings [84]. As shown, the stability of chitosan macromolecules depending on the functional substitute type can be written as: ($\text{Ni}^{2+}/\text{IMC}$) ($\text{Ni}^{2+}/2\text{-PEC}$) > ($\text{Ni}^{2+}/\text{chitosan}$) > ($\text{Ni}^{2+}/4\text{-PEC}$), which is consistent with the experimental data [84].

In 2018, Costa and colleagues studied the use of polyelectrolyte complexes (PEC's) formed in aqueous solution by using sodium alginate (SA) and chitosan (CS), which are ionic polysaccharides of natural origin with high availability and low-cost [87]. Hydrogels formed by PECs are one of the most notable materials used for incorporation of bioactive molecules in controlled release delivery systems [4]. Furthermore, due to the highly porous structure of the hydrogels, they can also encapsulate herbicides and pesticides for controlled release into the soil. This ensures constant levels of these agrochemicals in the soil for a significant period of time [4]. In addition, this procedure has the advantage of simplifying the handling and reducing the evaporative losses of these harmful agents, thereby reducing their environmental impact [87].

As well as controlled release in the soil, the polymeric matrices such as SA/CS have widely been employed to incorporate various agrochemical formulations for the removal of waste from water [87]. Hence, the objective of this theoretical study

was to evaluate the possible interactions that stabilize the formation of the SA/CS complex, from dimeric structures of both polysaccharides [87].

Theoretical results showed that the optimized structures of the isolated dimers are maintained by intramolecular hydrogen (H) bonds, as well as investigation on the calculated torsion angles involving the glycosidic bond is in agreement with those found experimentally by X-ray diffraction measurements [87]. Hence, the interaction between the alginate and chitosan dimers was mediated by the addition of two Na^+ cations, but only one of them remains coordinated by both dimers. Intermolecular H bonds involving the $-\text{COO}^-$ and $-\text{NH}_3^+$ groups are also formed, aiding the formation of the SA/CS complex [87].

However, in this case, the LMOEDA method indicates a significant covalent contribution to SA/CS stabilization [87]. In turn, this result also is corroborated by the NBO analysis, which shows a high contribution of the overlap of LP (O) $\rightarrow \sigma^*$ (NH), with an average energy of about 30 kcal mol^{-1} for the formed H bonds [87]. Finally, two water molecules neighboring the complex increase their stability and also promote an octahedral coordinate arrangement around Na^+ [87]. Glyphosate interacts with SA/CS by coordinating Na^+ and binding to the chitosan dimer by H-bond, according to fluorescence microscopy measurements [87].

Another interesting article was developed by Anota and collaborators, in 2014, on the functionalization of graphene with chitosan polymers or other functional groups to vary properties and find new future applications in optoelectronic devices and/or drugs [88]. In this context, the monomer is oriented perpendicularly to the graphene nanosheet (remaining unchanged) at a distance of 3.9 \AA . Also, the functionalization of the boron nanosheet (to form an epoxy group) and the interaction with the monomer provided better adsorption [88].

6 Synthesis of Chitosan Nanoparticles

As is well-known, the antimicrobial potential of chitosan is intensified when it is in the form of nanoparticles, because the larger specific area and density of charges favor a higher degree of interaction between chitosan and the negative charges of bacterial cells [89].

Hence, in this perspective, diverse strategies have widely been used to synthesis of chitosan nanoparticles, such as emulsion method, ionic gelation method, reverse micellar method, self-assembling method and so on, owing to their fascinating physical and chemical properties [90–128]. However, in view that the selection of the method of nanoparticle synthesis depends on numerous factors, such as the final properties required (e.g., particle size, thermal and chemical stability, and zeta potential), time of synthesis, reproducibility of the kinetic profiles, toxicity of the final product, use of shear forces and the need to use specific equipment for each synthesis [4, 129].

6.1 Ionic Gelation or Ionotropic Gelation

Ionic gelation or ionotropic gelation of chitosan in the form of nanoparticles was initially proposed by Calvo et al. [102]. It additionally is the most used method so far to obtain chitosan in the form of nanoparticles, presumably because it presents a simple, fast methodology, which does not require organic solvents or sonication techniques, and also allows the development of nanoparticles of determined size, shape and surface charge [102, 103]. The control of these physical characteristics of chitosan, in principle, is fundamentally important for many of their applications [4, 102–106].

This strategy, however, is usually based on the ionic interactions generated when a solution containing a polyanion, such as citrate, sulfate or tripolyphosphate (pH 7–9) is dripped [104] on an acidic aqueous solution (pH 4–6) of positively charged chitosan ($-\text{NH}_3^+$ protonated amino groups) under mild conditions (i.e., temperature and pressure). From the interaction between these two species, ionic crosslinking

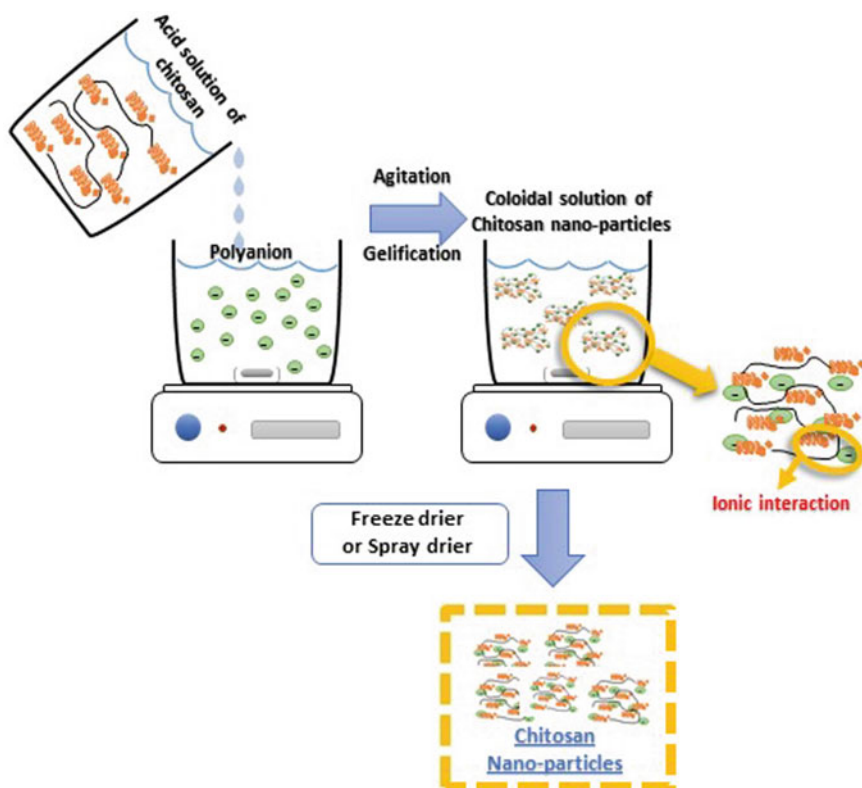


Fig. 2 Schematic design of Ionic gelation or ionotropic gelation

occurs, causing coagulation and then generating stable colloidal systems of spherical-like chitosan nanoparticles, as shown in Fig. 2.

Sodium tripolyphosphate (TPP- $\text{Na}_5\text{P}_3\text{O}_{10}$), in particular, is the most used polyanion as a reducing agent. This likely is due to, in fact, it is a non-toxic compound, does not present mutagenic or carcinogenic effects, is multivalent and has a high capacity to form gels (through ionic interactions) [106]. It also has low-cost and, unlike other crosslinking agents, does not have severe restrictions on handling and storage. In this methodology, it is well-known that tuning of many synthetic variables can, in principle, influence the size, shape and zeta potential of the nanoparticles obtained, which directly affect their antimicrobial activity in this case [106–108]. Likewise, when using smaller gauge needles in the peristaltic pump or atomizers, in particular, can aid in smaller size chitosan nanoparticles are obtained. Other experimental parameters that also influence on the particle size are changes in concentration of the crosslinking agent, method/rate/speed of agitation of both chitosan and polyanion solution, pH conditions, temperature and also drying method [4, 107].

Additionally, a detailed study reported by Jonassen et al. [108] shows that they obtained smaller and more stable nanoparticles when sodium chloride was added to the solvent. This likely is due to the reduction of the electrostatic attraction between the NH_3 groups of the chitosan chain. In addition, this study points to the increased the flexibility of the polymer chains in solution, as well as, thus the stability of the nanoparticles formed in this case [108].

6.2 *Polyelectrolyte Complexation—PEC or Self-assembling Method*

As shown in Fig. 3, the synthesis of chitosan-based nanoparticles by the PEC method is very similar to the ionic gelation process. However, in view that the difference between them relies on the fact that the first uses anionic macromolecules, while the second uses relatively smaller molecules, like phosphate, citrate, and sulfate [109, 110].

In the same way, the PEC method can in principle be applied to spontaneously form chitosan-based nanoparticles, as already discussed for the case of ionic gelation process, i.e., after the addition of RNA or alginate in the form of solution [111] in an aqueous solution of chitosan with acetic acid (under mechanical agitation) at about room temperature. To end, in this case, it is well-known that the shape of chitosan-based nanoparticle prepared by the PEC method is strongly dependent on the type of negatively charged polyelectrolytes used in this synthesis process [109–111].

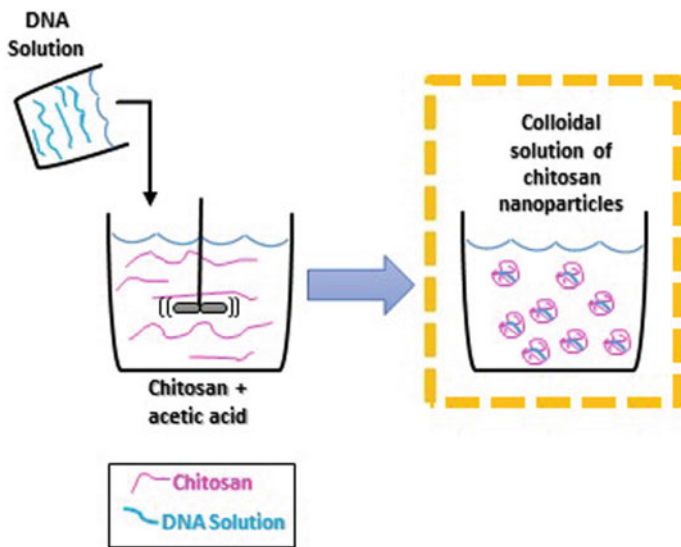


Fig. 3 Schematic design of Polyelectrolyte Complexation—PEC

6.3 Microemulsion Method

In general the microemulsion method was initially developed by De et al. [131], which is based on the formation of chitosan nanoparticles at the center of reverse micelles and subsequent cross-linking with glutaraldehyde (Fig. 4).

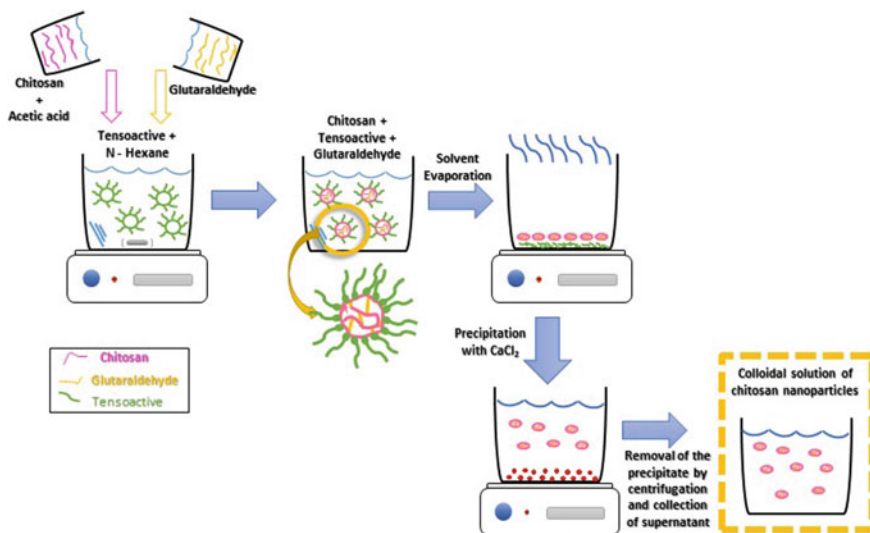


Fig. 4 Schematic design of microemulsion method

In general, the preparation of microemulsion consists of a surfactant dissolved in N-hexane and an acetic solution of chitosan. Chitosan-based nanoparticles are usually formed in the presence of the surfactant inside the reverse micelles [132]. Glutaraldehyde, a kind of homobifunctional reagent (i.e., that have identical reactive groups), is then added to the mixture, under continuous stirring at ordinary room temperature, for the occurrence of crosslinking of the chitosan chains, i.e., being responsible for the formation of a bond that occurs between the free amine group of chitosan and glutaraldehyde. Hence, in this case, the organic solvent is to remove by evaporation, and then the excess surfactant is generally precipitated with calcium chloride and removed through centrifugation. Prior to lyophilization, however, the nanoparticle suspension should be dialyzed. By using this strategy of synthesis, in particular, Sailaja et al. synthesized nanoparticles of chitosan with an average size of about 100 nm [113].

Futhermore, studies have reported that the main disadvantage of this technique is the need to use glutaraldehyde, a very toxic agent, which, therefore, limits the biomedical application of the chitosan nanoparticles formed. Subsequently, as an adaptation of the microemulsion method, the reverse micellar method has been investigated and proposed by Brunel et al. [114]. Summarizing, this approach is fundamentally based on the addition of a chitosan solution in a surfactant dissolved in an organic solvent, under continuous stirring at ordinary room temperature (see Fig. 5) [114]. Notably, the main highlight of this attractive route is the absence of toxic crosslinking organic solvents [115, 128]; however, this procedure has to be further optimized for enhanced functional properties.

6.4 Emulsification Solvent Diffusion Method

The typical emulsification solvent diffusion method, as shown in Fig. 6. Is fundamentally based on the partial miscibility of the organic solvent in water for the subsequent formation of the chitosan-based nanoparticles [4, 110, 116]. In addition, it is well-known that this method consists of adding an organic phase (e.g., methylene chloride and acetone) in a solution prepared of chitosan with stabilizers (e.g., poloxamer and lecithin) under mechanical agitation, which in turn results in an oil/water emulsion [110, 116]. Hence, the emulsion then undergoes a high-pressure homogenization in this case. When excess water is added, then the organic solvent (acetone) diffuses into the aqueous phase (e.g., acetone is partially miscible in water or any other organic solvent), thus reducing the polymer solubility and resulting in the precipitation of the chitosan nanoparticles [116]. However, in this case, the particular elimination of the solvent (methylene chloride) can directly occur either by evaporation or by filtration [116].

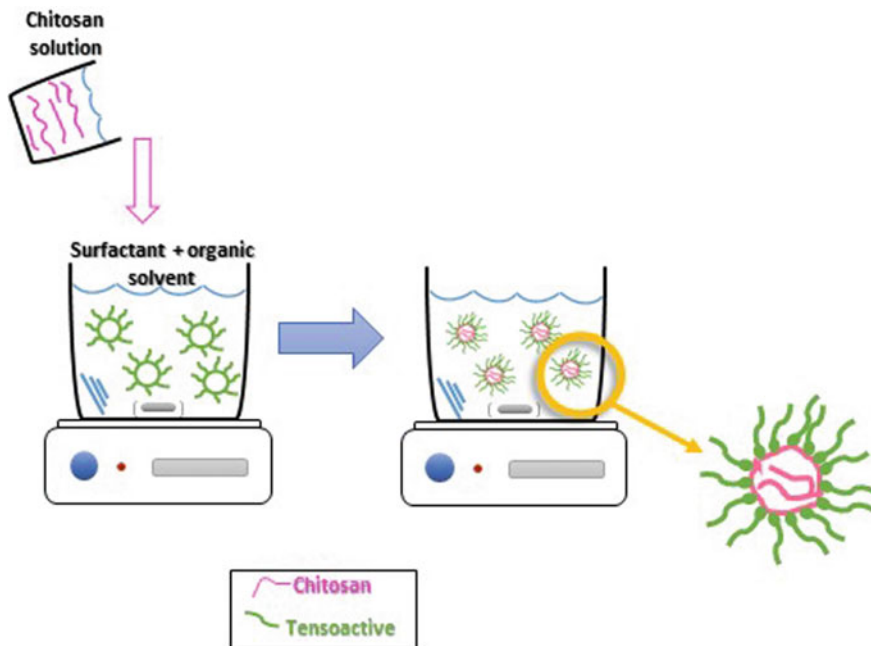


Fig. 5 Schematic design of Reverse micellar method

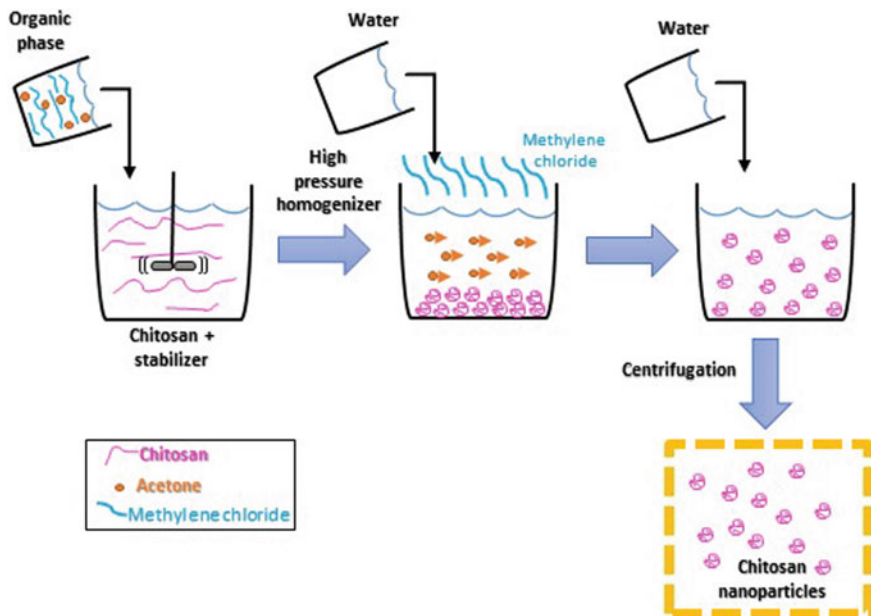


Fig. 6 Schematic design of Emulsification solvent diffusion method

On the other hand, in view of the major disadvantages of this methodology, however, include the particular use of organic solvents and the application of high shear forces [133]. According to Grenha [110], the main parameters that influence the size of the nanoparticles obtained and their final physicochemical properties are related to the molecular weight of chitosan, homogenization rate and reaction time (i.e., period of evaporation and diffusion).

7 Modifications in Chitosan Nanoparticles for the Antimicrobial Effect Potentialization

Chitosan-based nanoparticles have widely been used as a matrix in antimicrobial drug delivery systems (Table 1). They are usually used either in pure form or in combination with other polymers [117–121] or metals [122], in order to enhance their antimicrobial effects.

Du et al. [122] synthesized chitosan nanoparticles from the ionic gelation method and in the sequence modified them by adding solutions of five different metals (Ag^+ , Cu^{+2} , Zn^{+2} , Mn^{+2} or Fe^{+2}) in the final chitosan nanosuspension. Except for the case of Fe^{+2} containing sample, in particular, it was verified that the antimicrobial activity of the chitosan nanoparticles (against *Escherichia coli*, *Salmonella choleraesuis* and *Staphylococcus aureus*) have significantly increased by the metal ions used. The synergism between Cu^{+2} and chitosan resulted in a reduction of the minimal inhibitory concentration in 21 and 42 times for the *E. coli* and *S. choleraesuis*, respectively [122].

Since the conventional antibiotic agent delivery systems have some serious side effects, such as: high toxicity due to the instant release of the agent, intoxication of healthy cells and high frequency of the drug dosing. The limitations identified above, however, can in principle be overcome by using the chitosan nanoparticle matrices system for controlled release.

Nguyen et al. [92] found that small size chitosan nanoparticles and large zeta potential values present the best antimicrobial activity against *Streptococcus pneumoniae*. Garg et al. [117] prepared spherical-like chitosan nanoparticles with isoniazid (INH) and rifampicin (RIF) antibiotics by the ionic gelation method. In this case, the nanoparticles were dried using a spray drier with mannitol (1% w/v) and leucine (0.25% w/v). As a result, spherical nanoparticles of about 230 ± 4.5 nm were obtained in this case. After a period of 24 h of nebulization, the drugs were then detected in various organs (e.g., lungs, liver, spleen and also kidneys), i.e., suggesting that the antibiotics modified with nanoparticles were more effective against *Mycobacterium tuberculosis* than the free drugs [117]. This positive result, however, was then attributed to the synergism between the biodegradable and mucoadhesive nature of chitosan and the antimicrobial effect of the drugs, as well [117]. On the other hand, the chitosan nanoparticles controlled the drug release rate, in addition to prolonging the therapeutic effects and aid

Table 1 Chitosan nanoparticles, pure or modified with metals or antibiotics

Method	Particle size (nm)	Pure/ combination of other components	Relevant results	References
Microemulsion method	300–400	Nanoparticle of pure chitosan	Cells treated with chitosan nanoparticles suffered nuclear disintegration and fragmented causing programmed cell death	[123]
Ionic gelation method	244 ± 12	Nanoparticle of pure chitosan	The produced Nanoparticles showed strong and fast activity against Staphylococci (MRSA and MSSA) with low MIC values. Nanoparticles inhibit biofilm production	[93]
Emulsion technique	408.30 ± 53.17	Cefadroxil chitosan nanoparticles	In vivo tests in rats showed a high degree of synergism between the drug and the chitosan nanoparticle, resulting in the acceleration of wound healing and bacterial extinction (<i>S. aureus</i>), which was confirmed by histopathological examination of skin biopsies	[124]
Ionic gelation	166–1230	Chitosan nanoparticle with amoxicillin complex	Lower chitosan nanoparticle and higher zeta potential showed higher antibacterial activity Streptococcus pneumoniae	[92]
Ionic gelation	332. 2	Nanoparticle of pure chitosan	Stable chitosan nanoparticles showed significant antimicrobial activity against Streptomyces species, Pseudomonas fluorescense Staphylococcus aureus, Aspergillus niger and Aspergillus flavus	[125]

(continued)

Table 1 (continued)

Method	Particle size (nm)	Pure/ combination of other components	Relevant results	References
Ionic gelation	257	Chitosan nanoparticles and copper-loaded nanoparticles	The activity of the nanoparticles was evaluated against <i>E. coli</i> , <i>S. choleraesuis</i> , <i>S. typhimurium</i> , and <i>S. aureu</i> . Their MIC values were less than 0.251g/mL	[126]
Ionic gelation	157	Chitosan nanoparticles and <i>Mentha longifolia</i>	The incorporation of peppermint extract into chitosan nanoparticles resulted in increased antifungal effects against the growth of <i>A. niger</i> mycelium	[101]

in administering the drug to specific body parts, preferably the ones rich in macrophages for the treatment of the disease. Thus, modification of these drugs with chitosan nanoparticles allows a reduction in the drug dosing and its frequency, as well as an improvement in the patient's adherence to the treatment [117].

On the other hand, Pathania et al. [118] synthesized chitosan-g-poly(acrylamide)/CuS (CPA/CS) nanocomposites for the controlled release of the antibiotic ofloxacin, which exhibits antimicrobial effect against a variety of systemic infections. In particular, the maximum amount of drug released was about 76% in a period of 18 h. The antibacterial activity of the CPA/CS nanocomposite was investigated against *E. coli*. Inhibition occurred likely is due to the formation of a bond between the nanocomposite and the outer cell membrane of the bacterium, leading to its lysis, and also due to the inhibition of the dehydrogenase enzyme, periplasmic enzymatic activity, and active transport [127].

Chitosan nanoparticles can in principle be functionalized with the addition of metals, such as gold nanoparticles, and antibiotic ampicillin to further enhance the antimicrobial effect. For instance, Chamundeeswari et al. [128] found that the antimicrobial activity of the nanocomposite (C-AuNp-Amp) was twice as large as that of free ampicillin. The main advantage of using the nanocomposite is that, by reducing the dosage of antibiotics to 50%, the side effects can be minimized and this can effectively improve the patient's quality of life [128]. Other antibiotics, in practice, may also be used in the functionalization of chitosan nanoparticles, such as amoxicillin [119], doxycycline [120], and berberine [121], all effective against gram-positive and/or gram-negative bacteria.

8 Pharmacological Potential from Chitosan and Its Derivatives

Different methodologies and strategies of chitosan applications have widely been proposed in the literature. Hence, the growing interest in this biomolecule stems from its biological properties as biofunctional, biocompatible, antioxidant, non-toxic and able to form antimicrobial films and its applications in the biomedical, agricultural, food, cosmetic areas, in the processes of clarification and deacetylation of fruit juices and in water purification [4, 130, 134–145].

There is considerable scientific interest in the subject of this chapter. More than 13,000 articles were found only using the SCOPUS[®] database. Figure 7 shows the number of papers published in the last five years on chitosan-related compounds bioactivity studies in the various areas of knowledge. It is noteworthy that about 80% of this works have been published during this last decade.

A wide variety of studies have concluded that chitosan-based nanoparticles are a beneficial and safe substance for human consumption, due to their lower toxicity than glucose or sucrose, for example [93]. Thus, the ANVISA (BRAZIL, 1999) includes it in the list of “Foods with claims of functional and or health properties, novel foods/ingredients, bioactive substances and probiotics” [135].

Antimicrobial activity is one of the main biological properties conferred to chitosan-related compounds and distinguishes it from other polysaccharides. Unfortunately, the mechanism of action for this antimicrobial activity has not yet been fully elucidated in the literature [136, 137]. However, it is known that this mechanism of microbial inhibition is closely related to the physicochemical properties of the molecule that allow it to bind to the cell membrane of microorganisms.

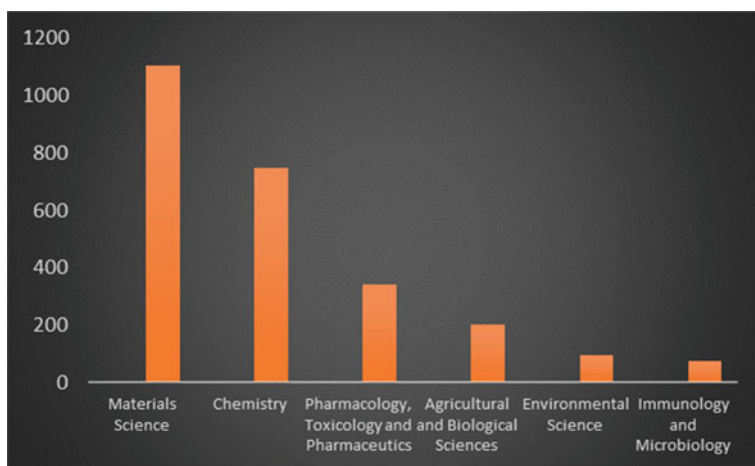


Fig. 7 Publications of the last five years (2014–2019 by the Scopus database) related to chitosan-related compounds bioactivity studies

This is achieved by means of its protonated amino groups by selectively binding to the cell surface via anionic interactions, resulting in a likely degradation or loss of intracellular components [138]. Other important mechanisms related to their antimicrobial activity are usually attributed to their chelating action that selectively binds to traces of essential elements or nutrients. This inhibits bacterial growth by sequestering water and inhibiting various enzymes, activating various defense mechanisms in the hosts [139].

This polymer also has polar characteristics and may play a role as the chelating agent of metal ions, which can act against lipid oxidation [140], such as studies with foods such as meat and seafood. When tested, the high amounts of unsaturated fatty acids observed revealed that the simple addition of chitosan was effective in controlling lipid oxidation, both in cod (*Gadus morhua*) and minced meat [141].

The versatility of chitosan-related compounds in antimicrobial products likely is due to the fact that this polymer can, in principle, be prepared in different forms, such as viscosity-controlled solutions, gels, films, and membranes [142].

Studies indicate that the chitosan partially deacetylated, in particular, is an insoluble polymer in most solvents [4, 5]. On the other hand, the vast majority of studies showed that the solubility of the chitosan-related compounds in solutions of most organic acids (i.e., with a pH below 6.0) occurs due to the protonation of the amino groups, present in its glycosamine units, generating positive charges ($-\text{NH}_3^+$) in the solution [143]. When solubilized at a pH below 6.5, it forms viscous solutions that contribute to the diverse characteristics, for example, coatings that are edible, flexible, long-lasting or difficult to break [144]. However, its solubilization requires strong agitation for long periods and, in some cases, requires heating to completely dissolve [4, 5, 143, 144].

On the other hand, the broad spectrum of chitosan antimicrobial action can also be expressed in terms of the number of different bacterial strains that are inhibited by this polymer, such as *Staphylococcus aureus*, *Escherichia coli*, *Salmonella typhimurium*, *Streptococcus faecalis*, *Salmonella entérica*, *Listeria monocytogenes*, *Bacillus cereus*, *Shigella dysenteriae*, as well as a wide variety of fungi and yeast [4, 134–150].

However, this mode of action will depend on some parameters such as the type of chitosan used, degree of deacetylation, molar mass, temperature and pH conditions of the medium [146]. Chitosan is an amino polysaccharide directly obtained from the deacetylation processing of chitin, in which the acetamido ($-\text{NHCOCH}_3$) groups of chitin are transformed into amino groups [5]. These protonated amino groups probably bind selectively to the negatively charged cell surface of target microorganisms, which may, as a result, alter the activity and permeability of their membranes, i.e., resulting easily in their complete inhibition [86, 145–148]. However, it is important to emphasize that the mode of antimicrobial action of chitosan-based nanoparticles is different for Gram-positive and Gram-negative bacteria and depends mainly on the molecular weight of the polymer [148].

According to Kim and Rajapakse [149], it could be that high molecular weight chitosan forms a film around the gram-positive bacteria cell and inhibits their

absorption of nutrients. In contrast, low molecular weight chitosan can penetrate Gram-negative bacteria more easily and reach DNA, which ultimately hinders its transcription and translation, destabilizing them completely [150]. Analysis using electrophoresis from free cell supernatants of chitosan-treated cell suspensions, have shown that the interaction of chitosan nanoparticles with Gram-negative bacteria did not involve the release of lipopolysaccharide or other membrane lipids [150–153].

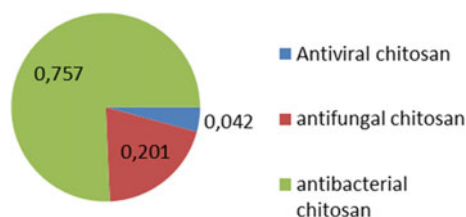
There have been multiple studies aimed at obtaining a washable, non-toxic, and environmentally friendly antibacterial preservation material [151, 152]. These materials can be formed by reaction of succinic anhydride with chitosan and lysozyme-N-succinyl chitosan (denoted as LSZ-NSC). When tested, they showed that lysozyme activity in LSZ-NSCs increased about 256% compared to free lysozyme activity and their bacteriostatic activity also exhibited a significant increase at low concentrations [152]. The authors concluded, then, that the active group introduced by the NSC was particularly located in the chitosan group C_2-NH_2 [152].

Other important research in this area has been successfully developed such as, for example, the study by Zhang et al. [153] which aimed to prepare a natural and active chitosan coating loaded with nano-encapsulated *Paulownia Tomentosa* essential oils (PTEO). This was done to investigate the effects of the coating on lipid oxidation, microbial growth and sensory attributes of ready-to-cook foods. The results obtained suggested that the nano-encapsulated PTEO-based chitosan coating may be a potential active packaging to extend the shelf life of ready-to-cook pork chops [153].

One of the greatest and most effective advances in the therapeutic treatment of people with HIV is, undoubtedly, gene therapy. As interfering RNA (siRNA) technology is one of the key strategies that help improve the outcomes of current therapeutic systems against HIV-1 infection, many studies have been conducted in this area [154, 155]. A recent study was conducted using a trimethyl chitosan-coated (TMC) superparamagnetic iron oxide nanoparticle (SPION) to deliver siRNA against HIV-1 nef (anti-nef siRNA) in two cell lines, HEK293 and RAW 264.7 macrophage. The results obtained showed significant reduction of the nef HIV-1 expression in stable HEK293 cells. Modified siRNA-loaded SPIONs also had no toxic or apoptosis-inducing effects on cells [155].

Thus, due to the antibacterial and antifungal properties of this biopolymer there is great potential for its application in biofilm preparation and in food preservation in combination with other compounds [4, 156]. Therefore, as a result of their excellent antimicrobial properties, the chitosan nanoparticles has been approved e.g. as a biopesticide (insecticide, fungicide, and rodenticide) by the US Environmental Protection Agency (EPA registration number 91664-2) and also as a food additive (use in foods generally including meat and poultry for multiple technical purposes), by the Food and Drug Administration of EUA (FDA, GRAS Notice N° 443) [157]. Figure 8 presents information obtained from SCOPUS® database relating to the antimicrobial activity evaluation study of chitosan and its derivatives.

Fig. 8 Percentage of the number of publications targeting antimicrobial activity studies with chitosan and its derivatives



An important beneficial action of the chitosan compounds for the health of consumers is related to its ability to decrease the cholesterol associated with low-density protein (LDL) and increase that associated with high-density protein (HDL), in addition to reducing body weight [158] and can thus be used in nutritional and therapeutic products for related pathologies. This biopolymer has also been shown to be an excellent therapeutic alternative for the treatment of skin lesions, since it is an aminoglucofuran composed of monomers N-acetyl-D-glucosamine (GlcNac) and D-glycosamine (GlcN), from crustacean waste from the fishing industry [159].

Other studies reveal that chitosan compounds can act as a promising wound healer, as well as having good tissue adhesion capacity [160] and also describe the stimulating effect of chitosan on the healing process, granulation tissue formation, angiogenesis, formation of collagen fibers and activation of the immune response [161]. Diverse studies have widely been developed in order to obtain new products based on chitosan-related nanoparticles that can in principle be used as dressings that act directly in the wound healing process.

Many studies have revealed that chitosan-based nanoparticles displays an important role in the recovery of acute cutaneous lesions of rats, accelerating the healing process and reducing the width of the lesion, which reinforces its potential for medical application [147]. In addition, many studies with this polymer point to a safe and beneficial substance for human consumption and indicate that it has lower toxicity than glucose or sucrose. In mammals, it is well known that the lethal dose of glucose is on the order of 8–12 g, whereas about 18 g of chitosan per kilogram body mass shows no sign of toxicity or mortality [86].

Hence, there the necessity of developing new chitosan-based materials, especially because of its excellent anti-inflammatory and/or antibiotic properties, which in turn can act as healing as well as promote pain relief and quality of life for affected patients [162, 163]. Biopolymer films from this compound have particularly been studied for this purpose, mainly due to their hemostatic, antimicrobial and biocompatibility capabilities, whose cell adhesion tests have shown that cells do not adhere to films, which is a desirable feature for a dressing [162]. And yet because of its potential for biodegradability, biocompatibility and bioactivity, chitosan has created significant interest in a variety of biomedical applications [163].

Another important potential application is the prevention of infection in wounds during the healing process. This has been achieved with chitosan due to its inherent antibacterial activity and many other advantages such as its analgesic effect and hemostatic activity [164].

Important research has highlighted the role of chitosan as a stimulant of polymorphonuclear leukocytes (PMN) and macrophages. Chitosan is able to induce migration of PMN cells into wounds and then promote active biodebridement by these cells [165].

Thus, research with this biopolymer has focused on molecular variations of this polysaccharide in order to increase its solubility and broaden the spectrum of its therapeutic applications, including as biocide [147, 160–177]. For instance, it is well-known that the quaternization at the chitosan nitrogen atom leads to producing highly water-soluble chitosan derivatives [4, 166]. These changes, in principle, can induce an excellent antimicrobial activity, most likely due to the permanent positive charge on nitrogen atoms which are bonded laterally to the polymer backbone [165]. Therefore, in this perspective, chitosan derivatives have long been a key issue of great interest in many experimental and theoretical studies, because they enhance the functional properties observed in chitosan compounds, i.e., especially in relation to its bactericidal property against Gram-positive and Gram-negative bacteria [166].

Among the chitosan derivatization studies to improve biological activity are the alkylation processes. For example, to obtain hydroxypropyl chitosan, chitosan must be modified by alkylation and sodium maleic acid must be grafted to the hydroxypropyl group [167]. Chitosan derivatives show better antibacterial activity for certain bacteria, such as tests against *Staphylococcus aureus* [168]. This likely is related to the amphiphilic structures of these derivatives, which generate structural affinity of bacteria cell walls, i.e., leading to cell wall destruction and apoptosis [168].

In this sense, Sankar et al. [169] manufactured crosslinked sponges of this biopolymer with lyophilized glutaraldehyde for application in blood hemostasis and found that it can act as a mechanical barrier in the blood, causing its immediate coagulation. Intracutaneous tests on rabbit and guinea pig claimed the good absorption capacity and biological compatibility of these sponges for hemostatic products. Huang et al. [170] also demonstrated the efficacy of a hydrophobically modified chitosan bandage for the treatment of non-compressible hemorrhage, which performed an in vitro toxicity assessment on 3T3 cells, together with the hemostatic effect, tissue biocompatibility and antimicrobial tests and noted that chitosan-based hemostatic agent was useful for the treatment of external and internal hemorrhagic lesions.

In addition to compounds obtained by derivatization of this polysaccharide, mixtures of chitosan copolymers with natural and synthetic materials have shown success in the development of tissue engineering materials (such as 3D freeze-dried scaffolds, hydrogels and also films) [171].

Studies developed by Leceta et al. [172] prepared with about 1 wt% Chitosan in a 1 wt% solution of acetic acid with glycerol as a plasticizer and subjected to the evaluation of the effect of coatings applied by dipping or spraying on the quality attributes of commercial carrots under packaging conditions. Modified atmosphere showed that the use of chitosan coating was also beneficial in preventing surface

whitening, i.e., providing better color retention and preserving the texture of the product during a 15-day refrigerated storage period [172].

Derivatives of this polysaccharide have other therapeutic applications. There are also several reports on the anticoagulant, antioxidant, anti-tumor, immune-enhancing, and anti-HIV activities of polysaccharide derivatives [173]. For example, a chitosan nanoparticle system conjugated with anti-transferrin and anti-bradykinin B2 antibody that has been used to increase inhibition of HIV replication [174].

Many pharmacological studies conclude that the good antimicrobial activity of chitosan nanoparticles depends on several factors such as concentration, pH conditions, degree of deacetylation, molecular weight and also of the solvent used [166, 175–177]. These researches have emphasized the potential of chitosan-based nanoparticles as a bioactive polymer with a wide variety of applications due to its functional properties such as antibacterial activity, nontoxicity, ease of modification and biodegradability [4, 138, 166, 171–184].

In addition to these properties already mentioned, due to its unique polycationic, non-toxic, antimicrobial and bioabsorbable nature, chitosan has a wide spectrum of applications in medical fields, such as controlled drug administration, dressings, tissue engineering, blood anticoagulant, bone regeneration biomaterial and antimicrobial agent [185–191].

An important application in this biomedical area is drug delivery [4]. Orally administered tablets offer several advantages over passive first-generation targeted systems, such as improved efficacy, reduction/elimination of unwanted side effects, and drug levels that are continuously maintained in a therapeutically range desirable without peaks and valleys. These experiments have been shown to be easier to develop in many drug delivery systems [188].

Chitosan-based products such as films have also attracted interest in other areas such as Food Chemistry for use in active food packaging. Talón et al. [189] prepared starch and pea films enriched with thyme extract and tannic acid and found that the antioxidant activity of tannic acid/chitosan films was higher than that of thyme/chitosan extract films.

Other studies with chitosan and its derivatives have revealed that these compounds may induce plant resistance to viral infection [190]. In chemotherapy of leishmaniasis, C-6 oxidized chitosan showed antileishmanial activity against *Leishmania infantum* LIPA 137 [191]. Furthermore, it also showed potent algicidal activity against harmful algal cells caused by an influx of intracellular components [152, 192]. Moreover, chitosan conjugated with chloroquine nanoparticles can be used to attenuate *Plasmodium berghei* infection in Swiss mice. However, in this perspective, few studies address the pharmacokinetics involved with using chitosan derivatives as antiparasitic drugs [160].

In chemotherapy and chemoprevention, chitosan derivatives have been considered as safe, effective products with fewer side effects on normal cells. In chemoprevention, micronutrient microencapsulation with chitosan increased blood circulation time to improve drug administration while chemotherapy showed highly specific tumor activity [158, 161]. Chitosan and some derivatives (mainly chitosan

oligosaccharides) may suppress the iNOS expression in activated microglial cells and changes in protein conformations, e.g., oxidation or glycation have also been reported as structural modifications related to Alzheimer's disease and associated dementia [147, 162].

Another important pharmacological action is in Immunotherapy, where chitosan thermogels allow CD8+ T to be released into the tumor microenvironment, produce Th1 cytokines and cytotoxic markers and subsequently kill their target cells [163].

In biotechnology, chitosan has also stood out as a potent biostimulant. Analysis of the potential of chitosan microparticles as promoters of tomato growth, which is one of the most consumed vegetable crops in the world, has shown a positive effect in improving germination index and vigor [192, 193]. In addition to triggering an improvement in root and shoot biomass, reinforcing tomato performance before transplantation reinforcing the potential of this association as a sustainable input for tomato production [164]. In recent years many studies have widely been developed focusing on the synthesis and bioactivity of chitosan hybrids and modification of their functional groups playing an important role in its pharmacological action [4, 165, 166].

References

1. Campos, E.V.R., Proença, P.L.F., Oliveira, J.L., Melville, C.C., Della Vecchia, J.F., de Andrade, D.J., Fraceto, L.F.: Chitosan nanoparticles functionalized with β -cyclodextrin: a promising carrier for botanical pesticides. *Sci. Rep.* **8**, 2067 (2018). <https://doi.org/10.1038/s41598-018-20602-y>
2. Mudgal, J., Mudgal, P.P., Kinra, M., Raval, R.: Immunomodulatory role of chitosan-based nanoparticles and oligosaccharides in cyclophosphamide-treated mice. *Scand. J. Immunol.* **89**, e12749 (2019). <https://doi.org/10.1111/sji.12749>
3. Yu, S., Xu, X., Feng, J., Liu, M., Hu, K.: Chitosan and chitosan coating nanoparticles for the treatment of brain disease. *Int. J. Pharm.* **560**, 282–293 (2019). <https://doi.org/10.1016/j.ijpharm.2019.02.012>
4. Rufato, K.B., Galdino, J.P., Ody, K.S., Pereira, A.G.B., Corradini, E., Martins, A.F., Paulino, A.T., Fajardo, A.R., Aouada, F.A., La Porta, F.A., Rubira, A.F., Muniz, E.C.: Hydrogels based on chitosan and chitosan derivatives for biomedical applications, hydrogels. In: *Smart Materials for Biomedical Applications*. Lăcrămioara Popa, Mihaela Violeta Ghica and Cristina-Elena Dinu-Pîrvu. IntechOpen (in press) (2018). <https://doi.org/10.5772/intechopen.81811>
5. Silva, D.S., Delezuk, J.A.M., La Porta, F.A., Longo, E., Campana-Filho, S.P.: Comparison of experimental and theoretical data on the structural and electronic characterization of chitin and chitosan. *Curr. Phys. Chem.* **5**, 206–213 (2016)
6. Kumirska, J., Weinhold, M.X., Thöming, J., Stepnowski, P.: Biomedical activity of chitin/chitosan based materials—influence of physicochemical properties apart from molecular weight and degree of N-Acetylation. *Polym. (Basel)*. **3**, 1875–1901 (2011). <https://doi.org/10.3390/polym3041875>
7. Prabakaran, M.: Review paper: chitosan derivatives as promising materials for controlled drug delivery. *J. Biomater. Appl.* **23**, 5–36 (2008). <https://doi.org/10.1177/0885328208091562>

8. Wang, X., Chi, N., Tang, X.: Preparation of estradiol chitosan nanoparticles for improving nasal absorption and brain targeting. *Eur. J. Pharm. Biopharm.* **70**, 735–740 (2008). <https://doi.org/10.1016/j.ejpb.2008.07.005>
9. Babu, A., Ramesh, R.: Multifaceted applications of chitosan in cancer drug delivery and therapy. *Mar. Drugs.* **15**, 1–19 (2017). <https://doi.org/10.3390/md15040096>
10. Gopal, J., Muthu, M., Dhakshnamurthy, T., Kim, K.J., Hasan, N.: Sustainable ecofriendly phytoextract mediated one pot green recovery of chitosan. *Sci. Rep.* 1–12 (2019). <https://doi.org/10.1038/s41598-019-50133-z>
11. Yadav, S.B., Bhise, A.V.: Chitosan: a potential biomaterial effective against typhoid. *Curr. Sci.* **87**, 1176–1178 (2004)
12. Sarvaiya, J., Agrawal, Y.K.: Chitosan as a suitable nanocarrier material for anti-Alzheimer drug delivery. *Int. J. Biol. Macromol.* **72**, 454–465 (2015). <https://doi.org/10.1016/j.ijbiomac.2014.08.052>
13. Cojocaru, C., Samoila, P., Pascariu, P.: Chitosan-based magnetic adsorbent for removal of water-soluble anionic dye: artificial neural network modeling and molecular docking insights. *Int. J. Biol. Macromol.* **123**, 587–599 (2019). <https://doi.org/10.1016/j.ijbiomac.2018.11.080>
14. Sant’Anna, C.M.R.: Molecular modeling methods in the study and design of bioactive compounds: an introduction. *Rev. Virtual Química.* **1** (2009). <https://doi.org/10.5935/1984-6835.20090007>
15. Taft, C.A., Canchaya, J.G.S.: Review on simulation models for materials and biomolecular study and design BT. In: Longo, E., La Porta, F.A. (eds.) *Recent Advances in Complex Functional Materials: From Design to Application*, pp. 373–408. Springer, Cham (2017). https://doi.org/10.1007/978-3-319-53898-3_15
16. Barcelos, M.P., Federico, L.B., Santos, C.B.R., Almeida, P.F.D., da Silva, C.H.D.P., Taft, C.A.: Pharmacophore and structure-based drug design, molecular dynamics and admet/tox studies to design novel potential Pad4 inhibitors. *Biomol. Struct. Dyn.* **37**, 1–33 (2018)
17. Taft, C.A., da Silva, C.H.T.P. (eds.): (2010, 2014) *New developments in medicinal chemistry*. In: *Chemistry*, vols 1, 2. U.A.E. Bentham Science (UAE)
18. Coelho, L.W., Junqueira, G.M.A., Machuca Herrera, J.O., Machado, S.D.P., Machado, B.D.C.: Aplicação de mecânica molecular em química inorgânica. *Quim. Nova.* **22**, 396–404 (1999). <https://doi.org/10.1590/s0100-40421999000300018>
19. Azevedo, F., Jr.: Molecular dynamics simulations of protein targets identified. In: Rapaport, D.C. (ed.) *The Art of Molecular Dynamics Simulation*, pp. 1353–1366 (2011). (Online ISBN: 9780511816581, Hardback ISBN: 9780521825689, Paperback ISBN: 9780521532754) <https://doi.org/10.1017/CBO9780511816581>
20. molecular dynamics simulations and binding free energy: K.D. Dubey, R.K.T. and R. P. Ojha, *Recent advances in protein–ligand interactions*. *Curr. Comput. Aided-Drug Des.* **9**, 518–531 (2013). <https://doi.org/10.2174/15734099113096660036>
21. Namba, A.M., Da Silva, V.B., Da Silva, C.H.T.P.: Dinâmica molecular: Teoria e aplicações em planejamento de fármacos. *Eclét. Quim.* **33**, 13–24 (2008). <https://doi.org/10.1590/S0100-46702008000400002>
22. Kitchen, D.B., Decornez, H., Furr, J.R., Bajorath, J.: Docking and scoring in virtual screening for drug discovery: methods and applications. *Nat. Rev. Drug Discov.* **3**, 935 (2004). <https://doi.org/10.1038/nrd1549>
23. Liu, J.-Y., Chen, X.-E., Zhang, Y.-L.: Insights into the key interactions between human protein phosphatase 5 and cantharidin using molecular dynamics and site-directed mutagenesis bioassays. *Sci. Rep.* **5**, 12359 (2015). <https://doi.org/10.1038/srep12359>
24. Thomsen, R., Christensen, M.H.: MolDock: a new technique for high-accuracy molecular docking. *J. Med. Chem.* **49**, 3315–3321 (2006). <https://doi.org/10.1021/jm051197e>
25. Friesner, R.A., Murphy, R.B., Repasky, M.P., Frye, L.L., Greenwood, J.R., Halgren, T.A., Sanschagrin, P.C., Mainz, D.T.: Extra precision glide: docking and scoring incorporating a model of hydrophobic enclosure for protein–ligand complexes. *J. Med. Chem.* **49**, 6177–6196 (2006). <https://doi.org/10.1021/jm051256o>

26. Jones, G., Willett, P., Glen, R.C., Leach, A.R., Taylor, R.: Development and validation of a genetic algorithm for flexible docking. *J. Mol. Biol.* **267**, 727–748 (1997). <https://doi.org/10.1006/jmbi.1996.0897>
27. Morris, G.M., Goodsell, D.S., Olson, A.J.: Automated docking of flexible ligands: applications of autodock. *J. Comput. Aided Mol. Des.* **10**, 293–304 (1996). <https://doi.org/10.1007/BF00124499>
28. Brozell, S.R., Mukherjee, S., Balius, T.E., Roe, D.R., Case, D.A., Rizzo, R.C.: Evaluation of DOCK 6 as a pose generation and database enrichment tool. *J. Comput. Aided Mol. Des.* **26**, 749–773 (2012). <https://doi.org/10.1007/s10822-012-9565-y>
29. Azevedo, L.S., Moraes, F.P., Xavier, M.M., Pantoja, E.O., Villavicencio, B., Finck, J.A., Proenca, A.M., Rocha, K.B., de Azevedo, W.F.: Recent progress of molecular docking simulations applied to development of drugs. *Curr. Bioinform.* **7**, 352–365 (2012)
30. A de Castro, A, Caetano, S., Silva, M.C., Mancini, T.T., Pereira Rocha, E., da Cunha, F.F.: Molecular docking, metal substitution and hydrolysis reaction of chiral substrates of phosphotriesterase. *Comb. Chem. High Throughput Screen.* **19**, 334–344 (2016)
31. Assis, L.C., Santos-Garcia, L., Ramalho, T.C., da Cunha, E.F.F.: Interactions of pyrimidine derivatives with dihydrofolate reductase and thymidylate synthase: directions toward combating toxoplasmosis. *Curr. Bioact. Compd.* **9**, 153–166 (2013). <https://doi.org/10.2174/22115528112019990010>
32. Hansch, C., Fujita, T.: ρ - σ - π analysis. a method for the correlation of biological activity and chemical structure. *J. Am. Chem. Soc.* **86**, 1616–1626 (1964). <https://doi.org/10.1021/ja01062a035>
33. Ma, W., Wang, Y., Chu, D., Yan, H.: 4D-QSAR and MIA-QSAR study on the Bruton's tyrosine kinase (Btk) inhibitors. *J. Mol. Graph. Model.* **92**, 357–362 (2019). <https://doi.org/10.1016/j.jmglm.2019.08.009>
34. Pratim Roy, P., Paul, S., Mitra, I., Roy, K.: On two novel parameters for validation of predictive QSAR models. *Molecules* **14** (2009). <https://doi.org/10.3390/molecules14051660>
35. Neves, B.J., Braga, R.C., Melo-Filho, C.C., Moreira-Filho, J.T., Muratov, E.N., Andrade, C. H.: QSAR-based virtual screening: advances and applications in drug discovery. *Front. Pharmacol.* **9**, 1275 (2018). <https://doi.org/10.3389/fphar.2018.01275>
36. Arroio, A., Honório, K.M., Da Silva, A.B.F.: Propriedades químico-quânticas empregadas em estudos das relações estrutura-atividade. *Quim. Nova* **33**, 694–699 (2010). <https://doi.org/10.1590/S0100-40422010000300037>
37. Fourches, D., Ash, J.: 4D-quantitative structure–activity relationship modeling: making a comeback. *Expert Opin. Drug Discov.* 1–9 (2019). <https://doi.org/10.1080/17460441.2019.1664467>
38. Sutherland, J.J., O'Brien, L.A., Weaver, D.F.: A comparison of methods for modeling quantitative structure–activity relationships. *J. Med. Chem.* **47**, 5541–5554 (2004). <https://doi.org/10.1021/jm0497141>
39. Hayriye, Y., Güzel, Y., Önal, Z., Alt, G., Kocakaya, S.O.: 4D-QSAR study of p 56 lck protein tyrosine kinase inhibitory activity of flavonoid derivatives using MCET method. In: Chapter 6—alternative ensembles, vol. 32, pp. 153–175. Cambridge University Press (2011). <https://doi.org/10.1017/CBO9780511816581.009>
40. Santos-Filho, O.A., Hopfinger, A.J.: The 4D-QSAR paradigm: application to a novel set of nonpeptidic HIV protease inhibitors. *Quant. Struct. Relationships.* **21**, 369–381 (2002)
41. Haile, J.M.: *Molecular Dynamics Simulation: Elementary Methods*, 1st edn. Wiley, New York, NY, USA (1992)
42. Rapaport, D.C.: *The Art of Molecular Dynamics Simulation*, 2nd edn. Cambridge University Press, Cambridge (2004). <https://doi.org/10.1017/cbo9780511816581>
43. Durrant, J., McCammon, J.: Molecular dynamics simulations and drug discovery. *BMC Biol.* **9**, 71 (2011). <https://doi.org/10.1186/1741-7007-9-71>
44. Ramalho, T.C., Rocha, M.V.J., da Cunha, E.F.F., Oliveira, L.C.A., Carvalho, K.T.G.: Understanding the molecular behavior of organotin compounds to design their effective use

- as agrochemicals: exploration via quantum chemistry and experiments. *J. Biomol. Struct. Dyn.* **28**, 227–238 (2010)
45. Verlet, L.: Computer “Experiments” on classical fluids. I. Thermodynamical properties of Lennard-Jones Molecules. *Phys. Rev.* **159**, 98–103 (1967). <https://link.aps.org/doi/10.1103/PhysRev.159.98>
 46. Schumann, U., Sweet, R.A.: A direct method for the solution of Poisson’s equation with Neumann boundary conditions on a staggered grid of arbitrary size. *J. Comput. Phys.* **20**, 171–182 (1976). [https://doi.org/10.1016/0021-9991\(76\)90062-0](https://doi.org/10.1016/0021-9991(76)90062-0)
 47. Hockney, R.W.: The potential calculation and some applications. *Methods Comput. Phys.* **9**, 136 (1970)
 48. Arfken, G.: Introduction BT—Mathematical Methods for Physicists, 3rd edn., pp. xxi–xxii. Academic Press (1985). <https://doi.org/10.1016/B978-0-12-059820-5.50008-2>
 49. Morse, P.M., Feshbach, H.: *Methods of Theoretical Physics*. McGraw-Hill, New York (1953)
 50. Hestenes, M.R., Stiefel, E.: Methods of conjugate gradients for solving linear systems. *J. Res. Natl. Bur. Stand.* **49**(1952), 409 (1934). <https://doi.org/10.6028/jres.049.044>
 51. Grossmann, C., Fletcher, R.: *Unconstrained Optimization. Practical Methods of Optimization 1*, vol. VIII, 120 S., £ 8.80. Wiley, Chichester, New York, Brisbane-Toronto (1980). ISBN 0–471–27711–8, ZAMM. *J. Appl. Math. Mech./Zeitschrift Für Angew. Math. Und Mech.* **61**, 408 (1981). <https://doi.org/10.1002/zamm.19810610824>
 52. Berendsen, H.J.C., Postma, J.P.M., Van Gunsteren, W.F., Dinola, A., Haak, J.R.: Molecular dynamics with coupling to an external bath. *J. Chem. Phys.* **81**, 3684–3690 (1984). <https://doi.org/10.1063/1.448118>
 53. Hoover, W.G.: Canonical dynamics: equilibrium phase-space distributions. *Phys. Rev. A.* **31**, 1695–1697 (1985). <https://link.aps.org/doi/10.1103/PhysRevA.31.1695>
 54. Nosé, S.: A molecular dynamics method for simulations in the canonical ensemble. *Mol. Phys.* **52**, 255–268 (1984). <https://doi.org/10.1080/00268978400101201>
 55. Parrinello, M., Rahman, A.: Polymorphic transitions in single crystals: a new molecular dynamics method. *J. Appl. Phys.* **52**, 7182–7190 (1981). <https://doi.org/10.1063/1.328693>
 56. Karplus, M., McCammon, J.A.: Molecular dynamics simulations of biomolecules. *Nat. Struct. Biol.* **9**, 646–652 (2002). <https://doi.org/10.1038/nsb0902-646>
 57. Carvalho, I., Pupo, M.T., Borges, Á.D.L., Bernardes, L.S.C.: Introdução a modelagem molecular de fármacos no curso experimental de química farmacêutica. *Quim. Nova* **26**, 428–438 (2003). <https://doi.org/10.1590/S0100-40422003000300023>
 58. Alcácer, L.J.: *Introdução a Química Quântica Computacional*. IST Press, Lisboa (2007)
 59. Ryde, U.: *QM/MM Calculations on Proteins*, 1st edn. Elsevier (2016). <https://doi.org/10.1016/bs.mie.2016.05.014>
 60. Zheng, M., Waller, M.P.: Adaptive quantum mechanics/molecular mechanics methods. *Wiley Interdiscip. Rev. Comput. Mol. Sci.* **6**, 369–385 (2016). <https://doi.org/10.1002/wcms.1255>
 61. Senn, H.M., Thiel, W.: QM/MM methods for biomolecular systems. *Angew. Chemie Int. Ed.* **48**, 1198–1229 (2009). <https://doi.org/10.1002/anie.200802019>
 62. van der Kamp, M.W., Mulholland, A.J.: Computational enzymology: insight into biological catalysts from modelling. *Nat. Prod. Rep.* **25**, 1001–1014 (2008). <https://doi.org/10.1039/b600517a>
 63. de Almeida, J.S.F.D., Cuya Guizado, T.R., Guimarães, A.P., Ramalho, T.C., Gonçalves, A. S., de Koning, M.C., França, T.C.C.: Docking and molecular dynamics studies of peripheral site ligand–oximes as reactivators of sarin-inhibited human acetylcholinesterase. *J. Biomol. Struct. Dyn.* **34**, 2632–2642 (2016). <https://doi.org/10.1080/07391102.2015.1124807>
 64. Humphrey, W., Dalke, A., Schulten, K.: VMD: visual molecular dynamics. *J. Mol. Graph.* **14**, 33–38 (1996). [https://doi.org/10.1016/0263-7855\(96\)00018-5](https://doi.org/10.1016/0263-7855(96)00018-5)
 65. Meng, X.-Y., et al.: *Curr. Comput. Aided Drug Des.* **7**(2), 146–157 (2011)

66. Correa-Basurto, J., Bello, M., Rosales-Hernández, M.C., Hernández-Rodríguez, M., Nicolás-Vázquez, I., Rojo-Domínguez, A., Trujillo-Ferrara, J.G., Miranda, R., Flores-Sandoval, C.A.: QSAR, docking, dynamic simulation and quantum mechanics studies to explore the recognition properties of cholinesterase binding sites. *Chem. Biol. Interact.* **209**, 1–13 (2014). <https://doi.org/10.1016/j.cbi.2013.12.001>
67. Matta, C.F., Gillespie, R.J.: Understanding and interpreting molecular electron density distributions. *J. Chem. Ed.* **79**(9), 1141–1152 (2002)
68. Capelle, K.: A bird's-eye view of density-functional theory. *Braz. J. Phys.* **36**(4A), 1318–1343 (2006)
69. Hohenberg, P., Kohn, W.: Inhomogeneous electron gas. *Phys. Rev.* **136**, B864–B871 (1964). <https://doi.org/10.1103/PhysRev.36.B864>
70. Kohn, W., Sham, L.J.: Self-consistent equations including exchange and correlation effects. *Phys. Rev.* **140**, A1133–A1138 (1965). <https://doi.org/10.1103/PhysRev.140.A1133>
71. ud Din, F., et al.: Effective use of nanocarriers as drug delivery systems for the treatment of selected tumors. *Int. J. Nanomed.* **12**, 7291–7309 (2017)
72. Singh, R., Lillard, J.W., Jr.: Nanoparticle-based targeted drug delivery. *Exp. Mol. Pathol.* **86**(3), 215–223 (2009)
73. Lombardo, D., Kiselev, M.A., Caccamo, M.T.: Smart nanoparticles for drug delivery application: development of versatile nanocarrier platforms in biotechnology and nanomedicine. *J. Nanomater.* **2019**(Article ID 3702518), 26 (2019)
74. Yadav, P., Bandyopadhyay, A., Chakraborty, A., Sarkar, K.: Enhancement of anticancer activity and drug delivery of chitosan-curcumin nanoparticle via molecular docking and simulation analysis. *Carbohydr. Polym.* **182**, 188–198 (2018)
75. Khan, M., Husain, Q., Ahmad, N.: Elucidating the binding efficacy of β -galactosidase on polyaniline–chitosan nanocomposite and polyaniline–chitosan–silver nanocomposite: activity and molecular docking insights. *J. Chem. Technol. Biotechnol.* (2018). <https://doi.org/10.1002/jctb.5831>
76. Al-Fifi, Z., Saleh, N.A., Elhaes, H., Ibrahim, M.: On the molecular modeling analyses of novel HIV-1 protease inhibitors based on modified chitosan dimer. *Int. J. Spectrosc.* **2015**, 1–9 (2015). <https://doi.org/10.1155/2015/174098>
77. Yadav, A.V., Bhise, S.B.: Chitosan: a potential biomaterial effective against typhoid. *Curr. Sci.* **87**, 1176–1178 (2004). <http://www.jstor.org/stable/24109427>
78. Mousavi, S.V., Hashemianzadeh, S.M.: Molecular dynamics approach for behavior assessment of chitosan nanoparticles in carrying of donepezil and rivastigmine drug molecules. *Mater. Res. Express* **6**, 45069 (2019). <https://doi.org/10.1088/2053-1591/aaefc6>
79. Deepa, G., Sivakumar, K.C., Sajeevan, T.P.: Molecular simulation and in vitro evaluation of chitosan nanoparticles as drug delivery systems for the controlled release of anticancer drug cytarabine against solid tumours. *3 Biotech.* **8**, 493 (2018). <https://doi.org/10.1007/s13205-018-1510-x>
80. Dhanasekaran, S., Rameshthangam, P., Venkatesan, S., Singh, S.K., Vijayan, S.R.: In vitro and in silico studies of chitin and chitosan based nanocarriers for curcumin and insulin delivery. *J. Polym. Environ.* **26**, 4095–4113 (2018). <https://doi.org/10.1007/s10924-018-1282-8>
81. Omar, A., El-Sayed, E.-S.M., Talaat, M.S., Ibrahim, M.: DNA hybridization on chitosan-functionalized silicon substrate. *Med. Chem. (Los. Angeles)* **12**, 464–471 (2016). <https://doi.org/10.2174/1573406412666151112124836>
82. Rashid, J.I.A., Yusof, N.A.: The strategies of DNA immobilization and hybridization detection mechanism in the construction of electrochemical DNA sensor: a review. *Sens. Bio-Sens. Res.* **16**, 19–31 (2017)
83. Trevino, V., Falciani, F., Barrera-Saldaña, H.A.: DNA microarrays: a powerful genomic tool for biomedical and clinical research. *Mol. Med.* **13**(9–10), 527–541 (2007)
84. Portnyagin, A.S., Bratskaya, S.Y., Pestov, A.V., Voit, A.V.: Binding Ni(II) ions to chitosan and its N-heterocyclic derivatives: density functional theory investigation. *Comput. Theor. Chem.* **1069**, 4–10 (2015). <https://doi.org/10.1016/j.comptc.2015.07.001>

85. Deka, B.C., Bhattacharyya, P.K.: DFT study on host-guest interaction in chitosan–amino acid complexes. *Comput. Theor. Chem.* **1110**, 40–49 (2017). <https://doi.org/10.1016/j.comptc.2017.03.036>
86. Franconetti, A., Carnerero, J.M., Prado-Gotor, R., Cabrera-Escribano, F., Jaime, C.: Chitosan as a capping agent: insights on the stabilization of gold nanoparticles. *Carbohydr. Polym.* **207**, 806–814 (2019). <https://doi.org/10.1016/j.carbpol.2018.12.046>
87. Costa, M.P.M., Prates, L.M., Baptista, L., Cruz, M.T.M., Ferreira, I.L.M.: Interaction of polyelectrolyte complex between sodium alginate and chitosan dimers with a single glyphosate molecule: a DFT and NBO study. *Carbohydr. Polym.* **198**, 51–60 (2018). <https://doi.org/10.1016/j.carbpol.2018.06.052>
88. Chigo Anota, E., Torres Soto, A., Cocoltzi, G.H.: Studies of graphene–chitosan interactions and analysis of the bioadsorption of glucose and cholesterol. *Appl. Nanosci.* **4**, 911–918 (2014). <https://doi.org/10.1007/s13204-013-0283-0>
89. Shi, Z., Neoh, K.G., Kang, E.T., Wang, W.: Antibacterial and mechanical properties of bone cement impregnated with chitosan nanoparticles. *Biomaterials* **27**, 2440–2449 (2006). <https://doi.org/10.1016/j.biomaterials.2005.11.036>
90. De Almeida, V.L., Leitão, A., Barrett Reina, L.D.C., Montanari, C.A., Donnici, C.L., Lopes, M.T.P.: Câncer e agentes antineoplásicos ciclo-celular específicos e ciclo-celular não específicos que interagem com o DNA: Uma introdução. *Quim. Nova.* **28**, 118–129 (2005). <https://doi.org/10.1590/s0100-40422005000100021>
91. Riegger, B.R., Kowalski, R., Hilfert, L., Tovar, G.E.M., Bach, M.: Chitosan nanoparticles via high-pressure homogenization-assisted miniemulsion crosslinking for mixed-matrix membrane adsorbers. *Carbohydr. Polym.* **201**, 172–181 (2018). <https://doi.org/10.1016/j.carbpol.2018.07.059>
92. Nguyen, T.V., Nguyen, T.T.H., Wang, S.L., Vo, T.P.K., Nguyen, A.D.: Preparation of chitosan nanoparticles by TPP ionic gelation combined with spray drying, and the antibacterial activity of chitosan nanoparticles and a chitosan nanoparticle–amoxicillin complex. *Res. Chem. Intermed.* **43**, 3527–3537 (2017). <https://doi.org/10.1007/s11164-016-2428-8>
93. Costa, E.M., Silva, S., Vicente, S., Neto, C., Castro, P.M., Veiga, M., Madureira, R., Tavaría, F., Pintado, M.M.: Chitosan nanoparticles as alternative anti-staphylococci agents: bactericidal, antibiofilm and antiadhesive effects. *Mater. Sci. Eng., C* **79**, 221–226 (2017). <https://doi.org/10.1016/j.msec.2017.05.047>
94. Gomathi, T., Sudha, P.N., Florence, J.A.K., Venkatesan, J., Anil, S.: Fabrication of letrozole formulation using chitosan nanoparticles through ionic gelation method. *Int. J. Biol. Macromol.* **104**, 1820–1832 (2017). <https://doi.org/10.1016/j.ijbiomac.2017.01.147>
95. Souto, G.D., Farhane, Z., Casey, A., Efeoglu, E., McIntyre, J., Byrne, H.J.: Evaluation of cytotoxicity profile and intracellular localisation of doxorubicin-loaded chitosan nanoparticles. *Anal. Bioanal. Chem.* **408**, 5443–5455 (2016). <https://doi.org/10.1007/s00216-016-9641-6>
96. Prabakaran, M.: Chitosan-based nanoparticles for tumor-targeted drug delivery. *Int. J. Biol. Macromol.* **72**, 1313–1322 (2015). <https://doi.org/10.1016/j.ijbiomac.2014.10.052>
97. He, Z., Santos, J.L., Tian, H., Huang, H., Hu, Y., Liu, L., Leong, K.W., Chen, Y., Mao, H.-Q.: Scalable fabrication of size-controlled chitosan nanoparticles for oral delivery of insulin. *Biomaterials* **130**, 28–41 (2017). <https://doi.org/10.1016/j.biomaterials.2017.03.028>
98. Vauthier, C., Zandanel, C., Ramon, A.L.: Chitosan-based nanoparticles for in vivo delivery of interfering agents including siRNA. *Curr. Opin. Colloid Interface Sci.* **18**, 406–418 (2013). <https://doi.org/10.1016/j.cocis.2013.06.005>
99. Bernkop-Schnürch, A., Dünnhaupt, S.: Chitosan-based drug delivery systems. *Eur. J. Pharm. Biopharm.* **81**, 463–469 (2012). <https://doi.org/10.1016/j.ejpb.2012.04.007>
100. Sagar, S.R., Singh, D.P., Panchal, N.B., Das, R.D., Pandya, D.H., Sudarsanam, V., Nivsarkar, M., Vasu, K.K.: Thiazolyl-thiadiazines as beta site amyloid precursor protein cleaving enzyme-1 (BACE-1) inhibitors and anti-inflammatory agents: multitarget-directed

- ligands for the efficient management of Alzheimer's disease. *ACS Chem. Neurosci.* **9**, 1663–1679 (2018). <https://doi.org/10.1021/acscemneuro.8b00063>
101. El-Aziz, A.R.M.A., Al-Othman, M.R., Mahmoud, M.A., Shehata, S.M., Abdelazim, N.S.: Chitosan nanoparticles as a carrier for *Mentha longifolia* extract: Synthesis, characterization and antifungal activity. *Curr. Sci.* **114**, 2116–2122 (2018). <https://doi.org/10.18520/cs/v114/i10/2116-2122>
 102. Calvo, P., Remuñán-López, C., Vila-Jato, J.L., Alonso, M.J.: Novel hydrophilic chitosan-polyethylene oxide nanoparticles as protein carriers. *J. Appl. Polym. Sci.* **63**, 125–132 (1997). [https://doi.org/10.1002/\(SICI\)1097-4628\(199710103\)63:1%3c125:AID-APP13%3e3.0.CO;2-4](https://doi.org/10.1002/(SICI)1097-4628(199710103)63:1%3c125:AID-APP13%3e3.0.CO;2-4)
 103. Gupta, S., Jassal, P.S., Chand, N.: Chitosan nanoparticles : synthesis and their applications. **3**, 686–689 (2016)
 104. Barratt, G.: Colloidal drug carriers: achievements and perspectives. *Cell. Mol. Life Sci.* **60**, 21–37 (2003). <https://doi.org/10.1007/s000180300002>
 105. Gan, Q., Wang, T., Cochrane, C., McCarron, P.: Modulation of surface charge, particle size and morphological properties of chitosan–TPP nanoparticles intended for gene delivery. *Colloids Surf. B Biointerfaces* **44**, 65–73 (2005). <https://doi.org/10.1016/j.colsurfb.2005.06.001>
 106. Ali, S.W., Joshi, M., Rajendran, S.: Modulation of size, shape and surface charge of chitosan nanoparticles with reference to antimicrobial activity. *Adv. Sci. Lett.* **3**, 452–460 (2010). <https://doi.org/10.1166/asl.2010.1152>
 107. Asiri, I. A.M., Mohammad, A.: *Applications of Nanocomposite Materials in Drug Delivery*. Elsevier (2018). ISBN 978-0-12-813741-3
 108. Jonassen, H., Kjøniksen, A.-L., Hiorth, M.: Stability of chitosan nanoparticles cross-linked with tripolyphosphate. *Biomacromol* **13**, 3747–3756 (2012). <https://doi.org/10.1021/bm301207a>
 109. Bhattarai, N., Gunn, J., Zhang, M.: Chitosan-based hydrogels for controlled, localized drug delivery. *Adv. Drug Deliv. Rev.* **62**, 83–99 (2010). <https://doi.org/10.1016/j.addr.2009.07.019>
 110. Grenha, A.: Chitosan nanoparticles: a survey of preparation methods. *J. Drug Target.* **20**, 291–300 (2012). <https://doi.org/10.3109/1061186X.2011.654121>
 111. Sailaja, A.K., Amareshwar, P., Chakravati, P.: Biological and chemical sciences chitosan nanoparticles as a drug delivery system. *J. Pharm. Pharm. Sci.* **1**, 474 (2010)
 112. Maitra, A., Ghosh, P.K., De Tapas, K.: Process for the preparation of highly monodispersed polymeric hydrophilic nanoparticles (1997) **5**. <https://patents.google.com/patent/US5874111A/en>
 113. Sailaja, A.K., Amareshwar, P., Chakravati, P.: Different techniques used for the preparation of nanoparticles using, natural polymers and their application. *Int. J. Pharm. Pharm. Sci.* **3**, 975–1491 (2011)
 114. Brunel, F., Véron, L., David, L., Domard, A., Delair, T.: A novel synthesis of chitosan nanoparticles in reverse emulsion. *Langmuir* **24**, 11370–11377 (2008). <https://doi.org/10.1021/la801917a>
 115. Divya, K., Jisha, M.S.: Chitosan nanoparticles preparation and applications. *Environ. Chem. Lett.* **16**, 101–112 (2018). <https://doi.org/10.1007/s10311-017-0670-y>
 116. Quintanar-Guerrero, D., de la Luz Zambrano-Zaragoza, M., Gutiérrez-Cortez, E., Mendoza-Muñoz, N.: Impact of the emulsification-diffusion method on the development of pharmaceutical nanoparticles. *Recent Pat. Drug Deliv. Formul.* **6**, 184–194 (2012). <https://doi.org/10.2174/187221112802652642>
 117. Garg, T., Rath, G., Goyal, A.K.: Inhalable chitosan nanoparticles as antitubercular drug carriers for an effective treatment of tuberculosis. *Artif. Cells Nanomed. Biotechnol.* **44**, 997–1001 (2016). <https://doi.org/10.3109/21691401.2015.1008508>
 118. Pathania, D., Gupta, D., Agarwal, S., Asif, M., Gupta, V.K.: Fabrication of chitosan-g-poly (acrylamide)/CuS nanocomposite for controlled drug delivery and antibacterial activity. *Mater. Sci. Eng. C* **64**, 428–435 (2016). <https://doi.org/10.1016/j.msec.2016.03.065>

119. Anirudhan, T.S., Deepa B.J.R.: Functionalized polymeric silver nanoparticle hybrid network as a dual antimicrobe: synthesis, characterization, and antibacterial application. *J. Appl. Polym. Sci.* **133** (2016). <https://doi.org/10.1002/app.43479>
120. Sahoo, S., Sasmal, A., Sahoo, D., Nayak, P.: Synthesis and characterization of chitosan-polycaprolactone blended with organoclay for control release of doxycycline. *J. Appl. Polym. Sci.* **118**, 3167–3175 (2010). <https://doi.org/10.1002/app.32474>
121. Zou, Q., Li, Y., Zhang, L., Zuo, Y., Li, J., Li, J.: Antibiotic delivery system using nano-hydroxyapatite/chitosan bone cement consisting of berberine. *J. Biomed. Mater. Res. Part A* **89A**, 1108–1117 (2009). <https://doi.org/10.1002/jbm.a.32199>
122. Du, W.-L., Niu, S.-S., Xu, Y.-L., Xu, Z.-R., Fan, C.-L.: Antibacterial activity of chitosan tripolyphosphate nanoparticles loaded with various metal ions. *Carbohydr. Polym.* **75**, 385–389 (2009). <https://doi.org/10.1016/j.carbpol.2008.07.039>
123. Asiri, S.M., Khan, F.A., Bozkurt, A.: Synthesis of chitosan nanoparticles, chitosan-bulk, chitosan nanoparticles conjugated with glutaraldehyde with strong anti-cancer proliferative capabilities. *Artif. Cells Nanomed. Biotechnol.* **46**, S1152–S1161 (2018). <https://doi.org/10.1080/21691401.2018.1533846>
124. Basha, M., AbouSamra, M.M., Awad, G.A., Mansy, S.S.: A potential antibacterial wound dressing of cefadroxil chitosan nanoparticles in situ gel: fabrication, in vitro optimization and in vivo evaluation. *Int. J. Pharm.* **544**, 129–140 (2018). <https://doi.org/10.1016/j.ijpharm.2018.04.021>
125. Supraja, T.N., Prasad, T.S.: Synthesis and characterization of chitosan nanoparticles and evaluation of antimicrobial activity antioxidant activity. *Adv. Bioequiv Availab.* **2** (2018)
126. Qi, L., Xu, Z., Jiang, X., Hu, C., Zou, X.: Preparation and antibacterial activity of chitosan nanoparticles. *Carbohydr. Res.* **339**, 2693–2700 (2004). <https://doi.org/10.1016/j.carres.2004.09.007>
127. Pavlidou, S., Papaspyrides, C.D.: A review on polymer-layered silicate nanocomposites. *Prog. Polym. Sci.* **33**, 1119–1198 (2008). <https://doi.org/10.1016/j.progpolymsci.2008.07.008>
128. Chamundeeswari, M., Sobhana, S.S.L., Jacob, J.P., Kumar, M.G., Devi, M.P., Sastry, T.P., Mandal, A.B.: Preparation, characterization and evaluation of a biopolymeric gold nanocomposite with antimicrobial activity. *Biotechnol. Appl. Biochem.* **55**, 29–35 (2010). <https://doi.org/10.1042/BA20090198>
129. Gao, X., Lowry, G.V.: Progress towards standardized and validated characterizations for measuring physicochemical properties of manufactured nanomaterials relevant to nano health and safety risks. *NanoImpact* **9**, 14–30 (2018)
130. Gómez-Estaca, J., López de Lacey, A., López-Caballero, M.E., Gómez-Guillén, M.C., Montero, P.: Biodegradable gelatin–chitosan films incorporated with essential oils as antimicrobial agents for fish preservation. *Food Microbiol.* **27**, 889–896 (2010). <https://doi.org/10.1016/j.fm.2010.05.012>
131. De, T.K., Ghosh, P.K., Maitra, A., Sahoo, S.K.: Process for the preparation of highly monodispersed polymeric hydrophilic nanoparticles. Google Patents (1999)
132. Gupta, S., Jassal, P.S., Chand., N.: Chitosan nanoparticles: synthesis and their applications. *J. Basic Appl. Eng. Res.* **3**, 8 (2016). ISSN 2350-0077
133. Mohammed, M.A., Syeda, J.T.M., Wasan, K.M., Wasan, E.K.: An overview of chitosan nanoparticles and its applications in non-parenteral drug delivery. *Pharmaceutics* **9**, 53 (2017)
134. Danczuk, M.: Eletrólitos Sólidos Poliméricos a Base de Quitosana **126** (2007)
135. Kanmani, P., Kumar, R.S., Yuvaraj, N., Paari, K.A., Pattukumar, V., Arul, V.: Effect of cryopreservation and microencapsulation of lactic acid bacterium *Enterococcus faecium* MC13 for long-term storage. *Bioch. Eng. J.* **58**, 140–147 (2011). <https://doi.org/10.1016/j.bej.2011.09.006>
136. Maricato, É.S.O.: Desenvolvimento de filmes de quitosana insolúveis em meio ácido com actividade antioxidante. 2010. 62 f. (Mestrado em bioquímica) - Departamento de Química, Universidade de Aveiro (2010)

137. Azevedo, V.V.C., Chaves, S.A., Bezerra, D.C., Lia Fook, M.V., Costa, A.C.F.M.: Quitina e Quitosana: aplicações como biomateriais. *Revista Eletrônica de Materiais e Processos. Campina Grande*, **2**(3), 27–34, dez. (2007)
138. Kong, M., Chen, X.G., Park, H.J.: Antimicrobial properties of chitosan and mode of action: a state of the art review. *Int. J. Food Microbiol.* **144**, 51–63 (2010). <https://doi.org/10.1016/j.ijfoodmicro.2010.09.012>
139. Santos, C.A.A., Castro, J.V., Picoli, A.A., Rolim, G.S.: Uso de quitosana e embalagem plástica na conservação pós-colheita de pêssegos ‘Douradão’. *Revista Brasileira de Fruticultura* **30**, 88–93 (2008). http://www.scielo.br/scielo.php?pid=S0100-294520080001000017&script=sci_abstract&tlng=pt
140. Borderías, A.J., Sánchez-Alonso, I., Pérez-Mateos, M.: New applications of fibres in foods: addition to fishery products. *Trends Food Sci. Technol.* **16**(10), 458–465 (2005). <https://doi.org/10.1016/j.tifs.2005.03.011>
141. Shahidi, F., Kamil, J., Jeon, Y.-J., Kim, S.K.: Antioxidant role of chitosan in a cooked cod (*Gadus morhua*) model system. *J. Food Lipids* **9**, 57–64 (2002). <https://doi.org/10.1111/j.1745-4522.2002.tb00208.x>
142. Mortazavian, A.M., et al.: Principles and methods of microencapsulation of probiotic microorganisms. *Iran. J. Biotechnol.* **5**, 1–18 (2007)
143. Pillai, C.K.S., Paul, W., Sharma, C.P.: Chitin and chitosan polymers: chemistry, solubility and fiber formation. *Prog. Polym. Sci.* **34**, 641–678 (2009). <https://doi.org/10.1016/j.progpolymsci.2009.04.001>
144. Roy, J.C., Salaün, F., Giraud, S., Ferri, A., Chen, G., Guan, J.: Solubility of chitin: solvents, solution behaviors and their related mechanisms. In: Xu, Z. (ed.) *Solubility of Polysaccharides*, 109–127. InTech, Vienna, Austria (2017). <https://doi.org/10.5772/intechopen.71385>
145. Fai, A.E.C., Stamford, T.C.M., Stamford, T.L.M.: Potencial biotecnológico de quitosana em sistemas de conservação de alimentos. *Revista Iberoamericana de Polímeros* **9**(5), 435 (2008)
146. Khan, A.: A potencialidade do reagente metacrilato de glicidila imobilizado no biopolímero quitosana para a remoção de cátions. 2011, 252f. Dissertação (Mestrado)- Universidade Estadual de Campinas, Campinas: São Paulo (2011)
147. Yadav, A.V., Bhise, S.B.: Chitosan: a potential biomaterial effective against typhoid. *Curr. Sci.* **87**(9), 1176–1178 (2004)
148. Goy, R.C., de Britto, D., Assis, O.B.G.: A review of the antimicrobial activity of chitosan. *Polímeros* **19**(3), 241–247 (2009)
149. Kim, S.K., Rajapakse, N.: Enzymatic production and biological activities of chitosan oligosaccharides (COS): a review. *Carbohydrate Polym.* **62**, 357–368 (2005)
150. Santos, M.C.: Efeitos dos subprodutos da aroeira e do biofilme a base de quitosana pós-colheita e controle de antracnose em goiabas “paluma”. 2012, 94f. Dissertação (Mestrado em Agroecossistemas) - Universidade Federal de Sergipe, São Cristóvão, 2012
151. Helander, I.M., Nurmiaho-Lassila, E.L., Ahvenainen, R., Rhoades, J., Roller, S.: Chitosan disrupts the barrier properties of the outer membrane of Gram negative bacteria. *Int. J. Food Microbiol.* **71**, 235–244 (2001)
152. Niu, X., Zhu, L., Xi, L., Guo, L., Wang, H.: An antimicrobial agent prepared by N-succinyl chitosan immobilized lysozyme and its application in strawberry preservation. *Food Control* **106829** (2019)
153. Zhang, H., Li, X., Kang, H.: Chitosan coatings incorporated with free or nano-encapsulated Paulownia Tomentosa essential oil to improve shelf-life of ready-to-cook pork chops. *LWT* **108580** (2019)
154. Downward, J.: RNA interference. *BMJ* **328**, 1245 (2004). <https://doi.org/10.1136/bmj.328.7450.1245>
155. Kamalzare, S., Noormohammadi, Z., Rahimi, P., Atyabi, F., Irani, S., Tekie, F.S.M., Mottaghtalab, F.: Carboxymethyl dextran-trimethyl chitosan coated superparamagnetic iron

- oxide nanoparticles: an effective siRNA delivery system for HIV-1 Nef. *J. Cell. Physiol.* (2019)
156. Kean, T., Thanou, M.: Biodegradation, biodistribution and toxicity of chitosan. *Adv. Drug Deliv. Rev.* **62**, 3–11 (2010)
 157. Wang, D., Han, J., Yu, Y., Li, X., Wang, Y., Tian, H., Guo, S., Jin, S., Luo, T., Qin, S.: Chitosan oligosaccharide decreases very-low-density lipoprotein triglyceride and increases high-density lipoprotein cholesterol in high-fat-diet-fed rats. *Exp. Biol. Med.* **236**(9), 1064–1069 (2011)
 158. Peter, M.G.: Chitin and chitosan from animal sources. In: Steinbüchel, A. (ed.) *Biopolymers: Polysaccharides II: Polysaccharides from Eukaryotes*, vol. 6, pp. 481–574. Wiley, Weinheim (2012)
 159. Alemдарođlu, C., Deđim, Z., Celebi, N., Zor, F., Oztürk, S., Erdođan, D.: An investigation on burn wound healing in rats with chitosan gel formulation containing epidermal growth factor. *Burns* **32**(3), 319–327 (2006)
 160. Ueno, H., Nakamura, F., Murakami, M., Okumura, M., Kadosawa, T., Fujinaga, T.: Evaluation effects of chitosan for the extracellular matrix production by fibroblasts and the growth factors production by macrophages. *Biomaterials* **22**(15), 2125–2130 (2001)
 161. Fráguas, R.M., Rocha, D.A., Queiroz, E.D.R., Abreu, C.M.P.D., Sousa, R.V.D., Oliveira Júnior, E.N.D.: Caracterização química e efeito cicatrizante de quitosana, com baixos valores de massa molar e grau de acetilação, em lesões cutâneas. *Polímeros* **25**(2), 205–211 (2015)
 162. Genesi, B.P.: Desenvolvimento de curativo a base de quitosana e gelatina contendo óleo de copaiba para tratamento de queimados (2015)
 163. Shigemasa, Y., Minami, S.: Applications of chitin and chitosan for biomaterials. *Biotechnol. Genet. Eng. Rev.* **13**, 383–420 (1995)
 164. Zhao, X., Wu, H., Guo, B., Dong, R., Qiu, Y., Ma, P.X.: Antibacterial anti-oxidant electroactive injectable hydrogel as self healing wound dressing with hemostasis and adhesiveness for cutaneous wound healing. *Biomaterials* **122**, 34–47 (2017)
 165. Minami, S., Okamoto, Y., Tanioka, S. I., Sashiwa, H., Saimoto, H., Matsuhashi, A., Shigemasa, Y.: Effects of chitosan on wound healing. In: Yalpani, M. (ed.) *Carbohydrates and carbohydrate polymers*, pp. 141–152 (1993)
 166. Martins, A., Facchi, S., Follmann, H., Pereira, A., Rubira, A., Muniz, E.: Antimicrobial activity of chitosan derivatives containing N-quaternized moieties in its backbone: a review. *Int. J. Mol. Sci.* **15**(11), 20800–20832 (2014)
 167. Tan, H., Ma, R., Lin, C., Liu, Z., Tang, T.: Quaternized chitosan as an antimicrobial agent: Antimicrobial activity, mechanism of action and biomedical applications in orthopedics. *Int. J. Mol. Sci.* **14**, 1854–1869 (2013)
 168. Xie, W., Xu, P., Wang, W., Liu, Q.: Preparation and antibacterial activity of a water-soluble chitosan derivative. *Carbohydr. Polym.* **50**, 35–40 (2002)
 169. Sankar, P.K., Rajmohan, G., Rosemary, M.J.: Physico-chemical characterisation and biological evaluation of freeze dried chitosan sponge for wound care. *Mater. Lett.* **208**, 130–132 (2017)
 170. Huang, Y., Feng, L., Zhang, Y., He, L., Wang, C., Xu, J., Wu, J., Kirk, T.B., Guo, R., Xue, W.: Hemostasis mechanism and applications of N-alkylated chitosan sponge. *Polym. Adv. Technol.* **28**(9), 1107–1114 (2017)
 171. Sivashankari, P.R., Prabakaran, M.: Prospects of chitosan-based scaffolds for growth factor release in tissue engineering. *Int. J. Biol. Macromol.* **93**, 1382–1389 (2016)
 172. Leceta, I., Molinaro, S., Guerrero, P., Kerry, J.P., De la Caba, K.: Caba, Quality attributes of MAP packaged ready-to-eat baby carrots by using chitosan-based coatings. *Postharvest. Biol. Technol.* **100**, 142–150 (2015)
 173. Li, S., Xiong, Q., Lai, X., Li, X., Wan, M., Zhang, J., Yan, Y., Cao, M., Lu, L., Guan, J., Zhang, D.: Molecular modification of polysaccharides and resulting bioactivities. *Comprehens. Revi. Food Sci. Food Safety* **15**(2), 237–250 (2016)

174. Gu, J., Al-Bayati, K., Ho, E.A.: Development of antibody-modified chitosan nanoparticles for the targeted delivery of siRNA across the blood-brain barrier as a strategy for inhibiting HIV replication in astrocytes. *Drug Delivery Transl. Res.* **7**(4), 497–506 (2017)
175. Mellegard, H., Strand, S.P., Christensen, B.E., Granum, P.E., Hardy, S.P.: Antibacterial activity of chemically defined chitosans: influence of molecular weight, degree of acetylation and test organism. *Int. J. Food Microbiol.* **148**, 48–54 (2011)
176. A. Anitha, S. Sowmya, P.T. Sudheesh Kumar, S. Deepthi, K.P. Chennazhi, H. Ehrlich, M. Tsurkan, R. Jayakumar, Chitin and chitosan in selected biomedical applications, *Prog. Polym. Sci.* **39** (2014) 1644–1667
177. Bugnicourt, L., Ladavière, C.: Interests of chitosan nanoparticles ionically cross-linked with tripolyphosphate for biomedical applications. *Prog. Polym. Sci.* **60**, 1–17 (2016)
178. Vunain, E., Mishra, A.K., Mamba, B.B.: Fundamentals of chitosan for biomedical applications. In: Jennings, J.A., Bumgardner, J.D. (eds.) *Chitosan Based Biomaterials*, Volume 1: Fundamenta
179. Kamaly, N., Yameen, B., Wu, J., Farokhzad, O.C.: Degradable controlled-release polymers and polymeric nanoparticles: mechanisms of controlling drug release. *Chem. Rev.* **116**, 2602–2663 (2016)
180. Talón, E., Trifkovic, K.T., Nedovic, V.A., Bugarski, B.M., Vargas, M., Chiralt, A., González-Martínez, C.: Antioxidant edible films based on chitosan and starch containing polyphenols from thyme extracts. *Carbohydr. Polym.* **157**, 1153–1161 (2017)
181. Jia, R., Duan, Y., Fang, Q., Wang, X., Huang, J.: Pyridine-grafted chitosan derivative as an antifungal agent. *Food Chem.* **196**, 381–387 (2016)
182. Salah-Tazdaït, R., Tazdaït, D., Harrat, Z., Eddaikra, N., Abdi, N., Mameri, N.: In: *Antiparasite Activity of Chitosan*, Proceedings of 2015 International Conference on Chemical, Metallurgy and Environmental Engineering (CMAEE 2015), Istanbul, Turkey, 3–4 June 2015, pp. 277–280
183. Tripathy, S., Das, S., Chakraborty, S.P., Sahu, S.K., Pramanik, P., Roy, S.: Synthesis, characterization of chitosan–tripolyphosphate conjugated chloroquine nanoparticle and its in vivo anti-malarial efficacy against rodent parasite: a dose and duration dependent approach. *Int. J. Pharm.* **434**, 292–305 (2012)
184. Abulaihaiti, M., Wu, X.W., Qiao, L., Lv, H.L., Zhang, H.W., Aduwayi, N., Wang, Y.J., Wang, X.C., Peng, X.Y.: Efficacy of albendazole–chitosan microsphere-based treatment for alveolar Echinococcosis in mice. *PLoS Negl. Trop. Dis.* **9**, e0003950 (2015)
185. Botlagunta, M.: Nutraceuticals-loaded chitosan nanoparticles for chemoprevention and cancer fatigue. *Nutraceuticals* 783–839 (2016)
186. Salah, R., Michaud, P., Mati, F., Harrat, Z., Lounici, H., Abdi, N., Drouiche, N., Mameri, N.: Anticancer activity of chemically prepared shrimp low molecular weight chitinevaluation with the human monocyte leukaemia cell line, THP-1. *Int. J. Biol. Macromol.* **52**, 333–339 (2013)
187. Kerch, G.: The potential of chitosan and its derivatives in prevention and treatment of age-related diseases. *Mar. Drugs* **13**, 2158–2182 (2015)
188. Wei, P., Ma, P., Xu, Q.S., Bai, Q.H., Gu, J.G., Xi, H., Du, Y.G., Yu, C.: Chitosan oligosaccharides suppress production of nitric oxide in lipopolysaccharide-induced N9 murine microglial cells in vitro. *Glycoconjugate J.* **29**, 285–295 (2012)
189. Monette, A., Ceccaldi, C., Assaad, E., Lerouge, S., Lapointe, R.: Chitosan thermogels for local expansion and delivery of tumor-specific T lymphocytes towards enhanced cancer immunotherapies. *Biomaterials* **75**, 237–249 (2016)
190. Colman, S.L., Salcedo, M.F., Mansilla, A.Y., Iglesias, M.J., Fiol, D.F., Martín-Saldaña, S., Alvarez, V.A., Chevalier, A.A., Casalagué, C.A.: Chitosan microparticles improve tomato seedling biomass and modulate hormonal, redox and defense pathways. *Plant Physiol. Biochem.* (2019)
191. Muslim, T., Morimoto, M., Saimoto, H., Okamoto, Y., Minami, S., Shigemasa, Y.: Synthesis and bioactivities of poly (ethylene glycol)–chitosan hybrids. *Carbohydr. Polym.* **46**(4), 323–330 (2001)

192. Sharif, R., et al.: The multifunctional role of chitosan in horticultural crops; a review. *Molecules* **23**(4), 872 (2018)
193. Al-Amri, S.M.: Improved growth, productivity and quality of tomato (*Solanum lycopersicum* L.) plants through application of shikimic acid. *Saudi J. Biol. Sci.* **20**(4), 339–345 (2013)

Effect of Light Stimulation on a Thermo-Cellulolytic Bacterial Consortium Used for the Degradation of Cellulose of Green Coconut Shells



Pedro Jorge Louro Crugeira, F. A. Chinalia, H. N. Brandão, J. B. T. L. Matos, A. L. B. Pinheiro and P. F. Almeida

Abstract The green coconut business is responsible for the generation of large amounts of waste. Sustainable development requires the transformation of such waste into value-added biotechnological products. The aim of this study was to optimize, by photostimulation, the hydrolysis of the coconut biomass. The thermo-cellulolytic consortium was collected from a composting pile, subjected to nutritional stress and irradiated either by Laser ($\lambda 660 \text{ nm}$) or LED ($\lambda 632 \pm 2 \text{ nm}$). Microbial quantification after irradiation showed a significant stimulatory biological response. Despite cultures irradiated by LED significantly differed from the Laser-irradiated ones ($p < 0.0001$) both were significantly different from the control ($p < 0.0001$). The microbial consortium irradiated either by Laser or LED light showed the increase of RNA production and consequently protein synthesis causing anticipation and increase of the RBBR catabolism. The generation of products by

P. J. L. Crugeira (✉) · F. A. Chinalia · J. B. T. L. Matos · P. F. Almeida
Laboratory of Biotechnology and Ecology of Micro-organisms, Institute of Health Science,
Federal University of Bahia, Reitor Miguel Calmon Ave, S/N, Salvador, BA 40110-100,
Brazil
e-mail: pedrocrugeira@yahoo.com.br

F. A. Chinalia
e-mail: chinalia@hotmail.com

J. B. T. L. Matos
e-mail: josilene.lima@ufba.br

P. F. Almeida
e-mail: pfatk@yahoo.com.br

H. N. Brandão
Department of Saude, Feira de Santana State University, Feira de Santa, BA 44036-900,
Brazil
e-mail: hugo@uefs.br

A. L. B. Pinheiro
Center of Biophotonics, Federal University of Bahia, 62, Araujo Pinho Ave, Canela,
Salvador, BA 40110-150, Brazil
e-mail: albp@ufba.br

© Springer Nature Switzerland AG 2020

F. A. La Porta and C. A. Taft (eds.), *Emerging Research in Science and Engineering Based on Advanced Experimental and Computational Strategies*, Engineering Materials, https://doi.org/10.1007/978-3-030-31403-3_5

cellulose hydrolysis (TRS and glucose) was significantly higher in the photostimulated groups, being the most effective catabolism observed within the first 48-h in the LED group and, after 144-h, in the Laser group. Photostimulation, especially by LED, might be considered as a booster of the bioprocess at low cost.

Keywords Biomass lignocellulolytic · Bacterial consortium · Laser · LED · Photostimulation

1 Introduction

The combination of population exponential growth and the indiscriminate exploitation of natural resources tends to culminate in the exhaustion of environmental resources. New approaches based on the use of residual biomass is one of the viable alternatives for obtaining natural resources with commercial value.

The incessant search for both recycling and reuse of agroindustrial wastes have prompted the development of innovative biotechnological processes capable of transforming waste into commercial compounds or products. This sustainable approach in the use of resources contributes to solving the problems caused by the accumulation of wastes and their consequent adverse effects on the environment. Furthermore, this is achieved by making them economically more profitable [36].

The market of coconut products has become a highly relevant in the economy of many countries. The coconut residual biomass is a valuable source of raw material for enhancing soil fertility and animal feed. In addition, there is significant evidence that this material can be used for second generation ethanol. On the other hand, it is yet necessary to clear two major bottlenecks in the production of reducing sugars from coconut fibers. The first is the disaggregation of lignin from hemicellulose/cellulose and the second is the reduction of costs with carbohydrate hydrolytic activity. In conjunction, they perform a synergistic bioprocess that allows greater lignocellulolytic activity [11].

Cellulose degradation is directly influenced by the degree of crystalline microfibrils and the presence of polymers in the cellulosic micropores matrix. A group of enzymes carries out cellulose hydrolysis (enzymatic complex). They are highly specific biocatalysts that synergistically act for the release of sugars. However, so far, few fungi and bacteria produce a comprehensive enzymic complex capable of extensively degrading lignocellulosic biomass in an economically viable manner. These enzymes include the ones which are carbohydrate active and the ones that are lignin oxidative enzymes [5, 45].

Microbial physiological state and enzymatic specificity can be modified by energetic modulation [10, 14, 41]. The metabolic response from the absorption of low-intensity radiation result in significant biochemical changes that causes either maintenance or the normalization of cellular functions. For the photobiomodulation process to occur, it is important that the target cells are not in the homeostasis phase [7].

When light is irradiated towards a living organism, energy is introduced into the biological system affecting several metabolic pathways. The resultant effect is directly related to energy dose, wavelength, power and the size of irradiated surface. The effectiveness of light irradiation is, therefore, closely related to an adequate energy fluency, that define the boundary between a stimulatory or inhibitory response [2].

Studies on the influence of low power laser and LED emitters on microbial populations have been discussed in the literature. They indicate biostimulant or proliferative results, postulating that such effects are due to the modifications generated by the increased energy level, caused by the light irradiation, in the microbial respiratory chain [9, 13, 14, 41].

The cytochrome C complex is one of the targets of red spectrum irradiation that, when photo-excited, it increases proton pumping leading to an increase in the amount of available cellular ATP. In such a case, the intramolecular target capable of absorbing light is the copper centers [1, 9].

Copper and zinc are commonly present in the protein structure or as enzymatic cofactors. These metals, especially zinc, are abundant in microorganisms and the metalloproteins containing them are commonly associated with transcriptional events that trigger the increase in the number of bacteria in the irradiated organisms [31].

Light emissions can “trigger” reactions in the respiratory chain or cell membrane. These will propagate through consecutive secondary reactions in the cytoplasm and the cell’s nucleus, triggering a series of chain reaction [22].

The aim of this study was to evaluate and compare the influence on the degradation process of green coconut fibers by a thermo-cellulolytic bacterial consortium photostimulated by laser or LED.

2 Methods

2.1 Pretreatment of Coconut Shell

The green coconut shell was subjected to two different alkaline pretreatments: 5% sodium hydroxide (NaOH) solution or 5% potassium hydroxide (KOH) solution in order to evaluate the best delignification performance.

Pretreatments were carried out in a water bath (Unique - USC 2500 ultrasonic cleaner, Illinois, Chicago, USA) at 100 °C for one hour in triplicate. Volumes of 400 mL of each solution were used for 20 g of green coconut shell, previously dehydrated in greenhouse (Biopar, Porto Alegre-RS, Brazil) at 60 °C for six hours. After pretreatments, the coconut fibers were washed with distilled water until pH neutralization (7.0).

Samples were taken after pretreatments for qualitative evaluation by scanning electron microscopy (SEM). The scanning electron microscope JEOL, model JSM-6610 LV, with 10 kV acceleration was used.

2.2 Microbial Sample Collection

Samples were collected from a lignocellulolytic residue composting pile at different points and depths during the active degradation phase (65–70 °C). Thirty aliquots of 100 g were removed and placed in a sterile environment at 4 °C and transported to the Laboratory of Biotechnology and Ecology of Microorganisms (LABEM), Federal University of Bahia–UFBA.

2.3 Selection of the Thermo-Cellulolytic Microorganisms

The samples were subjected to microbial extraction in a 0.01% sterile Tween 80 sterile saline phosphate buffer (PBS) (Merck, Germany) at 60 °C; 100 rpm for 2-h on a shaking table (New Brunswick Scientific Co I26, San Diego-CA, USA).

Serial decimal dilutions of the microbial culture in synthetic broth were carried out with the following composition: NaNO₃ (3.0 g/L); (NH₄)₂SO₄ (1.0 g/L); MgSO₄ (0.5 g/L); KCl (0.5 g/L); FeSO₄·7H₂O (10.0 mg/L), in Erlenmeyers containing 5 strips of filter paper Whatman n°1 (1 × 6 cm; Start Bioscience, Brazil) as a carbon source. After incubation at 60 °C; 100 rpm (New Brunswick Scientific Co I26 Incubator Shaker Series, São Diego-CA, USA) for 120-h, the cellulolytic capacity of the consortium was identified by analyzing the degradation of the filter paper. Cell quantification was performed by the most probable number method (MPN). Analyzes were performed in triplicate.

2.4 Characteristics of the Thermo-Cellulolytic Consortium

2.4.1 Cellulolytic Activity

Cellulolytic activity was assessed by quantification of Congo red discoloration method (Sigma-Aldrich, India).

After incubation of the bacterial pool for 36-h at 50 °C in mineral culture medium: NaNO₃ (2.0 g/L); K₂HPO₄ (1.0 g/L); MgSO₄ 7H₂O (0.5 g/L); KCl (0.5 g/L); FeSO₄·7H₂O (0.001 g/L); agar (10.0 g/L) with carboxymethylcellulose (CMC 5.0 g/L) as carbon source, 10 ml Congo red solution (2.5 g/L) in 0.1 M Tris HCl buffer, pH 8.0 was added. After 15 min the solution was discarded and the plates were washed with 5 mL of 0.5 M NaCl solution. Fifteen minutes were waited for halo and colony analysis.

2.4.2 Morphological Analysis of the Microbial Consortium

1 mL of sample was taken from the microbial consortium, centrifuged (Eppendorf 5804 R, Westbury-NY, USA) for 10 min at 10.000 rpm, then the pellet was washed with sterile PBS solution (three times) and re-suspended in orange acridine dye (Sigma-Aldrich, India) in a dark environment. After 10 min, 10 μ l aliquots were prepared for microscope viewing (Olympus BX 51, U-TVO.5XC-3 lens, Shinjuku, Tokyo, Japan).

2.4.3 Growth Curve of the Microbial Consortium

An inoculum of microbial culture consortium (25 ml) was transferred into Erlenmeyers containing (250 mL) mineral broth with the following composition: NaNO₃ (2.0 g/L); K₂HPO₄ (1.0 g/L); MgSO₄ 7H₂O (0.5 g/L); KCl (0.5 g/L); FeSO₄.7H₂O (0.001 g/L); CMC (5.0 g/L) with CMC as the sole carbon source under agitation at 100 rpm at 60 ° C (New Brunswick Scientific, San Diego-CA, USA).

Consortium growth was monitored for 72-h and samples were taken every four hours for microbial quantification by the direct counting method of fluorochrome staining using a fluorescence microscope (Olympus BX 51, U-TVO lens. 5XC-3, Shinjuku, Tokyo, Japan).

The samples collected for quantification were treated by the methodology described in Sect. 2.4.2. The visualized slides were photographed in 20 distinct fields of each sample and applied to Eq. 1 [28];

$$\text{Cells/mL} = (N \times A) / (d \times V_f \times A_g) \quad (1)$$

N Number of cells quantified

A Coverslip area

D Dilution factor

Vf Volume of sample

Ag Grate area of count (field of objective x numbers)

Table 1 Light emission parameters used

Parameters	Laser	LED
Wavelength (nm)	660	632 \pm 2
Mode	Continuous	Continuous
Spot size (cm ²)	0.04	0.5
Power output (mW)	40	145
Exposure Time (s)	325	44
Energy density (J/cm ²)	13	13

2.5 *Evaluation of the Photostimulation of the Microbial Consortium*

After the physiological activation of the microbial inoculum, culture was carried out in mineral medium described in Sect. 2.4.3 at 60 °C; 100 rpm for a period of 35-h (end of exponential phase). The culture was then centrifuged (Eppendorf 5804 R, Westbury-NY, USA) and the pellet washed with sterile PBS solution (three times) to initiate the nutritional stress phase.

The induction of functional disorder in the thermo-cellulolytic consortium was established through total nutritional deprivation (PBS), so that it was possible to photomodulate the metabolic system according to the energy offered.

One of the studied groups was irradiated with a laser device (Twin flex - MMOptics São Carlos, SP, Brazil) and another with the LED prototype (MMOptics São Carlos, SP, Brazil). The light emission parameters are described in Table 1.

The energy density of 13 J/cm² used to irradiate the microbial consortium was adopted based on studies reported by Crueira et al. [10].

The irradiation protocol was carried out under conditions of total nutrient deprivation (PBS) for a period of 68-h in petri dishes. Six irradiations were performed at 12-h intervals, being the first application carried out after 8-h of nutrient deprivation. The culture was kept in PBS solution at 60 °C and 100 rpm, for the time necessary for the following irradiations. The microbial consortium subjected to exactly the same methodology was used as control, without any irradiation.

After the irradiation protocol, samples were collected to quantify the number of viable cells. Serial dilutions were made in triplicate and 100 µl and inoculated into each Petri dish containing agar culture medium (Merck, Germany), diluted 10 times so that to avoid nutritional shock. After incubation for 48-h (TE-392/I Tecnal, Piracicaba-SP, Brazil) at 50 °C, colony forming units (CFU) were assessed.

2.6 *Assessment of the Lignolytic Activity*

The degradation evaluation of Remazol-R Bright Blue polymeric dye (RBBR) (Sigma-Aldrich, India) was used to evaluate the consortium in terms of its lignolytic activity as well as the effect of the Laser or LED irradiation in the catabolic process.

Following the irradiation protocol, 10 mL of the thermo-cellulolytic consortium was inoculated into 100 mL of mineral medium with 0.02% RBBR dye (Sigma-Aldrich, Germany), and the triplicates were incubated on a shaking table at 100 rpm, 60 °C (New Brunswick Scientific Co I26, San Diego-CA, USA) in a dark environment. The first sample was taken after 24-h and the others at every 48-h for 240-h. Absorbance readings at 595 nm by spectrophotometry was carried out in each sample (Molecular Devices Spectramax[®] 190 Microplate Reader, Hampton-NH, USA) [16].

2.6.1 Nucleic Acid Analysis by Epifluorescence

Triplicate samples were collected at 48-h intervals during the RBBR dye hydrolysis process and subjected to the acridine orange fluorochrome staining method (Sigma-Aldrich, India) described in Sect. 2.4.3 in order to identify single strand and double strand nucleic acids [27].

Background was subtracted from the images obtained by microscopy and the region of interest was selected using the contrast image which was binarized and used as a mask to filter the original image. The fluorescence intensity of each photomicrograph was quantified using the “Image J” software according to the analysis protocols of O’neal et al. [40], Bakr [3] and Jensen [20].

2.7 Quantification of the Cellulose Hydrolysis Products

2.7.1 Determination of the Total Reducing Sugars

Total soluble reducing sugars were determined during the coconut shell microbial hydrolysis process by the 3, 5-dinitrosalicylic acid (DNS) method.

For this, 25 mL of the bacterial consortium was inoculated into 250 mL of CMC-free mineral broth using 4.0 g of green coconut shell as a carbon source (pretreated with 5% NaOH) forming the study groups described in Table 2.

Each group was incubated in the agitation table at 60 °C, 100 rpm (New Brunswick Scientific Co I26 Incubator Shaker Series) in triplicate for 240-h. The supernatant samples were collected at the end of 24-h thereafter at 48-h intervals for quantification of total reducing sugars (TRS) according as described by Vasconcelos et al. [47]. The calibration curve was initially performed with standard

Table 2 Distribution of the experimental groups

Control group	Laser group	LED group
25 mL of the consortium with no irradiation	25 mL of the consortium with Laser irradiation	25 mL of the consortium with LED irradiation
+	+	+
4.0 g of 5% NaOH pretreated coconut shell with no irradiation	4.0 g of 5% NaOH pretreated coconut shell with Laser irradiation	4.0 g of 5% NaOH pretreated coconut shell with LED irradiation
+	+	+
250 mL Mineral broth medium	250 mL Mineral broth medium	250 mL Mineral broth medium
+	+	+
no irradiation	Laser irradiation	LED irradiation

D-glucose solutions to determine total reducing sugar (TRS) concentrations in g/L according to Eq. 2:

$$TRS = abs \times f \times d \quad (2)$$

in that:

abs is the average absorbance readings;

f is the concentration factor;

d is the inverse of sample dilution.

2.7.2 Quantification of the Glucose

The glucose content in the samples was quantified by HPLC chromatography analysis (High performance Liquid Chromatograph).

Samples were collected from the shaker at 60 °C and 100 rpm (New Brunswick Scientific Co I26 Incubator Shaker Series, San Diego-CA, USA) at the end of 24, 48, 96, 144, 192 and 240-h of incubation. They were then filtered through 0.22 µm Kasvi[®] PES membranes (Kasvi, Italy), and vialled for injection on the high performance refractive index detector (HPLC-IR) chromatograph.

The chromatographic experiments were performed on an EZChrom Elite HPLC system consisting of VRW HITACHI L-2130 pump, VRW HITACHI L-2200 automatic injector and VRW HITACHI L-2490 refractive index (IR) detector. HPX-87H Aminex[®] column (300 mm × 7.8 mm i.d./9 µm/BIO-RAD, California, USA) was used. The injection volume was 20 µL, the mobile phase used was 0.01 N aqueous H₂SO₄ solution with a flow rate of 0.6 mL/min. The analysis was performed at room temperature, the total analysis time was of 20 min.

Samples were analyzed for glucose pattern identification by comparing peak retention times in the sample chromatograms with that of the standard. The quantification was performed using the standard calibration analytical curves, interpolating the area value of the samples found in the obtained line equations.

Validation was performed according to parameters of the International Council for the Harmonization of Technical Requirements for Medicinal Products for Human Use using the parameters of selectivity, linearity, precision, accuracy, limit of detection and limit of quantification [19].

Selectivity was determined by comparing the peak of the standard with the corresponding peaks in the samples, taking into account retention time.

Linearity was determined by graphing the responses as a function of the analyte concentration through the calibration curve graph, projecting the equation of the regression line of y into x, estimated by the least squares method, taking into account the coefficient correlation (r) and determination (r²). The equations of the line were obtained by injections of solutions with different concentrations of external standards, ranging from 12 to 100 µg/mL for glucose. The external standard solution was prepared by dissolving the standard in ultrapure water.

Accuracy was determined by triplicate injection of three standard solutions according to the International Union of Pure and Applied Chemistry (IUPAC). This parameter was expressed as the relative standard deviation (SDR) according to Eq. 3:

$$DPR = \frac{DP}{CMD} \cdot 100 \quad (3)$$

in that:

DP is the standard deviation.

CMD is the average concentration determined.

Accuracy was verified by the recovery factor. A pool of samples was made and fortified with three standard solutions of known concentrations 80, 50 and 30 $\mu\text{g}/\text{mL}$ for glucose. Accuracy was assessed using experimentally determined concentration values compared to the theoretical concentration as can be seen in Eq. 4:

$$Accuracy = \frac{\text{Mean experimental concentration}}{\text{Theoretical concentration}} \cdot 100 \quad (4)$$

The limit of detection (DL) was estimated, according to IUPAC, by the ratio of the standard deviation of the linear coefficient and the slope of the calibration curve according to Eq. 5:

$$LD = \frac{DPa.3}{IC} \quad (5)$$

in that:

DPa is the standard deviation of the intercept with the y-axis of three calibration curves.

IC is the slope of the calibration curve.

The limit of quantification (QL) was estimated, according to the IUPAC, by the ratio of the standard deviation of the linear coefficient and the slope of the calibration curve according to Eq. 6:

$$LQ = \frac{DPa.10}{IC} \quad (6)$$

in that:

DPa is the standard deviation of the intercept with the y-axis of three calibration curves.

IC is the slope of the calibration curve.

2.8 Bacterial Quantification by Epifluorescence

Supernatant samples were collected during the pre-treated coconut shell hydrolysis process in triplicate after 48 and 144-h. Sample treatment was performed according to the methodology described in Sect. 2.4.2. The slides were visualized and photographed in 20 fields of each sample and microbial quantification by epifluorescence was performed as described in Sect. 2.7.1.

2.9 Statistical Analysis

Analysis of the results obtained in the different assays was performed using the ANOVA statistical test with the Tukey multiple comparison post-test with 95% confidence, using GraphPad Prism[®] 6.0 software (San Diego-CA, USA).

3 Results and Discussion

3.1 Pretreatments of the Coconut Shell

Pretreatments should prevent carbohydrate degradation or loss and formation of byproducts capable of inhibiting the hydrolysis process. Alkaline pretreatments were used because they allow both less sugar degradation and formation of furan derivatives when compared to acid treatments [6, 37].

The micrographs showed a reduction in the amount of lignin in both alkaline pretreatments, showing a decrease in globular protrusions, small pores and even components such as waxes and fatty acids that are part of the fill and fiber connections (Fig. 1) [4].

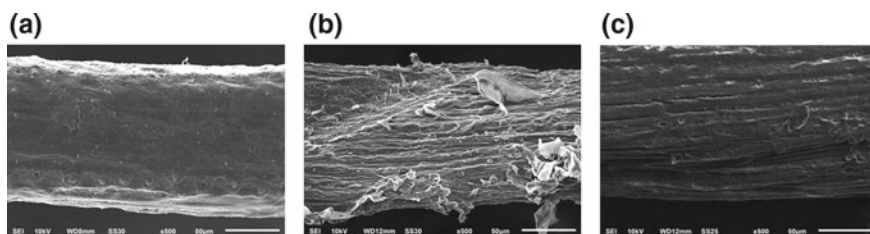


Fig. 1 SEM micrographs comparing the used pretreatments of coconut shells 500x. (a) No pretreatment; (b) Pretreatment with 5% NaOH, 100 °C, 1-h; (c) Pretreatment with 5% KOH, 100 °C, 1-h

The analysis of the micrograph showed a more effective delignification in alkaline treatment by 5% NaOH, having the advantage of being a more economical process, which led us to choose this pretreatment for the rest of this study.

In a study by Mwaikambo and Ansell [38] on hemp, jute, sisal and kapok fibers, it was demonstrated that the 6% NaOH solution was the most effective in delignification, without altering the fiber crystallinity index.

Gonçalves [17] performed the alkaline pretreatment on the mature coconut substrate reaching the best cellulosic conversion 90.72% after 96-h of enzymatic hydrolysis, using as a pretreatment the 2.5% (v/v) NaOH solution at 180 °C for 30 min.

Alkaline hydrothermal pretreatment at temperatures below 140 °C induces cleavage of ester bonds that bind phenolic acids. Nucleophilic substitution of the acyl ester linkage group occurs with the reaction of sodium hydroxide to form a carboxylic salt and an alcohol at room temperature [42].

Pretreatment is considered effective when it maximizes accessibility to biochemical and/or biological attack by minimizing the formation of inhibitor by-products. It is important that waste generation and energy expenditure be reduced as well as the operating cost for the process to be economically viable.

3.2 Selection of the Do Thermo-Cellulolytic Consortium

Cellulolytic microbial activity was tested using the whatman 1 filter paper strips protocol (Start Bioscience, Brazil). Total degradation of the filter paper was verified in the triplicates at distinct dilutions (10^{-2} , 10^{-3} , 10^{-4} and partial in the 10^{-5}) of an initial thermos-cellulolytic inoculum density of 4.6×10^4 MPN/ml. A microbial consortium was used with the intention of promote a synergistic action in order to optimize cellulose hydrolysis [15]. The incubation temperature was of 60 °C.

Due to the recalcitrance of lignocellulosic biomass, the microbial attack with greater possibility and versatility in the catabolic process will be hypothetically when coexisting in the microbial co-culture system [33].

Currently the catalysis of lignocellulosic biomass by microorganisms is slow, being essential the elaboration of studies and introduction of new technologies in order to optimize the hydrolysis process, making it economically sustainable [43].

3.3 Characteristics of the Thermo-Cellulolytic Consortium

3.3.1 Cellulolytic Activity

The evaluation of microbial cellulolytic potential was done by the analysis of the hydrolysis of Congo red assessed by the discoloration test, that demonstrated the endoglucanase activity in CMC (Fig. 2). The formation of halos in Petri dishes

Fig. 2 Halo of hydrolysis of CMC, red congo staining



cultures resulted from the cleavage of CMC into fragments smaller than hexoses, to which Congo red does not bind [9].

Studies by Theather and Wood [44] demonstrate a strong interaction of Congo red with polysaccharides (β 1–4) bound in D-glucopyranosyl units providing the basis for a sensitive assay for identifying cellulase-producing bacterial colonies.

3.3.2 Morphological Analysis of Microbial Consortium

It was possible, through fluorescence microscopy, to morphologically analyze the microorganisms present in the consortium, among them cocci, diplococci, streptococci, staphylococci, bacilli, diplobacilli and streptobacilli (Fig. 3).

3.3.3 Growth Kinetics of the Microbial Consortium

The thermo-cellulolytic consortium growth curve showed two exponential phase, one in the first eight hours of incubation, followed by another 30 to 36-h. Consecutively, the stationary phase was observed in the lasts 16-h and followed by the significant decline within 72-h (Fig. 4).

The growth curve began with a phase of cell multiplication, which could hypothetically indicate that the microorganisms had stored nutritional reserves before starting the carbon source hydrolysis (CMC) process or that they performed the degradation of the CMC in a first phase, generating by-products and products, such as easily assimilated glucose, thus stimulating cell division from 28-h of growth.

As it is a consortium, composed by several bacterial populations, it is natural that there is a competition for the easily accessible carbon source and that the growth curve of the microbial population suffers variations. In any case, it provides information on the symbiosis that exists between the various species of microorganisms required to perform an irradiation protocol.

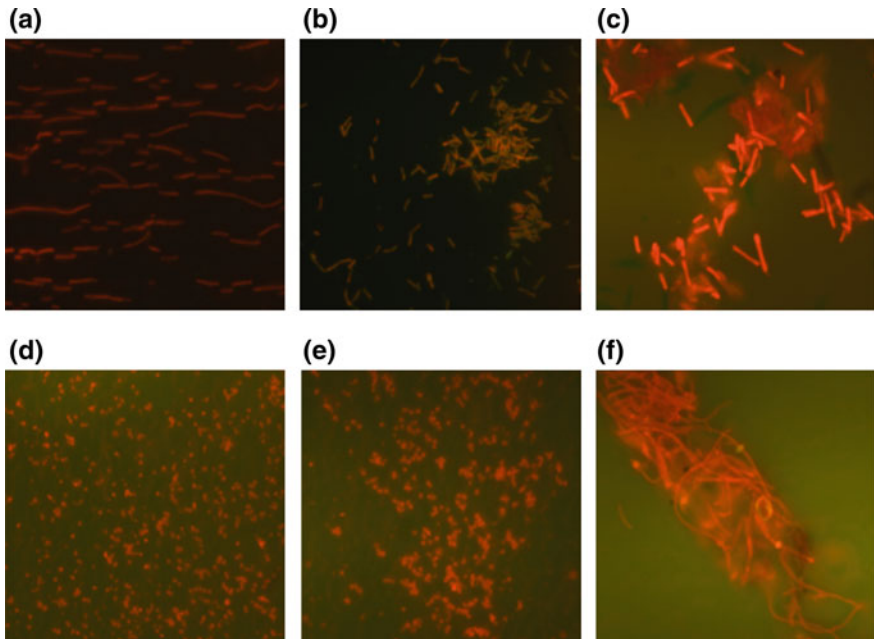
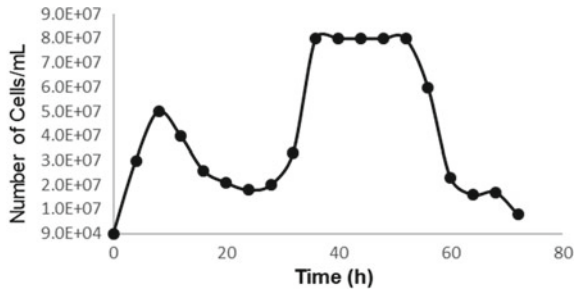


Fig. 3 Fluorescence microscopy images of morphologies and arrangements of microorganisms of the Consortium. (a) bacilli, diplococci and streptobacillus; (b) bacilli in irregular aggregates; (c) bacilli with terminal endospores; (d) cocci and diplococci in aggregates; (e) cocci in irregular aggregates; (f) Long filaments of cocci with endospores (Reproduced from [9])

Fig. 4 Growth curve of the thermo-cellulolytic consortium in Czapek mineral medium



3.4 Assessment of the Photobiomodulation of the Thermo-Cellulolytic Consortium

The irradiation protocol was performed in the consortium under nutritional stress (PBS solution), and radiation absorption occurs mainly when the cells are affected by a functional disorder [7].

Cell imbalance was encouraged to increase light absorption by photoacceptive molecules, triggering primary physicochemical changes and a sequence of secondary biochemical reactions in the microorganisms involved. Thus, it was intended to induce the physiological modulation of the microorganisms. The absorbed energy will be transformed into biochemical energy and used in metabolic processes in order to restore the homeostasis state of the microorganisms [21].

Energy density is undoubtedly one of the most important parameters for achieving the desired molecular effect, it may be the boundary between the stimulatory or inhibitory response [22].

The energy dose used was based on a study by Crugeira et al. [10], in a thermo-cellulolytic microbial consortium, that identified an energy density of 13 J/cm^2 as the one that induced the best response.

After the irradiation protocol, the numbers of CFUs of the study groups were compared. Laser-irradiated cultures showed a proliferation of 2.0×10^7 CFU/mL while those submitted to LED irradiation reached 5.5×10^7 CFU/mL, both superior to the control group in which the cell count was of 9×10^5 CFU/mL.

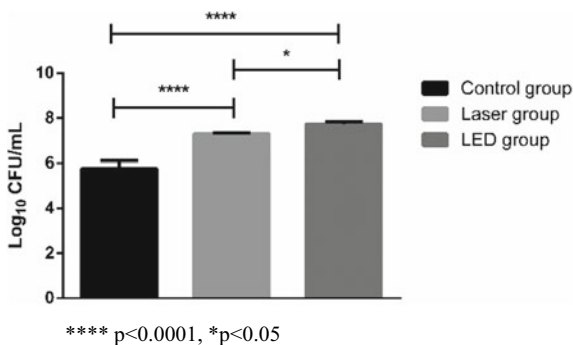
The results were statistically analyzed using ANOVA with the 95% confidence Tukey test. In the groups irradiated by both light sources, there was a significant increase in the number of cells compared to the control group, demonstrating thus a photostimulatory biological response in the microbial consortium (Fig. 5).

Both Laser- and LED-irradiated groups showed a significantly higher proliferation in comparison to the control group (respectively $p = 0.0057$ and < 0.0001). Comparing the two light sources a significant difference was also detectable ($p < 0.0001$) being the LED-irradiated group the one with higher count.

Karu et al. [26] established the basis for understanding the molecular mechanisms associated with light effects on cells by recording a photoreponse graph in the visible region stimulating *Escherichia coli* growth by DNA and ribonucleic acid synthesis rate.

Irradiated photoreceptors by specific wavelength and adequate energy density leads to the absorption of photons that take them to an electronically excited state capable of triggering primary molecular processes that causes biological effects [22].

Fig. 5 Microbial quantifications after irradiation protocol on logarithmic scale



The results of cellular quantification in the present study showed that, after irradiation by a non-coherent light (LED), microbial metabolic stimulation occurred as suggested by Karu [24]. It has been suggested that the cellular response to photostimulation is not directly associated to specific properties of the laser light, such as the coherence, as it is lost during the interaction of light with the matter and consequently it is not an essential condition for the photostimulation.

Studies on the effect of laser radiation on bacteria indicate biostimulation or proliferative effects, postulating that such effects are due to changes caused by increased energy supply by radiation in the bacterial respiratory chain [9, 23, 29]. One of the targets of light irradiation is the cytochrome C complex also present in bacteria. It has been suggested that when it is photostimulated there is an increase in its proton pumping capacity and consequently increases the amount of available cellular ATP [23].

Zinc and copper are found in protein metal centers or even acting as an enzymatic cofactor. These metals, especially zinc, are abundant in microorganisms and the metalloproteins that commonly contain them are associated with transcriptional events. Thus, the increase in the number of bacteria on the irradiated groups may also be related to the activation of such metalloproteins [1, 31].

One of the factors that may explain the higher effectiveness of LED irradiation found in this paper is based on studies by Karu [22] who showed that the microbial cytochrome has its maximum absorption peak at $\lambda 633 \text{ nm}$. This fact may corroborate the higher efficacy of LED ($\lambda 632 \text{ nm}$) in increasing microbial proliferation when compared to the control group or even to the Laser-irradiated group ($\lambda 660 \text{ nm}$).

On the other hand, the electromagnetic action spectrum of the light emitted by the LED is wider than that of the laser. Laser is characterized by a higher concentration of the energy fluency over a very small spectral range. While in the LED, the energy density is distributed in a larger electromagnetic band and can interact with a larger group of specific photoreceptors.

Primary chemical or physical changes caused by light radiation in the photoactive molecules are followed by a cascade of secondary biochemical reactions. These reactions occur in the absence of light and may occur within hours or days after irradiation [26].

The process is complex and wide ranging, depending on the photoreceptors and consequently the metabolic pathways involved, it is possible to change the pH and redox state of the cell, for example. In addition to the antiport carrier enzyme Na^+/H^+ , other ions carriers, sodium cation (Na^+), potassium cation (K^+), ATPase enzyme and enzymes that control cyclic AMP levels in a cell are also activated by irradiation and other secondary responses may arise in the cellular membrane [13, 25].

The inherent reactions to light emission that trigger biological stimulatory responses are vast and influence a large part of cell metabolism, culminating in an increased cell proliferation.

3.5 Assessment of the Lignolytic Activity in the Photostimulated Microbial Consortium

The determination of lignolytic activity by polymeric dyes was initially suggested by Glenn and Gold [16] and was established as a method for identifying microorganisms capable of degrading xenobiotic compounds. RBBR offers the advantage of low toxicity to microorganisms and its polymeric nature ensures that its degradation, at least in the early stages, occurs extracellularly [35, 39].

Although RBBR presents a complex and recalcitrant molecular structure, its degradation was identified in the photostimulated bacterial consortium within the first hours of analysis, demonstrating that the catalytic stimulation of extracellular lignolytic enzymes compared to the control group (Fig. 6).

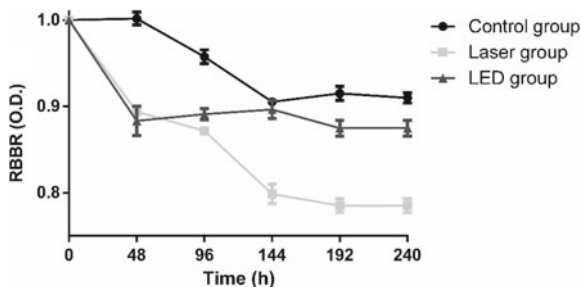
The results obtained in the first 48-h showed that the LED-irradiated group showed greater degradation of the RBBR (40.24%), while the Laser-irradiated one presented a degradation of 39.49%, both significantly higher than on the control group ($p < 0.0001$). No significant difference was observed between LED- and Laser-irradiated groups.

This finding indicates the possibility that light irradiation caused the excitation of prosthetic groups (heme and copper), that are mediating agents of the oxidizing reduction in the catalytic action of the RBBR dye. These mediators may be involved in the generation of reactive oxygen species (ROS), and directly or indirectly attack lignin and/or xenobiotic molecules [46].

The catalytic action of the control group only began after 48-h of incubation, revealing that irradiation stimulated extracellular enzymatic processes. After 96-h a significant statistical difference ($p = 0.0001$) was observed between the irradiated groups and the control group. On the other hand, after 144-h significant differences ($p = 0.0003$) were observed between the Laser-irradiated and the control and between the Laser- and the LED-irradiated groups.

The highest degradation (45.49%) was observed in the Laser-irradiated group at 192-h. The result was statistically significant ($p < 0.0009$) in comparison to both control and LED-irradiated groups (39.37%). At the end of the experiment (240-h) the catalytic activity in the Laser-irradiated group was significantly higher than in

Fig. 6 Evaluation of the hydrolysis of RBBR dye by the bacterial consortium over time. (Reproduced from [8])



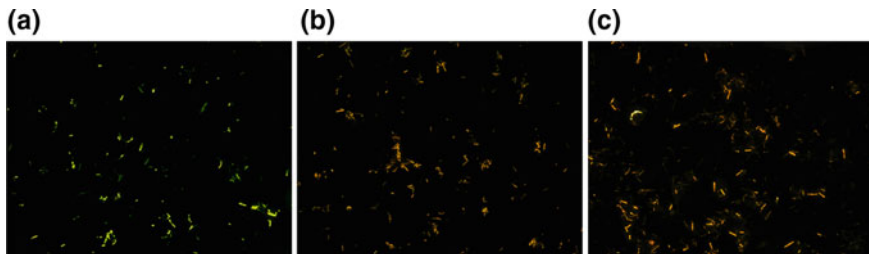


Fig. 7 Epifluorescence of the microbial consortium in different experimental settings after 48-h of incubation. (a) Control group showed green-marked cells, indicative of bifilamentary DNA. (b) Laser-irradiated group showed the cells orange-marked, indicative of monofilament nucleic acids. (c) LED-irradiated group showing the cell orange-marked indicative of monofilament nucleic acids. (Reproduced from [8])

the others study groups ($p < 0.0001$). LED-irradiated group showed significant difference ($p < 0.05$) when compared to the control group.

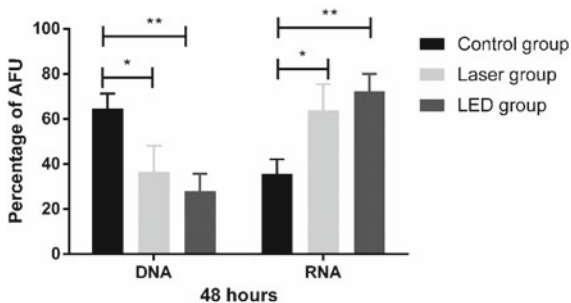
Nucleic acid analysis by epifluorescence at 48-h of incubation showed alteration of the green to orange staining pattern in the irradiated groups, demonstrating the increase of RNA production at this time (Fig. 7).

The quantification of the degradation of the RBBR at 48-h of incubation showed, in the control group, a higher percentage of double strand DNA (64.56%) and lower RNA (35.43%) per arbitrary fluorescence unit (AFU). In relation to the bifilamentary DNA there were significant differences in relation to the Laser- ($p < 0.0357$) and LED-irradiated ($p < 0.0049$) groups. In relation to single strand nucleic acid (RNA), the irradiated both groups showed a 28% increase in production when compared to the control group. There was no significant difference between the two irradiated groups (Fig. 8).

Effects produced by light on activating transcriptional and translational processes have been described [18, 48].

The metabolic pathways used in RBBR degradation are possibly different in the $\lambda 632 \text{ nm}$ and $\lambda 660 \text{ nm}$ irradiated groups. This fact can be explained by the initial

Fig. 8 Epifluorescence analysis of nucleic acids mono and bifilamentary in the experimental groups at the end of 48-h of RBBR hydrolysis. (Reproduced from [8])



** $p < 0.01$; * $p < 0.05$

difference of cells after the irradiation protocol, as well as by the direct or indirect photoactivation of extracellular metalloproteins.

In the LED group the hydrolysis of RBBR showed its degradation peak at 48-h, confirming the studies by Karu [26], which report the occurrence of photostimulatory effect, increase in the number of cells, up to 2 or 3 generations after irradiation causing increased metabolic activity and possibly direct activation of lignolytic metalloproteins.

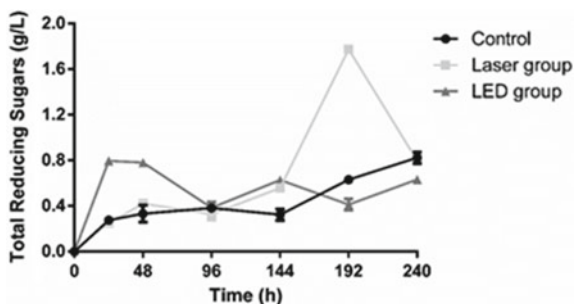
However, irradiation emitted at a wavelength of $\lambda 660$ nm may have induced activation of intracellular metalloproteins that actively participate in modulating extracellular enzymes or acting directly on lignolytic metalloproteins [32]. This last possibility is related to the absorption of photons by the prosthetic groups and/or aromatic peptide residues that may increase the catabolic capacity or assist in the maintenance of the three-dimensional conformation of the enzymes making them more resistant to the metabolic action denaturation [30].

The radiation emitted by light sources in the red spectrum can act as a trigger of enzymatic metabolic activation, i.e. as an oxidative substrate, providing the “activation” of redox mediators, metal prosthetic groups of lignolytic enzymes. On the other hand, during the excitation of the electronic states (primary reaction) a part of the energy is converted into heat, raising the temperature of the absorbing chromophores locally, causing structural changes and triggering biochemical activities, secondary reactions in the absence of light, such as enzyme activation by light [7].

3.6 Determination of Reducing Sugars

The TRS dosage from the hydrolysis of the residual biomass was quantified in each study group: Control, Laser and LED. A higher concentration of TRS was found in the LED-irradiated group up to 144-h of incubation, however the highest sugar production was found in the Laser-irradiated group after 192-h of incubation (Fig. 9).

Fig. 9 Quantification of reducing sugars over time



Significant differences between the LED-irradiated group and control were seen at 24 and 48-h intervals ($p < 0.05$) evidencing a higher hydrolytic performance of the LED-irradiated bacterial consortium within the first hours of incubation. After 144-h, the comparison between the Laser-irradiated group and the control group showed higher effectivity in the Laser-irradiated group that was found to be statistically significant ($p = 0.0104$) at 192-h. Despite no significant difference was seen when comparing the two irradiated groups at 240-h, both differed from the control ($p < 0.05$).

The greater bacterial proliferation observed in the LED group after the irradiation protocol is undoubtedly an advantage for the occurrence of greater initial biomass degradation, but by quantifying the TRS we can consider that different metabolic and enzymatic pathways are activated, as identified in the Laser-irradiated group that showed greater hydrolytic activity after 144-h of incubation.

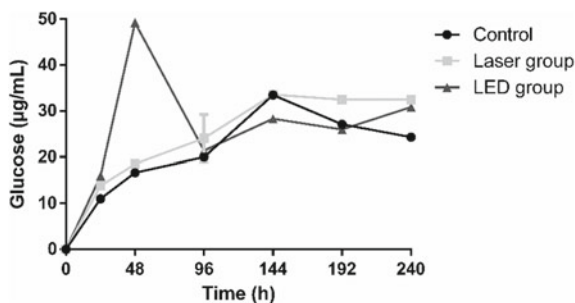
The observed fluctuation of biomass hydrolysis products over time can be explained by the concept of negative feedback. As the catabolic process of biomass occurs, reducing sugars accumulate which may inhibit cellulose degradation until they are used as a carbon source of the consortium. The degradation of biomass generates byproducts and products, such as glucose with easy microbial assimilation inhibiting substrate catabolism [34].

3.7 Quantification of Glucose

Glucose concentrations were determined by HPLC over 240-h for the purpose of evaluating cellulose degradation by the photostimulated bacterial consortium.

Analysis of glucose curves in the pretreated substrate showed a catabolic predominance of the group irradiated by LED in the first hours of the study, showing agreement with the results obtained in the determination of TRS. A fluctuation in glucose concentration over time was found, probably due to the microbial use of monosaccharide as a carbon source, confirming that found in the analysis of TRSs (Fig. 10) [34].

Fig. 10 Quantification of glucose over time



The group irradiated by LED showed its peak glucose concentration at 48-h, the same identified in the determination of TRS. A significant difference was seen ($p < 0.001$) when compared to both control and Laser-irradiated groups. After this period, the glucose consumption obtained by the LED-irradiated consortium was verified until 96-h. From 96-h onwards, the Laser-irradiated group presented a better performance with significant differences being observed ($p < 0.001$) at 192 and 240-h of incubation in comparison to the control group. The higher performance of cellulose hydrolysis was observed in the irradiated groups.

3.8 Microbial Quantification by Epifluorescence

The microbial quantifications performed during the biomass hydrolysis process, at the end of 48 and 144-h showed higher cell proliferation in the LED-irradiated group. This shows that after the irradiation (time zero) this group achieved higher microbial cell counts, “initiating in a privileged condition the process of hydrolysis of biomass”.

By treating the results obtained by the ANOVA statistical method, with the Tukey test, 95% confidence, it was possible to identify a significant difference ($p = 0.0005$) between the LED-irradiated group and the remaining two study groups (Fig. 11a). This difference was reduced in 144-h with a higher growth rate being observed in the Laser-irradiated group at this time. This is indicative of a higher relative cellular proliferation in the Laser-irradiated group at a later stage. On the other hand, significant difference ($p = 0.0327$) was seen when comparing the LED-irradiated and control groups (Fig. 11b).

The determined cell proliferation was aligned with the products of the cellulose hydrolysis quantified being indicative that the LED-irradiated group was the most effective, especially within 48-h.

In the Laser-irradiated group it was noticeable an increase in cell numbers up to the 3rd generation, a phenomenon already described by Karu [26] in

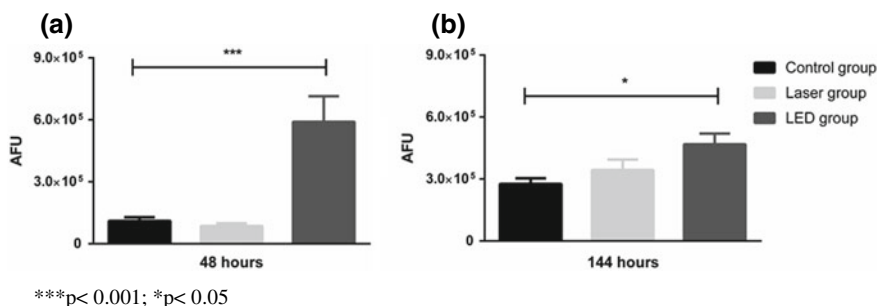


Fig. 11 Statistic analysis of the microbial quantification. (a) Microbial proliferation in 48-h of incubation; (b) Microbial proliferation in 144-h

Laser-irradiated *E. coli* cultures that, when incubated in nutrient medium, the increase in cell number occurred only for 2 or 3 generations after irradiation.

The action of LED light is broader than that of Laser, with the energy density being distributed over a larger electromagnetic band, enabling interaction with a larger number of specific photoreceptors [12].

Studies by Karu [22] showing that the microbial cytochrome has its maximum absorption peak at λ 633 nm. This fact may underlie the higher efficacy of LED (λ 632 nm) in increasing microbial proliferation.

Dobrowolski et al. [14] identified photostimulation as one of the new biotechnologies applicable to biomass degradation to obtain sustainable energy.

4 Conclusion

Pretreating coconut fiber with 5% NaOH improved the liberation and accessibility to the cellulose macromolecule. The production of products of the cellulose hydrolysis (TRS and glucose) was significantly higher in the photostimulated groups, being the most effective catabolism observed within the first 48-h in the LED group and after 144-h in the Laser group. Photostimulation, especially by LED, might be considered as a booster of the bioprocess at low cost.

References

1. Argüello, J.M., Raimunda, D., Padilla-Benavides, T.: Mechanisms of copper homeostasis in bacteria. *Front. Cell. Infect. Microbiol.* **3**, 1–14 (2013). <https://doi.org/10.3389/fcimb.2013.00073>
2. Bagnato, V.S., Mariyama, L.T.: Dosimetria na terapia com laser de baixa intensidade. *J. Bras. Laser.* **1**, 26–29 (2007)
3. Bakr, E.M.: A new software for measuring leaf area, and área damaged by *Tetranychus urticae* Koch. *JEN* **129**(3), 173–175 (2005). <https://doi.org/10.1111/j.1439-0418.2005.00948.x>
4. Bismarck, A., Mohanty, A.K., Aranberri-Askargorta, I., et al.: Surface characterization of natural fibers; surface properties and the water up-take behavior of modified sisal and coir fibers. *Green Chem.* **3**, 100–107 (2001)
5. Cantarel, B.L., Coutinho, P.M., Rancurel, C., Bernard, T., Lombard, V., Henrissat, B.: The carbohydrate-active enzymes database (CAZy): an expert resource for glycogenomics. *Nucleic Acids Res.* **37**, 233–238 (2009). <https://doi.org/10.1093/nar/gkn663>
6. Chen, W.H., Ye, S.C., Sheen, H.K.: Hydrolysis characteristics of sugarcane bagasse pretreated by dilute acid solution in a microwave irradiation environment. *Appl Energy* **93**, 237–244 (2012). <https://doi.org/10.1016/j.apenergy.2011.12.014>
7. Chavantes, M.A., et al.: Laser em Biomedicina Princípios e Práticas. São Paulo (2009)
8. Crugeira, P.J.L., Pinheiro, A.L.B., Almeida, P.F., et al.: Effects of photostimulation on the catabolic process of xenobiotics. *J. Photochem. Photobiol.* **191**, 38–43 (2019). <https://doi.org/10.1016/j.jphotobiol.2018.12.004>

9. Crueira, P.J.L., Almeida, P.F., Pinheiro, A.L.B., et al.: Photobiological effect of Laser or LED light in a thermophilic microbial consortium. *J. Photochem. Photobiol.* **181**, 115–121 (2018). <https://doi.org/10.1016/j.jphotobiol.2018.03.006>
10. Crueira, P.J.L., Santos, G.M.P., Chinalia, F.A., Almeida, P.F., Pinheiro, A.L.B.: In: Longo, L. (ed.) *Advances in Laserology: Selected Papers of Laser Florence 2015*, vol. 1, pp. 5–9. Medimond, Bologna. ISBN: 978-88-7587-732-3 (2016)
11. Cunha, E., Hatem, C., Barrick, D.: Natural and designed enzymes for cellulose degradation in advanced biofuels and bioproducts. In: Lee, W.J. (ed.) *Advanced Biofuels and Bioproducts*, pp. 339–367. Springer, NY (2013). <https://doi.org/10.1007/978-1-4614-3348-4>
12. Dacosta, R.S., Andersson, H., Wilson, B.C.: Molecular fluorescence excitation-emission matrices relevant to tissue spectroscopy. *Photochem. Photobiol.* **78**(4), 384–392 (2003). <https://doi.org/10.1562/0031-8655>
13. Dias, I.F.L., Siqueira, C.P.C.M., Durante, H.: Efeitos da luz em sistemas biológicos. *Ciências Exatas e Tecnológicas, Londrina* **30**(1), 33–40 (2009)
14. Dobrowolski, J.W., Bedla, D., Czech, T., et al.: Integrated innovative biotechnology for optimization of environmental bioprocesses and a green economy. In: Purohit, J.H., Kalia, V. C., Vaidya, A.N., Khardenavis, A.A. (eds.) *Optimization and Applicability of Bioprocesses*, pp. 27–72. Springer, Singapore (2017)
15. Gan, Q., Allen, S.J., Taylor, G.: Kinetic dynamics in heterogeneous enzymatic hydrolysis of cellulose: an overview, an experimental study and mathematical modelling. *Process Biochem.* **38**, 1003–1018 (2003). [https://doi.org/10.1016/S0032-9592\(02\)00220-0](https://doi.org/10.1016/S0032-9592(02)00220-0)
16. Glenn, J.K., Gold, M.H.: Decolorization of several polymeric dyes by the Lignin-degrading basidiomycete *Phanerochaete chrysosporium*. *Appl. Environ. Microbiol.* **45**(6), 1741–1747 (1983)
17. Gonçalves, F., Ruiz, A.H.A., Nogueira, C.C.: Comparison of delignified coconuts waste and cactus for fuel-ethanol production by the simultaneous and semi-simultaneous saccharification and fermentation strategies. *Fuel* **131**, 66–76 (2014). <https://doi.org/10.1016/j.fuel.2014.04.021>
18. Hemphill, J., Chou, C., Chin, J.W., Deiters, A.: Genetically encoded light-activated transcription for spatio-temporal control of gene expression and gene silencing in mammalian cells. *J. Am. Chem. Soc.* **135**, 13433–13439 (2013). <https://doi.org/10.1021/ja4051026>
19. International Conference on Harmonisation. ICH. International council on harmonization of technical requirements for registration of pharmaceuticals for human use. Guidance for industry: Q2B validation of analytical procedures: methodology. Geneva: ICH (1996)
20. Jensen, E.C.: Quantitative analysis of histological staining and fluorescence using imagej. *Anat. Rec.* **296**, 378–381 (2013). <https://doi.org/10.1002/ar.22641>
21. Karu, T.: Low-power laser therapy. In: Vodinh, T. (ed.) *Biomedical Photonics Handbook*, vol. 48, pp. 1–25. CRC Press, Boca Raton (2003)
22. Karu, T.: Primary and secondary mechanisms of action of visible to near-IR radiation on cells. *J. Photochem. Photobiol. B* **49**(1), 1–17 (1999). [https://doi.org/10.1016/S1011-1344\(98\)00219-X](https://doi.org/10.1016/S1011-1344(98)00219-X)
23. Karu, T.: *The Science of low power laser therapy*, edn 1, London (1998)
24. Karu, T.: Photobiological fundamentals of low-power laser therapy. *IEEE J. Quant. Electron.* **23**, 1703–1717 (1987). <https://doi.org/10.1109/JQE.1987.1073236>
25. Karu, T.I., Kolayakov, S.F.: Exact action spectra for cellular responses relevant to phototherapy. *Photomed. Laser Surg.* **23**(4), 355–361 (2005). <https://doi.org/10.1089/pho.2005.23.355>
26. Karu, T., Tiphlova, A.O., Letokhov, V.S., Lobko, V.V.: Stimulation of *E. coli* growth by laser and incoherent red light. *Nuovo Cimento D* **2**(4), 1138–1144 (1983)
27. Kasten, F.H.: Cytochemical studies with acridine orange and the influence of dye contaminants in the staining of nucleic acids. *Int. Rev. Cytol.* **21**, 141–202 (1967)
28. Kepner, R.L., Pratt, J.R.: Use of fluorochromes for direct enumeration of total bacteria in environmental samples: past and present. *Microbiol. Rev.* **58**(4), 603–613 (1994)

29. Kipshidze, N., Nikolaychi, V., Keelan, M.H., et al.: Low-power helium: neon laser irradiation enhances production of vascular endothelial growth factor and promotes growth of endothelial cells in vitro. *Lasers Surg. Med.* **28**(4), 355–364 (2001). <https://doi.org/10.1002/lsm.1062>
30. Kopka, B., Magerl, K., Savitsky, A., et al.: Electron transfer pathways in a light, oxygen, voltage (LOV) protein devoid of the photoactive cysteine. *Sci. Rep.* **7**, 1–16 (2017). <https://doi.org/10.1038/s41598-017-13420-1>
31. Latorre, M., Low, M., Gárate, E., et al.: Interplay between copper and zinc homeostasis through the transcriptional regulator Zur in *Enterococcus faecalis*. *Metallomics* **7**(7), 1137–1145 (2015). <https://doi.org/10.1039/c5mt00043b>
32. Liebert, A.D., Bicknell, B.T., Adams, R.D.: Protein conformational modulation by photons: a mechanism for laser treatment effects. *Med. Hypotheses* **82**, 275–281 (2014). <https://doi.org/10.1016/j.mehy.2013.12.009>
33. Lynd, L.R., Weimer, P.J., Zyl, W.H.V., Pretorius, I.S.: Microbial cellulose utilization: fundamentals and biotechnology. *Microbiol. Mol. Biol. Rev.* **66**(3), 506–577 (2002). <https://doi.org/10.1128/MMBR.66.3.506-577.2002>
34. Lynd, L.R., Laser, M.S., Bransby, D., et al.: How biotech can transform biofuels. *Nat. Biotechnol.* **26**(2), 169–172 (2008). <https://doi.org/10.1038/nbt0208-169>
35. Machado, K.M.G., Matheus, D.R., Bononi, V.L.R.: Ligninolytic enzymes production and remazol brilliant blue R decolorization by tropical brazilian basidiomycetes fungi. *Braz. J. Microbiol.* **36**, 246–252 (2005). <https://doi.org/10.1590/S1517-83822005000300008>
36. Menezes, C.R., Silva, I.S., Durrant, L.R.: Bagaço de cana: fonte para produção de enzimas lignocelulolíticas. *Estudos tecnológicos.* **5**(1), 68–78 (2009). <https://doi.org/10.4013/ete.2009.51.05>
37. Mood, S.H., Golfeshan, A.H., Tabatabaei, M., et al.: Lignocellulosic biomass to bioethanol, a comprehensive review with a focus on pretreatment. *Renew. Sustain. Energy Rev.* **27**, 77–93 (2013). <https://doi.org/10.1016/j.rser.2013.06.033>
38. Mwaikambo, L.Y., Ansell, M.P.: Chemical modification of hemp, sisal, jute and kapok fibers by alkalization. *J. Appl. Polym. Sci.* **84**(12), 2222–2234 (2002). <https://doi.org/10.1002/app.10460>
39. Okino, L.K., Machado, K.M.G., Fabris, C., et al.: Ligninolytic activity of tropical rainforest basidiomycetes. *World J. Microbiol. Biotechnol.* **16**, 889–893 (2000). <https://doi.org/10.1023/A:1008983616033>
40. O'neal, M.E., Landis, D.A., Isaacs, R.: An inexpensive, accurate method for measuring leaf area and defoliation through digital image analysis. *J. Econ. Entomol.* **95**(6), 1190–1194 (2002). <https://doi.org/10.1603/0022-0493-95.6.1190>
41. Pereira, P.R., Paula, J.B., Bahten, L.C.: Efeitos do Laser de baixa intensidade em cultura bacteriana in vitro e ferida infectada in vivo. *Revista do Colégio Brasileiro de Cirurgiões*, vol. 41, n 1, Rio de Janeiro (2014). <http://dx.doi.org/10.1590/S0100-69912014000100010>
42. Pedersen, M., Meyer, A.S.: Lignocellulose pretreatment severity—relating pH to biomatrix opening. *New Biotechnol.* **27**, 739–750 (2010). <https://doi.org/10.1016/j.nbt.2010.05.003>
43. Sukumaran, R.K., Singhanian, R.R., Mathew, G.M., et al.: Cellulase production using biomass feed stock and its application in lignocelluloses saccharification for bio-ethanol production. *Renew. Energy* **34**, 421–424 (2009). <https://doi.org/10.1016/j.renene.2008.05.008>
44. Teather, R.M., Wood, P.J.: Use of congo red-polysaccharide interactions in enumeration and characterization of cellulolytic bacteria from the bovine rumen. *Appl. Environ. Microbiol.* **43**, 777–780 (1982)
45. Ueda, M., Goto, T., Nakazawa, M., et al.: A novel cold-adapted cellulase complex from *Eisenia foetida*: characterization of a multienzyme complex with carboxymethylcellulose, β -glucosidase, β 1,3 glucanase and β -xylosidase. *Comp. Biochem. Physiol. Part B* **157**, 26–32 (2010). <https://doi.org/10.1016/j.cbpb.2010.04.014>
46. Van aken, B., Agthos, S.N.: Implications of manganese (III), oxalate, and oxygen in the degradation of nitroaromatic compounds by manganese peroxidase (MnP). *Adv. Appl. Microbiol.* **58**, 345–351 (2002). <https://doi.org/10.1007/s00253-001-0888-1>

47. Vasconcelos, N.M., Pinto, G.A.S., Aragão, F.A.S.: Determinação de Açúcares Redutores pelo Ácido 3,5-Dinitrosalicílico. *Bol. Pesquisa e Desenvolvimento* **88**, Embrapa, 10–22 (2013)
48. Wang, W., Wildes, C.P., Pattarabanjird, T., et al.: A light- and calcium-gated transcription factor for imaging and manipulating activated neurons. *Nat. Biotechnol.* **35**, 864–871 (2017). <https://doi.org/10.1038/nbt.3909>

High Coverage of H₂, CH₄, NH₃ and H₂O on (110) SnO₂ Nanotubes



Júnio César Fonseca Silva, José Divino dos Santos,
Jorge Luiz Costa Junior, Carlton Anthony Taft,
João Batista Lopes Martins and Elson Longo

Abstract We start with short review of inorganic nanotubes leading to gas sensors, which among others, can be important application of semiconductor oxides. We investigate the interaction of H₂, CH₄, NH₃ and H₂O gases at high internal and external coverage with the [(SnO₂)₁₈]₃ nanotube designed from the (110) plane of SnO₂ in the rutile structure. We have used the PM7 and DFT methods, and B3LYP as the functional with Huzinaga and LANL2DZ basis sets to determine adsorption energies, interatomic distances, LUMO, HOMO, energy gaps and hardness. DFT was used in order to investigate these systems formed by the high coverage of internal and external adsorbed gases on the nanotube. The adsorption energies, and inter/intra atomic distances indicate stronger interaction of the nanotube with the NH₃ and H₂O gases. Our calculated adsorption energies, interaction distances, energy gaps and sensitivity trends are in agreement with reported theoretical and experimental values. For these large systems (~ 1000 atoms), it is observed that the selected computational methods, despite their lower computational demand, can provide satisfactory physical/chemical insights. The intermolecular distances of the adsorbed gas suggest hydrogen bonding among the adsorbed gases of H₂O and NH₃ which helps to stabilize the interaction process.

Keywords Gas sensors · Ab initio · Interaction with gases · Inorganic nanotubes · DFT · Tin Dioxide · Simulation models

J. C. F. Silva · J. D. dos Santos · J. L. C. Junior
UEG, Br 153, 3105, CP 459, 75132-903, Anápolis, Goiás, Brazil

C. A. Taft
CBPF, Centro Brasileiro de Pesquisas Físicas, Rua Dr. Xavier Sigaud, 150, Rio de Janeiro
22290-180, Brazil

E. Longo
Universidade Estadual Paulista, UNESP, LIEC, Araraquara, SP CEP 14801-907, Brazil

J. B. L. Martins (✉)
Instituto de Química, UnB, Universidade de Brasília, Campus Universitário Darcy Ribeiro,
Brasília, DF 70910-900, Brazil
e-mail: Lopes@unb.br

1 Inorganic Nanotubes

It was observed [13], under the transmission electron microscope, unusual structures of carbon, wherein there was rolling and folding of graphene sheets, forming hollow structures, named nanotubes (concentric cylinders of graphene sheets). The hexagonal networks of carbon graphene sheets are stacked one above the other in the *c*-direction forming bulk graphite. Since then, intense research was done on carbon nanotubes (CNTs) which can be closed by caps via five-membered rings, or open-ended, which can be single-(SWNTs) or multi-walled (MWNTs). The nanotubes are classified as zigzag, chiral or armchair depending on the way one folds the graphene sheets, which affects the electrical conductivity [29, 45, 46, 49].

Nanotubes (NTs), in particular those of carbon, as well as C_{60} , during the last decades, have evolved to represent symbols of developing nanotechnology. Strong financial support followed their discovery which obtained great interest from the scientific and technological community. There has also been a great production of numerous nanosized devices and materials.

Since 1992, an important and increasing part in NT research can be attributed to inorganic NTs, indicating a large variety of promising chemistry and physical possibilities. The cylindrical geometry of a tubular crystal, which possesses a curved/strained lattice, can be considered counterpart of nanoparticle morphology/relaxed nanowire yielding technological challenges. Considering factors such as lattice defects/spontaneous minimization of free energy, there may be deviations requiring new visions in low-dimensional phenomena/self-assembly/miniaturization. Geometry/size effects in low-dimensional materials are of conceptual importance whereas NTs can be used as active/passive electronic components depending on their electric, magnetic and size-effect properties.

For almost 100 years inorganic 2d materials with layered structures have been investigated with research dedicated to natural occurring materials such as chrysotile, kaolinite, etc. Much of the work in the 20th century indicated discovery of high efficiency and stable photoelectrochemical/photovoltaic cells based on 2D-materials as well as charge density waves in layered metal dichalcogenides applied to research on structural and electrical properties at various temperatures. Subsequently, superconductivity was discovered in potassium intercalated MoS_2 and other compounds. The role of chemical and electrochemical intercalation of alkali metal ions in 2d-materials were recognized as important routes for storage of electrical energy which stimulated intensive research in the field of intercalation batteries. Nanoparticles (NP) decorated with Co and Ni atoms were important for industrial applications such as hydrodesulfurization [49].

Discovery of “massless” (Dirac) electrons was followed by graphene research and stimulated analogous research in exfoliated 2d-materials, i.e., graphene related materials (GRMs). With the advent of carbon nanotubes and C_{60} research, new paradigm for formation of fullerene-like and nanotube structures emerged. The reactive metal/non-metal rim atoms, only bonded partially, are the key stimulus for the formation of such hollow closed structures. From an energetic viewpoint it is

more favorable for the materials 2D monolayers to fold into closed seamless structures that compensates for elastic folding energy.

Over the last decades workers synthesized generic nanostructures from a number of 2d compounds. Theoretical-computer calculations were also used to determine structure/properties of nanotubes from 2d-compounds. Inorganic nanotubes were synthesized in pure/substantial phases indicating stability in the nano-size regime. Analyses of these nanostructures were provided by fingerprints via optical, electrical and mechanical measurements which clearly distinguished them from bulk phase whereas the large bending energy of these formations need to be compensated by multiple layers, favoring multiwall inorganic nanotubes instead of single wall nanostructures. These nanomaterials have important applications for solid lubricants, medical technologies, shock-resistant fabrics, with facile dispersion into various matrices as well as biocompatibility and low toxicity.

Considering difficulties of synthesizing nanotubes from 2d binary materials, the rich chemistry of 2d materials from quaternary and ternary compounds was also exploited. This included ternary layered compounds (MLCs) due to their relative stability/propensity to closed-cage hollow nanostructures. Combining the c-axis asymmetry (built-in) of layered compounds (Pauling's mechanism), as well as fine-tuning conditions for reaction to allow edge seaming of 2D nanocrystals (Kroto-Iijima-Tenne's mechanism), offered strong synthesis approaches for nanotubes from MLCs. During 50 s to 70 s of 20th century, tubular nanostructures of clay minerals (halloysite, imogolite) were investigated. These NT lengths can be up to few microns forming single-layers with diameters of less than 2 nm whereas their internal surface can be modified by replacing Si atoms. Functionalization is also possible with organic moieties yielding interesting properties which are attractive for industry such as applications in catalysis, gas separation and capture, composites, controlled drug delivery and others [28, 46].

In general, the driving force for formation of INT lies in intrinsic instability of layered two-dimensional crystalline compounds in planar form. The main energetic is from the dangling bonds (peripheral atoms). This can overcome elastic strain due to bending of layers and drive reaction to connect the layers. This is important in the case of crystalline layers of nano systems where dangling bonds are great part of total slab atoms yielding stable NTs below 200 nm diameters.

Chemical synthesis of nanotubes, regardless of 2d chemical composition, mostly involves high temperature reactions required to soften 2d layers and increase structural fluctuations, enhancing probability of seaming/folding of 2d layers and generating hollow closed nanotubes. These reactions often require good control of parameters necessary to control diffusion/nucleation rates.

The synthesis of core-shell nanotubes present new templating strategy to obtain INT from layered metals, difficult to obtain otherwise [15]. The 2d clusters (formed within hollow core on inner/outer surface of the outer nanotube perimeter fold forcible and seam eventually into core-shell nanotube structures. Core-shell nanotubular structures should be limited to hollow cores of 8 nm diameters. The templating strategy can be particularly useful for synthesis of nanotubes which possess relatively low melting points and are highly hygroscopic (difficult to work

with). Notable, single-wall boron nitride nanotubes (SW-BNNTs) were obtained inside SW carbon NTs using nano-templating reactions. The first catalytic-induced grown INT was done for SnS_2 tubes. Synthesis of GaS nanotubes, via solar ablation, has also been confirmed. There is a versatile chemical/physical stability methodology developed for the synthesis of nanotubes from different inorganic layered compounds. There is considerable room for systematic exploration of physical chemical properties of layered compound nanotubes [49].

Doping is another strategy for controlling/modifying properties of matrices, whereas, a demanding task in the process, is control of concentration and position of atoms incorporated into host lattice [21]. The synthesis of various metals oxides involves hydrothermal treatment of bulk layered compounds in the presence of organic templates at temperatures of 150–230 °C. The growth mode of titanate nanotubes is an example of synthetic mechanism of NTs in the absence of templates at low temperatures. VO_x , GaS, GaSe and other NTs can be synthesized in the presence of different organic templated due for example to the ability of aliphatic amines to self-assemble into wire-shaped aggregates whereas their hydrophobic nature serve as a nucleation surface that induces the precipitation of the layers in tubular structures. BN nanotubes can be synthesized from atomic layer deposition of precursors onto electrospun carbon nanofibers followed by high-temperature annealing. The synthesis of misfit sulphide INTs can occur in the gas phase after a chemical vapor transport mechanism. However, in general for these types of compounds a general growth pattern via chemical vapor transport can be delineated.

Extensive work has been done to investigate mechanical and tribological characteristics of INTs. Promising tribological results were also obtained for BNNTs opening pathway for various applications. Ultrahigh interlayer friction was found in multi-walled BNNTs with a difference of 22% regarding CNTs, attributed to the iconicity of bonds which provokes faceting between layers and consequently interlayer locking and stiffness. In general, faceting of NTs leads to stiffening/larger resistance towards torsion. Also, notable, these NTs reinforce silica, polymers and metallic matrices. Their elastic modulus is between 0.8 and 1.3 TPa, similar to that of CNTs, making BNNT good candidates to participate in composite materials [49].

Transition-metal dichalcogenide multiwall nanotubes indicate rich optical behavior. For example, $\text{Au}@\text{MoS}_2$ core-shell heterostructures exhibited coupling between MoS_2 excitonic transitions and Au nanoparticles leading to strong modulation of optical spectra in visible and enhanced Raman scattering as well as PL emission of these heterostructures. Electrical devices based on nanotubes (field effect transistors, electromechanical, etc) have increased considerable after solution of technological issues (contacts fabrication, selective etching, undercutting/suspending tubes, etc). Applications include FET transistors, electromechanical resonators, etc). WS_2 nanotubes indicated quasi-1D superconductivity characteristics whereas the critical temperature decreases with reducing diameter of the nanotubes. BNNTs indicate isolating character with band gaps independent of diameters, layers, chirality as well as optical properties (excitonic effects), luminescence characteristics, tunable deep-subwavelength light-trapping systems with potential applications as nano-sensors, nonlinear optics, etc.

Regarding stability, the proposed basis regarding growth mechanism of inorganic NTs is the lack of resistance to bending of crystal flakes (quasi-two-dimensional) including spontaneous (transition-metal dichalcogenides and misfit layered NT compounds), grown from vapor phase, forced geometrically from template growths, as coatings of nanofibers. Cylindric structure can occur spontaneously in some compounds as intrinsic property, from liquid/vapor phase, whereas ternary/quaternary compounds generally require template methods.

Rolling crystal flakes does not simple usually lead to NT longitudinal growth. Orientation relationships and stacking orders between two adjacent turns should be satisfied. Although the folded flake can be cylindrical, there can only be growth in radial direction when strain energy does not exceed energy gain (van der Waals interactions) between layers. There is usually weak interaction between layers whereas there is arbitrary interlayer distances. Regarding the driving forces for scrolling, they lie, first, in the asymmetry (intrinsic) of unit cell (along zone axis) and, secondly, thermal stress which exists at high temperatures and initiates the scrolling of layered sheets having at edges reduced interlayer forces. This causes local anisotropy of layers. Rolling-up/bending of thin layers for tubes is driven thermally. From kinetics, layered structure rolling can start by stress from structure/ of electrical nature resulting from asymmetry of layer. In soft chemistry, various layered materials (CeO₂, WO₃, SrAl₂O₄) were prepared within scroll-like morphology. The interaction between adjacent turns is strong when conditions are satisfied for stacking order. However, on bending, dislocations will be generated when van der Waals interaction energies between planes are smaller than covalent bonds. Otherwise, there should not be dislocations on bending.

Important methods for growing inorganic NTs include decomposition of precursor crystals, sulfurization, template growth, misfit rolling, precursor-assisted pyrolysis, electrospinning, self-assembly, precipitation, direct synthesis from vapor phase. In nontemplate growth from vapor phase, diffusion of adatoms on the inner/ outer phase can be important. A diffusion growth NTs process can yield so-called 'mama' tubes produced by decomposition/recrystallization of nanowires in the process of sulfurization at high temperatures.

The inorganic NTs can be found in various states of crystallinity and can be described as semi-single crystal lattices (translational periodicity along two directions) with curved third translation trajectory. Semi-single crystallinity is appropriate term for nonhelical/monohelical NTs having low density of defects. Polycrystallinity appears in structure of NT wall (composed of small thin crystal flakes). Polycrystallinity also appears in the radial direction as multi-helicity. Stability in cylindrical geometry found in narrow range of thermodynamical conditions such as gas flow, temperature and stoichiometry. Supposedly, nanotubes grow at a balance of two possible states far from equilibrium defined as minimum of total free energy. Nanotubes produced by diffusion suggest that cylindrical geometry can be intrinsic property of some compounds (under certain conditions).

Among the early workers, Rubio et al. [31] proved that single-wall BN nanotubes were stable when compared with unfolded analogs and subsequently workers showed that multiwall WS₂ (MoS₂) nanotubes of outer (4–7 layers) are

more stable than any conceivable unfolded structure with the same number of atoms. Single-wall phosphorus nanotubes were also shown to be more stable than their unfolded analogs.

The authors have investigated over the last decade the electronic structure, structural properties and stability of inorganic nanotubes such as GaAs, SiC, GaN, TiO₂, ZnO, MgF₂ [7, 9, 23, 33, 39–41] and have recently reported on the stability of GaAs [38].

The inorganic NTs can be classified as belonging to different families. We thus have transition-metal halogenic NTs, transition-metal chalcogenide NTs, transition-metal nitride NTs, transition-metal carbide NTs, oxide NTs, mixed-phase NTs, rare-earth fluoride NTs, metal-doped NTs, boron- and silicon-based NTs, metal NTs, metal-oxide NTs, organic NTs, inorganic NTs [29].

The very promising properties of the inorganic nanotubes makes them promising materials for usage in technological areas which includes photovoltaics, catalysis optoelectronics, energy harvesting, medicinal and sensors. There are also limitations attributed to difficulties associated with mass-production of good quality NTs, complex structures could hinder applications, possible unsolved atomic structures and difficulties in growth mechanism.

2 Metal Oxides

The semiconducting nature of many oxides makes them very attractive as materials for industrial/economical applications. Metal oxides, in particular, have a wide variety of chemical and electronic properties which makes them exciting for basic research as well as technological applications. These oxides, from more than five decades ago, in form of thick or thin films, have been used for monitoring presence of air pollutants. These materials span a good range of properties, such as electrical, from insulators (wide band-gap) to superconducting and metallic. Quasi-one-dimensional metal oxide nanostructures, such as nanotubes, indicate promising features including optoelectronics, gas sensing and energy applications [2, 29, 45].

Oxides, in chemical applications, can be used as support for dispersed metal catalysts as well as exhibit catalytical activity. The active phase of some metal oxide catalysts can be oxides and not the pure metal. Oxides also play an important role as solid state gas sensors. Numerous oxides show sensitivity to reducing and oxidizing gases by variation of their electrical properties whereas SnO₂ is one of the first considered/used for such applications. Since the 1950s (gas sensing effects first described for metal oxides) there has been an ongoing vision for developing cheap, robust, user-friendly gas sensing devices. Realizing this vision has been a challenging task for scientists working in the field (gas-sensors which are metal oxide-based).

Metal oxides including (ZnO, In₂O₃, SnO₂, CdO, MnO, NiO, WO₃, TiO₂, Cu₂O, VO₂, V₂O₅, among others) are attractive materials for studying gas response to reducing and oxidizing gases. More often, metal oxide materials, which are gas sensitive, are porous thick films. Molecular reaction/adsorption of molecules, in a

gas sensor, with pre-adsorbed chemical species, should result in changes of electrical conductivity. The fundamental process of solid-state gas sensing, is the reaction/adsorption of molecules at oxide surface making this a multidisciplinary problem, including surface science.

There is a net surface charge, due to the charge transfer from the oxide to the chemi- or ionosorbed molecule inducing a space charge region in the surface region of the oxide that balances the surfaces charges. One can describe this space charge region by energy levels, band bending or change of chemical potential (charge carrier). There is a shift in Fermi level which causes an accumulation/depletion of charge carriers (dependent on the sign of the surface charge). A change in charge carrier concentration, due to adsorbate induced band bending can be one of the causes for gas response in sensitive solid-state gas sensors. Notable, charged surface species, pre-adsorbed oxygen species can also play an outstanding role for detection of combustible gases.

A number of reactions of organic molecules at surfaces of oxides can be described by using the framework of surface base-acid reactions, i.e. the metal cations can be described as Lewis acid sites and the oxygen anions can act as Bronsted or Lewis base sites. Numerous Bronsted acids dissociate on oxide surfaces. This can result in dissociative adsorption, i.e. availability of pairs of undercoordinated metal cations as well as oxygens (surface base sites). Consequently, coordination environment of surface anions and cations can be critical surface characteristics than can be used to describe surface reactions of Bronsted acids. Metal oxides have found wide application as gas sensors (low-cost) with SnO₂, among preferred materials, for commercial devices due to the appealing characteristics.

2.1 Tin Dioxide (SnO₂)

The semiconducting nature of many oxides makes them very attractive as materials for industrial/economical applications. SnO₂ (stannic oxide) is a wide-bandgap n-type semiconductor with optical, electrical and electrochemical properties that are close to that of ZnO. This class of materials, combining optical transparency with high electrical conductivity, constitutes important components for optoelectronic applications. The properties of SnO₂ are similar to that of ZnO with a band gap in experiment which is wider than that of ZnO, and presents high exciton binding energy. SnO₂ has also attracted interest including transparent electrodes for liquid crystal displays, catalytic support material, chemoresistive portable gas sensors, solar cells, photocatalysis, optoelectronic devices and varistors. It has been studied for SO₂ oxidation into SO₃ as early as 1920s and starting from last century (middle) for CO oxidation, hydrocarbon combustion and other types of catalytic processes. Optical properties, lattice dynamics and electronic properties for SnO₂ have attracted both experimental and theoretical sustained investigations. As an n-type semiconductor, SnO₂ has been applied in gas sensing whereas their nanomaterials have been investigated for properties such as prominent selectivity, high chemical stability and fast-response speed [2, 8, 24, 34, 50, 51].

The valency of Sn and the coordinative environment are very dependent on surface preparation of surfaces of SnO₂. Consequently, structure-activity relations for oxide surfaces can vary by changing the preparation condition. For SnO₂ three stoichiometric surfaces can be prepared by high pressure oxygen annealing of plasma treatment, i.e. stoichiometric (1 × 1) surfaces; (1 × 1) surfaces with bridging oxygen rows removed and surfaces with all bridging oxygen removed; surfaces with all bridging atoms removed with additional in-plane oxygen vacancies. There is a similar situation for the (101) and (100) surfaces, stoichiometric and reduced SnO₂ surfaces with Sn⁴⁺ and Sn²⁺ surface cations.

It is possible to design for these surface adsorption sites having different steric and electronic properties, i.e. reduction of number of oxygen atoms which could have significant impact on surface reactivity. Molecular adsorption, for example, could be affected by transformation of valency of surface Sn species. Three could thus be change from valency IV to valency II as well as formation of fairly inactive 5s Sn lone pairs which all affect molecular absorption. It is possible to probe diverse surface reactivities for SnO₂ surface according to environmental coordination as well as state of charge of Sn cation.

Due to the close relationship between gas sensitivity of oxides and their surface chemical activity these two properties need to be considered together. The wide diversity of oxide materials is best demonstrated by the wide variety of self-assembled nanoscale materials discovered for tin oxides, including nanobelts, nanodiskettes, and nanotubes. The tin oxide nanostructures can have the bulk-like rutile structure and remain on the order of 10 × 100 nm in cross-section. Many of these tin oxide nanostructures can be formed from vapor phase transport growth. These kind of materials can be controlled selecting parameters, i.e. evaporation material (SnO₂ or SnO), gas flow, temperature, gas composition. The orthorhombic phase of SnO₂ is at high pressures the thermodynamic stable form. In addition to tin (IV) oxide the existence of tin(II) oxide illustrates the dual Sn valency which is crucial to understand surface properties of low index SnO₂ surfaces. Depending on oxygen chemical potential of the system (temperature/pressure) surfaces with either oxides of Sn(IV) or Sn(II) composition are thermodynamically possible. The variation (easy) of oxygen composition of SnO₂ surfaces is important for understanding important surface properties.

SnSO₂ combines electrical conductivity with optical transparency, as well as heterogeneous oxidation catalysis and solid state gas sensor properties, whereas same fundamental chemical/physical properties are responsible for suitability in different applications. The high charge carrier mobility and the dispersing conduction band are important ingredients making it good gas sensing material. The basic concept of gas sensing lies in acceptor/donor like adsorption of molecules which consequently induces band bending in the Debye layer of SnO₂ surface region resulting in changes in conductivity and consequently gas response. We note that details of adsorption/charge transfer of specific molecules require investigation.

3 Adsorption of Gases on SnO₂

Among the materials that are used as chemical sensors, nanomaterials are outstanding, indicating important properties such as electrical conductivity, high superficial area, wide interaction and diffusion of gas molecules as well as sensitivity and selectivity. The sensitivity depends on a number of factors including the presence of vacancies, adsorbed molecules on the surface, temperature and doping with metals [14, 16, 19, 20, 32].

SnO₂ is the compound currently studied for the development of gas sensors, beside other oxides, e.g. ZnO, CdO, MnO, NiO, WO₃, TiO₂, Cu₂O, VO₂, and V₂O₅, which play important role making possible the usage of a wide range of temperature for detection of various gases such as CH₄, NH₃, NO₂, CO, H₂S, H₂, H₂O, NH₃ [11, 22, 24, 26, 30].

H₂ has important characteristics making it necessary to develop devices that control and detect its presence [11, 18]. CH₄ is a gas that indicates different applications ranging from industrial to domestic use. Its identification and quantification are important due to inflammability, toxicity and explosive potential [17, 47, 48]. NH₃ is a pollutant, which is dangerous, and potential candidate for production of clean energy, whereas its speed of propagation in flame makes even at diluted concentrations it is highly toxic for amphibians and fishes. Real-time detection of NH₃ for control of power production plants, air quality monitoring in commercial airplanes as well as chemical industries is important line of research [25]. Understanding the role of water (moisture, humidity) on the sensing performance of SnO₂ nanosystems is of scientific/technological interest.

The importance of studying semiconductor compounds for the development of chemical sensors is due to their sensitivity in gas environments. Gas sensors could detect the presence of certain species via variation of conductance that occurs when the gas molecules interact with the surface causing a change in the charge concentration of the material [5].

The interest regarding the study of metallic oxides is focused mainly on understanding the interaction mechanisms between the gas and surface as well as the changes in the properties of electronic structure. Applications are growing in the development of gas nano sensors, i.e. chemical sensors capable of detecting toxic gases, which are generally used in areas ranging from monitoring gases liberated by automotive vehicles, to industrial control and even food safety [11, 18].

In the group of metallic oxides, SnO₂ is considered actually as one of the most promising materials for the fabrication of gas sensors, for fuels or pollutants. Compared to other oxides, they indicate advantages due to the easy synthesis, low fabrication cost, quick response time, quick recovery and response, long useful life and chemical stability [17, 18].

SnO₂ is an n-type semiconductor oxide, with 3.6 eV gap at 300 K, which is outstanding in relation to other group IV elements of the periodic table due to its optical and electrical properties, transparency, conductivity and chemical stability. Furthermore, the diverse geometries in which it can be found; e.g., nanotubes,

nanoparticles, nanowires, nanobelts, nanorods and nanoribbons, design a number of applications, such as chemical sensors, solar cells, lithium-ion battery, catalytic materials, fabrication of transparent conducting films and ultra-sensible gas sensors [5, 8, 25].

4 Simulation Models for Materials Study and Design

The properties of a N particle system can be determined from a $3N$ wave function (obeying Schrodinger equation (SE)), however, since the number of atoms in a macroscopic material is very large, we are faced with a non trivial problem to solve and approximations or alternative models have to be used. Hartree introduced single-electron wave functions/mean field approximations/ for electrons reducing problem to three-dimensional space. In the Born approximation the motion of nuclei is neglected. The Hartree-Fock (HF) method is obtained by introducing antisymmetric wave functions, the i th electron interacts with average electrostatic field. Electrons with same spin are kept apart by the exchange term. Quantum mechanics provide the theoretical foundation for materials and biomolecular study and design. Approximations to the theoretical framework leads to post-HF (CI, MRCI, CC, MCSCF, CASSCF, MBPT, LMP2, CCSD(T), semiempirical (Huckel, CNDO, INDO, NNDO, MNDO, AM1, OMx, PM7, RM1), density functional theory [4, 6, 43, 44].

Three approaches are used to solve the SE. In the quantum chemical ab initio method there is a convergent path to accurate solutions but are very expensive and restricted to smaller molecules. The orbitals can be represented by a linear combination of functions whereas Gaussian type orbitals are often used. In the density functional theory there is good performance/cost ratio with good accuracy for medium-sized molecules although there is not a systematic path for improvement. In the semiempirical quantum-chemical method, approximations and parametrizations are used allowing efficiency for modeling larger molecules with a limited accuracy.

For practical purposes, more simplifications can be used to solve the many-body problem, i.e. taking advantage of periodicity and symmetry of solids. Using the periodicity of the crystal structures the molecular orbitals can also be written in terms of plane waves whereas the periodicity of the lattice yields a potential (periodic) which is imposed on the density. Plane waves (independent of nuclei position, delocalized in space) can be used to expand orbitals using vectors in reciprocal space yielding simple forms for total electronic energy. These plane waves are actually lattice-symmetry-adapted three-dimensional Fourier decomposition of the orbitals. Core electrons can be removed explicitly (considered inert) or represented by smooth nodeless effective potentials.

Among early semiempirical approaches, the noninteractive Huckel methods use connectivity matrix of molecules to generate MOs. Among the first SCF approaches, the Pariser-Parr-Pople method was restricted to π electrons. Generalization to valence electrons was made by Pople yielding CNDO, INDO and NDDO

equations. Dewar introduced parameterization strategy via calibration against experimental data yielding INDO, MNDO, AM1, PM3. Extensions from sp to spd basis led to PM6 and PM7 covering the whole periodic table with applications to molecular as well as solid state properties.

Although it was known in the early 20s that the kinetic energy density in a uniform electron gas approximation, could lead to ground-state-energy functional, only in 1964 did Hohenberg and Kohn show that many-body properties are functions of ground-state densities. For an all-electron system a universal functional for the energy of the density can be defined whereas the global minimum for a given potential (external) would introduce the exact ground-state energy creating a new independent electron problem to substitute the many-body problem. The Kohn-Sham density functional theory (DFT) defines self-consistent equations to be solved for orbitals with densities defined as exact solutions of real systems. The cost/performance of DFT is better than that of WFT and is now very popular in physics/chemistry/biology. However, there are different approximations since the exchange-correlation potential is not well known. Improving description of dispersion/van der Waals interactions and reaction barriers are some of the challenges for DFT. The popular B3LYP is a hybrid functional model which is a linear combination of various approximations (HF, LDA, b88, LYP and VWN).

5 PM7 and DFT Calculations

Theoretical studies about SnO₂ were carried out at different levels of theory. It was investigated [47] the adsorption energy of tin oxide including characteristic gases dissolved in transformer oil using DFT level investigated the adsorption mechanism of Cu-doped SnO₂ (110) surface toward H₂ dissolved in power transformer [48]. Periodic hybrid-exchange density functional was used to study the adsorption of water on SnO₂ [27]. The electronic structure, density of states as well as effective electron and hole masses for SnO₂ was analyzed by ab initio electronic structure calculations [30]. The structural, electronic and optical properties of the rutile phase of SnO₂ were evaluated by Shao and co-workers [35–37].

We used the PM7 and DFT methods to describe the interaction of H₂, CH₄, NH₃ and H₂O gases with the SnO₂ nanotube, from the (110) rutile crystal plane. The semiempirical method was employed in the optimization processes due to the large size of the clusters and our previous experience with nanotubes such as GaAs, SiC, GaN, TiO₂, ZnO, MgF₂ [7, 9, 23, 33, 39–41]. DFT using the B3LYP functional with Huzinaga and LANL2DZ basis were used to investigate adsorption energies, interatomic distances, HOMO and LUMO orbitals, energy gaps and hardness with the objective of evaluating the sensor properties of the [(SnO₂)₁₈]₃ nanotube for different gases.

6 Computational Details

For the interaction of the gas molecules with the nanotube we adopted the single-walled nanotube SnO_2 with 324 atoms, identified as $[(\text{SnO}_2)_{18}]_3$ with a radius (r) of approximately 18.00 Å and height of 16.20 Å. This geometry adopted as basis for the interaction of the gases was generated via repetition of the 54 units of $(\text{SnO}_2)_2$ belonging to the (110) rutile crystal plane, whereas each unit is formed by 6 atoms, i.e. two Sn and four O atoms. The choice of (110) plane to generate the nanotube is attributed to the thermodynamic stability and the significant interest in relation to the study of its properties [3, 33]. Herewith, d_{Sn} represents the distance between the Sn atoms, and the structure of nanotube cluster was generated in the same way as in previous work [7, 9, 23, 33, 39–41].

In order to determine the reactivity of the $[(\text{SnO}_2)_{18}]_3$ nanotube, we made a saturation of the geometry approximating the gas molecules in both the external and internal areas of the nanotube. Taking into account the number of atoms of the nanostructure and number of gas molecules. In this manner, we made a simultaneous interaction of 162 molecules of H_2 , CH_4 , NH_3 , and H_2O . We placed 108 molecules in the external part and 54 molecules in the internal part in order to avoid steric effects due to the walls of the nanotube. The geometry of the $[(\text{SnO}_2)_{18}]_3$ nanotube was optimized using the Parametric Method 7 (PM7) Hamiltonian available in the MOPAC program [42]. This optimized structure was used as a basis for interaction with the gases. In each case, optimization of gas/nanotube geometry was made, using PM7 and maintaining fixed nanotube structure.

The calculation of the adsorption energy, HOMO, LUMO, energy gaps, hardness, were done using B3LYP hybrid functional, with the Huzinaga and LANL2DZ basis sets, available in Gaussian09 [10]. The adsorption energy (E_{ads}) of the molecules H_2 , CH_4 , NH_3 , H_2O was calculated using Eq. (1).

$$E_{\text{ads}} = \frac{E_{\text{cluster}} - (n_{\text{gas}} * E_{\text{gas}} + E_{\text{nanotube}} + E_{\text{inter}})}{n_{\text{gas}}} \quad (1)$$

Herewith, E_{cluster} is the nanotube energy optimized with gas molecules, n_{gas} is the number of gas molecules, E_{gas} is the energy of a molecule of isolated gas, E_{nanotube} is the energy of the pure nanotube and E_{inter} is the interaction energy of the gas molecules. For analysis of the contribution that the entire set of molecules make towards the total adsorption energy (E_{ads}), we calculated the interaction energy between the gas molecules (E_{inter}), keeping the position in which, they were oriented in relation to the nanotube, from optimized structure, using Eq. (2).

$$E_{\text{inter}} = E_{\text{gas-gas}} - 162 * E_{\text{gas-pure}} \quad (2)$$

E_{inter} represents the interaction energy between the gas molecules, whereas $E_{\text{gas-pure}}$ is the energy of an isolated molecule and $E_{\text{gas-gas}}$ is the energy of the 162 gas molecules with the same conformation obtained after the optimization process.

Information regarding the energy gap (E_g) and hardness (η) of the nanotube were obtained from the orbital energies (HOMO and LUMO) via Eqs. (3) and (4).

$$E_g = \text{HOMO} - \text{LUMO} \quad (3)$$

$$\eta = (\text{HOMO} - \text{LUMO})/2 \quad (4)$$

7 Results and Discussion

For the interaction of the gases we used as reference the $[(\text{SnO}_2)_{18}]_3$ nanotube. In this work, the cluster formed between the nanotube and the H₂ molecules, represented by $[(\text{SnO}_2)_{18}]_3\text{-H}_2$ is composed of 648 atoms, the $[(\text{SnO}_2)_{18}]_3\text{-CH}_4$ composed of 1134 atoms, the $[(\text{SnO}_2)_{18}]_3\text{-NH}_3$ has 972 atoms and the cluster formed by water molecules $[(\text{SnO}_2)_{18}]_3\text{-H}_2\text{O}$ has 810 atoms.

In Fig. 1 is depicted the interaction of H₂, CH₄, NH₃ and H₂O molecules with the $[(\text{SnO}_2)_{18}]_3$ nanotube after the optimization process. The density of these systems is approximately 0.013, 0.101, 0.107, and 0.113 g/cm³, for H₂, CH₄, NH₃ and H₂O molecules, respectively. It can be observed through frontal and lateral views that the gases used in this study adopt different orientations in space as well as distributions in relation to the external and internal surfaces of the nanotube. Two cases are produced, the first is the adsorption of CH₄ and H₂, apolar molecules, where the adsorbed molecules are spread inside the nanotube. The second is the

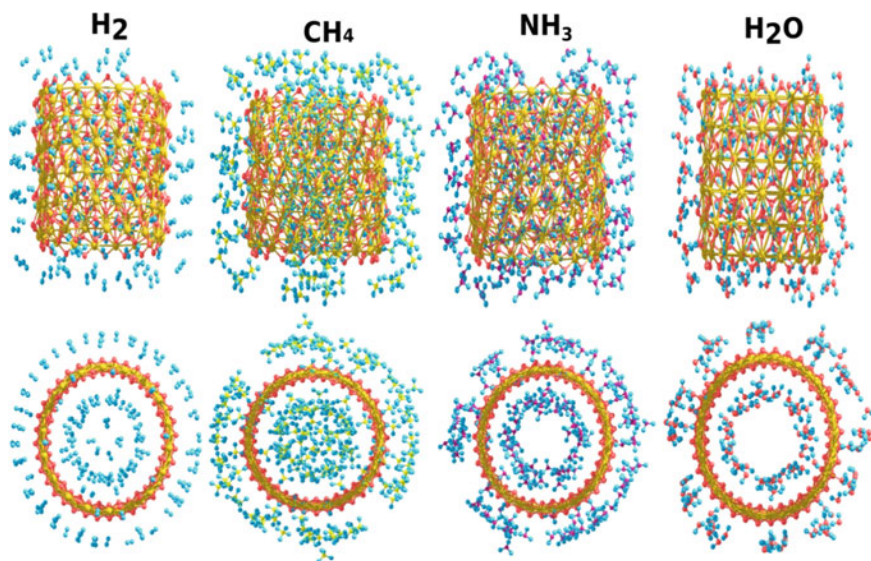


Fig. 1 Frontal and internal view of the interactions of the H₂, CH₄, NH₃ and H₂O molecules with the $[(\text{SnO}_2)_{18}]_3$ nanotube after optimization

adsorption of polar molecules NH_3 and H_2O , which have a well-structured adsorption due to the large effect of intermolecular forces.

Comparing the geometries of adsorbed gas molecules, we note that the O sites of the nanotubes tend to have smaller interaction distances with the gas molecules. The closest gases to the nanotube surface indicate the tendency to orient the H atoms in relation to the O atoms of the nanotube, suggesting that the interactions of these molecules occur preferentially between the H atoms of the gas molecules and oxygen atoms of the nanotube. These type of interactions for such gases with SnO_2 (110) have also been observed in the literature [11, 12, 35, 36, 50, 51].

The interaction of H_2 , CH_4 , NH_3 and H_2O gases is in agreement with SnO_2 (110) surface studies. It was indicated [35, 36] that the sensing mechanism of NH_3 in SnO_2 can be explained in terms of the interaction between ammonia molecules and oxygen species at the surface. It was concluded [47] that the adsorption energy of H_2 on oxygen site of SnO_2 is relatively higher than other sites. This is also consistent with other work [50]. It was reported by Hahn et al. [12] adsorption of H_2O molecules bent towards the surface, in a parallel associative adsorption configuration with the H atoms of H_2O closer to surface oxygen of SnO_2 [12, 32, 27]. It was also reported [47, 48] CH_4 adsorption at oxygen site.

Our calculations indicated that beginning with H_2 , it was noted that after the optimization process the molecules closest to the oxygen atoms of the surface were in the range of 2.20–2.80 Å, with these molecules separated by an average distance of 3.40 Å, that is related to the small adsorption energy.

For CH_4 it was observed that the closest gases are at distances between 3.20 and 3.60 Å whereas the C-H atoms have bonding distances of 1.08 Å. It was also found [47] exothermic adsorption of CH_4 at oxygen sites of SnO_2 (110) surface.

For the NH_3 molecule, the smallest distances occur between 1.80 and 2.20 Å having a bond length for N-H of 1.01 Å and intermolecular (N—H) and (N—N) distance of approximately 2.48 Å and 3.49 Å respectively. These values are characteristic of intramolecular hydrogen bonding. It was also found [35, 36] NH_3 adsorption close to surface oxygen of the SnO_2 surface, and indicated that the sensing mechanism of NH_3 is explained by the interaction of ammonia molecules with oxygen species at the SnO_2 surface.

The H_2O molecules closest to the nanotube are about 1.40–1.80 Å. Hahn et al. [12] found at high coverage H atoms at 1.42–1.88 Å from surface SnO_2 oxygens in agreement with our work. These small distances are related to the larger adsorption energies.

We obtain for H_2O molecules O-H bonding lengths of approximately 0.95 Å, whereas the intermolecular (O—O) and (O—H) distances are 2.70 Å and 1.74 Å respectively. These values are characteristic of intramolecular hydrogen bonding. Stabilized H_2O molecules on surface of SnO_2 (110) surface was also found [12]. The relative stability of water adsorption on SnO_2 (110) is governed largely by the strength of the chemisorption and hydrogen bonds at the surface of adsorbate-substrate system (Patel et al. 2017). Notwithstanding, it was indicated that an increasing number of H_2O molecules at the surface is stabilized by

Table 1 Adsorption energies (kJ/mol) for the H₂, CH₄, NH₃, and H₂O molecules

	B3LYP/Huzinaga	B3LYP/LANL2DZ
[(SnO ₂) ₁₈] ₃ -H ₂	-11.58	-0.96
[(SnO ₂) ₁₈] ₃ -CH ₄	-15.44	-0.96
[(SnO ₂) ₁₈] ₃ -NH ₃	-31.84	-4.82
[(SnO ₂) ₁₈] ₃ -H ₂ O	-38.59	-10.61

associative adsorption [1]. Therefore, our results are in agreement with the literature, where the small distance found suggests hydrogen bonding formation.

Table 1 shows the calculated adsorption energies using Eq. (1) for H₂, CH₄, NH₃ and H₂O on the [(SnO₂)₁₈]₃ nanotube for B3LYP with Huzinaga and LANL2DZ basis sets [10]. Comparing the adsorption energies from both basis sets it can be noted that the gases H₂, CH₄, NH₃, and H₂O indicate common tendency, i.e., an exothermic process. Using both basis sets indicate the same trend for the adsorption energies.

For the gases analyzed in Table 1, those that present polar character (NH₃ and H₂O) tend to be more strongly adsorbed on the surface of the nanotube, whereas the apolar molecules indicate a weaker interaction. In this form, it may be established that for the molecules analyzed the nanotube [(SnO₂)₁₈]₃ indicate more sensitivity for the NH₃ and H₂O molecules whereas H₂O is more strongly adsorbed. Another important point is that LANL2DZ basis set underestimates the adsorption energies. However, doing geometry optimization of these large systems, would be prohibitive, using more expensive ab initio methods.

Our calculations of adsorption energies yields good agreement with reported values in the literature. For H₂ we obtain using Huzinaga basis an adsorption energy of -11.58 kJ/mol on SnO₂ (110) in agreement with the exothermic adsorption for H₂ on oxygen site of SnO₂ surface [48], with values of -5.21 and -12.15 kJ/mol [47, 48]. Our results suggest a lower selectivity for H₂ molecules in relation to NH₃ and H₂O.

Thermoconductive and conductometric sensors rely on change of conductance (or resistance) of the sensing layer of semiconducting oxides. Using, for example, fuel in automotive applications with no emission of greenhouse gases to the environment becomes of utmost importance to monitor hydrogen leak, which could be hazardous and explosive. Our results herewith confirm the reported experimental disadvantage of this type of sensor, due to their weaker selectivity towards H₂, i.e., potential cross-sensitivity to other gases. Doping has been suggested to increase the selectivity to H₂ [16, 17].

For the adsorption energy of CH₄ on SnO₂ (110) we obtain -15.44 kJ/mol in agreement with the theoretical calculations of -13.51 kJ/mol [47, 48]. Our calculations indicate NH₃ adsorption on (110) SnO₂ of -31.84 kJ/mol. TPD spectra indicated that ammonia adsorption was unimolecular with typical energy of -66.57 kJ/mol [36]. For adsorption of H₂O on SnO₂ (110) our calculations yield -38.59 kJ/mol, and in the literature, theoretical calculations gives -94.55 kJ/mol for H₂O adsorption on SnO₂ surface [12].

Molecular adsorption of water molecules is more effective than the other gases such as NH_3 . For SnO_2 under normal humidity conditions high surface coverage of water is expected as indicated by our calculations. Water concentrations in typical humid environments can be exceedingly high whereas water coverage can partially block adsorption of other gases resulting in serious problems for experimental applications. Design of devices should consider these effects or use external filters to minimize effects.

In summary, our calculations suggest the presence of intermolecular interactions among the H_2O and among the NH_3 molecules, suggesting occurrence of hydrogen bonding. These molecules have these potential properties as well as average distances between molecules of H_2O (2.70 Å) and NH_3 (3.48 Å) which are within the range in which this type of interaction occurs. In recent studies, the intermolecular distance for the H_2O molecules was computed at 2.49 Å [36], compared with 2.70 Å in this work, suggesting the presence of intermolecular attractive interactions. To complement this information it was observed that the adsorption of H_2O occurs preferentially via chemisorption whereas the stabilization is mainly done via hydrogen bonding [27]. Our work is in agreement with these results.

We thus note that the $[(\text{SnO}_2)_{18}]_3$ nanotube indicates larger sensitivity to H_2O and NH_3 where the adsorption of these gases are favored by the formation of hydrogen bonding. For these systems we observe smaller distances between the gas and surface of the nanotube. The sensitivity should be larger for $\text{H}_2\text{O} > \text{NH}_3 > \text{CH}_4 > \text{H}_2$ from the results of adsorption energies and interatomic distances.

We also investigated the molecular orbitals (HOMO, LUMO), and thus energy gaps and hardness before and after gas adsorption on the nanotubes $[(\text{SnO}_2)_{18}]_3$. These calculations are shown in Table 2.

The interaction of the nanotube with the gases occurs with a variation of energies of HOMO and LUMO molecular orbitals compared to the pristine structure. Therefore, the clusters formed between the nanotubes $[(\text{SnO}_2)_{18}]_3$ and the gases indicate for most cases substantial reduction of band gaps compared to the pristine structure.

The HOMO levels are lowered and the LUMO levels are raised resulting in reduction of the band gaps. In this manner, the clusters formed between the nanotubes $[(\text{SnO}_2)_{18}]_3$ and the gases indicate for H_2O and NH_3 largest reduction of band gaps compared to the pristine clusters. For the hardness (η) the trends

Table 2 HOMO (eV), LUMO (eV), gap (eV), and hardness (eV)

	B3LYP/Huzinaga				B3LYP/LANL2DZ			
	HOMO	LUMO	Gap	Hardness	HOMO	LUMO	Gap	Hardness
Pristine	-6.88	-3.48	3.40	-1.70	-12.68	-1.96	10.72	-5.36
H_2	-7.18	-3.92	3.25	-1.63	-12.74	-2.04	10.69	-5.35
CH_4	-7.24	-3.84	3.43	-1.70	-12.44	-2.03	10.40	-5.20
NH_3	-5.18	-4.97	0.21	-0.10	-7.88	-4.28	3.60	-1.8
H_2O	-6.10	-5.92	0.18	-0.09	-9.68	-5.37	4.31	-2.15

observed suggests that the adsorption of H₂O and NH₃ molecules favors the formation of a structure with less hardness in relation to the other gases.

The B3LYP/Huzinaga calculated band gap 3.40 eV for pure SnO₂ is in agreement with the experimental value of 3.6 eV. The large reduction of the band gap after adsorption (Table 2) supports usage of these nanotubes for measuring sensitivity via conductivity measurements.

8 Conclusion

Nanotube [(SnO₂)₁₈]₃ generated from (110) rutile, such as unit cell parameters, with the support of programming algorithms served as internal and external surfaces to study adsorbed H₂, CH₄, NH₃ and H₂O gases. These systems were subsequently investigated using density functional theory at the B3LYP functional with the LANL2DZ and Huzinaga basis sets to explore the interaction of gases with the nanotubes.

The results obtained suggests that all the gases investigated tend to interact with the oxygen atoms present at the surface of the nanotube [(SnO₂)₁₈]₃ via the hydrogen atoms of the gases. The calculated adsorption energies of the gases on the nanotubes indicated for all clusters an exothermic process. Our calculated adsorption energies and inter/intra atomic values are in reasonable agreement with some experimental and theoretical values.

The polar molecules NH₃ and H₂O indicate largest adsorption energies and stronger interaction with the surface of the nanotube and should indicate large nano gas-sensor sensitivity. For the polar molecules our calculations suggest the presence of attractive intermolecular forces such as hydrogen bonding. The interatomic distances in the polar molecules support hydrogen bonding in these gases.

The larger adsorption energies and smaller interaction distances of gases with surfaces suggest a descending order (H₂O, NH₃, CH₄, H₂) for strength of interaction and sensitivity of the nanotube for gases.

Our calculated band gap (E_g) is in agreement with experimental values. The NH₃ and H₂O gases promote relatively large changes in HOMO and LUMO yielding substantial modifications of HOMO and LUMO.

Adsorbate induced band modification has the potential to induce strong electrical conductivity changes and trigger gas response signals. Our results indicate for NH₃ and H₂O that upon adsorption there is increase of the HOMO levels and a lowering of the LUMO levels with a subsequent substantial reduction of the energy gaps which would increase the conductivity and trigger appropriate gas response signals.

Acknowledgements We acknowledge financial support from CNPq.

References

1. Bandura, A.V., Kubicki, J.D., Sofo, J.O.: Comparisons of multilayer H₂O adsorption on the (110) surfaces of TiO₂ and SnO₂ as calculated with density functional theory. *J. Phys. Chem. B* **112**, 11616–11624 (2008)
2. Batzill, M., Diebold, U.: The surface and materials science of tin oxide. *Prog. Surf. Sci.* **79**, 47–154 (2005)
3. Beltrán, A., Andrés, J., Sambrano, J.R., Longo, E.: Density functional theory study on the structural and electronic properties of low index rutile surfaces for TiO₂/SnO₂/TiO₂ and SnO₂/TiO₂/SnO₂ composite systems. *J. Phys. Chem. A* **112**, 8943–8952 (2008)
4. Canchaya, J.G.S., Furtado, N.C., Taft, C.A.: An overview of fuel cells and simulation models: review on solid oxide fuel cells. *Curr. Phys. Chem.* **5**, 223–252 (2015)
5. Chen, J.S., Lou, X.W.: SnO₂-based nanomaterials: synthesis and application in lithium-ion batteries. *Small* **9**, 1877–1893 (2013)
6. Cohen, A.J., Mori-Sánchez, P., Yang, W.: *Chem. Rev.* **112**, 289–320 (2012)
7. Costa, R.J., Martins, J.B.L., Longo, E., Taft, C.A., Santos, J.D.: Methodology to obtain and study geometries of single and double wall silicon carbide nanotubes. *Curr. Phys. Chem.* **6**, 60–80 (2016)
8. Das, S., Jayaraman, V.: SnO₂: a comprehensive review on structures and gas sensors. *Prog. Mater. Sci.* **66**, 112–255 (2014)
9. Ferreira, M.D., Santos, J.D., Taft, C.A., Longo, E., Martins, J.B.L.: Single walled MgF₂ nanotubes. *Comput. Mater. Sci.* **46**, 233–238 (2009)
10. Frisch, M.J., Trucks, G.W., Schlegel, H.B., Scuseria, G.E., Robb, M.A., Cheeseman, J.R., Scalmani, G., Barone, V., Mennucci, B., Petersson, G.A., Nakatsuji, H., Caricato, M., Li, X., Hratchian, H.P., Izmaylov, A.F., Bloino, J., Zheng, G., Sonnenberg, J.L., Hada, M., Ehara, M., Toyota, K., Fukuda, R., Hasegawa, J., Ishida, M., Nakajima, T., Honda, Y., Kitao, O., Nakai, H., Vreven, T., Montgomery, J.A., Peralta, J.E., Ogliaro, F., Bearpark, M., Heyd, J.J., Brothers, E., Kudin, K.N., Staroverov, V.N., Kobayashi, R., Normand, J., Raghavachari, K., Rendell, A., Burant, J.C., Iyengar, S.S., Tomasi, J., Cossi, M., Rega, N., Millam, J.M., Klene, M., Knox, J.E., Cross, J.B., Bakken, V., Adamo, C., Jaramillo, J., Gomperts, R., Stratmann, R.E., Yazyev, O., Austin, A.J., Cammi, R., Pomelli, C., Ochterski, J.W., Martin, R.L., Morokuma, K., Zakrzewski, V.G., Voth, G.A., Salvador, P., Dannenberg, J.J., Dapprich, S., Daniels, A.D., Farkas, O., Foresman, J.B., Ortiz, J.V., Cioslowski, J., Fox, D.J.: *Gaussian 09, Revision A.02* (2009)
11. Hahn, S.H., Bårsan, N., Weimar, U., Ejakov, S.G., Visser, J.H., Soltis, R.E.: CO sensing with SnO₂ thick film sensors: role of oxygen and water vapour. *Thin Solid Films* **436**, 17–24 (2003)
12. Hahn, K.R., Tricoli, A., Santarossa, G., Vargas, A., Baiker, A.: First principles analysis of H₂O adsorption on the (110) surfaces of SnO₂, TiO₂ and their solid solutions. *Langmuir* **28**, 1646–1656 (2012)
13. Iijima, S.: Helical nanotubes of graphitic carbon. *Nature* **354**, 58–68 (1991)
14. Inyawilert, K., Wisitorsaat, A., Tuantranont, A., Phanichphant, S., Liewhiran, C.: Ultra-sensitive and highly selective H₂ sensors based on FSP-made Rh-substituted SnO₂ sensing films. *Sens. Actuators B: Chem.* **240**, 1141–1152 (2017)
15. Kreizman, R., Hong, S.Y., Sloan, J., Popovitz-Biro, R., Albu-Yaron, A., Ballesteros, T.B., Davis, B.G., Green, M.L.H., Tenne, R.: Core-shell PbI₂@WS₂ inorganic nanotubes from capillary wetting. *Angew. Chem. Int.* **48**, 1230 (2009)
16. Lavanya, N., Sekar, C., Fazio, E., Neri, F., Leonardi, S.G., Neri, G.: Development of a selective hydrogen leak sensor based on chemically doped SnO₂ for automotive applications. *Int. J. Hydrogen Energy* **42**, 10645–10655 (2017)
17. Liewhiran, C., Tamaekong, N., Tuantranont, A., Wisitorsaat, A., Phanichphant, S.: The effect of Pt nanoparticles loading on H₂ sensing properties of flame-spray-made SnO₂ sensing films. *Mater. Chem. Phys.* **147**, 661–672 (2014)

18. Li, C., Lv, M., Zuo, J., Huang, X.: SnO₂ highly sensitive CO gas sensor based on quasi-molecular-imprinting mechanism design. *Sensors* **15**, 3789–8000 (2015)
19. Liu, L., Song, P., Wei, Q., Zhong, X., Yang, Z., Wang, Q.: Synthesis of porous SnO₂ hexagon nanosheets loaded with Au nanoparticles for high performance gas sensors. *Mater. Lett.* **201**, 211–215 (2017)
20. Liu, Y., Huang, J., Yang, J., Wang, S.: Pt nanoparticles functionalized 3D SnO₂ nanoflowers for gas sensor application. *Solid State Electron.* **130**, 20–27 (2017)
21. Marques, T.M.F., Luz-Lima, C., Sacilloti, M., Fujisawa, K., Perea-Lopez, N., Terrones, M., Silva, E.N., Ferreira, O.P., Viana, B.C.: Photoluminescence enhancement of titanate nanotubes by insertion of rare earth ions in their interlayer spaces. *J. Nanomater.* **2**, 3809807 (2017)
22. Minh Nguyet, Q.T., Van Duy, N., Phuong, N.T., Trung, N.N., Hung, C.M., Hoa, N.D., Van Hieu, N.: Superior enhancement of NO₂ gas response using n-p-n transition of carbon nanotubes/SnO₂ nanowires heterojunctions. *Sens. Actuators B: Chem.* **238**, 1120–1127 (2017)
23. Moraes, E., Martins, J.B.L., Moraes, E.D.E., Gargano, R., José, R., Politi, S., Castro, E.A.S.: A theoretical investigation of ZnO nanotubes: size and diameter. *Curr. Phys. Chem.* **3**, 400–407 (2013)
24. Mizsei, J.: Forty years of adventure with semiconductor gas sensors. *Procedia Eng.* **168**, 221–226 (2016)
25. Nejati-Moghadam, L., Bafghi-Karimabad, A.E., Salavati-Niasari, M., Safardoust, H.: Synthesis and characterization of SnO₂ nanostructures prepared by a facile precipitation method. *J. Nanostruct.* **5**, 47–53 (2015)
26. Noei, M.: Probing the electronic sensitivity of BN and carbon nanotubes to carbonyl sulfide: theoretical study. *J. Mol. Liq.* **224**, 757–762 (2016)
27. Patel, M., Sanches, F.F., Mallia, G., Harrison, N.M.: A quantum mechanical study of water adsorption on the (110) surfaces of rutile SnO₂ and TiO₂: investigating the effects of intermolecular interactions using hybrid-exchange density functional theory. *Phys. Chem. Chem. Phys.* **16**, 21002–21015 (2014)
28. Panchakaria, L.S., Popovitz-Biro, L., Houben, L., Dunin-Borkowski, R.E., Tenne, R.: Lanthanide-based functional misfit-layered nanotubes. *Angew. Chem. Int. Ed.* **126**, 7040–7044 (2014)
29. Remskar, M.: Inorganic nanotubes beyond cylindrical matter. *Nanosci. Nanotechnol.* **1**, 237–253 (2011)
30. Rödl, C., Schleife, A.: Photoemission spectra and effective masses of n- and p-type oxide semiconductors from first principles: ZnO, CdO, SnO₂, MnO, and NiO. *Phys. Status Solidi Appl. Mater. Sci.* **211**, 74–81 (2014)
31. Rubio, A., Corkill, J.L., Cohen, M.L.: Theory of graphitic boron nitride nanotubes. *Phys. Rev. B* **49**, 5081–5084 (1994)
32. Santarossa, G., Hahn, K., Baiker, A.: Free energy and electronic properties of water adsorption on the SnO₂(110) surface. *Langmuir* **29**, 5487–5499 (2013)
33. Santos, J.D., Ferreira, M.D., Martins, J.B.L., Taft, C.A., Longo, E.: Computational studies of [(SnO₂)_n]_m nanotubes. *Curr. Phys. Chem.* **3**, 451–476 (2013)
34. Sensato, F.R., Custódio, R., Calatayud, M., Beltrán, A., Andrés, J., Sambrano, J.R., Longo, E.: Periodic study on the structural and electronic properties of bulk, oxidized and reduced SnO₂(110) surfaces and the interaction with O₂. *Surf. Sci.* **511**, 408–420 (2002)
35. Shao, F., Hernandez-Ramirez, F., Prades, J.D., Morante, J.R., Lopez, N.: Assessment and modeling of NH₃-SnO₂ interactions using individual nanowires. *Procedia Eng.* **47**, 293–297 (2012)
36. Shao, F., Hoffmann, M.W.G., Prades, J.D., Morante, J.R., López, N., Hernández-Ramírez, F.: Interaction mechanisms of ammonia and Tin oxide: a combined analysis using single nanowire devices and DFT calculations. *J. Phys. Chem. C* **117**, 3520–3526 (2013)
37. Shao, T.T., Zhang, F.C., Zhang, W.H.: First principles studies on structural, electronic and optical properties of SnO₂. *Adv. Mater. Res.* **900**, 203–208 (2014)

38. Silva, J.C.F., dos Santos, J.D., Taft, C.A., Martins, J.B.L., Longo, E.: Stability of rolled-up GaAs nanotubes. *J. Mol. Model.* **23**, 204–210 (2017)
39. Silva, J.C.F., dos Santos, J.D., Taft, C.A., Longo, E.: Theoretical study of gallium arsenide nanotubes built from crystal plane (110). *Curr. Phys. Chem.* **6**, 85–95 (2016)
40. Silva, G.O., Santos, J.D., Martins, J.B.L., Taft, C.A., Longo, E.: Simulations and analysis of titanium dioxide nanotubes (rutile (110) and anatase (101)). *Curr. Phys. Chem.* **6**, 10–21 (2016)
41. Sodré, J.M., Longo, E., Taft, C.A., Martins, J.B.L., dos Santos, J.D.: Electronic structure of GaN nanotubes. *C. R. Chim.* **20**, 190–196 (2017)
42. Stewart, J.J.P.: MOPAC2012 (2012)
43. Taft, C.A., Canchaya, J.G.S.: Review on simulation models for materials and biomolecular study and design, In: Longo, E., La Porta, F.A. (eds). *Recent Advances in Complex Functional Materials: From Design to Applications*, pp. 373–408. Springer, Cham (2017)
44. Taft, C.A., da Silva, C.H.T.P. (eds.): *New Developments in Medicinal Chemistry*. Chemistry, vol. 2. Bentham Science (UAE), UAE (2014)
45. Tenne, R., Olabi, A.G.: Inorganic nanotube materials. *Mater. Sci. Mater. Eng.* **3**, 1–3 (2015)
46. Visic, B., Panchakaria, L.S., Tenne, R.: Inorganic nanotubes and fullerene-like nanoparticles at the crossroads between solid-state chemistry and nanotechnology. *J. Am. Chem. Soc.* **139**, 12865–12878 (2017)
47. Wang, Q., Hao, J., Huang, H., Zhou, M., Zhou, Q.: Adsorption energy and charge transfer of tin oxide to characteristic gases dissolved in transformer oil. In: *ICHVE 2016 – 2016 IEEE International Conference on High Voltage Engineering and Application*, pp 1–3 (2016)
48. Wang, F., Fan, J., Sun, Q., Jiang, Q., Chen, S., Zhou, W.: Adsorption mechanism of Cu-doped SnO₂ (110) surface toward H₂ dissolved in power transformer. *J. Nanomater.* 3087491 (2016)
49. Weber, M., Latsunsky, I., Coy, E., Miele, P., Cornu, D., Bechelany, M.: Novel and facile route for the synthesis of tunable boron nitride nanotubes combining atomic layer deposition and annealing processes for water purification. *Adv. Mater. Interfaces* **5**, 1800056 (2018)
50. Wen, Z., Tian-Mo, L., Xiao-Fei, L.: Hydrogen sensing properties of low-index surfaces of SnO₂ from first-principles. *Phys. B: Condens. Matter* **405**, 3458–3462 (2010)
51. Wu, Q., Li, J., Sun, S.: Nano SnO₂ gas sensors. *Curr. Nanosci.* **6**, 525–538 (2010)

Surface Engineering in Alloyed CdSe/CdSe_xCdS_{1-x}/CdS Core-Shell Colloidal Quantum Dots for Enhanced Optoelectronic Applications



Sidney A. Lourenço, Anielle Christine A. Silva, Victor M. Zelaya, Carlos E. Cava, Gabriel D. A. Rocha, Marco A. T. da Silva, José L. Duarte, Flavio Franchello, Felipe de Almeida La Porta and Noelio O. Dantas

Abstract The optical properties of nanocrystal (NC) colloidal quantum dots (QDs) largely depend on their size and shape. These properties can be easily tuned by temperature and the concentration of ligands during their synthesis to generate QD particles with different optical features. However, the enormous complexity of these QD systems limits the understanding of the critical impact of passivating ligands and surface defects on their optical properties. In the present study, we systematically investigated the effect of different strategies on the optical properties of alloyed CdSe/CdSe_xCdS_{1-x}/CdS core shell (CS) QDs capped with several ligands, including trioctylphosphine (TOP) and hexadecylamine (HDA). The CdSe covered with TOP ligands were produced using the hot injection method, whereas CdSe covered with HDA ligands were produced by the exchange reaction method from as-synthesized samples. The CdSe/CdSe_xCdS_{1-x}/CdS QDs samples were prepared from a simple chemical route that involved an increasing concentration of thioglycerol to grow the CdS shell on the top of the as-precipitated CdSe core with different ligands in a controlled manner. Two emission peaks (at approximately 595 and 635 nm) were observed for three different surface coverages beyond the exciton recombination. These emissions were mainly attributed to the surface localized state

S. A. Lourenço · C. E. Cava · G. D. A. Rocha · M. A. T. da Silva
Laboratório de Dispositivos Fotônicos e Materiais Nanoestruturados, Universidade Tecnológica Federal do Paraná – UTFPR, 86036-370 Londrina, PR, Brazil

A. C. A. Silva · N. O. Dantas
Laboratório de Novos Materiais Isolantes e Semicondutores (LNMIS),
Instituto de Física, Universidade Federal de Uberlândia, CP 593, 38400-902
Uberlândia, MG, Brazil

V. M. Zelaya · J. L. Duarte · F. Franchello
Departamento de Física, Universidade Estadual de Londrina, 86051-970 Londrina, PR, Brazil

F. A. La Porta (✉)
Laboratório de Nanotecnologia e Química Computacional, Universidade Tecnológica Federal do Paraná – UTFPR, 86036-370 Londrina, PR, Brazil
e-mail: felipelaporta@utfpr.edu.br

in all samples and the charge carrier transfer between the exciton and surface states. Our findings revealed an increase in the photoluminescence (PL) intensity with increasing temperature for the alloyed CdSe/CdSe_xCdS_{1-x}/CdS CS QDs. The findings also revealed a continuous red-shift in the optical absorption peak, as a function of ligand concentration. This suggests a strong electronic coupling between the surface localized states and delocalized excitonic alloyed CdSe/CdSe_xCdS_{1-x}/CdS CS QDs. However, such colloidal nanocrystals (NCs) need to be further investigated to gain an in-depth understanding of their nanoscale behavior as well as explore their huge potential for several emerging technological applications.

Keywords Colloidal quantum dots · Surface states · Passivating ligands · Charge carrier transfer

1 Introduction

In recent decades, nanocrystalline colloidal quantum dots (QDs) have emerged as a promising option for several optoelectronic technologies, owing to the continuous tunability of their electronic and optical properties, which, in turn, results from the ease of alteration of their size, shape, and surface [1–6]. Moreover, novel physical properties of QDs have demonstrated potential applications in different technologic areas, such as light-emitting devices (LEDs) [7–10], low-threshold lasers [11], optical amplifiers [12], photovoltaic devices [13–16] field-effect transistors (FETs) [17], biological labels [18–20], antibacterial control [21], and cancer therapy [22].

The extremely small size of QDs, in the range of nanoscale, confers the property of a high surface-to-volume ratio to them, such that majority of the atoms are located on the surface [23]. The atoms at the surface of QDs can generate diverse surface defect sites (e.g., dangling bonds) that act as trap sites for charged carriers. For example, the trapping of charge carriers at the surface defect sites results in an exciton delocalization that may theoretically cause non-radiative recombination pathways with low photoluminescence quantum yields (PLQYs) [5, 24, 25]. These adverse effects may decrease the performance of several optoelectronic devices based on QDs systems [5, 24, 25]. Thus, intense efforts are being made to understand the role of charge carrier trapping at surface defects in physical processes such as carrier relaxation and recombination dynamics, which can provide great opportunities in the field of nanotechnology. However, knowledge related to surface trapping is still limited with several questions remaining unanswered [26–28].

A frequent method used to reduce the number of defect states and dangling bonds present on the nanocrystal (NC) surface, and thus the exciton delocalization, is the direct passivation of the QD surface with organic ligands, such as hexadecylamine (HDA), thioglycolic acid (TGA), mercaptopropionic acid (MPA), and trioctylphosphine (TOP). It has been demonstrated that the passivation of QD systems with organic capping agents strongly influences the electron and hole transport from QDs. Thus, passivation acts as a critical factor for the delivery of

photoexcited carriers in photovoltaic devices [5, 29–31], and in biomedical and clinical imaging applications [20, 32, 33].

Another method used to reduce surface trap states is the synthesis of core/shell structures. Here, two materials with different energy band gaps are used, thus creating a potential barrier at the semiconductor interface. This can increase the confinement potential of the charge carriers in the core region. That is, if the core QD gets encapsulated by another system of interest as a shell with a wide band gap, this generates two possibilities of alignment to confine either both (type-I) or a single (quasi-type-II) charge carrier to the core and minimize their surface overlap [34, 35]. However, the abrupt boundary between the core and shell materials can also induce strain owing to lattice mismatch and hence introduce new trap states at the core/shell interface [36]. Thus, recently it was proposed that a thick-graded shell could be considered as an efficient strategy to cover the semiconductor QD core and provide better enhancement of fluorescence with a significant impact on light-emitting devices (e.g., PLQY greater than 90% has been observed for such systems) [35, 36]. This particular structure has been shown to reduce Auger recombination, a non-radiative process, in semiconductor QDs, particularly the graded alloyed CdSe/CdSe_xCdS_{1-x}/CdS system; delocalize the electron into the *thick* CdS shell; reduce its overlap with the core-localized hole; [37] and improve the multi-exciton performance of the complex QD [30, 38, 39]. Hence, different strategies based on *inorganic or organic* surface cover have been employed to improve the PLQY, as well as, facilitate the charge energy transfer process in QD-based optical devices [27, 40, 41].

Thus, in the present work, we used steady-state photoluminescence (PL) as a function of temperature and time-resolved PL to study the electronic coupling between surfaces and excitonic states in three sets of CdSe QDs covered with different ligands. The set-1 (as-synthesized QDs) consisted of five samples of CdSe QDs with the size ranging from 2.16 to 2.46 nm and covered by TOP molecules. The set-2 consisted of five samples of CdSe QDs (the same of set-1) but functionalized, after exchange reaction process, with HDA molecules. The set-3, was proposed by Silva et al. [42], and resulted from a novel methodology to grow core-shell quantum dots (CS-QDs), using an aqueous-based wet chemistry protocol, in which the thickness of the CdS shell could be controlled by tuning the thio-glycerol concentration. This system, with a *thin*-graded CdSe_xS_{1-x}/CdS shell, which allowed surface states from 1-thioglycerol residual ligand to strongly couple with confined states, led to a strong quenching of excitonic recombination.

2 Samples and Experimental Section

The synthesis of CS-QDs was carried out by using an aqueous-based wet chemistry protocol. The proposed chemical route uses increasing concentration of 1-thioglycerol, a bifunctional linker molecule, (**HS-CH₂CH₂COOH**) to grow the CdS shell on top of the as-precipitated CdSe core in a controllable way. It was found

that lower concentration of 1-thioglycerol (3 mmol) added into the reaction medium limits the growth of the CdSe core, and to higher concentration (5–11 mmol) of 1-thioglycerol (TG) promotes the growth of CdS shell on top of the CdSe core with an increase from 0.50 to 1.25 nm in shell thickness. More details about synthesis methodology can be obtained in the following Ref. [42]. Briefly, CdSe QDs and CdSe/CdSe_xS_{1-x}/CdS CS-QDs were grown in aqueous solutions at room temperature using the following steps. Selenium powder (mmol, 99.999%), and a strong reduction agent, sodium Borohydride NaBH₄ (mmol, 98%), were dispersed in ultrapure water (20 mL) in a three-neck flask under argon flow. After that, 2 mmol of Cd(ClO₄)₂ · 6H₂O and x mmol of 1-thioglycerol were mixed in ultrapure water, and the pH was adjusted to 11 by adding 0.1 M NaOH. Then, cadmium- and selenium-containing solutions were mixed under magnetic stirring in a three-neck flask under argon flow at room temperature for 30 min. CdSe QDs and CdSe/CdSe_xS_{1-x}/CdS CS-QDs were precipitated with ethanol and centrifuged four times at 6000 rpm for 10 min. In this procedure, a thin intermediary alloy of CdSe_xS_{1-x} is formed on CdSe QDs. The confirmation of the CdSe_xS_{1-x} alloying, while using 1-thioglycerol, was supported by the change of the bandwidth value related to the LO branch with respect to bulk CdSe ($\Delta\omega = 118 \text{ cm}^{-1}$) [42]. The resulting nanopowders were dried in vacuum (mechanical pump) at room temperature and further dispersed in ultrapure water. With increasing TG concentration, five samples were obtained, which were analyzed in this paper. They were labeled as: CdSe:1TG, this sample has CdSe core with average size of 1.9 nm; CdSe:5TG, CdSe/CdS core-shell with core size of 1.7 nm and shell size of 0.514 nm; CdSe:7TG, CdSe/CdS core-shell with core size of 1.7 nm and shell size of 0.665 nm; CdSe:9TG, CdSe/CdS core-shell with core size of 1.7 nm and shell size of 0.869 nm and CdSe:11TG, CdSe/CdS core-shell with core size of 1.7 nm and shell size of 0.975 nm. Sizes of the core and shell were obtained from the analysis of optical absorption, X-ray diffraction and Raman techniques [42].

After synthesis, evaporation processes were initialized to obtain CS-QDs in a powder form. Photoluminescence (PL) was measured with a 405 nm ($\sim 3.06 \text{ eV}$) continuous wave laser focused at $\sim 200 \mu\text{m}$ and with low excitation power, 1.34 mW. These powders were put into a circular cavity of copper-cold finger closed by a quartz window. Luminescence spectra were collected from 15 to 300 K using a USB4000 Ocean Optics spectrometer equipped with a Toshiba TCD1304AP 3648-element linear CCD-array detector and a GG 435 nm long-wave-pass filter. Sample temperatures were controlled by a closed-cycle He cryostat (Janis, model CCS—150) equipped with a Lake Shore temperature controller (Model 805). Photoluminescence decay time measurements were performed by a Picoquant system (Fluotime 200), with a time-correlated single photon counting (TCSPC) technique, equipped with a MCP detector. For this measurement, samples were diluted in 23 mg/mL of deionized water. A picosecond pulsed diode laser (at 440 nm), 2.5 MHz repetition rate, 55 ps pulse, was used as excitation source.

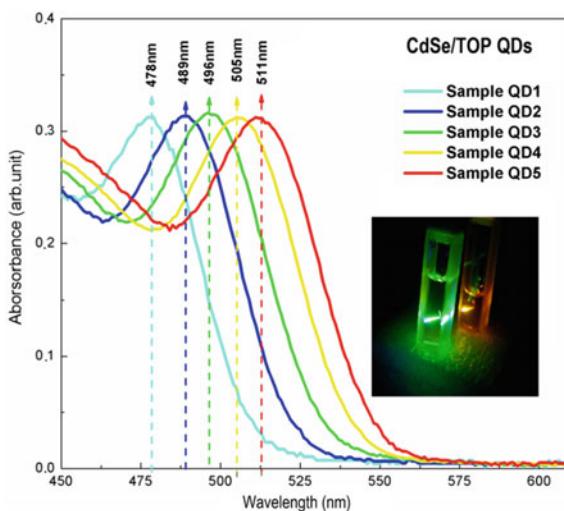
For comparison purpose, it was synthesized five as-synthesized CdSe, covered with TOP molecules, with different size and other five CdSe QDs surface-stabilized

with HDA, both diluted in toluene. The CdSe QDs were synthesized via the hot injection method [43]. It begins with the preparation of two solutions: a solution of TOP-Se and other of Cd. In the preparation of the first solution, 30 mg of Se and 5.0 ml of octadecene were added in a 10 ml flask on inert atmosphere (Ar gas). Then, it is adding 0.40 mL of TOP via a syringe. In this stage, the solution temperature was mantled at 100 °C. For the second solution, it was added 13 mg of CdO, 0.60 mL oleic acid (OA) and 10 ml of octadecene in a three-necked flask. This process should also be in an inert atmosphere to prevent the O₂ released to not oxidize the TOP when the first solution is injected. When the temperature of the second solution reaches 225 °C, it is injected TOP-Se within the Cd precursor solution to induce nucleation and nanoparticle growth. In this route synthesis, the TOP cap is grown on CdSe surface, which protect the CdSe QD. All reagents used in the synthesis procedure were purchased from Sigma-Aldrich (Brazil) and used without further purification.

Figure 1 illustrates the optical absorption spectra of aliquots of the CdSe QDs dissolved in toluene obtained for different times after injected TOP-Se solution into Cd precursor solution. The redshift of the absorption peak of the samples obtained at different time evidence the quantum size effect. The inset of Fig. 1 shows picture of two samples with different QDs size, in a cuvet, illuminated with 475 nm laser. Here, ones can observe the Tyndall effect in colloidal CdSe QDs. The QD size was obtained by using the optical absorption peak, related to first excitonic absorption, and the relation proposed by Willian et al. [44]. Thus, the QDs diameters of set-1, were: 2.16 nm (QD1); 2.26 nm (QD2); 2.31 nm (QD3); 2.40 nm (QD4) and 2.46 nm (QD5).

The ligand exchange reaction method is a common procedure used to functionalize QDs structures [6, 45]. In such a procedure, the native ligands, TOP in our

Fig. 1 It shows the optical absorption of set-1, CdSe QDs surface stabilized with TOP molecules. The quantum size effect leads to a red-shift of the optical absorption. Inset shows the Tyndall effect in colloidal CdSe QDs. A 405 nm laser pass thought two solution of toluene contained CdSe QDs of different size



case, are exchanged with less sterically demanding ligands that ideally still impart solution dispersibility and passivate the QDs surface [6, 45].

3 Results and Discussion

3.1 Steady-State and Time-Resolved Photoluminescence

Figure 2a shows the normalized PL spectra, at ordinary room temperature, of CdSe as-synthesized QDs (Set-1) with different sizes. The spectra show the excitonic transition, peaks of high intensity with the spectral position shifted from 490 to 551 nm as a function of QD size, and a broad PL peak at a higher wavelength, around 650 nm. Figure 2b shows the PL spectra of QDs in a lower scale. Here, it is observed that the broad PL peak originates from four transitions, identified as E_1 , E_2 , E_1^s , and E_2^s . The emission at 708 and 768 nm is attributed to well-known deep defect levels, labeled as (E_1) and (E_2), respectively, for CdSe QDs. Deep defect levels in CdSe QDs with a hexagonal wurtzite structure, a common phase for these materials [46], are related to two energetically different *divacancy* defects, V_{Cd} and V_{Se} , associated with the absence of Cd^{2+} and Se^{2-} ions in the crystalline QD structure [47]. One *divacancy* is oriented along the hexagonal c -axis of the wurtzite CdSe structure and assigned to trap E_1 , whereas the other is oriented along the basal

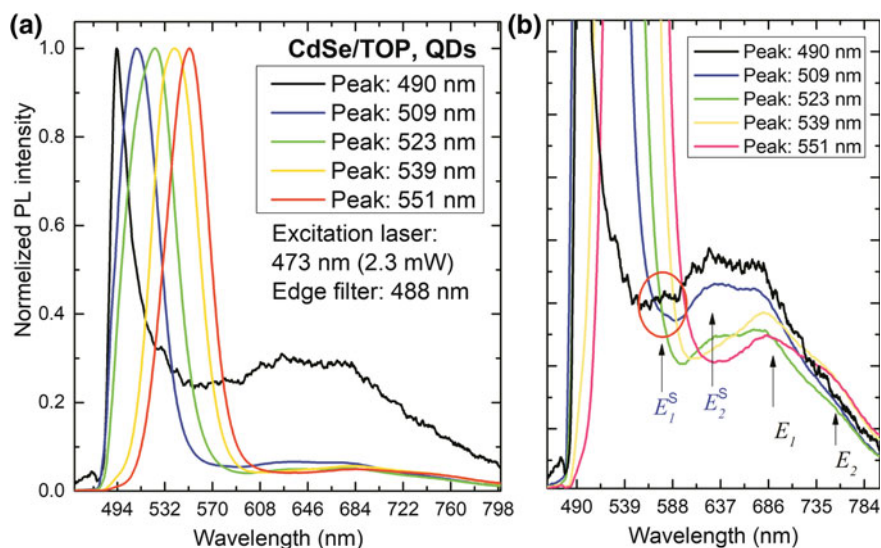


Fig. 2 (Color online) **a** Normalized PL spectra of CdSe/TOP QDs (set-1—*as-synthesized* CdSe QDs) with different size obtained at room temperature. **b** Shows a lower scale PL spectra where can be seen four PL peak: vacancy states labelled as E_1 and E_2 , and surface states labelled as E_1^s and E_2^s

Cd–Se bond directions and assigned to trap E_2 [47]. In addition to the *divacancy* defect, if CdSe QDs are not properly surface passivated, surface trap states could originate from surface defects [28, 48]. Moreover, traps states can originate from an incomplete surface passivation, oxidation of the surface by exposure to air, or by reaction with reducing/oxidizing ligands present in the synthesis reaction [28, 48].

Surface defects have been known for decades to play an important role in QDs, mainly in the energy transfer between the NCs and their environment [29, 49]. For example, in SiO₂ NCs, two stable broad luminescence peaks in the visible electromagnetic spectra of the silica NCs have been reported in the past years [50–53]. The stable light emission band at approximately 1.79 eV (692 nm) in the silica NCs was assigned to the non-bridging oxygen hole center –NBOHC–(≡Si–O^{*}) at the surface of NCs [50, 52]. The –OH groups on the SiO₂ NCs surface are other green emission fonts in SiO₂ NCs [51, 53]. The surface states are likely to trap electrons and/or holes, thus inducing recombinations. Therefore, we believe that emissions at 595 nm (E_1^s) and at 635 nm (E_2^s), shown in Fig. 2b, originated from a localized state due to surface defects in CdSe QDs, one shallow state (S_1) and the other deep state (S_2) present near the QD conduction and valence bands (VBs), respectively. As the size of the QD decreases, E_1 and E_2 transitions become less intense than E_1^s and E_2^s transitions, resulting in the broad PL peaks, around 650 nm, to present a blueshift.

Figure 3a shows PL spectra of the CdSe, with different QD sizes, after exchange reaction with HDA ligand. CdSe surface cover with HDA creates new QD surface states [45, 54]. The PL signal of the surface states, relative to excitonic transition, shows higher intensity after surface functionalization and results in a blueshift of the broad PL peak, as shown in Fig. 2a. As the size of the QD decreases, it becomes possible to detect the surface state clearly. Thus, we can tune the localized state from conduction band (for large QD size) to semiconductor band-gap energy (for smaller QD size). In this simple model, the energy of the surface state is static. For QD with larger size and emission at 610 nm, the surface states are into the conduction band (CB) and luminescence is only from excitonic transitions. As the QD size is reduced, the surface states are tuned to the band-gap and their luminescence is more intense, as shown in Fig. 3a. It is important to note that the broad PL peak from surface states is of the same spectral wavelength before and after the surface exchange reaction. Similar results were observed recently in CdTe QDs functionalized with MPA ligand [55]. However, the PL intensity of the surface states improved with relation to the PL intensity of the core-only QDs (surface capped with TOP). This could be interpreted as additional surface states (midgap states) from HDA ligands that improve surface states recombination.

Figure 3b presents normalized PL spectra of CS-QDs as a function of thio-glycerol concentration at 16 K. In all spectra, five recombinations can be observed, namely E_1 , E_2 , E_1^s , E_2^s , and the excitonic transition at 487 nm. Here, the excitonic transition has a strong PL quenching effect relative to the PL signal of surface states. In comparison with other two previously discussed QDs sets, new surface (E_1^s , and E_2^s) and vacancy (E_1 and E_2) recombinations occur at the sample wavelength as CdSe/TOP QDs (Fig. 2) and CdSe/HDA QDs (Fig. 3a), respectively.

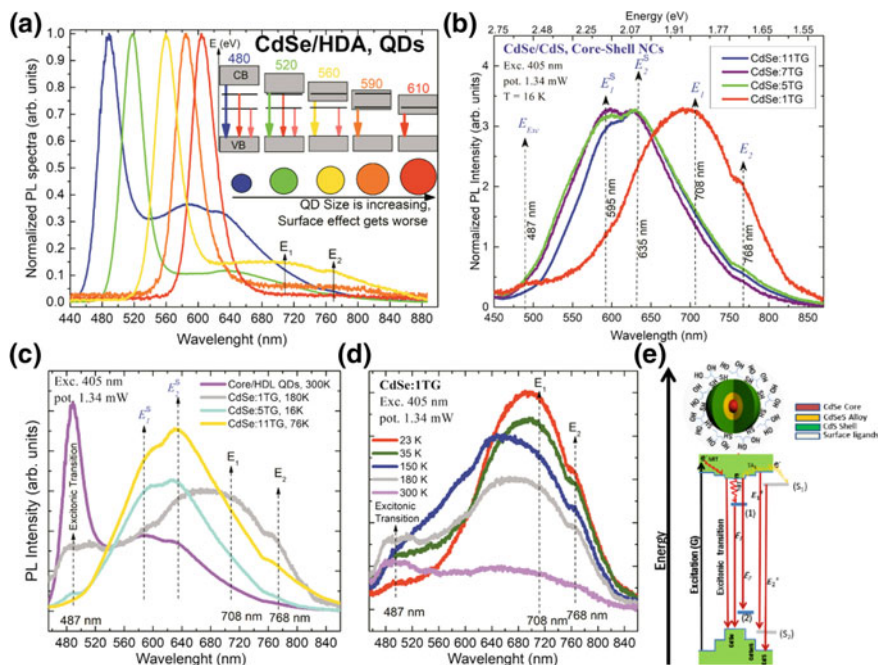


Fig. 3 Normalized PL spectra of the HDA functionalized CdSe QDs (a), at room temperature, and TG-capped CdSe/CdS QDs at 16 K with increasing thioglycerol concentrations (b). Their recombination aspects are depicted, where the emissions from both the QD (E_{exc}) and the vacancy states (E_1) and (E_2) are clearly identified. It also shows the characteristic emission from surface states at 595 and 635 nm, E_1^s and E_2^s , respectively. a Shows electronic surface states tuned from CB to band gap of QDs as QDs size reduction (QDs in quantum confinement regime). c Shows, for comparison, the PL spectra of the CdSe HDA functionalized and CS-CdSe with different TG concentration and d shows PL spectra of the CdSe:1TG for different temperatures. e Depicts the radiative and non-radiative process in the Core-Shell QDs capped with TG. The red arrows represent the non-radiative transitions (NRT) and green arrows represent the thermal activation (TA) processes involving surface states

The sample with 1 TG concentration presents strong vacancy PL intensity (Fig. 3b). As the TG concentration increases, the PL intensity of the surface states increases. Thus, CdSe/CdS structures with 1 TG concentration could have more selenium vacancies than CdSe/CdSe, with a higher TG concentration. CdSe:1TG displays residual dangle-bonds at the QD surface owing to partially capped surface, where virtual QD surface levels (shallow carrier traps) can emit radiations. With the increase in the TG concentration, the PL spectrum of the TG-capped CdSe QDs exhibited significant changes, as subsequent layers of CdS and TG were added to the QD surface. Figure 3c proposes the comparison method of the PL spectra of CdSe/HDA, in magenta, and CS-QDs with different TG concentrations. This figure shows that the surface and vacancy transitions are in the same energy position as CS-QDs or CdSe/HDA. Figure 3d presents the PL spectra of CdSe:1TG at different

temperatures. Here, one can observe the energy transfer from deeper localized states to surface states, depicting energy proximity between the states.

It is known that thiols form an important class of capping molecules; they have a polar head group and are used to synthesize water-soluble QDs. However, thiols can also introduce surface electronic levels (trap states) on the QD surface [5]. For instance, a recent work demonstrated that the hybridization intensity of the surface states in the QD systems could control energy position of VB and CB [28, 54]. Previous studies on CdSe QDs capped with the thiol group have particularly observed two radiative emission peaks near 600 and 640 nm, which are characteristic of CdSe QDs smaller than 3.6 nm [32, 55]. Also, emissions with a peak at around 595 nm (labeled in this article by E_1^s) and at 635 nm (by E_2^s), as shown in Figs. 2b, 3a, b, originated from localized surface states from different groups with similar energies. Thus, an increase in the concentration of thiols may, in principle, lead to an increase in the localized surface states, and subsequently an improvement in the surface PL signal, as shown in Fig. 3b.

When TG concentration was increased from 1 to 5 mmol, the surface shielding, in particular, improved, i.e., incomplete bonds and defect states levels reduced [56, 57]. At this moment, a *thin* shell of CdSe_xS_{1-x} developed around the CdSe core. Hence, the stabilizer, thioglycerol molecules, localized the electronic levels in the CdS surface that could be coupled by charge tunneling, depending on the shell thickness. The charge tunneling was then changed from the CdS surface to the CdSe core. This quantum process could increase the probability of non-radiative electron-hole recombination up to a specific shell thickness, a finding consistent with other studies [5, 58].

A study reported that the creation of electron trap states on the QD surface following the binding of the thiol functional group significantly influenced the electron transfer kinetics [59]. Recent analyses of QD-ligand interactions have reported delocalization of the charge-carrier wave functions onto organic ligands based on the ligand structure and functional group, specifically stressing on the hole-accepting ability of amine functional groups [54, 60]. Thus, the passivation of QDs with thioglycerol has been shown to create electron-trapping states on the QD [5, 29]. Different studies have shown that thiol ligands bind very strongly to the cadmium atoms on the surface of CdSe QDs [6]. Moreover, it has been demonstrated that thiol and thiolate ligands act as photogenerated hole traps and passivate electron traps [61]. Wuister et al. [62], and Baker et al. [29], have shown that hole trapping is the principal process for excitonic PL quenching in CdSe QDs capped with thiols. On the contrary, recent studies reported that graded alloy CdSe/CdSe_xS_{1-x}/CdS structure, with a *thick*-shell, could suppress hole-trapping process, reducing the non-radiative Auger recombination and subsequently improving the excitonic photoluminescence efficiency [30, 38].

In our synthesis process, the CdSe/CdSe_xS_{1-x}/CdS shell was constructed using 1-thioglycerol. In this process, the existence of residual thiol ligands on the CdSe/CdSe_xS_{1-x}/CdS surface resulted in a higher hole-trapped states density. As the shell was thin, we believe that charge tunneling from QD to surface states could have

occurred. This cannot occur in a thick-shell structure. The CdSeS/CdS shell structure form a quasi-type-II band structure of the graded alloy CdSSe QDs in which the excess electron energy (photoexcited in the PL experiment) in the CB is greater than the confinement potential of the CB offset of only $\sim 0.0\text{--}0.1$ eV between the CdSe core and the CdS shell [38]. Therefore, the electron is delocalized throughout both the core and shell materials. Figure 3e shows an illustrative band alignment and the radiative and non-radiative processes in the core-shell QDs capped with TG. The red arrows represent the non-radiative transitions (NRTs) and green arrows represent the thermal activation (TA) processes involving surface states.

In an analysis of electron transfer kinetics at the QD–metal oxide interface in CdSe QDs capped with MPA, Hines and Kamat [5, 63], showed that MPA created electron-trapping states on the surface of CdSe QDs. This is evident from the formation of shallow S_1 states, as shown in Fig. 3e. Recently, Frederick et al. [54, 64], proposed, within second-order perturbation theory and experimental data, a strong electronic coupling between delocalized orbitals of the VB of CdSe QDs and the HOMO orbitals of capping ligands. The mixing of ligand orbitals with the orbitals of the QD that are delocalized over both core and surface generates new hybridized orbitals that split the states from energies of isolated orbitals [38]. These results show that surface states in QDs can couple with electronic states of QDs, leading to new possibilities for charge transfer from the surface to the nucleus or vice versa. Moreover, the new hybridized states can be tunneled to QD outside the band gap, leading to QD surface functionalization [28].

Figure 4 shows the fluorescence decay of CdSe: x TG ($x = 1, 5, 7, 9$ and 11 mmol) with decays monitored at 635 nm and emission of E_2^s , (Fig. 4a). The PL decay from the CdSe capped QDs had a multi-exponential form, a finding consistent with earlier studies [5, 25, 65, 66]. The lifetime traces were fitted to a tri-exponential decay function, resulting in long ($\tau_1 \sim 23.0$ ns), medium ($\tau_2 \sim 3.5$ ns), and short ($\tau_3 \sim 0.36$ ns) lifetimes using the following equation: ($I = A_1\exp(-t/\tau_1) + A_2\exp(-t/\tau_2) + A_3\exp(-t/\tau_3)$), where I is the emission intensity; A_1, A_2 , and A_3 are pre-exponential factors; and τ_1, τ_2 , and τ_3 are the lifetimes. The lifetime of channel 1 was similar to that of the core-only CdSe QDs (22.0 ns; obtained from samples presented in Fig. 2a).

Channel 3 with a lifetime of ~ 0.36 ns (τ_3) is similar to that reported for biexciton recombination in CdSe/CdSe/CdSe $_x$ CdS $_{1-x}$ /CdS [65, 67]. In the biexciton recombination, a non-radiative process, the Auger decay and the lifetime increased with QD volume [67]. For CdSe/CdS CS QD, the biexciton lifetime (τ_{2x}) increased from 60 ps to 23 ns with an increase in the shell thickness from 0.0 to 5.6 nm [67]. Similar results were observed in the present study, as shown in Fig. 4a. However, the shell of our samples was lower. Figure 4a shows that as the thickness of the shell increases, the suppression of the Auger recombination increases, similar to that observed early [68]. This is an evidence of alloy formation between CdSe and the CdS shell.

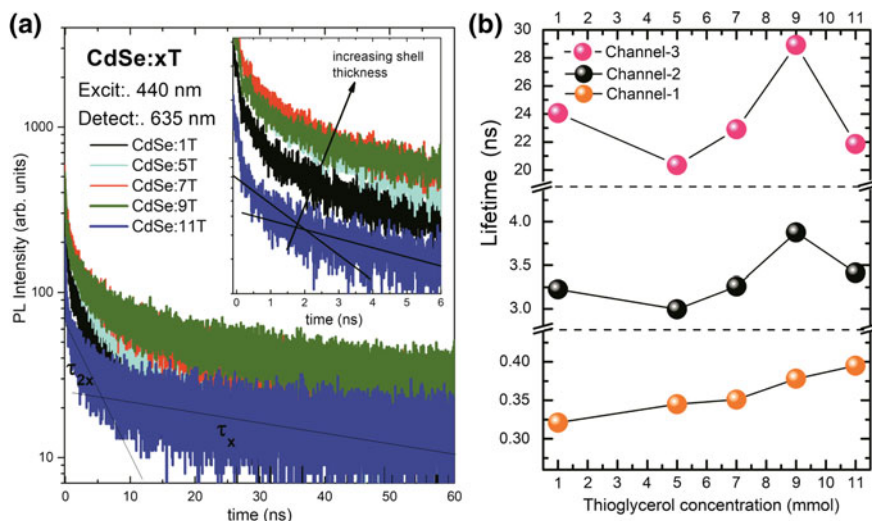


Fig. 4 **a** The fluorescence decay curves as a function of thioglycerol concentration for detection at 635 nm. The lifetime was obtained after a fitting procedure with a triexponential decay. **b** Life time for tree different channels as a function of thioglycerol concentration

Figure 4a, b shows that the average lifetime increased from 1 to 7 mmol of thioglycerol concentration and decreased at higher concentrations (see general behavior of fluorescence decay curves). Recent measurements of steady-state fluorescence in CdSe CS-QDs, with increasing concentration of thioglycerol, have shown that the fluorescence intensity increased as the thioglycerol concentration increased from 1 to 9 mmol, and it decreased at 11 mmol concentration [42], similar to the results observed in our lifetime data.

It is known that localized states proximal to or resonant with the extended states of CB have similar lifetimes. In this case, the lowest energy state, a localized state with longer lifetime, can serve as a charge reservoir for the state with a shorter lifetime. This charge reservoir could be accessed by thermal activation [69]. Lifetimes similar to that obtained in our experimental data were recently obtained by Mohamed et al., when analyzing the recombination of thiol-capped CdS nanoparticle films [70].

3.2 Photoluminescence as a Function of Temperature: Thermal Carrier Transfer

To further study the emissions at 595 and 635 nm from the surface states of TG-capped CdSe QDs, we analyzed PL as a function of temperature. Figures 5a, b shows the energy transfer process among surfaces states and the CS-QDs band edge

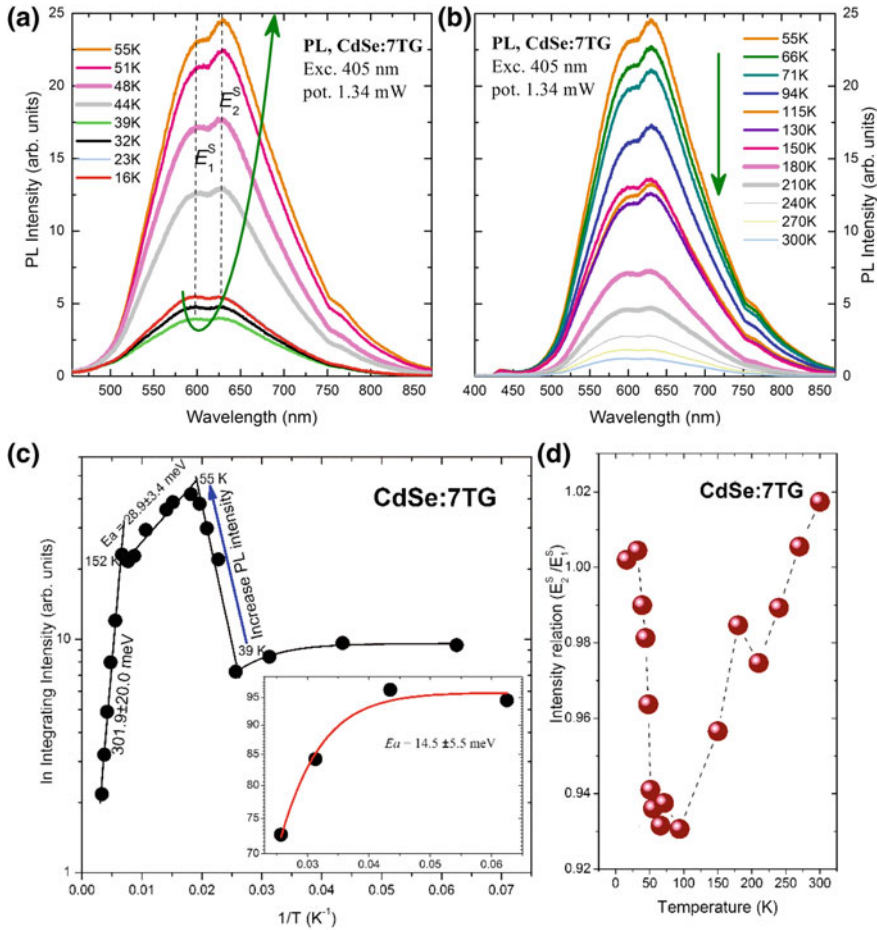


Fig. 5 a, b Show PL spectra of CdSe:7TG as a function of temperature. c shows integrated PL intensity as a function of $1/T$ for CdSe:7TG. The inset shows an expanded linear scale in the low temperature interval. The red line, in the inset, represents the best fit of a phenomenological expression: $I(T) = I_0/[1 + A \exp(-\frac{Ea}{KT})]$ [71, 72], Here Ea is the thermal activation energy and K is the Boltzmann constant. d Shows the relation of the PL peak intensity between E_2^S and E_1^S as a function of temperature

state. From 16 to 39 K, the PL spectrum depicts a reasonable intensity reduction as the temperature increases, a natural behavior for semiconductor materials. From 39 to 55 K, the PL intensity undergoes a sudden and unexpected increase, which, however, is not symmetrical between the components E_1^S and E_2^S . In this case, the increase in the emission intensity of E_2^S is more than that in the emission intensity of E_1^S . This behavior can be seen in Fig. 5d. For temperatures higher than 55 K, the intensity of the PL decreases. These PL(T) behaviors show the complex processes

of energy transfer by thermal activation of electronic states in CdSe:xTG materials and involve delocalized states of QDs and localized states of the capping agent.

Figure 5c shows the integrated PL intensity of CdSe:7TG sample as a function of inverse temperature. From 16 to 39 K, the PL intensity undergoes a moderate thermal quenching with an activation energy of 14.5 meV. We believe thermal quenching is relatively weaker in this temperature interval owing to the transfer of charge carriers from S₁ states to the electronic levels of QD via thermal activation TA₁, as shown in Fig. 3e. This low activation energy reflects proximity between the S₁ states and the electronic level of CS-QDs. However, at 39 K, the integrated PL intensity rapidly increases until 55 K, where it attains the thermal activation of a non-radiative channel have an energy barrier of about 28.9 meV (between 55 and 152 K). Hence, we found that the thermal activation energy of 39 K at TA₂ is sufficient to overcome the potential barrier between the electronic states of the CdSe core and the CdS shell. As shown in Fig. 5b, activation energy of approximately 28.9 meV in this simple model provides the thermal energy to pump holes of the S₂ state on the top of the VB, thereby significantly reducing the emission intensity E_2^s than the emission E_1^s , in agreement with the PL peak evolution for different temperatures. Figure 2c depicts the thermal activation energy TA₃. From 152 K, integrated PL intensity undergoes another thermal quenching process, causing the intensity to rapidly decrease with temperature. This process has activation energy of 301.9 meV and may be associated with non-radiative vacancy states.

4 Conclusions

Three sets of CdSe quantum dots (QDs) covered with different ligand molecules were growth and analyzed by optical spectroscopy. Set-1 (as-synthesized QDs) is composed by five samples of CdSe with size between 2.16 nm and 2.46 nm covered by TOP. Set-2 is composed by five samples of CdSe QDs, Set-1, functionalized, after exchange reaction process, with HDA molecules. Set-3 is composed by CdSe/CdSe_xS_{1-x}/CdS alloyed, core-shell (CS-QDs) capped with different thio-glycerol concentration, a different synthesis process. All these sets present luminescence of ligand states (surfaces, and vacancy E_1 , E_2 states) and excitonic transitions. Interestingly, all surfaces (E_1^s and E_2^s) and vacancy (E_1 , E_2) recombinations occur at sample energy position for the three set of QDs. Similar results were observed recently in CdTe QDs functionalized with MPA ligand [55]. However, the PL intensity of the surface states, in CS-QDs, are interestingly improved with relation to PL intensity of the core-only QDs (surface capped with TOP).

Anomalous increases in the luminescence intensity of the core-shell QDs, with increasing temperature, and a continuous redshift in the optical absorption peak, as a function of ligand concentration, evidence a strong electronic coupling between surface localized orbitals and delocalized excitonic CdSe QD states. Thus, we

believe that both shell of CdS as thiol states on the surface of CS-QDs can serve as a reservoir of charges to the core of CdSe. We believe that the main results of our paper will be useful to many groups working in this field, stimulating further investigations and applications mainly in the control of the carrier pathways after its photo- or electric-excitation in core-shell quantum dots that can be an important strategy to improve efficiency of photovoltaic or photodetector devices.

References

1. Talapin, D.V., Haubold, S., Rogach, A.L., Kornowski, A., Haase, M., Weller, H.: *J. Phys. Chem. B* **105**, 2260–2263 (2001)
2. Talapin, D.V., Rogach, A.L., Kornowski, A., Haase, M., Weller, H.: Highly luminescent monodisperse CdSe and CdSe/ZnS nanocrystals synthesized in a hexadecylamine- trioctylphosphine oxide- trioctylphosphine mixture. *Nano Lett.* **1**, 207–211 (2001)
3. Murray, C.B., Norris, D.J., Bawendi, M.G.: Synthesis and characterization of nearly monodisperse CdE (E = sulfur, selenium, tellurium) semiconductor nanocrystallites. *J. Am. Chem. Soc.* **115**, 8706–8715 (1993)
4. Alivisatos, A.P.: Semiconductor clusters, nanocrystals, and quantum dots. *Science* **271**, 933–937 (1996)
5. Hines, D.A., Kamat, P.V.: Quantum dot surface chemistry: ligand effects and electron transfer reactions. *J. Phys. Chem. C* **117**, 14418–14426 (2013)
6. Buckley, J.J., Couderc, E., Greaney, M.J., Munteanu, J., Riche, C.T., Bradforth, S.E., Brutchey, R.L.: Chalcogenol ligand toolbox for CdSe nanocrystals and their influence on exciton relaxation pathways. *ACS Nano* **8**, 2512–2521 (2014)
7. Colvin, V.L., Schlamp, M.C., Alivisatos, A.P.: Light-emitting diodes made from cadmium selenide nanocrystals and a semiconducting polymer. *Nature* **370**, 354–357 (1994)
8. Park, S.S., Kim, D.H., Jeon, Y.P., Kim, T.W.: Enhancement of the stabilization in white organic light-emitting diodes utilizing a color conversion layer containing CdSe/ZnS quantum dots. *J. Nanosci. Nanotechnol.* **13**, 7194–7197 (2013)
9. Kim, Y., Greco, T., Ippen, C., Wedel, A., Oh, M.S., Han, C.J., Kim, J.: Indium phosphide-based colloidal quantum dot light-emitting diodes on flexible substrate. *Nanosci. Nanotechnol. Lett.* **5**, 1065–1069 (2013)
10. Shen, H.B., Lin, Q.L., Wang, H.Z., Qian, L., Yang, Y.X., Titov, A., Hyvonen, J., Zheng, Y., Li, L.S.: Efficient and bright colloidal quantum dot light-emitting diodes via controlling the shell thickness of quantum dots. *ACS Appl. Mater. Interfaces* **5**, 12011–12016 (2013)
11. Klimov, V.I., Mikhailovsky, A.A., Xu, S., Malko, A., Hollingsworth, J.A., Leatherdale, C.A., Eisler, H.J., Bawendi, M.G.: Optical gain and stimulated emission in nanocrystal quantum dots. *Science* **290**, 314–317 (2000)
12. Harrison, M.T., Kershaw, S.V., Burt, M.G., Rogach, A.L., Kornowski, A., Eychmüller, A., Weller, H.: Colloidal nanocrystals for telecommunications. complete coverage of the low-loss fiber windows by mercury telluride quantum dot. *Pure Appl. Chem.* **72**, 295–307 (2000)
13. Thon, S.M., Sargent, E.H.: In: Eldada, L.A. (ed.) *Thin Film Solar Technology*, 3rd edn. (2011)
14. Tang, J.A., Sargent, E.H.: Infrared colloidal quantum dots for photovoltaics: fundamentals and recent progress. *Adv. Mater.* **23**, 12–29 (2011)
15. Li, X.M., Li, Y.F., Zeng, H.B.: Multiexciton generation in semiconductor nanocrystals: a potential avenue toward efficient solar cells. *Sci. Adv. Mater.* **5**, 1585–1595 (2013)
16. Chen, Z., Zhang, H., Yu, W., Li, Z., Hou, J., Wei, H., Yang, B.: Inverted hybrid solar cells from aqueous materials with a PCE of 3.61%. *Adv. Energy Mater.* **3**, 433–437 (2013)

17. Zhao, L., Hu, L., Fang, X.: Growth and device application of CdSe nanostructures. *Adv. Funct. Mater.* **22**, 1551–1566 (2012)
18. Bruchez, M., Moronne, M., Gin, P., Weiss, S., Alivisatos, A.P.: Semiconductor nanocrystals as fluorescent biological labels. *Science* **281**, 2013–2016 (1998)
19. Dong, M.T., Fu, S.S., Liu, S.X., Xu, J.Y., Huang, C.B.: One-pot synthesis of CdSe quantum dots in aqueous solution for biological labeling. *J. Chin. Chem. Soc.* **60**, 1328–1332 (2013)
20. Almeida Silva, A.C., Barbosa Silva, M.J., Cordero da Luz, F.A., Silva, D.P., Vieira de Deus, S.L., Dantas, N.O.: Controlling the cytotoxicity of CdSe magic-sized quantum dots as a function of surface defect density. *Nano Lett.* **14**, 5452–5457 (2014)
21. Xiu, Z.-M., Zhang, Q.-B., Puppala, H.L., Colvin, V.L., Alvarez, P.J.: Negligible particle-specific antibacterial activity of silver nanoparticles. *Nano Lett.* **12**, 4271–4275 (2012)
22. He, S.-J., Cao, J., Li, Y.-S., Yang, J.-C., Zhou, M., Qu, C.-Y., Zhang, Y., Shen, F., Chen, Y., Li, M.-M., Xu, L.-M.: *World J. Gastroenterol.* **22**, 5012–5022 (2016)
23. Kim, B.H., Hackett, M.J., Park, J., Hyeon, T.: Synthesis, characterization, and application of ultrasmall nanoparticles. *Chem. Mater.* **26**, 59–71 (2014)
24. Kamat, P.V., Christians, J.A., Radich, J.G.: Quantum dot solar cells: hole transfer as a limiting factor in boosting the photoconversion efficiency. *Langmuir* **30**, 5716–5725 (2014)
25. Yun, H.J., Paik, T., Edley, M.E., Baxter, J.B., Murray, C.B.: Enhanced charge transfer kinetics of CdSe quantum dot-sensitized solar cell by inorganic ligand exchange treatments. *ACS Appl. Mater. Interfaces.* **6**, 3721–3728 (2014)
26. Li, X., Feng, D., Tong, H., Jia, T., Deng, L., Sun, Z., Xu, Z.: Hole surface trapping dynamics directly monitored by electron spin manipulation in CdS nanocrystals. *J. Phys. Chem. Lett.* **5**, 4310–4316 (2014)
27. Maity, P., Debnath, T., Ghosh, H.N.: Slow electron cooling dynamics mediated by electron–hole decoupling in highly luminescent CdS_xSe_{1-x} alloy quantum dots. *J. Phys. Chem. C* **119**, 10785–10792 (2015)
28. Houtepen, A.J., Hens, Z., Owen, J.S., Infante, I.: On the origin of surface traps in colloidal II–VI semiconductor nanocrystals. *Chem. Mater.* **29**, 752–761 (2017)
29. Baker, D.R., Kamat, P.V.: Tuning the emission of CdSe quantum dots by controlled trap enhancement. *Langmuir* **26**, 11272–11276 (2010)
30. Park, Y.-S., Bae, W.K., Padilha, L.A., Pietryga, J.M., Klimov, V.I.: Effect of the core/shell interface on Auger recombination evaluated by single-quantum-dot spectroscopy. *Nano Lett.* **14**, 396–402 (2014)
31. Lu, H., Joy, J., Gaspar, R.L., Bradforth, S.E., Brutchey, R.L.: Iodide-passivated colloidal PbS nanocrystals leading to highly efficient polymer: nanocrystal hybrid solar cells. *Chem. Mater.* **28**, 1897–1906 (2016)
32. Larson, D.R., Zipfel, W.R., Williams, R.M., Clark, S.W., Bruchez, M.P., Wise, F.W., Webb, W.W.: Water-soluble quantum dots for multiphoton fluorescence imaging in vivo. *Science* **300**, 1434–1436 (2003)
33. Pelley, J.L., Daar, A.S., Saner, M.A.: State of academic knowledge on toxicity and biological fate of quantum dots. *Toxicol. Sci.* **112**, 276–296 (2009)
34. Kim, S., Fisher, B., Eisler, H.J., Bawendi, M.: Type-II quantum dots: CdTe/CdSe(core/shell) and CdSe/ZnTe(core/shell) heterostructures. *J. Am. Chem. Soc.* **125**, 11466–11467 (2003)
35. Chen, O., et al.: Compact high-quality CdSe–CdS core–shell nanocrystals with narrow emission linewidths and suppressed blinking. *Nat. Mater.* **12**, 445–451 (2013)
36. McBride, J., Treadway, J., Feldman, L.C., Pennycook, S.J., Rosenthal, S.J.: Structural basis for near unity quantum yield core/shell nanostructures. *Nano Lett.* **6**, 1496–1501 (2006)
37. Gong, K., Kelley, D.F.: Lattice strain limit for uniform shell deposition in zincblende CdSe/CdS quantum dots. *J. Phys. Chem. Lett.* **6**, 1559–1562 (2015)
38. Keene, J.D., McBride, J.R., Orfield, N.J., Rosenthal, S.J.: Elimination of hole–surface overlap in graded CdS_xSe_{1-x} nanocrystals revealed by ultrafast fluorescence upconversion spectroscopy. *ACS Nano* **8**, 10665–10673 (2014)

39. Garcia-Santamaria, F., Chen, Y., Vela, J., Schaller, R.D., Hollingsworth, J.A., Klimov, V.I.: Suppressed auger recombination in “giant” nanocrystals boosts optical gain performance. *Nano Lett.* **9**, 3482–3488 (2009)
40. Wang, X.Y., Ren, X.F., Kahen, K., Hahn, M.A., Rajeswaran, M., Maccagnano-Zacher, S., Silcox, J., Cragg, G.E., Efros, A.L., Krauss, T.D.: Non-blinking semiconductor nanocrystals. *Nature* **459**, 686–689 (2009)
41. Lawrence, K.N., Dutta, P., Nagaraju, M., Teunis, M.B., Muhoberac, B.B., Sardar, R.: Dual role of electron-accepting metal-carboxylate ligands: reversible expansion of exciton delocalization and passivation of nonradiative trap-states in molecule-like CdSe nanocrystals. *J. Am. Chem. Soc.* **138**, 12813–12825 (2016)
42. Silva, A.C.A., da Silva, S.W., Morais, P.C., Dantas, N.O.: Shell thickness modulation in ultrasmall CdSe/CdS_xSe_{1-x}/CdS core/shell quantum dots via 1-Thioglycerol. *ACS Nano* **8**, 1913–1922 (2014)
43. Donega, C.M., Liljeroth, P., Vanmaekelbergh, P.: Physicochemical evaluation of the hot-injection method, a synthesis route for monodisperse nanocrystals. *Small* **1**(12), 1152–1162 (2005)
44. W. Willian, Y., et al.: Experimental Determination of the Extinction Coefficient of CdTe, CdSe, and CdS Nanocrystals. vol. 125, pp. 2854–2860 (2003)
45. Boles, M.A., Ling, D., Hyeon, T., Talapin, D.V.: The surface science of nanocrystals. *Nature mater.* **15**, 141–153 (2016)
46. Babentsov, V., Riegler, J., Schneider, J., Ehlert, O., Nann, T., Fiederle, M.: Deep level defect luminescence in cadmium selenide nano-crystals films. *J. Cryst. Growth* **280**, 502–508 (2005)
47. Freitas Neto, E.S., Dantas, N.O., Barbosa Neto, N.M., Guedes, I., Chen, F.: Control of luminescence emitted by Cd_{1-x}Mn_xS nanocrystals in a glass matrix: x concentration and thermal annealing. *Nanotechnology* **22** (2011)
48. Henglein, A.: Physicochemical properties of small metal particles in solution: “microelectrode” reactions, chemisorption, composite metal particles, and the atom-to-metal transition. *J. Phys. Chem.* **97**, 5457–5471 (1993)
49. Rosa, I.L.V., Nassar, E.J., Serra, O.A.: Eu³⁺ and Tb³⁺ organophosphonates: synthesis, characterization and luminescent properties. *J. Alloy. Compd.* **275**, 315–317 (1998)
50. Glinka, Y.D., Lin, S.H., Chen, Y.T.: Time-resolved photoluminescence study of silica nanoparticles as compared to bulk type-III fused silica. *Phys. Rev. B* **66**, 035404 (2002)
51. Zhao, Q.C., Chen, W.M., Zhu, Q.R.: Self-assembly and characterization of novel amorphous SiO_x (x = 2.1) nanospheres. *Nanotechnology* **15**, 958–961 (2004)
52. Rahman, I.A., Vejayakumaran, P., Sipaut, C.S., Ismail, J., Chee, C.K.: Size-dependent physico-chemical and optical properties of silica nanoparticles. *Mater. Chem. Phys.* **114**, 328–332 (2009)
53. Lourenco, S.A., Laureto, E., Andrade, A.A., Silva, A.C.A., Dantas, N.O.: Efficient energy transfer mediated by intrinsic SiO₂ nanocrystals in Eu⁺³-doped lead borosilicate glasses. *Mater. Chem. Phys.* **139**, 471–477 (2013)
54. Frederick, M.T., Amin, V.A., Swenson, N.K., Ho, A.Y., Weiss, E.A.: Control of exciton confinement in quantum dot–organic complexes through energetic alignment of interfacial orbitals. *Nano Lett.* **13**, 287–292 (2013)
55. Vale, B.R.C., Silva, F.O., Carvalho, M.S., Raphael, E., Ferrari, J.L., Schiavon, M.A.: Water-soluble cdte/cds core/shell semiconductor nanocrystals: how their optical properties depend on the synthesis methods. *Crystals* **6**, 133 (2016)
56. Pal, M., Mathews, N.R., Santiago, P., Mathew, X.: A facile one-pot synthesis of highly luminescent CdS nanoparticles using thioglycerol as capping agent. *J. Nanopart. Res.* **14**, 916 (2012)
57. Wuister, S.F., Meijerink, A.: Synthesis and luminescence of CdS quantum dots capped with a silica precursor. *J. Lumin.* **105**, 35–43 (2003)
58. Liu, I.-S., Lo, H.-H., Chien, C.-T., Lin, Y.-Y., Chen, C.-W., Chen, Y.-F., Su, W.-F., Liou, S.-C.: Enhancing photoluminescence quenching and photoelectric properties of CdSe quantum dots with hole accepting ligands. *J. Mater. Chem.* **18**, 675–682 (2008)

59. Turk, M.E., et al.: Ultrafast electron trapping in ligand-exchanged quantum dot assemblies. *ACS Nano* **9**, 1440–1447 (2015)
60. Tan, Y., Jin, S., Hamers, R.J.: Influence of hole-sequestering ligands on the photostability of CdSe quantum dots. *J. Phys. Chem. C* **117**, 313–320 (2012)
61. Knowles, K.E., Tice, D.B., McArthur, E.A., Salomon, G.C., Weiss, E.A.: Chemical control of the photoluminescence of CdSe quantum dot-organic complexes with a series of para-substituted aniline ligands. *J. Am. Chem. Soc.* **132**, 1041–1050 (2019)
62. Wuister, S.F., Donega, C., Meijerink, A.: Influence of thiol capping on the exciton luminescence and decay kinetics of CdTe and CdSe quantum dots. *J. Phys. Chem. B* **108**, 17393–17397 (2004)
63. Frederick, M.T., Amin, V.A., Cass, L.C., Weiss, E.A.: A molecule to detect and perturb the confinement of charge carriers in quantum dots. *Nano Lett.* **11**, 5455–5460 (2011)
64. Hines, D.A., Kamat, P.V.: Recent advances in quantum dot surface chemistry. *ACS Appl. Mater. Interfaces* **6**, 3041–3057 (2014)
65. Dibbell, R.S., Watson, D.F.: Distance-dependent electron transfer in tethered assemblies of CdS quantum dots and TiO₂ nanoparticles. *J. Phys. Chem. C* **113**, 3139–3149 (2009)
66. Robel, I., Subramanian, V., Kuno, M., Kamat, P.V.: Quantum dot solar cells. harvesting light energy with CdSe nanocrystals molecularly linked to mesoscopic TiO₂ films. *J. Am. Chem. Soc.* **128**, 2385–2393 (2006)
67. Bae, W.K., et al.: Controlled alloying of the core–shell interface in CdSe/CdS quantum dots for suppression of auger recombination. *ACS Nano* **7**, 3411–3419 (2013)
68. García-Santamaría, F., Brovelli, S., Viswanatha, R., Hollingsworth, J.A., Htoon, H., Crooker, S.A., Klimov, V.I.: Breakdown of volume scaling in auger recombination in CdSe/CdS heteronanocrystals: the role of the core–shell interface. *Nano Lett.* **11**, 687–693 (2011)
69. Vlaskin, V.A., Janssen, N., van Rijssel, J., Beaulac, R., Gamelin, D.R.: Tunable dual emission in doped semiconductor nanocrystals. *Nano Lett.* **10**, 3670–3674 (2010)
70. Mohamed, N.B.H., Haouari, M., Zaaboub, Z., Nafoutti, M., Hassen, F., Maaref, H., Ben Ouada, H.: Time resolved and temperature dependence of the radiative properties of thiol-capped CdS nanoparticles films. *J. Nanoparticle Res.* **16**, 2242 (2014)
71. Leroux, M., Grandjean, N., Beaumont, B., Nataf, G., Semond, F., Massies, J., Gibart, P.: Temperature quenching of photoluminescence intensities in undoped and doped GaN. *J. Appl. Phys.* **86**, 3721–3728 (1999)
72. Lourenco, S.A., Dias, I.F.L., Pocas, L.C., Duarte, J.L., de Oliveira, J.B.B., Harmand, J.C.: Effect of temperature on the optical properties of GaAsSbN/GaAs single quantum wells grown by molecular-beam epitaxy. *J. Appl. Phys.* **93**, 4475–4479 (2003)

Biomolecular, Antimicrobial Research Insights and Applications

Antimicrobial Activity of Nanocrystals



Marcelly Chue Gonçalves, César Augusto Tischer,
Renata Katsuko Takayama Kobayashi and Gerson Nakazato

Abstract Nanotechnology is applied in many topics of health sections with great benefits for humans. The concern with bacterial resistance has abruptly increased and the number of infections caused by multidrug-resistant (MDR) bacteria today is very high. Extending this problem, there is a struggle in developing new efficient antimicrobials. As an alternative solution, different nanoparticles have been studied to be used as antimicrobials due their promising activity and potentialized biological properties. Several studies about antimicrobials and nanotechnology have showed that nanocrystals can act as antimicrobial against different microorganisms such as bacteria, fungi and protozoa, including MDR bacteria. Some nanocrystalline metals have been applied in materials for wound care such as gold and silver nanocrystals in biomedical applications. Cellulose nanocrystals have exhibited antimicrobial properties in different materials such as food-packaging against important foodborne pathogens. Another aspect is about experimental methods for evaluation of antimicrobial activity of nanoparticles, including nanocrystals. The analysis of this antimicrobial effect is associated with chemical and physical properties of nanomaterials that can be affected depending on synthesis and kind of compounds. The study of the antimicrobial properties of nanocrystals is important for prevention of human infections, and development of new alternatives and strategies to control of pathogens as well as bacterial resistance.

Keywords Nanocrystalline · Nanocrystals · Microorganisms · Inhibition · Bacterial resistance

M. C. Gonçalves · R. K. T. Kobayashi · G. Nakazato (✉)
Department of Microbiology, Center of Biological Sciences,
Universidade Estadual de Londrina, Londrina, Paraná CP 6001, Brazil
e-mail: gnakazato@uel.br

C. A. Tischer
Department of Biochemistry and Biotechnology, Center of Exact Sciences,
Universidade Estadual de Londrina, Londrina, Paraná, Brazil

© Springer Nature Switzerland AG 2020
F. A. La Porta and C. A. Taft (eds.), *Emerging Research in Science
and Engineering Based on Advanced Experimental and Computational Strategies*,
Engineering Materials, https://doi.org/10.1007/978-3-030-31403-3_8

1 Overview of Antimicrobial Resistance

However, the selection and spread of resistant bacteria after the clinical introduction of a determined antimicrobial is very fast. Penicillin, the first antibiotic, was discovered at 1928 by Fleming, it was first used on humans in 1941 and in the same year bacteria resistant to it were isolated. Overall, it takes less than 10 years to a bacterium to become potentially resistant to an antibiotic [18].

Antimicrobial resistance (AMR) is a naturally occurring process, some genes that confer antibiotic resistance were detected in ancestral bacterial strains that lived millions of years ago before man discovered and used antibiotics [9]. However, the frequency of AMR isolation has increased in recent years, becoming an increasingly serious problem. In the past, multidrug resistant (MDR) bacterial were found predominantly in hospitals, but in the last decade, MDR bacterial are also found at the community and even in food [8, 33].

One reason is the non-rational use of antimicrobials, favoring the rapid selection of resistant bacteria. This inappropriate use of antimicrobials does not occur only in humans, but in the livestock and agricultural sector too. In addition, the development of new antimicrobials candidates is expensive and limited return on investment lead to declining private investment in AMR relevant research and development activities. This has led many pharmaceutical companies to abandon this business and, consequently, the number of new antimicrobials entering the market has decreased significantly [42]. Then, the scarcity of new antimicrobials to combat these superbugs results in a catastrophic scenario, a growing enemy with a widely depleted combat arsenal [44].

Therefore, AMR is a large and growing global problem, with large health and economic consequences. For this reason, AMR has become a prominent topic on the public health agenda of Organization for Economic Cooperation and Development (OECD) countries. In 2017, around 17% of bacterial infections in OECD countries were resistant to antibiotics, but in some others countries, as Indonesia, Brazil and Russian Federation, between 40 and 60% of infections were caused by antimicrobial resistance bacteria [42].

According to the World Health Organization (WHO) [62], 12 antimicrobial resistant bacteria pose a threat to human health. They are divided into three categories based to the urgency of need for new antibiotics: Urgency “Critical”, Urgency “High” and Urgency “Medium”. The critical group includes multidrug resistant bacteria as *Acinetobacter baumannii*, *Pseudomonas aeruginosa* and various Enterobacteriaceae (including *Klebsiella pneumoniae*, *E. coli*, *Serratia* spp., *Proteus* spp. and others), which cause severe and often deadly infections due to the difficult treatment. The high and medium priority categories—contain other increasingly drug-resistant bacteria that cause diseases such as Sexually transmitted Disease and food poisoning. In these categories are *Enterococcus faecium*, *Staphylococcus aureus* methicillin resistant (MRSA), *Helicobacter pylori*, *Campylobacter* spp., *Salmonella* spp., *Neisseria gonorrhoeae*, *Streptococcus pneumoniae*, *Haemophilus influenzae* and *Shigella* spp. It is noticeable the highlights to the threat for Gram-negative bacteria (GNB), of the 12 bacteria, 9 are GNBs [18].

If no proactive solutions are now adopted to slow the rise in antimicrobial resistance, it is estimated that of the 700,000 people currently dying from MDR, by 2050 there will be ten million deaths per year, with huge economic loss. Since microorganisms are in the environment and circulate without borders, the necessary measures will need to be implemented globally. WHO's global priority pathogen list is an important tool to guide research and development of new antimicrobials [44]. To avoid the post-antibiotic era, it is fundamental that governments to put in place policies that incentivize basic science and advanced Research and development by both publicly funded agencies and the private sector investing in new antimicrobial discovery, as metallic nanoparticles and associations.

2 Metallic Nanocrystals

With features of both nanomaterials and metallic materials, metallic nanocrystals (MNCs) have attained spotlight due to the possibility of targeted synthesis, controlling their characteristics according to the application, since their properties can be adjusted by changing physical parameters as composition, structure, geometric shape and size. These changes can also modulate the antimicrobial activity of the MNCs [40]. The appropriate control of these properties presented in nanostructured materials can lead us to a better comprehension of the nanoscience as well to the development of new devices and technologies for different areas [5, 50].

In order to explore the physical properties and phenomena concerning new applications of nanostructures and nanomaterials, the engineering of NCs has been greatly explored and keeps expanding. Nowadays there is wide range synthesis methodologies due to the variety of experimental parameters that leads to different MNCs with distinct applications [63]. By reason of the high sensitivity concerning these methodologies, each parameter of synthesis is crucial to reach the most suitable result in terms of applicability of MNCs [5]. Each set of parameters can show a different applicability, thus, after nanocrystals synthesis, it is essential to characterize physical and chemical structures, so one can associate these parameters with the goal of the MNCs usage, standardize the synthesis parameters and replicate if necessary.

The MNCs have an extensive range of applications, including catalysis, electronics, photograph, data storage, photonics, therapeutic, diagnostic, imaging and sensing to their antimicrobial use. In this chapter, we will focus on metal nanocrystals applied in antimicrobial usage, their synthesis approaches, characterization and comparison between different MNCs.

2.1 *Synthesis Approaches of MNCs*

The ability to modulate the final product by adjusting the synthesis parameters is one of the main reasons of the increasing interest in nanotechnology in the recent

past years. Given this attention, a considerable amount of papers present reviews about synthesis of metal nanocrystals. Here, we emphasize MNCs synthesis related to antimicrobial usage.

The great majority of MNCs synthesis rely on a redox process at the early stages of the synthesis. The electron transfer from a salt precursor and another reagent can be induced by a physical cause or by reductants from a chemical or biological source [5]. Thus, besides divided in top-down and bottom up approaches, the synthesis of nanoparticles, including MNCs, is classified in three categories according to the type of synthesis: physical, chemical and biosynthesis [12].

Approaches based on wet-chemical synthesis are indeed the most used methods, since they are the most well studied category comparing to the physical and biogenic nanoparticle synthesis [52]. A common wet-chemical synthesis of antimicrobial related MNCs is the hydrothermal method, a rapid and non-complex

Table 1 Recent reports associating metal nanocrystals with antimicrobial activity and their synthesis method

Study	Type of MNCs synthesis	Metal nanocrystal	Antimicrobial effect
[4]	Wet-chemical synthesis	ZnO nanoparticle within cellulose nanocrystal (ZnO/cellulose composite)	Antibacterial activity against <i>Staphylococcus aureus</i> and <i>Salmonella choleraesuis</i>
[36]	Reflux condensation method (wet chemical + heating)	Flower-shaped CuO	Antibacterial and antifungal activity
[57]	Wet-chemical synthesis	Spheres, cubes, rods and octahedra shaped Cu ₂ O	Bactericidal (G+ and G-); highly selective for <i>Bacillus subtilis</i>
[2]	Microwave-assisted hydrothermal treatment	TiO ₂ @Ag nanocrystalline heterostructures	Activity against MRSA and <i>Candida</i> spp. planktonic and biofilm-forming cells
[40]	Hydrothermal method	Tetragonal/dodecahedral PbMoO ₄ nanocrystal	Synergism with gentamicin against <i>S. aureus</i>
[16]	Microwave-assisted hydrothermal synthesis	Nanocrystals nanocomposites of Ag@Fe ₃ O ₄ @cellulose	Activity against <i>S. aureus</i> and <i>Escherichia coli</i>
[22]	Hydrothermal method	Pd cubic and octahedron nanocrystals	Activity against <i>S. aureus</i> and <i>E. coli</i>
[45]	Wet-chemical synthesis	Superparamagnetic Ni colloidal nanocrystal clusters	Activity against <i>Bacillus subtilis</i> and <i>E. coli</i>
[26]	Microwave-assisted solvothermal method	Highly crystalline round-shaped ZnO nanocrystal	Activity against <i>S. aureus</i> and <i>E. coli</i>

approach, which the mechanism can be explained as the operation of an autoclave: a high-pressure structure, where reactants are heated in a specific solvent, allowing the reaction to occur [12, 53]. Despite these advantages, the reaction rate of crystallization is slow. Thus, in order to speed crystallization reaction, microwaves systems are used to heat the synthesis solutions. This method is called microwave-assisted hydrothermal method [51]. When the synthesis reaction solution has organic solvents instead of water, the method is called solvothermal method [67]. Table 1 summarizes recent published reports presenting different synthesis related to antimicrobial MNCs.

2.2 MNCs Characterization Techniques

To comprehend the nanoparticle behavior, it is essential to analyze characteristics of the synthesized nanoparticle. Size, morphology, structure, physical and chemical are some of the properties that connect the nanomaterials aspects with their function, providing potential parameters associations with applications. In this manner, characterization of nanoparticles is a fundamental step in nanomaterials study [38].

The characterization techniques of MNCs are no distinct than techniques for nanoparticles in general. Commonly, characterization comprises methodologies like optical spectroscopy, X-ray diffraction (XRD), Raman spectroscopy, solid-state NMR, electron microscopy, among others for chemical and physical analysis. Associated with XRD, as crystals are structures very well defined, crystalline patterns of MNCs can be refined through various tools, such as Full Width at Half Maximum (FWHM) of the Bragg reflections, Scherrer equation, Rietveld method, Williamson–Hall equation (Table 2) [38]. XRD results can also be confirmed through comparison of patterns with the data banks, as the International Centre for Diffraction Data (ICDD) [40].

The Full Width at Half Maximum (FWHM) along with the Scherrer equation are tools to calculate the crystallite size, shape and arrangement [3]. The evaluation of the size, microstrain and homogeneity is calculated through the value of correlation coefficient using the Williamson–Hall equation (WH) [61]. Elemental analysis is done by Energy Dispersive Spectroscopy (EDS) using FEG scanning electron microscope with an X-ray detector [40].

Table 2 Some of the most used tools for analysis and refinement of nanocrystalline patterns along with XDR results

Tool for crystal refinement	Target pattern
FWHM of the Bragg reflections	Arrangement of the crystal components, shape and size of crystals
Scherrer equation	Crystal size
Rietveld method	Structure
Williamson–Hall equation	Crystallite size, microstrain and homogeneity

2.3 Applications of MNCs

Research involving metal nanocrystals has expanded due their tunable characteristics and special features, turning them accessible to a wide range of applications as electronic applications, data storage, diagnostics or therapeutic [34, 52]. Here, we are going to discuss about antimicrobials applications of MNCs.

Since before the first antibiotic discovery by Alexander Fleming in 1930s, the microbicidal potential of metals is well-known. Silver was used for medical purposes as wound healing and for water, milk, vinegar and wine vessels, increasing their expiration date [1], copper was utilized against bacterial infections [15], and gold was exploited in medical recipes to treat syphilis [25]. After the emergence of antimicrobials, the handling of metals for these purposes decreased. However, today this picture is reversed: antimicrobial resistance is a global health issue that pushes researchers to find new strategies against these microbial pathogens, and a potential solution is to reuse metals, but in nanometer scale.

Each nanocrystal shape along with size has unique properties and can also present action against a wide or narrow spectrum of microorganisms as observed in Table 1, showing the antimicrobial activity of diverse MNCs against a variety of microbial organisms. Usually, articles focus on the synthesis of a metal nanocrystal and apply them against microorganisms to verify antimicrobial activity. In an interesting study, Peng and collaborators [45] synthesized superparamagnetic nickel nanocrystals that self-organize into clusters, containing magnetic and antimicrobial properties, that allowed *E. coli* and *B. subtilis* (and spores) to be captured by binding, killed and extracted (through magnetism, move from one place to another). Thus, this study shows a potential antimicrobial strategy using MNCs.

As some metals can present toxicity [52], in vivo studies mostly comprehend topical applications of MNCs. Studies as Tineo and collaborators [58] and Dutta and collaborators [17] compared the action of silver nanocrystals and silver sulfadiazine on wounds. Both studies presented advantages of silver nanocrystals usage, as a positive impact in the general wound healing or better antimicrobial activity. There is a lack in studies showing other type of administration or the systemic behavior of metal nanocrystals when aiming microbial control in vivo.

Besides the nanometer scale or increased magnetism of some nanometals, other strategies are the surface functionalization or encapsulation of MNCs or other nanoparticles. Encapsulation with specific substances or functionalization with antibodies, proteins or other molecules allow interaction (or better interaction) between the MNCs and a specific microorganism [56, 59]. These strategies enable incorporation of MNC to surfaces or materials, as medical tools, dressings for wounds, healthcare, hygiene, cosmetics, and innumerable other products, with the objective of repressing or inhibiting microbial growth.

Metal nanocrystals offer a great variety of possibilities in applications due to their metal and nanoscale properties. Synthesis parameters are intimately linked with the desirable final application, so the characterization is a fundamental step to guarantee that the synthesis reached nanocrystals with the aspired properties.

Applications of MNCs as antimicrobials are still most studied for prevention, aiming the microbial growth control of MNCs incorporated in materials or surfaces. More in vivo studies are necessary to guarantee safety of MNCs usage other than topic administration. The association of nanotechnology and antimicrobial strategies is a hot topic nowadays, and perspectives are growing as the studies show great applicability of metal nanocrystals in this area.

3 Cellulose Nanocrystals

Researches in the fields of tissue engineering are being encouraged by many successful in medicine regenerative treatments that utilize both synthetic and biological polymers. Together with this success the application of cellulose as biomaterial is undergoing exponential growth in the last years. The biocompatibility of cellulose, facility of forms manipulation being used as powder, gels, membranes or pastes and pure, blended or chemically modified make it a important biomaterial with mimetic capacities for regenerated organs.

Cellulose, no other compound over earth is most abundant, being produced mainly by plant but also by fungi, algae and bacteria. Cellulose is the glucose polysaccharide, estimated on 180 millions of tons, the product of the Cellulose Synthases (CeSa) extrude linked β -(1 \rightarrow 4) anhydro-glucose, governed by the weak hydrogen linkages that imposes strongly the linearity to the chain [24]. The longitudinal distribution of the polysaccharide also the fibrillar arrange is driven by the agglomerate of the CeSa, that can vary from species to species, and craved on the membrane are particularly organized giving to the cellulose ribbon its shape, sizes and crystalline unit [14, 48].

The chain is constituted from dimers of cellobiose with 1.034 nm length, and the angle between each anhydro glucose of 180° giving to the structure the alternate option to hydrogen linkages that characterize it, represented on Fig. 1. The hydroxyls of the C2-OH, C3-OH and HC6-OH, with the half turn of each monomer

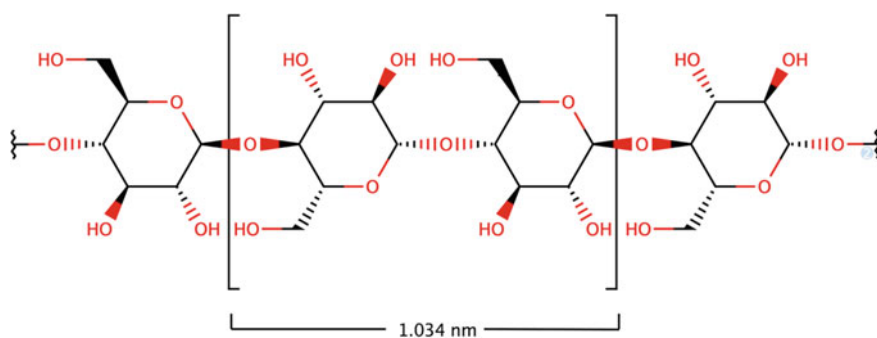


Fig. 1 Cellulose chain representation with anhydro cellobiose unit linked β -(1 \rightarrow 4) on the brackets. The C1 is the reducing end is at right

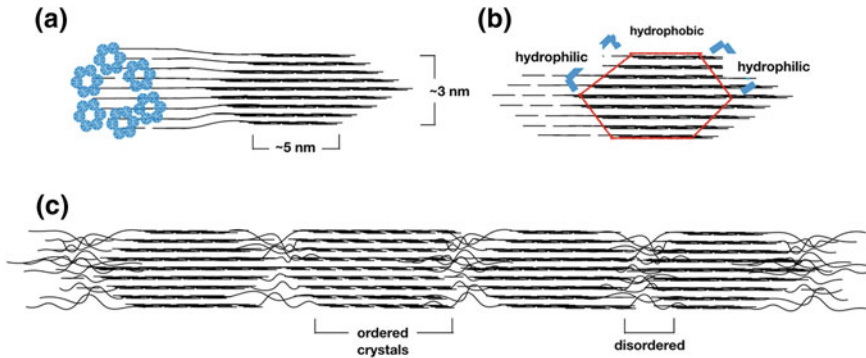


Fig. 2 The CeSA in blue is represented (a) extruding from each subunit the cellulose that aggregates on the microfibril bundle; it varies on high and wide, and the average sizes for plants are on the brackets. The (b) figure represents the crystalline arrangement with its hexagonal shape, constituting the ordered domain. On figure (c) one cellulose microfibril is represented showing its crystalline regions interposed with disordered chains

that by this way offer the these groups to linkage on one side another of the chain. Results from computational simulations attribute that the O3- links to -O5 on intrachain H bonds, as does O2-to-O6 intrachain H bonds. The strength of intralayer chain is given by O6-to-O3 H bond, as well O6-to-O2 [43].

The crystalline region it's a product of the polymerization and aggregation process, that occurs simultaneously connecting hydrogen bonds inter- and intramolecular stacking chains in microfibrils with 2.5–4 nm for cotton, or 5.8 nm for *Arabidopsis thaliana* [10].

The crystalline domains are separated by amorphous regions, and this highly ordered have dimension from 1 to 100 nm [49], that varies with the hexagonal distribution of the rosetta arrangement of CeSa [54], as can be seen on Fig. 2a. On the (b) the crystal arrangement the is formed transversally to the chain that keeps the dimensions given by the biosynthesis machinery; for plants the crystal structure is that hexagon. This heritage from enzyme complex machinery that drive the high ordered material and play a role on cellulose use as a polyvalent biopolymer is its amphiphilic character given by the distribution of the hydroxyls laterally distributed, and in other point the absence causes the affinity by hydrophobic compounds [39, 60]. The Cellulose microfibrils continuously grows with points where the sum of mismatches causes a rupture on the continuity, as represented by the disordered regions, Fig. 2c.

3.1 Nanocelluloses

The high performance cellulose can be catch using downsized fibers, usually called Nanocelluloses [35] that generates the highly ordered β -(1 \rightarrow 4) glucan chains. The

industrial rate nanocelluloses can be separated by its sizes and need to be, at least in one dimension, on nanometric scale. Three nanocelluloses are cited as potentially useful for a wide range of uses, in industrial amounts [6]: the cellulose nanocrystals (CNC), cellulose nanofibrils (CNF) and bacterial cellulose (BC).

The nanocellulose nanocrystals (CNC) corresponds to the highly ordered cellulose obtained after the hydrolysis with strong concentrated acid of amorphous parts [11, 31], and what left is mostly the crystalline region as well paracrystalline chains. Depends on the origin of the cellulose the nanofiber diameter could stay between 1 and 100 nm, but for plant ones, that has the viability to gain market, it round 2 and 10 nm.

Produced firstly on 1970s and deeply studied today its uses and production is gaining scale, being found as raw product or modified, as powder, paste, gel, slurry, considering the good aqueous dispersion [29], suspension stability and dispersibility [20], high compatibility with any chemical compound even hydrophobic.

Why nano? The aspect ratio, the rate between length and the diameter as well the crystallinity affects the comportment of the chain in water for example. Other important thing is that the hydrolysis process [7] that cut the amorphous regions and leave sulfate groups behind surrounding the nanofibril, playing an important role on the electric charge and other interesting properties that is the self-organization [13].

3.2 *Antibacterial Studies*

The cellulose nanofibrils (CNF) are produced by mechanical processes as grinding, homogenization or microfluidization [21] that separate the microfibrils that forms cell wall from each other. The gel formed is composed of nano-scale fibrils with 20–40 nm of diameter [65].

Bacterial cellulose (BC) is the product of the *Komagataeibacter* strains [66] that forms a thin film of mostly crystalline celluloses (CI ~ 70%). This material is interestingly resistant to the temperature and traction [41], as well if never dried retains 99% of its weight on water [47].

The anhydro glucose hydroxyls are good reaction sites to attach functional compounds [23, 27, 28, 46], and tens of years of chemical trials that has construct the worldwide chemotechnique could be crossed with this nano sized high performance carriers. However, the question of production viability should be immediately posed as part of the scientific question so that these products actually reach the patient user. The ways to got this results can be the use of nanocelluloses as physical barrier, the simple aggregation trough physical-chemical processes and covalently link compounds knew as microorganism killers.

Nanocellulose regenerated membranes can be made by conventional pressing devices to obtain filters, as Metreveli and cols. [37] does, that was able to filter successfully Influenza virus with pore size of ~ 19 nm. Singamaneni and cols. [30] include graphene during bacterial cellulose production to get a membrane with filtering capability to biofouling contaminated water; the ultrafiltration filter clean

water from algae and barnacles, getting twice of fast than commercial ultrafiltration ones. The cellulose producing bacteria is a kind of 3D bioprinter that aggregate to the material those compounds that was furnished together to the culture medium while extrudes the polysaccharide chain.

The be focused on antibiotics, the nanocelluloses could contribute to offer new alternatives to the bacterial resistance crises. For example, Tavakolian and cols. [55], has linked covalently trough aldehyde groups the lysozyme an nisin antibiotic polypeptides; the improvement on activity period for example for nisin, that in its free form usually loose its activity after 16–24 h, while immobilized retains its antibacterial activity against *Staphylococcus aureus* over all the time. The minimum inhibitory concentration, MIC, for both polypeptides immobilized on nanocellulose was better than the free form.

Daily products could be improved with antibiotic activity, for example the sponges of nanocellulose fibers, CNF, grafted with gentamicin [64] shown antibacterial effect with bactericidal rate of >99.9% for *Escherichia coli* and >99.9% for *S. aureus*.

After years of studies from the deep knowledge of structure [19, 32] to the consumer as ink additive [29] or the antibactericide dressing [55], nanocellulose has climb its importance together the rise of the green products and nanotechnology.

References

1. Alexander, J.W.: History of the medical use of silver. *Surg. Infect.* **10**, 289–292 (2009). <https://doi.org/10.1089/sur.2008.9941>
2. André, R.S., Zamperini, C.A., Mima, E.G., Longo, V.M., Albuquerque, A.R., Sambrano, J. R., Longo, E.: Antimicrobial activity of TiO₂:Ag nanocrystalline heterostructures: experimental and theoretical insights. *Chem. Phys.* **459**, 87–95 (2015). <https://doi.org/10.1016/j.chemphys.2015.07.020>
3. Azaroff, L.V.: Elements of X-ray crystallography. McGraw-Hill, New York (1968)
4. Azizi, S., Ahmad, M., Mahdavi, M., Abdolmohammadi, S.: Preparation, characterization, and antimicrobial activities of ZnO nanoparticles/cellulose nanocrystal nanocomposites. *BioResources* **8**(2) (2013). <https://doi.org/10.15376/biores.8.2.1841-1851>
5. Bai, L., Ouyang, Y., Song, J., Xu, Z., Liu, W., Hu, J., Wang, Y., Yuan, F.: Synthesis of metallic nanocrystals: from noble metals to base metals. *Materials* **12**(9), 1497 (2019). <https://doi.org/10.3390/ma12091497>
6. Blanco, A., et al.: Nanocellulose for industrial use: cellulose nanofibers (CNF), cellulose nanocrystals (CNC), and bacterial cellulose (BC). *Handbook of Nanomaterials for Industrial Applications*, pp. 74–126 (2018)
7. Börjesson, M., et al.: Increased thermal stability of nanocellulose composites by functionalization of the sulfate groups on cellulose nanocrystals with azetidinium ions. *J. Appl. Polym. Sci.* **135**(10), 45963 (2018)
8. Cyoia, P.S., Koga, V.L., Nishio, E.K., Houle, S., Dozois, C.M., Brito, K.C.T., Brito, B.G., Nakazato, G., Kobayashi, R.K.T.: Distribution of ExPEC virulence factors, *bla*_{CTX-M}, *fosA3*, and *mcr-1* in *Escherichia coli* isolated from commercialized chicken carcasses. *Front. Microbiol.* **9**, 3254 (2019)
9. D’Costa, V.M., et al.: Antibiotic resistance is ancient. *Nature* **477**, 457–461 (2011). <https://doi.org/10.1038/nature10388>

10. Davies, L.M., Harris, P.J.: Atomic force microscopy of microfibrils in primary cell walls. *Planta* **217**(2), 283–289 (2003)
11. De Souza Lima, M.M., Borsali, R.: Rodlike cellulose microcrystals: structure, properties, and applications. *Macromol. Rapid Commun.* **25**(7), 771–787 (2004)
12. Dhand, C., Dwivedi, N., Loh, X. J., Jie Ying, A.N., Verma, N.K., Beuerman, R.W., Lakshminarayanan, R., Ramakrishna, S.: Methods and strategies for the synthesis of diverse nanoparticles and their applications: a comprehensive overview. *RSC Advances* **5**(127), 105003–105037 (2015). <https://doi.org/10.1039/c5ra19388e>.
13. Diaz, J.A., et al.: Thermal expansion of self-organized and shear-oriented cellulose nanocrystal films. *Biomacromolecules* **14**(8), 2900–2908 (2013)
14. Doblin, M.S., et al.: Cellulose biosynthesis in plants: from genes to rosettes. *Plant Cell Physiol.* **43**(12), 1407–1420 (2002)
15. Dollwet, H.H.A., Sorenson, J.R.J.: Historic use of copper-compounds in medicine. *Trace Elem. Med.* **2**, 80–87 (1985)
16. Dong, Y.Y., Liu, S., Liu, Y.J., Meng, L.Y., Ma, M.G.: Ag@Fe₃O₄@cellulose nanocrystals nanocomposites: microwave-assisted hydrothermal synthesis, antimicrobial properties, and good adsorption of dye solution. *J. Mater. Sci.* **52**(13), 8219–8230 (2017). <https://doi.org/10.1007/s10853-017-1038-1>
17. Dutta, G., Das, N., Adhya, A., Munian, K., Majumdar, B.K.: Nanocrystalline silver gel versus conventional silver sulfadiazine cream as topical dressing for second-degree burn wound: a clinicopathological comparison. *Indian J. Burns* **26**, 29–37 (2018). https://doi.org/10.4103/ijb.ijb_9_18
18. Duval, R.E., Grare, M., Demoré, B.: Fight against antimicrobial resistance: we always need new antibacterials but for right bacteria. *Molecules* **24**, 3152 (2019)
19. Elazzouzi-Hafraoui, S., et al.: The shape and size distribution of crystalline nanoparticles prepared by acid hydrolysis of native cellulose. *Biomacromolecules* **9**(1), 57–65 (2008)
20. Endes, C., et al.: Risk assessment of released cellulose nanocrystals – mimicking inhalatory exposure. *J. Phys: Conf. Ser.* **429**(1), 012008 (2013)
21. Espinosa, E., et al.: Production of lignocellulose nanofibers from wheat straw by different fibrillation methods. Comparison of its viability in cardboard recycling process. *J. Clean. Prod.* **239**, 118083 (2019)
22. Fang, G., Li, W., Shen, X., Perez-Aguilar, J.M., Chong, Y., Gao, X., Chai, Z., Chen, C., Ce, C., Zhou, R.: Differential Pd-nanocrystal facets demonstrate distinct antibacterial activity against Gram-positive and Gram-negative bacteria. *Nat. Commun.* **9**(1) (2018). <https://doi.org/10.1038/s41467-017-02502-3>
23. Faria-Tischer, P.C.S., Ribeiro-Viana, R.M., Tischer, C.A.: Bio-based nanocomposites. In: Grumezescu, V., Grumezescu, A.M. (eds.) *Materials for Biomedical Engineering*, pp. 205–244. Elsevier, Amsterdam (2019)
24. Festucci-Buselli, R.A., Otoni, W.C., Joshi, C.P.: Structure, organization, and functions of cellulose synthase complexes in higher plants. *Braz. J. Plant. Physiol.* **19**(1), 1–13 (2007)
25. Fricker, S.P.: Medical uses of gold compounds: past, present and future. *Gold Bull.* **29**, 53 (1996). <https://doi.org/10.1007/BF03215464>
26. Garino, N., Sanvitale, P., Dumontel, B., Laurenti, M., Colilla, M., Izquierdo-Barba, I., Cauda, V., Vallet-Regi, M.: Zinc oxide nanocrystals as a nanoantibiotic and osteoinductive agent. *RSC Adv.* **9**(20), 11312–11321 (2019). <https://doi.org/10.1039/c8ra10236h>
27. Gilbert, R.D.: Cellulose and cellulose derivatives as liquid crystals. In: [s.l: s.n.], pp. 259–272 (1990)
28. Hu, W., et al.: Functionalized bacterial cellulose derivatives and nanocomposites. *Carbohydr. Polym.* **101**, 1043–1060 (2014)
29. Isogai, A.: Development of completely dispersed cellulose nanofibers. *Proc. Jpn. Acad. Ser. B: Phys. Biol. Sci.* (2018). Available from: <https://pdfs.semanticscholar.org/0006/20e05de074056cded8979cdc12b98feabbf2.pdf>. Accessed 31 Aug 2019

30. Jiang, Q., et al.: Photothermally active reduced graphene oxide/bacterial nanocellulose composites as biofouling-resistant ultrafiltration membranes. *Environ. Sci. Technol.* **53**(1), 412–421 (2019)
31. Klemm, D., et al.: Nanocelluloses: a new family of nature-based materials. *Angew. Chem. Int. Ed.* **50**(24), 5438–5466 (2011)
32. Klemm, D., et al.: Nanocellulose as a natural source for groundbreaking applications in materials science: today's state. *Mater. Today* **21**(7), 720–748 (2018)
33. Koga, V.L., Maluta, R.P., da Silveira, W.D., Ribeiro, R.A., Hungria, M., Vespero, E.C., Nakazato, G., Kobayashi, R.K.T.: Characterization of CMY-2-type beta-lactamase-producing *Escherichia coli* isolated from chicken carcasses and human infection in a city of South Brazil. *BMC Microbiol.* **19**(1), 174 (2019). <https://doi.org/10.1186/s12866-019-1550-3>. PMID: 31362706; PMCID: PMC6664532
34. Kovalenko, M.V., Manna, L., Cabot, A., Hens, Z., Talapin, D.V., Kagan, C.R., Klimov, V.L., Rogach, A.L., Reiss, P., Milliron, D.J., Guyot-Sionnest, P., Konstantatos, G., Parak, W.J., Hyeon, T., Korgel, B.A., Murray, C.A., Heiss, W.: Prospects of nanoscience with nanocrystals. *ACS Nano* **9**(2), 1012–1057 (2015). <https://doi.org/10.1021/nm506223h>
35. Lin, N., Dufresne, A.: Nanocellulose in biomedicine: current status and future prospect. *Eur. Polym. J.* **59**, 302–325 (2014)
36. Mageshwari, K., Sathyamoorthy, R.: Flower-shaped CuO nanostructures: synthesis, characterization and antimicrobial activity. *J. Mater. Sci. Technol.* **29**(10), 909–914 (2013). <https://doi.org/10.1016/j.jmst.2013.04.020>
37. Metreveli, G., et al.: A size-exclusion nanocellulose filter paper for virus removal. *Adv. Healthc. Mater.* **3**(10), 1546–1550 (2014)
38. Modena, M.M., Rühle, B., Burg, T.P., Wuttke, S. Nanoparticle characterization: what to measure? *Adv. Mater.* 1901556 (2019). <https://doi.org/10.1002/adma.201901556>
39. Moreau, C., et al.: Tuning supramolecular interactions of cellulose nanocrystals to design innovative functional materials. *Ind. Crops Prod.* **93**, 96–107 (2016)
40. Moura, J.V.B., Freitas, T.S., Silva, A.R.P., Santos, A.T.L., da Silva, J.H., Cruz, R.P., Coutinho, H.D.M.: Synthesis, characterizations, and antibacterial properties of PbMoO₄ nanocrystals. *Arab. J. Chem.* **11**(6), 739–746 (2017). <https://doi.org/10.1016/j.arabjc.2017.12.014>
41. Nainggolan, H., et al.: Mechanical and thermal properties of bacterial-cellulose-fibre-reinforced Mater-Bi[®] bionanocomposite. *Beilstein J. Nanotechnol.* **4**(1), 325–329 (2013)
42. OECD: Stemming the superbug tide: just a few dollars more. OECD Health Policy Studies, OECD Publishing, Paris (2018). <https://doi.org/10.1787/9789264307599-en>
43. Oehme, D.P., et al.: Unique aspects of the structure and dynamics of elementary Iβ cellulose microfibrils revealed by computational simulations. *Plant Physiol.* **168**(1), 3–17 (2015)
44. O'Neill, J.: Review on Antimicrobial Resistance. Tackling Drug-Resistant Infections Globally: Final Report and Recommendations (2016). Available from: https://amr-review.org/sites/default/files/160518_Final%20paper_with%20cover.pdf. Accessed 2 Sept 2019
45. Peng, B., Zhang, X., Aarts, D.G.A.L., Dullens, R.P.A.: Superparamagnetic nickel colloidal nanocrystal clusters with antibacterial activity and bacteria binding ability. *Nat. Nanotechnol.* **13**(6), 478–482 (2018). <https://doi.org/10.1038/s41565-018-0108-0>
46. Rajwade, J.M., Paknikar, K.M., Kumbhar, J.V.: Applications of bacterial cellulose and its composites in biomedicine. *Applied Microbiology and Biotechnology*. Springer, Berlin, Heidelberg (2015). Available from: <http://link.springer.com/10.1007/s00253-015-6426-3>. Accessed 27 Jun 2017
47. Rebelo, A., et al.: Dehydration of bacterial cellulose and the water content effects on its viscoelastic and electrochemical properties. *Sci. Technol. Adv. Mater.* **19**(1), 203–211 (2018)
48. Römling, U., Galperin, M.Y.: Bacterial cellulose biosynthesis: diversity of operons, subunits, products, and functions. *Trends Microbiol.* (2015)
49. Rongpipi, S., et al.: Progress and opportunities in the characterization of cellulose – an important regulator of cell wall growth and mechanics. *Front. Plant Sci.* (2019). Available from: <https://www.frontiersin.org/article/10.3389/fpls.2018.01894/full>. Accessed 30 Aug 2019

50. Ruditskiy, A., Xia, Y.: The science and art of carving metal nanocrystals. *ACS Nano* **11**(1), 23–27 (2017). <https://doi.org/10.1021/acsnano.6b08556>
51. Schmidt, R., Prado-Gonjal, J., Morán, E.: Microwave-assisted hydrothermal synthesis of nanoparticles. In: Kharisov, B.I., Ortiz-Mendez, O.V.K.U. (eds.) *CRC Concise Encyclopedia of Nanotechnology*, pp. 585–596. CRC Press Taylor & Francis Group, Boca Raton, FL, USA (2015). ISBN 9781466580343
52. Shankar, S.S., Deka, S.: Metal nanocrystals and their applications in biomedical systems. *Sci. Adv. Mater.* **3**, 169–19 (2011). <https://doi.org/10.1166/sam.2011.1150>
53. Sobhani, A., Salavati-Niasari, M.: Optimized synthesis of ZnSe nanocrystals by hydrothermal method. *J. Mater. Sci.: Mater. Electron.* **27**(1), 293–303 (2015). <https://doi.org/10.1007/s10854-015-3753-1>
54. Sorieul, M., et al.: Plant fibre: molecular structure and biomechanical properties, of a complex living material, influencing its deconstruction towards a biobased composite. *Materials* **9**(8), 1–36 (2016)
55. Tavakolian, M., et al.: Developing antibacterial nanocrystalline cellulose using natural antibacterial agents. *ACS Appl. Mater. Interfaces* **10**(40), 33827–33838 (2018)
56. Taylor, E.N., Kummer, K.M., Durmus, N.G., Leuba, K., Tarquinio, K.M., Webster, T.J.: Superparamagnetic iron oxide nanoparticles (SPION) for the treatment of antibiotic-resistant biofilms. *Small* **8**(19), 3016–3027 (2012). <https://doi.org/10.1002/sml.201200575>
57. Theja, G.S., Lawrence, R.C., Ravi, V., Nagarajan, S., Anthony, S.P.: Synthesis of Cu₂O micro/nanocrystals with tunable morphologies using coordinating ligands as structure controlling agents and antimicrobial studies. *CrystEngComm* **16**(42), 9866–9872 (2014). <https://doi.org/10.1039/c4ce01649a>
58. Tineo, C., Nuñez, C.M., Sosa, O., Pichardo, D., Hernández, J.L., Collado, G.: Effect of the use of silver nanocrystals and silver sulfadiazine in the management of soft tissue lesions. *Chronic Wound Care Manag. Res.* **4**, 17–24 (2016). <https://doi.org/10.2147/CWCMR.S120177>
59. Vikesland, P.J., Wigginton, K.R.: Nanomaterial enabled biosensors for pathogen monitoring – a review. *Environ. Sci. Technol.* **44**(10), 3656–3669 (2010). <https://doi.org/10.1021/es903704z>
60. Wicholm, K., Larsson, P.T., Iversen, T.: Assignment of non-crystalline forms in cellulose I by CP/MAS ¹³C NMR spectroscopy. *Carbohydr. Res.* **312**(3), 123–129 (1998)
61. Williamson, G.K., Hall, W.H.: X-ray line broadening from fided aluminum and wolfram. *Acta Metall.* **1**, 22–31 (1953)
62. World Health Organization: WHO Publishes List of Bacteria for Which New Antibiotics are Urgently Needed (2017). Available from: <http://www.who.int/mediacentre/news/releases/2017/bacteria-antibiotics-needed/fr/>. Accessed 2 Sept 2019
63. Xia, Y., Xiong, Y., Lim, B., Skrabalak, S.E.: Shape-controlled synthesis of metal nanocrystals: simple chemistry meets complex physics? *Angew. Chem. Int. Edn.* **48**(1), 60–103 (2009). <https://doi.org/10.1002/anie.200802248>
64. Xiao, Y., et al.: A light-weight and high-efficacy antibacterial nanocellulose-based sponge via covalent immobilization of gentamicin. *Carbohydr. Polym.* **200**, 595–601 (2018)
65. Xu, X., et al.: Cellulose nanocrystals vs. cellulose nanofibrils: a comparative study on their microstructures and effects as polymer reinforcing agents. *ACS Appl. Mater. Interfaces* **5**(8), 2999–3009 (2013)
66. Zhang, H., et al.: Complete genome sequence of the cellulose-producing strain *Komagataeibacter nataicola* RZS01. *Sci. Rep.* **7**(1), 1–8 (2017)
67. Zhong, H., Mirkovic, T., Scholtes, G.D.: Nanocrystal synthesis. *Comprehensive Nanoscience and Technology*, vol. 5. Academic Press, Amsterdam, The Netherlands, pp. 153–201 (2011). <https://doi.org/10.1016/b978-0-12-374396-1.00051-9>

Connecting Pathway Errors in the Insulin Signaling Cascade: The Molecular Link to Inflammation, Obesity, Cancer, and Alzheimer’s Disease



Yessica J. Sosa, Harolin M. Sosa, Victor A. Epiter-Smith,
Gemma R. Topaz and Kimberly A. Stieglitz

Abstract Insulin resistance is characterized by molecular defects in the insulin-signaling pathway. Such defects disrupt cellular homeostasis and impede normal biochemical response. The mechanistic obstruction of biomolecules in the pathway leads to a number of health consequences that are grouped into a cluster of illnesses widely known as “metabolic syndrome” which creates abnormal health states of chronic condition like heart disease, diabetes, cancer, and Alzheimer’s disease, a type of dementia also known as “diabetes type 3,” which all have a profound effect and greatly impact the overall health. The interplay of major pathways leading to glucose homeostasis and energy production is explored. Molecular docking is utilized to understand possible intermolecular forces between key molecules in the signaling pathways. Emphasis is placed on the major components of insulin signaling, especially on how individual protein molecules of the pathways are interacting with each other in the signaling cascade. The relationship between the respective diseases and the signaling cascades is explored. Molecular links in the insulin pathway will be explored in detail, in order to correlate major mechanisms that lead to insulin resistance and related pathological conditions.

Keywords Insulin pathway · Insulin resistance · Hyperglycemia · Obesity · Alzheimer’s disease · Insulin-signaling pathway · Inflammation · Dementia · Diabetes

Y. J. Sosa · H. M. Sosa · V. A. Epiter-Smith · K. A. Stieglitz (✉)
STEM Biotechnology Division, Roxbury Community College, Boston, USA
e-mail: kastieglitz@rcc.mass.edu

G. R. Topaz
Department of Biology, College of Arts & Sciences, Boston University, Boston, USA

K. A. Stieglitz
Department of Chemistry, College of Arts & Sciences, Boston University, Boston, USA

Abbreviations

4EBP1	Eukaryotic translation initiation factor 4E-binding protein 1
AD	Alzheimer's disease
Akt	Protein kinase B (PKB)
APP	Amyloid precursor protein
APS	Adaptor protein with pleckstrin homology
AS160	TBC1 domain family member 4 (TBC1D4)
A β	Amyloid beta
BAD	BCL2 associated agonist of cell death
C3G	Cyanidin 3-glucoside
CAP	Cbl-associated protein
Cbl	Cas-Br-M ecotropic retroviral transforming sequence homologue
CrK	Adapter molecule CrK (proto-oncogene c-Crk)
elk1	ETS like-1 protein Elk-1
eNOS	Endothelial NO synthase
ERK	Extracellular regulated kinase
ET-1	Endothelin-1
FFAs	Free fatty acids
FOXO	Forkhead box O
GAP	GTPase-activating protein
GEF	Guanine nucleotide exchange factor
GLUT4	Glucose transporter type 4 (SLC2A4)
GRB10	Growth factor receptor-bound protein 10; insulin receptor-binding protein Grb-IR
Grb2	Growth factor receptor-bound protein 2
GSK-3	Glycogen synthase kinase 3
GSK-3 β kinase	Glycogen synthase kinase 3 beta
IDE	Insulin degrading enzyme
IKK	I κ B kinase
IKK- β	I κ B kinase- β (inhibitor of nuclear transcription factor kappa-B kinase subunit beta)
IR	Insulin receptor
IRS	Insulin receptor substrate
JNK	c-jun N-terminal kinases
L803-mts	Selective peptide inhibitor of glycogen synthase kinase-3 (GSK-3)
MAPK	Mitogen-activated protein kinase
MAP2K	Mitogen-activated protein kinase kinase
MAP3K	Mitogen-activated protein kinase kinase kinase
MCP-1	Monocyte chemoattractant protein-1
MEK	MAPK and ERK kinases
MIP-1	Macrophage inflammatory protein 1
Mnk	Mitogen-activated protein kinase interacting protein kinase
mTOR	Mammalian target of rapamycin

NF- κ B	Nuclear factor kappa-light-chain-enhancer of activated B cells
NFT	Neurofibrillary tangles
NO	Nitric oxide
PKC	Protein kinase C
PKD-1	Pyruvate dehydrogenase lipoamide kinase isozyme 1
PI3K	Phosphoinositide 3-kinase (phosphatidylinositol 3 kinase)
PIP ₂	Phosphatidylinositol 4,5-bisphosphate
PIP ₃	Phosphatidylinositol-trisphosphate
PKC	Protein kinase C
POS	Polycystic ovarian syndrome
PPAR- γ	Thiazolidinedione family of Insulin-sensitizing peroxisome proliferator-activated receptor gamma
PTEN	Phosphatase and tensin homolog
PTP1B	Protein-tyrosine phosphatase 1B
Raf	Raf kinase family member (rapidly accelerated fibrosarcoma); RAF proto-oncogene serine/threonine-protein kinase
Ras	Ras GTPase
ROS	Reactive oxygen species
RSK	Ribosomal S6 kinase
RTK	Receptor tyrosine kinase
S6K	Ribosomal protein S6 kinase beta-1
Shc	Src-homology-2-containing protein
SHP2	Tyrosyl phosphatase
SOS	Guanyl nucleotide exchange factor son-of-sevenless
STZ	Streptozotocin
T2DM	Type 2 diabetes mellitus
TC10	Ras homologue gene family, member Q (ARHQ)
TLR	Toll-like receptor
TLR4	Toll-like receptor 4
TNF	Tumor necrosis factor
TNF- α	Tumor necrosis factor- α
TSC	Tuberous sclerosis 1
TZD	Thiazolidinediones

1 Introduction

1.1 Pathophysiology of Insulin Resistance and Resulting Comorbidities

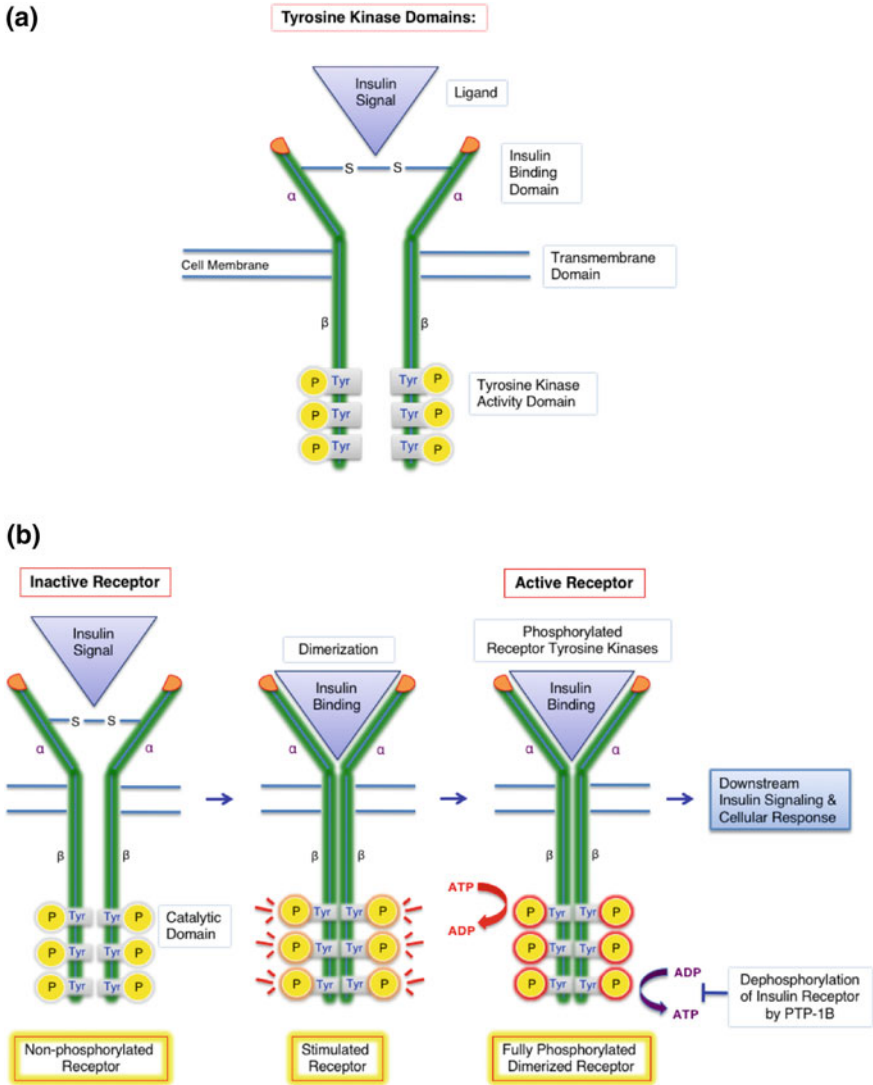
It is well known that the insulin pathway is disrupted by many of the pathological avenues that yield to insulin resistance, and that the resulting biochemical conditions create a direct path towards the development of major health risks with acute,

chronic, and often fatal potential [1, 2]. Insulin resistance is a central physiological defect where normal insulin signaling is disrupted by impaired biochemical pathways that control blood glucose levels [3, 4]. By definition, insulin resistance is a defect in signal transduction [5, 6]. Any step in the biochemical pathway involved in glycemic control has the propensity of developing major biochemical defects that fall under the metabolic syndrome umbrella, also widely known as “insulin resistance syndrome” [7–9]. The constellation of disorders under this umbrella includes hyperglycemia, hypertension, dyslipidemia, and obesity [9–12]. These insulin resistance-associated disorders create debilitating consequences in the overall health due to the development of major chronic health conditions that sabotage the overall health, such as cardiovascular disease [13, 14] diabetes [3, 8, 9], cancer [15–19], and neurodegeneration [20–23]; among other disorders like polycystic ovarian syndrome (POS) [17].

The mitogenic and metabolic disturbances incurred by the biochemical insults in the insulin pathway are affected by states of hyperinsulinaemia, glucose intolerance, oxidative stress, lipid accumulation, and pro-inflammatory states, which manifest in the multifactorial pathologic condition of insulin resistance [9, 12, 19]. There is ample evidence that indicates a clear link between circulating glucose, insulin, free fatty acids (FFAs) [12, 24, 25], reactive oxygen species (ROS) [1, 26], cytokines [26, 27], and insulin resistance. In addition, biomarkers like Tau and A β (amyloid beta) proteins in the brain play a significant role in the development of insulin resistance and the onset of Alzheimer’s disease, a provocative link in science which offers potential treatments in an often-critical mortal combat [20, 21, 28–30]. In general, the insulin-signaling pathway and its multi-array of pathological conditions serve as a platform for the study of molecular intermediates and interactions involved in the molecular defects of the interrelated insulin-signaling cascades. Such knowledge is substantial in science in order to improve the health and well-being of affected individuals and create better therapeutics which could stabilize reckless molecular interactions.

1.2 The Insulin Receptor and the Insulin Signaling Cascade

By ameliorating and targeting the molecules involved in the disease process, the disease states can be controlled chemically, which opens an avenue of possibilities in the field of biochemistry and pharmacology in regards to the treatment and multifactorial progeny of pathological insulin resistance conditions. Under normal physiological conditions, the insulin cascade proceeds uneventful, with turning on and off situations proceeding in a synchronized, canonical/established fashion. Insulin, the key that opens the insulin receptor device in the cell membrane, allows glucose to enter the cell. In turn, the insulin receptor is the gate that, once opened, sends the insulin signal to downstream effectors in the cell with the aim of lowering blood glucose levels. A picture of the insulin receptor is in Fig. 1a, and a picture in its inactive and reactive forms is depicted in Fig. 1b. Insulin primarily starts the



pathway by binding to the alpha subunit of the insulin receptor, which triggers the tyrosine kinase activity of the beta subunit and causes the phosphorylation of specific enzymes in a signaling kinase cascade of events [7, 12, 31] (Fig. 1a, b). The signaling cascade ultimately turns on a number of mechanisms that lead to the consumption and utilization of glucose. This process eventually lowers blood glucose levels and avoids cell starvation by allowing glucose to enter the cell.

The beta cells in the pancreas, also known as islets of Langerhans, play a vital role in glucose metabolism. When blood glucose levels are high, the beta cells react by releasing insulin, whose job is also to offset excess fuel and maintain a constant

◀**Fig. 1** **a** Schematic diagram of the insulin receptor. The insulin molecule is a ligand that activates the insulin receptor. The insulin receptor is composed of two alpha subunits and two beta subunits joined by disulfide bonds [3]. The alpha subunit is on the cell exterior and contains binding sites for the insulin molecule. Insulin turns on the cascade by adhering to the insulin binding domain of the insulin receptor, which triggers the intrinsic tyrosine kinase activity of the beta subunit. The beta subunit has a transmembrane domain that extends to the cytosol. The insulin molecule generates a signal that is transferred to the catalytic domain of the receptor when the receptor is phosphorylated. Ultimately, this causes the phosphorylation of specific enzymes in a signaling kinase cascade of events. **b** Schematic Representation of Receptor Tyrosine Kinase (RTK) Activity. The insulin receptor has two tyrosine kinase receptors made by two alpha subunits on the extracellular compartment of the cell, and two beta subunits embedded on the cytosol connected by disulfide bonds. The heterotetrameric protein is a highway for insulin passage across the cell membrane. Insulin signal transmission starts when the insulin ligand binds the alpha subunit on the cell exterior, causing beta subunits to cross-phosphorylate each other on specific tyrosine residues of the transmembrane protein. This autophosphorylation activates the insulin receptor and induces a conformational change of the beta subunit, which catalyze the activation of subsequent protein kinases responsible for propagating the insulin signal to the target cell in a cascade fashion of events [3, 6, 10, 25]

state of normoglycemia. However, with progressive decline in function, these pancreatic islets slowly lose the battle against insulin resistance by compromising the overall glucose homeostasis. The pancreatic islets continue to release insulin without receiving a signal to stop while hyperglycemia keeps increasing. In the insulin resistant state, the surge of insulin secretion by the pancreas is unable to unlock the cells to allow glucose utilization, which could lower blood glucose levels. In a desperate attempt to revert hyperglycemia, glucose knocks at the door of the insulin receptors to get into the cell, but insulin is unable to open the gate because the passage is blocked by a likely defect in the insulin signaling mechanism. Consequently, the insulin receptor remains closed, and insulin keeps accumulating outside of the cell in an effort to compensate hyperglycemia. As a result, hyperinsulinaemia builds up without being able to relay the message to the cell interior. This blockage is known as insulin resistance [15, 24, 32].

1.3 Insulin Resistance and Cell Starvation

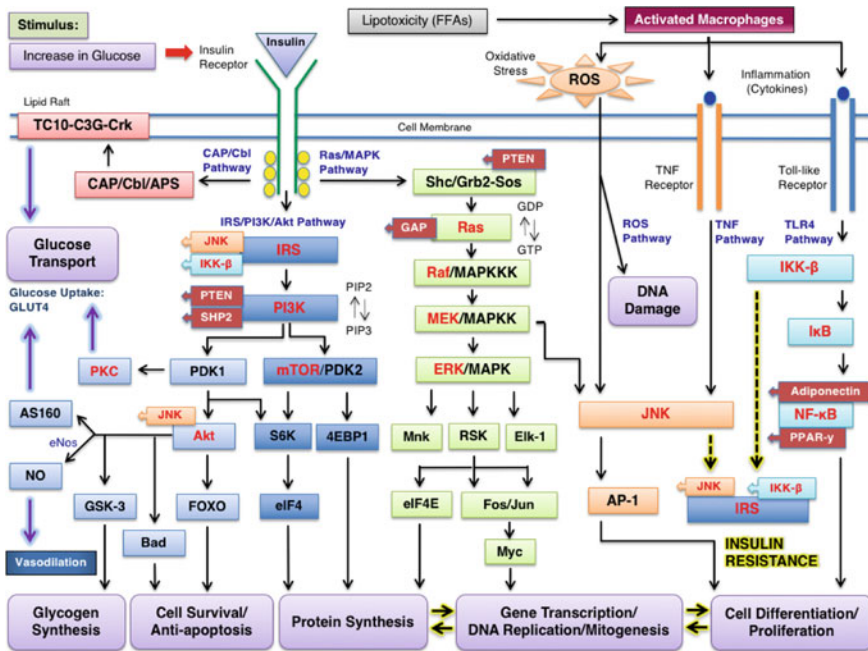
With insulin resistance, glucose cannot get past unresponsive receptors, and an adverse effect on the cell is created whereby the cell cannot consume glucose. Thus, hyperglycemia and hyperinsulinaemia continue to escalate in an uncontrolled fashion on the cell exterior. Insulin is unable to enter the cell and pass on the message that there is excess blood glucose outside of the cell waiting to be consumed by the cell. Therefore, cells starve when the insulin signal is not transduced to the interior of the cell and insulin resistance remains rampant [15, 24, 32]. This condition can be treated with insulin sensitizers like Thiazolidinediones (TZD), which are anti-diabetic agents which aim to improve receptor sensitivity to insulin by enhancing insulin action on the cell [8, 14, 33–35]. For example, a recent study

proposing a link between insulin resistance and neuroinflammation suggests that Rosiglitazone and Pioglitazone, two TZDs designed to treat Type 2 Diabetes Mellitus (T2DM), are therapeutic drugs that target neurodegeneration, improve insulin receptor site sensitivity, and prevent cognitive decline [20, 29, 36].

As it is formally known/gradually accepted, T2DM is a chronic systemic disease widely studied in the broad spectrum of associated metabolic diseases that is characterized by impaired B-cell function and insulin resistance [17, 24, 37, 38]. While Type 1 Diabetes is mainly a disease in which pancreatic islets become dysfunctional, Type 2 Diabetes is a disease characterized by insulin resistance and the resulting biochemical defects of the pathway [5, 12, 17, 24]. As the premise states, aberrations in the insulin circuitry create intracellular blockages with major repercussions to the normal flow of insulin signal transmission. For example, deregulation of inhibitory signaling pathways creates an avenue towards various malignancies that require alteration in therapy [39, 40]. More specifically, if the negative regulator of PI3K signaling, tumor suppressor PTEN, is mutated or even deleted, it can trigger unrestrained signaling events along the PI3K pathway which could render cancer cells insensitive to the current therapeutic regimen [40]. Alternative approaches to treatment need to be sought in light of such functional disorder to reactivate PTEN activity and halt tumor progression [39]. The diagrams depicted in Figs. 2 and 3 relate the molecular link of insulin resistance to the major pathological consequences of interrelated illnesses.

1.4 Insulin Resistance: Downregulation of the Insulin Signaling Pathway

Opposing mechanisms are important for a stable, homeostatic, biochemically-regulated environment. The “molecular switch” of the insulin resistance interplay is turned on until counter-regulatory mechanisms intercept the pathway with the purpose of switching the mechanism off (Fig. 3) [41]. Maintaining a moderate molecular climate in the cell, which aims to regulate euglycemia, is imperative for energy homeostasis. A chemical imbalance in the system could lead to the comorbid conditions that create the renowned insulin syndrome that is so challenging to treat. For example, when compensatory mechanisms of the insulin pathway fail to correct aberrant defects on the pathway, the consequences of hyperglycemia and hyperinsulinaemia, leading to inflammation [1, 23], oxidative stress [19, 42], DNA damage, proliferative states [15, 19, 43], and signs of dementia [20, 28] may be detrimental (Fig. 2, 3, and 4). The integrated understanding about insulin signaling and its interrelated pathways can facilitate further research to continue investigating selected mechanisms in order to target specific molecular disruptions that lead to insulin resistance and its associated and multifaceted pathological ailments.



1.5 Insulin Signaling Pathway: Up Regulation of Insulin Transmission Mechanisms

The insulin receptor is a highway for insulin passage across the cell membrane responsible for insulin signal transmission. The heterotetrameric protein is composed of two alpha subunits located on the extracellular compartment of the cell and two beta subunits embedded in the cytosol. Both glycoprotein subunits create a transmembrane dimer united by disulfide bonds [1, 31, 38]. The alpha subunit contains the hormone-binding domain and the beta subunit contains the ATP-binding and tyrosine kinase domain (Fig. 1a) [12, 27]. The whole receptor unit functions as a receptor tyrosine kinase (RTK), which is a specialized enzyme that transfers phosphate groups from ATP to tyrosine residues of intermediate substrates. Once the insulin ligand binds the alpha chain of the insulin receptor, it causes the catalytic domain of the receptor to be activated. The beta subunits dimerize and undergo a conformational change on the cytoplasmic domain, which facilitates autophosphorylation and subsequent activation of the receptor kinase (Fig. 1b) [7, 44]. The intrinsic cross-phosphorylation of tyrosine residues on the insulin receptor trigger other enzymes along the pathway called kinases to further propagate the insulin signal to target cells on a cascade fashion of events [44].

◀**Fig. 2** Insulin signaling pathway, inflammatory mediators, obesity and cancer. Three major intracellular pathways emanate from the activation of the insulin receptor: the Ras/MAPK Pathway, the IRS/PI3K/Akt Pathway, and the CAP/Cbl Pathway (Fig. 2). The three-protein kinase signaling systems propagate the signal in their respective chemical way. As illustrated in Fig. 2, the Ras/MAPK pathway conveys the insulin signal to adaptor protein, Shc. Shc recruits Grb2, SOS, Ras, and Raf, which activates MAPK via MEK. MAPK is a major contributor to the mitogenic part of the process, which allows expression of genes for cell differentiation and growth by controlling gene transcription and cellular proliferation [3, 6, 15]. Another set of adaptor proteins in the insulin pathway leads to a different signaling transduction mechanism, the IRS/PI3K/Akt pathway. In this specific pathway, IRS protein activates a PI3K cascade that phosphorylates kinase enzymes PDK1 and mTOR, which further activate effectors: S6 K, 4EBP1, Akt, and PKC, respectively (Fig. 2). Akt is a major downstream receptor substrate which is responsible for the activation of the following intracellular mediators: FOXO, BAD, GSK-3, and AS160. PI3K ultimately mediates glycogen synthesis via GSK-3 inactivation and facilitates transport of glucose into the cell via AS160 and PKC, which complies with the metabolic part of the process that lowers blood glucose levels [6, 10, 15]. The downstream effectors of PI3K, FOXO and BAD, comply with the cell survival part of the process by inhibiting cells from apoptosis or programmed cell death [4, 14]. A third mechanism, which emanates from the insulin receptor, is the CAP/Cbl pathway. In this specific pathway, adaptor proteins, APS and Cbl, are recruited to exert glucose control in the cell by promoting GLUT4 translocation [3, 6, 25]. The three pathways diverge from the insulin receptor and are activated independently in order to control and give precision to the pleiotropic actions of insulin [14, 15, 22]. In summary, insulin signaling activates several chain reactions that yield a diverse number of responses from the cell [6]. Upon high levels of glucose in the blood, the pancreas releases insulin to counteract the surge of glucose and maintain homeostasis. Insulin binds the alpha subunit of the insulin receptor on beta cells of the pancreas. Binding of the insulin-ligand to the alpha subunit triggers the beta subunit to activate tyrosine kinase and cause phosphorylation of other enzymes in a signaling kinase cascade of events. Adaptor protein Shc recruits Grb2, SOS, Ras, and Raf, which activate MAPK. MAPK allows expression of genes for cell differentiation and growth. Another set of adaptor proteins in the insulin pathway leads to a different signaling transduction mechanism. The IRS protein activates a PI3K cascade that phosphorylates an array of enzymes that ultimately stimulate glycogen synthesis and transport of glucose into the cell. There is yet another system governed by another set of proteins, APS/Cbl, which also exerts glucose transport control, but by a different pathway. Thus, ligand-binding to designated insulin receptor activates several chain reactions which yield a diverse number of responses from the cell [6]. Solid black line arrows signify pathway stimulation, and rectangular block arrows represent insulin signaling regulators which turn-off the normal response to insulin, or inhibit the insulin-signaling effect

2 Insulin Signaling Cascades

2.1 *The Three-Protein Kinase Signaling Systems*

Three major intracellular pathways emanate from the activation of the insulin receptor: the Ras/MAPK Pathway, the IRS/PI3K/Akt Pathway, and the CAP/Cbl Pathway (Fig. 2). The three-protein kinase signaling systems propagate the signal uniquely in their respective and associated biochemistry.

1. The Ras/MAPK Pathway

As illustrated in Fig. 2, the Ras/MAPK pathway conveys the insulin signal to adaptor protein, Shc. Shc recruits Grb2, SOS, Ras, and Raf, which activate MAPK

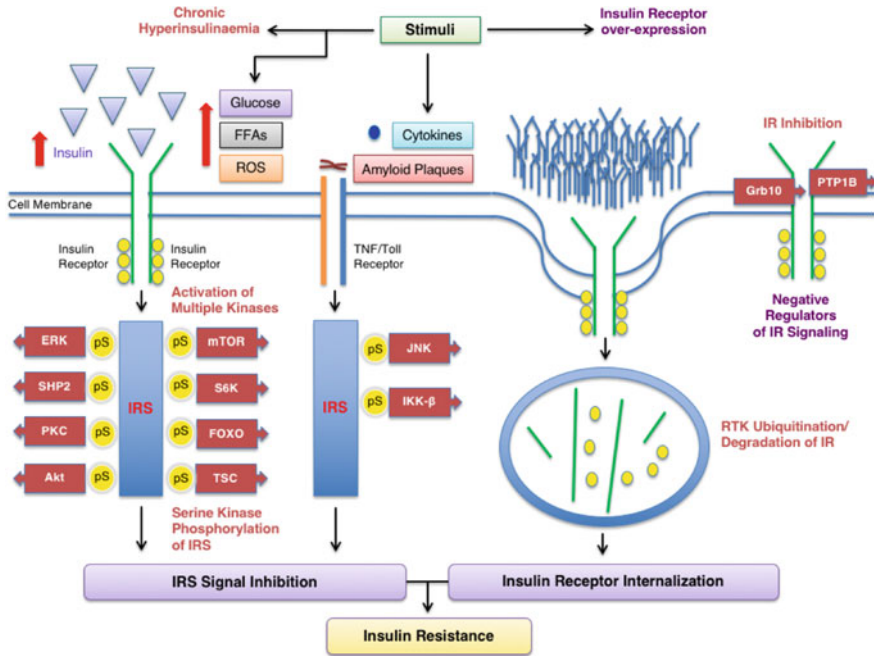


Fig. 3 Inhibitory mechanisms in insulin resistance. Schematic diagram of inhibitory mechanisms in insulin resistance, and resulting effect of insulin resistance. High levels of glucose call for cellular mediators that interact with the IRS protein and signal a high insulin level, which exhibits an inhibitory effect. As a result, insulin signal transduction is blocked. Furthermore, the insulin receptor is internalized when its receptor is bombarded with excess signaling. These biochemical culprits give rise to insulin resistance and its pathological consequences. Rectangular block arrows exemplify the down-regulators or inhibitors of insulin signaling that interrupt normal effector functioning and turn off normal cellular response triggered by the insulin signaling cascade

via MEK. MAPK is a major contributor to the mitogenic part of the process, which allows expression of genes for cell differentiation and growth by controlling gene transcription and cellular proliferation [7, 12, 17].

2. The IRS/PI3K/Akt Pathway

Another set of adaptor proteins in the insulin pathway lead to a different signaling transduction mechanism, the PI3K/Akt pathway. In this specific pathway, IRS protein activates a PI3K cascade that phosphorylates kinase enzymes, PDK-1 and mTOR, which further activate effectors: S6 K, 4EBP1, Akt, and PKC, respectively (Fig. 2). Akt is a major downstream receptor substrate which is responsible for the activation of the following intracellular mediators: FOXO, BAD, GSK-3, and AS160. PI3K ultimately mediates glycogen synthesis via GSK-3 inactivation and facilitates transport of glucose into the cell via AS160 and PKC, which complies with the metabolic part of the process that lowers blood glucose levels [7, 17, 38].

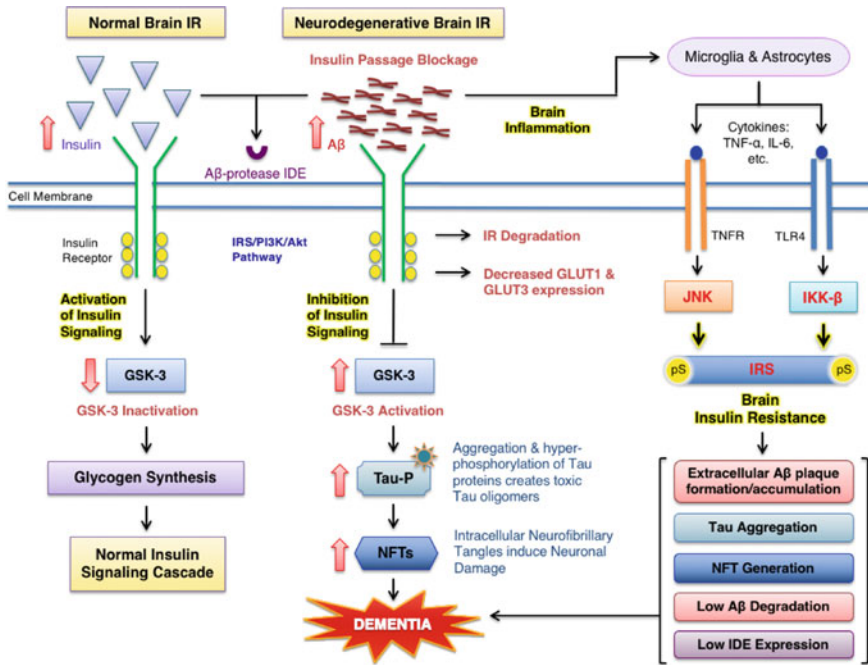


Fig. 4 Insulin signaling pathway leading to dementia. Schematic diagram illustrating the insulin signaling pathway leading to dementia. There is cross reactivity between the insulin receptor and the amyloid beta molecules which prevent insulin from binding. In hyperinsulinaemia, the amyloid beta protease also known as Insulin Degrading Enzyme (IDE) (*upper left*) degrades excess insulin to balance normal insulin levels in the blood. IDE is unable to degrade amyloid beta when mutated causing accumulation of amyloid beta molecules. Under normal conditions, insulin activates the normal insulin pathway to proceed, which inactivates GSK-3 and causes glycogen synthesis to occur. Note that inactivation of GSK-3 prevents tau phosphorylation as shown in the center of the figure, where activated GSK-3 hyperphosphorylates Tau leading to Neurofibrillary Tangles (NFTs) and dementia. As amyloid beta accumulates, there is brain inflammation and brain cells produce cytokines which trigger TNF and TLR4 receptors, activating JNK and IKK-beta, receptively phosphorylating IRS, causing insulin resistance (*right side of figure*). This leads to amyloid beta accumulation, plaque formation, Tau aggregation, NFT generation and even lower IDE expression

The downstream effectors of PI3K, FOXO and BAD, facilitate cell survival by inhibiting cells from apoptosis or programmed cell death [3, 45].

3. The CAP/Cbl Pathway

A third mechanism, which emanates from the insulin receptor, is the CAP/Cbl pathway. In this specific pathway, adaptor proteins, APS and Cbl, are recruited to exert glucose control in the cell by promoting GLUT4 translocation [12, 31, 38]. The three pathways diverge from the insulin receptor and are activated independently in order to control and give precision to the pleiotropic actions of insulin [3, 11, 17].

2.2 *The Insulin Transduction Mechanism*

The insulin transduction mechanism governs a diverse array of cellular effects. For example, one substrate within the system can regulate multiple functions within the cell, like Akt [46]. As illustrated in Fig. 2, Akt is a pleiotropic molecule that directs the path of the insulin signal and culminates in the following respective physiological responses: glycogen synthesis activation via induced-glycogen synthase kinase 3 (GSK-3) phosphorylation and inactivation [17, 38, 47], inhibition of apoptosis or programmed cell death via effectors FOXO and BAD [3, 45, 48], vasodilation through Nitric Oxide (NO) release by phosphorylation of endothelial NO synthase (eNOS) [12, 14, 30], and glucose transport via AS160 and PKC [7, 17]. In general, the PI3K/Akt pathway plays a major role in protein synthesis, cell survival and anti-apoptotic events, cellular growth and the overall control of cellular metabolism [7, 17, 37, 41, 49], including cardiovascular health [27, 41]. Any defect in this system could easily lead to metabolic disease and the associated insulin resistance syndrome [46]. In fact, insulin resistance is a risk factor to many of the other pathologies that characterize the associated metabolic diseases [9].

Akt, also known as protein kinase B (PKB), is a member of the serine/threonine protein kinase family that is involved in cellular metabolism, growth, proliferation and survival. It exists in three isoforms: Akt1, Akt2 and Akt3, and it is activated at two different sites, T308 and S473 [32, 40]. The three-dimensional structure of Akt1 has been solved and was used in docking studies for this review [50]. Additionally, the three-dimensional structure of the protein, GSK-3 β kinase, has also been solved and used in docking studies for this review [51]. The GSK-3 β kinase is a regulatory protein where inhibition of molecules can be added to produce a therapeutic approach for drugs in neurodegenerative diseases, Type 2 Diabetes, and cancer. GSK-3 β is a serine threonine protein kinase that is a substrate of the PI3K/Akt pathway. This is also important for docking because Akt directly binds to the β -isoform of GSK-3, inhibits its activity and, in turn, promotes glycogen synthesis and neuronal survival [52] (Figs. 2 and 4). In addition, the molecular intermediate, Akt, activates kinases (AS160) that facilitate glucose uptake via GLUT4 translocation, which prevent cell starvation. Using the ZDOCK program, the Akt protein was docked as a receptor [50] with the GSK-3 β as ligand [51]. As shown in Fig. 5a, Akt1 is colored orange. Molecular docking suggests interactions with dimer, GSK-3, where monomer A is yellow and monomer B is magenta (Fig. 5a). Examples of GSK-3 dimer residues and Akt1 monomer residues—which are predicted to interact—are shown in Fig. 5b. Generally, Akt acts as a negative regulator of GSK-3, whereas, Akt inhibits GSK-3 activity and precipitates insulin signaling (Fig. 2). A derailment in this activity down-regulates insulin signaling, but precipitates neuronal apoptosis and signs of dementia, as detailed in Fig. 4 [52, 53].

As it is well-known, insulin resistance is a molecular impairment in the insulin transduction circuitry, which blocks the normal pathway of insulin [3, 24, 32, 55]. When the insulin signal pathway is interrupted, the insulin cascade does not turn on,

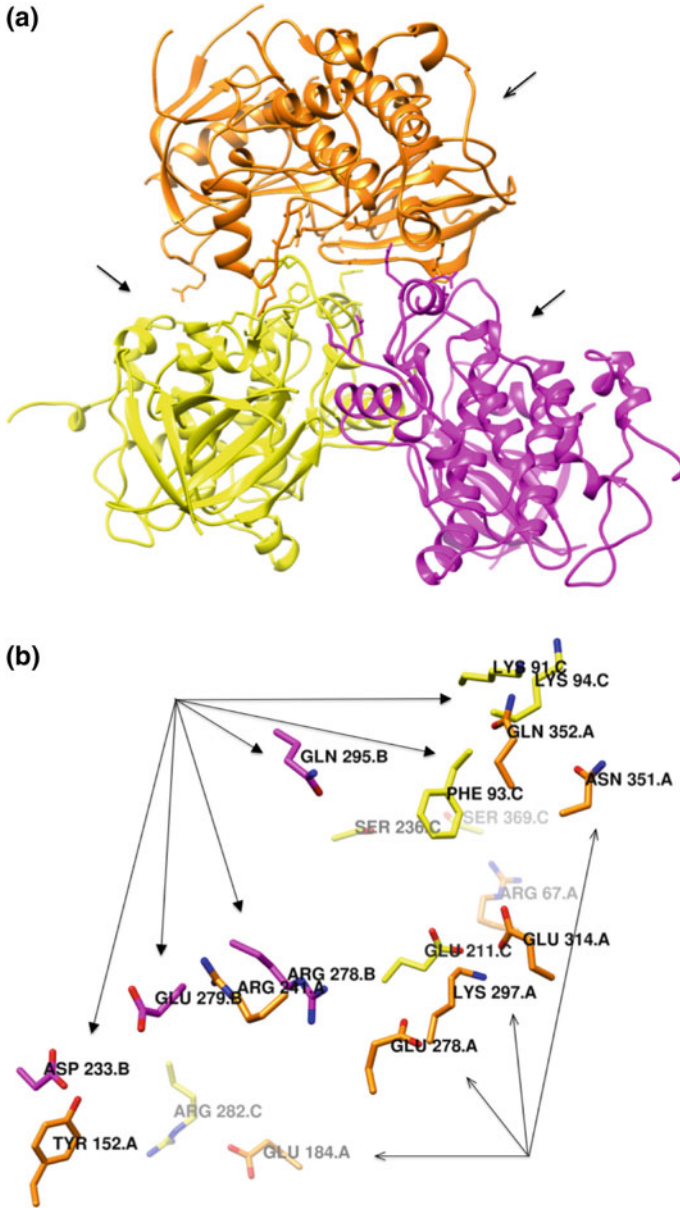


Fig. 5 a The predicted interaction between Akt1 and GSK-3 Dimer. Akt1 monomer (*top, open arrow*) PDB code 3O96 [49] docked with GSK-3 dimer (*bottom left and right, closed arrows*) PDB code 1Q3 W [50] using ZDOCK [54]. b Close-up of the Interface between Akt and GSK-3. Docking of Akt monomer (*right, open arrows*) and GSK-3 dimer (*left, closed arrows*) shows multiple interactions including potential hydrogen bonding and hydrophobic interactions between the two proteins

and insulin cannot deliver its message to effector cells to lower blood glucose levels. The insulin receptor becomes desensitized to the receptor ligand and results in hyperglycemia, hyperinsulinaemia, and overt diabetes [15, 32]. Beta cells in the pancreas try to overcome hyperglycemia by producing more insulin until they become exhausted by the workload of constant insulin production that does not exert an effect on the cell. Defects in tissue sensitivity to insulin and decreased insulin secretion by pancreatic B-cells are main characteristics that define Type 2 Diabetes Mellitus (T2DM) [17, 24, 35, 37, 38]. At this point, the insulin transduction pathways start losing their battle against the chronic metabolic syndrome and resulting diabetes due to failing compensatory mechanisms [15]. The main focus of pharmacological therapy in the mainstream of insulin resistance is to target the intracellular defects that are causing its associated intra-molecular derangement. The antidiabetic agent, Thiazolidinedione (TZD), for example, targets insulin resistance in the skeletal muscle by improving glucose transport, glycogen synthesis, and redistribution of fat [24]. In addition, GSK-3 inhibitors, like L803-mts, have shown to reduce neurotoxicity and improve cognition by targeting key kinases of the PI3K-Akt pathway (GSK-3) which aim to improve insulin signaling [52, 55]. By understanding the molecular interactions of specific kinases of the insulin cascade and their substrates, better designs against the aberrant activities that compound the insulin signaling system can be designed and developed [55].

2.3 The Role of Insulin as a Regulator, Mediator, and Modulator in the PI3K/Akt and CAP/Cbl Pathways

Insulin is an anabolic hormone that promotes the synthesis of vital macromolecules of metabolism, which include glycogen, carbohydrates, proteins, and lipids [2, 6, 12, 31]. In order to create these crucial biomolecules, insulin exerts a tight control in the passage of glucose into the cell. For example, if blood glucose is high, insulin turns on the signaling transduction pathway that leads to glucose uptake, or glucose influx into the cell, which leads to blood glucose reduction. Consequently, the PI3K/Akt pathway and the CAP/Cbl pathway are activated by insulin signaling mechanisms. Therefore, when the insulin signal turns on the IRS protein, it finds docking molecules in the PI3K/Akt intracellular pathway. PKC is recruited to activate the translocation of GLUT4 from the intracellular space to the plasma membrane and induces the transport of glucose into the cell, which lowers blood glucose levels [31, 41] (Fig. 2). Likewise, the intracellular signaling protein, TC10, from the CAP/Cbl pathway, triggers membrane translocation of GLUT4 in an effort to increase glucose uptake and decrease hyperglycemia [16, 17]. In general, glucose transport is the rate-limiting step in peripheral insulin-sensitive tissues like skeletal muscle and liver [6, 24, 56, 57]. A biochemical defect such as mutations in GLUT4, which is the molecule that transports glucose across the cell membrane in response to insulin, is a major contributor to insulin resistance [2, 31, 56]. Additionally, a molecular defect of glucose transporters in the brain, GLUT1 and GLUT3, greatly

affects brain glucose metabolism and eventually leads to the neurodegeneration characteristic of Alzheimer's Disease (AD) (Fig. 4) [58]. The antibiotic compound, streptozotocin (STZ), has been used in mouse models of diabetes because it destroys the insulin-producing beta cells of the pancreas and are therefore capable of demonstrating the major pathways leading to insulin resistance, diabetes, and states of dementia [58, 59].

Any defect in the proteins involved in the insulin cascade can have major repercussions in cellular homeostasis and cause major disturbances which may lead to the development of the diverse conditions that fall under the insulin resistance syndrome [1, 2, 39]. Generally, impaired glucose transporters, B-cell dysfunction, and defective insulin signaling transductions are known to cause dysregulation of glucose homeostasis that lead to the onset of Type 2 Diabetes mellitus [2, 24]. Furthermore, advances with the drug, Wortmannin, which blocks glucose uptake and GLUT4 translocation, have proven that PI3K is an important modulator of insulin signaling which blocks most of insulin actions [11, 31, 40, 60]. Evidence also shows that PI3K inhibitors, in general, affect the Akt and PKC substrates from the PI3K/Akt pathway by interfering with glucose transport and causing insulin resistance [6]. However, the pathway interference can be compensated by a second signal, the CAP/Cbl pathway, although research also suggests that both signals are necessary for proper metabolic maintenance [6, 31].

The CAP/Cbl pathway is a separate insulin-signaling pathway independent of PI3K and MAPK. This pathway affects a group of lipid raft molecules embedded in the plasma membrane (Crk, C3G, TC10), which directly stimulates glucose transporters (GLUT4) [11]. GLUT4 transporters facilitate glucose entry into the cell by bringing glucose molecules from the cell exterior to the cell interior in response to insulin signaling and facilitative diffusion. They metabolize glucose according to energy needs, and are recycled within the cell by means of proteolytic cleavage and vesicle sequestration [11]. A mutated GLUT4 transporter could greatly affect glucose translocation and cause a major impairment in glucose homeostasis which could ultimately lead to insulin resistance and diabetes (refer to Fig. 2) [31]. The PI3K/Akt and CAP/Cbl pathways intersect atypical PKC, elucidating a point of convergence between these two insulin pathways [31].

2.4 The Role of Insulin as a Mediator in Ras/MAPK Signaling

A parallel pathway to PI3K is the Ras/MAPK pathway, and is vital for major cellular processes, like gene expression, cell differentiation, proliferation, and cell growth. Once the pathway is activated, the insulin receptor autophosphorylates in the inner compartment of the cell and attracts SH2-containing proteins, which are adaptor proteins that bind with high affinity to phospho-tyrosine residues (pTyr), and bind less to phospho-serine (pSer) and phospho-threonine (pThr) residues [3].

The activated receptor phosphorylates adaptor protein Shc and interacts with Grb2. Grb2 is another adaptor protein that lacks enzymatic activity, yet is able to bind phosphorylated insulin receptor tyrosine kinase and cause SOS, a guanine nucleotide exchange factor (GEF) for Ras, to activate monomeric G protein Ras, a GTPase enzyme [39, 61]. SOS, another adaptor protein, binds to Grb2, in order to accomplish this task. The Grb2-SOS complex activates Ras GTPases by releasing its bound GDP and exchanging it with GTP. In its GTP-bound state, Ras is able to relay the signal to the transcriptional apparatus of the nucleus and activate many effector proteins within the cell [41, 62].

The Ras/MAPK cascade is triggered by the activation of Ras [41, 60]. As shown in Fig. 2, Ras-GTP activates the kinase cascade, which unfolds in the following sequence: Ras-GTP, Raf (MAPKKK) MEK (MAPKK), ERK (MAPK). Once activated, MAPK migrates from the cytosol to the nucleus of the cell and transduces the signal to the following molecular intermediates: Mnk, RSK, and elk1, which turn on early genes like eIF4E, cfos, cjun, and cmc, respectively (Fig. 2). The polypeptide, eIF4E, is a eukaryotic translation initiation factor that facilitates translation of mRNA messages into protein with precise cellular instructions, and the following transcription factors: cfos, cjun, and cmc, are potent mitogens that increase gene expression and facilitate the synthesis of proteins necessary to replicate DNA and promote mitogenesis. In summary, when insulin activates the Ras/MAPK signaling pathway, the result is an increase in protein synthesis that supports gene expression, cell proliferation and differentiation.

Of additional note is the commitment of the Ras/MAPK pathway to angiogenesis and vascular stability. For example, MAPK stimulates angiogenesis through the expression of genes that build blood vessels [61, 63]. Activated MAPK stimulates the release of endothelin-1 (ET-1), which promotes vasoconstriction of endothelial cells. Conversely, Akt promotes vascular relaxation by producing NO through eNos release [30]. Therefore, the insulin pathway has cardiac implications with respect to the vascular effects of the given pathways.

2.5 The Connection Between PI3K and CAP/Cbl

Research evidence suggests that insulin-mediated biochemical pathways work in conjunction with each other to potentiate synergistic effects of insulin. For example, PI3K activation is not enough to stimulate glucose uptake, as it has been shown in multiple experiments which target PI3-kinase. Studies show that PI3K mutants only partially stimulate GLUT4 translocation to the plasma membrane in response to insulin [6, 11, 31]. Therefore, a hypothesis has been formulated about whether another mechanism works with PI3K synergistically in order to transport glucose in and out of the cell. The CAP/Cbl Pathway also mediates glucose transport via GLUT4 translocation to the cell membrane. Studies also show that this pathway alone cannot fully drive glucose transport activity [6, 31]. This phenomenon is further explained when TC10, coupled with active mutant PI3K, restores insulin

action [11, 64]. PI3K and TC10 complement each other. These independent, but convergent pathways, work in parallel to bring about insulin-mediated effects on the cell [6, 11, 31, 49].

The insulin transduction pathway is an interrelated network of associated proteins that converge, diverge, communicate, and continue to associate biochemically. Like PI3K and TC10, MAPK and PI3K are also involved in the molecular cross-talk. For example, when inactivated IRS inhibits PI3K signaling, the MAPK pathway is activated, leading to mitogenesis, continued cell growth, and a resulting obesity [7]. Likewise, mTOR inactivation leads to MAPK activation in a PI3K-dependent manner, which proves the fact that blocking one pathway can activate the other in a feedback loop of events [40]. For example, PI3K inhibition can drive tumorigenesis by upregulation of MAPK [65, 66]. This knowledge can help develop better tactics in terms of drug development. For instance, one option is to consider pharmacologic inhibitors that target both pathways for better therapeutic effects, or drugs that target two kinases in one pathway simultaneously [40]. Some inhibitors like PI3K and Akt inhibitors should be refined to target specific isoforms in order to improve selectivity. When one inhibitor fails, another inhibitor targeting a different pathway should be readily available in order to combat toxicity, resistance, and oncogenic changes of tumor-associated cells [20, 40, 65]. More importantly, potent dual inhibitors should be readily accessible to intervene with aggressive treatment that yields promising results [40, 67].

The PI3K pathway generally governs a cell survival pathway of cell growth and expansion [43]. As shown in Fig. 2, the interaction between IRS and PI3K is critical in the signal transduction cascade to activate PDK-1 and mTOR and downstream effectors resulting in protein synthesis, gene transcription, and cell survival. Therefore, a detailed understanding of molecular interactions between IRS and PI3K is useful as a potential target for modulators of this pathway. Using the ZDOCK program [54], the IRS protein [68] was docked as a receptor with the PI3K as ligand [69]. Details of the 3-dimensional predicted interactions were analyzed in Chimera [70]. As shown in Fig. 6, the IRS dimer (blue and green) is interacting at the dimer interface with the C-terminal helix of the IRS protein. The IRS helix spans from residues Thr1081-Leu1090 and predicts along with Arg1076 of previous helix to be involved in both hydrophobic and hydrogen bonding interactions with PI3K. The crystal structure of the protein-protein complex has yet to be solved to confirm these predictions. However, the fact that there are 8 hydrogen-bonding interactions between the C-terminal helix of IRS and polar residues of PI3K is very intriguing. Current studies of protein-protein interactions of the different components of the IRS signaling pathway continue to elucidate molecular details of the interactions, which span from activation, inactivation and degradation of the proteins involved.

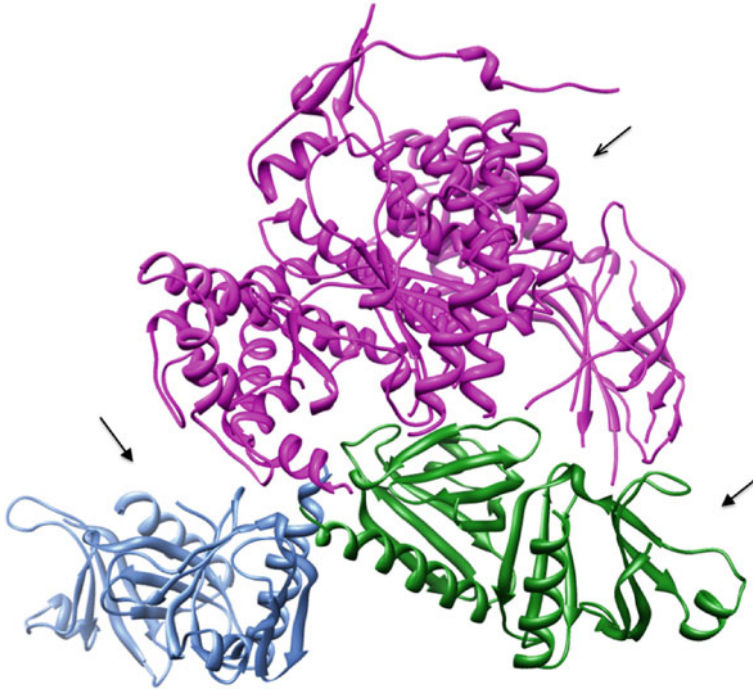


Fig. 6 The Predicted Interaction between IRS Dimer (*bottom left and right, closed arrows*) and PI3K Monomer (*top, open arrow*). Docking of IRS dimer (PDB code 1QQG [68]) with PI3K monomer (PDB code 4HVB [69]) was performed using ZDOCK [54]

3 Regulation of the Insulin Signaling Pathway

3.1 Cancer and Hyperinsulinaemia

Insulin is an anabolic hormone that promotes cell division and proliferation [19, 37]. It is well known that insulin has stimulatory functions and oncogenic properties with established links in cancer progression [15, 19, 65, 71–73]. The growth-promotion capabilities of insulin can be potentiated by states of hyperinsulinaemia [45]. For instance, in an environment of hyperinsulinaemia, there is an additional drive for committed kinases to initiate protein synthesis, cell growth, and proliferation. However, cell proliferation can be preserved even while therapeutically inhibiting one pathway because of the crosstalk among the different pathways. For example, insulin signaling via the MAPK pathway remains intact despite the PI3K pathway is inhibited [15]. Similarly, by suppressing the MAPK pathway, cell division might be inhibited, but not the metabolic actions of insulin governed by the convergent PI3K pathway [4]. Thus, a therapeutic action intended to control one pathway may actually drive tumor growth on the other, defeating the intended

action of a specific therapeutic drug. Consequently, drug therapy can be very challenging in cancer therapy as well as a variety of metabolic diseases, as previously discussed [40].

The Ras/MAPK signaling pathway plays a critical role in cancer. For example, its integrant molecule, Ras, is a critical molecule in cancer studies because of its sensitivity to be switched on or off. The Ras-GTPases act as “molecular switches,” which can be turned on and off depending on the environmental conditions of the cell [61]. For example, the signaling cascade is inactivated by the action of protein phosphatases and GTP hydrolysis, and GAP (GTPase-activating protein) is an enzyme which inactivates the Ras GTPases by catalyzing the rate of GTP hydrolysis from GTP to GDP + P [15, 61]. In turn, SOS is a GEF (Guanine Nucleotide Exchange Factor) with enzymatic-like properties, which catalyzes the guanine nucleotide exchange from GDP to GTP in monomeric Ras. Basically, GAPs keep Ras in its inactive form (Ras-GDP) while GEFs activate Ras to its active form (Ras-GTP) [61]. The activity of Ras-GTPases is tightly regulated by intrinsic enzymatic mechanisms which, when mutated, open an avenue to carcinogenesis [62].

Ras protein is a molecule that is highly expressed in cancer cells, with point mutations comprising of 30% of all human cancers [15, 61]. When insulin receptors are up-regulated, Ras enhances insulin action. Insulin receptors are normally internalized in the cell as a compensatory feedback inhibition mechanism aimed at decreasing hyperinsulinaemia and the possible dangerous hypoglycemic states [45]. Research evidence also suggests that when the PI3K pathway is suppressed, for example, in breast cancer cells, Ras/MAPK signaling takes over, and vice versa [72]. This is generated by the established crosstalk among the signaling networks, assigned by the signaling feedback loop. This is noteworthy in drug therapy, which often requires a combination of drugs like PI3K inhibitors and MAPK inhibitors that target a combination of pathways in order to restrain tumor regression [40, 74]. An example of a dual inhibitor of the PI3K and MAPK pathways, which targets the proliferation of breast cancer, is miR-564 [66]. MAPK inhibitors turn off Ras signaling downstream of Ras. Oncogenic changes or perturbations in any of the proteins involved in any corresponding insulin pathway can render cells resistant to certain cancer treatment [40]. For example, if Ras is mutated, the monomeric G protein can be fixated in its “ON” state, and if the Ras oncogene is resistant to kinase inhibitors, and tumor will progress [61]. In general, when Ras genes are overexpressed, insulin can also exert a stronger effect on cell growth [15].

Many defects in the pathway could interrupt the flow of insulin signaling and lead to aberrant effects. Models of insulin resistance show impaired insulin signal transduction at the level of various enzymes and intermediates of the interconnected pathways [32, 59]. For example, mTOR is crucially involved in cell proliferation and differentiation. Therefore, a defect in this cell mediator would facilitate tumor growth by promoting protein synthesis [40, 43]. In addition, a defect on the tumor suppressor protein, PTEN, which also acts as a lipid phosphatase that cleaves PI(3, 4, 5) P3 back into PI(4, 5)P2, could lead to upregulation of the PI3K signaling pathway, and eventually lead to cancer. PTEN has an antagonizing effect to PI3K,

downregulating PI3K activity. If PTEN is defective, it will remain incapable of turning the PI3K pathway off. In mouse models, PTEN loss either by gene mutation or deletion leads to carcinogenic activities, which could potentiate malignant transformation of cells into hyperplastic tumors [40]. PTEN suppression, or inactivation of any of the phosphatases that supposed to halt insulin action, could lead to tumor progression because the insulin pathway is unrestrained [39, 40]. Since PI3K contributes to cell growth and survival, including insulin-mediated glucose transport and metabolism, pharmaceutical companies are working aggressively towards the development of inhibitors that target the PI3K pathway. For example, Wortmannin is one of the first generation PI3K inhibitors that have revolutionized the understanding of the major insulin signaling pathways [38, 59]. However, since germline mutations and oncogenic changes in the PI3K pathway may render the signaling mechanism defective, different alternatives need to be sought to reach to the same conclusion [38]. For this reason, it is very important to consider the interaction of interconnected pathways that reach to the same end in insulin signaling.

Dysregulation in the complicated meshwork of insulin signaling interconnections often require aggressive treatments in order to treat carcinogenic diseases. For example, dual inhibition might be necessary in order to target a specific cellular response like tumor progression. The microRNA, miR-564, is an example of a dual inhibitor that targets PI3K and MAPK by causing G1 arrest. It has been shown to markedly reduce tissue invasion in aggressive breast cancer and the number of relapses in affected patients [75]. Another dual inhibitor currently in development is Semafore's SF1126, which targets PI3K and mTOR. SF1126 has been proven to be effective at inducing apoptosis and inhibiting cell proliferation [38], and targets cancer more effectively than an mTOR inhibitor alone [67]. Despite complications of side effects due to selectivity, scientists continue to work for better therapeutic drugs that offer the best treatment and the less complications. Dual inhibition is a fascinating approach that scientists and pharmaceutical companies are continually investigating in order to offer better prognosis in treatment and disease remission.

3.2 Down Regulation: Prevention of Insulin Overload

In order to create balance in the body, there should be an inhibitory pathway in place that could stop the propagation of stimulating signals. Otherwise, insulin would create catastrophic effects in the human body. Excess insulin could turn on pathways that if left unchecked could lead to obesity, excess proliferation and differentiation, excess metabolic actions that create excess protein synthesis and mediators in glucose control that could be detrimental if not well controlled. These controlled mechanisms are discussed below.

Insulin overload destabilizes the cell environment and make the cell prone to transduction inhibition and insulin resistance. Multiple molecules in the cell contribute to the cell destabilization by opening the highway to other pathways that are

precipitated by multiple disease states. In particular, states of oxidative stress, obesity, inflammation, hyperglycemia, lipotoxicity, including Alzheimer's disease, intervene in the insulin pathway by secreting biomolecules which affect the normal flow of insulin signaling events, leading to insulin transduction inhibition, insulin resistance, and cancer, among other cellular effects. The schematic representations of these processes are illustrated in Fig. 3. Inhibitory molecules that affect kinase activity and induce insulin resistance include: phosphatases, cytokines, free fatty acids (FFAs) [11, 41], free radicals, and excess blood glucose levels [41]. In particular, cells of obesity secrete FFAs and adipocytokines, which impart an immune response, increase inflammatory processes, lead to insulin resistance and/or cancer [19]. These molecules exert a negative feedback mechanism on insulin signaling that changes the course of the intended pathway towards insulin signaling termination (Fig. 3).

3.3 Insulin Receptor Degradation

One aspect of hyperinsulinaemia is IR (insulin receptor) internalization due to overexpression regulation of insulin receptors. Generally, IRs are upregulated by hyperinsulinaemic conditions in the extracellular compartment of the cell. IR over-expression leads to IR ubiquitination or degradation in the endosomal compartment. When insulin binds to IR, the complex is internalized into the cell, and then it dissociates allowing the free insulin to return to the surface. IR internalization prevents over-abundant receptors outside of the cell to keep turning the insulin signaling pathway on and activating a perpetual insulin signaling circuitry from propagating [12] (Fig. 3). It is equally important to note that there is a close link in the literature between hyperinsulinaemia, insulin receptor over-expression and cancer [15, 71], as it has been shown that patients who take metformin, an insulin sensitizer which increases insulin uptake and lower insulin levels in the blood, have a 25–40% lower risk of developing cancer as opposed to patients who depend on insulin to lower blood glucose levels [71]. Scientific evidence shows that metformin decreases tumor growth by decreasing Akt signaling, which is a favorable link for metformin, anticancer therapy, and a decreased risk of cancer development [43]. Even though nonmalignant transformed cells can overexpress insulin receptors, prolonged chronic exposure to insulin have been shown to result in malignant transformed phenotype. Although these upregulated receptors appear to be structurally normal, they have chronic receptor kinase hyper-activity, which may lead to gene transcription, cell growth and cell division [15]. Additional signaling mechanisms will prevent prolonged activation of IRS signaling stimulated by high level of insulin [for example: ERK, SHP2, PKC, Akt, JNK, mTOR, S6 K, FOXO, TSC, IKK (Fig. 3)].

3.4 *IRS Degradation*

IRS signaling is also inhibited as a result of hyperinsulinaemia by a process called, IRS ubiquitination. There are many theories that have tried to explain what makes IRS dysfunctional and IR unresponsive to increased insulin signals and hyperglycemia. The IRS/PI3K signaling is inhibited by a negative feedback mechanism, which down-regulates the expression of the insulin receptor and results in sustained desensitization of IRS [15]. The inhibitory effect on IRS signaling ascertains that excess insulin signaling is not constantly activated [45]. When insulin is not associated with its receptor, IRS is degraded by ubiquitin-dependent pathway, preventing further signaling to its nearby insulin receptor. This is a protective mechanism that prevents sustained insulin transmission, rather than an insult of the pathway. The downregulation of receptors is a negative regulation of insulin signaling which brings about insulin resistance or insensitivity of receptors that react to insulin when insulin levels are sustained [45]. Using ZDOCK [54], the IRS dimer (bottom left/right) and JNK monomer (top) were docked (Fig. 7a). Specific interactions at the interface are shown between the JNK monomer and IRS dimer in Fig. 7b. Three types of potential interactions are observed: (1) Hydrogen bonding between SER261 of the IRS dimer and GLN120 of the JNK monomer, (2) Hydrophobic interactions between Ile231 of JNK with PHE160 of the IRS dimer, and (3) Electrostatic interaction between JNK Lys222 and IRS SER261. These interactions are important to elucidate in order to design potential inhibitors for this specific protein interactions.

3.5 *Phosphatases*

Molecules involved in reversible protein phosphorylation, or retrophosphorylation pathways, are critical for cells to live in healthy, stable conditions. Lipid phosphatases antagonize PI3K-dependent signaling by catalyzing the removal of phosphate groups and downgrading PIP3 to PIP₂. As a result, the intracellular signaling is inhibited. PTEN and SHIP2 are two examples of phosphatases, which inactivate PIP-lipid second messengers to prevent further downstream kinase activation (Fig. 2) [75, 77]. PTEN attenuates PI3K activation by hydrolyzing 3-phosphates and SHIP2 by removing 5-phosphatases from the inositol ring of PI (3, 4, 5) PI₃(31). PIP3 dephosphorylation precipitates insulin resistance. In addition, PTEN has a role in MAPK signaling inhibition by targeting Shc/Grb2-SOS (Fig. 2). Conversely, studies with knock-out (KO) mice, where the PTEN and SHIP2 genes have been deleted, have resulted in mice with increased insulin sensitivity and insulin action [75, 77]. SHIP2 deficiency, in particular shows marked induction of Akt-transduction with resulting hypoglycemia [41]. In general, these PI3K inhibitors are key regulators of glucose transport, metabolism, and survival [11, 20].

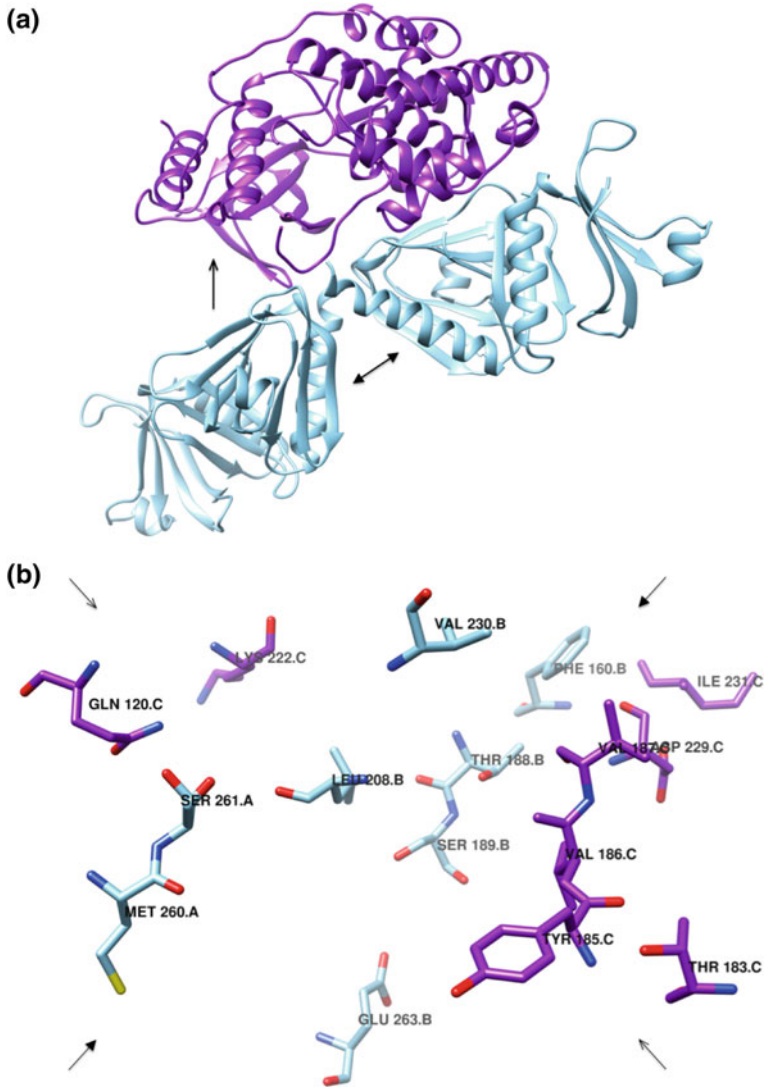


Fig. 7 **a** The predicted interaction between IRS (PDB code 1QQG [68]) and JNK (PDB code 4QTD [76]) proteins docked using ZDOCK [54]. The JNK protein (*top, open single arrow*) is shown interacting with IRS (*bottom left and right, closed double arrow*), **b** Close-up of the predicted interface between IRS (*middle, closed arrows*) and JNK (*left and right, open arrows*). Several potential electrostatic and hydrophobic interactions are shown

3.6 *Other Phosphatases and Insulin Receptor Regulators*

Downregulators of insulin signaling are an important component for the stability of normal metabolism. Particularly, phosphatases are molecules that terminate insulin signaling. Another molecule which blocks insulin action and cause insulin resistance is tyrosine phosphatase SHIP2, which catalyze the dephosphorylation of PIP₃ into PIP₂ [11]. In turn, PTP1B is another protein tyrosine phosphatase that achieves the same inhibitory effects, but by targeting the dephosphorylation of tyrosine residues on activated tyrosine receptor kinases (RTKs) [41, 78]. If the genes of these corresponding phosphatases are also disrupted, insulin sensitivity is also improved [11]. In addition, GRB10 is another molecule that exerts a negative regulation of IR by binding to it. GRB10 belong to a class of cytoplasmic adaptor proteins that induce a negative feedback inhibition on insulin action [41] and ubiquitinates IR [49]. Other negative regulators of insulin action involve molecules, which interfere with Ras signaling, like GTPase-activating protein, or GAP, as mentioned above.

3.7 *Serine Phosphorylation*

Reversible protein phosphorylation is a technique used by the cell that maintains metabolic homeostasis. Indeed, insulin transduction is governed by the fine-tuning of protein modifications guided by tyrosine and serine/threonine phosphorylation techniques [3], which collaborate by turning the pathway on and off, respectively [41]. Additional signaling mechanisms function to turn the pathway off. In the retrograde phosphorylation of protein kinases, guided by Ser/Tyr phosphorylation methods, the prolonged activation of the insulin signaling cascade provoked by high levels of insulin is haltered. Molecules involved in reversible protein phosphorylation include: ERK, SHP2, PKC, Akt, JNK, mTOR, S6 K, FOXO, TSC, IKK (Fig. 3). The cell resorts to additional pathways to downregulate insulin signaling when insulin levels are too high. Serine/threonine (Ser/Thr) phosphorylation methods halter the prolonged activation of the insulin signaling cascade provoked by high levels of insulin [11, 79]. Molecules involved in this pathway exhibit reversible protein phosphorylation, which deactivates the insulin signaling cascade preventing the prolonged activation of the insulin signaling cascade provoked by high levels of insulin. Such molecules include: ERK, SHP2, PKC, Akt, JNK, mTOR, S6 K, FOXO, TSC, IKK (Fig. 4). These molecules are capable of inducing a negative response on insulin signaling that stops insulin transduction. Despite insulin builds up to turn the pathway on, the insulin transduction pathway is not turned on. As a consequence, the insulin signaling pathway is less sensitive to the chronic insulin signaling and excess glucose affecting the cell. Eventually, sustained hyperinsulinaemia leads to uncompensated insulin resistance, impaired cell growth

and survival mechanism [15]. Insulin signaling inhibitors suppress insulin action and could be potential therapeutic agents for insulin resistance states (Fig. 3).

It is well understood that tyrosine phosphorylation turns physiological mechanisms on and serine/threonine (Ser/Thr) phosphorylation turns cellular responses off [41]. Ser/Thr phosphorylation inhibits IR and IRS signaling, as depicted in Fig. 3. The beta cells in the pancreas respond to hyperglycemia by increasing insulin levels, but when beta cells become less and less responsive to high glucose levels and Type 2 Diabetes (T2D) progresses, hyperglycemia stimulates chronic elevations of insulin in the blood. Insulin normally stimulates phosphorylation of tyrosine residues on IRS molecules in order to turn the insulin pathway on, and carry on with the respective insulin signaling pathways that depart from IRS signaling. However, serine and threonine phosphorylation can cause an attenuation of the insulin response [41], as illustrated in Fig. 3. As the beta cells in the pancreas become less and less responsive to high glucose levels and Type 2 Diabetes (T2D) progresses, hyperglycemia stimulates chronic elevations of insulin in the blood].

Hyperinsulinaemia stimulates phosphorylation of Ser/Thr residues on IRS, including IR and other effector molecules in the pathway, causing the downregulation of insulin signaling and a resulting insulin resistance. Serine and threonine kinases build up a negative effect on IR and IRS that desensitize cells from the effects of insulin [11, 41]. For example, Ser/Thr kinase activation inhibits IRS stimulation (Fig. 3) and PI3K activity (Fig. 2), and ultimately decreases glucose transport in skeletal muscle cells and adipocytes [24]. Cellular mediators, discussed in this review, which interact with the IRS protein and activate serine/threonine kinase activity are: ERK, SHP2, PKC, Akt, mTOR, S6 K, FOXO, TSC [45, 46], JNK, IKK [41, 78]. Additional molecules participate to attenuate the insulin response by targeting the insulin receptor include: GRB10 and PTP1B. Stressful events, inflammatory states, hyperglycemia, and obesity play a role in the etiology and pathogenesis of insulin resistance by impairing the insulin signaling pathway [19, 41]. Under stressful situations, proinflammatory cytokines, fatty acid metabolites, and reactive oxygen species (ROS) stimulate serine kinases to induce serine phosphorylation of IR and IRS-1 at specific serine residues [11, 41]. Serine/threonine kinase activation hinders tyrosine phosphorylation of the IRS proteins, thereby hindering their function (inactivate insulin signaling/cause insulin resistance) [11, 75]. As shown in Figs. 1 and 4, IKK and JNK are two serine/threonine kinases that are responsible for the phosphorylation of IRS-1 at the serine-307 site [3, 7]. In addition, JNK targets a serine phosphorylation on Akt, which inhibits Akt activation and reduce insulin signaling [15] (Fig. 2). JNK, in turn, can be phosphorylated by MEK, through cross talk with the Ras/MAPK pathway [19]. In general, serine activation attenuates the insulin response and augments insulin resistance [12, 15]. Additional molecules, which interfere with normal insulin transduction by activating serine kinases of IRS include: ERK, PKC, Akt, mTOR, S6 K, FOXO, TSC [45, 46].

3.8 *Inflammation*

The inflammatory pathway is of vital concern for the development of insulin resistance and cancer. Inflammatory molecules are activated in response to a variety of forms of stressors generated in and around the cell environment. In general, inflammation is a reactive response to threats in equilibrium happening within the organism. For example, inflammation is activated by oxidative stress [79]. Oxidative stress builds up Reactive Oxygen Species (ROS) called free radicals. Free radicals are very damaging for the cell. The buildup of free radicals that accumulate could potentially cause DNA damage and lead to cancer. Free radicals destabilize stable molecules by breaking their stable chemical bonds and converting them into reactive species, which cause oxidative damage to DNA, mutations, and tumor progressions [15]. In general, ROS activates macrophages and start an immune response that leads to cell proliferation and differentiation [15, 19]. In addition, ROS is also induced by hypoxia [19, 79]. According to research, anti-inflammatory agents like NSAIDs and antioxidants are useful to potentially treat and prevent colorectal cancer, with a documented reduction of 40–50% of colorectal cancers with drug use [15, 19]. Documented research has also shown that anti-inflammatory agents are useful to prevent fat-induced insulin resistance in rodents, a clear indication that inflammation plays an important role in the pathogenesis of insulin resistance in obesity [80]. NSAIDs, as well as salicylates like aspirin, are known to reverse insulin resistance in patients with Type 2 Diabetes [43] and are also used as cancer-reduction efforts [15]. Oxidative stress, inflammation, hyperglycemia, hyperinsulinaemia, and obesity are closely linked to cancer and insulin resistance [19].

3.9 *Obesity*

In obesity, cells become hyperplastic and hypertrophies as new adipocytes form. The cells become hypoxic as new cells accumulate. The added stress causes adipocytes to secrete inflammatory cytokines, called adipocytokines, or adipokines, which stimulate angiogenesis in the adipose tissue [19, 26, 81]. Adipocytokines are inflammatory mediators that are upregulated in obese states [78] and are produced by both adipocytes and immune cells like macrophages [41]. The pro-inflammatory cytokines of adiposity include an array of inflammatory mediators such as tumor necrosis factor- α (TNF- α), interleukin-6 (IL-6), IL-8, IL-10, macrophage inflammatory protein 1 (MIP-1), and monocyte chemoattractant protein-1 (MCP-1). These inflammatory mediators play an important role in the induction of insulin resistance [12, 19]. Deletion of inflammatory mediators like MCP-1 have proven insulin sensitivity in mice studies [41]. In general, insulin resistance is directly correlated with body weight, and obesity is highly linked to the development of metabolic inflammation, diabetes, and cancer [26]. From a list of preventable cancers, the

cancer rates for obesity are only second to smoking, with 20% of all cancers caused by obesity according to an epidemiology studies conducted over the last 25 years [26]. It is also interesting to note that ~60% of the patients with Type 2 Diabetes are obese [7] and the metabolic imbalance is often corrected with bariatric surgery and insulin-sensitizers (e.g., Metformin), which confers that lean body mass is an attractive therapeutic zone in the area of hyperinsulinaemia and insulin resistance [7, 82, 83]. Similarly, a study proved that lowering chronic elevations of FFAs in obese individuals with T2DM improved insulin sensitivity 50%, which ascertains the role of excess energy stores and lipid accumulation in the development of insulin resistance and diabetes type 2 [83, 84].

Adipose tissue is considered an endocrine organ because it is also capable of secreting cytokines and hormones that influence insulin sensitivity and metabolic homeostasis [7]. Another adipokine secreted by adipose tissue and circulating macrophages is adiponectin, the most abundant adipokine. While deleterious pro-inflammatory cytokines, TNF α and IL-6, are over-secreted in obesity, adiponectin is markedly decreased [7, 82]. Adiponectin has protective role in the cell by enhancing insulin sensitivity and decreasing carcinogenesis. Adiponectin is also implicated in the downregulation of the TLR4 pathway by targeting NF- κ B. Adiponectin inhibits NF- κ B, and the result halts cell proliferation and insulin resistance [7, 15, 26, 82]. Summed in the author's words, "the suppression of inflammation increases insulin sensitivity and reduces metabolic dysfunction in Type 2 Diabetes Mellitus" [7].

The compact mass of adipose tissue releases Free Fatty Acids (FFAs) into circulation. Plasma FFA levels increase in obese individuals and induce a low-grade inflammation, causing insulin resistance [82]. The fat mass, along with free circulating fatty acids, triggers a large release of cytokines, which can, disrupt glucose uptake [80]. Persistently high levels of FFAs in the blood ultimately leads to Type 2 Diabetes [79] and cancer [19]. Plasma concentrations of cytokines (like TNF- α) normally increase with obesity and decrease with weight loss, suggesting a possible link between obesity and insulin resistance in the inflammatory pathway. Thus, weight loss seems to restore insulin sensitivity [80], while TNF- α induces lipolysis, thereby triggering the release of FFAs from adipocytes [26]. In turn, fatty acids freely flowing in the blood turn macrophages on, and stimulate TNF- α production by macrophages [26] (Fig. 2, Activated Macrophages). This process ultimately shuts down the PI3K/Akt pathway, enabling the transport of excess glucose into the cell, resulting in lower blood glucose levels. Opposite to inflammatory molecules, insulin inhibits lipolysis in adipocytes and restrains release of FFA into circulation. If increasing levels of FFAs reach a "lipotoxic" level, insulin signaling is impaired [4]. This denotes a clear convergence between obesity, diabetes, and inflammatory pathways.

3.10 The Connection Between Inflammation and Obesity

The inflammatory pathway has great implications in the development of insulin resistance and proliferative states. It has been hypothesized that FFAs cause ROS formation as well as the subsequent influx of cytokines which deactivate the insulin signaling cascade, and augments situations of cancer progression and invasion [80, 84]. ROS is induced by oxidative stress and plays a role in the induction of insulin resistance by activating JNK (c-Jun NH₂-terminal Kinase) [79]. JNK is a serine/threonine kinase that has been shown to disrupt insulin signaling by inhibiting tyrosine phosphorylation of IRS, and Akt [15]. When stress kinases like JNK binds to IRS and Akt, insulin signaling is suppressed and the action of insulin is blocked [15, 84]. The stress molecule, JNK, is also activated by inflammatory mediator TNF- α via the TNF receptor, which inhibits insulin signaling [7, 15 78]. Other inflammatory mediators like I κ B kinase- β (IKK- β), interrupt insulin signaling in a similar way as JNK. IKK- β is a serine/threonine kinase that is triggered by an increase in plasma FFA levels, and interrupts insulin signaling by decreasing tyrosine phosphorylation on IRS [84]. IKK- β therefore plays a critical role in tumorigenesis, cell proliferation, inhibition of apoptosis, and metastasis [19].

Furthermore, obesity (FFAs) and inflammation (TNF- α) play an active role in the activation of the IKK- β pathway [85]. NF- κ B is modulated via the toll-like receptor (TLR). TLR is a membrane receptor inherent in macrophages and adipocytes which activate the inflammatory pathway [79]. When TLR is activated, the IKK- β /NF- κ B pathway is turned on [79]. IKK- β , also known as Inhibitor of Nuclear Transcription factor kappa-B kinase subunit beta, phosphorylates the protein Inhibitor of NF- κ B (I κ B), which binds NF- κ B and inactivates its function. Activated I κ B is subsequently degraded by proteasomes via the ubiquitination pathway, which allows NF- κ B to be released from I κ B. NF- κ B is then translocated to the nucleus, whereby it regulates gene expression of pro-inflammatory molecules [80]. NF- κ B is involved in the production of cytokines and the development of insulin resistance and cell proliferation. Inhibition of IKK kinases via the IKK- β /NF- κ B pathway and TLR receptor yield promising avenues for the treatment of inflammation and cancer, although the drug development in this area is in its infancy [85].

Anti-inflammatory drugs significantly improve insulin sensitivity and reverse insulin resistance [43, 80]. For example, NSAIDs, as well as salicylates like aspirin, are known to reverse insulin resistance in patients with Type 2 Diabetes [43] and are also used as cancer-reduction efforts [15]. In particular, aspirin has anti-proliferative properties, which reduces cancer progression via the TLR pathway. By inhibiting the I κ B kinase- β (IKK- β) signaling, aspirin prevents inflammation and proliferative states [15]. Another molecule which antagonize NF- κ B action via the TLR is PPAR- γ . PPAR- γ is a nuclear receptor protein called, Peroxisome-Proliferator-Activated Receptor- γ , which prevents NF- κ B activation, inhibit cytokine production, suppress insulin resistance, and limits proliferation of cancer cells [15]. TZD (thiazolidinediones) drugs are potent PPAR γ agonists which are highly expressed in

adipocytes. These type of antidiabetic agents promote insulin sensitivity in skeletal muscle and liver by redistributing fat into adipocytes [24].

3.11 Role of Insulin Signaling Pathway in Vascular Stability

In addition to metabolic and mitogenic roles, insulin also has a major role in maintaining vascular stability. Insulin exerts a vascular function on endothelial cells by initiating vasodilation through the PI3K/Akt pathway and vasoconstriction through Ras/MAPK signaling, which adds another important mechanism to the pleiotropic effects of the insulin cascade [30]. Basically, insulin imparts vascular actions on the endothelium by producing nitric oxide (NO), which improves vasodilation. For example, Akt directly phosphorylates serine residues of endothelial NO synthase (eNOS) via the PI3K/Akt pathway [12, 14]. Activated eNOS produce nitric oxide, which are potent vasodilators [12, 14, 30] (Fig. 2). Similarly, activated MAPK stimulates the release of endothelin-1 (ET-1), which promotes vasoconstriction of endothelial cells [30] (Not on the picture). Interruptions in any of the implicated insulin pathways due to the insulin resistance aftermath could create vascular changes with cardiac repercussions. For example, if the PI3K/Akt pathway is affected and Akt is defective, eNOS will not be activated to produce NO. Therefore, a decrease in NO could bring about a reduction in vasodilation, which would increase the risk of developing hypertension [84]. The opposite is speculated if MAPK is the affected kinase. In addition, inflammation also has an effect on cardiac health. Elevated FFAs turn on the TLR4 pathway and activate an avenue that creates low grade inflammation. This effect causes atherosclerotic vascular disease and non-alcoholic fatty liver disease [86]. Moreover, decreased glucose uptake and increased glucose production characterize diabetes, the major illness that affect multiple organ systems and lead to deleterious health effects [14, 84]. In short, insulin resistance is related to the metabolic syndrome for the major actions insulin exerts.

4 Implications of Insulin in Alzheimer's Disease

4.1 Alzheimer's Disease

Alzheimer's disease (AD) is another debilitating and deleterious disease that is being closely studied for its pathological link with insulin resistance is Alzheimer's disease (AD). Insulin resistance is markedly noticed in patients who have both AD and diabetes [2], which implies that there could be some mechanistic link between the two diseases. AD is molecularly defined as a neurological disease affected by

the accumulation of two kinds of proteins in the brain, Tau proteins and amyloid beta ($A\beta$) peptides. Tau and $A\beta$ proteins are the defining markers of AD responsible for the formation of the well-known neurofibrillary tangles (NFTs) and $A\beta$ plaques, respectively. Insulin signaling acts as a protective mechanism in AD by inhibiting tau phosphorylation via GSK-3 inhibition and by altering the processing of the amyloid precursor protein (APP), resulting in reduced generation of $A\beta$. Normally, an $A\beta$ -protease called, Insulin Degrading Enzyme (IDE), creates a competition between insulin and $A\beta$ for the insulin receptor-binding site (Fig. 4). IDE usually degrades $A\beta$ over insulin, but when insulin levels are too high, as in hyperinsulinaemia, IDE preferably degrades insulin [28]. Therefore, insulin is a protective mechanism against AD up to certain extent because hyperinsulinaemia could also induce $A\beta$ production and create states of dementia [28].

Insulin resistance generally results in low levels of IDE, less $A\beta$ degradation outside of the cell, and more neurodegenerative disorders [20]. Hyperinsulinaemia and insulin resistance play a role in $A\beta$ and tau regulation by controlling IDE expression at the synapse [21, 30]. As it has been demonstrated in post mortem brain tissue studies, insulin resistance in AD brains usually results in low IDE expression and low $A\beta$ degradation [21, 30]. $A\beta$ is a normal by-product of metabolism, but when $A\beta$ accumulates to neurotoxic levels, the defining plaque features of AD form, which turn on various mechanisms that potentiate $A\beta$ production and the persistence of the degenerative insult [21].

A major pathway affected by insulin with respect to AD is the PI3K/Akt pathway. In normal physiological conditions, insulin depresses GSK-3 activity by promoting the dephosphorylation of glycogen synthase, an action that also stimulates glycogen synthesis, among other processes [87] (Fig. 4). However, when insulin signaling transduction is decreased or impaired, GSK-3 is activated and can lead to AD. Activated GSK-3 induces Tau phosphorylation and aggregation [30, 58], which forms NFTs. In addition, dysfunctional/deregulated GSK-3 leads to substantial increase in $A\beta$ levels on cell exterior, forming plaques [58]. Plaques, in turn, remove insulin receptors from the plasma membrane and induce insulin receptor degradation/internalization and an inherent insulin resistance [30]. Cell surface IR expression is also reduced by $A\beta$ [21]. Additionally, neuroinflammation is precipitated by proinflammatory mediators like TNF- α and IL-6, which reduce insulin sensitivity and accelerates the progression of AD.

The dementia biomolecules of AD, $A\beta$ and Tau, accumulate in the brain and create an immune response called neuroinflammation [36]. Microglia and astrocytes respond by secreting CNS cytokines like TNF- and IL-6, in response to low-grade inflammation [53]. In general, insulin resistance, diabetes, obesity, and AD activate stress molecules (JNK, IKK- β) of the inflammatory pathway that leads to a low-chronic systemic inflammation [21]. The inflammatory and stress pathways are known to activate TNF and TLR4 receptors, respectively, which activate kinases that serine phosphorylate IRS (JNK and IKK) and cause insulin resistance, including AD (Fig. 4). Serine IRS phosphorylation of IRS is the signature for insulin signaling impairment [21], which is also marked by AD.

AD is an end-result of diabetes, and it is usually referred to as, diabetes type 3 [2, 21, 57, 88], after the long-term consequences [2]. However, it is worth mentioning, “AD is not a normal process of aging,” and there are no current treatments available, which can cure AD, but reduce its progression [30]. Currently, anti-inflammatory drugs are sought as a therapeutic/preventive modality to reduce the risk of metabolic and degenerative disease processes. Insulin resistance, AD, and other metabolic and degenerative disorders, are targeted with anti-inflammatory drugs to control the disease process. Anti-inflammatory drugs have also been used as a therapeutic approach in AD to control the disease-induced inflammatory pathways. For example, the link between diabetes and AD is prominent in epidemiology studies that consider patients who take NSAIDs and demonstrate a reduced risk in developing AD [30] and insulin resistance [21]. It is also important to note that patients with systemic infections have increased propensity towards developing dementia symptoms like cognitive impairment and memory loss [21]. In addition, insulin therapy may correct the pathological events of abnormal cognition as it reduces pathological A β accumulation and binding of A β at synapses [21]. Intranasal insulin therapy has been sought as an alternative avenue in regards to this approach [30]. In addition, insulin sensitizers like TZD and other PPAR- γ agonists, have also been used to control the disease process by targeting the inflammatory process and markedly reducing A β and tau pathology in AD (36). In addition, TZD drugs decrease FFA concentrations in the blood, which decreases diabetes in obese individuals and the neurotoxicity driven by cerebral inflammation [36]. Furthermore, GSK-3 inhibitors that target tau-phosphorylation and NFT formation are currently under study as potential treatment for AD [30]. GSK-3 are considered potential treatment for diabetes and neurodegenerative diseases with current investigations and innovations under way [30].

The excess A β accumulation in the brain related to AD also plays a role in mitochondrial dysfunction and oxidative stress, which are common pathological landmarks of metabolic disorders and neurodegeneration [42]. Moreover, AD, with its defining characteristics of plaque formation and NFTs, is also related to cancer development through activation of inflammatory processes that yield to insulin resistance [21].

Generally, Akt acts as a negative regulator of GSK-3, whereas, Akt inhibits GSK-3 activity and precipitates insulin signaling. A derailment in this activity promotes neuronal apoptosis, insulin resistance, and signs of dementia [52] (Fig. 2 and 4). Normally, Akt negatively correlates GSK-3, whereas activation of Akt inhibits GSK-3, activates insulin signaling and reduces signs of dementia, as depicted in Fig. 4 [52]. A derailment in this activity (GSK-3 β activation) could promote neuronal apoptosis, negative regulation of insulin signaling, and precipitate the signs of dementia [52]. Akt correlates negatively with GSK-3 by inhibiting GSK-3 activity and precipitating insulin signaling. Additionally, a molecular defect of glucose transporters in the brain, GLUT1 and GLUT3, have major repercussions in brain glucose metabolism which impedes the normal flow of insulin signaling and eventually may lead to the neurotoxicity and neurodegeneration characteristic of Alzheimer’s Disease (AD) [58] (Fig. 4). Additionally, a molecular defect of

glucose transporters in the brain, GLUT1 and GLUT3, have major repercussions in brain glucose metabolism which impedes the normal flow of insulin signaling and eventually create situations of neurotoxicity that favors states of dementia [58] (Fig. 4).

5 Conclusion

The insulin pathway intersects molecular mechanisms that lead to a constellation of pathologies. Inflammation, stress, obesity, AD, cardiovascular disease, and cancer are all interrelated in an array of molecules that converge and diverge and turn molecules on or off according to biochemical conditions [89, 90]. Insight into the insulin signaling pathway offers invaluable knowledge about the insulin resistance syndrome and its comorbid effects, including cancer progression and AD. In-depth knowledge about the insulin transduction pathway broadens the scientific understanding about the multiple pathological features that contribute to disorders of metabolism and its mitogenic properties. By creating an overall picture of the insulin pathway, scientists can have a better idea about what molecules to target in order to control a desired cellular response. In fact, the pathologic conditions that emerge from defects in the insulin signaling cascade share similarities and points of convergence that offer a platform for continued research. Careful introspection into such mechanisms can open a door of invaluable information that could possibly generate better treatments or possible cures for complex deleterious cases of the insulin nature. For example, it is our hope to crystallize molecules in the pathway to verify their docking with specific molecules that could possibly be used in clinical medicine in a nearby future. This information is vital for drug development and therapeutic regimens that center on targeting molecular derailment of the insulin transduction network. In fact, defects in the biochemical circuitry of insulin signaling are major targets that can nowadays yield promising results in the microscopic and challenging world of insulin resistance.

References

1. Hirabara, S.M., Gorjao, R., Vinolo, M.A., et al.: Molecular targets related to inflammation and insulin resistance and potential intervention. *J. Biomed. Biotechnol.* **379024**, 1–16 (2012)
2. Zhang, J.J., Liu, F.: Tissue-specific insulin in the regulation of metabolism and aging. *IUBMB Life* **66**(7), 485–495 (2014)
3. He, H.J., Zong, Y., Bernier, M., et al.: Sensing the insulin signaling pathway with an antibody array. *Proteomics Clin. Appl.* **3**(12), 1440–1450 (2009)
4. Abdul-Ghani, M.A., DeFronzo, R.A.: Pathogenesis of insulin resistance in skeletal muscle. *J. Biomed. Biotechnol.* **476279**, 1–19 (2010)
5. Chakraborty, C.: Biochemical and molecular basis of insulin resistance. *Curr. Protein Pept. Sci.* **7**(2), 113–121 (2006)

6. Pessin, J.E., Saltiel, A.R.: Signaling pathways in insulin action: molecular targets of insulin resistance. *J. Clin. Investig.* **106**(2), 165–169 (2000)
7. Guo, S.: Insulin signaling, resistance, and the metabolic syndrome: insights from mouse models to disease mechanisms. *J. Endocrinol.* **220**(2), T1–T23 (2014)
8. Govindarajan, G., Gill, H., Rovetto, M., et al.: What is insulin resistance? *Heart Metab.* **30**, 30–34 (2006)
9. Roberts, C.K., Hevener, A.L., Barnard, J.: Metabolic syndrome and insulin resistance: underlying causes and modification by exercise training. *Compr. Physiol.* **3**(1), 1–58 (2013)
10. Moller, D.E., Kaufman, K.D.: Metabolic syndrome: a clinical and molecular perspective. *Annu. Rev. Med.* **56**, 45–62 (2005)
11. Saltiel, A.R., Pessin, J.E.: Insulin signaling pathways in time and space. *Trends Cell Biol.* **12**(2), 65–71 (2002)
12. Sesti, G.: Pathophysiology of insulin resistance. *Best Pract. Res. Clin. Endocrinol. Metab.* **20**(4), 665–679 (2006)
13. Aganović, I., Dušek, T.: Pathophysiology of metabolic syndrome. Department of Internal Medicine. Division of Endocrinology, University Hospital Center Zagreb, Croatia. *EJIFCC* **18**(1), 3–6 (2007)
14. Muniyappa, R., Montagnani, M., Koh, K.K., et al.: Cardiovascular actions of insulin. *Endocr. Rev.* **28**(5), 463–491 (2007)
15. Godsland, I.F.: Insulin resistance and hyperinsulinaemia in the development and progression of cancer. *Clin. Sci.* **118**, 315–332 (2010)
16. Lizcano, J.M., Alessi, D.R.: The insulin signaling pathway. *Curr. Biol.* **12**(7), R236–R238 (2002)
17. Mlinar, B., Marc, J., Janez, A., et al.: Molecular mechanisms of insulin resistance and associated diseases. *Clin. Chim. Acta* **475**, 20–35 (2007)
18. Mendonça, F.M., de Sousa, F.R., Barbosa, A.L.: Metabolic syndrome and risk of cancer: which link? *Metabolism* **64**(2), 182–189 (2015)
19. Pothiwala, P., Jain, S.K., Yaturu, S.: Metabolic syndrome and cancer. *Metab. Syndr. Relat. Disord.* **7**(4), 279–288 (2009)
20. Dineley, K.T., Jahrling, J.B., Denner, L.: Insulin resistance in Alzheimer’s disease. *Neurobiol. Dis.* **72PA**, 92–103 (2014). (PMC. Web., 20 June 2018)
21. Ribe, E.M., Lovestone, S.: Insulin signaling in Alzheimer’s disease and diabetes: from epidemiology to molecular links. *J. Intern. Med.* **280**(5), 430–442 (2016)
22. Verdile, G., Keane, K.N., Cruzat, V.F.: Inflammation and oxidative stress: the molecular connectivity between insulin resistance, obesity, and Alzheimer’s disease. *Mediat. Inflamm.* **105828**, 1–17 (2015)
23. Hotamisligil, G.S.: Inflammation and metabolic disorders. *Nat. Publ. Group* **444**, 860–867 (2006)
24. Petersen, K.F., Shulman, G.I.: Pathogenesis of skeletal muscle insulin resistance in type 2 diabetes mellitus. *Am. J. Cardiol.* **90**(5A), 11G–18G (2002)
25. Reaven, G.M.: Banting lecture 1988. Role of insulin resistance in human disease. *Diabetes* **37**, 1595–1607 (1988)
26. Cao, H.: Adipocytokines in obesity and metabolic disease. *J. Endocrinol.* **220**(2), T47–T59 (2014)
27. Wilcox, G.: Insulin and insulin resistance. *Clin. Biochem.* **26**(2), 19–39 (2005)
28. Stanley, M., Macauley, S.L., Holtzman, D.M.: Changes in insulin and insulin signaling in alzheimer’s disease: cause or consequence? *J. Exp. Med.* **213**(8), 1375–1385 (2016)
29. Perez, M.J., Quintanilla, R.A.: Therapeutic actions of the thiazolidinediones in Alzheimer’s disease. *PPAR Res. J.* **957248**, 1–8 (2015)
30. Bedse, G., Domenico, F.D., Serviddio, G., et al.: Aberrant insulin signaling in Alzheimer’s disease: current knowledge. *Front. Neurosci.* **9**(204), 1–13 (2015)
31. Chang, L., Chiang, S.H., Saltiel, A.R.: Insulin signaling and the regulation of glucose transport. *Mol. Med.* **10**(7–12), 65–71 (2004)

32. Serrano, R., Villar, M., Gallardo, N.: The effect of aging on insulin signalling pathway is tissue dependent: central role of adipose tissue in the insulin resistance of aging. *Mech. Ageing Dev.* **130**(3), 189–197 (2009)
33. Petersen, K.F., Shulman, G.I.: Etiology of insulin resistance. *Am. J. Med.* **119**(5A), 10S–16S (2006)
34. Hinke, S.A.: Epac2: a molecular target for sulfonylurea-induced insulin release. *Science Signaling* **2**(85), e54 (2009). (pp. 1–4)
35. Thareja, S., Aggarwal, S., Bhardwaj, T.R., Kumar, M.: Protein tyrosine phosphatase 1b inhibitors: a molecular level legitimate approach for the management of diabetes mellitus. *Med. Res. Rev.* **32**(3), 459–517 (2010)
36. Hildreth, K.L., Van Pelt, R.E., Schwartz, R.S.: Obesity, insulin resistance, and Alzheimer's disease. *Obesity (Silver Spring, MD)* **20**(8), 1549–1557 (2012)
37. Wang, Q., Jin, T.: The role of insulin signaling in the development of β -cell dysfunction and diabetes. *Islets* **1**(2), 95–101 (2009)
38. Li, C., Zhang, B.B.: Insulin signaling and action: glucose, lipids, protein. In: De Groot, L.J., Chrousos, G., Dungan, K., et al. (eds.) *Endotext* [Internet], pp. 2000–2009. MDText.com, Inc., South Dartmouth (MA) (2007)
39. McCubrey, J.A., Steelman, L.S., Chappell, W.H., Abrams, S.L., Montalto, G.: Mutations and deregulation of Ras/Raf/MEK/ERK and PI3K/PTEN/Akt/mTOR cascades which alter therapy response. *Oncotarget* **3**(9), 954–987 (2012)
40. Liu, P., Cheng, H., Roberts, T.M., Zhao, J.J.: Targeting the phosphoinositide 3-kinase (PI3K) pathway in cancer. *Nat. Rev. Drug Discovery* **8**(8), 627–644 (2009)
41. Boucher, J., Kleinridders, A., Kahn, R.: Insulin receptor signaling in normal and insulin-resistant states *Cold Spring Harb Perspect. Biology* **6**(1), pii.a009191 (2014)
42. Ravichandran, K.S.: Signaling via Shc family adapter proteins. *Oncogene* **20**(44), 6322–6330 (2001)
43. Braun, S., Bitton-Worms, K., LeRoith, D.: The link between the metabolic syndrome and cancer. *Int. J. Biol. Sci.* **7**(7), 1003–1015 (2011)
44. Berg, J.M., Tymoczko, J.L., Stryer, L.: Some receptors dimerize in response to ligand binding and signal by cross-phosphorylation. In: *Biochemistry*, 5th edn. W. H. Freeman, New York (2002) (Section 15.4)
45. Rhodes, C.J., White, M.F., Leahy, J.L., Kahn, S.E.: Direct autocrine action of insulin on β -cells: does it make physiological sense? *Diabetes* **62**(7), 2157–2163 (2013)
46. Copps, K.D., White, M.F.: Regulation of insulin sensitivity by serine/threonine phosphorylation of insulin receptor substrate proteins IRS1 and IRS2. *Diabetologia* **55**(10), 2565–2582 (2012)
47. Vats, R.K., Kumar, V., Kothari, A., Mital, A., Ramachandran, U.: Emerging targets for diabetes. *Curr. Sci.* **88**(2), 241–249 (2005)
48. McGonnell, I.M., Grigoriadis, A.E., Lam, E.W.F., Price, J.S., Sunter, A.: A specific role for phosphoinositide 3-kinase and Akt in osteoblasts? *Front. Endocrinol.* **3**(88), 1–8 (2012)
49. Wu, W.I., Voegtli, W.C., Sturgis, H.L., Dizon, F.P., Vigers, G.P.: Crystal structure of human Akt1 with an allosteric inhibitor reveals a new mode of kinase inhibition. *PLoS ONE* **5**, 12913 (2010)
50. Bertrand, J.A., Thieffine, S., Vulpetti, A., Cristiani, C., Valsasina, B.: Structural characterization of the Gsk-3 β active site using selective and non-selective ATP-mimetic inhibitors. *J. Mol. Biol.* **333**, 393–407 (2003)
51. Reddy, P.H.: Amyloid β -induced glycogen synthase kinase 3 β phosphorylated VDAC1 in Alzheimer's disease: implications for synaptic dysfunction and neuronal damage. *Biochem. Biophys. Acta.* **1832**(12), 1913–1921 (2013)
52. Hooper, C., Killick, R., Lovestone, S.: The GSK-3 hypothesis of Alzheimer's disease. *J. Neurochem.* **9**(104), 1433–1439 (2008)
53. Eldar-Finkelman, H., Martinez, A.: GSK-3 inhibitors: preclinical and clinical focus on CNS. *Front. Mol. Neurosci.* **4**(2011), 32 (2013). (PMC. Web., 20 June 2018)

54. Chen, R., Li, L., Weng, Z.: ZDOCK: an initial-stage protein-docking algorithm. *Proteins* **52** (1), 80–87 (2003)
55. Kahn, B.B.: Facilitative glucose transporters: regulatory mechanisms and dysregulation in diabetes. *J. Clin. Investig.* **89**(5), 1367–1374 (1992)
56. Shulman, G.I.: Cellular mechanisms of insulin resistance. *J. Clin. Investig.* **106**(2), 171–176 (2000)
57. Deng, Y., Li, B., Liu, Y., Iqbal, K., Grundke-Iqbal, I., Gong, C.X.: Dysregulation of insulin signaling, glucose transporters, O-GlcNAcylation, and phosphorylation of tau and neurofilaments in the brain. *Am. J. Pathol.* **175**(5), 2089–2098 (2009)
58. Wu, J., Yan, L.J.: Streptozotocin-induced type 1 diabetes in rodents as a model for studying mitochondrial mechanisms of diabetic B cell glucotoxicity. *Diabetes Metab. Syndr. Obes. Targets Ther.* **8**, 181–188 (2015). (PMC. Web., 20 June 2018)
59. Haag, M., Dippenaar, N.G.: Dietary fats, fatty acids and insulin resistance: short review of a multifaceted connection. *Med. Sci. Monit.* **11**(12), RA359–RA367 (2005)
60. Castellano, E., Downward, J.: RAS interaction with PI3K: more than just another effector pathway. *Genes Cancer* **2**(3), 261–274 (2011)
61. Santarpia, L., Lippman, S.L., El-Naggar, A.K.: Targeting the mitogen-activated protein kinase RAS-RAF signaling pathway in cancer therapy. *Expert. Opin. Ther. Targets* **16**(1), 103–119 (2012). (PMC. Web. 20 June 2018)
62. Molina, J.R., Adjei, A.A.: The Ras/Raf/MAPK pathway. *J. Thorac. Oncol.* **1**(1), 7–9 (2006)
63. Ramalingam, L., Oh, E., Thurmond, D.C.: Novel roles for insulin receptor (IR) in adipocytes and skeletal muscle cells via new and unexpected substrates. *Cell Mol. Life Sci.* **70**(16), 2815–2834 (2013)
64. Kiemper, S.J., Myers, A.P., Cantley, L.C.: What a tangled web we weave: emerging resistance mechanisms to inhibition of the phosphoinositide 3-kinase pathway. *Cancer Discov.* **3**(12), 1345–1354 (2013)
65. Belfiore, A., Malaguarnera, R.: Insulin receptor and cancer. *Endocr. Relat. Cancer* **18**, R125–R147 (2011)
66. Xie J, Wang X, Proud CG mTOR inhibitors in cancer therapy. *F1000 Res.*, 5 (2016) (F1000 Fac. Rev. 2078. PMC. Web., 20 June 2018)
67. Chen, J., Zhao, K.N., Li, R., Shao, R., Chen, C.: Activation of PI3K/Akt/mTOR pathway and dual inhibitors of PI3K and mTOR in endometrial cancer. *Curr. Med. Chem.* **21**(26), 3070–3080 (2014)
68. Dhe-Paganon, S., Ottinger, E.A.: Crystal structure of the pleckstrin homology-phosphotyrosine binding (PH-PTB) targeting region of insulin receptor substrate 1. *Proc. Natl. Acad. Sci. U.S.A.* **96**, 8378–8383 (1999)
69. Cheng, H., Li, C., Bailey, S., Baxi, S.M., Goulet, L., Guo, L.: Catalytic unit of PI3K γ in complex with PI3K/mTOR dual inhibitor PF-04979064. *ACS Med Chem Lett* **4**, 91–97 (2013)
70. Pettersen, E.F., Goddard, T.D., Huang, C.C., Couch, G.S., Greenblatt, D.M., Meng, E.C., Ferrin, T.E.: UCSF Chimera—a visualization system for exploratory research and analysis. *J Comput Chem* **25**(13), 1605–1612 (2004)
71. Liu, J., Visser-Grieve, S., Boudreau, J., Yeung, B., Lo, S., Chamberlain, G.: Insulin activates the insulin receptor to downregulate the PTEN tumour suppressor. *Oncogene* **33**, 3878–3885 (2014)
72. Bollig-Fischer, A., Dewey, T.G., Ethier, S.P.: Oncogene activation induces metabolic transformation resulting in insulin-independence in human breast cancer cells. *PLoS ONE* **6** (3), e17959 (2011)
73. Serra, V., Scaltriti, M., Prudkin, L., Eichhorn, P.J.A., Ibrahim, Y.H., Chandarlapaty, S., Markman, B., Rodriguez, O., Guzman, M., Rodriguez, S., Gili, M., Russillo, M., Parra, J.L., Singh, S., Arribas, J., Rosen, N., Baselga, J.: PI3K inhibition results in enhanced HER signaling and acquired ERK dependency in HER2-overexpressing breast cancer. *Oncogene* **30**, 2547–2557 (2011)

74. Mutlu, M., Saatci, Ö., Ansari, S.A., Yurdusev, E., Shehwana, H., Konu, Ö., Raza, U., Şahin, Ö.: MiR-564 acts as a dual inhibitor of PI3K and MAPK signaling networks and inhibits proliferation and invasion in breast cancer. *Sci. Rep.* **6**, 32541 (2016)
75. Kim, Y.J., Jahan, N., Bahk, Y.Y.: Biochemistry and structure of phosphoinositide phosphatases. *BMB Rep.* **46**(1), 1–8 (2013)
76. Chaikuad, A., Tacconi, E.M.C., Zimmer, J., Liang, Y., Gray, N.S., Tarsounas, M., Knapp, S.: A unique inhibitor binding site in ERK1/2 is associated with slow binding kinetics. *Nat. Chem. Biol.* **10**, 853–860 (2014)
77. Tang, X., Powelka, A.M., Soriano, N.A., Czech, M.P., Guiherme, A.: PTEN, but not SHIP2, suppresses insulin signaling through the phosphatidylinositol 3-Kinase/Akt Pathway in 3T3-L1 adipocytes. *J. Biol. Chem.* **280**(23), 22523–22529 (2005)
78. Mardilovich, K., Pankratz, S.L., Shaw, L.M.: Expression and function of the insulin receptor substrate proteins in cancer. *J. Cell Commun. Signal.* **7**(14), 1–15 (2009)
79. Tanti, J.F., Gremeaux, T., van Obberghen, E., Le Marchand-Brustel, Y.: Serine/threonine phosphorylation of insulin receptor substrate 1 modulates insulin receptor signaling. *J. Biol. Chem.* **269**(8), 6051–6057 (1994)
80. Ye, J.: Mechanisms of insulin resistance in obesity. *Front. Med.* **7**(1), 14–24 (2013)
81. Du, Y., Wei, T.: Inputs and outputs of insulin receptor. *Protein Cell* **5**(3), 203–213 (2014)
82. Bastard, J., Maachi, M., Lagathu, C., Kim, M.J., Caron, M.: Recent advances in the relationship between obesity, inflammation, and insulin resistance. *Eur. Cytokine Netw.* **17**(1), 4–12 (2006)
83. Boden, G.: Obesity and free fatty acids. *Endocrinol. Metab. Clin. N. Am.* **37**(3), 635–646 (2008)
84. Samuel, V.T., Petersen, K.F., Shulman, G.I.: Lipid-induced insulin resistance: unravelling the mechanism. *Lancet* **375**(9733), 2267–2277 (2010)
85. Jung, U.J., Choi, M.S.: Obesity and its metabolic complications: the role of adipokines and the relationship between obesity, inflammation, insulin resistance, dyslipidemia and nonalcoholic fatty liver disease. *Int. J. Mol. Sci.* **15**(4), 6184–6223 (2014)
86. Hajduch, E., Litherland, G.J., Hundal, H.S.: Protein kinase B (PKB/Akt)—a key regulator of glucose transport? *FEBS Lett.* **492**, 199–203 (2001)
87. Lee, H.K., Kumar, P., Fu, Q., Rosen, K.M., Querfurth, H.W.: The insulin/Akt signaling pathway is targeted by intracellular B-amyloid. *Mol. Biol. Cell* **20**(5), 1533–1544 (2009)
88. Sosa, H.M., Keyes, R., Stieglitz, K.A.: Structural analysis of relevant drug targets for Alzheimer's disease: novel approaches to drug development. *Curr. Bioact. Compd.* **13**(2), 90–100 (2017)
89. Tripathy, D., Mohanty, P., Dhindsa, S., Ghanim, H.: Elevation of free fatty acids induces inflammation and impairs vascular reactivity in healthy subjects. *Diabetes* **52**, 2882–2887 (2003)
90. Pergola, G.D., Silvestris, F.: Obesity as a major risk factor for cancer. *J. Obes.* **2013**, 1–11 (2013)

Prediction of the Three-Dimensional Structure of Phosphate-6-mannose PMI Present in the Cell Membrane of *Xanthomonas citri* subsp. *citri* of Interest for the Citrus Canker Control



Mariana Pegrucci Barcelos, Leonardo Bruno Federico,
Carlton A. Taft and Carlos H. T. de Paula da Silva

Abstract Citrus canker, caused by the bacterium *Xanthomonas citri* subsp. *citri* (XAC) is one of the most important diseases in citrus, presenting a significant impact on the Brazilian economy. A promising target enzyme for such disease control is phosphomannose isomerase (PMI). Phosphomannose isomerase is an enzyme that catalyses the interconversion of fructose-6-phosphate (F6P) and mannose-6-phosphate (M6P) and allows the synthesis of GDP-mannose in eukaryotic organisms. In *Xanthomonas* sp., phosphomannose isomerase is related to the production of xanthan gum, which is a defense mechanism of bacteria to prevent dehydration in harmful environments. Due to the lack of a resolved protein structure, a PMI model was created using the protein homology modeling method and, after protein selection by a BLASTp algorithm and subsequent alignment using ClustalOmega, the model was built using the MODELLER Software. The model was analysed and validated using the WhatIf, ProCheck, Errat, Prove and Verify-3D softwares. The *Xanthomonas* PMI model proved reliable through the validation and evaluation tests.

Keywords Citrus canker · Phosphomannose isomerase (PMI) · Homology modeling

M. P. Barcelos · L. B. Federico · C. H. T. de Paula da Silva (✉)
Laboratório Computacional de Química Farmacêutica (LCQF), Faculdade de Ciências Farmacêuticas de Ribeirão Preto (FCFRP), Universidade de São Paulo, Av. do Café, s/n, Ribeirão Preto 14040-903, Brazil
e-mail: tomich@fcrp.usp.br

M. P. Barcelos · C. H. T. de Paula da Silva
Departamento de Química, Faculdade de Filosofia, Ciências e Letras de Ribeirão Preto (FFCLRP), Universidade de São Paulo, Av. Bandeirantes, 3900, Ribeirão Preto 14090-901, Brazil

C. A. Taft
Centro Brasileiro de Pesquisas Físicas, Rua Dr. Xavier Sigaud 150, Urca, 22290-180 Rio de Janeiro, Brazil

1 Introduction

During the last ten years, four diseases have plagued the world's citrus, among them, citrus cancer has attracted special attention. This disease is one of the main and most impacting threats to citrus, responsible for a great economic loss to citrus producers. This fact is due to current control measures that are based on the eradication and exclusion of large areas of production in view of the low incidence of the disease.

The causative agent of citric cancer is a gram-negative bacterium belonging to the genus of *Xanthomonas*, with oxidative, aerobic and non-nitrogen-fixing metabolism [1], been the most severe type being caused by *Xanthomonas citri* subsp *citri* (XAC). It is the strain with the largest range of hosts and is also the most widespread in the world, reaching several countries such as Japan, Argentina, Brazil, among others.

The most striking feature of XAC-infected plants is the circular, protruding, cortical, brownish-colored eruptive lesions on leaves, branches, and fruits [2]. The spread of citrus disease occurs at short distances through the action of rain and wind, while the spread over longer distances occurs due to the transport of infected plant material [3, 4]. Thus, it is of utmost importance that disinfection of crop equipment and spraying of vehicles occur to prevent the spread of disease in uninfected places.

In addition to the precautions to be taken by the spread of the disease by man, natural phenomena such as rainfall. The rains that cause a large accumulation of water in the leaves, force the entry of water through the stomata and contribute to the entry of bacteria in the intracellular environment. In addition, thorns, pruning and other activities can cause leaf injury, also becoming a gateway to bacterial infection and/or transmission. After infection, lesions develop which, with the help of wind, dew and rain, will carry the bacteria to the next plant and start the citrus cancer cycle again [5].

Today, citrus canker control is based on regulatory measures that determine the eradication and exclusion of infected plants [6], and management measures aimed at reducing the impact of the disease on the plantation. If there is an area where the pest occurs with low incidence, the control is mainly done by planting healthy seedlings and eliminating contaminated citrus plants and those suspected of contamination. Now, if there is an area where citrus canker is already distributed among plants, a set of management measures should be undertaken to reduce the impact of the disease on the production [7].

Among the management measures adopted, there is a control of the citrus mining caterpillar (*Phyllocnistis citrella*) in the orange groves, whose presence contributes to the increased incidence of citrus canker [8] and the use of a copper syrup that helps reduce the amount of symptoms in plants and fruit drop, but does not prevent bacteria from entering the orchard.

Symptoms caused in the plant are believed to come from proteins transferred directly to the host cell cytosol via a conductive pore created by a type III secretion

system. In this system, the bacteria “perceive” the plant or environmental conditions as favorable and activate protein production. At this stage, there are two important gene sets: *avr* (avirulence) and *hrp* (hypersensitivity response and pathogenicity). The *avr* genes are responsible for determining the specificity of genotype-genotype interaction while *hrp* genes are related to pathogenicity and induction of hypersensitivity responses in non-host plants [9].

Xanthomonas sp. also use the type IV secretion system, which consists of a conjunction mechanism to export proteins or DNA-protein complexes to the extracellular or cytosol medium of host cells during infection, involving direct cell-cell contact [10].

1.1 Recent Discoveries in Citrus Canker Bacteria

Several researches under development aim to control XAC in citrus orchards. A recent and important discovery was the complete sequencing of the XAC genome by FAPESP’s Organization for Nucleotide Sequencing and Analysis (ONSA) network laboratories [11]. The results show that the XAC genome consists of 5,175,554 base pairs, which encode 4313 proteins. Carnielli and collaborators [12] of the Laboratory of Biochemistry and Applied Molecular Biology of the Federal University of São Carlos—UFSCar published a scientific article reporting the identification of 6 important proteins on the XAC surface present only in infectious conditions. These proteins are possibly related to binding of XAC to the host, and thus to triggering pathogenicity [12].

One of the structures discovered on the surface of XAC was protein phosphomannose isomerase (PMI). PMI is a monomeric enzyme responsible for the inter-conversion of fructose-6-phosphate (F6P) and mannose-6-phosphate (M6P) and is considered a bifunctional enzyme as it belongs to the families of mannose-1-phosphate guanyltransferase and mannose-6 phosphate isomerase [13]. This enzyme has important contributions to the metabolic pathways, since F6P belongs to the glycolytic pathway and M6P is a cell identifier used for cell transport and cell membrane identification in prokaryotic and eukaryotic organisms [14]. In addition, this enzyme may be useful in the development of new antifungal treatments, since lack of PMI activity in yeast cells may lead to cell lysis and the enzyme may be inhibited [15].

In *Xanthomonas*, PMI is related to the production of xanthan gum, which is a defense mechanism for bacteria to prevent dehydration in harmful environments [16]. In studies previously conducted at LBBMA–UFSCar by Zandonadi [17], it was noted that PMI has a higher induction in XAC in inducing medium compared to another strain of the bacterium.

Another evidence that also points to PMI as a potential therapeutic target is its participation in the survival and pathogenicity of other microorganisms, as in *Saccharomyces cerevisiae* [18], *Candida albicans* [15], *Mycobacterium smegmatis* [19] and *Leishmania mexicana* [20] e *Xanthomonas* sp. However, the literature

reports only three known inhibitors: erythros-4-phosphate, mannitol-1-phosphate and, to a lesser extent, the alpha anomer of mannose-6-phosphate [21].

Thus, the inhibition of PMI identified in the XAC membrane proves to be an innovative and promising strategy to combat citric cancer. A very efficient and inexpensive methodology for proposing new protein inhibitors is called rational planning. This methodology is able to contribute at all stages of the process, from the discovery of prototypes (also known as “lead compounds”), their optimization (with respect to affinity, specificity, efficacy and side effects), to the elaboration of clinical trial candidate compounds [22]. This methodology is based on the inhibition or stimulation of the biological activity of macromolecules, such as proteins or nucleic acids (DNA or RNA) associated with different diseases. Structural information from the bioreceptor (and ligands) enables discovery and directs the synthesis of compounds to their binding site, which may become potent bioactive compounds. What makes this approach even more attractive when used with proteins is the knowledge that 78% of current drugs target this type of biomolecule receptor [22].

Thus, the three-dimensional structure of the bioreceptor becomes important information for studies of bioactive molecule development that can be obtained through experimental studies such as x-ray crystallography and NMR. However, when experimental data are non-existent, the theoretical contribution guarantees satisfactory results for the determination of protein structure with the prediction of structures through the structural homology technique.

1.2 Molecular Modelling: Treading/Folding Recognition and Homology Modelling

In-silico techniques have been used for the computational prediction of three-dimensional protein structures, making possible molecular interaction studies, drug discovery and improving the results of Quantitative Structure-Activity Relationship (QSAR) techniques. The computational modeling of proteins uses structures solved by techniques such as NMR spectroscopy, X-ray crystallography, among others. The protein modeling technique has some methodologies employed, but this introduction will only address the modeling by homology and threading/fold recognition [23, 24].

Folding Recognition or Threading is a protein modeling methodology used to model proteins that have folding equal to known structures but do not have resolved homologous structures (those deposited in PDB) [25, 26]. This technique was described in 1991 for Bowie, Luthy and David Eisenberg [25] and the word threading was defined in 1992 for David Jones, Will R. Taylor and Janet Thornton [26], referring to a 3D structure of a protein model based on the folding.

Modeling is done by evaluating the amino acids of the target sequence so that they fit into a model, selecting the one that best fits. The methodology is effective

and widely used due to some factors. The first is that there are a limited number of different folding in nature, thanks to the evolution and restrictions imposed by the chemistry and physics of amino acids; there is a high chance that the protein will have a fold similar to that already studied by other techniques such as X-ray crystallography and NMR spectroscopy deposited in the PDB. whereas 90% of the structures resolved in recent years submitted to the PDB have similar folding [27].

Although both threading and homology modeling are methods used for modeling, the protein structures used of their targets are different. The first technique, homology modeling, is for targets that have resolved homologous proteins deposited in the PDB. On the other hand, threading is for targets that have bend resemblance and low sequence identity when homology modeling cannot be efficient [28].

The threading method is divided into those based on 1-D profile, aligning the target sequence with each structure in the folding library and 3-D profile, which consider the complete protein structure [29].

A simple form for the depicted approach would be to analyze the amino acid and classify it if it is present on the nucleus or surface of the protein; however, the most elaborate ones analyze the secondary structure that the amino acid is present and how conserved it is [29, 30].

In the 3-D profile the interatomic distances between all pairs of atoms of the structure are analyzed. Although it is a more detailed analysis of the structure, it has greater difficulty in aligning with the target sequence [30].

Molecular modeling by homology refers to the construction of a protein model using the target amino acid sequence and experimentally resolved three-dimensional structures (template). The amino acid sequence of these three-dimensionally resolved structures must be similar to the target protein sequence for such a technique to be developed [31].

Studies have shown that the three-dimensional protein structure is more conserved from an evolutionary point of view than expected with respect to sequence [32].

The most common errors that occur in homology modeling are inaccuracies in the alignment of the target sequence with the template sequence [33, 34]. The quality of the model structure mainly depends on the quality of sequence alignment. Some problems encountered in homology model creation are the presence of alignment gaps, interfering with the target structural region and when some template gaps were not resolved due to the low resolution in the experimental part used to solve the structure. However, the biggest errors occur in loop regions, as the target sequence and template can differ greatly in these regions [35]. One way to minimize errors in alignment is by using multiple alignment and refining regions with low similarity [36, 37].

The models, which have a sequential identity above 50%, are highly reliable with only minor errors regarding side chain packaging. When this identity drops to 25–50%, errors become more severe and appear mainly in loop regions. Finally, below 25%, errors become extremely severe, resulting in protein folding problems [38]. In this region of low identity, homology modeling is extremely difficult, and the threading method [39] is more appropriate.

Thanks to the difficulty and time, it takes for protein structures to be resolved by experimental methods such as x-ray crystallography as well as NMR, homology modeling provides useful and often essential models for other experimental studies.

In-silico structural models can be used for protein-protein interaction studies, molecular fitting, among others [40]. Low precision models can also be used for these purposes, as most errors are located in the handles. of protein. The functional regions of these models tend to be highly conserved throughout evolution and are therefore more accurately modeled [38].

2 Theoretical Support for the Prediction of a Protein Model Through the Protein Structural Homology Technique

The structural protein homology technique is based on the development of a three-dimensional receptor model by comparing two or more similar protein sequences. Thus, at least one experimentally resolved structure is required to develop a model and this structure must share a sequential identity of at least 25% with the protein to be modelled [41].

The procedure for developing a protein model by the structural homology protein modeling method follows four steps: Starting with the search for homologous sequences (1), followed by sequence alignments (2), and ending with the construction of the model (3) and evaluation (4) [42]. A good suggestion for developing these steps is to use the program sequence: Blastp, Clustal Omega, Modeller, WhatIf and Save.

The first step in building a protein model through the structural homology technique, searching for homologous sequences, is performed by software or online servers that detect similarities between nucleotide sequences and proteins such as the server **BLAST** (*Basic Local Alignment Search Tool*) criado pelo *National Center for Biotechnology*. **BLAST** works by an algorithm that is capable of comparing protein sequences with protein databases in any combination, among other functions. For protein search there are five algorithms to choose from: (1) Quick **BLASTp** (Accelerated protein-protein BLAST), (2) BLASTP (protein-protein BLAST), (3) PSI-BLAST (Position-Specific Iterated BLAST), (4) PHI-BLAST (Pattern Hit Initiated BLAST), (5) DELTA-BLAST (Domain Enhanced Lookup Time Accelerated BLAST) [43].

First, **BLASTp** looks for three similar amino acids (hit) to the template sequence in other sequences available in various databases. When these hits are found, they get a score. Then the analysis is expanded to the ends of the sequences to obtain a higher score. Another analysis by **BLASTp** is the randomness with which a homologous sequence was obtained. This score is called e-value and indicates the likelihood of finding an alignment in another sequence. Thus, the lower the value of e-value, the more reliable the result obtained.

An important point to consider at the early stage of the prediction process of a protein structure is the percentage of sequential identity. This data measures the degree of correspondence between two substrings. An identity of 25% or greater implies similarity of function, while 18–25% similarity may imply structural or even similarity of function. Another important piece of data analyzed during sequence alignment is which mutations (insertions and/or deletions) of amino acid residues these proteins have undergone throughout evolution, estimating that function should be preserved in sections where identity (or even similarity) sequential should be longer.

The second step of building a protein model, the most important step in the process, [44] can be performed well through the online server **CLUSTAL Omega (European Bioinformatics Institute EMBL-EBI)** [45]. Such a program works in five steps to generate multiple sequence alignment. The first and second steps consist of pairwise and grouping [46]. Then there is the construction of a ‘guide’ tree, in which two closer groups are combined. This step follows until a final tree can be parsed. Finally, multiple sequence alignment is generated [47].

Finally, for the actual construction step the program **Modeller (University of California San Francisco–UCFS)** [48]. The program **Modeller** was used for the construction of the PMI model and it is an automated algorithm used for protein structure modelling through comparison with solved three-dimensional structures [49]. This program uses at least one input structure as a reference (or template) and, from other provided alignments, generates a homologous three-dimensional model [48]. For the construction of the three-dimensional model, the program uses some spatial constraints such as distances and dihedral angles, length and binding angles, secondary structure folding, among others. After model generation, an evaluation and modeling of the loop regions can occur using an algorithm, followed by the structural optimization of the generated model [49].

To ensure the reliability of the generated model, an evaluation step is necessary. Online server **WhatIf (Centre for Molecular and Biomolecular Informatics–CMBI)** [50] is an important analysis option because it does the analysis between atomic contacts between atoms of each amino acid residue present in the model. In addition to this server the suite **SAVE v5.0 (NIH MBI Laboratory)** (<http://servicesn.mbi.ucla.edu/SAVES/>) has important analyzes to be evolved as the **ProCheck** [51], **Verify 3D**, **Errat e Prove**.

Using the **WhatIf** server allows analysis of atomic contacts. The program identifies bad contacts and favorable contacts (such as intermolecular interactions), generating scores for each residue. Additionally, the program provides a flexible environment for displaying, manipulating and analyzing small molecules, proteins, nucleic acids and their interactions, as well as for the validation and correction of protein structures.

Another very important program for the analysis of a predicted protein model is **ProCheck**. This program compares the generated model residues and high-resolution crystallographic protein structures. **ProCheck** is available from EMBL-EBI and, with it, e. It is through this analysis that the graphs of Ramachandran Diagram, planarity of peptide bonds, tetrahedral distortion of alpha

carbons, energies of hydrogen bonds, measurements of non-ligand interactions (van der Waals, hydrogen bonds, electrostatic interactions) are generated. General Factor (G-Factor), the latter being an average of the general stereochemistry of the model.

Also in the SAVE suite, there is the Verify 3D program that analyzes the compatibility between the 3D model and its location-based amino acid sequence (alpha, beta, loop) and a chemical environment sequence (polar, nonpolar) using a proposed matrix by Bowie and collaborators [25]. This matrix allows a probability analysis of finding the 20 amino acids in different chemical environments, based on the amino acid type and nature of the chemical environment. Next, alignment is performed between the 3D model and the amino acid sequence; allowing detection of badly resolved regions.

Unbound interactions between different atoms in the model compared to highly refined structures can be analyzed by **ERRAT**. This analysis graphs an error function through a window consisting of nine residuals. Generally speaking, it is a more effective method than the **3-D Profile** proposed by Bowie and collaborators [25], but it is no better than **ProCheck**.

Finally, it is possible to calculate the volume of atoms present in the predicted macromolecule with the **PROVE** program. **PROVE** generates a statistical deviation called Z-score and this statistical data comes from comparing the model with refined high resolution structures deposited in the PDB.

3 Development and Evaluation of the Generated PMI Model

Next, the 4 steps of protein model prediction will be elucidated by the structural homology modeling technique (homologous sequence search, alignment, model construction and evaluation) using the XAC PMI protein as an example.

3.1 Approval Sequence Identification Step

The initial step of the protein modeling prediction process is the identification of sequence-homologated protein structures in search that have crystallographic data, that is, their structure resolved and reported in a database of crystallographic structures, such as Protein Data Bank [52]. For greater reliability of the generated model it is desired that the sequential identities are above 25% in relation to the protein sequence under study [35]. This process can be efficiently performed through the **BLAST** online server with the protein blast algorithm (**BLASTp**).

Therefore, the use of Blastp for the XAC PMI amino acid sequence identified four structures with sequential identity above 25% (Table 1). Due to the fact that the model to be generated is of interest for Structure-Based Drug Discovery

Table 1 Sequence identity and e-value results of protein sequences obtained from the **BLAST** online server using the protein blast algorithm (**BLASTp**) for screening for XAC PMI homologated proteins

PDB ID	Identity (%)	E-value
2QH5_A	38	7×10^{-63}
2X5S_A	38	5×10^{-64}
2CU2_A	38	2×10^{-59}
1H5R_B	29	0.033

(SBDD) studies the choice of the crystallographic structure for its construction took into consideration the presence of a complex ligand to the protein site. Thus, the choice of the homologous protein used to predict an XAC PMI structure was the protein B chain (*Escherichia coli* strain K12 Thymidyltransferase) which holds the PDB code ID: 1H5R

In possession of the homologous sequences the sequence under study, the next step is determined by the alignment of the sequences and their evaluation. In order to approach as many options as possible, allowing the construction of a more reliable model, the alignment was performed with the five obtained sequences. Thus, it was possible to obtain four alignments between the protein sequence under study and the protein sequences from **BLASTp** individually and one fifth regarding a multiple alignment between all sequences.

For greater process robustness, alignment can be combined with a visual inspection of overlapping crystallographic structures. Thus, it is possible to analyze whether the insertions or deletions suggested by **Clustal Omega** are as expected. That is, they have not been placed in regions containing secondary structures. This structural overlap allowed the visualization of all secondary structures of the proteins and, due to this, some modifications were made in the alignment proposed by **Clustal Omega**. Thus, the most promising alignment was the multiple alignment proposed by the program combined with the visual inspection presented in Fig. 1.

Overlapping the generated model with the reference structure also reveals important data that increases the reliability of the obtained model (Fig. 2). It can be observed in the region of the active site that the amino acid residues described by Zuccotti and co-works [53]. As responsible for the formation of the ligand-PMI complex, Gln147, Glu162 and Val173, remain allocated in the same region when compared to the PDB ID 1H5R reference framework. However, in the model created based on the *Xanthomonas* sequence, the amino acid valine is replaced by an asparagine, but both (model asparagine and reference structure valine) are present in the same region and over the same main chain conformation.

1H5R	-KMRKGIILAGGSGTRLYPVTMA-VSKQLLPIYD-KPMIYYPLSTLMLAGIR--DILIIST	57
2CU2	-MKTYALVMAGGRGERLWPLSREDRPKPFPLFEGKTLLEATLERLAPL-VPPERTLLAVR	59
2X5S	--VMKALILAGGSGERFWPLSTPETPKQFLKLFGNKSLMRWTFERVLEE-MDPKDVIIVVTH	58
2QH5	-LKIKNILLSG-----YPKQFLKLFDHKSLFELSFKRNASL-VD--ETLIVCN	57
PMI	MSDVLPIILSGSGSTRWLPLSRESYPKQFLPLVGDKSMQLQSTWLRAPV-AG-HAPIVVAN	59
	...** *:*:* : *:* * : : :	
1H5R	PQDTPRFQQLLDGGSQWGLNL---QYKVPSPDGLAQAFIIGEE---FIG---GDDCALVLG	110
2CU2	RDQEAVAR-PYADG-----I---RLLLLEPLGRDTAGAVLLGVA---EALKEGAERLLVPA	108
2X5S	KDYVERTKKELEPE-----LPDENIAEPMKKNTAPACFIGTKL---AD--DD-EPVLVLP	108
2QH5	EKHVFLALEEIKNEIK--NKS-VGFLLESLSKNTANAIALSALM---SD--KE-DLLIVTFS	110
PMI	EEHRFMAAEQLQ-QLG--VKPS-AILLEPKGRNTAPAIAVAALAEATRDLG--AD-PLLLVLPS	114
	. : : : : : . : : :	
1H5R	DNIFYG-HDLPKLMEAAVNK-ES--GATVFAYHVNDPE-RYGVVEFDKN-----GTAISLEE	162
2CU2	DHVVGDDEAYREALATMLEAAEEG-FVVALGLRPTRPETEYGYIRLGPREG-	
	AWYRGEFVLE	168
2X5S	DHRIPDTKKFWKTVKKALDALEKYDGLFTFGIVPTRPETGYGYIEIGEELEEYVHKVAQFR	170
2QH5	DHLIKDLQAYENAIAKKAIDLAQKG-FLVTFGVSIDKPNTEFGYIESP----NGLD-VKRFIE	175
PMI	DHVIQNEAAFQAAVTLAATAAEEQG-KLVTFGIKPTAPETGYGYIKAS--AGAGASAVERFVE	182
	*. . : : : : : : : : : : : : : : : : *	
1H5R	KP-----LEP--K-SNYAVTGLYFYDN-DVVQMAKNLKPSAR-----	195
2CU2	KPSYAEALEYIRK-GYVWNGGVFAFAPATMAELFRRHLPSSHE-ALER-LLAGAS-----	220
2X5S	KPDLEAKKFVESGRFLWNSGMFLWKAREFIEEVKVCESPIYENLKDVDPRNFEE-----	225
2QH5	KPSLDKAIEFQKSGGFYFNSGMFVFAQAGVFLDELKKHAPTILK-GCER-AFESLENAYFFEK	226
PMI	KPDLATAQSYLASGEYVWNSGMFLFRASRYLEELRKFHPAIAAD-ACQK-AWENKRDADFT-232	
	** * .. : : : : : : : : : : *	
1H5R	-----GELEITD-INRIYLEQGRLSVAMMGRGYAWLDTGTHQSLEASN	238
2CU2	----L EEVYAGLPKISIDYGVMEKA-E--RVRVVLGR--FPWDDVGNWRALERVFS	267
2X5S	----LKKAYEKVPSISVDYAVMEKS-K--KVRVVKAD--FEWSDLGNWSSVREIEG	272
2QH5	KIARLSEKMQDLEDMSIDIALMQQS-H--KIKMVELN--AKWSDLGNFNAL----	273
PMI	--TRLDKDAFAASPSDSIDYAVMEKT-A--DAVVVPLD--AGWINDVGSWSSSL-----	277
	: : : : : : : : : : * * * * : :	

Legend: Dark-blue amino acids belong to β -leaf whereas green-colored amino acids belong to α -helices. The active site is highlighted in yellow and the amino acids that have had their rotamers modified are highlighted in blue.

Fig. 1 Alignment of amino acid sequences of protein phosphomanose isomerase (PMI) and structure sequences obtained by BLASTp (1H5R, 2CU2, 2X5S and 2QH5)

3.2 Model Construction and Evaluation Stage

After the alignment step is completed, the next step is conducted by constructing the model itself. Such a step is possible through the MODELLER program, which was used and thus generated 5 model hypotheses. In possession of the generated models, the evaluation step emerges to determine the most reliable and fit model for further studies.

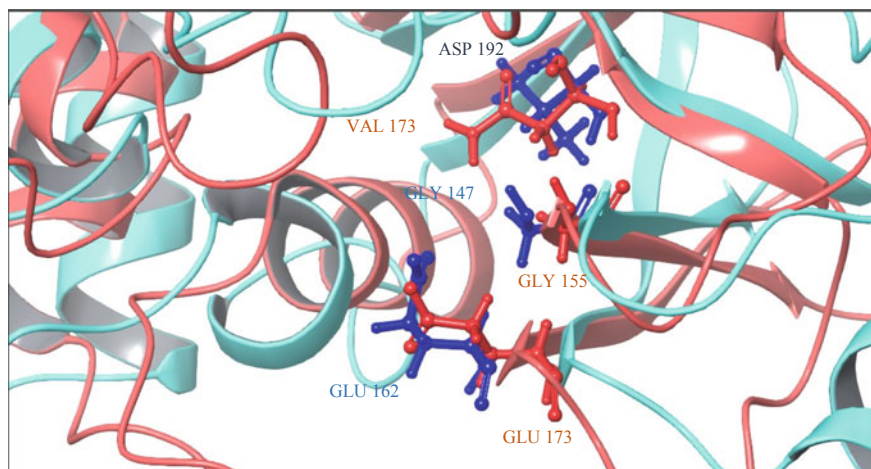


Fig. 2 Final PMI model of *Xanthomonas citri* subsp. *citri*, obtained by comparative modeling, highlighting the amino acids present in the active site. In blue color, residues belonging to the model that were allocated in the same region observed for the structure used herein as reference (PDB ID 1H5R), which is in red color

Table 2 Presentation of the results of general score (**WhatIf**), forbidden regions (**Ramachandran**) and G-Factor (**ProCheck**) obtained in the validation stage of the generated models

Models	General Score (WhatIf)	Forbidden Regions (Ramachandran Plot)	G-Factor
<i>1H5R</i>	-0.813	1	0
<i>Hypothesis 1</i>	-0.697	0	-0.1
<i>Hypothesis 2</i>	-0.745	1	-0.1
<i>Hypothesis 3</i>	-0.734	0	-0.1
<i>Hypothesis 4</i>	-0.758	0	-0.1
<i>Hypothesis 5</i>	-0.667	1	-0.1

Therefore, it is advisable to evaluate the presence of good or bad atomic contacts and also to make a comparison between model residues based on parameters observed in high-resolution crystallographic protein structures. And these studies were developed with the **WHATIF** online server and the **PROCHECK** program, respectively and the main results view in Table 2.

Given the results obtained by **WHATIF** it can be observed that the best hypothesis evaluated was *Hypothesis 4*, which had a total **WHATIF** score of -0.758, it is noteworthy that the reference value for this study is -0.813, which corresponds to the General Score for the crystallographic structure (1H5R) used as reference.

Another point of attention is the identified regions of the Ramachandran chart. The **Ramachandran Diagram** is divided into four regions: highly favorable, favorably permitted, generously permitted, and forbidden. When an amino acid is in the forbidden region, this means that any interatomic distance between unbound atoms is less than the Van der Waals distance corresponding to those atoms. In the case of *Hypothesis 4*, no amino acid residue is found in the forbidden region, favoring its selection as a model.

Another important point to consider is the G-Factor. It is a score based on the observed stereochemical parameters of a given structure. In the case of the PMI model, the hypotheses presented a G-Factor of -0.1 , a value that is within the region for a protein with a resolution of 1.9 \AA (referring to 1H5R).

An important point to be analyzed at this stage of the process are the conformations of amino acid residues that are part of the interaction site under study. This visual inspection is intended to analyze, and if necessary, modify the conformation of certain residues through the use of a library of rotamers. The choice of the best rotamer should take into account the direction of the residues of the structure used as a reference for the development of the model and the absence of contact with the neighboring residues.

We highlight that for the generated PMI model it was necessary to modify some residues, which can be seen in Fig. 1. With this change of rotamers, the value of **What If** for *Hypothesis 4* was changed to -0.782 , approaching the value of the reference structure (1H5R).

3.2.1 Evaluation of Dihedral Angles Ψ Versus Versus ϕ Through the Ramachandran Diagram

The Ramachandran Diagram is an essential tool for protein analysis as it shows the errors contained in the tertiary structure of these macromolecules. By showing which amino acids are in energetically favorable or unfavorable regions, this instrument allows an evaluation of the quality of experimental and theoretical models [54].

The graph is formed by two axes with values between -180° and $+180^\circ$, corresponding to the angles Phi and Psi of the provincial chain and comprising all possible energetic combinations of amino acid residues with these dihedral angles [54]. However, there are two amino acids that can be found in unfavorable regions: glycine and proline.

Since glycine has only one hydrogen in its side chain, and thus the least sterically hindered residue, it can assume forbidden conformations to other amino acids. On the other hand, proline, because it has a cyclic lateral chain, which makes its rotation restricted around the binding, is the most conformationally restricted amino acid.

The final **Ramachandran Diagram** obtained for the generated PMI model (Fig. 3) did not indicate unfavorable phi and psi angles for the residues present in the model, especially in the region of the interaction site. The model presented

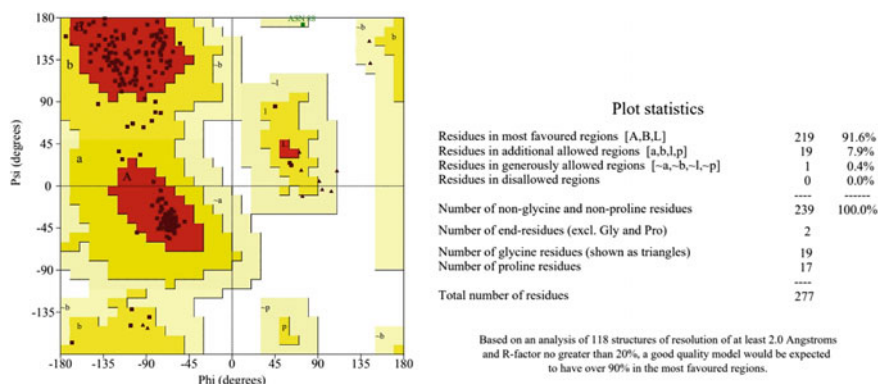


Fig. 3 Ramachandram diagram of *Xanthomonas citri* subsp. *citri* obtained by ProCheck: 91.6% waste in favorable regions, 7.9% waste in permitted regions, 0.4% waste in generously permitted regions and 0% waste in prohibited regions

91.6% of its residues in highly favorable regions and although the ASN88 residue appears in a “generously allowed” region, its torsional angles were “inherited” from the crystallographic structures used as reference.

3.2.2 Other Important Parameters for the Analysis (Suite SAVE v5)

Other important tools for analyzing a predicted protein model can be found in the SAVE v5 suite. Using **ProCheck** allows analysis of the planarity of peptide bonds, poor atomic contacts, tetrahedral distortion of alpha carbons, energy of hydrogen bonds and G-Factor. For the generated PMI model all values are within the expected values for 1.9 Å resolution protein structures (referring to the PDB ID 1H5R structure, used here as a reference for modeling) (Fig. 2) and the tetrahedral distortion of the alpha carbons presented a better value than the crystallographic one.

The parameters presented together in Figs. 1 and 2 help to evaluate the overall stereochemical quality of the selected model. The graphs show that the model obtained values within the **PROCHECK** reference range and, when analyzing the values presented by **WHATIF** for the amino acids belonging to the PMI interaction site, none presented values below -5 , which, if they existed, they should be reviewed and refurbished.

In addition to the atomic bonds that occur in the peptide chain there are also interactions between unlinked atoms. The tertiary structure of a protein is highly dependent on these interactions and there are six types of likely interactions between unbound atoms and they do not occur at random. Thus, it is possible through the **ERRAT** program to identify regions and make one in the statistical analysis of these interactions.

By looking at the graph developed by ERRAT for the PMI model (Fig. 4), it is possible to identify three distinct regions: one green, one yellow and one red. The green region shows that all amino acids are within expected values for highly resolved and refined structures. The yellow region corresponds to those amino acids that exceed the expected result and can be rejected with 95% confidence. A good protein structure is expected to have 5% of its structure in this region. Finally, the red regions are those that can be rejected with 99% confidence. The model generated for PMI has few yellow regions and only a single amino acid in the red region (ALA167). No amino acids present in these regions are part of the active site, so there will be no problems for future testing. In addition to this data, the quality factor, value related to unbound atomic interactions of 85.5019 determines a high quality structure (result for values above 50) (Fig. 5).

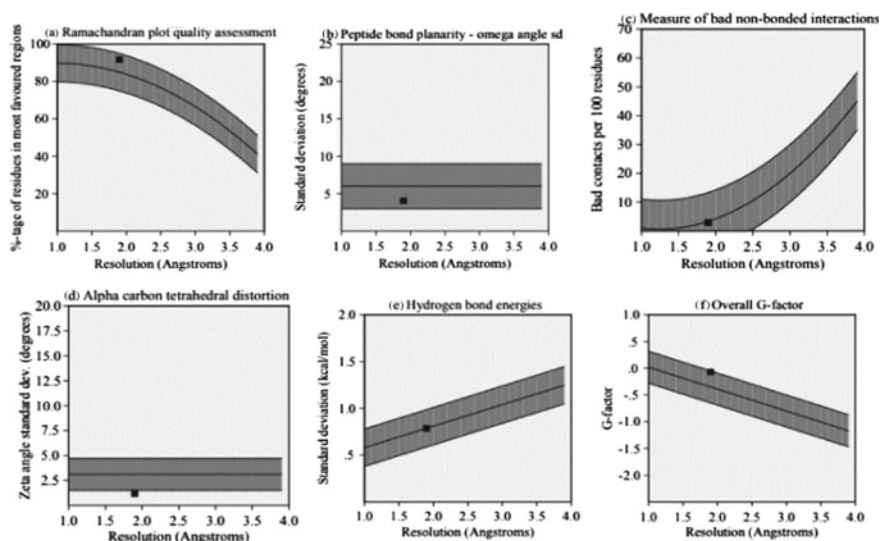


Fig. 4 Summary of the stereochemical evaluation of the selected model constructed by structural homology for PMI



Fig. 5 ERRAT obtained for the generated PMI model of *Xanthomonas* sp. The red bar indicates the amino acid with error above 99%, the yellow bars indicate regions with errors between 95% and 99%, and the green bars indicate the regions with minor error percentage for protein folding

Another interesting analysis is to check if an amino acid residue matches the environment it is in, in other words whether there is compatibility of the model with its amino acid sequence. This analysis can be performed using Verify-3D, in the PMI study it can be observed that at least 80% of amino acids had a score equal to or greater than 0.2 in the 3D-1D profile. In addition, there is a region (ALA66 to LEU82) that has fallen below the threshold, indicating a probable misfolding in that region; however, it is not a cause for concern because it is not in the region of the active site of the model (Fig. 6).

Finally, as a last analysis it is possible to verify the volume of atoms. The PROVE program correlates the volume obtained for each amino acid of the protein with the high resolution protein volumes. As a result, PROVE provides a score value called the Z-score that corresponds to the programmed statistical deviation from highly resolved and refined structures. In the case of the PMI model under study, both the Z-score and the Z-score RMS were above the region of interest. In addition, 4.6% of the analyzed residues were considered outliers, indicating that more attention should be given to the model. However, along with all the other analyzes done, it can be determined that this is a good model for the PMI of *Xanthomonas* sp (Fig. 7).



Fig. 6 Verify-3D obtained for the generated PMI model of *Xanthomonas* sp

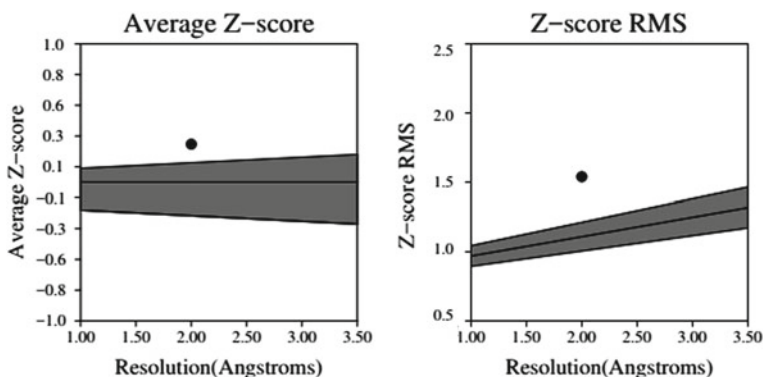


Fig. 7 PROVE obtained for the generated PMI model of *Xanthomonas* sp. Z-score corresponds to the deviations of atomic volume values from standard values. Z-score rms measures the average of irregular volumes in the protein structure

4 Conclusion

The three-dimensional structure of a receptor is an important tool for computational chemists working in the area of molecular modeling. By exploring interactions in a ligand-receptor complex, it is possible to perform a deeper analysis of these studies, expanding the impact of these tools.

The *Xanthomonas* PMI model proved reliable through the validation and evaluation of the interaction site residues. Consequently, this model can also be used in virtual screening studies to select compounds that interact with this target, possibly in the management of citrus cancer.

Acknowledgements We acknowledge financial support from CNPq.

References

1. Hasse, C.H.: *Pseudomonas citri*, the cause of citrus canker. *J. Agric. Res.* **4**, 97–104 (1915)
2. Vernière, C.J., Gottwald, T.R., Pruvost, O.: Disease development and symptom expression of *Xanthomonas axonopodis* pv. *citri* in various citrus plant tissues. *Phytopathology* **93**, 832–843 (2003)
3. Danos, E., Berger, R.D., Stall, R.E.: Temporal and spatial spread of citrus canker within groves. *Phytopathology* **74**, 904–908 (1984)
4. Gottwald, T.R., McGuire, R.G., Garran, S.: Asiatic citrus canker: spatial and temporal spread in simulated new planting situations in Argentina. *Phytopathology* **78**, 739–745 (1988)
5. Gottwald, T. R., Graham, J.H., & Schubert, T.S.: *Citrus canker*. *Plant Health Prog.* (2000)
6. Gottwald, T.R., Hughes, G., Graham, J.H., Sun, X., Riley, T.: The citrus canker epidemic in Florida: the scientific basis of regulatory eradication policy for an invasive species. *Phytopathology* **91**, 30–34 (2001)
7. Portaria da Coordenadoria de Defesa Agropecuária (CDA). Resolução SAA-10. Available at <https://www.defesa.agricultura.sp.gov.br/legislacoes/resolucao-saa-10-de-20-02-2017,1093.html> (2017)
8. Seille, R., Christiano, C.: Universidade de São Paulo Escola superior de Agricultura “Luiz de Queiroz” Cancro cítrico (2006)
9. Bonas, U.: Hrp genes of phytopathogenic bacteria. *Curr. Top. Microbiol. Immunol.* **192**, 79–84 (1994)
10. EL Yacoubi, B.: Bacterial citrus canker: molecular aspects of a compatible plant-microbe interaction. *Mater. Japan.* <https://doi.org/10.2320/materia.44.24> (2005)
11. Da Silva, A.C.R., et al.: Comparison of the genomes of two *Xanthomonas* pathogens with differing host specificities. *Nature* **417**, 459–463 (2002)
12. Carnielli, C.M., Artier, J., de Oliveira, J.C.F., Novo-Mansur, M.T.M.: *Xanthomonas citri* subsp. *citri* surface proteome by 2D-DIGE: ferric enterobactin receptor and other outer membrane proteins potentially involved in citric host interaction. *J. Proteomics* **151**, 251–263 (2017)
13. InterPro: Protein sequence analysis & classification. Available at <http://www.ebi.ac.uk/interpro/entry/IPR016305>
14. Stryer, L., Berg, J.M., Tymoczko, J.: *Biochemistry*. WH Freeman, New York (2007)
15. Cleasby, A., et al.: The x-ray crystal structure of phosphomannose isomerase from *Candida albicans* at 1.7 angstrom resolution. *Nat. Struct. Biol.* **3**, 470–479 (1996)

16. Papoutsopoulou, S.V., Kyriakidis, D.A.: Phosphomannose isomerase of *Xanthomonas campestris*: a zinc activated enzyme. *Mol. Cell. Biochem.* **177**, 183–191 (1997)
17. Zandonadi, F.D.S.: Análise proteômica diferencial da fração periplasmática das estirpes A, B e C de *Xanthomonas* spp. que diferem na patogenicidade e espectro de citros hospedeiros. Universidade Federal de São Car (2012)
18. Payton, M.A., Rheinneck, M., Klig, L.S., DeTiani, M., Bowden, E.: A novel *Saccharomyces cerevisiae* secretory mutant possesses a thermolabile phosphomannose isomerase. *J. Bacteriol.* **173**, 2006–2010 (1991)
19. Patterson, J.H., Waller, R.F., Jeevarajah, D., Billman-Jacobe, H., McConville, M.J.: Mannose metabolism is required for mycobacterial growth. *Biochem. J.* **372**, 77–86 (2003)
20. Garami, A., Ilg, T.: Disruption of mannose activation in *Leishmania mexicana*: GDP-mannose pyrophosphorylase is required for virulence, but not for viability. *EMBO J.* **20**, 3657–3666 (2001)
21. Gao, H., Yu, Y., Leary, J.A.: Mechanism and kinetics of metalloenzyme phosphomannose isomerase: measurement of dissociation constants and effect of zinc binding using ESI-FTICR mass spectrometry. *Anal. Chem.* **77**, 5596–5603 (2005)
22. Oprea, T.: Introduction to Chemoinformatics in Drug Discovery. Wiley-VCH, Hoboken (2005)
23. Hoof, R.W.W., Sander, C., Vriend, G.: Objectively judging the quality of a protein structure from a Ramachandran plot. *Comput. Appl. Biosci.* **13**, 425–430 (1997)
24. Rodriguez, R., Chinea, G., Lopez, N., Pons, T., Vriend, G.: Evaluation: three related resources. *Bioinformatics* **14**, 523–528 (1998)
25. Bowie, J.U., Ltcy, R., Eisenberg, D.A.: Method to identify protein sequences that fold into a known three-dimensional structure. *Science* **253**, 164–170 (1990)
26. Jones, D.T., Taylor, W.R., Thornton, J.M.: A new approach to protein fold recognition. *Nature* **358**, 86–89 (1992)
27. Peng, J., Xu, J.: Low-homology protein threading. *Bioinformatics* **26**, i294–i300 (2010)
28. Peng, J., Xu, J.: A multiple-template approach to protein threading. *Proteins: Struct. Funct. Bioinf.* **79**, 1930–1939 (2011)
29. Yang, Y., Faraggi, E., Zhao, H., Zhou, Y.: Improving protein fold recognition and template-based modeling by employing probabilistic-based matching between predicted one-dimensional structural properties of query and corresponding native properties of templates. *Bioinformatics* **27**, 2076–2082 (2011)
30. Gront, D., Blaszczyk, M., Wojciechowski, P., Kolinski, A.: BioShell Threader: protein homology detection based on sequence profiles and secondary structure profiles. *Nucleic Acids Res.* **40**, 257–262 (2012)
31. Chothia, C., Lesk, A.M.: The relation between the divergence of sequence and structure in proteins. *EMBO J.* **5**, 823–826 (1986)
32. Kaczanowski, S., Zielenkiewicz, P.: Why similar protein sequences encode similar three-dimensional structures? *Theor. Chem. Acc.* **125**, 643–650 (2010)
33. Venclovas, Č., Margelevičius, M.: Comparative modeling in CASP6 using consensus approach to template selection, sequence-structure alignment, and structure assessment. *Proteins Struct. Funct. Genet.* **61**, 99–105 (2005)
34. Ginalski, K.: Comparative modeling for protein structure prediction. *Curr. Opin. Struct. Biol.* **16**, 172–177 (2006)
35. Chung, S.Y., Subbiah, S.: A structural explanation for the twilight zone of protein sequence homology. *Structure* **4**, 1123–1127 (1996)
36. Martí-Renom, M.A., Stuart, A.C., Fiser, A., Sánchez, R., Melo, F., Sali, A.: Comparative protein structure modeling of genes and genomes. *Annu. Rev. Biophys. Biomol. Struct.* **29** (1), 291–325 (2000)
37. Mückstein, U., Hofacker, I.L., Stadler, P.F.: Stochastic pairwise alignments. *Bioinformatics* **18**, S153–S160 (2002)
38. Baker, D., Sali, A.: Protein structure prediction and structural genomics. *Science* **294**, 93–96 (2001)

39. Blake, J.D., Cohen, F.E.: Pairwise sequence alignment below the twilight zone. *J. Mol. Biol.* **307**, 721–735 (2001)
40. Gopal, S., et al.: Homology-based annotation yields 1,042 new candidate genes in the *Drosophila melanogaster* genome. *Nat. Genet.* **27**, 337–340 (2001)
41. Schwede, T., Kopp, J., Guex, N., Peitsch, M.C.: SWISS-MODEL: an automated protein homology-modeling server. *Nucleic Acids Res.* **31**, 3381–3385 (2003)
42. Sanchez, R., Sali, A.: Advances in comparative protein-structure modelling. *Curr. Opin. Struct. Biol.* **7**(2), 206–214 (1997)
43. Altschul, S.F., Gish, W., Miller, W., Myers, E.W., Lipman, D.J.: Basic local alignment search tool. *J. Mol. Biol.* **215**, 403–410 (1990)
44. Zhorov, B.S., Folkman, E.V., Ananthanarayanan, V.S.: Homology model of dihydropyridine receptor: implications for L-type Ca(2+) channel modulation by agonists and antagonists. *Arch. Biochem. Biophys.* **393**, 22–41 (2001)
45. Sievers, F., et al.: Fast, scalable generation of high-quality protein multiple sequence alignments using clustal omega. *Mol. Syst. Biol.* **7**, 1–6 (2011)
46. Blackshields, G., Sievers, F., Shi, W., Wilm, A., Higgins, D.G.: Sequence embedding for fast construction of guide trees for multiple sequence alignment. *Algorithms Mol. Biol.* **5**, 1–11 (2010)
47. Profile Hidden Markov Model Analysis (2018). Available at: www.biology.wustl.edu
48. Sali, A.: Modeller: generation and refinement of homology-based protein structure models. *Methods Enzymol.* **374**, 461–491 (2004)
49. Eswar, N., Webb, B., Marti-Renom, M.A., Madhusudhan, M.S., Eramian, D., Shen, M.Y., Pieper, U., Sali, A.: Comparative protein structure modeling using MODELLER. *Curr. Protoc. Protein Sci.* **50**(1), 2–9 (2007)
50. Vriend, G.: WHAT IF: a molecular modeling and drug design program. *J. Mol. Graph.* **8**, 52–56 (1990)
51. Laskowski, R.A., MacArthur, M.W., Moss, D.S., Thornton, J. M.: Procheck: a program to check the stereochemical quality of protein structures. *J. Appl. Crystallogr.* **26**, 283–291 (1993)
52. Kirchmair, J., et al.: The Protein Data Bank (PDB), its related services and software tools as key components for in silico guided drug discovery. *J. Med. Chem.* **51**, 7021–7040 (2008)
53. Zuccotti, S., et al.: Kinetic and crystallographic analyses support a sequential-ordered bi bi catalytic mechanism for Escherichia coli glucose-1-phosphate thymidyltransferase. *J. Mol. Biol.* **313**, 831–843 (2001)
54. Ramachandran, G.N., Ramakrishnan, C., Sasisekharan, V.: Stereochemistry of polypeptide chain configurations. *J. Mol. Biol.* **7**, 95–99 (1963)

Design of Inhibitors of the Human Fibroblast Activation Protein α as a Strategy to Hinder Metastasis and Angiogenesis



Daniel F. Kawano, Carlos H. T. de Paula da Silva and Carlton A. Taft

Abstract In many cancers such as breast, colon and pancreatic carcinomas, the tumor-associated stroma constitutes the microenvironment necessary to provide their nutritional support and survival/growth factors. In these tissues, cancer-associated fibroblasts express the fibroblast activation protein α (FAP), a dipeptidyl peptidase involved in the proteolytic remodeling of the stromal extracellular matrix of the tumor. Accordingly, high levels of stromal FAP correlate with a rapid progression of colorectal cancers, for example, increasing the potential for the development of metastasis. The presence of FAP on the surface of the cells is associated with other enzymes (specially metalloproteinases) and their regulators in order to promote an extensive degradation of the extracellular matrix. FAP is the only peptidase able to type-I collagen as a substrate and it acts in association with matrix metalloproteinases to produce biologically active fragments of denatured collagen. Therefore, the resulting proteolytic degradation (remodeling) of the extracellular matrix allows the neoplastic cells to invade the surrounding tissues, to migrate to distant sites (metastasis) and the increase in the microvessel density (angiogenesis) to provide the proper nutrition of the tumor. Herein we reviewed the role of FAP in cancers and the main synthetic and computer-aided strategies for the development of FAP inhibitors. As an example of structure-based drug design, we also used docking simulations coupled to *in silico* analyses of pharmacokinetics and toxicity profiles to identify new potential FAP inhibitors. In this concern, we started from 60,000 structures and applied a shape-fitting sampling algorithm to select compounds that could potentially fit into the binding pocket of FAP. The top 2%

D. F. Kawano (✉)

Faculty of Pharmaceutical Sciences, University of Campinas—UNICAMP,
Rua Cândido Portinari 200, Campinas 13083-871, São Paulo, Brazil
e-mail: dkawano@unicamp.br

C. H. T. de Paula da Silva

Faculty of Pharmaceutical Sciences of Ribeirão Preto, University of São Paulo,
Av. do Café s/n, Ribeirão Preto, São Paulo 14040-903, Brazil

C. A. Taft

Brazilian Center for Physics Research, Rua Dr. Xavier Sigaud 150, Rio de Janeiro,
RJ 22290-180, Brazil

© Springer Nature Switzerland AG 2020

F. A. La Porta and C. A. Taft (eds.), *Emerging Research in Science and Engineering Based on Advanced Experimental and Computational Strategies*, Engineering Materials, https://doi.org/10.1007/978-3-030-31403-3_11

277

compounds were rescored and had their binding affinity energies calculated. We studied the binding modes for the top-twelve compounds, estimating their drug-likeness and predicted some toxicity endpoints. All ligands displayed significant binding affinity energies, and none was potentially mutagenic or tumorigenic and only one was expected to be teratogenic. Nine of the twelve selected compounds displayed drug-likeness scores that would confer a proper lipophilicity balance for oral use. Although these compounds must be subjected to experimental validation concerning FAP inhibition, they seem promising due to the good predicted binding affinities, adequate pharmacokinetic profiles and general low toxicity.

Keywords Fibroblast activation protein α (FAP) · Cancer · Tumor-associated stroma · Dipeptidyl peptidases

1 Introduction

Cancer is a highly heterogeneous disease, triggered by intrinsic (genetically inherited) or acquired (environmental) stimuli, as one can observe by the strong correlation between ultraviolet radiation and skin cancer [1], benzene and myeloid leukemia [2], human papillomavirus and cervical cancer [3], *Helicobacter pylori* and gastric cancer [4] or persistent smoking and lung cancer [5]. The underlying etiology and progression of this disease may be explained by the occurrence of two major alterations: (1) mutations (including additions, deletions, substitutions and rearrangements of certain genes or chromosomes) that allow cells to begin an uncontrolled growth and (2) a compensatory disruption of the survival signaling pathways, which physiologically block the apoptotic process and, ultimately, ensure the excessive persistence of these hyperproliferative cells [6–8].

Cancer will only occur when these two abnormalities happen simultaneously since a deregulated proliferation in health cells will conduce to the prompt activation of apoptosis to destroy these cells. On the other hand, suppression of apoptosis alone will confer little advantage to a cell in a non-proliferative scenario. Consequently, these two processes have an additive character because, although the inhibition of apoptosis is not intrinsically mutagenic, its suppression will allow the survival of mutated cells that, otherwise, would have been efficiently eliminated [6].

Therefore, reactivation of a functional apoptotic process in cancer cells is a typical strategy to achieve tumor-selective eradication without compromising the majority of healthy cells. However, the ‘classic’ chemotherapeutic agents, which ultimately kill cells by inducing apoptosis, are also lethal to healthy rapidly dividing cells such as the bone marrow, gastrointestinal/oral mucosa, skin and hair follicle cells [7, 9]. Alternative approaches are then necessary to achieve tumor suppression and the study of its surroundings (i.e., the tumor microenvironment) may provide the required answer. The tumor depends on its associated stroma for the nutritional support and for survival/growth factors, while the stroma may account for more than 90% of the tumor mass in carcinomas such as breast, colon and pancreatic [10].

Several studies demonstrate the role of the tumor microenvironment in promoting drug resistance [11–15] and angiogenesis [16–21], while the presence of carcinoma-associated fibroblasts [22–24] and inflammatory infiltrating cells [25–27] in the tumor-associated stroma correlates with a poor disease out-come [28].

2 The Role of the Fibroblast Activation Protein α (FAP) in Cancers

In the normal stroma of organs and tissues, the connective tissue is composed of fibroblasts, which are immersed in a vast extracellular matrix of connective tissue fibers and proteoglycan aggregates to form a viscous hydrated gel. These fibroblasts produce nearly all the components of the extra-cellular matrix including structural (e.g., fibrous collagen and elastin) and adhesive proteins (e.g., laminin and fibronectin), and ground substance (e.g., glycosaminoglycans, such as hyaluronan and glycoproteins) [29]. In cancers, the stromal fibroblasts (now denominated cancer-associated fibroblasts) compose the tumor microenvironment, playing a role in several processes that confer the malignant behavior of tumors including proliferation, angiogenesis and remodeling of the extracellular matrix to favor the invasion and metastasis of carcinoma cells [30].

A main characteristic of the cancer-associated fibroblasts is the expression of the fibroblast activation protein α (FAP), which is detected on the surface of fibroblasts in the stroma surrounding more than 90% of the epithelial cancers [31]. It has also been found in epithelial tumor cells of breast, gastric, and colorectal cancers, as well as on melanocytes and melanoma cells [32–37]. High levels of stromal FAP correlate with a rapid progression of colorectal cancers, increasing the potential for the development of metastasis [38].

FAP is an integral membrane dipeptidyl peptidase (of which the dipeptidyl peptidase IV is the prototypical member) and, accordingly, it is able to cleave a Pro-Xaa peptide bond (where Xaa represents any amino acid) (Fig. 1) [39]. FAP and the dipeptidyl peptidase IV share 50% of sequence identity considering the whole proteins and 70% in the comparison of the catalytic domains [40–42].

Although both FAP and dipeptidyl peptidase IV show similar peptidase activities, FAP is the only peptidase able to have gelatin, α 2-antiplasmin and the type-I collagen as substrates [32, 41, 43–45], while some studies suggest that FAP may act in association with matrix metalloproteinases to produce biologically active fragments of denatured collagen [46, 47]. The neuropeptide Y (NPY), B-type natriuretic

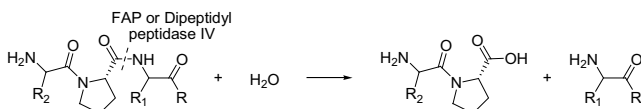


Fig. 1 General mechanism of peptide hydrolysis by FAP and dipeptidyl peptidase IV

peptide, substance P and peptide YY are natural hormone substrates for both FAP and the dipeptidyl peptidase IV [48].

As FAP is able of degrading the type-I collagen, it is involved in the proteolytic degradation (remodeling) of the extracellular matrix, allowing the neoplastic cells to invade the surrounding tissues and to migrate to distant sites (metastasis). In addition, remodeling of the extracellular matrix will favor angiogenesis and tumors expressing FAP have a 3-fold higher microvessel density as compared with tumors from cells not expressing FAP. Additionally, abolition of FAP enzymatic activity reduces tumor growth, providing an attractive target for the development of new drugs [49].

The presence of FAP on the surface of the cells is associated with invadopodia, which are sites where proteases (e.g., metalloproteinases) and their regulators are concentrated within the plasma membrane to promote the degradation of the extracellular matrix, then allowing improved cell motility and the invasive behavior of these cells [50]. Therefore, FAP expression by fibroblasts promotes changes in the composition and organization of the extracellular matrix to favor invasion not only because of the FAP's proteolytic activity itself but, mainly, in a coordinated action with metalloproteinases [34].

3 Strategies for the Design of FAP Inhibitors

Chemical synthesis is an important issue and often a limiting factor in the drug discovery process [51]. Although bioinformatics, chemo informatics and theoretical drug optimization strategies are valuable and integral parts of the drug design process, they may sometimes generate structures that are quite complicated and, consequently, hard to synthesize by requiring long-step synthesis with carefully controlled reactions, especially if the stereochemical configuration is a concern [52]. Therefore, the factors that conspire to make a synthesis difficult to execute (i.e., those which give rise to molecular complexity) [53] must be considered when selecting a hit or preparing analogs of a hit of interest.

Medicinal chemists typically aim to synthesize as many new compounds as quickly as possible which will then be tested by biologists against a chosen biological target [54]. In this context, synthetic accessibility can be thought as their efforts to use the smallest number of chemical steps to synthesize a drug from common laboratory reactants [55]. However, synthetic accessibility and structural complexity are not only central issues in determining potential drug candidate molecules. They also must be carefully analyzed in the subsequent creation, exploration, and evaluation of short, efficient, safe, reproducible, scalable, ecological but still economical syntheses for the selected clinical candidates, i.e. in process optimization and scale up synthesis [54].

From the structural point of view, several features contribute to molecular complexity such as molecular size, element and functional-group content, cyclic connectivity, stereocenter content, chemical reactivity and structural instability [53]. Although these factors had been primarily identified based on the experience of

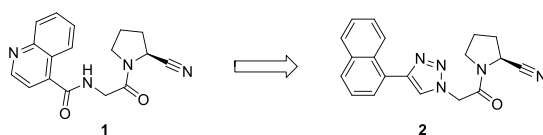
organic chemists regarding what features in the structure of a compound make it hard to be synthesized, there are also theoretical reasons for recognizing some of these features as sources of complexity. As stated by Goodwin [56] “*the more functional groups that a structure has, the more likely it is that one of those functional groups will interfere with an attempt to apply a standard chemical reaction to modify a structure in a predictable way. Similarly, the more structurally unstable a molecule is, the more likely an attempted chemical modification of it will result in a range of possible products. Not only are reagents often capable of reacting at multiple sites in a complex molecule, but also structural complexity can alter the chemical environment in a way that interferes with the mechanism of a desired reaction so that it will no longer produce the desired product to the anticipated extent* [56].”

Tough bioisosteres are classically used by medicinal chemists to improve potency, selectivity, bioavailability and/or metabolic stability, to decrease side effects or even to achieve patentability. Bioisosteric replacements can also result in compounds with reduced structural complexity and, consequently, better synthetic accessibility [57]. This can be achieved by improving structural stability, for example, when an amide group is replaced by a 4-substituted 1, 2, 3-triazole ring (Fig. 2), which is resistant to hydrolysis. This was the strategy employed by Jansen et al. [58] for the design of FAP inhibitors. Starting from **1** (Fig. 2), which displayed an IC_{50} concerning FAP inhibition of 0.01 μM , they designed the analog **2**, with improved metabolic stability. As the 4-alkynyl derivatized quinolines required to obtain the triazole analogues of **1** were, however, found not to be readily accessible, this group was replaced by a naphthalene moiety. However, FAP inhibition was considerably reduced, yielding an IC_{50} of 12.5 μM [58].

Another synthetic strategy to mask metabolically vulnerable groups is the design of a prodrug, compounds that are inactive in themselves, but which are converted in the body to the active drug. Usually, a metabolic enzyme is involved in converting the prodrug to the active drug, and so a good knowledge of drug metabolism and the enzymes involved allows the medicinal chemist to design a suitable prodrug which turns drug metabolism into an advantage rather than a problem [57]. As the target here is a peptidase, one can design prodrugs that are specific for tumor cells and tumor microenvironment upon activation by FAP.

In this context, LeBeau et al. [59] designed peptide protoxins by adding the FAP substrate sequences into the prodomain of melittin (Fig. 3), the main toxic component in the venom of the common European honeybee *Apis mellifera*. The designed peptide protoxins were efficiently activated by FAP and selectively toxic to FAP-expressing cell lines with IC_{50} values in the low micromolar range. Intratumoral injection of these compounds produced significant growth inhibition of human breast and prostate cancer xenografts, with minimal toxicity to the host animal [59].

Fig. 2 Design of FAP inhibitors based on bioisosteric replacement



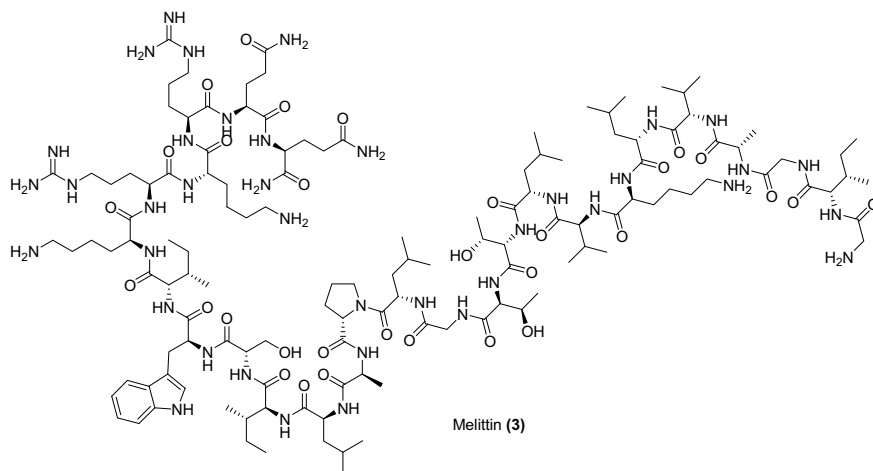


Fig. 3 Structure of the main toxic component in the venom of honeybees, Melittin

Another interesting approach concerns the prodrugs of dipeptide boronic acids, as illustrated in Fig. 4. Although Val-boroPro (**6**) is a potent inhibitor of DPPIV, FAP, as well of other serine hydrolyses that cleave after proline (e.g., DPPII, DPP8, DPP9 and PREP), and is an effective and long-acting compound *in vivo*, the drug demonstrated to be very toxic in pre-clinical trials, with a maximum tolerated dose of 0.025 mg/kg [60]. Therefore, Poplawski et al. [61] described a very clever strategy concerning the design of prodrugs of **6** (Fig. 4). While the very toxic Val-boroPro will be released in the FAP-expressing tumor tissues to inhibit the local dipeptidyl peptidases, the active drug may also diffuse to distant sites. However, in aqueous solution, **6** undergoes a reversible, pH-dependent conversion to the cyclic inactive form **7**, which is the predominant form in the physiological pH, then providing an attenuation of the inhibitory potency in more than 100-fold and, consequently, also excellent gains in terms of efficacy and safety [61].

Apart from the unquestionable importance of the synthetic chemistry and the classical medicinal chemistry strategies to design new FAP inhibitors, the use of computer technology in the field of drug research has increased over the past decades. The availability of faster and cheaper computers in association with the development of more accurate software make it possible to hold information about the known properties of molecules, to perform drug docking calculations and to aid the recognition of protein binding sites and their interactions via 3-D visualization systems [62].

Computer-aided drug design (CADD) approaches are categorized into structure-based drug design (SBDD) and ligand-based drug design (LBDD), where the first refers to techniques that take into account the three-dimensional (3-D) structure of the therapeutic target for the design of new ligands (e.g., molecular docking). The ligand-based drug design techniques, on the other hand, use organic molecules with known biological activities as templates for the design of new chemical entities that are supposed to share some level of similarity and,

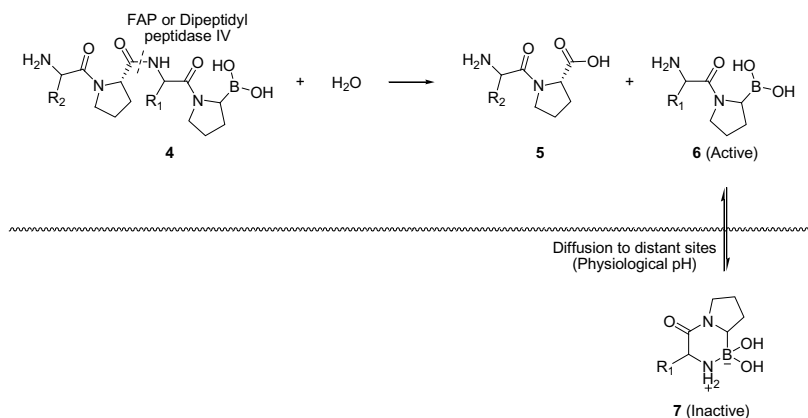


Fig. 4 Structure of the main toxic component in the venom of honeybees, Melittin

consequently, some extent of the biological activity with the parent templates [63]. Examples of LBDD approaches include pharmacophore modeling and quantitative structure-activity relationships, as described above.

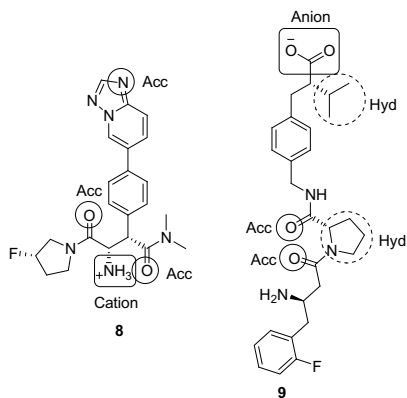
A pharmacophore can be viewed as the maximum common denominator of a group of molecules that exhibit similar pharmacological profiles by acting at the same site of a target [64]. If two compounds display similar chemical features at approximately the same distances to each other, they will also perform the same set of interactions with the target and, accordingly, they will share the same pharmacophore model. In other words, compounds exerting similar activities at the same enzyme or receptor possess, in most cases, closely related binding properties due to similar chemical features in sterically consistent locations [65].

Due to the high degree of phylogenetic relationship with other close dipeptidyl peptidases (e.g., DPPIV, DPPII, DPP8, DPP9 and PREP), selectivity is a potential point of concern for FAP inhibitors. Accordingly, the pharmacophores of these six cases of enzymes generally display substantial overlap [66], as illustrated by lack of selectivity of ValboroPro [61]. In this context, two general pharmacophore models for these enzymes (Fig. 5) were defined for DPPIV using a set of 358 known inhibitors. Both models were validated in a virtual screening campaign and the 28 best hits were assayed for enzyme inhibition, with the best compound displaying an IC₅₀ of 1.12 μM [67].

Since the observation in the 19th century that small changes in the molecular structure of certain drugs coincided with changes in their biological responses [68], medicinal chemists aim to predict the biological activities of compounds based on their chemical structures. This is the basis of the Structure-Activity Relationship (SAR) studies, relations between the molecular structure and the biological/physicochemical activity of chemicals [69]. SARs are commonly determined by promoting minor alterations in the structure of a lead compound to obtain close analogues that can be assayed to determine the effect that these structural changes have on biological activity [70].

Quantitative structure-activity relationship (QSAR) can be viewed as a special case of SAR (when relationships become quantified), and by employing QSAR

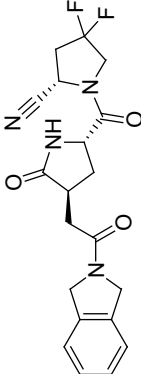
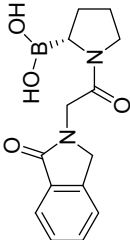
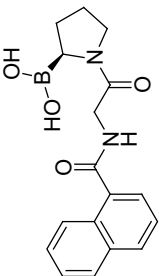
Fig. 5 Two main pharmacophore models for dipeptidyl peptidases defined from a set of 358 known inhibitors [67]. The pharmacophore features are highlighted in the structure of two DPPIV inhibitors with IC_{50} values in the low micromolar range. Abbreviations for pharmacophore features: Hyd = hydrophobic; Acc = hydrogen bond acceptor



models, the biological activity (or property) of a new/untested compound can be inferred from the molecular structure of “similar” compounds whose activities have already been experimentally assessed [71]. Many physiological activities of molecules can be related to their structures through molecular descriptors, which are numerical values that characterize the properties of these molecules. Some descriptors can be obtained directly from the structure of chemicals (constitutional, topological, geometrical, and electronic descriptors) while others represent physicochemical properties (electronic and hydrophilicity descriptors). Another characteristic of descriptors is that the values of some of them depend only on 2-D representation (constitutional and topological), whereas the values of others are influenced by the 3-D molecular conformations (electronic and geometrical descriptors) [72]. Constitutional descriptors are the simplest descriptors (1-D) used in QSAR studies since they only reflect the molecular composition of a molecule (e.g. molecular weight) without considering its electronic or geometric aspects. Topological descriptors are more complex because they give information about the atoms and bonds in a molecule (2-D descriptors). One example of topological descriptor is the topological polar surface area (TopoPSA), which represents the sum of surfaces of polar atoms in a molecule [73].

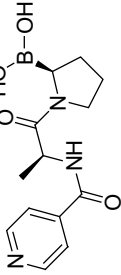
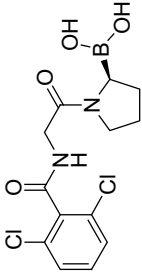
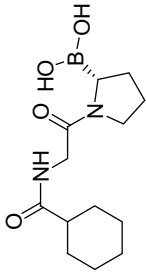
Geometric descriptors are obtained from three-dimensional structures of molecules defined by coordinates of atomic nuclei and size of the molecules [74]. Electronic descriptors are also obtained from 3-D structures of molecules, but they reflect the spatial distribution of the electrons in a molecule, being calculated with *ab initio* or semi-empirical approaches [75]. Starting from the data of 24 FAP inhibitors, Xu et al. [76] constructed a 3D-QSAR model based on comparative molecular field analysis considering steric, hydrophobic and hydrogen bond donor functional fields, which displayed a good discrimination between good and weak inhibitors, in accordance with the results independently suggested by molecular docking studies. Therefore, the authors argue that the model could be helpful to predict the inhibitory FAP activities of new compounds in the future [76]. The structures of other FAP inhibitors discovered based on different synthetic and/or CADD) approaches are depicted in the Table 1.

Table 1 Structures of some of the most potent FAP inhibitors reported in the literature

Structure	IUPAC Name	K_i (nM)	References
 <p style="text-align: center;">10</p>	(2S)-1-[(2S,4S)-4-[2-(2,3-dihydro-1H-isoindol-2-yl)-2-oxoethyl]-5-oxopyrrolidine-2-carbonyl]-4,4-difluoro pyrrolidine-2-carbonitrile	1.3	[77]
 <p style="text-align: center;">11</p>	[(2R)-1-[2-(1-oxo-2,3-dihydro-1H-isoindol-2-yl)acetyl]pyrrolidin-2-yl]boronic acid	7.5	[78]
 <p style="text-align: center;">12</p>	[(2S)-1-[2-[(naphthalen-1-yl)formamido]acetyl]pyrrolidin-2-yl]boronic acid	7.9	[77]

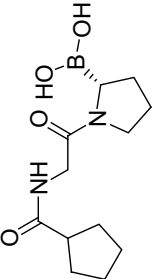
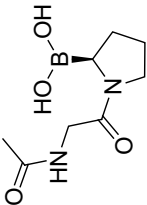
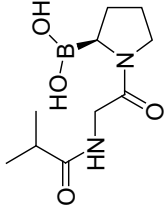
(continued)

Table 1 (continued)

Structure	IUPAC Name	K_i (nM)	References
 <p style="text-align: center;">13</p>	[(2 <i>S</i>)-1-[(2 <i>S</i>)-2-[(pyridin-4-yl) formamido]propanoyl] pyrrolidin-2-yl]boronic acid	9.0	[79]
 <p style="text-align: center;">14</p>	[(2 <i>S</i>)-1-[2-[(2,6-dichlorophenyl)formamido]acetyl]pyrrolidin-2-yl]boronic acid	12.0	[78]
 <p style="text-align: center;">15</p>	[(2 <i>R</i>)-1-[2-(cyclohexylformamido)acetyl]pyrrolidin-2-yl]boronic acid	14.0	[78]

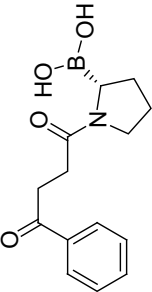
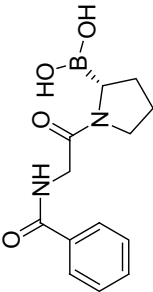
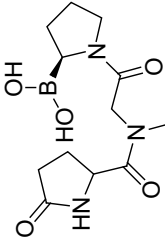
(continued)

Table 1 (continued)

Structure	IUPAC Name	K_i (nM)	References
 <p style="text-align: center;">16</p>	[(2 <i>R</i>)-1-[2-(cyclopentylformamido)acetyl]pyrrolidin-2-yl]boronic acid	20.0	[78]
 <p style="text-align: center;">17</p>	[(2 <i>S</i>)-1-(2-acetamidoacetyl)pyrrolidin-2-yl]boronic acid	23.0	[78]
 <p style="text-align: center;">18</p>	[(2 <i>S</i>)-1-[2-(2-methylpropanamido)acetyl]pyrrolidin-2-yl]boronic acid	51.0	[78]

(continued)

Table 1 (continued)

Structure	IUPAC Name	K_i (nM)	References
 <p style="text-align: center;">19</p>	[(2 <i>R</i>)-1-(4-oxo-4-phenylbutanoyl)pyrrolidin-2-yl]boronic acid	94.0	[78]
 <p style="text-align: center;">20</p>	[(2 <i>R</i>)-1-[2-(phenylformamido)acetyl]pyrrolidin-2-yl]boronic acid	142.0	[78]
 <p style="text-align: center;">21</p>	[(2 <i>S</i>)-1-[2-[<i>N</i> -methyl-1-(5-oxopyrrolidin-2-yl)formamido]acetyl]pyrrolidin-2-yl]boronic acid	146.0	[78]

4 An In Silico SBDD Workflow for the Discovery of FAP Inhibitors

Molecular docking approaches are useful tools to model the interactions between small molecules and proteins at the atomic level, both for characterizing the behavior of small compounds at the binding site of proteins as well as for the elucidation of fundamental biochemical processes [80]. However, as these programs are developed to work across a large set of target proteins (i.e., to be of general use) [81], an initial validation of the docking procedure must be performed to assure the method will be able to properly describe the ligand interactions with the desired target. Such validation may be conducted through redocking, a comparison of the conformation, position and orientation (which are collectively known as a pose) of the docked ligand with the corresponding ones of the ligand co-crystallized with the target [82].

In this section, we will describe a docking-based strategy (SBDD) coupled to in silico analyses of pharmacokinetics and toxicity profiles to identify new potential FAP inhibitors. As the only available crystallographic structure of the human FAP (PDB-ID: 1Z68) does not include a reference ligand [83], validation of the docking methods was performed via redocking using the structure of the dipeptidyl peptidase IV (PDB-ID: 4G1F). This enzyme which shares nearly 50% of overall amino acid sequence identity with FAP and is believed to hold a common ancestry with FAP [84]. Both the structures of FAP and the dipeptidyl peptidase IV were checked for missing atoms, side chains and residues using PDB_HYDRO (http://lorenz.immstr.pasteur.fr/pdb/frozen_submission.php). The virtual screening simulations were performed using the ChemBridge DIVERSet-CL library, which is currently composed of 60,000 diverse lead-like and drug-like compounds (http://www.chembridge.com/screening_libraries/diversity_libraries/diverset/).

To assure a minimum complementarity between these compounds and the binding site of FAP, an initial filtering was employed using a shape-based docking algorithm that approximates an exhaustive search, a process known to search systematically rotations and translations of the ligand within the active site [85]. Simulations were performed inside a 15 Å cubic grid, which included the catalytic triad of FAP (Ser⁶²⁴, Asp⁷⁰² and His⁷³⁴) [83] and their close residues: Arg¹²³, Asn⁷⁰⁴, Glu²⁰³, Glu²⁰⁴, Gly⁶²⁶, Phe³⁵⁰, Trp⁶²³, Trp⁶⁵³, Tyr⁵⁴¹, Tyr⁶²⁵, Tyr⁶⁵⁶, Tyr⁶⁶⁰, Val⁶⁵⁰ and Val⁷⁰⁵. Redocking of the crystallographic ligand into the binding site of dipeptidyl peptidase IV using the same settings yielded a heavy atom Root-Mean-Square Deviation (RMSD) value of 2.06 Å. Subsequently, the top 1% scored (i.e., 600) compounds were rescored using the GOLD software, as we previously described [86]. Briefly, the protonation states of the amino acid residues (essentially the histidine residues) were calculated at the physiological pH using the PROPKA module of the PDB2PQR Server (http://nbc-222.ucsd.edu/pdb2pqr_2.0.0/) and set in GOLD 5.4 for the simulations. GOLD is a molecular docking software widely used by pharmaceutical companies [87].

The program uses genetic sampling algorithms inspired by the Darwin's theory of evolution, where the degrees of freedom of the ligand are encoded as binary strings called "genes" that make up a "chromosome", thus actually representing the pose of the ligand. Therefore, genetic algorithms demand that the fittest "individuals" (poses) are carried on to the next generation and random or biased mutations can be made to increase genetic (conformational) diversity [88]. Simulations were then performed in a 10 Å sphere, for which the geometric center was set from Ser⁶²⁴, a residue that form the catalytic triad of FAP. Default values were set for the genetic algorithm parameters and ChemScore was defined as the score function. Redocking of the crystallographic ligand into the binding site of dipeptidyl peptidase IV using the same settings yielded a heavy atom RMSD of 0.44 Å.

The top 2% scored compounds had their best poses predicted via flexible ligand-docking in Gold. For the 12 best-ranked ligands in this step, the ten best poses were then calculated and selected for analyses of the main protein-ligand interactions using Pose View, a software that creates two-dimensional diagrams of interactions for a docked ligand and a protein complex with a known 3-D structure, according to chemical drawing conventions [89]. Drug-likeness and toxicity profiles were predicted using Osiris Property Explorer (<http://www.organic-chemistry.org/prog/peo/>). Osiris allows the estimation of toxicity effects (mutagenicity, tumorigenicity and adverse reproductive effects) through the identification of potentially hazardous fragments in the query compound based on the search in a database of known toxic molecules. The server also calculates drug-likeness scores and allows the prediction of other parameters that affect drug-likeness such as LogP, solubility, molecular weight and topological polar surface area [90].

The docking process may be subdivided into two basic steps: sampling conformations of the ligand into the active site of the protein (i.e., attempts of reproducing the experimental binding mode using a sampling algorithm) and then ranking these conformations via a scoring function (i.e., assessment of the binding affinity) [91]. We started from the 60,000 structures in the ChemBridge DIVERSet-CL library and applied a shape-fitting sampling algorithm to select compounds that could potentially fit into the binding pocket of FAP. According to this preliminary evaluation, the resulting top 1% scored compounds, 600 structures, displayed binding energies ranging from -18.65 to -11.65 kcal/mol.

This initial filtering ranked the compounds based on an empirical scoring function, which decomposes the predicted binding energies into several energy components, such as hydrogen bonds, van der Waals interactions, hydrophobic effects and deformation effects upon binding [92]. It is important to notice that binding affinity energies tend to be expressed as negative values because they are experimentally quantified through the binding Gibb's free energy ($\Delta G_{\text{binding}}$) which is related to binding constant as:

$$\Delta G_{\text{binding}} = -RT \ln K_b \quad (1)$$

where R is the gas constant, T is the temperature in Kelvin and K_b is the binding constant. As the binding energy indicates how good a protein and a ligand can bind

each other, then even more negative the binding energy, even more strength in binding between two molecules takes place [93]. Besides of having a more robust sampling algorithm (as suggested by the lower RMSD value achieved in the redocking simulation), the GOLD software also exhibits a more advanced built-in scoring function, the ChemScore fitness function. Therefore, these 600 compounds were rescored using this method to obtain more reliable binding modes and precise affinity energies. The ChemScore function accounts for hydrophobic-hydrophobic contact areas, hydrogen bonding, ligand flexibility and metal interactions, also incorporating protein-ligand atom clash and internal energy terms [94]. In this context, the top 2% rescored compounds, 12 structures, now displayed binding energies ranging from -48.28 to -40.17 kcal/mol (Table 2).

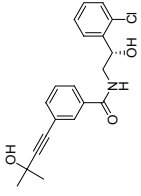
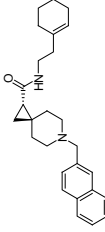
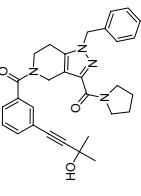
In the last decades, pharmaceutical companies have worked to reduce the number of projects halted or restarted because of toxicity and pharmacokinetics issues by predicting the pharmacokinetics and toxicities of chemical compounds along the drug discovery process rather than at the final stages [95]. In line with these efforts, we estimated the drug-likeness of the top-12 screened compounds to gain some insight into the ideal lipophilicity balance for oral use and we also predicted some of the main toxicity endpoints for drugs (mutagenicity, tumorigenicity and teratogenicity). The drug-likeness scores were calculated based on a database of 5,300 distinct substructure fragments from 3,300 traded drugs, and these analyses previously demonstrate that about 80% of the drugs have positive drug-likeness values while chemical reagents tend to display negative values [90]. In this regard, favorable drug-likeness scores were found for compounds **24**, **25** and **27–33**, while favorable toxicity profiles were observed for all the tested compounds, except for **32** (Table 2).

Analyses of the most probable binding modes of the screened compounds at the active site of FAP (Fig. 6) explain the significant and somewhat similar binding energies observed for all these twelve structures. All compounds (except for **25** and **28**, perhaps) displayed several hydrogen bonds, which certainly contribute to the estimated potencies of these potential inhibitors against FAP since the hydrogen bonds and electrostatic interactions are known to play a central role concerning the processes of molecular recognition and ligand-target binding [96].

For compounds **25** and **28**, fewer hydrogen bonds were observed and a large number of (weaker) hydrophobic or aromatic interactions were also predicted. At first glance, it seems contradictory to assume **25** as potent as a FAP inhibitor as **24**, for example, which displays a higher number of hydrogen bonds. However, it was observed that a single hydrogen bond, when adjacent to the hydrophobic groups of one ligand, tends to increase the strength of both interactions much more than what would be expected based upon on simple additivity. This occurs because, while the hydrogen bond will hold the hydrophobic side chain closer and more firmly against the hydrophobic pocket wall in the target, the apolar side chain will also increase the strength of the hydrogen bond by stabilizing its geometry and, consequently, both interactions will mutually reinforce each other [97].

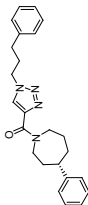
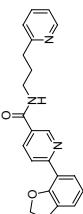
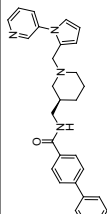
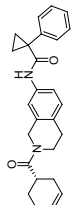
Although these twelve substances must be purchased and subjected to experimental validation concerning the inhibition of FAP, the twelve compounds seem

Table 2 Predicted Gibbs free energy for binding values, drug-likeness scores and main toxicity endpoints for the 12 top-ranked compounds from the ChemBridge DIVERSet (CB-DVS) Library

Compound	$\Delta G_{\text{binding}}$ (kcal/mol)	Drug-likeness	Mutagenicity	Tumorigenicity	Teratogenicity
 CB-DVS 18,829,867 (22)	-48.28	-2.56	Absent	Absent	Absent
 CB-DVS 16,676,717 (23)	-45.32	-0.69	Absent	Absent	Absent
 CB-DVS 14,108,708 (24)	-44.91	1.12	Absent	Absent	Absent

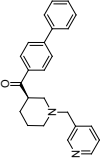
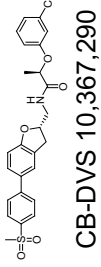
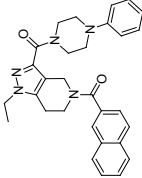
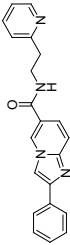
(continued)

Table 2 (continued)

Compound	$\Delta G_{\text{binding}}$ (kcal/mol)	Drug-likeness	Mutagenicity	Tumorigenicity	Teratogenicity
 CB-DVS 16,752,179 (25)	-44.58	1.85	Absent	Absent	Absent
 CB-DVS 10,728,518 (26)	-43.91	-0.85	Absent	Absent	Absent
 CB-DVS 12,216,790 (27)	-43.67	0.82	Absent	Absent	Absent
 CB-DVS 13,768,300 (28)	-42.16	2.40	Absent	Absent	Absent

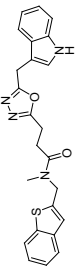
(continued)

Table 2 (continued)

Compound	$\Delta G_{\text{binding}}$ (kcal/mol)	Drug-likeness	Mutagenicity	Tumorigenicity	Teratogenicity
 CB-DVS 16,600,667 (29)	-42.04	2.78	Absent	Absent	Absent
 CB-DVS 10,367,290 (30)	-41.98	5.83	Absent	Absent	Absent
 CB-DVS 10,349,133 (31)	-41.79	9.22	Absent	Absent	Absent
 CB-DVS 10,144,801 (32)	-41.602	4.48	Absent	Absent	Yes

(continued)

Table 2 (continued)

Compound	$\Delta G_{\text{binding}}$ (kcal/mol)	Drug-likeness	Mutagenicity	Tumorigenicity	Teratogenicity
 CB-DVS 14,879,674 (33)	-40.17	6.74	Absent	Absent	Absent

A positive value for the drug-likeness score indicates the molecule contain structural features that are predominantly observed in traded oral drugs

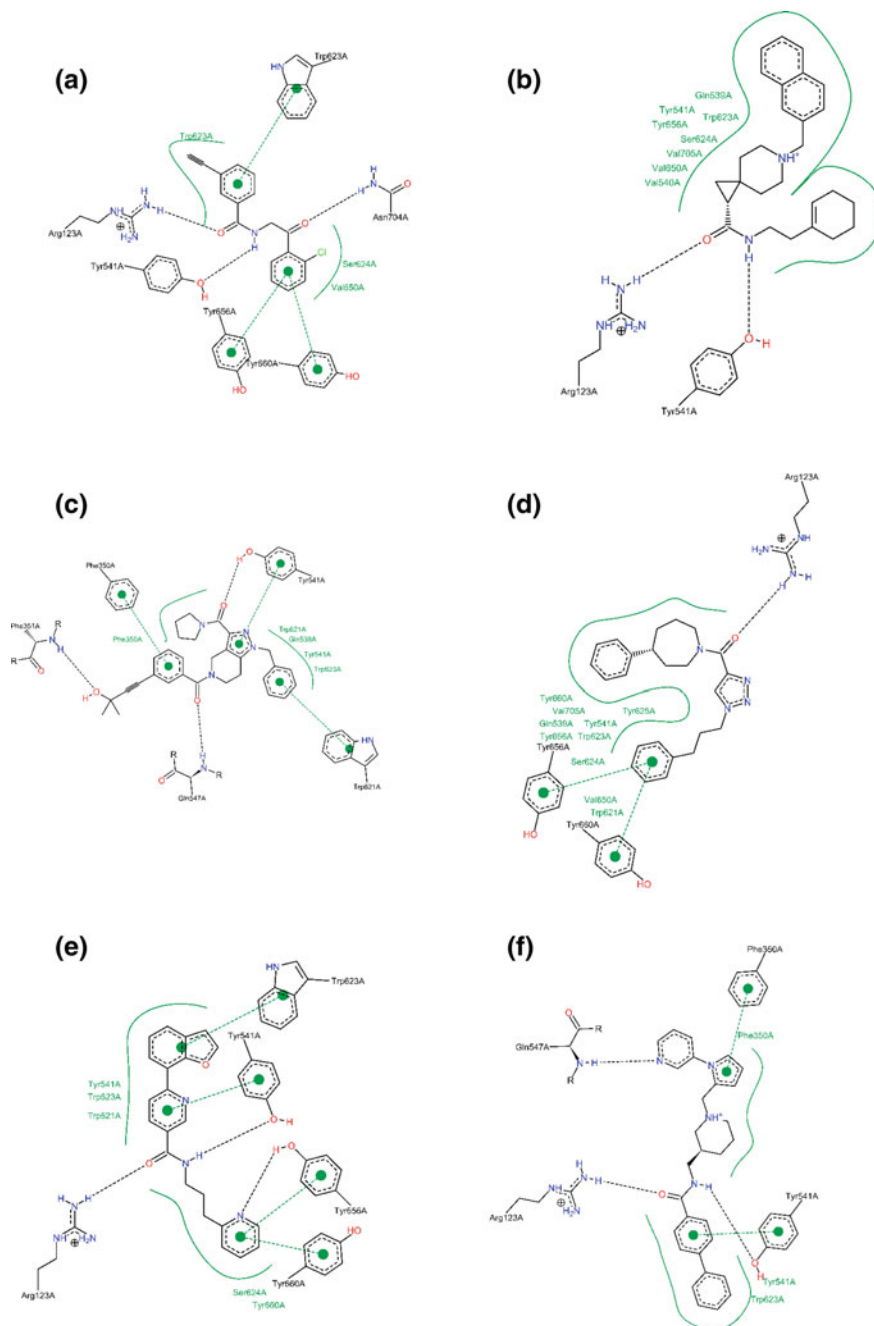


Fig. 6 Two-dimensional diagrams of ligand–FAP interactions based on the outputs generated with PoseView [89]. Dashed lines correspond to hydrogen bonds or π - π /cation- π interactions (aromatic features are indicated with green circles), while the solid green arches highlight hydrophobic interactions: **a** 22, **b** 23, **c** 24, **d** 25, **e** 26, **f** 27, **g** 28, **h** 29, **i** 30, **j** 31, **k** 32 and **l** 33

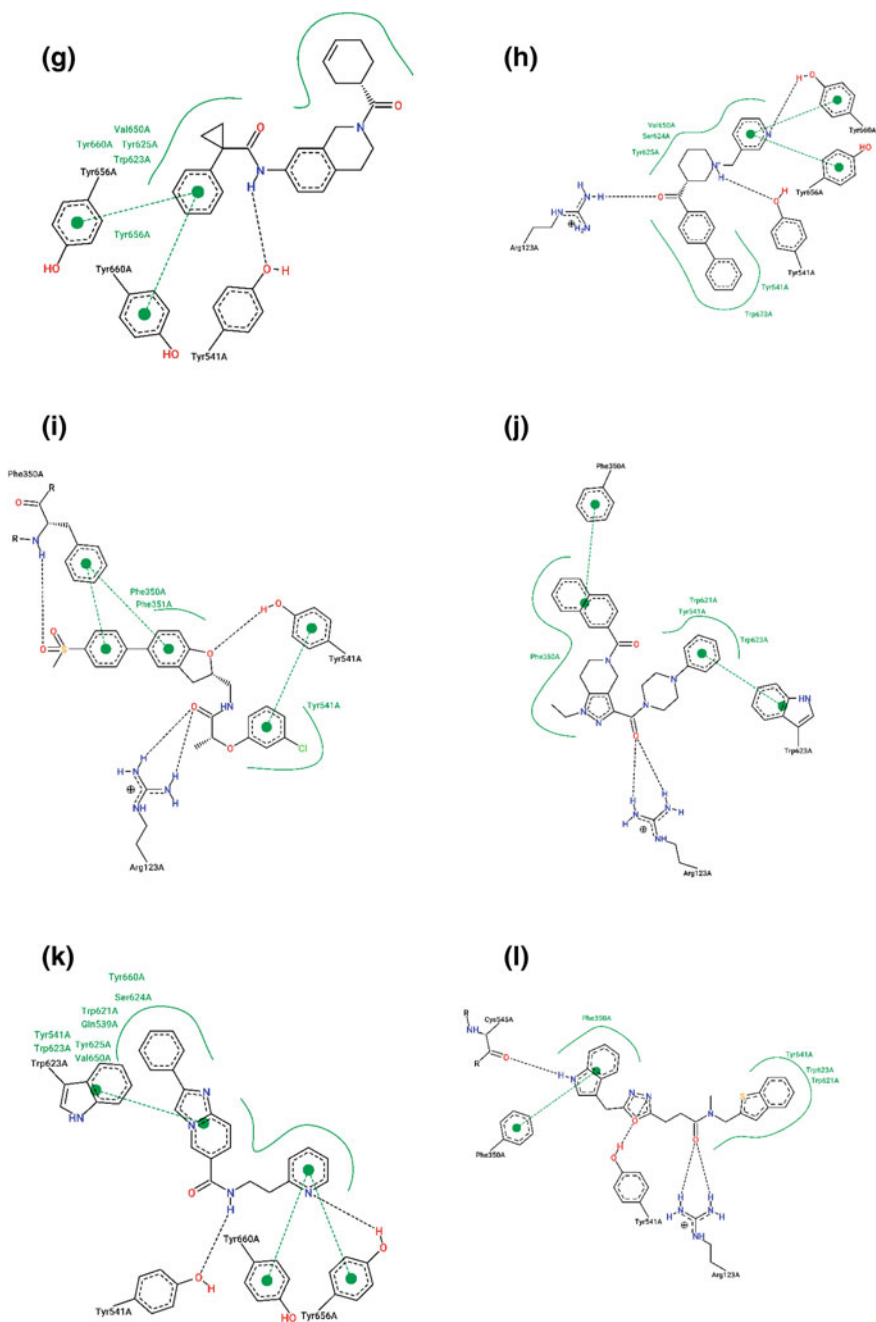


Fig. 6 (continued)

promising due to the good predicted binding affinities, adequate pharmacokinetic profiles (specially **24**, **25** and **27–33**) and low toxicity (except for **32**). Another interesting property of these structures is the amide group connecting rings that participate in hydrophobic and aromatic interactions. Amide linkages are known to favor the synthetic accessibility, thus allowing the fast exploration of structure-activity relationships (SARs) through the generation of libraries of analogues [98]. This approach can also be used in association with pharmacophoric and bioisosteric replacements to produce compounds with reduced structural complexity and, consequently, better synthetic accessibility, central issues in lead optimization and scale up synthesis [99].

5 Conclusions

The human fibroblast activation protein α (FAP) plays an important role in the proteolytic remodeling of the extracellular matrix of the tumor, allowing the neoplastic cells to invade the surrounding tissues, to undergo metastasis, and to perform angiogenesis, collectively promoting extensive tumor growth. Here we reported the use of a multistep molecular docking approach to identify potential FAP inhibitors. All the twelve best-ranked ligands displayed significant binding affinity energies, which are coherent with extensive hydrogen bonding or *H*-bonds plus hydrophobic/aromatic interactions that are known to mutually reinforce each other. Concerning the toxicity and pharmacokinetics of these compounds, none is expected to be mutagenic, tumorigenic and only one compound (**32**) is potentially teratogenic, and several compounds (**24**, **25** and **27–33**) displayed drug-likeness scores that are in accordance with a proper lipophilicity balance for oral use. In addition, they may be subjected to pharmacophoric and bioisosteric replacements to produce analogues with reduced structural complexity/better synthetic accessibility, which are central issues for lead optimization and scale up synthesis.

Acknowledgements The authors thank the Brazilian funding agencies CNPq (Conselho Nacional de Desenvolvimento Científico e Tecnológico) and PRP-UNICAMP (Pró-Reitoria de Pesquisa da Unicamp) for the financial support.

References

1. Brash, D.E., Ziegler, A., Jonason, A.S., et al.: Sunlight and sunburn in human skin cancer: p53, apoptosis, and tumor promotion. *J. Invest. Dermatol. Symp. Proc.* **1**(2), 136–142 (1996)
2. Kawasaki, Y., Hirabayashi, Y., Kaneko, T., et al.: Benzene-induced hematopoietic neoplasms including myeloid leukemia in Trp53-deficient C57BL/6 and C3H/He mice. *Toxicol. Sci.* **110**(2), 293–306 (2009)
3. Schiffman, M., Castle, P.E., Jeronimo, J., et al.: Human papilloma virus and cervical cancer. *Lancet* **370**(9590), 890–907 (2007)

4. Wang, C., Yuan, Y., Hunt, R.H.: The association between *Helicobacter pylori* infection and early gastric cancer: a meta-analysis. *Am. J. Gastroenterol.* **102**(8), 1789–1798 (2007)
5. Smith, C.J., Perfetti, T.A., King, J.A.: Perspectives on pulmonary inflammation and lung cancer risk in cigarette smokers. *Inhal. Toxicol.* **18**(9), 667–677 (2006)
6. Green, D.R., Evan, G.I.: A matter of life and death. *Cancer Cell* **1**(1), 19–30 (2002)
7. Kasibhatla, S., Tseng, B.: Why target apoptosis in cancer treatment? *Mol. Cancer Ther.* **2**(6), 573–580 (2003)
8. Gulliksen, A., Karlsen, F.: Microchips for the diagnosis of cervical cancer. *Methods Mol. Biol.* **385**, 65–86 (2007)
9. Ogle, O.E., Nikoyan, L.: Radiation and chemotherapy in oral and maxillofacial surgery. In: Motamedi, M.H.K. (ed.) *A Textbook of Advanced Oral and Maxillofacial Surgery*, pp. 257–278. InTech, Rijeka (2013)
10. Connolly, J.L., Schnitt, S.J., Wang, H.H., et al.: Principles of Cancer Pathology. In: Bast, R. C., Kufe, D.W., Pollock, R.E., et al. (eds.) *Holland-Frei Cancer Medicine*, 5th edn, pp. 384–399. BC Decker Inc., Hamilton (2000)
11. Li, Z.W., Dalton, W.S.: Tumor microenvironment and drug resistance in hematologic malignancies. *Blood Rev.* **20**(6), 333–342 (2006)
12. Trédan, O., Galmarini, C.M., Patel, K., et al.: Drug resistance and the solid tumor microenvironment. *J. Natl. Cancer* **99**(19), 1441–1454 (2007)
13. Sun, Y.: Tumor microenvironment and cancer therapy resistance. *Cancer Lett.* **380**(1), 205–215 (2016)
14. Son, B., Lee, S., Youn, H., et al.: The role of tumor microenvironment in therapeutic resistance. *Oncotarget* **8**(3), 3933–3945 (2017)
15. Shee, K., Yang, W., Hinds, J.W., et al.: Therapeutically targeting tumor microenvironment-mediated drug resistance in estrogen receptor-positive breast cancer. *J. Exp. Med.* **215**(3), 895–910 (2018)
16. Nyberg, P., Salo, T., Kalluri, R.: Tumor microenvironment and angiogenesis. *Front Biosci.* **13**, 6537–6553 (2008)
17. Sarah, J.L., Payne, S.J.L., Jones, L.: Influence of the tumor microenvironment on angiogenesis. *Future Oncol.* **7**(3), 395–408 (2011)
18. Watnick, R.S.: The role of the tumor microenvironment in regulating angiogenesis. *Cold Spring Harb. Perspect. Med.* **2**(12) (2012). <https://doi.org/10.1101/cshperspect.a006676a006676>
19. Samples, J., Willis, M., Klauber-DeMore, N.: Targeting angiogenesis and the tumor microenvironment. *Surg. Oncol. Clin. N. Am.* **22**(4), 629–639 (2013)
20. Mittal, K., Ebos, J., Rini, B.: Angiogenesis and the tumor microenvironment: vascular endothelial growth factor and beyond. *Semin. Oncol.* **41**(2), 235–251 (2014)
21. Gascard, P., Tlsty, T.D.: Carcinoma-associated fibroblasts: orchestrating the composition of malignancy. *Genes Dev.* **30**(9), 1002–1019 (2016)
22. Sewell-Loftin, M.K., Bayer, S.H., Crist, E et al.: Cancer-associated fibroblasts support vascular growth through mechanical force. *Sci. Rep.* **7**(1). (2017). <https://doi.org/10.1038/s41598-017-13006-x>
23. Ahrens, D., Bhagat, T.D., Nagrath, D., et al.: The role of stromal cancer-associated fibroblasts in pancreatic cancer. *J. Hematol. Oncol.* **10**(1), 76 (2017). <https://doi.org/10.1186/s13045-017-0448-5>
24. Tao, L., Huang, G., Song, H., et al.: Cancer associated fibroblasts: an essential role in the tumor microenvironment. *Oncol. Lett.* **14**(3), 2611–2620 (2017)
25. Lazennec, G., Richmond, A.: Chemokines and chemokine receptors: new insights into cancer-related inflammation. *Trends Mol. Med.* **16**(3), 133–144 (2010)
26. Banat, G.A., Tretyn, A., Pullamsetti, S.S. et al.: Immune and inflammatory cell composition of human lung cancer stroma. *PLoS ONE* **10**(9) (2015). <https://doi.org/10.1371/journal.pone.0139073.eCollection2015>

27. Jakubowska, K., Kisielewski, W., Kańczuga-Koda, L., et al.: Diagnostic value of inflammatory cell infiltrates, tumor stroma percentage and disease-free survival in patients with colorectal cancer. *Oncol. Lett.* **14**(3), 3869–3877 (2017)
28. Lorusso, G., Curzio Rüegg, C.: The tumor microenvironment and its contribution to tumor evolution toward metastasis. *Histochem. Cell. Biol.* **130**(6), 1091–1103 (2008)
29. Kendall, R.T., Feghali-Bostwick, C.A.: Fibroblasts in fibrosis: novel roles and mediators. *Front. Pharmacol.* **5**(123) (2014). <https://doi.org/10.3389/fphar.2014.00123>
30. Yamaguchi, H., Yoshida, N., Takanashi, M., et al.: Stromal fibroblasts mediate extracellular matrix remodeling and invasion of scirrhous gastric carcinoma cells. *PLoS ONE* **9**(1), e85485 (2014). <https://doi.org/10.1371/journal.pone.0085485.eCollection>
31. Garin-Chesa, P., Old, L.J., Rettig, W.J., et al.: Cell surface glycoprotein of reactive stromal fibroblasts as a potential antibody target in human epithelial cancers. *Proc. Natl. Acad. Sci. U. S. A.* **87**, 7235–7239 (1990)
32. Aoyama, A., Chen, W.T.: A 170-kDa membrane-bound protease is associated with the expression of invasiveness by human malignant melanoma cells. *Proc. Natl. Acad. Sci. U. S. A.* **87**, 8296–8300 (1990)
33. Monsky, W.L., Lin, C.Y., Aoyama, A., et al.: A potential marker protease of invasiveness, seprase, is localized on invadopodia of human malignant melanoma cells. *Cancer Res.* **54**, 5702–5710 (1994)
34. Kelly, T., Kechelava, S., Rozypal, T.L., et al.: Seprase, a membrane-bound protease, is over expressed by invasive ductal carcinoma cells of human breast cancers. *Mod. Pathol.* **11**, 855–863 (1998)
35. Okada, K., Chen, W.T., Iwasa, S., et al.: Seprase, a membrane-type serine protease, has different expression patterns in intestinal—and diffuse-type gastric cancer. *Oncology* **65**, 363–370 (2003)
36. Mori, Y., Kono, K., Matsumoto, Y., et al.: The expression of a type II transmembrane serine protease (Seprase) in human gastric carcinoma. *Oncology* **67**, 411–419 (2004)
37. Iwasa, S., Okada, K., Chen, W.T., et al.: Increased expression of seprase, a membrane-type serine protease, is associated with lymph node metastasis in human colorectal cancer. *Cancer Lett.* **227**, 229–236 (2005)
38. Henry, L.R., Lee, H.O., Lee, J.S., et al.: Clinical implications of fibroblast activation protein in patients with colon cancer. *Clin. Cancer Res.* **13**, 1736–1741 (2007)
39. Brennan, W.N., Isaacs, J.T., Denmeade, S.R.: Rationale behind targeting fibroblast activation protein-expressing carcinoma-associated fibroblasts as a novel chemotherapeutic strategy. *Mol. Cancer Ther.* **11**(2), 257–266 (2012)
40. Scanlan, M.J., Raj, B.K., Calvo, B., et al.: Molecular cloning of fibroblast activation protein alpha, a member of the serine protease family selectively expressed in stromal fibroblasts of epithelial cancers. *Proc. Natl. Acad. Sci. U.S.A.* **91**, 5657–5661 (1994)
41. Pineiro-Sanchez, M.L., Goldstein, L.A., Dodt, J., et al.: Identification of the 170-kDa melanoma membrane-bound gelatinase (seprase) as a serine integral membrane protease. *J. Biol. Chem.* **272**, 7595–7601 (1997)
42. Cheng, J.D., Valianou, M., Canutescu, A.A., et al.: Abrogation of fibroblast activation protein enzymatic activity attenuates tumor growth. *Mol. Cancer Ther.* **4**, 351–360 (2005)
43. Kelly, T.: Evaluation of seprase activity. *Clin. Exp. Metastasis* **17**, 57–62 (1999)
44. Park, J.E., Lenter, M.C., Zimmermann, R.N., et al.: Fibroblast activation protein, a dual specificity serine protease expressed in reactive human tumor stromal fibroblasts. *J. Biol. Chem.* **274**, 36505–36512 (1999)
45. Lee, K.N., Jackson, K.W., Christiansen, V.J., et al.: A novel plasma proteinase potentiates alpha2-antiplasmin inhibition of fibrin digestion. *Blood* **103**, 3783–3788 (2004)
46. Christiansen, V.J., Jackson, K.W., Lee, K.N., et al.: Effect of fibroblast activation protein and alpha2-antiplasmin cleaving enzyme on collagen types I, III, and IV. *Arch. Biochem. Biophys.* **457**, 177–186 (2007)

47. Huang, Y., Simms, A.E., Mazur, A., et al.: Fibroblast activation protein- α promotes tumor growth and invasion of breast cancer cells through non-enzymatic functions. *Clin. Exp. Metastasis* **28**, 567–579 (2011)
48. Keane, F.M., Nadvi, N.A., Yao, T.W., et al.: Neuropeptide Y, B-type natriuretic peptide, substance P and peptide YY are novel substrates of fibroblast activation protein- α . *FEBS J.* **278**, 1316–1332 (2011)
49. Liu, R., Li, H., Liu, L., et al.: Fibroblast activation protein: a potential therapeutic target in cancer. *Cancer Biol. Ther.* **13**(3), 123–129 (2012)
50. Chen, W.T.: Proteolytic activity of specialized surface protrusions formed at rosette contact sites of transformed cells. *J. Exp. Zool.* **251**, 167–185 (1989)
51. Schurer, S.C., Tyagi, P., Muskal, S.M.: Prospective exploration of synthetically feasible, medically relevant chemical space. *J. Chem. Inf. Model.* **45**, 239–248 (2005)
52. Gasteiger, J.: De novo design and synthetic accessibility. *J. Comput. Aid Mol. Des.* **21**, 307–309 (2007)
53. Corey, E.J., Chelg, X.M.: *The Logic of Chemical Synthesis*, 1st edn, p. 436. Wiley, New York (1995)
54. Karpf, M.: From milligrams to tons: the importance of synthesis and process research in the development of new drugs. In: Shioiri, T., Izawa, K., Konoike, T. (eds.) *Pharmaceutical process chemistry*, 1st edn., pp. 1–38. Wiley-VCH Verlag GmbH & Co., New York (2011)
55. Wunderlich, Z., Mirny, L.A.: Using the topology of metabolic networks to predict viability of mutant strains. *Biophys. J.* **91**, 2304–2311 (2006)
56. Goodwin, W.: Scientific understanding and synthetic design. *Brit. J. Philos. Sci* **60**, 271–301 (2009)
57. Patrick, G.L.: *An Introduction to Medicinal Chemistry*, 5th edn, p. 789. Oxford University Press, Oxford (2013)
58. Jansen, K., Heirbaut, L., Verkerk, R., et al.: Extended structure-activity relationship and pharmacokinetic investigation of (4-quinolinoyl)glycyl-2-cyanopyrrolidine inhibitors of fibroblast activation protein (FAP). *J. Med. Chem.* **57**(7), 3053–3074 (2014)
59. LeBeau, A.M., Brennen, W.N., Aggarwal, S., et al.: Targeting the cancer stroma with a fibroblast activation protein-activated promelittin protoxin. *Mol. Cancer Ther.* **8**(5), 1378–1386 (2009)
60. Connolly, B.A., Sanford, D.G., Chiluwal, A.K., et al.: Dipeptide boronic acid inhibitors of dipeptidyl peptidase IV: determinants of potency and in vivo efficacy and safety. *J. Med. Chem.* **51**, 6005–6013 (2008)
61. Poplawski, S.E., Lai, J.H., Sanford, D.G., et al.: Pro-soft Val-boroPro: a strategy for enhancing in vivo performance of boronic acid inhibitors of serine proteases. *J. Med. Chem.* **54**(7), 2022–2028 (2011)
62. Dalkas, G.A., Vlachakis, D., Tsagkrasoulis, D., et al.: State-of-the-art technology in modern computer-aided drug design. *Brief. Bioinform.* **14**(6), 745–752 (2013)
63. Veselovsky, A.V., Ivanov, A.S.: Strategy of computer-aided drug design. *Curr. Drug Targets Infect. Disord.* **3**(1), 33–40 (2003)
64. Langer, T., Hoffmann, R.D.: *Pharmacophores and Pharmacophore Searches*, 1st edn, p. 375. Wiley-VCH Verlag GmbH & Co., KGaA, Weinheim (2006)
65. Wermuth, C.G.: *The Practice of Medicinal Chemistry*, 3rd edn, p. 982. Academic Press, California (2008)
66. Waumans, Y., Baerts, L., Kehoe, K., et al.: The dipeptidyl peptidase family, prolyl oligopeptidase, and prolyl carboxypeptidase in the immune system and inflammatory disease, including atherosclerosis. *Front. Immunol.* **6**, 387 (2015). <https://doi.org/10.3389/fimmu.2015.00387.eCollection2015>
67. Al-Masri, I.M., Mohammad, M.K., Taha, M.O.: Discovery of DPP IV inhibitors by pharmacophore modeling and QSAR analysis followed by in silico screening. *Chem. Med. Chem.* **3**(11), 1763–1779 (2008)
68. Crum Brown, A., Fraser, T.R.: On the connection between chemical constitution and physiological action; with special reference to the physiological action of the salts of the

- ammonium bases derived from Strychnia, Brucia, Thebaia, Codeia, Morphia, and Nicotia. *J. Anat. Physiol.* **2**(2), 224–242 (1868)
69. Hulzebos, E.M., Janssen, P.A.H., Maslankiewicz, L., et al.: The Application of Structure-Activity Relationships in Human Hazard Assessment: A First Approach, RIVM Report No. 601516008, p. 55. Netherlands National Institute for Public Health and the Environment, Bilthoven (2001)
 70. Thomas, G.: *Fundamentals of Medicinal Chemistry*, 1st edn, p. 285. Wiley, New York (2003)
 71. Gramatica, P.: On the Development and Validation of QSAR Models. In: Reisfeld, B., Mayeno, A.N. (eds.) *Computational Toxicology*, vol. II, pp. 499–526. Springer Science +Business Media LLC, New York (2013)
 72. Todeschini, R., Consonni, V.: *Handbook of Molecular Descriptors*, 1st edn, p. 667. Wiley-VCH Verlag, Weinheim (2000)
 73. Prasanna, S., Doerksen, R.J.: Topological polar surface area: a useful descriptor in 2D-QSAR. *Curr. Med. Chem.* **16**(1), 21–41 (2009)
 74. Karelson, M.: *Molecular Descriptors in QSAR/QSPR*, 1st edn, p. 448. Wiley, New York (2000)
 75. Stanton, D.T., Jurs, P.C.: Development and use of charged partial surface area structural descriptors in computer-assisted quantitative structure-property relationship studies. *Anal. Chem.* **62**(21), 2323–2329 (1990)
 76. Xu, J., Huang, S., Zhang, T., et al.: The SAR studies on FAP inhibitors as tumor-targeted agents. *Med. Chem. Res.* **24**, 1744–1752 (2015)
 77. Tsai, T.Y., Yeh, T.K., Chen, X., et al.: Substituted 4-carboxymethylpyroglutamic acid diamides as potent and selective inhibitors of fibroblast activation protein. *J. Med. Chem.* **53**, 6572–6583 (2010)
 78. Tran, T., Quan, C., Edosada, C.Y., et al.: Synthesis and structure-activity relationship of *N*-acyl-Gly-, *N*-acyl-Sar- and *N*-blocked-boroPro inhibitors of FAP, DPP4, and POP. *Bioorg. Med. Chem. Lett.* **17**, 1438–1442 (2007)
 79. Poplawski, S.E., Lai, J.H., Li, Y., et al.: Identification of selective and potent inhibitors of fibroblast activation protein and prolyl oligopeptidase. *J. Med. Chem.* **56**, 3467–3477 (2013)
 80. McConkey, B.J., Sobolev, V., Edelman, M.: The performance of current methods in ligand-protein docking. *Curr. Sci.* **83**, 845–855 (2002)
 81. Kroemer, R.T.: Structure-based drug design: docking and scoring. *Curr. Protein Pept. Sci.* **8** (4), 312–328 (2007)
 82. Arooj, M., Kim, S., Sakkiah, S., et al.: Molecular modeling study for inhibition mechanism of human chymase and its application in inhibitor design. *PLoS ONE* **8**(4), e62740 (2003). <https://doi.org/10.1371/journal.pone.0062740>
 83. Aertgeerts, K., Levin, I., Shi, L., et al.: Structural and kinetic analysis of the substrate specificity of human fibroblast activation protein alpha. *J. Biol. Chem.* **280**, 19441–19444 (2005)
 84. Irwin, D.M.: Ancient duplications of the human proglucagon gene. *Genomics* **79**, 741–746 (2002)
 85. Joy, S., Nair, P.S., Hariharan, R., et al.: Detailed comparison of the protein-ligand docking efficiencies of GOLD, a commercial package and Argus Lab, a licensable freeware. *Silico Biol.* **6**(6), 601–605 (2006)
 86. Silva, V.B., Kawano, D.F., Gomes, A.S., et al.: Molecular dynamics, density functional, ADMET predictions, virtual screening, and molecular interaction field studies for identification and evaluation of novel potential CDK2 inhibitors in cancer therapy. *J. Phys. Chem. A* **112**(38), 8902–8910 (2008)
 87. Young, D.C.: *Computational Drug Design: A Guide for Computational and Medicinal Chemists*. Wiley, New Jersey (2009)
 88. Torres, F.C., Goncalves, G.A., Vanzolini, K.L., et al.: Combining the pharmacophore features of coumarins and 1,4-substituted 1,2,3-triazoles to design new acetylcholinesterase inhibitors: fast and easy generation of 4-methylcoumarins/1,2,3-triazoles conjugates via click chemistry. *J. Braz. Chem. Soc.* **27**(9), 1541–1550 (2016)

89. Stierand, K., Maaß, P., Rarey, M.: Molecular complexes at a glance: automated generation of two-dimensional complex diagrams. *Bioinformatics* **22**(14), 1710–1716 (2006)
90. Sander, T.: OSIRIS property explorer. Actelion Pharmaceuticals Ltd., Allschwil (2011). <https://www.organic-chemistry.org/prog/peo/>
91. Meng, X.Y., Zhang, H.X., Mezei, M., et al.: Molecular docking: a powerful approach for structure-based drug discovery. *Curr. Comput. Aided Drug Des.* **7**(2), 146–157 (2011)
92. Wang, R., Lai, L., Wang, S.: Further development and validation of empirical scoring functions for structure-based binding affinity prediction. *J. Comput. Aided Mol. Des.* **16**(1), 11–26 (2002)
93. Murphy, K.P.: Predicting binding energetics from structure: looking beyond ΔG° . *Med. Res. Rev.* **19**(4), 333–339 (1999)
94. Verdonk, M.L., Cole, J.C., Hartshorn, M.J., et al.: Improved protein-ligand docking using GOLD. *Proteins* **52**(4), 609–623 (2003)
95. Van de Waterbeemd, H., Gifford, E.: ADMET in silico modelling: towards prediction paradise? *Nat. Rev. Drug Discov* **2**(3), 192–204 (2003)
96. Nolan, T., Singh, N., McCurdy, C.R.: Ligand macromolecule interactions: theoretical principles of molecular recognition. In: Roque, A.C.A. (ed.) *Ligand-Macromolecular Interactions in Drug Discovery*, pp. 13–29. Humana Press, New York (2010)
97. Muley, L., Baum, B., Smolinski, M., et al.: Enhancement of hydrophobic interactions and hydrogen bond strength by cooperativity: synthesis, modeling, and molecular dynamics simulations of a congeneric series of thrombin inhibitors. *J. Med. Chem.* **53**(5), 2126–2135 (2010)
98. Sharman, G.J.: Conformation and stereochemical analysis of drug molecules. In: Everett, J.R., et al. (eds.) *NMR in Pharmaceutical Science*, pp. 207–220. Wiley, Chichester (2015)
99. Silva, V.B., Kawano, D.F., Rodrigues, R.P., et al.: Bioisosteric replacements in drug design. In: Taft, C.A., et al. (eds.) *New Developments in Medicinal Chemistry*, vol. 2, pp. 213–238. Bentham Science Publishers, San Francisco (2014)

Pharmacophore Mapping of Natural Products for Pancreatic Lipase Inhibition



Matheus Gabriel de Oliveira, Waléria Ramos Nogueira de Souza, Ricardo Pereira Rodrigues, Daniel F. Kawano, Leonardo Luiz Borges and Vinicius Barreto da Silva

Abstract The use of pancreatic lipase (LP) inhibitors to reduce the absorption of dietary fats has become one of the pharmacological approaches adopted for the treatment of obesity. Since natural products continue to play a significant role in drug discovery and development the search for natural compounds with PL inhibitory activity is an interesting approach to provide new lead compounds for drug discovery and to guide dietary trends in order to prevent or treat obesity. The consumption of Myrciaria genus plant species is also related to increased HDL cholesterol and improved triglycerides excretion in animal models. In addition, extracts of species from Myrciaria genus are related to in vitro inhibitory activity against PL. Hence it is important to identify which chemical markers from Myrciaria genus species are structurally related to PL inhibitory activity. Ligand-based pharmacophore modeling is one of the most applied approaches in medicinal chemistry in order to detect molecular features related to molecules that are able to modulate a particular biological target. Some Myrciaria genus chemical markers including polyphenols, glycosides and lactonic derivatives share molecular features found in classic PL inhibitors. Such phytomolecules from Myrciaria species are a starting point to develop novel therapeutic options for obesity with PL inhibitory activity.

M. G. de Oliveira · W. R. N. de Souza
Laboratório de Pesquisa em Produtos Naturais (LPPN), Faculdade de Farmácia,
Universidade Federal de Goiás (UFG), Goiânia, Goiás, Brazil

R. P. Rodrigues
Graduate Program in Pharmaceutical Sciences, Federal University
of Espírito Santo (UFES), Vitória, Espírito Santo, Brazil

D. F. Kawano
Faculdade de Ciências Farmacêuticas, Universidade Estadual de Campinas,
Campinas, São Paulo, Brazil

L. L. Borges · V. B. da Silva (✉)
Escola de Ciências Médicas, Farmacêuticas e Biomédicas,
Pontifícia Universidade Estadual de Goiás, Anápolis, Goiás, Brazil
e-mail: vbarreto@pucgoias.edu.br

Keywords Obesity · Myrciaria · Jaboticaba · Ligand-based drug design · Phytomolecules

1 Introduction

Natural products continue to play a significant role in the drug discovery and development process [1–4]. Between 1980 and 2013, more than 1500 new drugs were introduced into the market including approximately 300 natural products and natural product derivatives [5]. Since natural compounds exhibit pleiotropic action and could bind to multiple targets, therefore phytochemicals identified from traditional medicinal plants represent an opportunity for the discovery of lead compounds or even drugs [6, 7].

In the past two decades, the prevalence of obesity has increased dramatically around the world and it is primarily considered as a disorder of lipid metabolism associated with several pathological disorders, such as diabetes, cardiovascular disease and cancer [8, 9]. Lipase inhibitors have a wide range of applications in the fields of pharmaceuticals and the use of pancreatic lipase (PL) inhibitors to reduce the adsorption of dietary fats has become an important pharmacological approach adopted for the treatment of obesity [10].

The *Myrciaria* genus belongs to the Myrtaceae family and the plant species of this genus are spread across various Brazilian biomes. The bioactive compounds from *Myrciaria* genus have been related to several therapeutic activities such as antioxidant, antimicrobial, anti-inflammatory and hypolipidemic [11–13]. The consumption of the freeze-dried jaboticaba (*Myrciaria jaboticaba*) peel is related to increased HDL (High Density Lipoprotein) cholesterol and improved triglycerides excretion in obese rats [13, 14]. Moreover, jaboticaba raw extract showed inhibitory activity against PL ($IC_{50} = 1.08$ mg sample/mL reaction) and its polyphenols largely contributed to this effect [15]. Then *Myrciaria jaboticaba* is an interesting source to search for natural products with PL inhibitory activity.

One of the most important advances in the design and discovery of new drugs has been the use of molecular modeling [16]. Pharmacophores have proven to be extremely effective in silico filters in the search for bioactive molecules on several targets. Their use reduces the number of compounds and costs which have to be considered in large biophysical screenings [17].

2 Natural Products for Drug Discovery and Development

Natural products comprise substances produced by life organisms, such as microorganisms, plants and animals, with recognized chemical diversity and complexity developed during biosynthesis and properties that are evolutionary optimized for serving different biological functions [18]. They have been

historically recognized as invaluable sources of inspiration for chemistry, biology, and medicine and the exploration of these natural products has facilitated natural product-based drug discovery [19].

Historically, there are many examples of the development of medicines originated from natural products, including: (i) the anti-cholesterolaemic agents simvastatin, lovastatin, pravastatin and atorvastatin; (ii) the anti-hypertensive agents captopril and enalapril; (iii) the immunosuppressive agents cyclosporin A, tacrolimus (FK506) and rapamycin; (iv) the antitumoral agents taxol, docetaxel and camptothecin; and (v) the antibiotic and antifungal agents: penicillin, erythromycin, clarithromycin and amphotericin B [20, 21].

Natural-derived products constitute an extremely important resource for global pharmaceutical companies working on the development of new medicines. Newman and Cragg [22] assessed the role of natural products in the drugs approved by the U. S. Food and Drug Administration (FDA) between 1981 and 2014, and it was verified that in this period the FDA approved 1562 drugs, being 64 (4%) of unaltered natural products, 141 (9.1%) of botanical drugs (mixture), 320 (21%) of natural product derivatives and 61 (4%) of synthetic drugs but with natural products pharmacophore. These drugs were approved especially for antibiotic and anticancer fields [22].

Among the natural products, plant-based systems continue to play an essential role in healthcare and their use by different cultures has been extensively documented. The World Health Organization (WHO) estimated that approximately 80% of the population rely mainly on traditional medicines for their primary health care, being the medicinal plants the main component [23]. The traditional use of the plants proved to be an invaluable guide for screening of drugs and many important modern drugs like digitoxin, reserpine, tubocurarine, ephedrine, ergometrine, atropine, vinblastine and aspirin have been discovered by following leads from the traditional uses [24, 25].

Medicinal plants are often perceived as chemically complex molecules offering particular fragments into ligand-efficient and selective novel chemical entities. Its extracts are natural libraries of complex compounds and offer more drug-like features to molecules from combinatorial chemistry in terms of functional groups, chirality and structural complexity [26]. Medicinal plant research is often complex and multidisciplinary. In addition to the established ethnopharmacological approach to select plant material, the computational approach has allowed the selection of the test samples based on *in silico* bioactivity predictions data of constituents that often occur in certain families and genders of plants [27].

The isolation of natural compounds often follows a bioassay-guided isolation that begins with an active extract to identify the bioactive constituent(s) or isolation of new compounds and screening of the pure compounds for activity. Due to the diversity of the chemical and physical properties of natural compounds, various chromatographic [high-performance liquid chromatography (HPLC), gas chromatography] and spectroscopic techniques [nuclear magnetic resonance (NMR), mass spectroscopy (MS)] are often applied for the identification, with particular emphasis on hyphenated techniques [liquid chromatography–MS (LC-MS), LC-NMR] [28].

Although unaltered natural products continue to play an important role in drug discovery, it is important that the structures and its associated physicochemical properties are assessed for druggability. *In silico* tools may help the rational drug design from natural products by predicting and optimizing, for example, its pharmacokinetic, metabolic, and toxicity properties. Moreover, the concept of creating libraries of natural compounds with suitable physicochemical properties can be useful in avoiding the isolation of ones that do not satisfy lead-like and/or drug-like properties and, hence, are unlikely to proceed to the development stage [29].

The therapeutic activity of plant extracts is usually because of the synergistic and simultaneous action of several chemicals. The investigation of plant-derived substances was historically based on a forward pharmacology approach using *in vivo* animal tests, organ or tissue models, or bacterial preparations, followed by *in vitro* investigation of the mechanisms underlying the activity [30]. In the more recent past, this approach changed and is now usually starting with screening of large collections of plant-derived compounds (libraries) against pre-characterized disease-relevant protein targets, with the aim to identify hits, compounds with the desired activity that are then further studied in relevant *in vivo* models with the aim to validate them in a reverse pharmacology approach [31].

For long time, the massive amounts of genetic information responsible for the metabolic potential of the natural sources as producers of bioactive metabolites remained unexplored. However, developments in genomics have revealed the metabolic potential of natural sources. Genome-mining approaches have been developed to activate silent biosynthetic gene clusters in microorganisms to obtain cryptic natural products that are not detected under conventional laboratory conditions. Principal component analysis (PCA), combining molecular networking and metabolomics, is an especially valuable tool for extracts, allowing rapid comparison of metabolite profiles from complex crude extracts, allowing for effective chemical dereplication and discovery of novel compounds [32].

Innovative drug discovery from natural products requires a multidisciplinary approach utilizing available and innovative technologies to package such natural product compounds for medical practice and drug development. The combined use of biological approaches and medicinal chemistry offers promising opportunities to access natural product-like compounds. The successful use of such an approach will allow the development of next-generation drugs to combat the ever-increasing health challenges of today and the future [27].

3 Obesity

Obesity is characterized by an excess of body fat resulted from a chronic surplus in energy intake over energy expenditure. In clinical practice, the body fatness is usually estimated by body mass index (BMI). Patients with a BMI of 25 and 30 kg/m² are classified, respectively, as overweight and obese [33]. In the progression of obesity, the lipid deposition in adipose tissue can exceed the storage capacity of

adipocytes, resulting in elevated circulating concentrations and inappropriate accumulation in multiple tissues, most notably liver and skeletal muscle. Fat deposits in such ectopic tissues are unhealthy and can initiate tissue inflammation, endoplasmic reticulum stress, and endothelial dysfunction, accelerating the development of obesity associated pathologies [34].

According to the WHO, more than 2.1 billion adults were estimated to be overweight or obese globally in 2014, of which 1.5 billion were overweight and 640 million were obese. The estimated age-standardized prevalence of obesity in 2014 was 10.8% among adult men and 14.9% among adult women. These data would indicate that female sex is associated with higher risk of obesity, whereas overweight is more prevalent among men [35]. In 2016, approximately 39% (1.9 billion) of adults above the age of 18 years are overweight and 13% (603.7 million) were classified as obese, despite of efforts to slow the progress of the epidemic. This prevalence translates into a global health cost equivalent to 2.8% of the world's gross domestic product, or approximately US\$ 2 trillion. Furthermore, obesity is responsible for 3.4 million global deaths annually and accounts for about 4% of life lost per year [36, 37].

Population studies have clearly shown that individuals with obesity are at greater risk of developing numerous health complications that contribute to premature death than normal-weight individuals. In addition to an increased risk of developing features of the metabolic syndrome, other common comorbidities are endocrine disorders, such as type 2 diabetes mellitus, respiratory problems, cardiovascular diseases and cancers. Moreover, obesity has negative impacts not only on psychological and mood issues, but also on cognitive function [38].

The etiology of obesity is multifactorial, involving a complex interaction among genetics, hormones and the environment. Interfering genes described are beta-3-adrenergic receptor gene, peroxisome-proliferator-activated receptor gamma 2 genes, chromosome 10p, melanocortin-4 receptor gene and other genetic polymorphisms. Multiple hormones are involved in regulation and pathophysiology of obesity, including leptin, ghrelin, obestatin, nesfatin-1, endocannabinoids. Moreover, some environmental factors like energy-dense foods and increasingly fewer demands for physical activity in usual lifestyles may also influence obesity [39, 40].

The control of body weight and composition has to consider energy intake, energy expenditure and fat deposition. Current management of obesity is aimed at weight loss by taking a risk-based approach using low-risk treatments, such as lifestyle interventions, dietary changes and exercise, as the first-line choice, followed by pharmacotherapy and surgery in selected cases [40]. Pharmacotherapy should be a consideration for patients with a BMI of ≥ 30 kg/m² and BMI of ≥ 27 kg/m² with weight-related comorbidities, and is the next logical therapeutic approach for patients who have historically failed to benefit from lifestyle modification approaches and for those with difficulty maintaining weight loss over the long term [41].

Many weight-lowering pharmacotherapies that were initially approved for treatment of obesity were subsequently withdrawn as safety concerns emerged to

Table 1 US FDA-approved drugs for the treatment of obesity

Drug	Mechanism of action	Approved use	Adverse effects
Orlistat	Pancreatic lipase inhibitor	Long-term oral use	Bloating and diarrhea. Impaired absorption of fat-soluble vitamins
Lorcaserin	Serotonin receptor agonist	Long-term oral use	Headache, dizziness, nausea, dry mouth and constipation
Liraglutide	Glucagon-like receptor 1 agonist	Long-term use by subcutaneous injection	Nausea with vomiting, acute pancreatitis and hypoglycaemia
Diethylpropion, phentermine, phendimetrazine and benzphetamine	Noradrenergic drug	Short-term oral use	Dizziness, dry mouth, insomnia, constipation, irritability and cardiostimulatory effect
Phentermine-topiramate extended release	Appetite suppressants through the release of serotonin, noradrenaline and dopamine	Long-term oral use	Paraesthesia and change in taste (dysgeusia), metabolic acidosis and glaucoma
Naltrexone-bupropion sustained release	Appetite suppressants through inhibiting the reuptake of dopamine and noradrenaline, blocking μ -opioid receptor and activating pro-opiomelanocortin	Long-term oral use	Nausea, constipation and headache

dominate the pharmacological benefits. On the other hand, abuse of amphetamines, methamphetamine and phenmetrazine is well established, and these agents are approved by the FDA for short-term treatment, but not for long-term treatment, of the patient with obesity. Although historical weight-loss drugs failed to meet expectations, there has been important progress in recent years in the emergence of novel therapeutics [42]. Pharmacotherapeutic agents approved by US FDA and used to treat obesity include is shown in Table 1 [43, 44].

Among the existing treatments for obesity, development of nutrient digestion and absorption inhibitors is considered important strategies in the effort to decrease energy intake via gastrointestinal mechanisms. Since the dietary fat is not directly absorbed by the intestine unless the fat has been subjected to the action of pancreatic lipase, it is one of the most target widely studied for the development of new anti-obesity agents [45].

The only pancreatic lipase inhibitor approved by FDA is orlistat, a saturated derivative of lipstatin, produced from the actinobacterium *Streptomyces toxytricini*. Orlistat acts in the lumen of the stomach and small intestine by forming a covalent bond with the active serine site of gastric and pancreatic lipases and thus it inhibits

these lipases from hydrolyzing the ingested fat into absorbable free fatty acids and monoglycerides, leading to decreased systemic absorption of dietary fat by 30%. Despite its promising results, orlistat's use is limited by its gastrointestinal adverse effects, and patients should be advised to take a daily multivitamin supplement to make up for reduced absorption of fat-soluble vitamins [46].

4 Pancreatic Lipase as a Target for Anti-obesity Drugs

Pancreatic lipase (PL) belongs to the large family of serine esterases and is a key metabolic enzyme produced by the pancreas, being responsible for the hydrolysis of 50–70% of the total ingested fat [47]. PL is a glycoprotein of 50 KDa released in response of the hormone cholecystokinin and pancreatic acinar cells in the intestine, after the ingestion of a fatty meal. This enzyme releases fatty acids from the triglyceride skeleton at the C-1 and C-3 position. Lipase inhibition leads to interference with fat hydrolysis, which leads to decreased utilization of ingested lipids, reducing fat absorption [48].

Crystal structures of human PLs are described in Protein Data Bank (PDB) (<http://www.rcsb.org>), including: the pancreatic lipase-related protein 1 (PDB: 2PPL) and protein 2 (PDB: 2OXE), and the pancreatic lipase-colipase complex (PDB: 1LPB). Moreover, PL sequences have also been defined for several species by the screening of pancreatic cDNA libraries. Structurally, the *N*-terminus domain of PL comprises the residues 1–336 and contains the catalytic triad, whereas the *C*-terminus domain has smaller dimension, and comprises the residues from 337 to 449. The *C*-terminus domain allows the interaction with colipase, which is crucial for the enzymatic activity. The two domains are separated by a small aminoacidic chain, and are stabilized by seven disulphide bonds [49, 50].

The *N*-terminal domain belongs to the α/β hydrolase fold and contains the catalytic triad consisting of Ser-152, Asp-176, and His-263 (Fig. 1). Four main steps, involving changes in conformation or charge, occur to the pancreatic lipase molecule: (i) initial closed conformation: a loop structure within the *N*-terminal (residues 237–261), often referred to as the 'lid' domain, initially covers the active site. Two other domains maintain the lid in this closed confirmation by van der Waal's forces; $\beta 5$ (75–84) and $\beta 9$ (203–223); (ii) transition to open confirmation: the $\beta 5$ domain moves away from the lid domain, causing the lid domain to uncover the active site (the open conformation); (iii) formation of an oxyanion hole: the movement of the $\beta 5$ domain also creates an electrophilic region around the triad serine residue. This oxyanion hole helps stabilize the intermediate catalytic product formed during the reaction. Aromatic side chains from residues tyrosine 114, phenylalanine 215 and phenylalanine 77 endow the oxyanion hole with hydrophobicity, as does the presence of proline 180, isoleucine 209 and leucine 202; (iv) binding to substrate and catalysis: two acyl-binding sites in the $\beta 9$ domain allow the carbonyl carbon of the primary ester bond access to the triad serine 152 residue. The *sn*-1 (or because of molecular symmetry, the *sn*-3) acyl chain is held

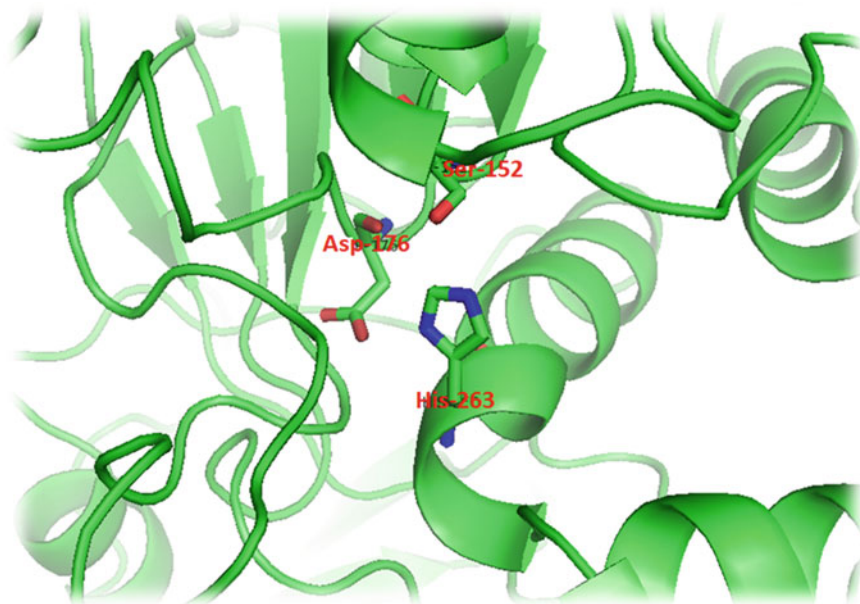


Fig. 1 Catalytic triad of the PL binding site formed by Ser-152, Asp-176 and His-263

within the oxyanion hole. The *sn*-2 chain lies within a second hydrophobic groove formed by side chains of lid domain residues (251–259) and by isoleucine 78 in the β 5 domain. This results in hydrolysis of the acylglycerol substrate. Two residues (leucine 213 and phenylalanine 215) on the β 9 domain contact with alkyl chains are implicated in increasing hydrolysis product stability [49, 50].

To carry out efficient lipolysis at a hostile lipid-water interface, PL indeed needs to complex with the amphipathic protein co-lipase to facilitate the opening of the lid, thus assisting its anchorage to the interface: following the conformational rearrangements of the β^5 -fold and the flap, this latter and the colipase surface form a large continuous hydrophobic plateau, extending over 50 Å, which strongly interacts with the lipid-water interface [51]. Phospholipids, bile salts, and amphiphilic proteins inhibit this process while several proteins such as serum albumin modulate this activity *in vivo*; plactoglobulin A, melittin, ovalbumin and myoglobin inhibit PL activity in light of the lipase desorption from its substrate, also protamine exerts an intense inhibitory activity on PL depending on the nature of the substrate emulsifier [52]. PL appears to lose catalytic activity below pH 5. This observation would suggest a potential exacerbation of low lipase activity in disorders causing pancreatic exocrine insufficiency, as not only will lower amounts of lipase be secreted into the duodenal lumen, but it may also be catalytically inactive due to low intestinal pH, caused by a lack of pancreatic bicarbonate secretion [53].

PL inhibitory properties have been extensively examined for the determination of the potential effect of new antiobesity agents and the discovery of orlistat has

increased the search for PL inhibitors compounds of natural products with a good safety profile. Studies have been reported in vitro inhibitory activity of natural products against PL, especially the chemo-diversity plant secondary metabolites, including polyphenols [54], saponins [55, 56], flavonoids [57, 58], alkaloids [59, 60], carotenoids [61], terpenes [62] and lignans [63]. The promising activities of medicinal plants have provided a direction for treatment of obesity and its secondary metabolites might provide a potential lead or pharmacophore for further development.

4.1 *Myrciaria Genus*

Myrciaria genus (Myrtaceae), presents a great importance due to its great technological potential of native species and its fruits with conditions for industrialization [64]. The fruits of this family possess a high pulp yield, flavor and several substances with antioxidant properties. This genus has species spread across various Brazilian biomes, such as Amazon Forest, Caatinga, Cerrado, Atlantic Forest, and Pampa. This genus presents about 99 known species [65]. Some species of *Myrciaria* genus are easily found in home yards, where has highlight the species known as jaboticabeira (*Myrciaria cauliflora* (Mart.) Berg) [66, 67] that produce fruit highly appreciated by the population and its fruits are consumed in forms of juices, jams, wines, and liqueurs, showing great potential in the food industry, in addition to possessing substances with the medicinal character that will be described later.

The geographical distribution of *Myrciaria* species occurs in many diversity centers, such as Brazil, Bolivia, Paraguay and Argentina, Central America and South Florida [68, 69]. In Brazil, these plants are cultivated mainly in the States of São Paulo, Rio de Janeiro, Minas Gerais, and Espírito Santo [70, 71].

According to the biological properties, rats fed with ration mixed with lyophilized barks of fruits from *Myrciaria jaboticaba* (Vell.) Berg showed an increase in antioxidant potential plasmatic in rats, and this effect could be due to anthocyanins content in this byproduct. However, excessive consumption of anthocyanins present in jaboticaba peels caused a reduction in antioxidant activity, showing the need to establish a recommended daily intake of these substances [72].

Besides the coloring given to plants, anthocyanins have properties that associate their intake with habits of healthy eating. There are several articles about these pigments reporting activities anticarcinogenic [73, 74], antioxidant [75], antiviral [74] and anti-inflammatory [76], agreeing with the properties of foods that contain considerable contents of anthocyanins. Beyond these effects, anthocyanins possess the effects: antimutagenic, cancer chemopreventive, in type 2 diabetes and Alzheimer's disease [77–79]. The consumption of foods rich in anthocyanins has been linked to the reduction of weight gain, regulation of hormones involving to obesity and improvement of insulin resistance in mice [80–82].

The peels of fruits and leaves of *Myrciaria cauliflora* (Mart.) O. Berg is astringent and popularly used against diarrhea and skin irritations [83]. It also presents indications for asthma, intestines inflammation, hemoptysis and was demonstrated that depsides and anthocyanins of jaboticaba fruits can reduce inflammation caused by exposure to cigarette smoke [84]. These compounds present strong antioxidant and anti-inflammatory properties, and some of these are of interest due to their potential to treat chronic obstructive pulmonary disease (COPD). The anti-inflammatory activity of jaboticaba against COPD also makes this fruit an emerging functional food for smokers, to reduce the lung damage in these patients [85]. Fruits of *Myrciaria vexator* also have an action against COPD, mainly due to the antioxidant capacity and the polyphenol content [86]. Besides, fruit extracts of *M. vexator* fruits exhibit antiradical activities by the ABTS method, much higher than the activity found to the so-called 'superfruits' such as blueberry [87]. The consumption of freeze-dried jaboticaba peel increased HDL-cholesterol (41.65% in animals fed with 2% freeze-dried peel jaboticaba in relation to the control group) and improve insulin resistance in obese rats (hyperinsulinemia was lower in animals that received freeze-dried jaboticaba peel) [88].

Hydroethanolic extracts (80%) of *M. cauliflora* leaves showed antifungal activity in vitro against strains of *Candida albicans* (dilution to 1: 2) and *C. krusei* (crude extract), while hydroethanolic extract from stem barks antifungal activity against the strains tested: *Candida albicans* (dilution to 1:2), *Candida guilliermondii* (dilution to 1:8) and *Candida krusei* (dilution to 1:8) [89].

In *Myrciaria dubia* (Kunth) McVaugh fruits (camu-camu) were found powerful antioxidative and anti-inflammatory properties in vivo in humans, these activities can be attributed to the presence of vitamin C, anthocyanins and β -carotene [90]. The camu-camu juice presented the same previous properties when compared to ascorbic acid and these effects may be due to the presence of unknown substances besides vitamin C or other compounds capable to modulate in vivo the vitamin C kinetics in camu-camu. The consumption daily of 70 mL of camu-camu juice for 1 week was capable to reduce urinary 8-hydroxydesoxyguanosine, a biomarker of DNA damage, which did not occur with equal amounts of isolated ascorbic acid [90]. Recently, Myoda et al. [91] studied the effects of several concentrations of methanolic extract of camu-camu juice residue such as seed and peel on the following microorganisms: *Staphylococcus aureus*, *Escherichia coli* and *Saccharomyces cerevisiae*. The extract showed antimicrobial activity against *Staphylococcus aureus* probably due to lipophilic compounds [91]. Besides, the compound 4-(α -rhamnopyranosyl) ellagic acid showed the strongest inhibition against human recombinant aldose reductase, is 60 times higher than quercetin [87, 92].

Genotoxic and antigenotoxic potential of *M. dubia* juice on blood cells of mice after acute, subacute and chronic treatment were evaluated and after treatments, there was not observed a signal of toxicity and death, which shows that camu-camu fruits it's safe for human consumption, however, depth studies are necessary. Besides, the camu-camu presented antigenotoxic activity, in the *ex vivo* test (comet assay) [93].

5 Pharmacophore-Based Drug Design

Computers have become a more prominent tool for rational strategies in drug discovery since the 1980s, mainly by the reduced time and costs of the process. The main goal of Computer-Aided Drug Design (CADD) is the identification of hits, which can then be used as starting point for hit-to-lead optimization [94]. The basis of all CADD methods is chemo-informatics, the application of data storage, handling, and retrieval methods to chemical structures, their properties, and biological activity. It also covers the calculation of molecular descriptors that describe a chemical or physical property based on the molecules' structure, and which can be used for filtering compounds. In order to be able to compare and quantify similarity between molecules, molecular fingerprints are often the methods of choice [94, 95].

In this context, the pharmacophore-based virtual screening emerged and largely evolved in the drug discovery process. The original concept of the pharmacophore was developed by Paul Ehrlich in 1909 that suggested that specific groups within a molecule are responsible for its biological activity and molecules with similar effect had similar functions in common [96]. Since 1997, pharmacophore has been defined by the International Union of Pure and Applied Chemistry (IUPAC), as: "The ensemble of steric and electronic features that is necessary to ensure the optimal supramolecular interactions with a specific biological target and to trigger (or block) its biological response". The pattern of features of a molecule that is responsible for a biological effect can be labeled as hydrogen bond donors or acceptors, cationic, anionic, aromatic, or hydrophobic, and any possible combinations [97].

Pharmacophore models can be derived by either ligand and structure-based approaches, depending on the availability of the three-dimensional structure of the binding site of the target. In the first approach, the identification of a pharmacophore, in principle, involves two steps: (i) the analysis of the modeling set molecules itself to identify pharmacophoric features, and (ii) the alignment of the assumed bioactive conformations of the molecules to determine the best overlay of corresponding features. If a molecule can fulfill the requirements of the model it has a high likelihood to be active in the experimental testing [98]. Che et al. [99] used this approach to identify novel CXC chemokine receptor 2 (CXCR2) antagonists for treatment of metastatic cancer. The compound selected by pharmacophore screening showed an antagonist activity with an IC_{50} value of 14.8 μM and anti-cancer metastatic effect (72% inhibition in cell migration at 50 $\mu\text{g ml}^{-1}$) [99].

An important step in ligand-based virtual screening of pharmacophore is the preparation of the database. Public sources such as ChEMBL [100], PubChem [101], BindingDB [102] and DrugBank [103] provide compound activity data, target information and compounds structures. Besides, collecting active compounds from literature and patents is doable. Compound activities can be filtered by descriptors such as IC_{50} or K_i . A well-constructed pharmacophore model should be able to cover as much as the active compounds and discard the inactive ones. Moreover, some elements need to be considered in the construction of the

pharmacophore model, including the number of compounds, the diversity and the activity magnitudes [104]. There are several commercially available programs and servers for automatic generation of pharmacophore models from a set of active ligands, including Discovery Studio (DS) [105], Phase [106], LigandScout [107] and Pharmagist [108].

When the structural information for the protein receptor is known, a pharmacophore model can be constructed by analyzing the binding interactions, the chemical properties, inclusion of shape and volume information of an active site of interest [109]. The structure-based pharmacophores have gained significant interest in the past years, since the number of experimentally determined 3D structure of targets has grown constantly and are being deposited, including in protein-ligand complexes, in databases such as the PDB [110]. There are several programs and servers that use the 3D atomic structures of protein binding sites into queries, including Catalyst [111], LigandScout [112] and PharmMapper [113]. Rochilla et al. [114] used a structure-based similarity search to identify inhibitors against IdeR, a transcription factor of *Mycobacterium tuberculosis*. The pharmacophore model provided insight into the features essential for IdeR inhibition and five molecules with promising IC₅₀ values inhibited *M. tuberculosis* growth with MIC₉₀ ranging from 17.5 µg/ml to 100 µg/ml [114].

Nevertheless, a very common approach in virtual screening is when different methods are combined consecutively. A combined ligand and structure-based drug design approach provides a synergistic advantage over either methods performed individually, as it was showed by Yadav et al. [115] in the identification of novel HIV-1 protease inhibitors [115]. On the other hand, pharmacophore models have been used as a filter for the analysis of molecular docking. Docking simulations are computational methods that aim to predict the binding mode of a compound for a given receptor as well as the quality of the interaction, often by attempting to predict the affinity (free energy of binding) using a scoring function. Several options are available for combining docking-based virtual screening with pharmacophore-based virtual screening: (i) the database of ligands can be pre-filtered using a pharmacophore query, prior to evaluation using docking simulations; (ii) the docking simulations can be post-filtered using a pharmacophore query to remove any compounds that fail to bind according to the pharmacophore query; (iii) to use the pharmacophore alignment to guide the placement during the docking simulations [116].

Besides screening, pharmacophore is a powerful model also in other applications of drug development, like ADME/Tox studies. It is known that poor ADME-tox is a major contributing factor to failures during drug development and clinical trials, thus these properties should be profiled early during the drug discovery process [117]. Kaur et al. [118] built a pharmacophore model for a CYP3A4-specific inhibitor derived from the structure/function studies on analogues of ritonavir. CYP3A4 inhibition has a greater impact on human health, as it can lead to xenobiotic-induced toxicity and drug–drug interactions, one of the reasons for late-stage clinical trial failures and withdrawal of marketed pharmaceuticals [118]. Moreover, pharmacophore models can also be used for anti-target screening to

predict the interaction of compound with targets with mediate potential harmful effects. Kratz et al. [119] develop a ligand-based pharmacophore model to identify human ether-a-go-go-related gene (hERG) potassium channel inhibitors. In this study, the tested compounds inhibited hERG channels expressed in HEK 293 cells with IC_{50} values ranging from 0.13 to 2.77 μM , attesting to the suitability of the model as cardiotoxicity prediction tools in a preclinical stage [119].

6 Pharmacophore Mapping of Chemical Markers from *Myrciaria* Genus Species for Pancreatic Lipase Inhibition

The aim of this work was to identify through pharmacophore approach the chemical markers from *Myrciaria* genus capable of inhibiting PL. In literature there are the description of several chemical markers already isolated from *Myrciaria* genus species that comprise an interesting library to find novel lead compounds with PL inhibitory activity, since *Myrciaria* genus plant extracts exhibit beneficial effects over fat metabolism.

7 Data Preparation

A search using BindingDB [120] and PubChem [121] was conducted to find compounds with PL inhibitory activity. The keyword “pancreatic lipase” was used in the search of bioassay records. The compounds were clustered according to their chemical classes and those five presenting the lowest IC_{50} (Inhibitory Concentration) values were selected to represent the dataset of their chemical class.

The chemical markers from plant species of *Myrciaria* genus that are already identified in literature were selected in scientific publications from PubMed, ScienceDirect and SciELO. This survey was carried out from 2014 to 2016 using the keywords “*Myrciaria*”, “secondary metabolites”, “chemical composition” and “active compounds”. A total of twenty full-text articles were considered. The two-dimensional chemical structures of these chemical markers and the PL inhibitors were sketched (Fig. 2), converted in 3D and optimized using ACD/ChemSketch (Freeware) 2017.2.1 [122], and subsequently converted to Sybyl MOL2 files using Accelrys Discovery Studio Client 2.5 [123].

Pharmacophoric models were generated using PharmaGist webserver which generates 3D pharmacophores from a set of molecules that are known to bind to a common target receptor. The method searches for possible pharmacophores and reports the highest-scoring ones. The candidate pharmacophores are detected by multiple flexible alignment of the input ligands, where the flexibility of the ligands is treated explicitly and in a deterministic manner in the alignment process [124].

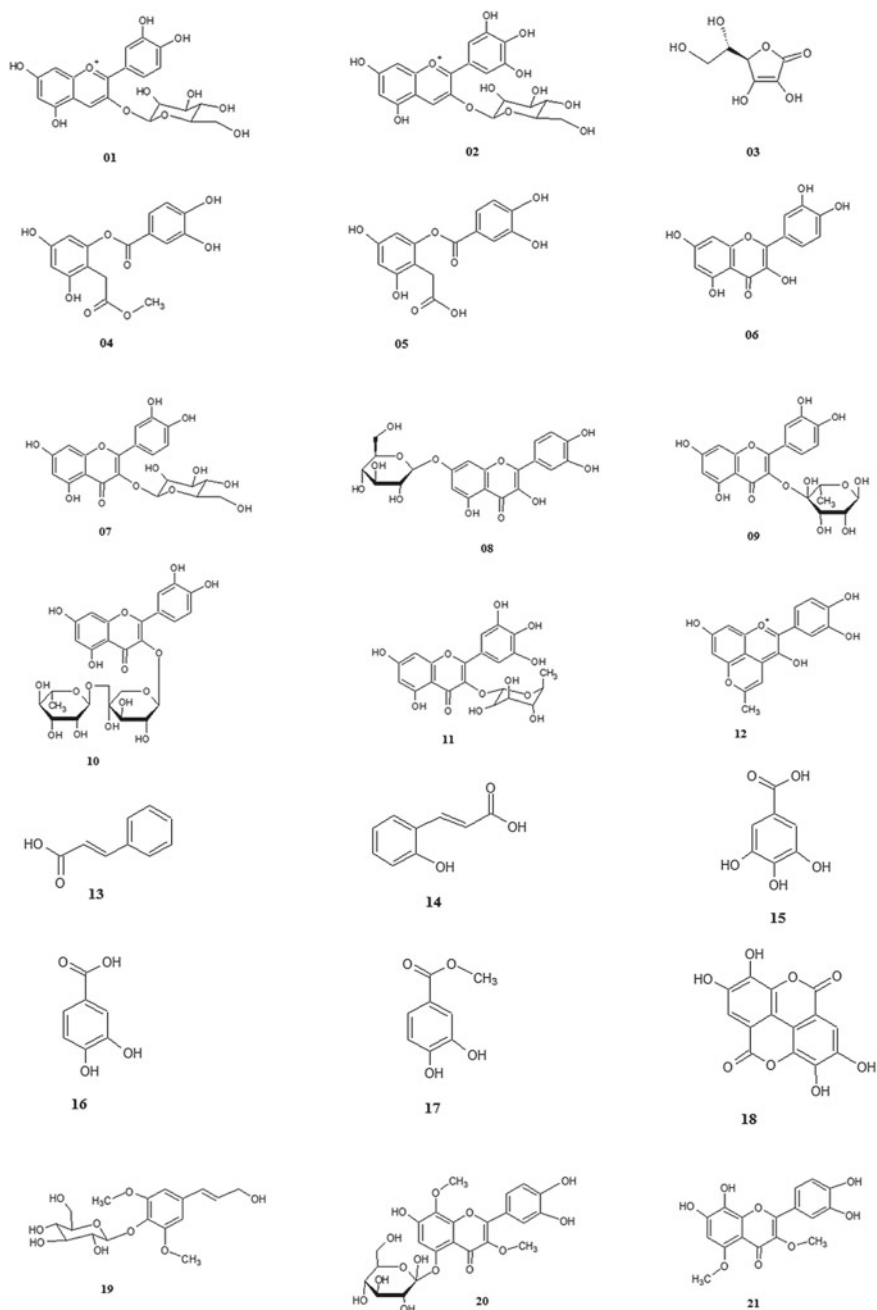


Fig. 2 Chemical markers from *Myrciaria* genus

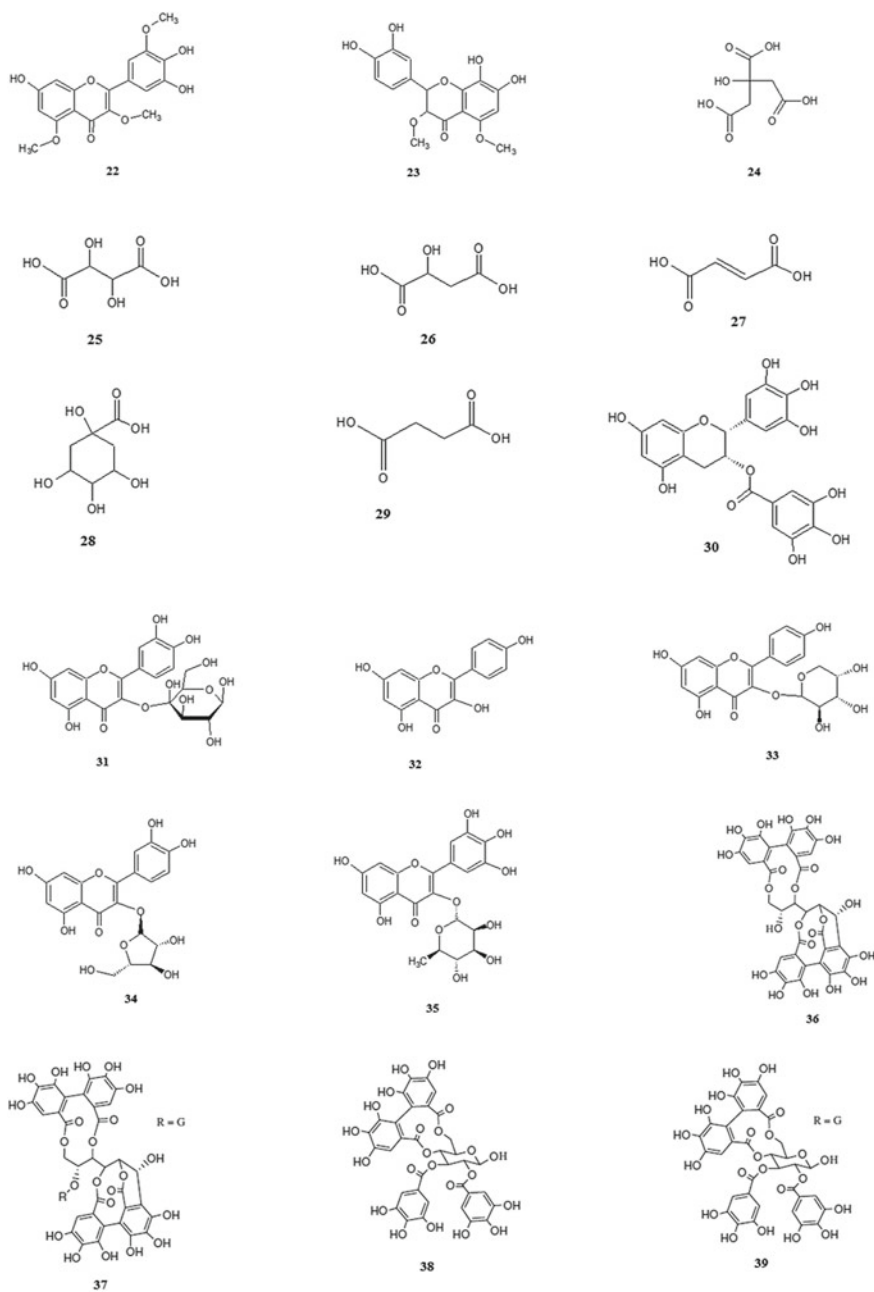


Fig. 2 (continued)

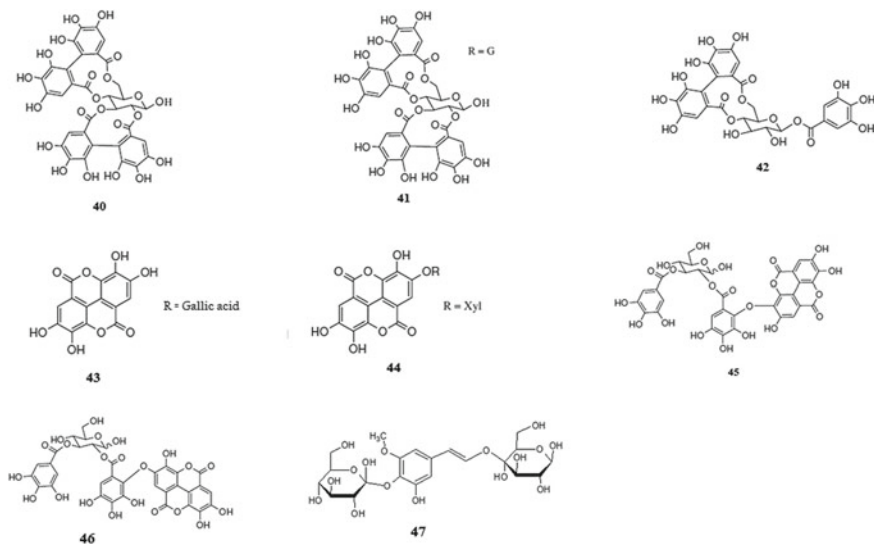


Fig. 2 (continued)

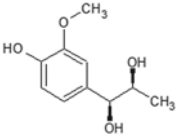
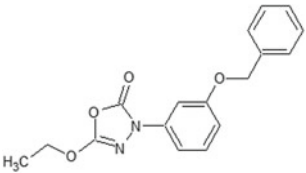
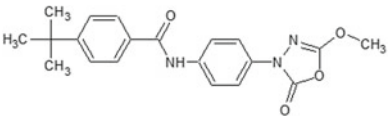
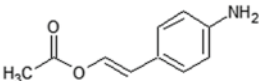
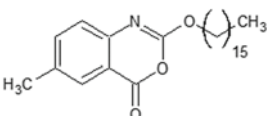
Pharmacophore modelling procedures were used to identify the main features of literature searched PL inhibitors and to align these features with the ones of *Myrciaria* genus chemical markers. Concerning the parameters, a minimum of 3 features including hydrogen-bond acceptor, hydrogen bond donor, hydrophobic, and ring aromatic features were selected for generating the pharmacophore models. The scoring weight assigned was 3.0 for aromatic rings, 1.0 for charge (anion/cation), 1.5 for hydrogen bond (donor/acceptor) and 0.3 for hydrophobic, which represent the default parameters of the webserver.

First, the PL inhibitors of the datasets (benzene derivatives (A), saponins and terpenoids (B), carotenoids (C), lactonic derivatives (D), triglycerides-like molecules (E) and glycosides and polyphenols (F)) were selected for pharmacophore perception, comprising a total of 30 compounds (Tables 2, 3, 4, 5, 6 and 7). Then, the chemical markers were inputted into each PL inhibitors dataset, in order to obtain the fitting pharmacophore models with *Myrciaria* genus chemical markers. The top-scored pharmacophore models were selected.

8 Pharmacophore Modeling

During literature search for PL inhibitory activity, many plant extracts, microbial products and synthetic compounds were identified for this activity. Natural compounds and dietary phytomolecules have an advantage of synergism and chemo-diversity [125]. Several chemical classes of PL inhibitors are reported in

Table 2 Chemical structure and IC₅₀ values for PL dataset of benzene derivatives

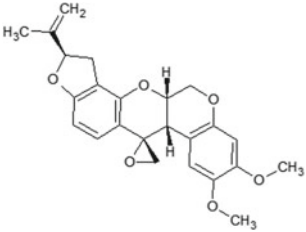
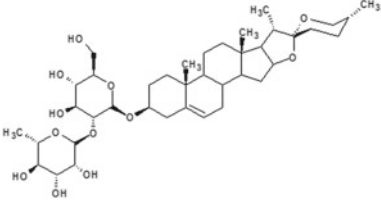
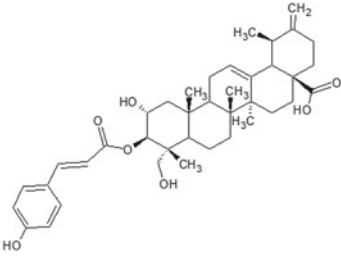
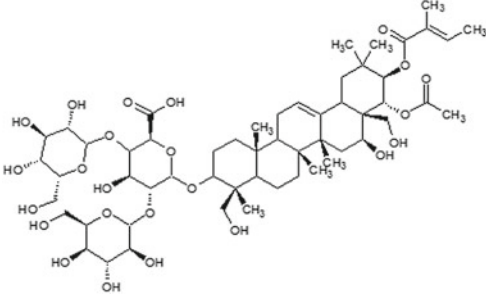
Structure	IC ₅₀ (μM)
	9.1
	0.01
	0.01
	7.46
	1

literature, which formed part of our dataset including: benzene derivatives, saponins, terpenoids, lactonic derivatives, carotenoids, triglycerides-like molecules, glycosides and polyphenols.

Many reported natural products, particularly the phenolics, terpenes and saponins have already shown inhibition of PL and among them the polyphenols represent the major class of PL inhibitors, then many fruits and herbal teas have been extensively studied for the PL inhibition due to the presence of polyphenols [125–127].

The structural diversity of inhibitors reported in literature resulted in different pharmacophoric models that might allow the fit of chemical markers phyto-molecules. A consensual model for all the classes was not obtained due to their

Table 3 Chemical structure and IC₅₀ values for PL dataset of saponins and terpenoids

Structure	IC ₅₀ (μM)
	6.3
	24.9
	14
	12

(continued)

Table 3 (continued)

Structure	IC50 (μM)
	15

structural differences, however the most representative features were the hydrophobic and hydrogen bond acceptor groups. According to the alignment of molecules, there are restrictive models such as the one for lactonic derivatives and on the other hand non restrictive models such as benzene derivatives (Fig. 3).

In the search for phytomolecules from *Myrciaria* genus, most of the existing studies about the chemical composition have concentrated on *M. cauliflora*, *M. dubia*, and *M. vexator*. Different types of polyphenol compounds such as flavonoids, tannins, anthocyanins and phenolic acids are found in extracts of *Myrciaria* fruits. Other compounds are also reported such as sesquiterpenes and organic acids [128–135].

With a vast composition of polyphenols the dataset of chemical markers (Fig. 2) have a predominance of molecules with aromatic rings, hydrogen bond acceptors and donors groups which favors the fit of such molecules in the pharmacophoric features of benzene derivatives, lactonic derivatives and the glycosides and polyphenols group. None of the chemical markers were capable to fit in the pharmacophoric features of saponins and terpenoids, the carotenoids and the triglycerides-like molecules group (Table 8).

Visualizing the fitting to the pharmacophore features of benzene derivatives, a large number of polyphenols attended the required features (Table 1), an aromatic group surrounded by two hydrogen bond acceptors. However as they are constituted of large molecules, only a part of their structure was aligned (Fig. 4).

Considering the pharmacophore model of lactonic derivatives, the chemical markers fitted only with some required features, however a greater part of the molecules was aligned (Fig. 5).

Finally, the pharmacophore of glycosides and polyphenols was the most representative for *Myrciaria* genus chemical markers, where most of them fitted with all the required features with a high score alignment when compared to benzene and lactonic derivatives models, mainly because PL inhibitors and chemical markers belong to the same chemical class (Fig. 6).

Sergent et al. [136] investigated the *in vitro* inhibitory activity of polyphenols on PL and, among them, epigallocatechin-3-gallate, kaempferol, quercetin and

Table 4 Chemical structure and IC₅₀ values for PL dataset of carotenoids

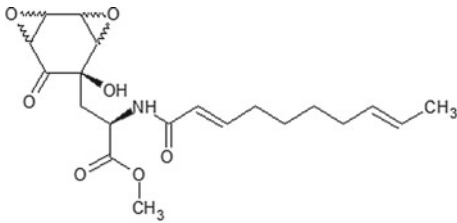
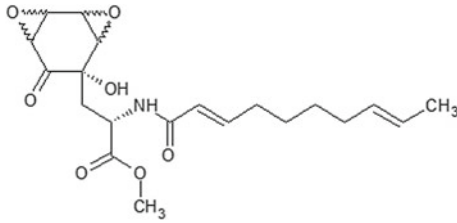
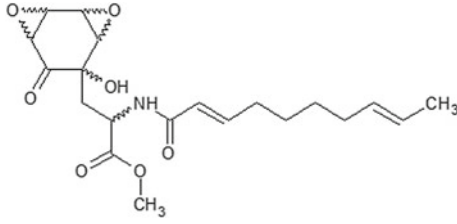
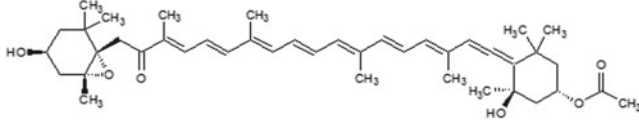
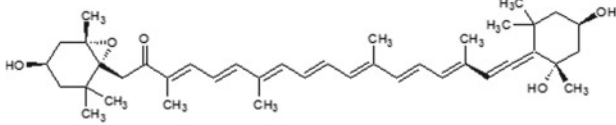
Structure	IC ₅₀ (μM)
 <p>The structure shows a substituted cyclohexane ring with a methyl ester group (-COOCH₃) and a hydroxyl group (-OH). It is connected via an amide bond to a long polyene chain ending in a methyl group (-CH₃).</p>	270
 <p>The structure is similar to the first one, but the stereochemistry of the hydroxyl group and the amide bond is different.</p>	27
 <p>The structure is similar to the first one, but the stereochemistry of the hydroxyl group and the amide bond is different.</p>	120
 <p>A complex carotenoid structure with multiple methyl groups (-CH₃) and hydroxyl groups (-OH) on the ring systems, and a long polyene chain with methyl substituents.</p>	0.66
 <p>A complex carotenoid structure similar to the previous one, but with different stereochemistry for the methyl and hydroxyl groups.</p>	0.76

Table 5 Chemical structure and IC₅₀ values for PL dataset of lactonic derivatives

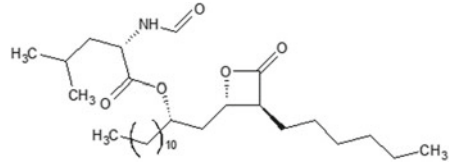
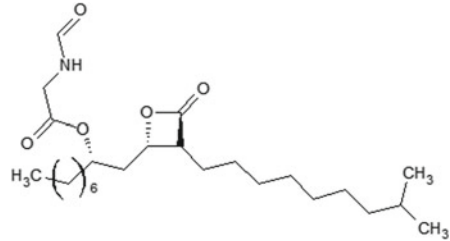
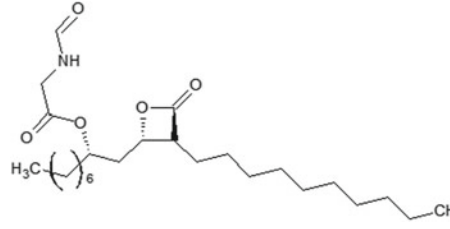
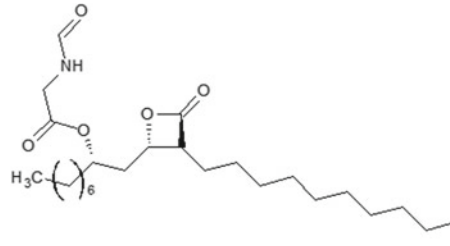
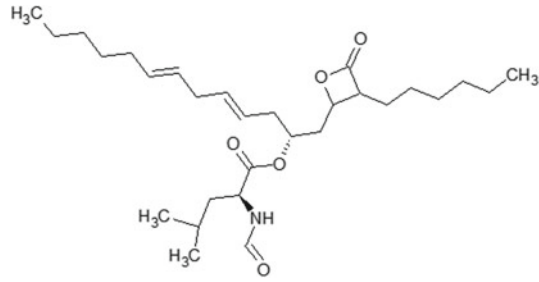
Structure	IC ₅₀ (μM)
 <p>Chemical structure of a lactonic derivative. It features a central lactone ring (a five-membered ring with one oxygen and two carbonyl groups). Attached to the ring are: a decyl chain (H₃C-(CH₂)₁₀-) on the left, a methyl group (CH₃) on the right, and a methyl ester group (-COOCH₃) on the bottom. A formamide group (-NHCHO) is attached to the decyl chain.</p>	0.068
 <p>Chemical structure of a lactonic derivative. It features a central lactone ring. Attached to the ring are: a hexyl chain (H₃C-(CH₂)₆-) on the left, and an isopropyl group (-CH(CH₃)₂) on the right.</p>	0.62
 <p>Chemical structure of a lactonic derivative. It features a central lactone ring. Attached to the ring are: a hexyl chain (H₃C-(CH₂)₆-) on the left, and a formamide group (-NHCHO) on the right.</p>	0.66
 <p>Chemical structure of a lactonic derivative. It features a central lactone ring. Attached to the ring are: a hexyl chain (H₃C-(CH₂)₆-) on the left, and a formamide group (-NHCHO) on the right.</p>	0.89
 <p>Chemical structure of a complex lactonic derivative. It features a central lactone ring. Attached to the ring are: a long chain with a double bond and a methyl group (H₃C-CH₂-CH₂-CH=CH-CH₂-CH₂-CH=CH-CH₂-) on the left, a decyl chain (H₃C-(CH₂)₁₀-) on the right, and a formamide group (-NHCHO) on the bottom. The formamide group is attached to a carbon that also has a methyl group (H₃C) and a methyl ester group (-COOCH₃).</p>	0.14

Table 6 Chemical structure and IC₅₀ values for PL dataset of triglycerides-like molecules

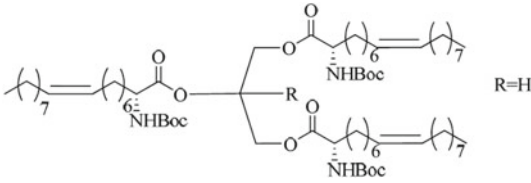
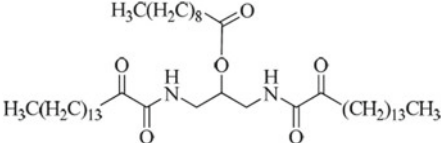
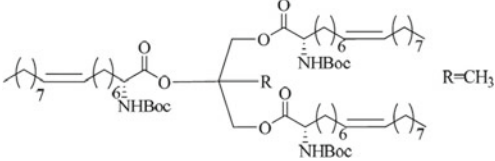
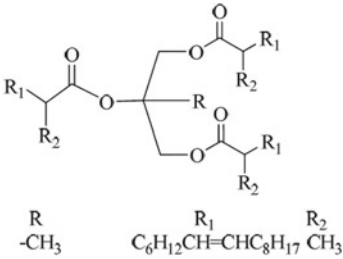
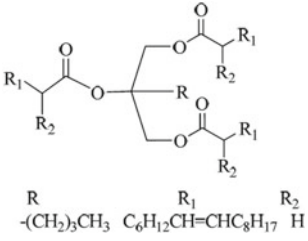
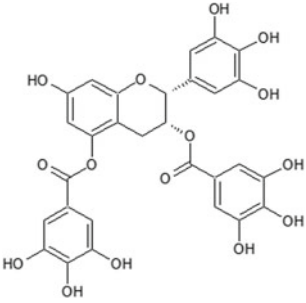
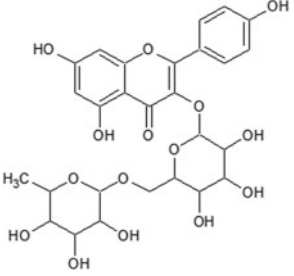
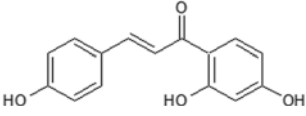
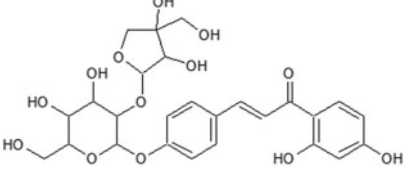
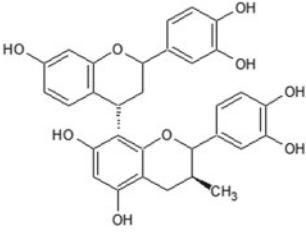
Structure	IC ₅₀ (μM)
 <p>R=H</p>	3
	76
 <p>R=CH₃</p>	2
 <p>R -CH₃</p> <p>R₁ C₆H₁₂CH=CHC₈H₁₇ R₂ CH₃</p>	3
 <p>R -(CH₂)₃CH₃</p> <p>R₁ C₆H₁₂CH=CHC₈H₁₇ R₂ H</p>	3

Table 7 Chemical structure and IC₅₀ values for PL dataset of glycosides and polyphenols

Structure	IC ₅₀ (μM)
	0.098
	2.9
	7.3
	14.9
	5.5

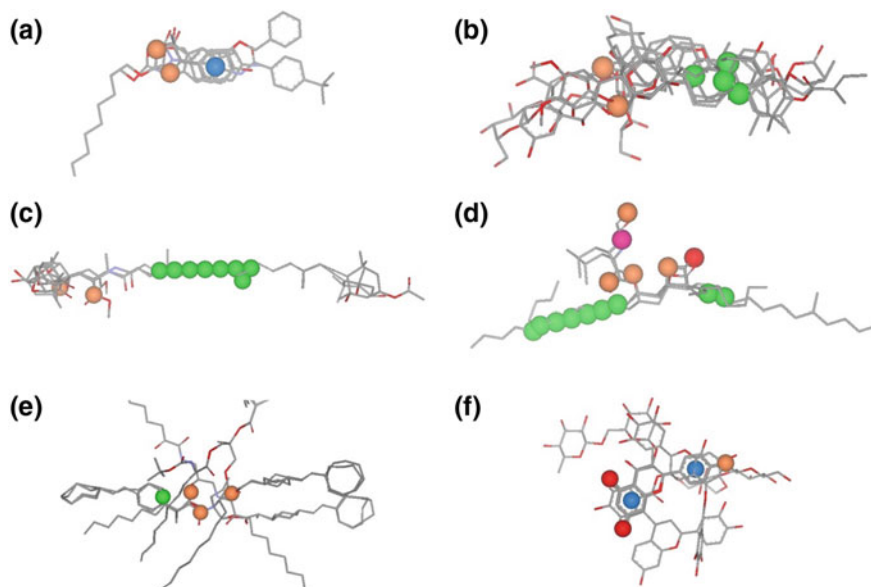


Fig. 3 Pharmacophore models of the PL inhibitors dataset obtained using PharmaGist. **a** Benzene derivatives. **b** Saponins and terpenoids. **c** Carotenoids. **d** Lactonic derivatives. **e** Triglycerides-like molecules. **f** Glycosides and polyphenols. Pharmacophore features are color-coded in orange for hydrogen-bond acceptors, blue for aromatic rings, green for hydrophobic, pink for hydrogen-bond donors and red for concomitant feature of hydrogen-bond acceptor and donors groups

Table 8 Distribution of chemical markers (1–47) from *Myrciaria* genus that fitted the pharmacophoric features of the PL inhibitors dataset

PL inhibitors dataset	Number of pharmacophore features				
	7	6	5	4	3
Benzene derivatives (3 ^a)	–	–	–	–	1, 2, 4, 5, 6, 7, 8, 9, 10, 11, 12, 13, 14, 15, 16, 17, 18, 19, 20, 21, 22, 23, 28, 30, 31, 32, 33, 34, 35, 36, 37, 38, 39, 40, 41, 42, 43, 45, 46 e 47
Lactonic derivatives (16 ^a)	–	9, 20, 31, 34, 37, 41, 42	4, 5, 8, 10, 11, 23, 30, 33, 35, 39, 43, 45, 46, 47	3	–
Glycosides and	1, 2, 4, 5, 6, 7, 9, 10, 11, 18,	8, 12, 20,	47	–	–

(continued)

Table 8 (continued)

PL inhibitors dataset	Number of pharmacophore features				
	7	6	5	4	3
polyphenols (7 ^a)	31, 32, 33, 34, 35, 37, 42, 43	21, 22, 23, 30, 41			

^aNumber of features of the dataset

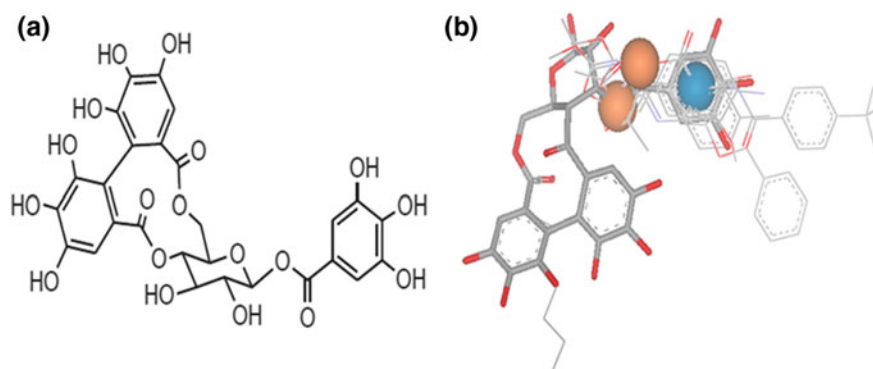


Fig. 4 Structure of the chemical marker number 42 (a) and its fitting to the pharmacophore of benzene derivatives (b). Pharmacophore features are color-coded in orange for hydrogen bond acceptors and blue for aromatic rings

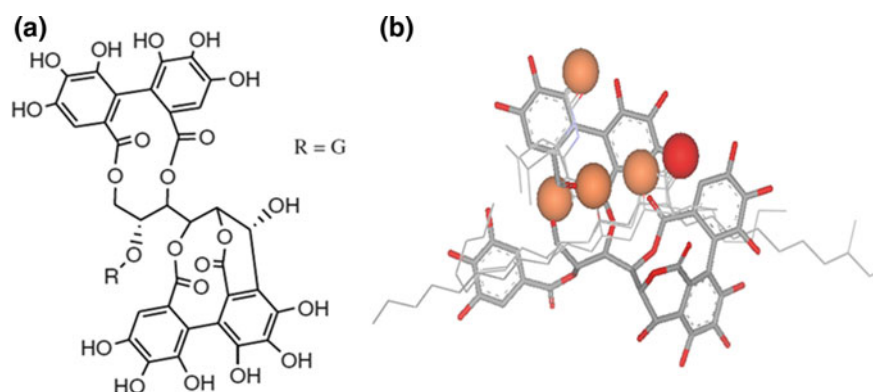


Fig. 5 Structure of the chemical marker number 37 (a) and its fitting to the pharmacophore of lactonic derivatives (b). Pharmacophore features are color-coded in orange for hydrogen-bond acceptors and red for concomitant feature of hydrogen-bond acceptor and donors groups

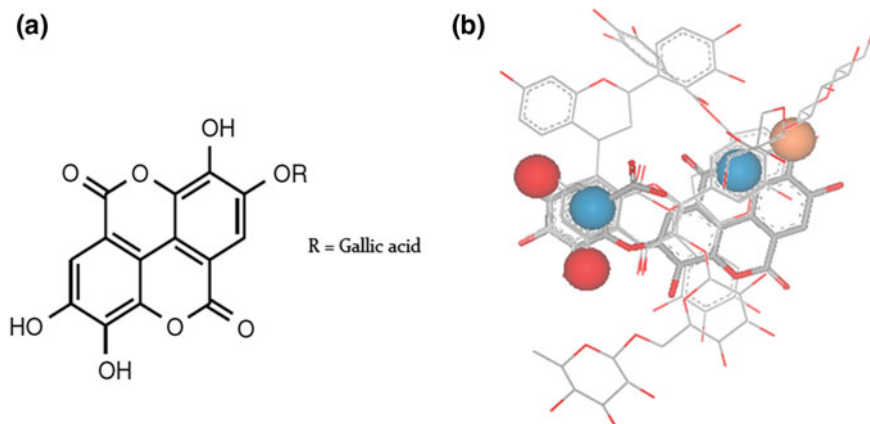


Fig. 6 Structure of the chemical marker number 43 (a) and its fitting to the pharmacophore of glycosides and polyphenols (b). Pharmacophore features are color-coded in orange for hydrogen-bond acceptors, blue for aromatic rings and red for concomitant feature of hydrogen-bond acceptor and donors groups

quercetin-3- β -D-glucoside showed the highest inhibitory activity [136]. These compounds are the chemical markers numbered as 30, 32, 6 and 31 respectively, and they were able to fit in at least in two of the constructed pharmacophore models (Table 8).

Regarding the structure-activity relationships for the polyphenols, Nakai et al. [137] suggested that the functional galloyl moieties in the structure and the polymerization of flavan-3-ol were needed for the expression of lipase inhibition [137]. This fact is also visualized in the pharmacophore model for glycosides and polyphenols (Fig. 6) by the presence of aromatic centers and hydrogen bond acceptor groups. The *Myrciaria* genus chemical markers were able to fit this model due to having these characteristics in their structures.

Hu et al. [138], evaluated the inhibitory activity of caffeoylquinic acid and its isomers against PL, and the authors suggest that smaller polyphenols provided fewer binding sites to the protein chain, causing weaker interactions or binding. We found polyphenols of larger structures in the chemical markers, then there is a possibility of them having more binding sites in the protein chain [138].

It is well known that the lipophilic catalytic site of the enzyme is perfectly suited to the lipophilic nature of orlistat, the only FDA-approved (Food and Drug Administration) PL inhibitor, indicating that there is a linear trend between the lipophilicity of the inhibitors and their inhibitory activity [139, 140]. The chemical markers have their lipophilicity represented mainly by aromatic rings, suggesting that these moieties may have an important role in the interaction with the PL.

It was possible to identify chemical markers able to fit concomitantly to three pharmacophore models (Fig. 7), indicating that ligands of multiple chemical classes

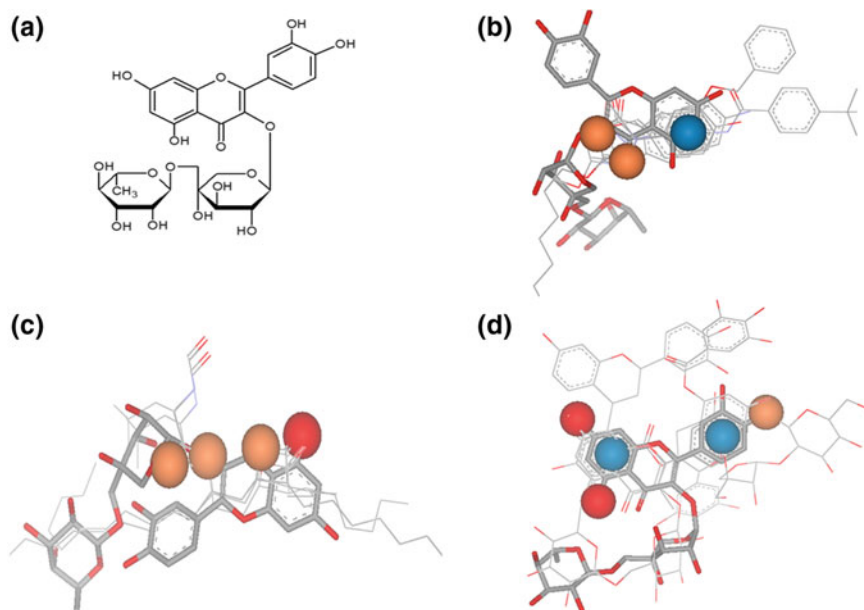


Fig. 7 Structure of the chemical marker number 43 (a) and its fitting to the pharmacophore of glycosides and polyphenols (b). Pharmacophore features are color-coded in orange for hydrogen-bond acceptors, blue for aromatic rings and red for concomitant feature of hydrogen-bond acceptor and donors groups

could inhibit PL. Moreover, there are many chemical markers with features which fulfill the minimum requirements expected of different types of PL inhibitors which evidences that these chemical markers may act by a synergistic effect.

9 Conclusion

Obesity has increased at an alarming rate in recent years, on the other hand, there is increasing interest in the anti-obesity effect of medicinal plants. The pharmacophoric approach demonstrated that the polyphenolic compounds from *Myrciaria* genus are promising PL inhibitors, because they share chemical features with different classes of PL inhibitors reported in literature. These facts may help to elucidate the effect of jaboriticaba, a fruit of a Brazilian native *Myrciaria* genus species, against obesity and to encourage further studies of other plants from this genus for anti-obesity and hypolipemic activity through inhibition of PL. Such phyto-molecules from *Myrciaria* species are a starting point to the development of novel therapeutic options with PL inhibitory action.

References

1. Newman, D.J., Cragg, G.M.: Natural products as sources of new drugs over the 30 years from 1981 to 2010. *J. Nat. Prod.* **75**(3), 311–335 (2012)
2. Haustedt, L.O., Mang, C., Siems, K., Schiewe, H.: Rational approaches to natural-product-based drug design. *Curr. Opin. Drug Discov. Devel.* **9**(4), 445–462 (2006)
3. Baker, D.D., Chu, M., Oza, U., Rajgarhia, V.: The value of natural products to future pharmaceutical discovery. *Nat. Prod. Rep.* **24**(6), 1225–1244 (2007)
4. Grabowski, K., Baringhaus, K.H., Shneider, G.: Scaffold diversity of natural products: inspiration for combinatorial library design. *Nat. Prod. Rep.* **25**(5), 892–904 (2008)
5. Haustedt, L.O.; Siems, K.: The role of natural products in drug discovery: examples of marketed drugs. In: Werngard, C., Peter, H. (eds.) *Small molecule medicinal chemistry: strategies and technologies*, p. 381. Wiley (2015)
6. Rollinger, J.M., Langer, T., Stuppner, H.: Strategies for efficient lead structure discovery from natural products. *Curr. Med. Chem.* **13**(13), 1491–1507 (2006)
7. Al-Masri, I.M.: Pancreatic lipase inhibition by papaverine: investigation by simulated molecular docking and subsequent in vitro evaluation. *Jordan. J. Pharmacol.* **6**(3), 271–279 (2013)
8. Tsai, A.G., Williamson, D.F., Glick, H.A.: Direct medical cost of overweight and obesity in the USA: a quantitative systematic review. *Obes. Rev.* **12**(1), 50–61 (2011)
9. Calle, E.E., Rodriguez, C., Walker-Thurmond, K., Thun, M.J.: Overweight, obesity, and mortality from cancer in a prospectively studied cohort of U.S. adults. *N. Engl. J. Med.* **348**(17), 1625–1638 (2003)
10. Carrière, F., Renou, C., Ransac, S., Lopez, V., De Caro, J., Ferrato, F., De Caro, A., Fleury, A., Sanwald-Ducray, P., Lengsfeld, H., Beglinger, C., Hadvary, P., Verger, R., Laugier, R.: Inhibition of gastrointestinal lipolysis by orlistat during digestion of test meals in healthy volunteers. *Am. J. Physiol. Gastrointest. Liver Physiol.* **281**(1), G16–G28 (2001)
11. Myoda, T., Fujimura, S., Park, B., Nagashima, T., Nakagawa, J., Nishizawa, M.: Exotic fruits reference guide. *J. Food Agric. Environ.* **8**, 304–307 (2010)
12. Dastmalchi, K., Flores, G., Wu, S.B., Ma, C., Dabo, A.J., Whalen, K., Reynertson, K.A., Foronjy, R.F., D’Armiento, J.M., Kennelly, E.J.: Edible *Myrciaria vexator* fruits: bioactive phenolics for potential COPD therapy. *Bioorgan. Med. Chem.* **20**(14), 4549–4555 (2012)
13. Lenquiste, S.A., Batista, A.G., Marinele, R.S., Dragano, N.R.V., Maróstica, M.R.: Freeze-dried jaboticaba peel added to high-fat diet increases HDL-cholesterol and improves insulin resistance in obese rats. *Food Res. Int.* **49**, 153–160 (2012)
14. Batista, G.B., Lenquiste, S.A., Moldenhauer, C., Godoy, J.T., Reis, S.M.P.M., Junior, M.R. M.: Jaboticaba (*Myrciaria jaboticaba* (Vell.) Berg.) peel improved triglycerides excretion and hepatic lipid peroxidation in high-fat-fed rats. *Rev. Nutr.* **25**, 571–581 (2013)
15. Alezandro, M.R., Granato, D., Genovese, M.L.: Análises químicas, propriedades funcionais e controle de qualidade de alimentos e bebidas: uma abordagem teórico-prática. *Food Res. Int.* **54**, 650–659 (2013)
16. Ewas, A.F., Maghrabi, I.A., Namarneh, A.I.: Advances in molecular modeling and docking as a tool for modern drug discovery. *Der Pharma Chem.* **6**, 211–228 (2014)
17. Sanders, M.P.A., McGuire, R., Roumen, L., Esch, I.J.P., Vlieg, J., Klomp, J.P.G., Graaf, C.: From the protein’s perspective: the benefits and challenges of protein structure-based pharmacophore modeling. *Med. Chem. Commun.* **3**, 28–38 (2012)
18. Harvey, A.L.: Natural products in drug discovery. *Drug Disc. Today* **13**, 894–901 (2008)
19. Baker, D.D., Chu, M., Oza, U., Rajgarhia, V.: The value of natural products to future pharmaceutical discovery. *Nat. Prod. Rep.* **24**, 1225–1244 (2007)
20. Strohl, W.R.: The role of natural products in a modern drug discovery program. *Drug Disc. Today* **5**, 39–41 (2000)
21. Harvey, A.: Strategies for discovering drugs from previously unexplored natural products. *Drug Disc. Today* **5**, 294–299 (2000)

22. Newman, D.J., Cragg, G.M.: Natural products as sources of new drugs from 1981 to 2014. *J. Nat. Prod.* **79**(3), 629–661 (2016)
23. WHO: National policy on traditional medicine and regulation of herbal medicines: report of a WHO global survey. World Health Organization, Geneva, Switzerland (2005)
24. Balunas, M.J., Kinghorn, A.D.: Drug discovery from medicinal plants. *Life Sci.* **78**, 431–441 (2005)
25. Sharma, S.B., Gupta, R.: Drug development from natural resource: a systematic approach. *Mini. Rev. Med. Chem.* **15**, 52–57 (2015)
26. Ghorbani, A., Naghibi, F., Mosaddegh, M.: Ethnobotany, ethnopharmacology and drug discovery. *Iran. J. Pharm. Sci.* **2**, 109–118 (2006)
27. Haustedt, L.O., Mang, C., Siems, K., Schiewe, H.: Rational approaches to natural-product-based drug design. *Curr. Opin. Drug Disc. Dev.* **9**, 445–462 (2006)
28. Wolfender, J.-L., Marti, G., Thomas, A., Bertrand, S.: Current approaches and challenges for the metabolite profiling of complex natural extracts. *J. Chromatogr. A* **1382**, 136–164 (2015)
29. Cheng, F., Li, W., Liu, G., Tang, Y.: In silico ADMET prediction: recent advances, current challenges and future trends. *Curr. Topics Med. Chem.* **13**, 1273–1289 (2013)
30. Ertl, P., Roggo, S., Schuffenhauer, A.: Natural product-likeness score and its application for prioritization of compound libraries. *J. Chem. Inf. Model.* **48**, 68–74 (2008)
31. Patwardhan, B., Vaidya, A.D.B., Chorghade, M., Joshi, S.P.: Reverse pharmacology and systems approaches for drug discovery and development. *Curr. Bioact. Compd.* **4**(4), 1–12 (2008)
32. Mukherjee, P.K., Harwansh, R.K., Bahadur, S., et al.: Metabolomics of medicinal plants—a versatile tool for standardization of herbal products and quality evaluation of ayurvedic formulations. *Curr. Sci.* **111**, 1624–1630 (2016)
33. Lenz, M., Richter, T., Mühlhauser, I.: The morbidity and mortality associated with overweight and obesity in adulthood: a systematic review. *Dtsch. Arztebl. Int.* **106**, 641–648 (2009)
34. Peeters, A., Barendregt, J.J., Willekens, F., et al.: Obesity in adulthood and its consequences for life expectancy: a life-table analysis. *Ann. Intern. Med.* **138**, 24–32 (2003)
35. World Health Organization: Obesity and Overweight (2014). <http://www.who.int/mediacentre/factsheets/fs311/en/>
36. World Health Organization: Obesity and Overweight (2016). https://www.who.int/gho/ncd/risk_factors/overweight/en/
37. GBD 2015 Obesity Collaboration: Health effects of overweight and obesity in 195 countries over 25 years. *N. Engl. J. Med.* **377**, 13–27 (2017)
38. Flegal, K.M., Kit, B.K., Orpana, H., Graubard, B.I.: Association of all-cause mortality with overweight and obesity using standard body mass index categories: a systematic review and meta-analysis. *JAMA* **309**, 71–82 (2013)
39. Racette, S.B., Deusinger, S.S., Deusinger, R.H.: Obesity: overview of prevalence, etiology, and treatment. *Phys. Ther.* **83**(3), 276–288 (2003)
40. Kaila, B., Raman, M.: Obesity: a review of pathogenesis and management strategies. *Can. J. Gastroenterol.* **22**(1), 61–68 (2008)
41. Jensen, M.D., Ryan, D.H., Apovian, C.M., et al.: 2013 AHA/ACC/TOS guideline for the management of overweight and obesity in adults: a report of the American College of Cardiology/American Heart Association Task Force on practice guidelines and the obesity society. *Circulation* **129**(Suppl 2), S102–S138 (2014)
42. Yanovski, S.Z., Yanovski, J.A.: Long-term drug treatment of obesity. A systematic and clinical review. *JAMA* **311**, 74–86 (2014)
43. Joo, J.K., Lee, K.S.: Pharmacotherapy for obesity. *J. Menopausal Med.* **20**(3), 90–96 (2014)
44. Srivastava, G., Apovian, C.M.: Current pharmacotherapy for obesity. *Nat. Rev. Endocrinol.* **14**(1), 12–24 (2018)
45. Xu, P.F., Dai, S., Wang, J., et al.: Preventive obesity agent montmorillonite adsorbs dietary lipids and enhances lipid excretion from the digestive tract. *Sci. Rep.* **6**, 19659 (2016)

46. Drew, B.S., Dixon, A.F., Dixon, J.B.: Obesity management: update on orlistat. *Vasc. Health Risk Manag.* **3**, 817–821 (2007)
47. Wang, H., Eckel, R.: Lipoprotein lipase: from gene to obesity. *Am. J. Physiol. Endocrinol. Metab.* **297**, E271–E288 (2009)
48. Mead, J.R., Irvine, S.A., Ramji, D.P.: Lipoprotein lipase: structure, function, regulation, and role in disease. *J. Mol. Med. (Berl.)* **80**, 753–769 (2002)
49. Winkler, F.K., D’Arcy, A., Hunziker, W.: Structure of human pancreatic lipase. *Nature* **343**, 771–774 (1990)
50. Lowe, M.E.: Structure and function of pancreatic lipase and colipase. *Annu. Rev. Nutr.* **17**, 141–158 (1997)
51. Bacha, A.B., Karray, A., Daoud, L., Bouchaala, E., Ali, M.B., Gargouri, Y., Ali, Y.B.: Biochemical properties of pancreatic colipase from the common stingray *Dasyatis pastinaca*. *Lipids Health Dis.* **10**, 69 (2011). <https://doi.org/10.1186/1476-511x-10-69>
52. Tsujita, T., Matsaura, Y., Okuda, H.: Studies on the inhibition of pancreatic and carboxylester lipases by protamine. *J. Lipid Res.* **37**(7), 1481–1487 (1996)
53. Brownlee, I.A., Forster, D.J., Wilcox, M.D., Dettmar, P.W., Seal, C.J., Pearson, J.P.: Physiological parameters governing the action of pancreatic lipase. *Nutr. Res. Rev.* **23**, 146–154 (2010)
54. Buchholz, T., Melzig, M.F.: Polyphenolic compounds as pancreatic lipase inhibitors. *Planta Med.* **81**, 771–783 (2015)
55. Li, F., Li, W., Fu, H., Zhang, Q., Koike, K.: Pancreatic lipase-inhibiting triterpenoid saponins from fruits of *Acanthopanax senticosus*. *Chem. Pharm. Bull. (Tokyo)* **55**, 1087–1089 (2007)
56. Subandi, Zakiyaturroddiyah, L., Brotosudarmo, T.H.P.: Saponin from purple eggplant (*Solanum melongena* L.) and their activity as pancreatic lipase inhibitor. *IOP Conf. Ser. Mater. Sci. Eng.* **509**, 012139 (2019)
57. Peng, Y.A.N.G., Yanqin, L.I.: Inhibitory effect of flavonoids and fagopyritols from buckwheat on pancreatic lipase. *Food Sci.* **36**(11), 60–63 (2015)
58. Rahim, A.T.M.A., Takahashi, Y., Yamaki, K.: Mode of pancreatic lipase inhibition activity in vitro by some flavonoids and non-flavonoid polyphenols. *Food Res. Int.* **75**, 289–294 (2015)
59. Birari, R., Roy, S.K., Singh, A., Bhutani, K.: Pancreatic lipase inhibitory alkaloids of *Murraya koenigii* leaves. *Nat. Prod. Commun.* **4**, 1089–1092 (2009)
60. Sridhar, S.N.C., Mutyra, S., Paul, A.T.: Bis-indole alkaloids from *Tabernaemontana divaricata* as potent pancreatic lipase inhibitors: molecular modelling studies and experimental validation. *Med. Chem. Res.* **26**, 1268–1278 (2017)
61. Matsumoto, M., Hosokawa, M., Matsukawa, N., Hagiom, Shinoki A., Nishimukai, M., et al.: Suppressive effects of the marine carotenoids, fucoxanthin and fucoxanthinol triglyceride absorption in lymph duct cannulated rats. *Eur. J. Nutr.* **49**, 243–249 (2010)
62. Ninomiya, K., Matsuda, H., Shimoda, H., Nishida, N., Kasajima, N., Yoshino, T., et al.: Carnosic acid, a new class of lipid absorption inhibitor from sage. *Bioorg. Med. Chem. Lett.* **14**, 1943–1946 (2004)
63. Ahn, J.H., Shin, E.J., Liu, Q., Kim, S.B., Choi, K.M., Yoo, H.S., Hwang, B.Y., Lee, M.K.: Lignan derivatives from *Fraxinus rhyncophylla* and inhibitory activity on pancreatic lipase. *Nat. Prod. Sci.* **18**, 116–120 (2012)
64. Camlofski, A.M.: Caracterização do fruto de Cerejeira ‘Eugenia Involocrata DC’ visando seu aproveitamento tecnológico. Dissertation, Universidade Estadual de Ponta Grossa, Ponta Grossa (2008)
65. IPNI: The International Plant Name Index (<http://www.ipni.org/>). In: The Royal Botanic Gardens. The Harvard University Herbaria; Australian National Herbarium, Kew (2012)
66. Mattos, J.R.: Jaboticabeiras. Instituto de Pesquisas de Recursos Naturais Renováveis. Porto Alegre, AP (1983)
67. Donadio, L.C.: Jaboticaba (*Myrciaria jaboticaba* (Vell.) Berg). Jaboticabal, Funep (2000)

68. Jham, G.N., Fernandes, S.A., Garcia, C.F., Palmquist, D.: Comparison of GC and HPLC for quantification of organic acids in two jaboticaba (*Myrciaria*) fruit varieties. *Quim. Nova* **30** (7), 1529–1534 (2007)
69. Balerdi, C.F., Rafie, R., Crane, J.: Jaboticaba (*Myrciaria cauliflora* Berg.) a delicious fruit with an excellent market potential. *Proc. Fla. Sta. Hortic. Soc.* **119**(1), 66–68 (2006)
70. Ascheri, D.P.R., Ascheri, J.L.R., Carvalho, C.W.P.: Caracterização da farinha de bagaço de jaboticaba e propriedades funcionais dos extrusados. *Ciênci. Tecnol. Aliment.* **26**(4), 897–905 (2006)
71. Oliveira, A.L., Neto, E.A.B., Fenerich, E.J., Alonso, C.O., Azevedo, J.S.A., Neto, P.O.: Efeito da aplicação pré-colheita de cálcio na qualidade dos frutos de jaboticaba. In: XX Congresso Brasileiro de Fruticultura. Vitória (2008)
72. Leite, A.V., Malta, L.G., Riccio, M.F., Eberlin, M.N., Pastore, G.M., Maróstica Júnior, M. R.: Antioxidant potential of rat plasma by administration of freeze-dried jaboticaba peel (*Myrciaria jaboticaba* Vell Berg). *J. Food Chem.* **59**, 2277–2283 (2011)
73. Hagiwara, A., Miyashita, K., Nakanishi, T., Sano, M., Tamano, S., Kadota, T., Koda, T., Nakamura, M., Imaida, K., Ito, N., Shirai, T.: Pronounced inhibition by a natural anthocyanin, purple corn color, of 2-amino-1-methyl-6-phenylimidazo[4,5-b]pyridine (PhIP)-associated colorectal carcinogenesis in male F344 rats pretreated with 1,2-dimethylhydrazine. *Cancer Lett.* **171**(1), 17–25 (2001)
74. Kapadia, G.J., Balasubramanian, V., Tokuda, H., Iwashima, A., Nishino, H.: Inhibition of 12-O-tetradecanoylphorbol-13-acetate induced Epstein-Barr virus early antigen activation by natural colorants. *Cancer Lett.* **115**(2), 173–178 (1997)
75. Wang, C.J., Wang, J.M., Lin, W.L., Chu, C.Y., Chou, F.P., Tseng, T.H.: Protective effect of Hibiscus anthocyanins against tert-butyl hydroperoxide-induced hepatic toxicity in rats. *Food Chem. Toxicol.* **38**(5), 411–416 (2000)
76. Kong, J.M., Chia, L.S., Goh, N.K., Chia, T.F., Brouillard, R.: Analysis and biological activities of anthocyanins. *Phytochemistry* **64**(5), 923–933 (2003)
77. Katsube, N., Iwashita, K., Tsushida, T., Yamaki, K., Kobori, T.: Induction of apoptosis in cancer cells by Bilberry (*Vaccinium myrtillus*) and the anthocyanins. *J. Agric. Food Chem.* **51**(1), 68–75 (2003)
78. Tsuda, T., Horio, F., Uchida, K., Aoki, H., Osawa, T.: Dietary cyanidin 3-O-b-D-glucoside-rich purple corn color prevents obesity and ameliorates hyperglycemia in mice. *J. Nutr.* **133**, 2125–2130 (2003)
79. Wang, J., Mazza, G.: Effects of anthocyanins and other phenolic compounds on the production of tumor necrosis factor alpha in LPS/IFN-gamma-activated RAW. *J. Agric. Food Chem.* **50**, 4183–4189 (2002)
80. DeFuria, J., Bennett, G., Strissel, K.J., Perfield II, J.W., Milbury, P.E., Greenberg, A.S., Obin, M.S.: Dietary blueberry attenuates whole-body insulin resistance in high fat-fed mice by reducing adipocyte death and its inflammatory sequelae. *J. Nutr.* **139**(8), 1510–1516 (2009)
81. Prior, R.L., Wu, X., Gu, L., Hager, T., Hager, A., Wilkes, S., Howard, L.: Purified berry anthocyanins but not whole berries normalize lipid parameters in mice fed an obesogenic high fat diet. *Mol. Nutr. Food Res.* **53**(11), 1406–1418 (2009)
82. Prior, R.L., Wilkes, S., Rogers, T., Khanal, R.C., Wu, X., Hager, T.J., Hager, A., Howard, L.: Dietary black raspberry anthocyanins do not alter development of obesity in mice fed an obesogenic high-fat diet. *J. Agric. Food Chem.* **58**(7), 3977–3983 (2010)
83. Souza-Moreira, T.M., Severi, J.A., Santos, E., Silva, V.Y.A., Vilegas, W., Salgado, H.R.N., Pietro, R.C.L.R.: Chemical and antiarrheal studies of *Plinia cauliflora*. *J. Med. Food* **14** (12), 1590–1596 (2011)
84. Boari Lima, A.J., Duarte Corrêa, A., Carvalho Alves, A.P., Patto Abreu, C.M., Dantas-Barros, A.M.: Caracterização química do fruto jaboticaba (*Myrciaria cauliflora* Berg) e de suas frações. *Arch. Latinoam. Nutr.* **58**(4), 416–421 (2008)

85. Reynertson, K.A., Wallace, A.M., Adachi, S., Gil, R.R., Yang, H., Basile, M.J., D'Armiento, J., Weinstein, I.B., Kennelly, E.J.: Bioactive depsides and anthocyanins from Jaboticaba (*Myrciaria cauliflora*) Kurt. J. Nat. Prod. **69**, 1228–1230 (2006)
86. Dastmalchi, K., Flores, G., Wu, S.B., Ma, C., Dabo, A.J., Whalen, K., Reynertson, K.A., Foronjy, R.F., D'Armiento, J.M., Kennelly, E.J.: Edible *Myrciaria vexator* fruits: bioactive phenolics for potential COPD therapy. Bioorg. Med. Chem. **20**(14), 4549–4555 (2012)
87. Akter, M.S., Oh, S., Eun, J.-B., Ahmed, M.: Nutritional compositions and health promoting phytochemicals of camu-camu (*Myrciaria dubia*) fruit: a review. Food Res. Int. **44**(7), 1728–1732 (2011)
88. Lenquiste, S.A., Batista, Â.G., Marineli, R.D.S., Dragano, N.R.V., Maróstica, M.R.: Freeze-dried jaboticaba peel added to high-fat diet increases HDL-cholesterol and improves insulin resistance in obese rats. Food Res. Int. **49**(1), 153–160 (2012)
89. Diniz, D.N., Macêdo-Costa, M.R., Pereira, M.S.V., Pereira, J.V., Higino, J.S.: Efeito antifúngico in vitro do extrato da folha e do caule de *Myrciaria cauliflora* Berg. sobre microrganismos orais. Rev. Odontol. UNESP **39**, 151–156 (2010)
90. Inoue, T., Komoda, H., Uchida, T., Node, K.: Tropical fruit camu-camu (*Myrciaria dubia*) has anti-oxidative and anti-inflammatory properties. J. Cardiol. **52**(2), 127–132 (2008)
91. Myoda, T., Fujimura, S., Park, B., Nagashima, T., Nakagawa, J., Nishizawa, M.: Antioxidative and antimicrobial potential of residues of camu-camu juice production. J. Food Agric. Environ. **8**(2), 304–307 (2010)
92. Ueda, H., Kuroiwa, E., Tachibana, Y., Kawanishi, K., Ayala, F., Moriyasu, M.: Aldose reductase inhibitors from the leaves of *Myrciaria dubia* (H. B. & K.) McVaugh. Phytomedicine **11**(7–8), 652–656 (2004)
93. Silva, F.C., Arruda, A., Ledel, A., Dauth, C., Romão, N.F., Viana, R.N., de Barros Falcao Ferraz, A., Picada, J.N., Pereira, P.: Antigenotoxic effect of acute, subacute and chronic treatments with Amazonian camu-camu (*Myrciaria dubia*) juice on mice blood cells. Food Chem. Toxicol. **50**(7), 2275–2281 (2012)
94. Yu, W., MacKerell Jr., A.D.: Computer-aided drug design methods. Methods Mol. Biol. **1520**, 85–106 (2017). https://doi.org/10.1007/978-1-4939-6634-9_5
95. Kore, P., Mutha, M., Antre, R., Oswal, R., Kshirsagar, S.: Computer-aided drug design: an innovative tool for modeling. Open J. Med. Chem. **2**(4), 139–148 (2012)
96. Yang, S.-Y.: Pharmacophore modeling and applications in drug discovery: challenges and recent advances. Drug Discov. Today **15**, 444–450 (2010)
97. Langer, T.: Pharmacophores in drug research. Mol. Inf. **29**, 470–475 (2010)
98. Kutlushina, A., Khakimova, A., Madzhidov, T., Polishchuk, P.: Ligand-based pharmacophore modeling using novel 3D pharmacophore signatures. Molecules **23**, 3094 (2018)
99. Che, J., Wang, Z., Sheng, H., et al.: Ligand-based pharmacophore model for the discovery of novel CXCR1 antagonists as anti-cancer metastatic agents. R Soc Open Sci. **5**(7), 180176 (2018). Published 4 Jul 2018
100. Mendez, D., Gaulton, A., Bento, A.P., Chambers, J., De Veij, M., Félix, E., Magariños, M. P., Mosquera, J.F., Mutowo, P., Nowotka, M., et al.: ChEMBL: towards direct deposition of bioassay data. Nucl. Acids Res. **47**, D930–D940 (2019)
101. Kim, S., Thiessen, P.A., Bolton, E.E., et al.: PubChem substance and compound databases. Nucl. Acids Res. **44**(D1), D1202–D1213 (2016)
102. Gilson, M.K., Liu, T., Baitaluk, M., Nicola, G., Hwang, L., Chong, J.: BindingDB in 2015: a public database for medicinal chemistry, computational chemistry and systems pharmacology. Nucl. Acids Res. **44**(D1), D1045–D1053 (2016)
103. Wishart, D.S., Feunang, Y.D., Guo, A.C., et al.: DrugBank 5.0: a major update to the DrugBank database for 2018. Nucl. Acids Res. **46**(D1), D1074–D1082 (2018)
104. Leach, A.R., Gillet, V.J., Lewis, R.A., Taylor, R.: Three-dimensional pharmacophore methods in drug discovery. J. Med. Chem. **53**, 539–558 (2010)
105. Dassault Systèmes BIOVIA: Discovery Studio v. 4.0, Dassault Systèmes, San Diego (2012)

106. Dixon, S.L., Smondyrev, A.M., Knoll, E.H., Rao, S.N., Shaw, D.E., Friesner, R.A.: PHASE: a new engine for pharmacophore perception, 3D QSAR model development, and 3D database screening: 1. Methodology and preliminary results. *J. Comput. Aided Mol. Des.* **20**, 647–671 (2006)
107. Wolber, G., Langer, T.: LigandScout: 3-D pharmacophores derived from protein-bound ligands and their use as virtual screening filters. *J. Chem. Inf. Model.* **45**, 160–169 (2005). <https://doi.org/10.1021/ci049885e>
108. Schneidman-Duhovny, D., Dror, O., Inbar, Y., Nussinov, R., Wolfson, H.J.: PharmaGist: a webserver for ligand-based pharmacophore detection. *Nucleic Acids Res.* **36**(Web server issue), W223–W228 (2008)
109. Hu, B., Lill, M.A.: Exploring the potential of protein-based pharmacophore models in ligand pose prediction and ranking. *J. Chem. Inf. Model.* **53**(5), 1179–1190 (2013)
110. Rose, P.W., Prilič, A., Altunkaya, A., et al.: The RCSB protein data bank: integrative view of protein, gene and 3D structural information. *Nucl. Acids Res.* **45**(D1), D271–D281 (2017)
111. Hecker, E.A., Duraiswami, C., Andrea, T.A., Diller, D.J.: Use of catalyst pharmacophore models for screening of large combinatorial libraries. *J. Chem. Inf. Comput. Sci.* **42**, 1204–1211 (2002)
112. Wolber, G., Langer, T.: LigandScout: 3-D pharmacophores derived from protein-bound ligands and their use as virtual screening filters. *J. Chem. Inf. Model.* **45**(1), 160–169 (2005)
113. Liu, X., Ouyang, S., Yu, B., Liu, Y., Huang, K., Gong, J., Zheng, S., Li, Z., Li, H., Jiang, H.: PharmMapper server: a web server for potential drug target identification using pharmacophore mapping approach. *Nucl. Acids Res.* **38**, W609–W614 (2010)
114. Rohilla, A., Khare, G., Tyagi, A.K.: Virtual screening, pharmacophore development and structure based similarity search to identify inhibitors against IdeR, a transcription factor of *Mycobacterium tuberculosis*. *Sci. Rep.* **7**, 4653 (2017)
115. Yadav, D., Paliwal, S., Yadav, R., Pal, M., Pandey, A.: Identification of novel HIV 1-protease inhibitors: application of ligand and structure based pharmacophore mapping and virtual screening. *PLoS ONE* **7**(11), e48942 (2012)
116. Kumar, A., Zhang, K.Y.J.: Hierarchical virtual screening approaches in small molecule drug discovery. *Methods*. Epub 27 July 2014
117. Alqahtani, S.: In silico ADME–Tox modeling: progress and prospects. *Exp. Opin. Drug Metab. Toxicol.* **13**(11), 1147–1158 (2017)
118. Kaur, P., Chamberlin, A.R., Poulos, T.L., Sevioukova, I.F.: Structure-based inhibitor design for evaluation of a CYP3A4 pharmacophore model. *J. Med. Chem.* **59**(9), 4210–4220 (2016)
119. Kratz, J.M., Schuster, D., Edtbauer, M., Saxena, P., Mair, C.E., Kirchebner, J., et al.: Experimentally validated hERG pharmacophore models as cardiotoxicity prediction tools. *J. Chem. Inf. Model.* **54**(10), 2887–2901 (2014)
120. Liu, T., Lin, Y., Wen, X., Jorissen, R.N., Gilson, M.K.: BindingDB: a web-accessible database of experimentally determined protein-ligand binding affinities. *Nucl. Acids Res.* **35**, D198–D201 (2007)
121. Kim, S., Thiessen, P.A., Bolton, E.E., Chen, J., Fu, G., Gindulyte, A.: *Nucl. Acids Res.* **78**, 1–12 (2015)
122. ACD/ChemSketch (Freeware) 2017.2.1. Advanced Chemistry Development, Inc
123. Discovery Studio Client, v2.5.0.9164. Accelrys Software Inc
124. Schneidman-Duhovny, D., Dror, O., Inbar, Y., Nussinov, R., Wolfson, H.J.: PharmaGist: a webserver for ligand-based pharmacophore detection. *Nucl. Acids Res.* **36**, W223–W228 (2008)
125. Lunagariya, N.A., Patel, N.K., Jagtap, S.C., Bhutani, K.K.: Inhibitors of pancreatic lipase: state of the art and clinical perspectives. *Excli J.* **13**, 897–921 (2014)
126. Sharma, N.K., Ahirwar, D.: A review on herbal medicinal plants for the treatment of obesity. *J. Harm. Res.* **2**, 01–33 (2013)
127. Sukhdev, S., Singh, K.S.: Therapeutic role of phytomedicines on obesity: importance of herbal pancreatic lipase inhibitors. *Int. Res. J. Med. Sci.* **1**(9), 15–26 (2013)

128. Wu, S.B.A., Dastmalchi, K., Long, C.L., Kennelly, E.J.: Metabolite profiling of jaboticaba (*Myrciaria cauliflora*) and other dark-colored fruit juices. *J. Agric. Food Chem.* **60**, 7513–7525 (2012)
129. Hussein, S.A.M., Hashem, A.N.M., Seliem, M.A., Lindequist, U., Nawwar, M.A.M.: Polyoxygenated flavonoids from *Eugenia edulis*. *Phytochemistry* **64**, 883–889 (2003)
130. Einbond, L.S., Reynertson, K.A., Luo, X.D., Basile, M.J., Kennelly, E.J.: Anthocyanin antioxidants from edible fruits. *Food Chem.* **1**(84), 23–28 (2004)
131. Vidigal, M.C.T.R., Minim, V.P.R., Carvalho, N.B., Milagres, M.P., Gonçalves, A.C.A.: Effect of a health claim on consumer acceptance of exotic Brazilian fruit juices: Açai (*Euterpe oleracea* Mart.), camu-camu (*Myrciaria dubia*), Cajá (*Spondias lutea* L.) and Umbu (*Spondias tuberosa* Arruda). *Food Res. Int.* **44**(7), 1988–1996 (2011)
132. Chirinos, R., Galarza, J., Betalleluz-Pallardel, I., Pedreschi, R., Campos, D.: Antioxidant compounds and antioxidant capacity of Peruvian camu camu (*Myrciaria dubia* [H.B.K.] McVaugh) fruit at different maturity stages. *Food Chem.* **120**, 1019–1024 (2010)
133. Akter, M.S., Oh, S., Eun, J.B., Ahmed, M.: Nutritional compositions and health promoting phytochemicals of camu-camu (*Myrciaria dubia*) fruit: a review. *Food Res. Int.* **44**, 1728–1732 (2011)
134. Tietbohl, L.A.C., Lima, B.G., Fernandes, C.P., Santos, M.G., Silva, F.E.B., Denardin, E.L.G., Bachinski, R., Alves, G.G., Silva-Filho, M.V., Rocha, L.: Comparative study and anticholinesterasic evaluation of essential oils from leaves, stems and flowers of *Myrciaria floribunda* (H. West ex Willd.) O. Berg. *Lat. Am. J. Pham.* **31**(4), 637–641 (2012)
135. Apel, M.A., Sobral, M., Zuanazzi, J.A., Henriques, A.T.: Essential oil composition of four Plini species (Myrtaceae). *Flavour Frag. J.* **21**, 565–567 (2006)
136. Sergent, T., Vanderstraeten, J., Winand, J., Beguin, P., Schneider, Y.J.: Phenolic compounds and plant extracts as potential natural anti-obesity substances. *Food Chem.* **135**(1), 68–73 (2012)
137. Nakai, M., Fukui, Y., Asami, S., Toyoda-Ono, Y., Iwashita, T., Shibata, H., Mitsunaga, T., Hashimoto, F., Kiso, Y.: Inhibitory effects of oolong tea polyphenols on pancreatic lipase in vitro. *J. Agric. Food Chem.* **53**(11), 4593–4598 (2005)
138. Hu, B., Cui, F., Yin, F., Zeng, X., Sun, Y., Li, Y.: Coffeoylquinic acids competitively inhibit pancreatic lipase through binding to the catalytic triad. *Int. J. Biol. Macromol.* **80**, 529–535 (2015)
139. Bentley, D., Young, A.M., Rowell, L., Gross, G., Tardio, J., Carlile, D.: Evidence of a drug-drug interaction linked to inhibition of ester hydrolysis by orlistat. *J. Cardiovasc. Pharmacol.* **60**(4), 390–396 (2012)
140. King, A.R., Lodola, A., Carmi, C., Fu, J., Mor, M., Piomelli, D.: A critical cysteine residue in monoacylglycerol lipase is targeted by a new class of isothiazolinone-based enzyme inhibitors. *Br. J. Pharmacol.* **157**(6), 974–983 (2009)

Perspectives and Strategies for Zeolites, Graphitic, Polymeric and Ferrite Systems

Theoretical Insights About the Chemical Dependent Role of Exchange-Correlation Functionals: A Case Study



Leonardo Konopaski Andreani, Renan Augusto Pontes Ribeiro,
Luis Henrique da Silveira Lacerda and Sérgio Ricardo de Lázaro

Abstract In this study, ab initio density functional theory calculations were performed for different materials considering the existence of different chemical bonds in NaCl, TiO₂ in anatase and rutile phases, and Graphite. Our insight was investigate materials with very specific and stablished chemical bonds, such as, strongly ionic (NaCl); mixed ionic-covalent bonds (TiO₂) and strongly covalent (Graphite) simulating each material in the PBE (pure), PBE0 (hybrid), B3LYP (parametrized and hybrid) functionals with Grimme dispersion (D) to build a case of study for this approach. We evaluated structural, mechanical and electronic properties as regards the role of different exchange-correlation functional. From such properties, the chemical nature dependence regarding to different exchange-correlations functionals was revised proving that the precision of DFT calculations depends on the chemical bond character showing the hard work in describe the chemical bond from general exchange-correlation functional. This proposition is an initial discussion for other theoretical studies.

Keywords DFT · Functionals · Chemical bond · Electronic density · Electronegativity

1 Introduction

1.1 Bravais Lattices

The Solid State is employed on the description of the matter in the solid-state, describing as molecular solid, as amorphous solids, as crystalline structures, and even for recently discovered quasicrystal. In this chapter, crystalline structures of

L. K. Andreani · L. H. da S. Lacerda · S. R. de Lázaro (✉)
Department of Chemistry, State University of Ponta Grossa, Ponta Grossa, Brazil
e-mail: srlazaro@uepg.br

R. A. P. Ribeiro
Department of Chemistry, Universidade Federal do Rio Grande do Norte, Natal, Brazil

© Springer Nature Switzerland AG 2020
F. A. La Porta and C. A. Taft (eds.), *Emerging Research in Science and Engineering Based on Advanced Experimental and Computational Strategies*, Engineering Materials, https://doi.org/10.1007/978-3-030-31403-3_13

materials were evaluated aiming to determine the role dependence of chemical-dependent role of exchange-correlation functional. This kind of material presents a high symmetry level of constituent atoms, which are observed in a periodic distribution and can be reproduced by translational symmetries. Thus, the crystalline structure is obtained through a translational movement from a lattice vector, resulting in the repetition of minimum unit that expresses the material's structure in its totality; such minimum unit is called unit cell. The unit cells are symmetrically and periodically stacked three-dimensionally in one of the fourteen possible symmetries, determined by crystallographic studies carried out by Bravais in 1848. Such symmetries are known as the Bravais lattice (Fig. 1) and are subdivided into seven crystalline systems according to the unit cell type: triclinic, monoclinic, orthorhombic, tetragonal, cubic, rhombohedral and hexagonal. The difference between each type of unit cell arises from a , b and c lattice parameters, α , β and γ unit cell angles, originating the 230 space groups [1–5].

Although all the crystalline structure shows symmetry associated to its structure, the symmetry degree observed in each Bravais unit cell is different, being that depending on the space group (atoms arrangement), lattice parameters and unit cell angles. Thereby, the symmetry degree on crystalline structures increases in the following order: triclinic < monoclinic < orthorhombic < rhombohedral < hexagonal < tetragonal < cubic. The symmetry degree has large influence on the

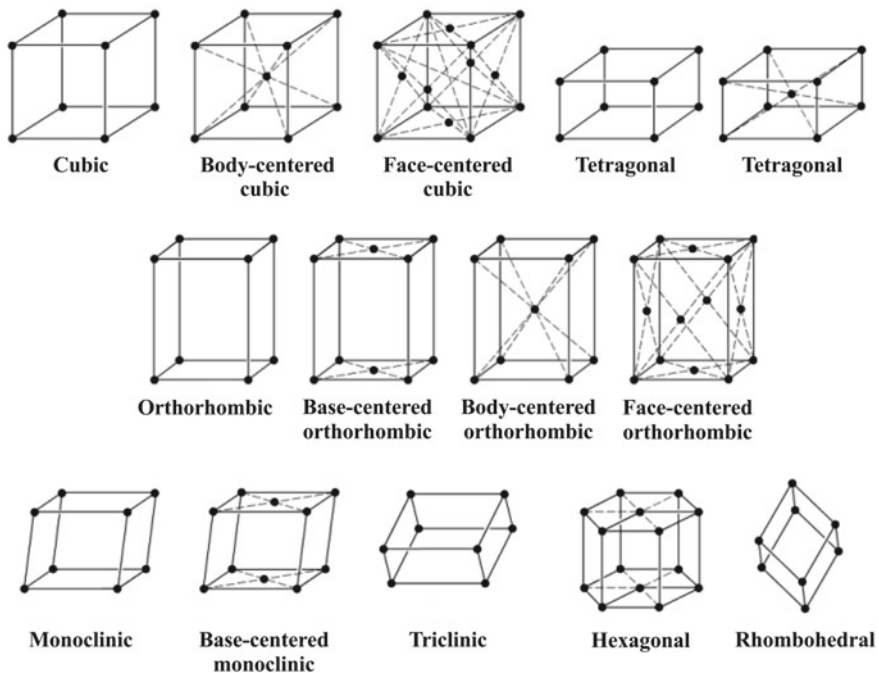


Fig. 1 Representation of the fourteen symmetries predicts by the Bravais lattice

properties of the material and, in general, the materials with non-center-symmetric sites exhibit the most interesting properties for technological application [5].

The periodicity and symmetry of crystal figures out as the most important features of a solid. Besides their influence on the materials property, they are very relevant in computational routines employed nowadays, causing the reduction of computational cost. It is possible due to the description of system by periodic models, which are essentially based on symmetry and atoms repetitions by translational operations [6]. In case of periodic models, it is required the construction of the Wigner Seitz unit cell of reciprocal lattice, also known as Brillouin Zone [7].

The application of Solid State materials on technological properties is possible mainly by its unique set of properties, such as electronic, optical and elastic properties. Hereafter, these properties are detailed described in the light of Solid-State theory.

2 Band Theory: Fundamentals for Electronic and Optical Properties

The crystalline structure of a solid is composed of atoms periodically distributed in an infinite lattice obtained from symmetry's operation and, for this reason, the energy levels of this kind the material presents a characteristic behavior described by the Band Theory for a crystalline solid. This theory predicts that, for one atom, the energy levels are quantized and discrete, corresponding to atomic orbitals; in a crystalline solid, the energy levels distribution is more complex, once the energy levels are slightly affected by neighbor atoms. Consequently, in a solid it is observed the formation of a big number of electronic states very closer each other, forming an almost continuous energy band. Thereby, an energy band is a continuous of electronic states closely spaced (Fig. 2) [2–4].

Based on band structures, the materials were grouped according to an elementary classification as conductors, semiconductors and insulators, being then differentiated by the energy difference between the conduction (CB) and valence bands (VB), i.e., the unoccupied and occupied energy levels, respectively. Such energy difference is called band gap and represents the energy required to excite an electron from VB to CB. As presented in Fig. 3, band gaps values minor than 1 eV are characteristic for conductor materials; intermediate differences (between 1 and 4 eV) are observed for semiconductor materials, while the insulator materials have band gap higher than 4 eV. In particular, the red region in Fig. 3 refers to the band gap energy range suggested for application on photocatalytic process or opt-electronic devices.

The electronic conduction process on solid-state materials occurs through the formation of electron-hole pair since one electron (e^-) is excited to CB forming a hole (h^\bullet) in VB. The conduction mechanism is dependent on the materials' electronic structure and crystalline structure symmetry points along the Brillouin Zone.

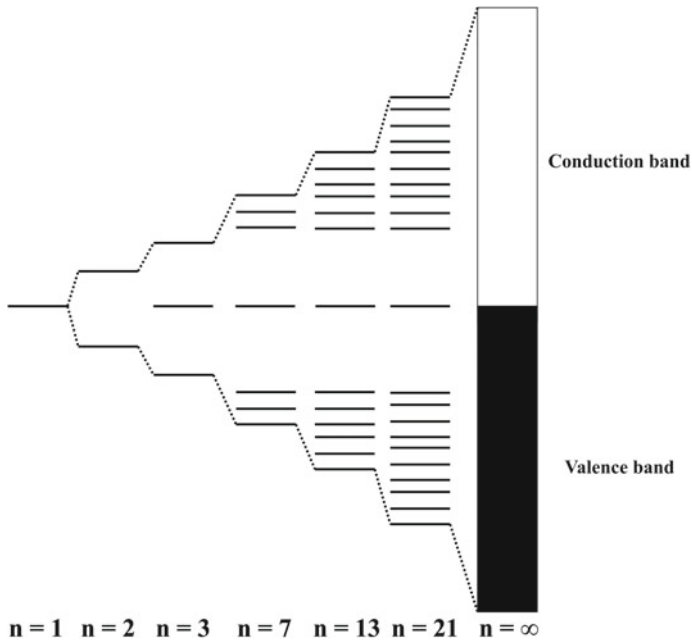


Fig. 2 Bands Theory representations on crystalline solids where n represents the number of atoms

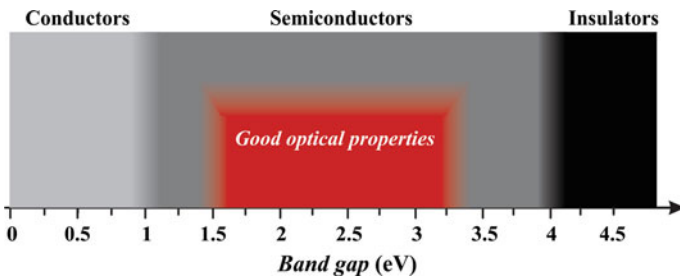


Fig. 3 Solid-State materials classification as conductors, semiconductors or insulators. The red region indicates the band gap value region required to the application on the photocatalytic process

Such symmetry points are intrinsically related to the unit cell space group and are label according to the atomic spatial coordinates. In summary, two kinds of conduction process are possible. The first refers to the direct excitation of an electron and occurs when the materials absorb energy equal or higher than the band gap. The second type occurs indirectly and consists of the excitation of an electron between two different symmetry points of Brillouin Zone; in turn, requires high energy since involves the coupling between phonons and photons [2].

Likewise, the optical properties of a solid-state material are also obtained as a result of Band Theory and determine how the material interacts with electromagnetic radiation. It is important to note that the interaction occurs only with radiations whose energy is equal or bigger than the material band gap.

In particular, the conductivity of solid-state materials depends on several factors, such as temperature and charge carriers' mobility. The temperature influence is justified by the perturbation of energy level, mainly evidenced by the variation on the Fermi energy level, which is a statistical measurement that provides the energy of the highest occupied energy orbital. However, the influence of temperature is relevant only for conductors and semiconductors, once on insulators the temperature contribution it is not enough to enable the electron excitation [3]. In turn, the charge carriers' mobility is a determinant factor for electronic conduction because, if the charge carriers are unstable, the conduction process is disadvantaged due to fast recombination of electron-hole pair [7].

3 Elastic Properties: Crystalline Materials Behavior Under Mechanic Forces

The crystalline structure of material presents high ordering, enabling its characterization by several techniques of crystallographic characterization. Although it is possible, a solid-state material may have its crystal structure altered as evidenced by uniform distortions resulting from mechanical forces or pressure. How a material responds to such perturbations is described by its elastic properties.

The external pressure exerted on the material is proportional to the force acting on a surface or area of the crystal structure; such effect is known as *Elastic Modulus* (Fig. 4). Thus, the degree of deformation presented by the structure is directly proportional to the magnitude of the pressure exerted and, in general, the elastic properties of a material depend on the type of bond between the constituent atoms, crystal structure, material composition, and the nature of the deformation about this.

The elastic properties of a solid are investigated according to the nature of the strain exerted on it. The first known type of deformation determines the resistance of a solid to linear pressures resulting in changes in material length; this type of deformation is called *Young Modulus*. Another type of deformation, called *Shear Modulus*, consists in applying parallel pressure to one of the surfaces of the crystal structure; while the opposite surface remains fixed and the planes are displaced in space by an angle Φ . Finally, the other type of deformation refers to the change in volume of the crystal structure by means of isostatic pressure (applied equally to all directions of the solid) and is called *bulk modulus*. In particular, the bulk modulus value may be positive or negative depending on the change in solid volume [7].

In this book chapter, the elastic properties of the investigated materials are determined from computational simulations based on the theory proposed by Birch-Murnaghan to investigate the *bulk modulus*. Through this approach, it is

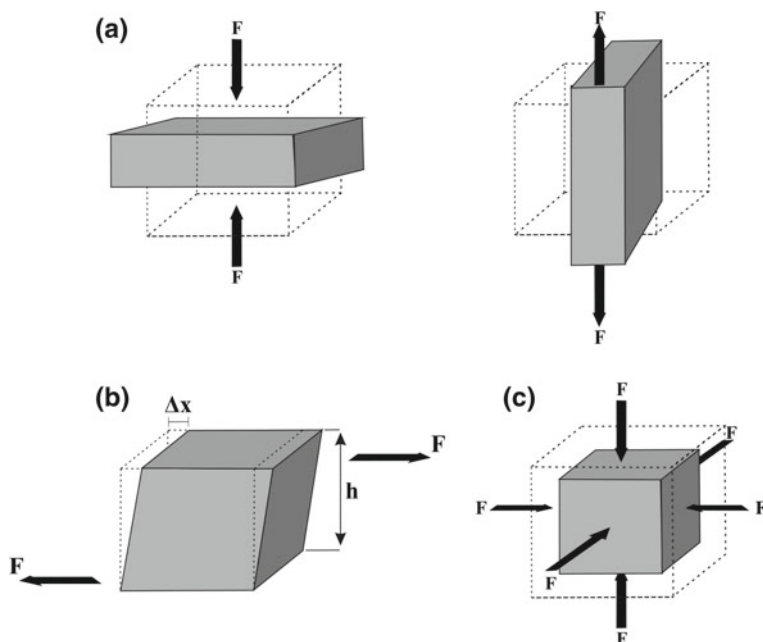


Fig. 4 Solid-state materials *Elastic Modulus* types: *Young Modulus* (a), *Shear Modulus* (b) and *Bulk Modulus* (c)

possible to determine the structural stability of the proposed systems mainly under high-pressure conditions [8–10]. Also, the values were also used to determine chemical-dependent role of exchange-correlation functionals.

4 Density Functional Theory: The Role of the Functional

One of more challenges for Computational Chemistry is a precise description for ionic, covalent and metallic chemical bonds. Such a description is complex because the electronic density distribution in each bond is very different. For example, ionic bonds have a high electronic density localization, while covalent bonds show an electronic density more homogeneous on atomic nucleus. The change in electronic density localization is controlled from electronegativity between atoms, i.e., a high difference between electro negativities is connected to ionic chemical bonds; whereas, the bond path between atoms with similar electronegativities is called covalent chemical bonds. However, quantum mechanics descriptions for sharing of the electronic density is subject of high-level research. The main factor of quantum chemistry regard to sharing of the electronic density is the exchange-correlation terms (E_{xc}), which are fundamentals because describe the electron-electron interactions in a volume around atomic nucleus.

In this aspect, theoretical-computational methods for chemical simulations have attracted much scientific interest to understand more accurately the E_{xc} effects. Nowadays, the Density Functional Theory (DFT) is a very well success tool to describe electron-electron interactions because, in its fundamental equations, the E_{xc} terms are precisely defined [11–13]. This theory was developed by Hohenberg and Kohn [14] using the electronic density (ρ) as fundamental property to describe electronic properties in molecular system. For a simple representation, DFT can be understood as a reformulation of quantum mechanics based on Schrodinger Equation because the wave function (ψ) was substituted by electronic density (ρ). More precisely, in DFT the E_{xc} terms can be represented from an exact functional of ρ . However, the mathematical formalism for such functions is still unacknowledged been needs several approximations to describe the functional and, consequently, chemical bonds. Then, the development of functionals to represent more precisely chemical and physical properties from chemical bonds is a fundamental subject of Computational Chemistry [15].

The most common functionals used to describe the electron interaction in solids are based on Generalized Gradient Approximation (GGA) and hybrid formalism that mix the GGA description with exact E_{xc} calculated from Hartree-Fock method. For GGA, the method developed by Perdew–Burke–Ernzerhof (PBE) can be understood as a continuous extrapolation of the exchange-correlation energy of the homogeneous electron gas [16].

$$E_{XC}^{PBE} = \int d^3r \rho(r) \epsilon_{XC}^{PBE}(r_S(r), s(r), \zeta(r)) \quad (1)$$

However, the PBE correlation energy does not vanish for a one-electron density, and the cancellation of the self-interaction requires a completely nonlocal functional as PBE0 and B3LYP. In this case, a technique became known as hybridization and gave rise to so-called Hybrids Functional [17, 18]. The existence of these functionalities is allowed by the adiabatic connection, a method that allows the connection of a system with non-interacting electrons to the system of N interacting electrons; then, that the electron density remains equal to the exact electronic density. The widely used B3LYP hybrid functional can be described as:

$$E_{XC}^{B3LYP}[\rho] = E_{XC}^{SVWN} + c_1 (E_X^{exata} - E_X^S) + c_2 \Delta E_X^{Becke} + c_3 \Delta E_c^{LYP} \quad (2)$$

In this equation, a , b and c represent semi-empirical coefficients that can be determined from a minimization relative to experimental data, ΔE_X^{Becke} the gradient correction for exchange energy proposed by Lee [19] and the gradient correction for the correlation energy developed by Lee et al. [19]. Since the LYP functional does not have an easily separable local component, the local functional for the correlation developed by Vosko, Wilk, and Nusair (SVWN) was used to provide different contributions of local and gradient-corrected terms. This functional was applied to different atoms and molecules of the Poples G1 database and from the minimization of E_{XC} in relation to atomization energies, proton and electron

affinities as well as ionization potentials the semi-empirical coefficients were determined as $a = 0.2$, $b = 0.72$ and $c = 0.81$, respectively.

In recent years, the B3LYP has become one of the most used functionals for the study of solid-state materials. The main constraint to this functional is in the representation of metals where the uniform electron gas boundary is not correctly reproduced. This error occurs because the local term for the correlation used in B3LYP superficially reproduces the slow decay of the electronic density at the boundary of the non-interacting system [20, 21].

These aspects were corrected by the PBE0 functional proposed by Perdew, Burke, and Ernzerhof (PBE) and developed by Adamo and Barone [22]. This functional is based on the increase of the percentage of the exact exchange term to 25% allied to the exchange term and PBE correlation. The final expression of this functional is represented in Eq. 3, where the absence of semi-empirical coefficients gives the free denomination of parameters for the functional PBE0.

$$E_{XC}^{PBE0} = E_{XC}^{PBE} + \frac{1}{4}(E_X^{HF} - E_X^{PBE}) \quad (3)$$

In order to complement the description of these functionalities, especially to describe long-distance or van der Waals interaction, the Grimme dispersion term (D) was developed, which helps the electronic description for low interaction energies and greater binding distances than those described by functional ones with or without parameters for the interaction region [23–25].

5 Crystalline Structures

In this study, a different class of solid-state materials was systematically investigated. In particular, we consider a fully ionic solid NaCl, a mixed ionic-covalent bond character for anatase and rutile phases of TiO₂, and the graphite (C_{graph}) as a fully covalent system, as depicted in Fig. 5.

The NaCl, is an ionic solid with a face-centered cubic structure (Fm-3m - 225) described by a lattice parameter of $a = b = c = 5.640$ Å. This material, has a bulk-modulus of 26.6 GPa, and behaves as insulating material with band-gap of 8.97 eV [26, 27].

Titanium dioxide, TiO₂, is a well-known solid-state material with several technological applications. This compound has different kinds of polymorphs, being the rutile and anatase phases the most common in nature, whereas other phases can be synthetically obtained under pressure[28, 29]. The fundamental properties of these polymorphs enable their use in the development of solar cells, photodegradation of water in H₂ and O₂, degradation of environmentally hazardous molecules and reduction of CO₂ in the burning of hydrocarbons. The difference between the valence and the conduction band determines the optical absorption property being essential for all these applications. The rutile phase is a semiconductor and its

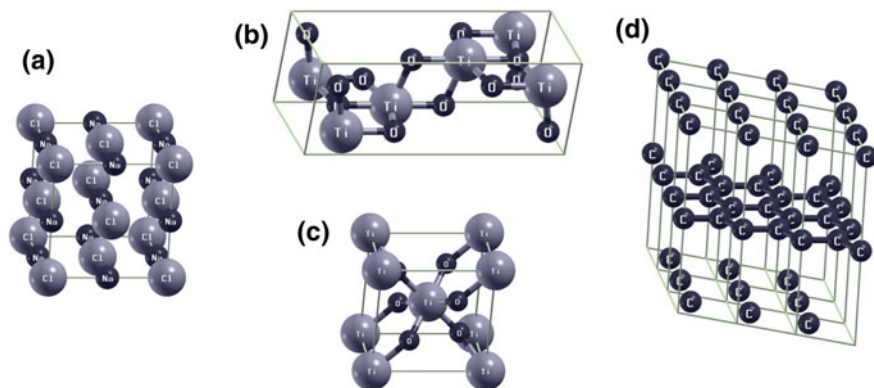


Fig. 5 Conventional unit cell for NaCl (a), TiO₂ rutile (b), TiO₂ anatase (c), and C_{graphite} (d)

crystal structure has a tetragonal space group ($P4_2/mnm-136$) with lattice parameters equal to $a = b = 4.594 \text{ \AA}$ and $c = 2.959 \text{ \AA}$. This material has a bulk modulus around 211 GPa and behaves as a semiconductor with band-gap of 3.0 eV. On the other hand, the Anatase phase has a tetragonal symmetry ($I4_1/amd-141$) and lattice parameters of $a = b = 3.785 \text{ \AA}$ and $c = 9.512 \text{ \AA}$. In addition, its bulk modulus is around 179 GPa, while the electronic structure has a band gap of 3.2 eV [30–32].

Graphite (C_{graph}) can be observed in the hexagonal and rhombohedral crystalline phases, being the hexagonal polymorph the most abundant in nature. The constituent carbon atoms have hybridization of the sp^2 type, in which each carbon atom forms three covalent bonds σ and a weak π bond. The structure can be described by the stacking of planes of carbon atoms, known as graphene, which are formed by carbon hexagons. Graphite is an anisotropic material, i.e. the band gap depends on the direction in which the current is applied. Indeed, the out-of-plane band gap is around 1.0 eV, whereas the in-plane is very small, giving a characteristic of conductive material [33–35].

In this study, a systematic theoretical investigation about the effect of Exchange-correlation functional (PBE, PBE0, B3LYP, PBE + D, PBE0 + D e B3LYP + D) on the reproduction of structural, mechanical and electronic properties of NaCl, rutile and anatase TiO₂, and C_{graph}.

6 Computational Method

In this study ab initio simulations based on Density Functional Theory (DFT) were carried out considering PBE, PBE0 and B3LYP functionals with and without Grimme dispersion correction (D). The CRYSTAL09 software in Linux operating system was used [36, 37].

NaCl crystalline structure was described from Fm-3m (225) group with $a = 5.64 \text{ \AA}$; while, TiO_2 in Rutile phase was represented from $\text{P4}_2/\text{mmn}$ (136) and $a = b = 4.59 \text{ \AA}$ and $c = 2.96 \text{ \AA}$, for Anatase phase the symmetry was $\text{I4}_1/\text{amd}$ (141) with $a = b = 3.77 \text{ \AA}$ and $c = 9.64 \text{ \AA}$. Graphite structure was simulated in $\text{P6}_3/\text{mmc}$ (194) symmetry and $a = b = 2.47 \text{ \AA}$ and $c = 6.79 \text{ \AA}$. All simulations were optimized regarding to total energy, the Coulomb integrals were truncated in 10^{-8} 10^{-8} 10^{-8} 10^{-16} convergence criteria; Monkhost-Pack mesh was defined as $10 \times 10 (4 \times 4)$ for Graphite (NaCl and TiO_2).

We have performed a systematic investigation considering a different kind of combinations between basis set and functionals to show how the nature of functional can influence different properties of materials mainly regarding chemical bonds. In Tables 1, 2 and 3 are organized all models from basis set and functionals previously selected.

Table 1 Combinations between basis set for each PBE, PBE0, B3LYP, PBE + D, PBE0 + D and B3LYP + D functionals for highly ionic NaCl material

Basis set combination		Cl		
		TZVP	86-311G	HAYWLC-31G
Na	TZVP	1	2	3
	8-511(1d)G	4	5	6

Table 2 Combinations between basis set for each PBE, PBE0, B3LYP, PBE + D, PBE0 + D and B3LYP + D functionals for ionic-covalent TiO_2 material in Rutile and Anatase structures

Basis set combination		O		
		8-411	TZVP	6-31d1
Ti	86-411(d31)G	1	2	3
	TZVP	4	5	6

Table 3 Combinations between basis set for each PBE, PBE0, B3LYP, PBE + D, PBE0 + D and B3LYP + D functionals for covalent Graphite material

Basis set	DURAND-21G*	6-21G*	TZVP
C	1	2	3

* is the representation for d orbitals from polarization gaussian functions

7 Results and Discussion

The main aim of our theoretical study was to evaluate structural, mechanical and electronic properties for NaCl, TiO₂ in Rutile and Anatase phases and Graphite materials regarding basis sets and different E_{xc} functionals. Such functionals were chosen because of high application in many material simulations and its performance to describe electronic and structural effects from different chemical bonds.

It is well-known the dependence of ab initio calculations with respect to basis sets choice for any molecular or solid systems. Table 4 presents the better basis sets combinations for each material taking account the different functionals. For highly ionic NaCl material, the better combinations were 1, 3 and 6 (Table 1); which are described by contracted pseudopotential basis sets, very adapted for electrons highly localized as ionic solids. Regarding TiO₂ material we found a deviation between Rutile and Anatase phases, which was not an expected result due to the same chemical bond nature that suggests in theory more proximity between the simulations. However, we noted that for Rutile phase, only basis sets combination 5 (Table 2) showed better result; this combination is formed by TZVP basis sets for both Ti and O atoms independently of functional description. In theoretical results for Anatase phase were evidenced 3 and 6 basis sets combinations, which present a strong influence of polarization functions in the atomic descriptions. At last for Graphite material, the better results were for 3 basis set and one for 2 basis set (Table 3) showing that polarization functions are important for hybridization effect.

Figure 6 shows the relative error for NaCl material with respect to each functional. Because of high difference in electronegativity, the electronic localization effect is very pronounced; then, the most expected tendency is that electronic exchange effect is more effective than electronic correlation effect. The lattice parameters showed good agreement for all functionals and the relative error had a low deviation. Band-Gap results were interesting because only PBE and PBE + D functionals overestimated this property; while other functionals underestimated this value. Such effect is linked to the nature of ionic bond in NaCl, where the correlation effect is low and PBE and PBE + D functionals have not correlation term include. The greatest relative errors were calculated for all functionals with Grimme dispersion, while functionals without this correction have minor relative errors. We commented that bulk modulus calculated were based on isostatic pressure; thus, the dispersion correction has a negative influence on such property in NaCl because in highly ionic solids the long-range effects are less pronounced.

Table 4 Selected basis set combinations for the different E_{xc} functionals for NaCl, TiO₂ Rutile and Anatase, and Graphite materials

	B3LYP	PBE	PBE0	B3LYP + D	PBE + D	PBE0 + D
NaCl	1	6	3	3	6	3
Rutile	5	5	5	5	5	5
Anatase	6	3	3	6	3	3
Graphite	3	3	2	3	3	3

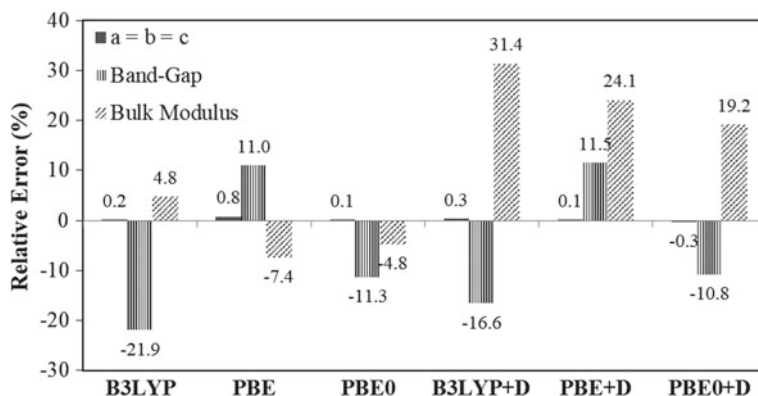


Fig. 6 Theoretical results for the relative error of structural, mechanical and electronic results as function of the different E_{xc} for NaCl

In general, the great charge separation caused by high electronegativity difference shows that functionals with correlation terms describe better a large set of properties. Therefore, B3LYP, B3LYP + D, PBE0 and PBE0 + D functionals represented with good agreement lattice parameters, underestimated the Band-Gap and showed minor relative error for bulk modulus. However, the PBE0 functional was the best functional for NaCl.

Figure 7 shows the obtained results for better basis sets combinations and functionals for TiO_2 in the Anatase structure. For structural properties, $a = b$ lattice parameters presented good agreement at 1% in relative error. In particular, PBE0 functional did not show relative error. Regarding c lattice parameter the relative errors were increased and all functionals overestimated its value. In this case, it was noted that B3LYP is the best functional with relative error of 1.5%. This result was

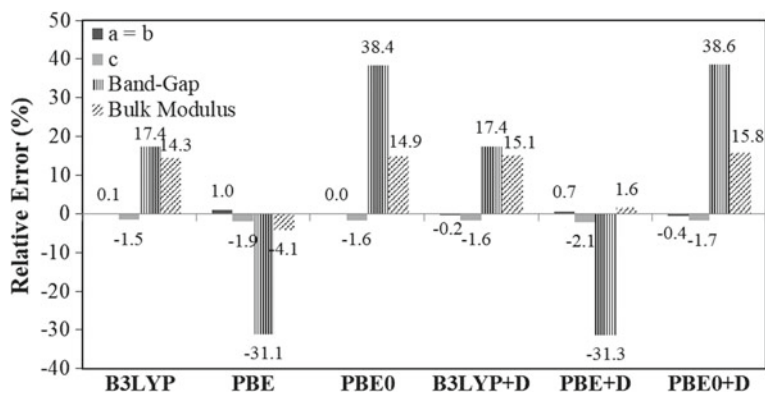


Fig. 7 Theoretical results for the relative error of structural, mechanical and electronic results as function of the different E_{xc} for TiO_2 anatase

expected because in *c* lattice parameter is localized an anisotropic electronic distribution, i.e., a region of mix between ionic and covalent bonds. For Band-Gap, PBE and PBE + D functionals underestimated this parameter, while B3LYP and B3LYP + D functionals showed the lower relative errors with 17.4%. With exception of PBE functional, all other functionals had a tendency to overestimate this property. However, PBE and PBE + D have the minor relatives errors in inverse directions, such results show a good representation from PBE functional, while the dispersion correction (PBE + D) was important to increase the precision in describing this property.

TiO₂ Rutile phase was simulated because of its similarity in composition with Anatase phase, however, the crystalline structure is different, being a good example for same Ti-O covalent bond in another molecular geometry. Figure 8 shows that the lattice parameters were well simulated from all functionals, being the bigger relative error found was -1.1% showing that basis set was very representative with respect to the different functionals. The lower band-gap values were calculated with B3LYP and B3LYP + D functionals, this result was expected because is well-know that hybrid and parameterized functionals describe with more efficiency the ionic-covalent bond in solids as TiO₂. In case of PBE and PBE + D descriptions was proved that bulk modulus has low agreement because of high relative errors, the high absence of a good description for correlation term. However, the inclusion of Grimme dispersion was superficial to improve all functional results.

Figure 9 shows relative error values for Graphite structure considering the better combination between basis sets. All functionals overestimated the values for *a* = *b* lattice parameters showing that results are independent of nature of these functionals. However, for *c* lattice parameter the PBE0 functional has the lower relative error and all other functionals underestimated such parameter. In general, the lattice

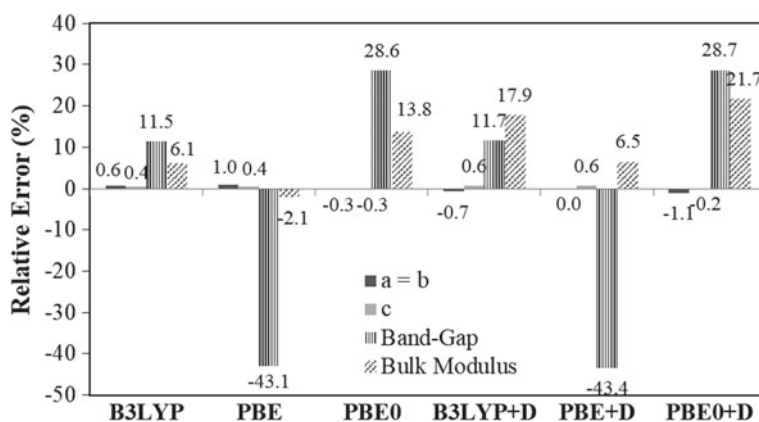


Fig. 8 Theoretical results for relative errors of structural, mechanical and electronic results as a function of the different E_{xc} for TiO₂ Rutile

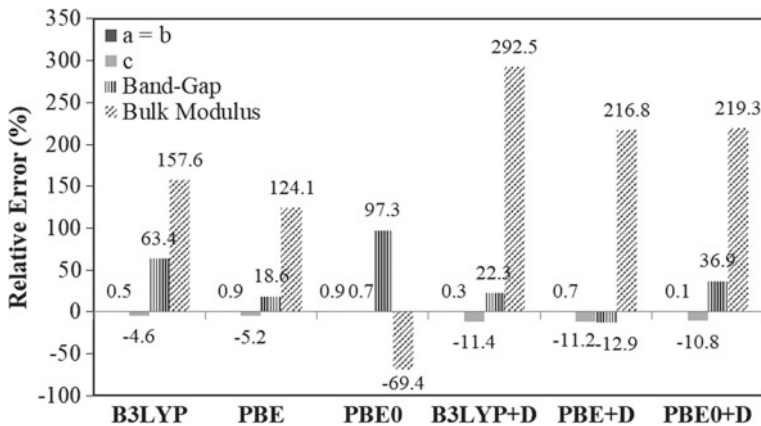


Fig. 9 Theoretical results for the relative error of structural, mechanical and electronic results as function of the different E_{xc} for Graphite

parameters were the values with lower relative error associated. Regarding Band-Gap results, the PBE + D approach obtained an underestimated result but more approximated to experimental results while the other functionals overestimated the Band-Gap. In particular, the better functionals for Graphite were PBE and PBE + D indicating that for this material the error can be associated with E_{xc} term and long-range electronic density description, such as van der Waals effect. For bulk modulus, all functional descriptions were poor to simulate this property. However, for PBE0 functional the relative error was underestimated and lower. Such result is expected because the Graphite structure is layered and bulk modulus applied was isotropic pressure, i.e., it was applied the same pressure in all directions simultaneously. Then, the response from Graphite structure is unusual and the relative error from simulation has tendency to increase.

In this section, our purpose was discuss briefly very specific charge distribution maps to present as kind of chemical bond can be associated with such analysis. Figure 10 shows the charge maps obtained from the best functionals for the investigated materials. In general, circular or centered charge densities on atomic nucleus are denominated as ionic bond (Fig. 10a), the charge density does not show entanglement between atoms; whereas, for Graphite structure in AA stacking (Fig. 10b), the charge map shows covalent bonds between carbon atoms representing sp^2 hybridization. TiO_2 material in both rutile (Fig. 10c) and anatase structure (Fig. 10d) has chemical bond with intermediary characteristics between ionic and covalent features. The ionic bond is more visualized among TiO_2 clusters, while covalent bond is very pronounced between Ti and O atoms inside of TiO_2 cluster, showing charge paths directed from covalent bonds due to the intrinsic nature of TiO_2 .

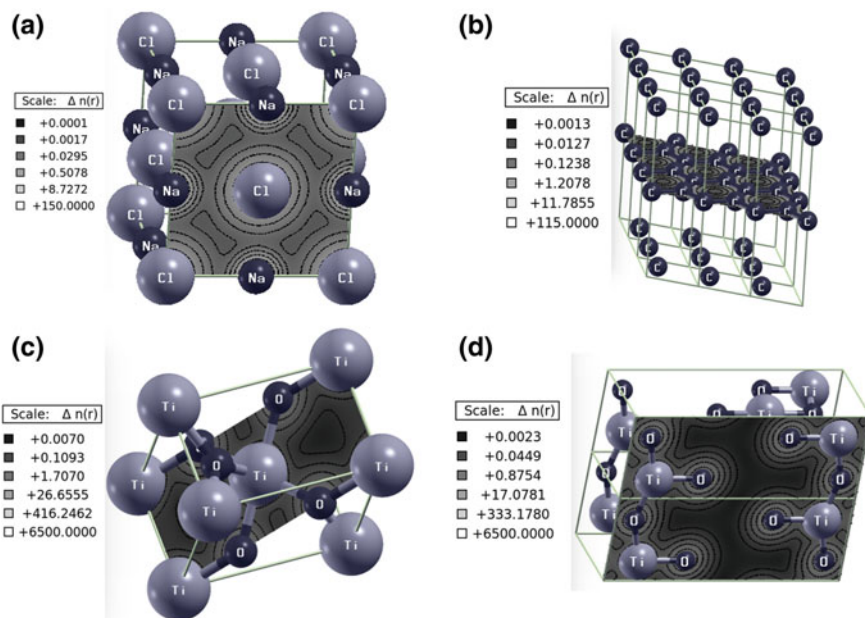


Fig. 10 Charge density maps for NaCl (a), Graphite (b) and TiO₂ in Rutile (c) and Anatase (d) phases

8 Conclusion

In this study, the role of chemical bond in the precision of different exchange-correlation functionals was revised for NaCl, TiO₂ Anatase and Rutile and Graphite. Theoretical results indicate that highly ionic, intermediary and highly covalent bonds show different relations with E_{xc} formalism depending on the description of exchange and correlation terms. Indeed, the obtained results indicate singular descriptions for PBE, PBE0 and B3LYP functionals with and without dispersion energy term; in general, the modification in chemical bond promotes changes in the electronic density extremely connected to exchange-correlation energy. In particular, our investigation has shown that functional based on hybrid formalism presented a performance more adapted for such chemical bonds proposed. Therefore, to find a functional that represents such changes in chemical bonds is a challenge of our time. Nowadays, there is hard work to describe the exchange-correlation energy and know-how such chemical property can be modeled from a single functional.

Acknowledgements The authors acknowledge the UEPG, CAPES, CNPq and Fundação Araucária (project 009/2017) for financial support.

References

1. Rössler, U.: *Solid State Theory: An Introduction*, 2nd edn. Physica—Verlag, Nova York (2009)
2. Kwok, H.L.: *Electronic Materials*. PWS Publishing Company, Boston (1997)
3. West, A.R.: *Basic Solid State Chemistry*, 2nd edn. Wiley, Chichester (2006)
4. Smart, L.E.: *Solid State Chemistry: An Introduction*, 3rd edn. Taylor & Francis, Boca Raton (2005)
5. Ropp, R.C.: *Solid State Chemistry*. Elsevier, Amsteram (2003)
6. Andrés, J., Beltran, J.: *Química teórica y Computacional*, 1st edn. Universidade Jaume I, Castello de La Plana (2000)
7. Harrison, W.A.: *Elementary Electronic Structure*. World Scientific Publishing, Danvers (2004)
8. Serway, R.A., Jewett, J.W.: *Physics for Scientists and Engineers*. Cengage Learning (2012) (Chapters 1–39)
9. Birch, F.: Finite Elastic Strain of Cubic Crystals. *Phys. Rev.* **71**, 809–824 (1947)
10. Murnaghan, F.D.: The compressibility of media under extreme pressures. *Proc. Natl. Acad. Sci.* **30**, 244–247 (1944)
11. Becke, A.D.: Perspective: fifty years of density-functional theory in chemical physics. *J. Chem. Phys.* **140**(18), 18A301 (2014)
12. Mardirossian, N., Head-Gordon, M.: Thirty years of density functional theory in computational chemistry: an overview and extensive assessment of 200 density functionals. *Mol. Phys.* **115**(19), 2315–2372 (2017)
13. Hautier, G., Jain, A., Ong, S.P.: From the computer to the laboratory: materials discovery and design using first-principles calculations. *J. Mater. Sci.* **47**(21), 7317–7340 (2012)
14. Hohenberg, P., Kohn, W.: Inhomogeneous electron gas. *Phys. Rev.* **136**(3B), B864–B871 (1964)
15. Jones, R.O.: Density functional theory: its origins, rise to prominence, and future. *Rev. Mod. Phys.* **87**(3), 897–923 (2015)
16. Perdew, J.P., Burke, K., Ernzerhof, M.: Generalized gradient approximation made simple. *Phys. Rev. Lett.* **77**(18), 3865–3868 (1996)
17. Cesare, F.: Hybrid functionals applied to perovskites. *J. Phys.: Condens. Matter* **26**(25), 253202 (2014)
18. Becke, A.D.: Density functional thermochemistry. III. The role of exact exchange. *J. Chem. Phys.* **98**(7), 5648–5652 (1993)
19. Lee, C., Yang, W., Parr, R.G.: Development of the Colle-Salvetti correlation-energy formula into a functional of the electron density. *Phys. Rev. B* **37**(2), 785–789 (1988)
20. Paier, J., Marsman, M., Kresse, G.: Why does the B3LYP hybrid functional fail for metals? *J. Chem. Phys.* **127**(2), 024103 (2007)
21. Perdew, J.P., et al.: Understanding band gaps of solids in generalized Kohn-Sham theory. *Proc. Natl. Acad. Sci.* **114**(11), 2801 (2017)
22. Adamo, C., Barone, V.: Toward reliable density functional methods without adjustable parameters: The PBE0 model. *J. Chem. Phys.* **110**(13), 6158–6170 (1999)
23. Grimme, S., et al.: A consistent and accurate ab initio parametrization of density functional dispersion correction (DFT-D) for the 94 elements H–Pu. *J. Chem. Phys.* **132**(15), 154104 (2010)
24. Grimme, S.: Semiempirical GGA-type density functional constructed with a long-range dispersion correction. *J. Comput. Chem.* **27**(15), 1787–1799 (2006)
25. Grimme, S.: Accurate description of van der Waals complexes by density functional theory including empirical corrections. *J. Comput. Chem.* **25**(12), 1463–1473 (2004)
26. Brown, F.C., et al.: Extreme-ultraviolet spectra of ionic crystals. *Phys. Rev. B* **2**(6), 2126–2138 (1970)

27. Lewis, J.T., Lehoczky, A., Briscoe, C.V.: Elastic constants of the Alkali Halides at 4.2 °K. *Phys. Rev.* **161**(3), 877–887 (1967)
28. Zhu, T., Gao, S.P.: The stability, electronic structure, and optical property of TiO₂ polymorphs. *J. Phys. Chem. C* **118**(21), 11385–11396 (2014)
29. Baur, W.H.: Über die Verfeinerung der Kristallstrukturbestimmung einiger Vertreter des Rutiltyps. III. Zur Gittertheories des Rutiltyps. *Acta Crystallogr. A* **14**(3), 209–213 (1961)
30. Isaak, D.G., et al.: Elasticity of TiO₂ rutile to 1800 K. *Phys. Chem. Miner.* **26**(1), 31–43 (1998)
31. Odling, G., Robertson, N.: Why is anatase a better photocatalyst than Rutile? The importance of free hydroxyl radicals. *ChemSusChem* **8**(11), 1838–1840 (2015)
32. Arlt, T., et al.: High-pressure polymorphs of anatase TiO₂. *Phys. Rev. B* **61**(21), 14414–14419 (2000)
33. Ooi, N., Rairkar, A., Adams, J.B.: Density functional study of graphite bulk and surface properties. *Carbon* **44**(2), 231–242 (2006)
34. González, J., Guinea, F., Vozmediano, M.A.H.: Unconventional quasiparticle lifetime in graphite. *Phys. Rev. Lett.* **77**(17), 3589–3592 (1996)
35. Kurakevych, O.O., Solozhenko, E.G., Solozhenko, V.L.: High-pressure study of graphite-like B-C phases. *High Press. Res.* **29**(4), 605–611 (2009)
36. Dovesi, R., et al.: CRYSTAL09 user's manual. CRYSTAL09. University of Torino, Torino (2009)
37. Dovesi, R., et al.: CRYSTAL: a computational tool for the ab initio study of the electronic properties of crystals. *Z. Kristallogr. Crystall. Mater.*, 571 (2005)

Design and Applications in Catalytic Processes of Zeolites Synthesized by the Hydrothermal Method



Patricia H. Y. Cordeiro, Heveline Enzweiler, Luiz Jardel Visioli,
Cássio Henrique Zandonai,
João Lourenço Castagnari Willimann Pimenta
and Gimerson Weigert Subtil

Abstract The zeolites are aluminosilicates with perfectly crystalline structure based on tetrahedral arrangements of silicon and aluminum. These materials present great potential for application in catalytic, adsorption and ion exchange processes. In addition, the zeolite crystallinity results in a highly stable material, with very organized micropores and network of channels. Zeolites have been widely used in chemical processes as heterogeneous catalysts, both in the research and development stage of technology and in applications already established in industry, such as the catalytic cracking of petroleum. The synthesis of this material occurs through the hydrothermal method, which consists on the steps of gel synthesis, crystallization at autogenous pressure, separation of the precipitated material and subsequent heat treatment to remove the structure directing agents. During preparation of

P. H. Y. Cordeiro (✉)

Laboratório de Engenharia, Colegiado de Engenharia Química, Universidade Tecnológica Federal do Paraná, PR Estr. dos Pioneiros 3131, Jardim Morumbi, Londrina, PR 86036-370, Brazil

e-mail: pcordeiro@utfpr.edu.br

H. Enzweiler · L. J. Visioli

Departamento de Engenharia de Alimentos e Engenharia Química, Universidade do Estado de Santa Catarina, Rodovia BR 282, km 573, Pinhalzinho- Santa Catarina, RS 89870-000, Brazil

e-mail: heveline.enzw@gmail.com

L. J. Visioli

e-mail: luizjvisioli@gmail.com

C. H. Zandonai · J. L. C. W. Pimenta · G. W. Subtil

Laboratório de Catálise, Departamento de Engenharia Química, Universidade Estadual de Maringá, Av. Colombo 5790, Zona 7, Maringá, PR 87020-900, Brazil

e-mail: chzandonai@gmail.com

J. L. C. W. Pimenta

e-mail: joaocwpimenta@gmail.com

G. W. Subtil

e-mail: weigert_subtil@hotmail.com

© Springer Nature Switzerland AG 2020

F. A. La Porta and C. A. Taft (eds.), *Emerging Research in Science and Engineering Based on Advanced Experimental and Computational Strategies*, Engineering Materials, https://doi.org/10.1007/978-3-030-31403-3_14

the synthesis gel, the composition of the material to be generated can be changed, by varying the Si/Al ratio (important parameter for zeolites) or by incorporating other metals into the crystalline structure, for example. It is also possible to vary the amount of synthesis water, which changes the solubility of the medium and also the autogenous pressure in the subsequent phase. In the crystallization step, the time and temperature in which nucleation and crystal growth occurs can be manipulated, altering the size of the crystallites formed. Finally, in the heat treatment step, the textural properties and the crystallinity can be altered by modifying the temperature, heating rate and calcination time. The possibility of altering the physical-chemical properties of the zeolites makes them very versatile materials for application in catalysis, making it possible to obtain materials with characteristics close to the ideal for specific processes. In this sense, zeolitic materials have been used as catalysts with acidic activity (property generated in the material structure itself), as supports for certain active phases in chemical reactions and even as active supports in photochemical reactions. Therefore, the aim of this chapter is to discuss the synthesis of zeolites through the hydrothermal method, with a focus on the manipulation of the synthesis conditions and their consequences on the physico-chemical properties and the implications for the applications in different catalytic processes.

Keywords Zeolites · Hydrothermal method · Applications

1 Introduction

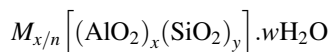
From the discovery of stilbite by Swedish Cronsted in 1746, a new class of mineral materials called “zeolites” has been recognized. At the time, this term was used only to denote a family of natural minerals that had ion exchange properties. The reversible desorption of water, property presented by all these materials, gave rise to the generic name of zeolites, which derived from the Greek words: *zeo* = “boiling” and *lithos* = “stone” [33].

Structurally, zeolites are crystalline polymers based on a three-dimensional arrangement of tetrahedral TO_4 (SiO_4 or AlO_4^-) bound by oxygen atoms to form subunits and huge networks of identical blocks. These tetrahedra are arranged in rings, which are combined to form regular and uniform channels and cavities, with dimensions in the order of angstroms. The channels and cavities allow the selective passage of certain molecules into their interior, depending on their size and shape [10, 33]. This property gave the zeolites the name of “Molecular Sieves”, and is one of the main characteristics that make this material widely used in industrial applications, such as catalysis and adsorption.

In the structural arrangement of a zeolite, tetrahedral $(\text{AlO}_4)^-$ induces the formation of negative charges by having oxidation number +3 and being coordinated by 4 oxygen atoms. This negative charge must be counterbalanced by a compensation cation that does not belong to the crystalline structure and is located within

the channels and cavities. This compensating cation, formed mainly by alkaline and alkaline earth metals, can easily be exchanged by an external cation (liquid or gaseous medium), giving this material an excellent ion exchange property.

The structural formula of zeolite can be written as [10]:



where M is the compensation cation with valence n , w is the number of water molecules and the ratio y/x usually varies from 1 to 5 depending on the structure. The sum $(x + y)$ is the total number of tetrahedra per unit cell.

Natural zeolites are formed through slow hydrothermal reactions when rock cavities of a basic nature (specifically aluminosilicates), whether metamorphic or volcanic, contain mineralizing solutions (high pH), are subjected to high temperatures. Over vast periods of time, in the order of thousands of years, the mineralization and recrystallization of aluminosilicates within such rocks gave rise to natural zeolites [91, 92]. As industrial applications require high purity and well-defined chemical composition, many studies have been performed to obtain synthetic zeolites.

Synthetic zeolites, although of higher purity compared to natural zeolites, the synthesis methods can produce a wide range of zeolites, many of which are not found in nature, containing Si/Al specific ratios, as well as with the addition of new elements to the zeolites structures.

This control over the characteristics of the synthesized materials brings great interest in the development and production of zeolites for heterogeneous catalysis, either in the form of supports or mass catalysts, since zeolites have very interesting characteristics, such as high specific areas, high porosity, extremely uniform pore sizes and the possibility of being produced both in neutral form, usually with a high Si/Al ratio, and in order to contain large amounts of acidic sites. The petrochemical industry, for example, makes extensive use of zeolites as heterogeneous catalysts, since much of today's gasoline is produced by cracking heavy hydrocarbons in a fluidized bed of zeolites [20].

Due to the great utility and interest attributed to these materials, as early as the 1940s and 1950s, researchers tried to find methods for synthesizing zeolites so they did not need to rely on natural deposits.

According to the literature [20, 46], the modern synthesis method is the result of the work of Richard Barrer and Robert Milton, who, initially guided by the natural process, synthesized zeolites by treating mineral phases with high pH solutions and under high temperatures (up to 270 °C), maintaining these conditions for hours or even days. This process then gave rise to the Hydrothermal Method for the synthesis of various types of zeolites. Using this method, Barrer and coworkers (Union Carbide Group Co.) synthesized the main commercial synthetic zeolites, which are still used in industry today: LTA (Linde Type A, relative to Linde Division from Union Carbide Organization), FAU (Linde Type X and Y) and a ZSM-5 zeolite.

After the discovery of the hydrothermal method, many types of zeolites were synthesized in laboratory using only inorganic reagents [20]. Two of the main types

of zeolites, widely used today and synthesized by the hydrothermal method, are described below: Zeolite Y and ZSM-5.

Zeolite Y has a faujasite type crystalline structure (FAU), with a Si/Al ratio varying from 1.5 to 3, and has large cubic cell units of approximately 25 Å and 192 tetrahedrons (Si, Al)O₄ [33]. It features six 6-6 tetrahedrons double rings (DR6) as secondary construction units used to join the sodalite enclosures. The union of these 6-6 rings with four hexagonal faces of the sodalite cavities (or beta cavities) forms a polyhedron, which englobes a large cavity (cavity α), with an internal diameter of 12.4 Å and pore openings delimited by rings of 12 oxygen atoms, with a free opening of 8 Å [33]. The combination of the α -supercavities with each other and with the sodalite cavities gives the final zeolite structure (Fig. 1a). The pore system of the faujasite three-dimensional crystal structure has openings of 7.8 and 2.2 Å (Fig. 1b) [33].

With an MFI type crystalline structure, zeolite ZSM-5 belongs to the pentasil family and has a high percentage of silicon (Si/Al > 15) (Fig. 2a). Its structure is formed by five rings that form columns and are connected to each other, as can be seen in Fig. 2b, which shows the porous structure of the ZSM-5, with its straight channels and their intersections. The opening of the straight channels varies from 5.3 to 5.6 Å, and the sinusoidal channels have openings of 5.1–5.5 Å, with an almost circular form [5].

To the present day, 231 structures have been approved by IZA-SC [6] and the main structural information of each zeolite, both natural and synthetic, can be viewed in the IZA-SC database (<http://www.iza-structure.org/databases/>).

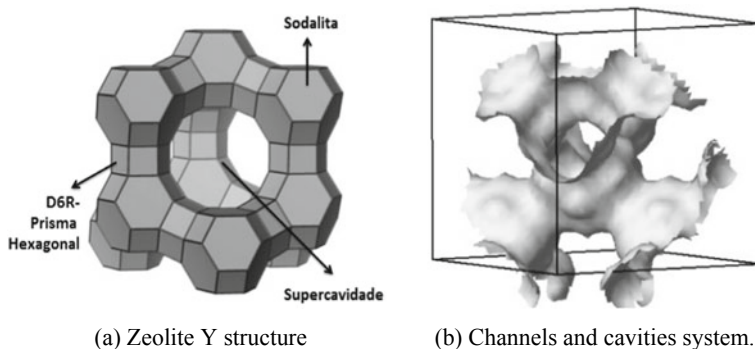


Fig. 1 Schematic representation of Zeolite Y. *Source* Adapted from Kulprathipanja [48]. Reproduced with permission from John Wiley and sons

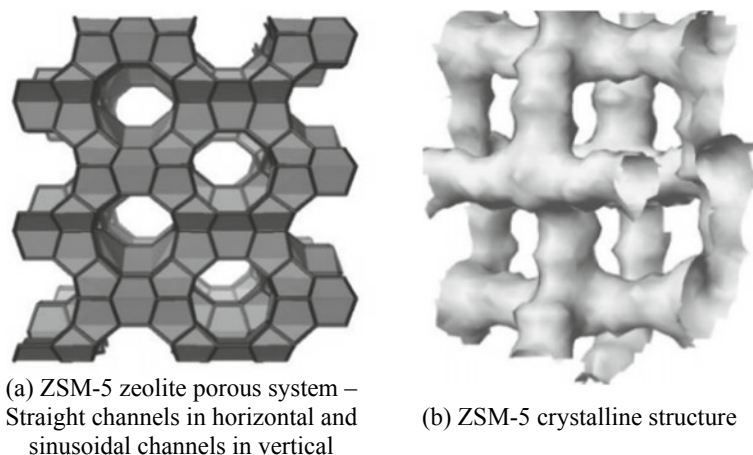


Fig. 2 Schematic representation of zeolite ZSM-5. *Source* Kulprathipanja [48]. Reproduced with permission from John Wiley and sons

2 The Hydrothermal Method for Zeolite Synthesis

During the synthesis of zeolites by the hydrothermal process, an aqueous mixture containing silicon sources (alkoxides, colloidal silica, silicates and others), aluminum sources (salts, boehmite, aluminates or even metal dust), structural directives (organic molecules) and metal cations (which later became compensating ions) gives rise to a supersaturated aluminosilicate solution. By the addition of seed crystals or spontaneous nucleation, crystal growth or gel formation occur. The complex mechanism behind these steps can be called zeolitization [27, 46].

The first step of zeolitization is the dissolution of amorphous solids (silicon or aluminum sources in the form of gels such as aerosil and boehmite silica), usually in a solution with high concentration of hydroxyls and therefore very alkaline. However, the fluoride ion, F^- , can also play the role of mineralizing agent, allowing the process to be conducted at a lower pH level [46, 91, 92].

The major advantage of using fluoride ions as mineralizers comes from the fact that complexing effects and lower pH allow a higher concentration of ions such as Fe^{3+} , Ti^{4+} and Ge^{4+} to be added to the solution, making it possible to produce zeolites with various metal ions in its structure. However, high fluoride concentrations may inhibit the polymeric condensation mechanism involved in the integration of monomers into the zeolite crystals, thus preventing the growth of zeolite crystals [91, 92]. Great interest also arises with the possibility of using the F^- ion for the preparation of grid crystals and differentiated structures [20].

After the initial combination of the precursors, the formed mixture may undergo an aging process. During this step, silica dissolution continues to occur, producing silicate ions in solution. Prolonged aging (hours or days) leads to the formation of

oligomeric species from silicate ion condensations [7]. The formation of these species is extremely important, since aluminum, present in the form of $\text{Al}(\text{OH})_4^-$, reacts preferentially with larger silicate ions, possibly due to the greater capacity of charge distribution, and from this interaction the oligomeric aluminosilicate species are formed [27].

With the constant dissolution of the silicon source and formation of ions in solution, this becomes supersaturated. Crystallization can then be initiated by two routes: seed addition or spontaneous nucleation [20, 27], the latter being greatly affected by the pH of the solution. According to Barrer [7], such effect can be explained by the faster dissolution of the silicon source gel and higher silicate concentrations at high pH, which would lead to faster core growth.

Precursor crystallization and dissolution occur in parallel, generally seen as amorphous gel depolymerization and crystalline lattice polymerization, so that the concentration of ions in solution can remain constant during crystallization, decreasing only after total dissolution of the amorphous phase (SiO_2 and Al sources), characterizing the final stages of zeolite synthesis.

Crystal growth, in most cases, occurs at the interface between crystal and mother liquor and not in a direct amorphous solid—crystalline solid transformation [27, 44].

The zeolitic crystallization process contrasts with crystallizations of common ionic compounds that occur when mother liquor ions move to the crystal surface, then undergo a desolvation process and reorganize into the crystal surface.

According to [20], aluminosilicate anions are rearranged in the presence of cations such as sodium or potassium, forming polyhedral units. The integration of these oligomers on the crystal surface occurs as a polymerization by covalent bonding of the species (monomers in solution) to the inorganic crystal lattice. This complex mechanism, then, is one of the rate limiting steps in the production of zeolites by the hydrothermal process.

The solution reorganization and integration of oligomeric species to the crystal surface occurs in parallel with the dissolution of the precursors (usually in the form of gels). Thus, the use of autoclave reactors for batch production of zeolites is very common.

Due to the nature of the solution, if the crystals are left in contact with the mother liquor for extended periods, they may continue to undergo depolymerization and repolymerization, leading to other unwanted phases. Therefore, it is interesting that the contact time between crystal and mother liquor is minimized after the production of the desired crystalline phase [27]. Simple filtration separation followed by washing and drying of the crystals is sufficient to prevent subsequent changes in the crystalline structure.

3 Influence of Synthesis Conditions on Zeolite Properties

3.1 Aluminum and Silicon Sources

The process of hydrothermal synthesis of zeolites involves sources of silica and alumina, reacting by means of a mineralizing agent such as hydroxide or fluoride, and may also use structure templates. The interaction between the mineralizing agents and the minerals used plays an important role in the process of the zeolite crystal formation. Thus, both the aluminum and silicon sources can influence the physical and chemical properties of the zeolite.

3.1.1 Silicon Sources

The most commonly used sources of silicon are sodium silicate, colloidal silica solution, fumed silicon dioxide (fumed silica), tetramethylorthosilicate (TMOS) and tetraethylorthosilicate (TEOS). They may differ mainly in their solubility and reactivity.

The zeolite ZSM-5 was synthesized using four different sources of silicon: tetraethylorthosilicate (TEOS), colloidal silica, sodium metasilicate and fumed silica [65]. ZSM-5 synthesis was possible for all reagents except sodium metasilicate, which resulted in quartz formation. The ZSM-5 zeolites presented different crystallinities; the highest was found for the one synthesized with fumed silica, followed by TEOS and finally colloidal silica, which presented the lowest crystallinity. The crystal shape was also different: in the synthesis with TEOS and colloidal silica twisted crystals were formed, while the synthesis with pyrogenic silica formed cubic crystals.

Comparing the crystal growth rate with hydrophobic fumed silica [96], it was observed that the behavior was similar for the synthesis with silicon dioxide and with sodium silicate nonahydrate and pentahydrate, indicating the same driving force behind this phenomenon. Regarding crystal yield, there was a big difference for longer crystallization times: the material synthesized with sodium silicate nonahydrate showed the highest yield, followed by both sodium silicate pentahydrate and hydrophobic fumed silica, and the lowest yield occurred in the synthesis with silicon dioxide. Thus, although the growth rate was similar, the yield was quite different for each species, indicating that for the sources tested in the same reaction medium, the yield was affected, but not the nucleation rate. In addition, the synthesis using silica hydrolyzed silicate (TEOS), producing ethanol as a byproduct, led to a decrease in linear crystal growth rates, while the nucleation rates were higher. With a higher number of nucleation centers, a narrow range of size distribution was also observed, since the crystals nucleated very early.

When comparing fumed silica (Carb-o-Sil) with anhydrous sodium metasilicate and pentahydrate as the sources of silica in the synthesis of zeolite X [87], in a gel composition of $4.76\text{Na}_2\text{O} : 1\text{Al}_2\text{O}_3 : 3.5\text{SiO}_2 : 454\text{H}_2\text{O}$, it was observed that the

anhydrous salt generated larger crystals, with twice the size of those produced by the hydrated salt, while fumed silica generated intermediate crystals, similar to the hydrated salt.

In the syntheses of zeolites X and Y two sources of silica were used: an aqueous colloidal solution with 30% SiO₂ and a solution with 29.5% SiO₂ containing Na₂O in water [89]. The synthesis gels were evaluated by Raman spectroscopy. The zeolite X synthesis spectroscopies revealed aluminate leftovers for the 29.5% SiO₂ solution and a slower crystallization rate, while the same did not occur for the 30% SiO₂ solution. It also presented a higher crystallization rate, indicating better incorporation of aluminum species. The synthesis of zeolite Y was strongly influenced by the silica source: the solution with 30% SiO₂ formed mainly zeolite Y, while the solution with 29.5% SiO₂ containing Na₂O in water, generated zeolite X, and may generate zeolite P depending on the concentration. The authors attributed this to the different rates of aluminate incorporation during synthesis.

In order to compare the silica source in the metal-free ITQ-13 synthesis [104], the process was performed with fumed silica and tetraethylortosilicate (TEOS) in a synthesis gel of composition 1.0SiO₂:0.29R(OH)₂:0.64F:xH₂O, varying x from 7 to 12. Zeolite could be obtained from fumed silica without the hydrolysis step, making synthesis faster. As TEOS releases ethanol into the medium, it slows down the crystallization rate, requiring 8 h more to achieve the same crystallinity as pyrogenic silica synthesis.

Comparison between the use of amorphous silica and TEOS was also performed for Beta zeolite synthesis [18]. The zeolite synthesized with TEOS showed higher activity and selectivity than that synthesized with fumed silica, for the same Si/Al ratio. However, using silica in the synthesis, larger and more stable crystals were observed in the process of dealumination, which resulted in higher catalytic activity as well as lower deactivation rate than the TEOS synthesis.

The specific surface of the silicon source can also influence the properties of the zeolite produced. Using silicas with different areas in the synthesis of zeolite A [63], it was observed that the larger area silicas had higher solubilization capacity in the alkaline solution, thus leading to higher nucleation rates, which consequently generated smaller crystals. Smaller area silicas took longer to dissolve into larger crystals. This effect was also observed in the synthesis of omega zeolite, where silica gel with different areas was used [26].

The polymerization level of the silica source affects its solubility and reactivity. In synthesis of zeolite Y diatoms from different regions were used as silica source [32]. Zeolite Y was obtained only under severe alkaline conditions, whereas at lower alkalinity there was little dissolution of diatom silica. Despite being a natural source, after treatment, the remaining impurities had little effect on the crystalline structure of the zeolite produced.

In the synthesis of ZSM-5, the influence of silicon sources on the crystallization with tetrapropylammonium as structure director was evaluated [29]. Silica gel (SiO₂.0.4H₂O) and colloidal silica (SiO₂.5H₂O) were used. The highly alkaline medium used in the synthesis with this director favored the solubility of silica gel, thus achieving a shorter induction period and higher crystallization rate, whereas

colloidal silica had a longer induction period. Using the silica gel in the synthesis, crystals were observed to grow from a sludge-like medium with a higher rate, yielding smaller twisted and spherical crystals, whereas with colloidal silica it was formed a more viscous medium within 24 h of reaction, generating larger crystals after a longer crystallization period. The effect of silica sources on the amount of aluminum in the synthesized material was also evaluated. Little difference was observed in the incorporation of aluminum using aluminum nitrate, whereupon in the synthesis with tetraethylorthosilicate (TEOS) and sodium silicate it was incorporated more aluminum atoms than in the synthesis with fumed silica.

3.1.2 Alumina Sources

There are several sources of alumina that can be used to produce zeolites by the hydrothermal method. These include aluminum hydroxide, chloride and nitrate, as well as less conventional ones such as aluminum butoxide.

The aluminum source can significantly influence the crystallization and morphology of the synthesized zeolite. This was observed in the synthesis of NaA zeolite using sulfate or chloride as aluminum source [58]. Evidence has been found that sulfate ions may act as catalysts for crystallization and phase change due to the strong interaction of these ions with the zeolitic structure of the material produced. Sulfate produced better crystallinity in half the time of that of chloride. In assays with long crystallization times and high alkalinity, NaX zeolites with chloride and sodalite with sulfate were produced, which may be due to the difference in the interaction between the alkali metal cations and the anions of these salts, which create regions with different ion concentrations, forming different materials. However, it is noteworthy that in the syntheses with tetraethylorthosilicate, there were no major differences in the properties of NaA zeolites produced when comparing the aluminum sources.

For the sodalite synthesis, aluminum hydroxide, metal isopropoxide and pseudoboemite were used as aluminum sources [36]. Under the experimental conditions used, when using aluminum hydroxide, no metal species were observed in the zeolite crystal lattice. Pseudoboemite resulted in a material containing mixtures of pure silicon sodalite and aluminum sodalite, but with large amounts of metal outside the zeolitic network. In the synthesis with isopropoxide the results were better, since the aluminum distribution was more homogeneous.

Four different Al sources, namely aluminum hydroxide, chloride, nitrate and butoxide, were tested to evaluate the incorporation of Al atoms into the zeolite ZSM-5 crystal lattice [29]. The complexity of the salt used for the synthesis influenced the metal incorporation in the structure. Three different Al atom coordinations were observed in the zeolitic structure. For the synthesis with butoxide, aluminum was incorporated into the zeolite lattice and more than 90% of the Al atoms were isolated from each other in the structure, and this effect also occurred using nitrate as Al source, but with a slightly smaller total incorporation. The hydroxide and chloride syntheses resulted in fewer isolated aluminum atoms in the

lattice, but a larger number of nearby aluminum was observed, separated by a silicon oxide ($\text{Al-O-(Si-O)}_{12}\text{-Al}$), with a higher total amount of Al found on the net.

Zeolite A synthesis was performed using ashes and the amount of Al was adjusted by using a sodium aluminate solution or an aluminum hydroxide powder [3]. In the synthesis with aluminum hydroxide, the zeolite obtained contained aluminum outside the crystal lattice, while the synthesis with aluminate did not present aluminum atoms with this organization. It was also observed that aluminate, by supplying sodium into the synthesis mixture, helped to stabilize the aluminosilicate anions, while in the synthesis with hydroxide the opposite was observed, since by adding hydroxide the crystallinity became smaller and the material became more sensitive to variations in Si/Al ratio.

Also in the synthesis of ZSM-5, aluminum sulfate, hydroxide, alumina and sodium aluminate were used as sources [39]. Synthesis with aluminum sulfate and sodium aluminate produced ZSM-5 zeolites, in which the aluminate generated higher crystallinity. On the other hand, the syntheses with alumina and hydroxide produced quartz phase materials. ZSM-5 with cubic crystals was produced in the synthesis with sulfate and aluminate, while the quartz produced presented needle-shaped crystals.

3.1.3 Alternative Sources of Aluminum and Silicon

In addition to using sources of alumina or silica from pure reagents, natural sources can also be used. It is common to find works that use ashes in the synthesis, because they are rich in alkali metals and silica, and in some cases have considerable amounts of aluminum. However, it is always necessary to adjust the content of alumina or silicon to obtain the desired zeolite and its Si/Al ratio.

Several sodium zeolites were produced by hydrothermal synthesis, using ashes without the addition of silicon or aluminum sources [74]. The materials obtained were zeolites NaP1, NaP, analcime and gelinin. The ashes obtained from various sources showed different compositions of aluminum, silicon and other metals and nonmetals. The syntheses were sensitive to the composition of the ash used; materials with the same molar ratio $\text{SiO}_2/\text{Al}_2\text{O}_3$ produced zeolites with different crystallinities, because they had different compositions of other species.

In an extensive review about the use of kaolin in hydrothermal synthesis of zeolites [42], it was found that after converting kaolin to metakaolin (in a process known as metakaolinization), both aluminum and silicon became amorphous and available for the synthesis of the desired material. Other parameters were also important, such as the Si/Al molar ratio. Low Si/Al ratios favored zeolites LTA and X, while higher ratios favored the synthesis of zeolites such as ZSM-5. Concentrations in the range of 3 mol/L of sodium hydroxide were found to be the best for the synthesis of zeolites, and at higher concentrations lower crystallinity was obtained. At temperatures below 70 °C no crystalline species were observed

and the best temperature range found was up to 200 °C. The minimum crystallization time was 24 h and the best crystallinity was found for the zeolite crystallized for 120 h.

3.2 *Crystallization Time and Temperature*

The stage of heat treatment in zeolites synthesis is of paramount importance, especially when considering the fine tuning of the material's porosity. Both micro and mesopores can be formed during calcination. In addition, the often-used structure directing agents (templates) are usually removed through heat. Therefore, the final structure of each zeolite is truly achieved after the heat treatment is completed.

In accordance to this, the heat treatment is one of the most important steps in zeolites preparations. A good control over this process is mandatory for the formation of the wanted structures, especially when considering the cases where it is desirable for metal ions present in the framework to be removed, forming extra-framework species, which eventually present new structures and new possibilities in application such as the production of new catalysts. The heat treatment also affecting properties such as crystal size, and even forming other materials by dissolving already formed metastable structures.

In their study [112] reported the preparation of composite molecular sieves with mesoporous and microporous structures by heat treating ZSM-5. Such a method is very advantageous, presenting itself as a low cost, easy controllable method that has a good repeatability for preparation of bimodal porous materials.

Zhang et al [112] tested temperatures in the range of 950–1100 °C and treatment from 2 to 10 h in air. As result of such treatment, a new kind of ZSM-5 with bimodal pore was developed, where a part of the original micropore had remained, but some narrow mesopores were formed in the same matrix. In a similar fashion, Groen et al. [35] prepared mesoporous modernite by controlling silicon extraction on alkaline treatment of high-silica mordenite, followed by thermal treatment. As a result, the material exhibited substantial mesoporosity and microporosity, a very important characteristic for catalyst synthesis.

In the synthesis of omega zeolite the effect of temperature on crystallization time was evaluated [26]. The synthesis performed at 100 °C for 15 days was observed to yield a material with properties equivalent to that produced by the same synthesis gel subjected to 135 °C for one day. Moreover, it was found that, even at the lowest temperature, the time necessary to produce the omega zeolite was as narrow as at the highest temperature.

The effect of temperature and crystallization time was evaluated on the NaA zeolite synthesis [58]. At lower temperatures (80 and 85 °C), there was no formation of zeolite or any crystal structure. Only at 90 °C NaA zeolite was produced, but at a higher temperature (95 °C), NaX zeolite was formed by the decrease in the crystallinity of NaA zeolite (these two zeolites have synthesis gel with similar

compositions). Evaluating the crystallization time between 1 and 12 h, it was observed that up to 2 h the amorphous gel changed to highly crystalline NaA zeolite, but as time passed the gel reorganized forming highly crystalline sodalite after 12 h of reaction, which may occur due to the metastable nature of NaA zeolite.

In the synthesis of zeolite NaY, the effect of process temperature and time on material diameters was evaluated [9]. Increasing the temperature during the gel formation step decreased the size of the zeolite particles produced. As the temperature increased during the aging stage, it was observed that the particle size of the material increased, as well as the transparency of the solution, obtaining micrometric zeolites in syntheses at low temperatures. These effects occurred because higher temperatures tend to further solubilize the solid phase by increasing the concentration of the reaction medium, which accelerates the formation of larger crystals and decreases the time of this phase. Tests at higher temperatures revealed this effect and also the formation of structures different than the desired ones.

Among other synthesis parameters, the effect of temperature and crystallization time were evaluated on NaX zeolite synthesis [113]. It was observed that with the crystallization time the gel changed from an amorphous phase to a NaX rich phase within 3 h. As time progressed, the amorphous band decreased as the crystallinity of the material increased, reaching good crystallinity within 7 h. The crystallinity increased with crystallization time, reaching a maximum up to 15 h, and from 15 to 34 h no improvements in zeolite crystallization were observed. The increase in temperature favored the formation of a sodalite phase, which is due to the dissolution of the metastable NaX structure that tends to reorganize into a more stable form.

In the same way, for the synthesis of ZSM-5 [66], it was observed that after reaching the optimum crystallinity, no changes were observed in the material crystallinity for longer times. However, different crystals were formed at different reaction times. Initially, when crystallization was not complete, orthorhombic crystals were formed, and as time progressed were observed orthorhombic and spherical crystals, whereas after complete crystallization only orthorhombic crystals were found. On the other hand, in the NaA zeolite synthesis [8], it was observed that increasing both the crystallization time and temperature, the crystallinity and particle size of the zeolite produced also increased. The temperature had more influence on the particle size and the reaction time affected more intensely the crystallinity.

3.3 Structure Directing Agents (SDAs) in Zeolite Synthesis

Currently, approximately 230 zeolite structures are known, but more than 2.6 million structures predicted [55]. This fact can be attributed due to the development of innovative synthetic strategies, such as the introduction of organic structure guiding agents (OSDA), the introduction of heteroatoms such as Ge in the synthesis

of OSDA-mediated zeolites, the topotactic transformation of zeolite precursors in two-dimensional layers, the method of assembly-disassembly-organization reassembly and others [68, 84].

The vast majority of overviews require a structure driver (OSDA—organic structure directing agent). Organic directors are molecules with size and shape proportional to the channels and cavities of the crystalline structure and thus can facilitate the crystallization of zeolites in specific structures. In the absence of a structure driver, only 50 natural and 30 synthetic zeolites exist or have been successfully synthesized in laboratories [76].

The ability to access more theoretical zeolite structures depends on the knowledge of structural targeting of the OSDAs with the specificity of controlling the kinetic step from pre-nucleation, nucleation and crystal growth [77]. According to [61], the template theory until 1983 could be divided in four main generations. Firstly, in 1960, tetramethylammonium, also known as TMA, was used as the first organic cation in zeolite synthesis, resulting in the synthesis of many structures containing small cages.

One year later, zeolite β was synthesized using tetraethylammonium (TEA). Others structures with high silica alumina, such as ZSM-5, 11, 12, 34, 39 and 48 were also synthesized using TPA, TBA and TMA as organic template. The third generation came with the use of organic amines, resulting in another important family of molecular sieves, the ALPOs. The fourth generation was brought with the use of alcohols, ketones, glycerol and organic sulfur as organic molecules.

Since then, high silica zeolite synthesis using alkylamines or alkylammonium have resulted in a host of materials with novelty framework topologies or in materials with known framework structures but with previously undiscovered compositional ranges. Early on, many of these organic SDAs were prepared from single-step alkylation reactions of an available amine with an appropriate alkyl halide.

Researchers had used N,N,N-trimethyladamantammonium to prepare SSZ-13 (CHA), SSZ-23 (STT), SSZ24 (AFI), and SSZ-25 (MWW) and SSZ-31 [12]. Studies had success with diquatary ammonium molecules (diquats), formed by reaction of a dihalide with a tertiary amine, such as trimethylamine, 1-methylpyrrolidine, or quinuclidine. The use of diquats has led to the discoveries of several zeolites including EU-1 (EUO) and Nu-87 (NES) [13], SSZ-16 (AFX) [60], ITQ-13 (ITH) [19], and ITQ-22 (IWW) [80].

In general, zeolite crystals are formed during the crystallization process in several stages, including the prenucleation stage, primary nucleation, core growth and finally, crystal growth, which may or may not be accompanied by simultaneous secondary nucleation.

The driving force of the process is the phenomenon of supersaturation, a very complex and difficult condition to investigate due to its metastable nature [62]. The pre-nucleation stage includes the partial or complete dissolution and hydrolysis of Si and Al sources, followed by the condensation of silicon and aluminum species in zeolytic precursors, until a metastable condition (supersaturation) is reached.

When supersaturation is achieved, a period, called induction time, is defined as the period between supersaturation and the beginning of the formation of nuclei with a detectable size [93]. During this stages of nucleation and growth of crystals, the “structuring”, “directing” or “shaping” agents will influence the structure of the molecular sieve produced.

The role of inorganic agents can be summarized as suppliers of OH^- (in some cases substituted by F^-), which influence the kinetics of gel dissolution by mineralization and generation of “precursors”, those, in the case of zeolites, are oligomers of silicates. Organic compounds will generally be responsible for the modeling action of crystals of the molecular sieve and stabilization of structures [41, 64].

The main factors affecting zeolite formation are crystallization temperature, time, precursors sources, the presence of impurities and concentrations of those, seed addition, the presence of structure drivers and the pH of the reaction mixture. It is clear that the structure drivers are vital in the formation of zeolites. Several chemical compounds present in the synthesis mixture can provide this effect in a cooperative way [59].

Structure drivers can be classified into groups. The first is charged molecules, mainly cations (organocations), which are also known as organic drivers or pore fillers, being primarily alkyl-ammonium cations. A second group is formed by inorganic cations, e.g. alkali- and earthy alkali metal cations, which are usually introduced into the synthesis mixture as bases to adjust the pH and can cause significant effects on nucleation and crystal growth. The third group contains neutral molecules, such as water, amines, and ionic pairs (e.g. salts). Those can also function as drivers for the stabilization of specific types of zeolites, since the porous architecture of zeolitic products depends on the size, shape, stiffness, compliance and card density of OSDA.

On the other hand, the selectivity of the crystallization phase is also strongly affected by inorganic structure drivers (ISDAs), such as 2A metal ions, hydroxide or fluoride anions, and heteroatoms other than Si [84]. In their review [53] accounted many new structures that were discovered and successfully synthesized.

The development of structure drivers has great important in the production of zeolites with larger pores, large cavities and mixed porosity with meso or macropores in already known structures [72]. Studies show that, in general, pore openings, their dimensions, connectivity and architecture in synthesized zeolites can be modified with the variation in size, load, stiffness, polarity and hydrophobicity of structure drivers. Each structure driver can lead to the formation of secondary units of specific constructions that induce corresponding zeolitic. Therefore, it is clear that the design of organic structure drivers is one of the most efficient ways to obtain new zeolytic structures [68].

For some types of zeolites, the addition of already formed crystals (seeds) with similar structure can accelerate the crystallization process, specifically the nucleation step, by the rapid (inter)crystalline growth promoted by such seeds. Due to the potential seed structure driving, this technique partially or completely eliminates the need for organic drivers in some zeolite synthesis [40].

This method comes with the great advantage of mitigating the usage of OSDAs, which are a main cause of environmental concerns, as the organic templates and organic solvents are usually toxic and expensive. The by-products contain abundant inorganic/organic species that could be reused, while the resultant products need to be calcined at high temperature to remove the occluded organic templates, increasing further concerns with environmental pollution. Many efforts have been made toward the development of more environmental friendly synthesis routes for zeolite materials [59].

One of the major concerns for the synthesis of new zeolites with extra wide pores is the fact that such routes would require large and rigid structural drivers with the polarity necessary to favor the formation of zeolites with a large volume of micropores and a system of multidimensional channels. One of the methods that stands out for the improvement of porosity is the creation of secondary porosity with the insertion of meso and macropores. A material with such characteristics is called hierarchical zeolites and the methods for its production are classified as assembly, demetallization and mixed methods.

The assembly methods, also called bottom up processes, create meso or macropores from the organization of zeolitic or nanocrystals precursor units. Subclassifications of the routes for such processes are hard templating, soft templating and indirect modeling routes. The first two are defined according to the nature of the driver used as a generator of meso and macropores, while the later does not have the addition of a driver in the reaction environment [94].

One of the key factors for the synthesis of these structures is the application of different types of surfactants, whose molecules tend to form micelles in aqueous solutions, which causes surfactant to act as mesoporous drivers. Surfactants are easily removed by calcination [83].

Other class of pore drivers include organosilanes that interact with the zeolite structure and thus prevent phase separation during the synthesis process. Burkett et al. [11] were the pioneers in developing synthesis of inorganic materials using organosilanes, using siloxanes [67]. This discovery increased the interest of the application of these compounds in the synthesis of zeolites as a co-director.

The use of aphylic organosilanes has stood out and proved efficient in the synthesis of mesoporous zeolites, obtaining hierarchically structured zeolites in known structures such as ATL, sodalite, BEA, FAU and FER [16, 17, 38, 98]. The “two-in-one” drivers have been highlighted by the possibility of synthesizing ordered mesoporous zeolites. Several new arrangements were discovered with its use, such as the RTH structure CIT-10, a lamellar material that contains small pores that are perpendicular to the layers, offering advantage in the separation of smaller molecules [81].

The molecular structure of ARDS is the most important factor in the structure topology of ALPO-type zeolites, as the direction of the ALPO structure depends heavily on the geometric and chemical properties of ARDS [61]. The molecular structures of the organic amines can be diversified by means of simple organic reactions. In aqueous acid medium, amines are protonized to form ammonium ions

and can be cooperatively mounted with inorganic anions via electrostatic interactions, thus being widely used for synthesis of ALPO as SDAs [109].

Other analogous structures to ALPOs such as SAPO-34, SAPO-31, ALPO-5 and VPI-5 were also synthesized using amines as SDAs [57, 79]. Organic quaternary ammoniums [82], N-containing chiral esters (Huang and Caro [37], metal complexes and sulfur compounds (sulfonic and sulfides) [51] were also tested for synthesis of ALPOs.

Xu et al. [101] related to the hydrothermal synthesis of ALPO-LTA using NPA as SDA, acquiring a perfectly cubic structure. With the content of NPA of 2.2%, they showed that perfect cubic crystals could grow to a size as large as 170 μm . In a similar fashion [102] used NPA in the hydrothermal synthesis of SAPO-47, varying the content from 1.5 to 3.9%, discovering that the size of SAPO-47 crystals increased dramatically by increasing the content of NPA in the gel until 2.3%. When the molar ratio increased from 3.1 to 3.9%, the size of SAPO-47 crystals decreased.

As the final crystal size highly depends on the relative rate of nucleation and crystal growth, they concluded that the rate of crystal growth is much faster than the rate of nucleation in the low concentration of NPA ($\leq 2.3\%$). Thus, the size of SAPO-47 increased by increasing the content of NPA in the gel. However, the rate of nucleation might be much faster than the rate of crystal growth when the content of NPA reaches higher values, leading to the decrease in the size of crystals.

One of the strategies for the development of new structures that has been reported is the combined use of Ge and OSDA in concentrated fluoride medium, which causes the formation of new structures with low structural density. The drawback of this route is the low thermal stability of the molecular sieves of germanosilicates. Of the various structures already reported, only eighteen of them present a good thermal stability compared to the other structures [84].

The research and tests of inorganic directing agents, combined with OSDAs has been predominantly by trial and error. Some zeolites, such as RHO and ZK-5, can be synthesized with or without OSDAs [14, 75]. With this in mind, the use of simulation to predict the behavior of structure drivers, has been growing in recent years.

Li et al. [55, 54] used the first principle methods to explore the interactions between N,N,N-trimethyl-1-adamantyl ammonium (TMAda⁺) and framework $[\text{AlO}_2]^-$ in the dilute limit within an SSZ-13 lattice. Their results indicated that the Al distribution patterns observed in relevant SSZ-13 samples are not consequences of the location bias for Al substitution within a single TMAda⁺-cage complex but likely involve long-range electrostatic interactions among multiple TMAda⁺-cage complexes. The computational protocol could be employed to examine other combinations of SDAs and zeolites of interest.

4 General Uses of Zeolites

Generally, natural zeolites are most applied in the environmental area or processes that require large amount of material, because they are cheaper and less pure than synthetic zeolites. On the other hand, these are mostly used in industrial and petrochemical processes.

As mentioned above, zeolites can act as molecular sieves. Their small pores allow the entry of small molecules, barring the largest. Due to their ability to selectively absorb molecules with different sizes, shapes and polarities, they can be used as adsorbents in separation and purification processes of gases and liquids, for example:

- Gas Drying: Zeolites A or X can be used to dry gases such as air, hydrogen, natural gas, LPG, ethylene and propylene.
- Gas Purification: Zeolites can be used in the purification of industrial gases containing sulfur, nitrous and mercury vapors and in the production of N₂ and O₂ from air (pressure swing adsorption).
- Hydrocarbon Separation: Zeolites X and Y may be used in several hydrocarbon separation processes, such as xylene (Asahi Parex process), ethylbenzene (EBEX process), n-paraffins from ramified and cyclic (Molex process), olefins and paraffins (Case Olex) and separation of isomeric mixture of glucose and fructose to produce concentrated fructose syrup.
- Dehydrated ethanol: zeolite can be used to remove water from hydrated ethanol in substitution of cyclohexane or another dehydrating agent to produce anhydrous ethanol.

Zeolites can also be used as catalysts or as support to catalysts in many industrial processes such as refining, petrochemical and fine chemicals. According to [33], zeolites replaced the conventional catalysts due to their improved activity and selectivity, high acidity and/or crystalline structures, and due to the size of their pores and cavities, which gives a geometric selectivity towards products or reagents.

The use of zeolites revolutionized the catalytic cracking process in fluidized bed (FCC—Fluid Catalytic Cracking) of oil to produce gasoline. About 90% of the industrial plants around the world use zeolite USY containing Re⁺³, ZSM-5 and other elements. The good performance of zeolite catalysts in this process is due to their good thermal and hydrothermal stability, high acidity, less coke formation, good friction resistance and pore sizes that allow selective cracking [33, 91, 92].

Other catalytic processes that use zeolites as catalysts include: hydroisomerization, hydrocracking, transformation of methanol into gasoline (MTG), C8 aromatic hydrocarbon isomerization, LPG aromatization (transformation of light hydrocarbon into aromatic), alkylation and disproportionation of aromatics.

In the applications mentioned above, are used mainly synthetic zeolites. In processes where it is necessary high zeolite volumes, the natural ones, such as clinoptilolite, chabazite, erionite, mordenite and phillipsite, are used. Due to their

microporosity, that provides the molecular sieve effect, the natural zeolites can be used as fluidized bed in the mechanical filtration of water, liquors, oils, removal of suspended particles and microorganisms. By presenting high content of silica and other elements such as aluminum, alkaline and alkaline earth metals, they can be used as raw material for industries of ceramics, materials for electronics and glass or be used as cement additives to confer it higher resistance [33, 91, 92].

As said before, one of the main characteristics of a zeolite is the ion exchange capacity. NaA zeolite can be used to reduce the hardness of domestic and industrial wastewater (extraction of the cations Ca^{2+} and Mg^{2+}), as support for fertilizers (soil conditioning), medicinal drugs, odor removal [91, 92], deodorizing air, gas filter (mask and cigarettes). A sodium zeolite can be used in the detergent formulation to replace polyphosphates and other highly polluting compounds. They can also be applied in the treatment of wastewater to remove NH_4^+ ions and heavy metals, in the storage of radioactive elements, by removing Cs^+ , Ca^+ and Sr^{2+} from the central cooling water system of the nuclear plant and as environmental anti-poisoning (processing of NO_x and SO_x from combustion gases).

According to the [115] group's report, the global market for zeolite is on the rise, with an estimated annual growth rate of 3.5% between 2015 and 2020. In 2014 the global market was evaluated at USD 3.50 billion, equivalent to 3000 kilo tons of zeolites, and 60% of the total volume consumed was natural zeolites.

The main producer of natural zeolites in 2014 was China, with an output in the range of 1.8–2.2 million tons. The second largest producer was the Republic of Korea (230,000 t) followed by the US (64,100 t) (U.S. Geological Survey Minerals Yearbook, 2015).

Of all the zeolite consumed worldwide in 2014, 50% was intended for incorporation in detergents [115]. Zeolite LTA (4A, NaA) is widely used as a substitute for sodium tripolyphosphate (STPP), as this can cause eutrophication (excessive algae growth in the surface of rivers). Thus, zeolite is widely used due to environmental issues, particularly in concentrated detergents.

The main world leaders in the zeolite market are [115]: Tosoh Corporation, Arkema Group, BASF SE, Interra Global Corporation, UOP LLC, Zeochem AG, Grace Catalysts Technologies, Chemiewerk Bad Köstritz GmbH (CWK), Tricat Group, KNT Group, Zeox Corporation, Anhui Mingmei MinChem Co., Ltd, Union Showa KK (USKK), Dalian Haixin Chemical Industrial Co., Ltd, Yingkou Zhongbao Molecular Sieve Co., Ltd, Clarian.

4.1 Catalytic Applications of Zeolites

In Table 1 are presented some recent articles (published in the past three years) addressing the catalytic applications of zeolites.

Pyrolysis is a thermochemical conversion process that converts biomass or other sources of long chain organic molecules into liquid and gaseous fuels or other valuable chemicals [45]. Generally, lignocellulosic biomass is used as a feedstock

Table 1 Catalytic applications of zeolites

Zeolite	Catalyst composite	Process	References
FAU	Co-Ni-Pt/FAU	Biodiesel production by esterification of oleic acid with ethanol. The FAU material was prepared using shale rock	[2]
Na-Y	La ₂ O ₃ /Na-Y	Transesterification of castor oil with ethanol using spherical catalyst particles	[23]
Y and ZSM-5	H-Y and ZSM-5	Palmitic acid esterification	[73]
Y	Li/Na-Y	Transesterification of castor oil with ethanol to produce biodiesel	[54]
Y	Ni-W/Y	Hydrocracking of n-heptane using zeolite Y impregnated nanoparticles	[4]
Y	Heteropolyacid-Ni/ Hierarchical mesoporous zeolite Y	Hydrodeoxygenation and hydrocracking of microalgae biodiesel to produce jet biofuel	[15]
Beta and Y	NiMo/zeolite-Al ₂ O ₃	Vacuum gas oil hydrocracking for production of more volatiles compounds	[21]
ZSM-5	ZSM-5	Catalytic cracking of soybean oil with acid catalyst to produce hydrocarbons for fuel use	[24]
USY	NiMo/USY-Al ₂ O ₃	Catalytic hexadecane hydrocracking to produce liquid hydrocarbons (C5-C15)	[43]
Y	Ni/meso-Y	Conversion of methyl palmitate into jet biofuel	[111]
Y	La/H-Y	Catalytic cracking of bulky hydrocarbon feed	[69]
A	Pt/Na-A (nanoencapsulated metal)	Water gas shift reaction without methane formation	[30]
Y	Mg/Na-Y	Glucose isomerization for production of fructose with high conversion and selectivity	[34]
FAU	Hierarchical FAU nanosheets	Benzylation of toluene with benzyl chloride	[110]
Beta	Fe/Beta	Glucose isomerization to fructose in aqueous media	[103]
Beta	HPA/Zr-Beta	One-pot conversion of furfural into γ -valerolactone	[97]
HZSM-5	Ga/HZSM-5	Aromatization of 2,5-dimethylfuran in the presence of ethylene	[90]
ZSM-5	Zn-Cr/ZSM-5	One-pot co-conversion of xylose and methane under solvent-free conditions	[71]

(continued)

Table 1 (continued)

Zeolite	Catalyst composite	Process	References
Beta	Beta nanoclusters/NiMo	Hydrodesulfurization of dibenzothiophene (DBT) as probe molecule	[22]
Y	NiMo/Ga-Y	Hydrodesulfurization of 4,6-dimethyldibenzothiophene (4,6-DMDBT) as probe molecule	[114]
ZSM-5	Pd/montmorillonite-modified HZSM-5	Hydrodesulfurization of diesel fuel with low sulfur concentration (about 350 ppm)	[107]
H-Beta, H-ZSM-5, SSZ-13	Cu/Zeolite	Reduction of NO _x in vehicle emissions with propane	[52]
various	Beta, ZSM-5, ZSM-11, ZSM-23, ZSM-35, MOR, MCM-22, MCM-49, EU-1, SAPO-11	Amination of isobutylene to tert-butylamine over zeolite catalysts with different structures and acidities	[31]
Beta	H-Beta	Esterification of succinic acid and phenol for production of diphenyl succinate in an one step reaction	[50]
MFI	MFI-Fe	Electro-Fenton oxidation process to remove the water contaminants	[49]
H-Beta; ZSM-5 and HY	Fe-Ni/zeolite	Production of Benzene, Toluene and Xilene from anisole by hydrodeoxygenation and transalkylation at ambient pressure	[100]
ZSM-5, MOR, MCM- 22, H β , and SAPO-34	Cu/zeolite	Selective catalytic oxidation of n-butylamine	[99]
Beta	H-Beta	Methylation of toluene with methanol in sub/supercritical toluene	[86]
ZSM-5	Pd-TiO ₂ /ZSM-5	Hydrogen production by photocatalytic water splitting	[25]
Y	Fe ₂ O ₃ /Y	Phenol photodegradation	[105]
ZSM-5	Ti/H-ZSM-5 (zeolite containing iron species)	Photocatalytic CO ₂ reduction	[88]
ZSM-5	Fe/ZSM-5 (hierarchical)	Fischer-Tropsch synthesis (converts syngas into aromatics)	[95]
Beta	Co/Beta (dealuminated)	Fischer-Tropsch synthesis with high selectivity towards liquid products	[78]

(continued)

Table 1 (continued)

Zeolite	Catalyst composite	Process	References
Beta	Co/Beta (hierarchical)	Fischer-Tropsch synthesis with high selectivity of isoparaffins	[56]
Y	Nb ₂ O ₅ /Zeolite (Na-Y, H-Y, H-USY)	Glycerol acetalization reaction for production of solketal	[28]
MCM-22	V/MCM-22	Gas phase oxidative dehydration of glycerol to acrylic acid in one single step using bifunctional catalysts	[85]
Y	M/Y (M = Ni, Fe, Mo, Ga, Ru, Co)	High density polyethylene pyrolysis for generation of aromatic compounds	[1]
Y	H-Y	Pyrolysis of lignin modified with phenolic hydroxyl for production of benzene, toluene, xylene and naphthalene	[45]
H-Beta, H-ZSM-5, MAS-7, MCM-41, SAPO-11	Ni-Cu/Zeolite	Alcoholysis of Kraft lignin for production of bio-oil mainly composed of alkanes, aliphatic acids/esters and aliphatic ketones/alcohols	[47]
MFI	MFI (Si/Al = 42)	Conversion of lignin-derived alkylphenol to phenol via transalkylation in benzene solvent	[108]
ZSM-5; beta and Y	Ni/zeolite	Syngas production from the pyrolysis-catalytic steam reforming of waste high density polyethylene	[106]
X; Y and ZSM-5	X; Y (Si/Al = 5.1; 5.2 and 80) and ZSM-5 (Si/Al = 80)	Catalytic fast pyrolysis of hydrolysis lignin for the production of bio-oils with high contents of monomeric aromatics/phenolics	[70]

in this process. In this context [70] reported that, by increasing the total Bronsted acidity of ZSM-5 zeolites, the content of monomeric aromatics and phenolics in the bio-oil produced by fast pyrolysis also increases. Kim et al. [45] showed that the pyrolysis of lignin modified with phenolic hydroxyl, using H-Y as catalyst, produced a stream with high selectivity towards aromatic compounds of industrial interest. Additionally [47] described the importance of the solvent used in the pyrolysis reaction as being, among other reasons, the hydrogen source during the reaction with metal/zeolite catalyst. The last authors have evaluated H-Beta, H-ZSM-5, MAS-7, MCM-41 and SAPO-11 zeolites as supports for Ni-Cu catalyst.

On the other hand [1] and [106] proposed the pyrolysis of waste high density polyethylene instead of biomass. The pyrolysis of this raw material could be very

important in the current scenario, where the society generates tons of plastic waste daily. Akubo et al. [1] demonstrated that the impregnation of transition metals (Ni, Fe, Mo, Ga, Ru, Co) in the H-Y zeolite increases the yield of aromatic hydrocarbons. However, the authors verified that an increase from 1 to 5% on the metal content did not present significant effect in the composition of the reaction products. By studying the Ni impregnated on different zeolites [106] found that the ZSM-5 zeolite presented the most promising activity and that Y zeolite showed significant coke deposition during the pyrolysis of high density polyethylene.

Other widely reported application for zeolites is the hydrocracking of long chain organic molecules [15], as could be seen in Table 1. This process can be coupled to a deoxygenation to generate hydrocarbons as reaction products (used ordinarily as fuels). Cheng et al. [15], Emori et al. [24] and Zhang et al. [111] researched the hydrocracking of materials originated from biomass. Cheng et al. [15] reported the use of hierarchical Y zeolite with $\text{H}_3\text{PW}_{12}\text{O}_{40}$ -Ni for hydrodeoxygenation and hydrocracking of biodiesel. The authors observed that the content of heteropolyacid (0–8%) highly influenced the yield and structure of the reaction products. Meanwhile [24], by using directly the ZSM-5 zeolite, were able to produce hydrocarbons like gasoline, kerosene and diesel from soybean oil. On the other hand, jet fuel was produced over Ni supported mesoporous Y zeolite from methyl palmitate [111]. The results indicated that the selectivity towards this product increased by previously desilicating the zeolite.

The hydrocracking of molecules from not renewable raw material is also very important for industrial application. In this scenario [43] described the use of NiMo/USY- Al_2O_3 to cracking the molecule of hexadecane. The authors described the importance of zeolite recrystallization and addition of alumina to change the catalyst acidity and the metal-support interaction. Anis et al. [4] reported the hydrocracking of n-heptane using nano and micro particles of Ni-W/Y. Comparing the results with those of similar micro-catalysts, the nanoparticles registered higher conversions.

Fischer-Tropsch synthesis is an important process for producing several chemical products from syngas (CO and H_2). Zeolites have been applied as support for the active metal particles in this process. According to [95], both high acidity and increase of mesoporosity of Fe supported on hierarchical ZSM-5 zeolite could improve the selectivity of aromatics in the oil product. In the same direction [56] employed hierarchical micro-meso-macroporous Beta zeolite supported Co catalyst. The authors reported that the modified zeolite had good macroporous structure, which reduced the internal diffusion limitations and also the methane selectivity.

Furthermore [78] studied cobalt catalyst supported on dealuminated Beta zeolite for Fisher-Tropsch synthesis in order to improve liquid products selectivity. They concluded that, besides the positive effects of increased mesoporosity, the reduction of acidity, resulted from the desalination treatment, increased the stability of the catalyst by improving the resistance to carbon deposition.

The biodiesel production is another process that can be catalyzed using zeolite materials. Prinsen et al. [73] studied the esterification of palmitic acid with methanol using H-Y and H-ZSM-5 catalysts. The main result obtained was that the

acid conversion was more related to the porosity and hydrophobicity/hydrophilicity of the materials than to their total acidity. Also [2, 23, 54] presented the transesterification reaction for biodiesel production. Ordinarily, this is a high rate reaction if the catalyst has alkaline activity. Li et al. [54] showed results indicating that there is an optimum amount of Li_2CO_3 in the catalyst for maximum ester production. Moreover the authors demonstrated the influence of the catalyst calcination temperature and time in the product yield.

As a result of the increase in biodiesel production by alcoholysis, processes that aim at the conversion of glycerol (by-product associated with this biofuel) into compounds with higher added value have been investigated. Table 1 presents two examples of application of zeolites in the formulation of catalysts used in processes with glycerol as reactant. Ferreira et al. [28] employed Y zeolite-supported niobium pentoxide catalysts for the glycerol acetalization reaction. The desired product was (2,2-dimethyl-1,3-dioxolan-4-yl)methanol (solketal), which is largely used as a solvent or plasticizer, and as a suspension agent in pharmaceutical preparations. The presence of Nb was proven to increase the hydrophobicity of the zeolite, affect surface acidity and generate higher conversions of glycerol into solketal. Additionally [85] evaluated a series of V/zeolite bifunctional catalysts (zeolite = FAU, FER, MEL, MFI, MOR, MWW and OFF) in gas phase oxidative dehydration of glycerol into acrylic acid in one single step. They reported that the selectivity towards acrylic acid was related to the ability of stabilizing the redox pair $\text{V}^{5+}/\text{V}^{4+}$ and that MCM-22 showed the highest activity as zeolitic support.

Regarding the environmental issues, the reduction of vehicles exhaust emissions of NO_x has been largely highlighted in the last years. Lee et al. [52] proposed the use of Cu/zeolite and propane as sacrificial reagent for this contaminant removal. The results indicated that the zeolites ZSM-5, SSZ-13 and Beta with 5% of Cu were able to reduce the NO_x concentration in the reaction products. Besides, the propane was converted by efficient process and CO was produced as result of partial oxidation of sacrificial reagent.

In the same way, the growing concern regarding the vehicular emissions of SO_2 instigated studies to improve the hydrodesulfurization process. Through this catalytic reaction, the sulfur is removed with the use of hydrogen. Zeolite containing catalysts were evaluated in hydrodesulfurization of probe molecules by Dong et al. [22] and Zhou et al. [114], using dibenzothiophene and 4,6-dimethylidibenzothiophene, respectively. Dong et al. [22] used Beta nanoclusters in the NiMo catalyst, which increased the total acidity and improved DBT direct desulfurization rate. On the other hand [114] employed Ga modified Y zeolite as NiMo catalyst support and stated that the framework Ga species promoted more metal-support interactions, resulting in higher catalytic activity.

Furthermore [107] used a HZSM-5 derived catalyst for hydrodesulfurization of diesel fuel with low sulfur concentration. According to the authors, the catalyst prepared by ion-exchange with tetraamminepalladium chloride solution exhibited the highest sulfur tolerance, which showed that the Pd adding method affects catalyst performance. The montmorillonite additive led to a decrease in the cracking function and improved catalytic activity.

Zeolites also have good potential applications in photocatalytic processes. They are generally used as catalyst supports due to their crystalline structure that could slow up the charge carrier recombination reaction and so improve photocatalytic activity. In Table 1 three examples of photocatalytic processes can be found, including down-hill and up-hill reactions. As down-hill process, thermodynamically favorable, phenol photodegradation over $\text{Fe}_2\text{O}_3/\text{Y}$ catalyst is presented. Yang et al. [105] reported that high catalytic activity in this Fenton reaction can be attributed to the bifunctional properties of strong surface Bronsted acidity and high reactivity of octahedral Fe^{3+} in the highly dispersed ultrafine Fe_2O_3 nanoparticles.

Tong et al. [88] employed Ti/H-ZSM-5 (zeolite containing iron species) in photocatalytic CO_2 reduction. Furthermore [25] described the use of ZSM-5 zeolite as support for TiO_2 semiconductor and combined Pd as cocatalyst in photocatalytic water splitting aiming to produce hydrogen. The authors discussed the influence of catalyst synthesis parameters on hydrogen production and pointed out that the zeolite improved photocatalytic activity.

Finally, the versatility and stability of zeolite materials as catalysts are evident in the research by Tangestanifard and Ghaziaskar [86]. The authors proposed the xylene production by methylation of toluene with methanol in pressurized conditions (including supercritical condition) using H-Beta as catalyst in the process. The results indicated that the zeolite did not present any changes after reaction at 623 K and 45 bar, demonstrating the high stability of the material. This stability is important because the authors reported the influence of operational conditions in the specific p-xylene isomer yield.

5 Conclusion

The art of synthesizing zeolites goes far beyond just mixing silicon and aluminum components. For hydrothermal synthesis it is necessary to choose the silicon and aluminum precursors, templates, compensation cation as well as the evaluation of parameters such as time and calcination temperature. The correct choice of these parameters is extremely important because it can result in zeolites with desirable or undesirable characteristics for specific processes such as catalytic, adsorption and ion exchange processes.

References

1. Akubo, K., Nahil, M.A., Williams, P.T.: Aromatic fuel oils produced from the pyrolysis-catalysis of polyethylene plastic with metal-impregnated zeolite catalysts. *J. Energy Inst.* **92**, 195–202 (2019). <https://doi.org/10.1016/j.joei.2017.10.009>
2. Alismaeel, Z.T., Abbas, A.S., Albayati, T.M., Doyle, A.M.: Biodiesel from batch and continuous oleic acid esterification using zeolite catalysts. *Fuel* **234**, 170–176 (2018). <https://doi.org/10.1016/j.fuel.2018.07.025>

3. Ameh, A.E., Fatoba, O.O., Musyoka, N.M., Petrik, L.F.: Influence of aluminium source on the crystal structure and framework coordination of Al and Si in fly ash-based zeolite NaA. *Powder Technol.* **306**, 17–25 (2017). <https://doi.org/10.1016/j.powtec.2016.11.003>
4. Anis, S.F., Singaravel, G., Hashaikheh, R.: Ni-W/nano zeolite Y catalysts for n-heptane hydrocracking. *Mater. Chem. Phys.* **212**, 87–94 (2018). <https://doi.org/10.1016/j.matchemphys.2018.03.032>
5. Auerbach, S., Carrado, K., Dutta, P.: *Handbook of zeolite science and technology* (2003)
6. Baerlocher, C., McCusker, L.B., Olson, D.H.: *Atlas of Zeolite Framework Types*. Elsevier (2007)
7. Barrer, R.M.: Zeolites and Their Synthesis. *Zeolite* **1**, 130–140 (1981). [https://doi.org/10.1016/S0144-2449\(81\)80001-2](https://doi.org/10.1016/S0144-2449(81)80001-2)
8. Bayati, B., Babaluo, A.A., Karimi, R.: Hydrothermal synthesis of nanostructure NaA zeolite: the effect of synthesis parameters on zeolite seed size and crystallinity. *J. Eur. Ceram. Soc.* **28**, 2653–2657 (2008). <https://doi.org/10.1016/j.jeurceramsoc.2008.03.033>
9. Bo, W., Hongzhu, M.: Factors affecting the synthesis of microsized NaY zeolite. *Microporous Mesoporous Mater.* **25**, 131–136 (1998). [https://doi.org/10.1016/S1387-1811\(98\)00195-4](https://doi.org/10.1016/S1387-1811(98)00195-4)
10. Breck, D.W.: *Zeolite Molecular Sieves: Structure, Chemistry, and Use*, 1st ed. Wiley, New York (1974)
11. Burkett, S.L., Sims, S.D., Mann, S.: Synthesis of hybrid inorganic–organic mesoporous silica by co condensation of siloxane and organosiloxane precursors. *Chem. Commun.* 1367–1368 (1996)
12. Burton, A.W., Zones, S.I.: Organic molecules in zeolite synthesis: their preparation and structure-directing effects. *Stud. Surf. Sci. Catal.* **168**, 137–179 (2007). [https://doi.org/10.1016/S0167-2991\(07\)80793-2](https://doi.org/10.1016/S0167-2991(07)80793-2)
13. Casci, J.L., Lowe, B.M., Whitam, T.V.: Zeolite EU-1, p. 42226. *Eur. Pat. Appl* (1981)
14. Chatelain, T., Patarin, J., Fousson, E., Soulard, M., Guth, J.L., Schulz, P.: Synthesis and characterization of high-silica zeolite RHO prepared in the presence of 18-crown-6 ether as organic template. *Microporous Mater.* **4**(2–3), 231–238 (1995). [https://doi.org/10.1016/0927-6513\(95\)00009-X](https://doi.org/10.1016/0927-6513(95)00009-X)
15. Cheng, J., Zhang, Z., Zhang, X., Liu, J., Zhou, J., Cen, K.: Hydrodeoxygenation and hydrocracking of microalgae biodiesel to produce jet biofuel over H3PW12O40-Ni/hierarchical mesoporous zeolite Y catalyst. *Fuel* **245**, 384–391 (2019). <https://doi.org/10.1016/j.fuel.2019.02.062>
16. Cho, K., Cho, H.S., de Ménorval, L.C., Ryoo, R.: Generation of mesoporosity in LTA zeolites by organosilane surfactant for rapid molecular transport in catalytic application. *Chem. Mater.* **21**(23), 5664–5673 (2009). <https://doi.org/10.1021/cm902861y>
17. Choi, M., Lee, D.H., Na, K., Yu, B.W., Ryoo, R.: High catalytic activity of palladium (II)-exchanged mesoporous sodalite and NaA zeolite for bulky aryl coupling reactions: reusability under aerobic conditions. *Angew. Chem. Int. Ed.* **48**(20), 3673–3676 (2009). <https://doi.org/10.1002/ange.200806334>
18. Corma, A., Gómez, V., Martínez, A.: Zeolite beta as a catalyst for alkylation of isobutane with 2-butene. Influence of synthesis conditions and process variables. *Appl. Catal A Gen.* **119**, 83–96 (1994). [https://doi.org/10.1016/0926-860X\(94\)85026-7](https://doi.org/10.1016/0926-860X(94)85026-7)
19. Corma, A., Puche, M., Rey, F., Sankar, G., Teat, S.J.: A zeolite structure (ITQ-13) with three sets of medium-pore crossing channels formed by 9- and 10-Rings. *Angew. Chem. Int. Ed.* **42**(10), 1156–1159 (2003). <https://doi.org/10.1002/anie.200390304>
20. Cundy, Colin S., Cox, Paul A.: The hydrothermal synthesis of zeolites: history and development from the earliest days to the present time. *Chem. Rev.* **103**, 663–702 (2003). <https://doi.org/10.1021/cr020060i>

21. Dik, P.P., Danilova, I.G., Golubev, I.S., Kazakov, M.O., Nadeina, K.A., Budukva, S.V., Pereyma, V.Y., Klimov, O.V., Prosvirin, I.P., Gerasimov, E.Y., Bok, T.O., Dobryakova, I. V., Knyazeva, E.E., Ivanova, I.I., Noskov, A.S.: Hydrocracking of vacuum gas oil over NiMo/zeolite-Al₂O₃: in fluence of zeolite properties. *Fuel* **237**, 178–190 (2019). <https://doi.org/10.1016/j.fuel.2018.10.012>
22. Dong, C., Yin, C., Wu, T., Wu, Z., Liu, D., Liu, C.: Effect of β -zeolite nanoclusters on the acidity and hydrodesulfurization activity of an unsupported Ni-Mo catalyst. *Catal. Commun.* **119**, 164–169 (2019). <https://doi.org/10.1016/j.catcom.2018.11.002>
23. Du, L., Ding, S., Li, Z., Lv, E., Lu, J., Ding, J.: Transesterification of castor oil to biodiesel using NaY zeolite-supported La₂O₃ catalysts. *Energy Convers. Manag.* **173**, 728–734 (2018). <https://doi.org/10.1016/j.enconman.2018.07.053>
24. Emori, E.Y., Hirashima, F.H., Zandonai, C.H., Ortiz-bravo, C.A., Fernandes-machado, N.R. C., Olsen-scaliante, M.H.N.: Catalytic cracking of soybean oil using ZSM5 zeolite. *Catal. Today* **279**, 168–176 (2017). <https://doi.org/10.1016/j.cattod.2016.05.052>
25. Enzweiler, H., Yassue-cordeiro, P.H., Schwaab, M., Barbosa-coutinho, E., Scaliante, M.H. N.O., Fernandes, N.R.C.: Evaluation of Pd-TiO₂/ZSM-5 catalysts composition effects on hydrogen production by photocatalytic water splitting. *Int. J. Hydrogen Energy* **3**, 6515–6525 (2018). <https://doi.org/10.1016/j.ijhydene.2018.02.077>
26. Fajula, F., Vera-Pacheco, M., Figueras, F.: Synthesis of zeolite omega. Influence of the temperature and the reagents on the crystallization kinetics. *Zeolites* **7**, 203–208 (1987). [https://doi.org/10.1016/0144-2449\(87\)90051-0](https://doi.org/10.1016/0144-2449(87)90051-0)
27. Feijen, E.J.P., Martens, J.A., Jacobs, P.A.: Zeolites and their mechanism of synthesis. *Stud. Surf. Sci. Catal.* **84**, 3–21 (1994). [https://doi.org/10.1016/S0167-2991\(08\)64074-4](https://doi.org/10.1016/S0167-2991(08)64074-4)
28. Ferreira, C., Araujo, A., Calvino-Casilda, V., Cutrufello, M.G., Rombi, E., Fonseca, A.M., Bañares, M.A., Neves, I.C.: Y zeolite-supported niobium pentoxide catalysts for the glycerol acetalization reaction. *Microp. Mesop. Mat.* **271**, 243–251 (2018). <https://doi.org/10.1016/j.micromeso.2018.06.010>
29. Gábová, V., Dědeček, J., Čejka, J.: Control of Al distribution in ZSM-5 by conditions of zeolite synthesis. *Chem. Commun.* **3**, 1196–1197 (2003). <https://doi.org/10.1039/b301634j>
30. Galeano, Y.M., Negri, F., Moreno, M.S., Múnera, J., Cornaglia, L., Tarditi, A.M.: Pt encapsulated into NaA zeolite as catalyst for the WGS reaction. *Appl. Catal. A, Gen.* **572**, 176–184 (2019). <https://doi.org/10.1016/j.apcata.2018.12.034>
31. Gao, S., Zhu, X., Li, X., Wang, Y., Xie, S., Du, S., Chen, F., Zeng, P., Liu, S., Xu, L.: Direct amination of isobutylene over zeolite catalysts with various topologies and acidities. *J. Energy Chem.* **26**, 776–782 (2017). <https://doi.org/10.1016/j.jechem.2017.03.018>
32. Garcia, G., Cardenas, E., Cabrera, S., Hedlund, J., Mouzon, J.: Synthesis of zeolite y from diatomite as silica source. *Microporous Mesoporous Mater.* **219**, 29–37 (2016). <https://doi.org/10.1016/j.micromeso.2015.07.015>
33. Giannetto Pace, G., Rendón, A.M., Fuentes, G.R.: Zeolitas: Características, propiedades y aplicaciones industriales, 2a ed. Venezuela. Edditorial Innovación Tecnológica—Facultad de Ingeniería, UCV (2000)
34. Graça, I., Iruretagoyena, D., Chadwick, D.: Glucose isomerisation into fructose over magnesium-impregnated NaY zeolite catalysts. *Appl. Catal. B Environ.* **206**, 434–443 (2017). <https://doi.org/10.1016/j.apcatb.2017.01.037>
35. Groen, J.C., Sano, T., Moulijn, J.A., Pérez-Ramírez, J.: Alkaline-mediated mesoporous mordenite zeolites for acid-catalyzed conversions. *J. Catal.* **251**(1), 21–27 (2007)
36. Herreros, B., Klinowski, J.: Influence of the source of silicon and aluminium in the hydrothermal synthesis of sodalite. *J. Chem. Soc., Faraday Trans.* **91**, 1147–1154 (1995). <https://doi.org/10.1039/FT9959101147>
37. Huang, A., Caro, J.: Preparation of large and well-shaped LTA-type AlPO₄ crystals by using crown ether Kryptofix 222 as structure directing agent. *Microporous Mesoporous Mater.* **129** (1–2), 90–99 (2010). <https://doi.org/10.1016/j.micromeso.2009.09.002>

38. Inayat, A., Knoke, I., Spiecker, E., Schwieger, W.: Assemblies of mesoporous FAU-type zeolite nanosheets. *Angew. Chem. Int. Ed.* **51**(8), 1962–1965 (2012). <https://doi.org/10.1002/anie.201105738>
39. Ismail, A.A., Mohamed, R.M., Fouad, O.A., Ibrahim, I.A.: Synthesis of nanosized ZSM-5 using different alumina sources. *Cryst. Res. Technol.* **41**, 145–149 (2006). <https://doi.org/10.1002/crat.200510546>
40. Iyoki, K., Itabashi, K., Okubo, T.: Progress in seed-assisted synthesis of zeolites without using organic structure-directing agents. *Microporous Mesoporous Mater.* **189**, 22–30 (2014). <https://doi.org/10.1016/j.micromeso.2013.08.008>
41. Jacobs, P.A.: Some thermodynamic and kinetic effects related to zeolite crystallization. In: *Zeolite Microporous Solids: Synthesis, Structure, and Reactivity*, pp. 3–18. Springer, Dordrecht (1992). <https://doi.org/10.1007/978-94-011-2604-5>
42. Johnson, E.B.G., Arshad, S.E.: Hydrothermally synthesized zeolites based on kaolinite: a review. *Appl. Clay Sci.* **97–98**, 215–221 (2014). <https://doi.org/10.1016/j.clay.2014.06.005>
43. Kazakov, M.O., Nadeina, K.A., Danilova, I.G., Dik, P.P., Klimov, O.V., Pereyma, V.Y., Paukshtis, E.A., Golubev, I.S., Prosvirin, I.P., Gerasimov, E.Y., Dobryakova, I.V., Knyazeva, E.E., Ivanova, I.I., Noskov, A.S.: Influence of USY zeolite recrystallization on physicochemical properties and catalytic performance of NiMo/USY-Al₂O₃ hydrocracking catalysts. *Catal. Today* **329**, 108–115 (2019). <https://doi.org/10.1016/j.cattod.2019.01.003>
44. Kerr, G.T.: Chemistry of crystalline aluminosilicates. I. Factors Affecting the Formation of Zeolite A. *J. Phys. Chem.* **70**(4), 1047–1050 (1966). <https://doi.org/10.1021/j100876a015>
45. Kim, J., Heo, S., Choi, J.W.: Effects of phenolic hydroxyl functionality on lignin pyrolysis over zeolite catalyst. *Fuel* **232**, 81–89 (2018). <https://doi.org/10.1016/j.fuel.2018.05.133>
46. Kirschhock, C.E., Feijen, E.J., Jacobs, P.A., Martens, A.: Handbook of heterogeneous catalysis. In: Ertl, G., Knözinger, H., Schüth, F., Weitkamp J. (eds.) pp. 160–78 (2008)
47. Kong, L., Liu, C., Gao, J., Wang, Y., Dai, L.: Efficient and controllable alcoholysis of Kraft lignin catalyzed by porous zeolite-supported nickel-copper catalyst. *Bioresour. Technol.* **276**, 310–317 (2019). <https://doi.org/10.1016/j.biortech.2019.01.015>
48. Kulprathipanja, S.: *Zeolites in Industrial Separation and Catalysis*. Wiley-VCH Verlag GmbH & Co. KGaA, Weinheim, Germany (2010)
49. Le, T.X.H., Drobek, M., Bechelany, M., Motuzas, J., Julbe, A., Cretin, M.: Application of Fe-MFI zeolite catalyst in heterogeneous electro-Fenton process for water pollutants abatement. *Microporous Mesoporous Mater.* **278**, 64–69 (2019). <https://doi.org/10.1016/j.micromeso.2018.11.021>
50. Le, S.D., Nishimura, S., Ebitani, K.: Direct esterification of succinic acid with phenol using zeolite beta catalyst. *Catal. Commun.* **122**, 20–23 (2019). <https://doi.org/10.1016/j.catcom.2019.01.006>
51. Lee, S., Jo, C., Park, H., Kim, J., Ryoo, R.: Sulfonium-based organic structure-directing agents for microporous aluminophosphate synthesis. *Microporous Mesoporous Mater.* **280**, 75–81 (2019). <https://doi.org/10.1016/j.micromeso.2019.01.048>
52. Lee, K., Kosaka, H., Sato, S., Yokoi, T., Choi, B., Kim, D.: Effects of Cu loading and zeolite topology on the selective catalytic reduction with C₃H₆ over Cu/zeolite catalysts. *J. Ind. Eng. Chem.* **72**, 73–86 (2019). <https://doi.org/10.1016/j.jiec.2018.12.005>
53. Li, J., Corma, A., Yu, J.: Synthesis of new zeolite structures. *Chem. Soc. Rev.* **44**(20), 7112–7127 (2015). <https://doi.org/10.1039/C5CS00023H>
54. Li, Z., Ding, S., Chen, C., Qu, S., Du, L., Lu, J., Ding, J.: Recyclable Li/NaY zeolite as a heterogeneous alkaline catalyst for biodiesel production: Process optimization and kinetics study. *Energy Convers. Manag.* **192**, 335–345 (2019). <https://doi.org/10.1016/j.enconman.2019.04.053>
55. Li, S., Gounder, R., DeBellis, A.D., Muller, I.B., Prasad, S., Moini, A., Schneider, W.F.: Influence of N, N, N-trimethyl-1-adamantyl Ammonium Structure Directing Agent on Al Substitution in SSZ-13 Zeolite. *J. Phys. Chem. C* **123**(28), 17454–17458 (2019). <https://doi.org/10.1021/acs.jpcc.9b05334>

56. Li, H., Hou, B., Wang, J., Qin, C., Zhong, M., Huang, X., Jia, L., Li, Debao: Direct conversion of syngas to isoparaffins over hierarchical beta zeolite supported cobalt catalyst for Fischer-Tropsch synthesis. *Molec. Catal.* **459**, 106–112 (2018). <https://doi.org/10.1016/j.mcat.2018.08.002>
57. Liu, G., Tian, P., Li, J., Zhang, D., Zhou, F., Liu, Z.: Synthesis, characterization and catalytic properties of SAPO-34 synthesized using diethylamine as a template. *Microporous Mesoporous Mater.* **111**(1–3), 143–149 (2008). <https://doi.org/10.1016/j.micromeso.2007.07.023>
58. Liu, X.D., Wang, Y.P., Cui, X.M., He, Y., Mao, J.: Influence of synthesis parameters on NaA zeolite crystals. *Powder Technol.* **243**, 184–193 (2013). <https://doi.org/10.1016/j.powtec.2013.03.048>
59. Liu, J., Yu, J.: Toward greener and designed synthesis of zeolite materials. In: *Zeolites and Zeolite-Like Materials*, pp. 1–32. Elsevier (2016). <https://doi.org/10.1016/C2014-0-00257-2>
60. Lobo, R.F., Zones, S.I., Medrud, R.C.: Synthesis and Rietveld refinement of the small-pore zeolite SSZ-16. *Chem. Mater.* **8**(10), 2409–2411 (1996). <https://doi.org/10.1021/cm960289c>
61. Lok, B.M., Cannan, T., Messina, C.A.: The role of organic molecules in molecular sieve synthesis. *Zeolites* **3**(4), 282–291 (1983). [https://doi.org/10.1016/0144-2449\(83\)90169-0](https://doi.org/10.1016/0144-2449(83)90169-0)
62. Masoumifard, N., Guillet-Nicolas, R., Kleitz, F.: Synthesis of engineered zeolitic materials: from classical zeolites to hierarchical core-shell materials. *Adv. Mater.* **30**(16), 1704439 (2018). <https://doi.org/10.1002/adma.201704439>
63. Meise, W., Schwochow, F.E.: Kinetic studies on the formation of zeolite A. *Adv. Chem.* **121**, 169–178 (1973). <https://doi.org/10.1021/ba-1973-0121.ch014>
64. Mintova, S., Olson, N.H., Valtchev, V., Bein, T.: Mechanism of zeolite A nanocrystal growth from colloids at room temperature. *Science* **283**(5404), 958–960 (1999). <https://doi.org/10.1126/science.283.5404.958>
65. Mohamed, R.M., Aly, H.M., El-Shahat, M.F., Ibrahim, I.A.: Effect of the silica sources on the crystallinity of nanosized ZSM-5 zeolite. *Microp Mesop Mater.* **79**, 7–12 (2005). <https://doi.org/10.1016/j.micromeso.2004.10.031>
66. Mohamed, R.M., Fouad, O.A., Ismail, A.A., Ibrahim, I.A.: Influence of crystallization times on the synthesis of nanosized ZSM-5. *Mater. Lett.* **59**, 3441–3444 (2005). <https://doi.org/10.1016/j.matlet.2005.06.009>
67. Moliner, M., Martínez, C., Corma, A.: Multipore zeolites: synthesis and catalytic applications. *Angew. Chem. Int. Ed.* **54**(12), 3560–3579 (2015). <https://doi.org/10.1002/anie.201406344>
68. Moliner, M., Rey, F., Corma, A.: Towards the Rational Design of Efficient Organic Structure-Directing Agents for Zeolite Synthesis. *Angew. Chem. Int. Ed.* **52**(52), 13880–13889 (2013). <https://doi.org/10.1002/anie.201304713>
69. Oruji, S., Khoshbin, R., Karimzadeh, R.: Combination of precipitation and ultrasound irradiation methods for preparation of lanthanum-modified Y zeolite nano-catalysts used in catalytic cracking of bulky hydrocarbons. *Mater. Chem. Phys.* **230**, 131–144 (2019). <https://doi.org/10.1016/j.matchemphys.2019.03.038>
70. Paysepar, H., Tirumala, K., Rao, V., Yuan, Z., Nazari, L.: Zeolite catalysts screening for production of phenolic bio-oils with high contents of monomeric aromatics/phenolics from hydrolysis lignin via catalytic fast pyrolysis. *Fuel Process. Technol.* **178**, 362–370 (2018). <https://doi.org/10.1016/j.fuproc.2018.07.013>
71. Peng, H., Wang, A., He, P., Harry, J., Meng, S., Song, H.: Solvent-free catalytic conversion of xylose with methane to aromatics over Zn-Cr modified zeolite catalyst. *Fuel*, **253**, 988–996 (2019). <https://doi.org/10.1016/j.fuel.2019.05.088>
72. Perez-Ramirez, J., Christensen, C.H., Egeblad, K., Christensen, C.H., Groen, J.C.: Hierarchical zeolites: enhanced utilisation of microporous crystals in catalysis by advances in materials design. *Chem. Soc. Rev.* **37**(11), 2530–2542 (2008). <https://doi.org/10.1039/b809030k>

73. Prinsop, P., Luque, R., González-arellano, C.: Zeolite catalyzed palmitic acid esterification. *Microp Mesop Mater.* **262**, 133–139 (2018). <https://doi.org/10.1016/j.micromeso.2017.11.029>
74. Querol, X., Plana, F., Alastuey, A., López-Soler, A.: Synthesis of Na-zeolites from fly ash. *Fuel* **76**, 793–799 (1997). [https://doi.org/10.1016/s0016-2361\(96\)00188-3](https://doi.org/10.1016/s0016-2361(96)00188-3)
75. Ren, L., Zhu, L., Yang, C., Chen, Y., Sun, Q., Zhang, H.,... Xiao, F.S.: Designed copper–amine complex as an efficient template for one-pot synthesis of Cu-SSZ-13 zeolite with excellent activity for selective catalytic reduction of NO_x by NH₃. *Chem. Commun.* **47**(35), 9789–9791 (2011). <https://doi.org/10.1039/c1cc12469b>
76. Rimer, J.D., Kumar, M., Li, R., Lupulescu, A.I., Oleksiak, M.D.: Tailoring the physicochemical properties of zeolite catalysts. *Catal. Sci. Technol.* **4**(11), 3762–3771 (2014). <https://doi.org/10.1039/C4CY00858H>
77. Rimer, J.D., Tsapatsis, M.: Nucleation of open framework materials: navigating the voids. *MRS Bull* **41**(5), 393–398 (2016). <https://doi.org/10.1557/mrs.2016.89>
78. Sadek, R., Chalupka, K.A., Mierczynski, P., Rynkowski, J., Millot, Y., Valentin, L., Casale, S., Dzwigaj, S., 2019. Fischer-Tropsch reaction on Co-containing microporous and mesoporous Beta zeolite catalysts : the effect of porous size and acidity. *Catal. Today In press*, 0–1. <https://doi.org/10.1016/j.cattod.2019.05.004>
79. Saha, S.K., Waghmode, S.B., Maekawa, H., Komura, K., Kubota, Y., Sugi, Y., ... Sano, T.: Synthesis of aluminophosphate molecular sieves with AFI topology substituted by alkaline earth metal and their application to solid acid catalysis. *Microporous Mesoporous Mater.* **81** (1–3), 289–303 (2005). <https://doi.org/10.1016/j.micromeso.2005.02.009>
80. Sastre, G., Pulido, A., Castañeda, R., Corma, A.: Effect of the germanium incorporation in the synthesis of EU-1, ITQ-13, ITQ-22, and ITQ-24 zeolites. *J. Phys. Chem. B* **108**(26), 8830–8835 (2004). <https://doi.org/10.1021/jp0378438>
81. Schmidt, J.E., Xie, D., Davis, M.E.: Synthesis of the RTH-type layer: the first small-pore, two dimensional layered zeolite precursor. *Chem. Sci.* **6**(10), 5955–5963 (2015). <https://doi.org/10.1039/C5SC02325D>
82. Seo, Y., Lee, S., Jo, C., Ryoo, R.: Microporous aluminophosphate nanosheets and their nanomorphic zeolite analogues tailored by hierarchical structure-directing amines. *J. Am. Chem. Soc.* **135**(24), 8806–8809 (2013). <https://doi.org/10.1021/ja403580j>
83. Serrano, D.P., Pizarro, P.: Synthesis strategies in the search for hierarchical zeolites *Chem. Soc. Rev.* **42**(9), 4004–4035 (2013). <https://doi.org/10.1039/C2CS35330J>
84. Shin, J., Jo, D., Hong, S.B.: Rediscovery of the importance of inorganic synthesis parameters in the search for new zeolites. *Acc. Chem. Res.* **52**(5), 1419–1427 (2019). <https://doi.org/10.1021/acs.accounts.9b00073>
85. Silva, T.Q., Santos, M.B., Santiago, A.A.C., Santana, D.O., Cruz, F.T., Andrade, H.M.C., Mascarenhas, A.J.S.: Gas phase glycerol oxidative dehydration over bifunctional V/H-zeolite catalysts with different zeolite topologies. *Catal. Today* **289**, 38–46 (2017). <https://doi.org/10.1016/j.cattod.2016.08.011>
86. Tangestanifard, M., Ghaziaskar, H.S.: The Journal of Supercritical Fluids Methylation of toluene with methanol in sub/supercritical toluene using H-beta zeolite as catalyst. *J. Supercrit. Fluids* **113**, 80–88 (2016). <https://doi.org/10.1016/j.supflu.2016.03.013>
87. Tekin, R., Bac, N., Warzywoda, J., Sacco, A.: Effect of reaction mixture composition and silica source on size distribution of zeolite X crystals. *J. Cryst. Growth* **411**, 45–48 (2015). <https://doi.org/10.1016/j.jcrysgro.2014.11.017>
88. Tong, Y., Chen, L., Ning, S., Tong, N., Zhang, Z., Lin, H., Li, F., Wang, X.: Photocatalytic Reduction of CO₂ to CO over the Ti-highly dispersed HZSM-5 Zeolite Containing Fe. *Appl. Catal B, Environ.* **203**, 725–730 (2016). <https://doi.org/10.1016/j.apcatb.2016.10.065>
89. Twu, J., Dutta, P.K., Kresge, C.T.: Raman spectroscopic studies of the synthesis of faujasitic zeolites: comparison of two silica sources. *Zeolites* **11**, 672–679 (1991). [https://doi.org/10.1016/S0144-2449\(05\)80170-8](https://doi.org/10.1016/S0144-2449(05)80170-8)

90. Uslamin, E.A., Luna-murillo, B., Kosinov, N., Bruijninx, P.C.A., Pidko, E.A., Weckhuysen, B.M., Hensen, E.J.M.: Gallium-promoted HZSM-5 zeolites as efficient catalysts for the aromatization of biomass-derived furans. *Chem. Eng. Sci.* **198**, 305–316 (2019). <https://doi.org/10.1016/j.ces.2018.09.023>
91. Van Bekkum, H., Flanigen, E.M., Jacobs, P.A., Jansen, P.A.: *Reaction Kinetics & Catalysis Letters Studies in Surface Science and Catalysis*, vol. 137, 2nd edn. Introduction to Zeolite Science and Practice (2001)
92. Van Bekkum, H., Flanigen, E.M., Jacobs, P.A., Jansen, J.C.J.: *Introduction to Zeolite Science and Practice*. 2ed, Elsevier (2001)
93. Vieira, L.H., Rodrigues, M.V., Martins, L.: Conventional zeolite and seed-induced crystallization. *Quím. Nova*, 1515–1524 (2014). <http://dx.doi.org/10.5935/0100-4042.20140229>
94. Wei, Y., Parmentier, T.E., de Jong, K.P., Zečević, J.: Tailoring and visualizing the pore architecture of hierarchical zeolites. *Chem. Soc. Rev.* **44**(20), 7234–7261 (2015). <https://doi.org/10.1039/C5CS00155B>
95. Wen, C., Wang, C., Chen, L., Zhang, X., Liu, Q.: Effect of hierarchical ZSM-5 zeolite support on direct transformation from syngas to aromatics over the iron-based catalyst. *Fuel* **244**, 492–498 (2019). <https://doi.org/10.1016/j.fuel.2019.02.041>
96. Wiersema, G.S., Thompson, R.W.: Nucleation and crystal growth of analcime from clear aluminosilicate solutions. *J. Mater. Chem.* **6**, 1693–1699 (1996). <https://doi.org/10.1039/jm9960601693>
97. Winoto, H.P., Fikri, Z.A., Ha, J., Park, Y., Lee, H., Suh, D., Jae, J.: Heteropolyacid supported on Zr-Beta zeolite as an active catalyst for one-pot transformation of furfural to γ -valerolactone. *Appl. Catal. B Environ.* **241**, 588–597 (2019). <https://doi.org/10.1016/j.apcatb.2018.09.031>
98. Wuamprakhon, P., Wattanakit, C., Warakulwit, C., Yuthalekha, T., Wannapakdee, W., Ittisanronnachai, S., Limtrakul, J.: Direct synthesis of hierarchical ferrierite nanosheet assemblies via an organosilane template approach and determination of their catalytic activity. *Micropor. Mesopor. Mat.* **219**, 1–9 (2016)
99. Xing, X., Li, N., Sun, Y., Wang, G., Cheng, J., Hao, Z.: Selective catalytic oxidation of n-butylamine over Cu-zeolite catalysts. *Catal. Today* In press, 1–8 (2019). <https://doi.org/10.1016/j.cattod.2018.12.001>
100. Xu, X., Jiang, E., Li, Z., Sun, Y.: BTX from anisole by hydrodeoxygenation and transalkylation at ambient pressure with zeolite catalysts. *Fuel* **221**, 440–446 (2018). <https://doi.org/10.1016/j.fuel.2018.01.033>
101. Xu, X.T., Zhai, J.P., Chen, Y.P., Li, I.L., Chen, H.Y., Ruan, S.C., Tang, Z.K.: Synthesis of large single crystals of AlPO-LTA by using n-Propylamine as structure directing agent. *J. Cryst. Growth* **407**, 1–5 (2014). <https://doi.org/10.1016/j.jcrysgro.2014.08.024>
102. Xu, X.T., Zhai, J.P., Chen, Y.P., Li, I.L., Ruan, S.C., Tang, Z.K.: Synthesis of large optically clear SAPO-47 single crystals using n-propylamine as template. *J. Cryst. Growth* **426**, 123–128 (2015). <https://doi.org/10.1016/j.jcrysgro.2015.05.029>
103. Xu, S., Zhang, L., Xiao, K., Xia, H.: Isomerization of glucose into fructose by environmentally friendly Fe/b zeolite catalysts. *Carbohydr. Res.* **446–447**, 48–51 (2017). <https://doi.org/10.1016/j.carres.2017.05.006>
104. Xu, G., Zhu, X., Li, X., Xie, S., Liu, S., Xu, L.: Synthesis of pure silica ITQ-13 zeolite using fumed silica as silica source. *Microporous Mesoporous Mater.* **129**, 278–284 (2010). <https://doi.org/10.1016/j.micromeso.2009.10.005>
105. Yang, X., Cheng, X., Elzatahry, A.A., Chen, J., Alghamdi, A., Deng, Y.: Recyclable Fenton-like catalyst based on zeolite Y supported ultrafine, highly-dispersed Fe₂O₃ nanoparticles for removal of organics under mild conditions. *Chinese Chem. Lett.* **30**, 324–330 (2019). <https://doi.org/10.1016/j.ccllet.2018.06.026>
106. Yao, D., Yang, H., Chen, H., Williams, P.T.: Investigation of nickel-impregnated zeolite catalysts for hydrogen/syngas production from the catalytic reforming of waste polyethylene. *Appl. Catal. B Environ.* **227**, 477–487 (2018). <https://doi.org/10.1016/j.apcatb.2018.01.050>

107. Yashnik, S.A., Urzhuntsev, G.A., Stadnichenko, A.I., Svintsitskiy, D.A., Ishchenko, A.V., Boronin, A.I., Ismagilov, Z.R.: Effect of Pd-precursor and support acid properties on the Pd electronic state and the hydrodesulfurization activity of Pd-zeolite catalysts. *Catal. Today* **323**, 257–270 (2019). <https://doi.org/10.1016/j.cattod.2018.07.058>
108. Yoshikawa, T., Umezawa, T., Nakasaka, Y., Masuda, T.: Conversion of alkylphenol to phenol via transalkylation using zeolite catalysts. *Today In Press, Catal* (2019). <https://doi.org/10.1016/j.cattod.2018.08.009>
109. Yu, J., Xu, R.: Insight into the construction of open-framework aluminophosphates *Chem. Soc. Rev.* **35**(7), 593–604 (2006). <https://doi.org/10.1039/B505856M>
110. Yutthalekha, T., Wattanakit, C., Warakulwit, C.: Hierarchical FAU-type zeolite nanosheets as green and sustainable catalysts for benzylolation of toluene. *J. Clean. Prod.* **142**, 1244–1251 (2017). <https://doi.org/10.1016/j.jclepro.2016.08.001>
111. Zhang, Z., Cheng, J., Qiu, Y., Zhang, X., Zhou, J., Cen, K.: Competitive conversion pathways of methyl palmitate to produce jet biofuel over Ni/desilicated meso-Y zeolite catalyst. *Fuel* **244**, 472–478 (2019). <https://doi.org/10.1016/j.fuel.2019.02.036>
112. Zhang, C., Liu, Q., Xu, Z., Wan, K.: Synthesis and characterization of composite molecular sieves with mesoporous and microporous structure from ZSM-5 zeolites by heat treatment. *Microp Mesop Mat* **62**(3), 157–163 (2003). [https://doi.org/10.1016/S1387-1811\(03\)00427-X](https://doi.org/10.1016/S1387-1811(03)00427-X)
113. Zhang, X., Tang, D., Zhang, M., Yang, R.: Synthesis of NaX zeolite: Influence of crystallization time, temperature and batch molar ratio $\text{SiO}_2/\text{Al}_2\text{O}_3$ on the particulate properties of zeolite crystals. *Powder Technol.* **235**, 322–328 (2013). <https://doi.org/10.1016/j.powtec.2012.10.046>
114. Zhou, W., Zhou, A., Zhang, Y., Zhang, C., Chen, Z., Liu, L., Zhou, Y., Wei, Q., Tao, X.: Hydrodesulfurization of 4,6-dimethyldibenzothiophene over NiMo supported on Ga-modified Y zeolites catalysts. *J. Catal.* **374**, 345–359 (2019). <https://doi.org/10.1016/j.jcat.2019.05.013>
115. Zion Research : Zeolite (Natural and Synthetic) Market for Catalysts, adsorbents, Detergent Builders and Other Applications, Global Industry Perspective, Comprehensive Analysis, Size, Share, Growth, Segment, Trends and Forecast 2020. Acessado em 01 de setembro de 2019 (2015). <https://www.marketresearchstore.com/news/global-zeolite-market-140>

Design and Applications of Spherical Infinite Coordination Polymers (ICPS)



Guilherme Arroyos, Caroline M. da Silva and Regina C. G. Frem

Abstract Since Alfred Werner published his work on coordination compounds in 1893, much progress has been made regarding this class of materials. Further studies evolved to the coordination polymers, among which the Metal-Organic Frameworks (MOFs), which are two- or three-dimensional coordination networks containing potentially empty cavities. Frequently, MOFs are crystalline materials with the coordination units repeating itself in an ordered manner in the structure, thus creating different topologies. However, synthetic parameters (pH, temperature, solvent) directly influence the kinetics and thermodynamics of the nucleation and growth of MOF crystals. In some cases, a material of low crystallinity may be formed, with short-range order. Most authors classify these compounds as Infinite Coordination Polymers (ICPs), Coordination Polymer Particles (CPPs) or Nanoscale Coordination Polymers (NCPs). Although not yet standardized by IUPAC, several articles, including recent review articles, name low-crystalline coordination polymers as ICPs. ICPs can show high tailorability regarding the particle size and morphology. They are usually obtained as micro- or nanoparticles, with spherical (mainly), cubic, rod-like and ring-like morphologies being reported. The major challenge in the study of ICPs lies in the structural elucidation, often performed by single crystal X-ray diffraction in crystalline MOFs. In this chapter, the synthetic routes, formation mechanisms, characterization techniques and potential applications of spherical ICP particles, such as in sensing, light-emitting devices, biomedicine, catalysis, gas sorption and separation, will be discussed.

Keywords Infinite coordination polymers · Metal-Organic frameworks · Spherical morphology · Coordination chemistry · Transition and lanthanide metal ions · Multitopic organic ligands

G. Arroyos (✉) · C. M. da Silva · R. C. G. Frem
Institute of Chemistry, São Paulo State University, UNESP,
PO Box 355, Araraquara, SP 14800-060, Brazil
e-mail: guiarroyos@gmail.com

© Springer Nature Switzerland AG 2020
F. A. La Porta and C. A. Taft (eds.), *Emerging Research in Science and Engineering Based on Advanced Experimental and Computational Strategies*, Engineering Materials, https://doi.org/10.1007/978-3-030-31403-3_15

391

1 Introduction

The coordination polymers are compounds essentially constructed by the interaction between metallic ions or clusters and organic multitopic bridging ligands [1]. The study of Metal-Organic Frameworks (MOFs), a special class of coordination polymers, has become a rising research topic since Professor Omar Yaghi's publication about reticular chemistry for framework design [2, 3]. IUPAC defines MOFs as two- or three-dimensional coordination networks containing potentially empty cavities [4]. Research in MOF area is of high scientific relevance, with several articles and books published and almost 70,000 structures indexed in the CSD (Cambridge Structure Database) until 2017 [5]. Being an area in the frontier of inorganic chemistry and solid-state chemistry, it has soon attracted scientists' attention due to different possible combinations between metals and organic linkers. These combinations can result in materials with several distinct properties, such as permanent porosity, high surface area, high thermal stability and multiple possibilities of functionalization [6].

MOFs usually shows high structural organization, thus showing crystallinity [7]. The metal ions or clusters and bridging organic ligands are named Secondary Building Units (SBUs), which build the structure of the MOF and form the crystal lattice [8]. These coordination units repeat itself in an ordered manner in the structure, creating different topologies. The formation of a MOF particle usually is thermodynamically favorable due to the equal distribution of repulsive forces in the crystal. A typical formation mechanism of a MOF involves coordinative self-assembly between metallic ions or clusters and linkers, originating the first crystal nuclei that later grow into larger crystallites [9]. However, the crystallization process can be arrested in early stages, resulting in amorphous phases in the material [10]. This process can be done via modification of some synthetic parameters, such as solvent type, pH, time, temperature and heat source. The amorphous coordination polymers' nomenclature is not yet standardized. It is somewhat confusing and a misnomer to refer to these structures as MOFs, since they lack crystallinity and therefore a well-defined framework. Mirkin et al. refers to these materials as Infinite Coordination Polymers (ICPs) [11], while other authors refers them as Coordination Polymer Particles (CPPs) [12–14], Nanoscale Coordination Polymers (NCPs) [15–17] or even as MOFs [18]. Due to the amorphous nature, ICP particles can exhibit different particle morphologies, such as spheres (most common), hollow-spheres, wheels, rods, etc. This is a key difference between MOFs and ICPs: MOFs' particles are usually faceted due to the crystal habits [19]. Figure 1 shows scanning electron microscopy (SEM) and transmission electron microscopy (TEM) images of some representative spherical ICP particles.

It is worth mentioning that the so-called "amorphous MOFs" are different compounds from ICPs, since they only lose their crystallinity after exposure to mechanical or thermal stress conditions. In a ball mill, for example, the mechanical pressure can cause the loss of crystallinity of the MOF, while ICPs have intrinsic low crystallinity [24]. The applications for ICPs are usually in the same fields as

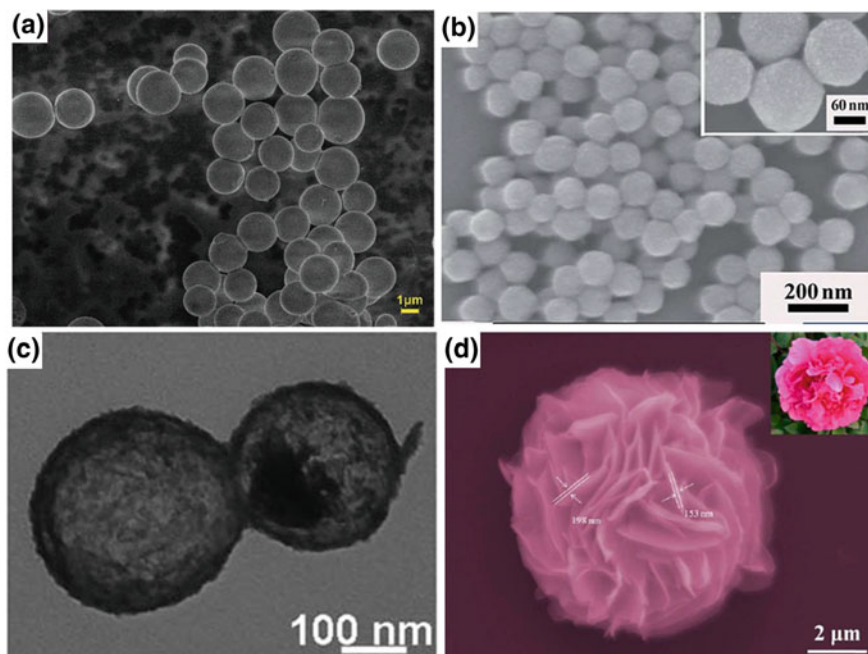


Fig. 1 Spherical ICP particle micrographs. **a** Smooth microspheres [20]; **b** nanospheres [21]; **c** hollow nanospheres [22]; **d** flower-like particle [23]. Adapted and reprinted with permission from *The Royal Society of Chemistry*

MOFs: sensing [21, 25–27], light-emitting devices [20, 22], biomedicine [16, 27, 28], drug delivery [15, 29] and to a lesser extent, catalysis [30], gas storage and separation [31, 32]. ICP particles are usually obtained as nano- or microspheres, which are easily dispersed in solvents for applications where bulk MOF materials are not suited. Uniform nano- and microspheres also can have other potential applications such as templates for other materials [33, 34] or standards for calibrating equipment [35].

In this chapter, the focus will be on ICPs exhibiting spherical particle morphology. The synthetic routes, formation mechanisms, characterization techniques, properties studies and potential applications of ICPs will be discussed.

2 Mechanism of Spherical ICP Particle Formation

ICPs are mainly reported as amorphous nano- or microspheres. It is a general consensus between authors that the particles adopt a spherical morphology to minimize the interfacial free energy between the solvent and the surface of the particle [36, 37]. A challenge in studying ICP particles rather than MOFs is working

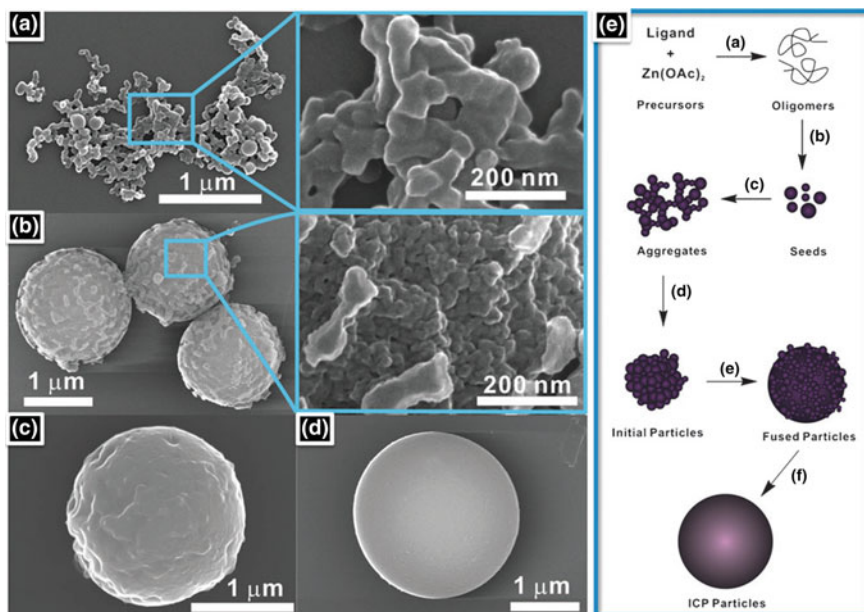


Fig. 2 A representative mechanism of spherical Zn-based particle formation based on a time-resolved SEM study. The photographs show the results after the process was interrupted at: **a** 5 min; **b** 10 min; **c** 30 min; **d** 40 min. **e** Shows the proposed mechanism of ICP particle formation. Reprinted with permission from The Royal Society of Chemistry

with amorphous rather than crystalline materials. Therefore, single crystal and powder X-ray diffraction techniques cannot be used to study the transformations that lead to the desired particles. One has to rely on other characterization techniques, such as scanning or transmission electronic microscopy, to understand how the atoms are organized. Figure 2 shows a time-resolved SEM study by Mirkin et al. on the mechanism of the formation of spherical Zn-based ICP particles [32].

In the precursor solution, the metallic ions and organic ligands bind together forming the first oligomers. These oligomers then combine producing seeds (nucleation process), which have well defined crystallographic planes. The surfaces of the seeds probably contain many unreacted sites for further polymerization, allowing rapid fusion and growth via coordination chemistry. The first steps are relatively fast at high concentrations of ligand and metal ion. The seeds produced can reduce the surface tension through agglomeration in the presence of the solvent. The concentration of ligands and metal ions decrease overtime as well the nucleation of new particles. The growth and fusion of existing nuclei become dominant, resulting in spherical ICP particles with smooth surfaces. However, the fusion of seeds is not organized, meaning that the aggregates contain different orientated crystallographic planes in random directions (high entropy). With a TEM study, Yin et al. could observe different nanoscale “crystal islands” on the surface of Gd-based ICP nanospheres, as shown in Fig. 3. The random orientations of

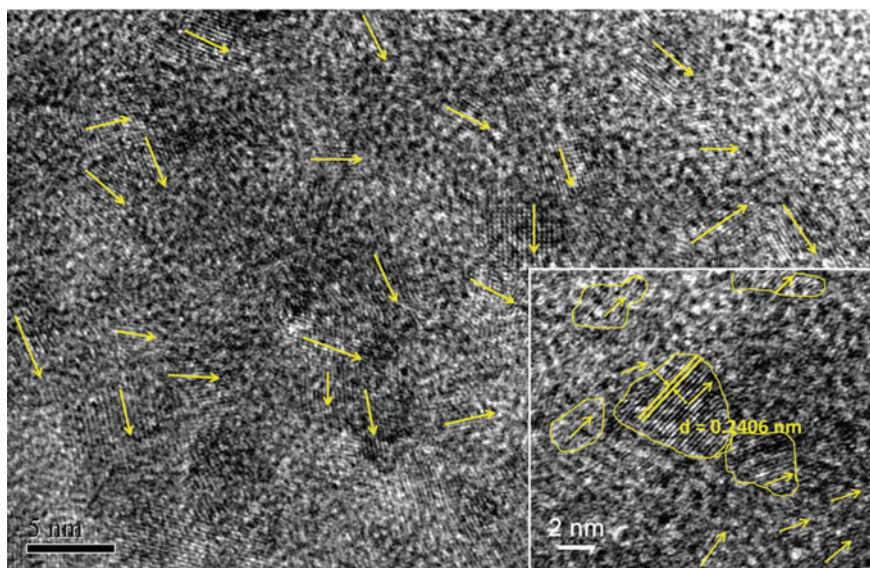


Fig. 3 High-resolution TEM image of an ICP nanosphere; lattice fringes are highlighted in yellow. Adapted and reprinted with permission from [28]

crystallographic planes explain the amorphous phases observed in powder X-ray diffraction (see Fig. 5).

Spherical and amorphous ICP particles are more frequently reported when using lanthanide(III) (Ln-ICPs) as metallic centers rather than transition metals. Yin et al. also proposed a self-limiting growth mechanism for the Gd-based ICP nanospheres. The ligand coordinates to the Ln^{3+} ions to form a crystal structure within a small region. The high coordination numbers limit the formation of large crystals. The crystal islands then connect to each other to form the ICP particle, meaning they do not grow epitaxially and form self-limited size and spherical structures, adopting this morphology to minimize the interfacial free energy between surfaces of particles and the solvent.

3 Synthesis of ICPs

Similar to MOFs, the reactants for ICPs are metal ions or clusters and bridging organic ligands dispersed in a solvent or solvent mixture. The synthesis of spherical ICPs involve two main reported procedures: direct precipitation at room temperature and heating through solvothermal or microwave-assisted synthesis.

Direct precipitation method. The direct precipitation method exploits the product particles' insolubility in a given solvent, usually at room temperature. The precipitation can also be induced by the addition of a poor solvent in the precursor

solution. Mirkin et al. reported one of the first spherical ICP particles in 2005 [11]. It was based on an organometallic ligand (carboxylate-functionalized binaphthyl bis-metallotridentate Schiff base) and zinc(II) acetate, using pyridine as solvent. After the addition of a non-polar solvent (diethyl ether or pentane), the spontaneous formation of the spherical inorganic polymer particles occurred through binding between carboxylate terminal groups of the ligand and the zinc(II) ion. The polymerization was reversible through the addition of excess pyridine. Diethyl ether or pentane addition to the polar precursor solution results in precipitation due to the low solubility of the particles in non-polar media. Slow diffusion of the non-polar solvents into the precursor solution resulted in micro-sized particles, while its rapid addition produced much smaller ICPs. These results were significant because they showed that growth processes could be arrested at an early stage of the reaction. At the same year, Wang et al. reported nanospheres constructed by mixing $\text{H}_2[\text{PtCl}_6]$ and *p*-phenylenediamine aqueous solutions [38]. The result of this mixture was monodisperse spheres of approximately 420 nm in diameter, taking advantage of the very low solubility of the product in water.

After these two initial reports, several other articles reported the growth of spherical ICP particles by direct precipitation [15, 17, 39–43]. Mirkin et al. synthesized spherical ICP microparticles using nickel(II) acetate and metallo-salen ligands as precursors, using the same strategy of slow diffusion of diethyl ether in pyridine starting solution [44]. After drying the solvents, the particles retained their spherical morphology, but converted into crystalline rods after the addition of methanol. By dissolving the rods into pyridine and diffusing diethyl ether, the process could be undone, producing the microspheres again, as can be seen in the SEM studies in Fig. 4. The major difference between the ICP spherical particles and

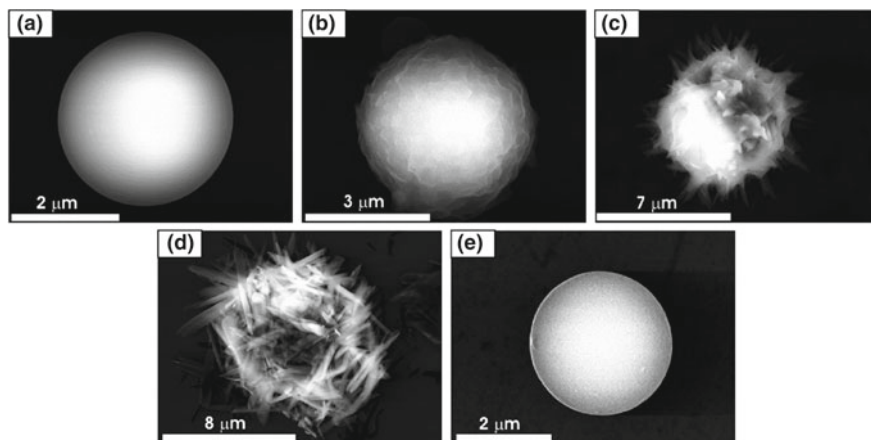


Fig. 4 Monitoring by SEM images the conversion of Ni^{2+} based ICP particles into crystalline rods. **a** Initial particle grown from precursor solution; **b** early intermediate after 5 min exposure to methanol; **c** intermediate at a later stage (30 min); **d** crystalline rods; **e** particle grown by first dissolving the crystalline rods with pyridine and then exposing to diethyl ether by vapor diffusion. Adapted and reprinted with permission from [44]

crystalline rods is the coordination of methanol to the nickel(II) ions in the crystal. The authors attributed this to be the driving force for the amorphous to crystalline transformation.

A newer strategy for direct precipitation is the use of spray technique to disperse small droplets of metal precursor on the surface of the ligand solution. By using this approach, Li et al. obtained monodisperse flower-like particles of Co^{2+} and Ni^{2+} with 1,4-benzenedicarboxylate ligand, as could be observed in Fig. 1d [23].

Solvothermal methods. One of the most common ways of synthesizing coordination polymers is heating the precursors and solvents mixture inside a sealed vial using an autoclave. Most reported spherical ICPs have been produced by using this method [22, 45–52]. The solvothermal synthesis can lead to either crystalline MOFs or amorphous ICPs depending on the reaction temperature and time, concentration of reactants, surfactant, solvent and pH values. Temperatures over 80 °C are usually required to give enough activation energy to start the coordination reactions and nucleation. For the production of amorphous ICPs, shorter synthesis times are required to prevent crystalline growth.

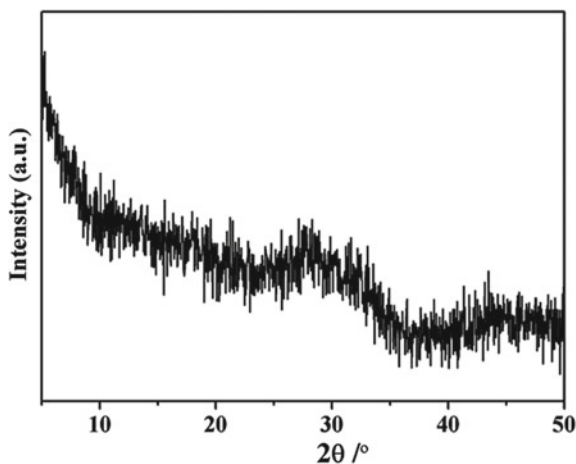
On a similar note, microwaves can also be used as a heating source when synthesizing ICPs. While microwave-assisted synthesis is a common way to produce nanoscale crystalline MOFs [53, 54], some amorphous ICPs are also reported. In microwave-assisted synthesis the heat is more evenly distributed through the reaction flask when compared to solvothermal technique. Shorter synthesis times are also commonly used, with reports of ICPs being synthesized in only 5 min [55]. The products are usually uniform in dimensions and composition. To our knowledge, only rare-earth based spherical ICPs have been produced by this method [20, 33, 36, 55].

4 Characterization and Property Studies of ICPs

Powder X-Ray Diffraction. The easiest way of differentiating crystalline MOFs from amorphous ICPs is by using powder X-ray diffraction. ICPs typically shows halos and noise in the diffractogram (see Fig. 5), similar to other amorphous materials such as glasses. In this case, the amorphous pattern appears due to the random orientated crystal islands, as explained above.

Powder X-ray diffraction cannot give structural information of amorphous ICPs. An approach used by Yin et al. was to synthesize a lanthanide(III)-based crystalline MOF with 1,3-terephthalic acid ligand, which is structurally similar to the 5-boronoisophthalic acid ligand used for the spherical Ln-ICP synthesis [18]. Single crystal X-ray diffraction could then be performed in the MOF, and since the structure and coordination modes of both ligands are similar, the authors could propose how the 5-boronoisophthalic acid ligand was coordinating the ions in the amorphous ICP.

Fig. 5 Typical PXRD pattern of amorphous ICPs. Adapted and reprinted with permission from [21]



Newer techniques such as pair distribution function (PDF-G(r)) can be used to ascertain the degree of local and intermediate ordering within amorphous solids, which is not possible using conventional X-ray technique, as can be seen in Fig. 6.

The top pattern (Fig. 6a) is from a crystalline sample, while the pattern in the middle (Fig. 6b) is from the same material in a disordered configuration after thermal and mechanical stress. Since there are fewer peaks, there are fewer information necessary to determine structure. PXRD patterns similar to that shown in Fig. 6b are considered as amorphous [56], even though this material (and many others that exhibit similar patterns) actually have short-range order and are nanocrystalline [24]. As noted by Bennett and Cheetham, the short-range order limit (Fig. 6c) is evidenced by the main peak in the PDF at 6 Å, which corresponds to the nearest neighbor Zn-Zn. To this date, however, this technique was not yet used to characterize ICPs.

FT-IR Spectroscopy. FT-IR spectroscopy can give information about the coordination of organic linkers to the metallic centers and about post-synthetic modifications. In many cases, it is used to confirm the formation of the final product. For example, Pan, Xu and Ni compared the FT-IR spectra of the organic linkers (4,4'-bipyridyl and 1,3,5-benzenetricarboxylic acid) and the microspheres particles obtained after coordination with Zn²⁺. The absence of the band $\nu_{\text{C}=\text{O}}$ of -COOH group was attributed to the deprotonation of carboxylic group. The presence of two peaks at 1616, 1606 cm⁻¹ and 1340, 1352 cm⁻¹ at the spectrum of the synthesized microspheres are associated to the stretching vibrations $\nu_{\text{as}}\text{COO}$ and $\nu_{\text{s}}\text{COO}$ of the carboxylated groups, which demonstrated the successful synthesis [40].

Thermogravimetric and Elemental Analysis. Thermogravimetric and elemental analysis are used for investigation of the components in the structure, thermal stability as well as stoichiometric ratio. As an example, Nie et al. reported the TG-DTG curves of Ce³⁺-microspheres doped with Yb³⁺ and Er³⁺, which exhibits three major stages of rapid weight loss in the temperature range from 20 to 800 °C

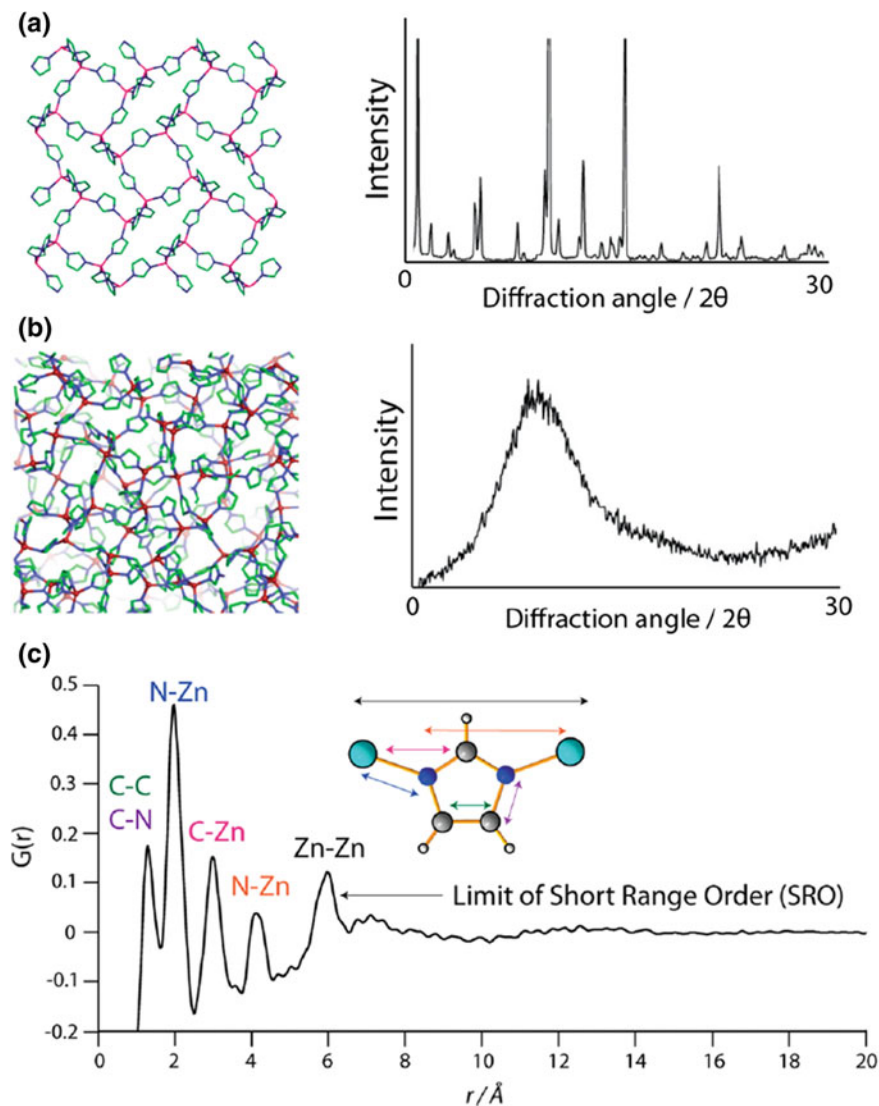


Fig. 6 PXRD patterns of the crystalline (a) and amorphous (b) phases of the MOF **ZIF-1** ($[\text{Zn}(\text{Imidazolate})_2]$) and pair distribution function $G(r)$ pattern of amorphous **ZIF-1** (c). Reprinted with permission from [24]

[49]. The first two weight losses below 327 °C can be attributed to the removal of the physically absorbed and structured water molecules with a mass loss of 22.8%. The latter weight loss from 327 to 582 °C is assigned to the decomposition of organic linker (2,5-pyridinedicarboxylic acid or 2,5- H_2PDC) with a mass loss of

40.9%. Above 582 °C, there is no weight loss, which indicated that the initial **Ce-ICP: Yb³⁺, Er³⁺** have been completely transformed to CeO₂: Yb³⁺, Er³⁺ after the heat treatment process. Elemental analysis results show that the percentage of C, H, N were 26.07%, 3.70% and 5.30%, respectively, giving a proposed formula of [RE₂(PDC)₃]·8H₂O (RE = Ce: Yb, Er).

Other characterization techniques. A complementary technique to elemental analysis is the inductively coupled plasma (ICP), mainly used for quantification of metals in coordination polymers. Zhong et al. used the ICP-OES analysis to find the terbium percentage in a Tb³⁺-based ICP. The CHN elemental analysis of the sample **Tb-BTB** (BTB = 4,4',4''-benzene-1,3,5-triyl-tri-benzonate) (%: C, 36.05; H, 2.77; N, 0.42) and the ICP-OES (Tb, 33.40%) allowed to propose the empirical formula of TbC₁₄H₁₃O₈N_{0.1} [22]. NMR spectroscopy can also be used for characterization studies. Zhang et al. measured solid-state ¹H NMR spectra to further identify the functional groups of **Eu-ICP** (terephthalic acid linker) nanospheres. The linker displayed two lines at chemical shifts of 8.07 and 13.30 ppm, which were attributed to the aromatic and acidic protons, respectively. In the case of **Eu-ICP**, there was only one broad peak at around 7.39 ppm, in which the disappearance of the peak assigned to the acidic protons indicated that the carboxylic acid had deprotonated [21]. The Dynamic Light Scattering (DLS) technique allows the study of average particle size, which is important depending on the application. DLS analysis was utilized by Nouri, Abedi and Morsali to characterize Zn-based ICPs with 1,3-bis(tetrazol-5-ylmethyl)benzene (btb) linker [30]. The studies show the influence of the initial metal and linker concentrations in the size of the obtained particles. The high concentration of the initial reagents leads to the formation of smaller **Zn(btb)** particle sizes compared to low concentrations. The DLS analysis confirm the average smaller size (96 nm) for high concentration (2.5 mol L⁻¹) and bigger size (667 nm) for low concentration (0.01 mol L⁻¹) of both metal and linker.

Gas Sorption. Similar to crystalline MOFs, ICPs usually exhibit micropores (<2 nm diameter) and ultramicropores (<0.7 nm diameter) [57]. However, the pore channels are not well organized due to the crystal island structure. This means that surface area calculated using BET method from 77 K N₂ sorption isotherms are usually similar to non-porous materials. For this reason, the most recommended method to use is CO₂, H₂ or Ar sorption, due to the smaller kinetic diameters and the temperature in the analysis (CO₂ sorption is usually done at 258 K, for example, diminishing the quadrupole interactions between the gas molecules and the pore windows). The highest surface area value reported for an amorphous ICP, to our knowledge, is 225 m²g⁻¹ (calculated from CO₂ sorption isotherm) for a Zn-based sphere [31], still much lower than classical MOFs. The calculated pore volumes are usually average values since the amorphous structure leads to the formation of different sized pores. Rare-earth based ICPs typically exhibits even lower values, due to the high coordination numbers and multiple geometries in the same structure closing the pore access [48].

Photoluminescence Spectroscopy. This technique is mainly used for studying luminescent lanthanide(III)-based ICPs, which can emit in the visible (400–750 nm), near infrared and infrared (750–1200 nm) regions of the electromagnetic

spectrum. It is possible to determine the excitation/emission wavelengths, excited state lifetime and quantum yield. As an example, Xu et al. reported a luminescence study of a terbium-based coordination polymer (**Tb-BTB**). Under 316 nm excitation, the emission spectrum exhibited terbium(III) $^5D_4 \rightarrow ^7F_J$ ($J = 6, 5, 4$ and 3) characteristic transition bands and luminescence lifetime equal to 53.02 μs [22].

5 Applications of ICPs

As previously highlighted, the potential applications for ICPs are similar to those reported for crystalline MOFs, with ICPs main advantage over MOFs being the high tailorability of morphology and size of the particles. Some applications, such as templating, rely on the morphology, while others take advantage of the higher dispersibility of ICPs in solvent media. Since most reported spherical ICPs are also rare-earth based materials, the most common applications harness their luminescent and magnetic properties [36].

5.1 Luminescent Sensors

One of the most reported applications for spherical ICPs is in luminescence-based sensors [25]. Compared to classical crystalline MOFs, micro- and nanosized ICPs displays higher dispersibility in solvent media, resulting in measurements that are more reliable. For Ln-ICPs, the luminescence is originated from $f-f$ transitions of lanthanide centers. The electrons from organic ligands can efficiently absorb the excitation radiation and transfer the energy to the lanthanide ion, which causes a population of higher energy electronic states (antenna effect) [58]. Analytes can perturb this process, thus causing a quenching or an enhancement in the luminescence intensity, or even a change in the emission color in doped samples. The quenching or enhancement of the emission intensity relationship to the analyte concentration can usually be described by using the linear Stern-Volmer's equation: $I_0/I = 1 + K_{sv} \cdot [A]$, in which I and I_0 correspond to the maximum emission intensity of the material at a specific wavelength in the presence and absence of the analyte, respectively; K_{sv} represents the quenching/enhancement rate constant, and $[A]$ is the analyte concentration. After calculating the linear fit, it is possible to create a calibration curve and determine the concentration of the analyte in other solutions. The main advantage of using luminescence-based sensors is the high sensitivity and low limits of detection (LOD) over other types of sensors. Examples of analytes and Ln-ICPs reported for their detection will be described below.

Oh et al. reported Eu^{3+} and Tb^{3+} -based ICPs for Cu^{2+} ion sensing in water [59]. The ICP spheres were grown as a shell over a silica core, mainly to reduce the amount of the sensing-active material used. The authors assigned the quenching

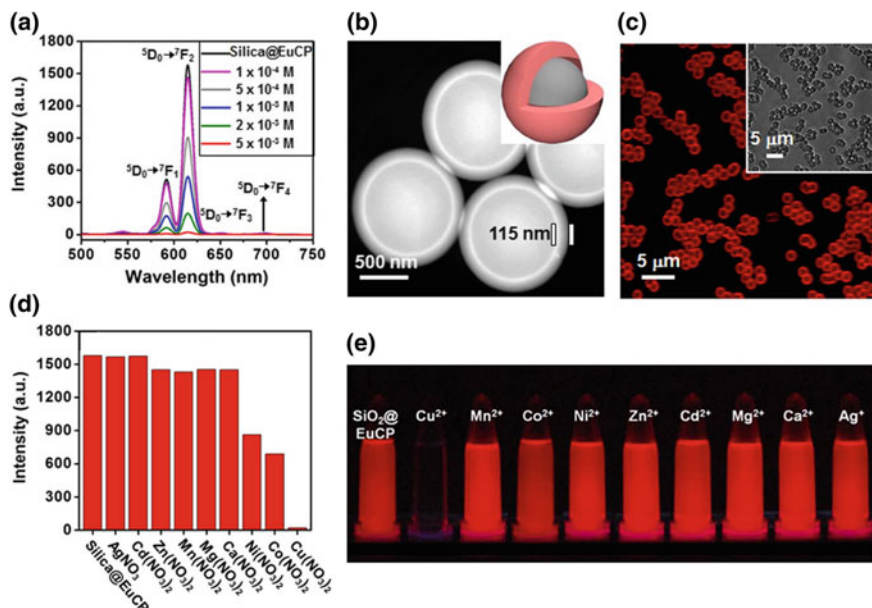


Fig. 7 **a** Emission spectra of silica@Eu-ICP showing the luminescence quenching caused by different concentrations of Cu²⁺ ion; **b** TEM image and schematic representation of the Eu-ICP shell over the silica core; **c** confocal microscopy and optical microscopy (inset) images of silica@Eu-ICP microspheres; **d** luminescent intensity changes of silica@Eu-ICP microspheres after immersion in various metal ion solutions (5 mmol L⁻¹); **e** photographs of silica@Eu-ICP microspheres suspensions after immersion in various metal ion solutions under UV irradiation. Adapted and reprinted with permission from [59]

process to the interaction of Cu²⁺ with the oxygen atoms of the carboxylate group from the isophthalic acid ligand. The quenching was selective when compared to other metallic ions (Mg²⁺, Ca²⁺, Mn²⁺, Co²⁺, Ni²⁺, Zn²⁺, Cd²⁺, Ag⁺) and could respond to concentrations of Cu²⁺ as low as 10⁻⁴ mol L⁻¹. The material could also be recycled multiple times through washing with acetonitrile. These results along with micrographs of the silica@Eu-ICP spheres can be seen in Fig. 7.

Ye et al. reported dye doped Ce³⁺/Tb³⁺-based ICPs for Hg²⁺ ion sensing in water [26]. Adenosine monophosphate (AMP) was used as the organic ligand, and after the synthesis coumarin dye was encapsulated in the ICPs spheres. The authors suggest that since AMP has stronger binding affinity for Hg²⁺, it displaces Tb³⁺ and Ce³⁺ in the coumarin@Ce/Tb-AMP material, thus reducing the intensity of Tb³⁺ *f-f* emission and enhancing the coumarin emission. The sensor was selective when exposed to other ions. The LOD was defined as 0.03 nmol L⁻¹, which is much lower than the safety limit of 0.002 mg L⁻¹ in drinking water set by the United States Environmental Protection Agency (USEPA), meaning it could be used as a potential sensor for monitoring Hg²⁺ in potable water. A similar approach was used

by Chen et al., which reported a Tb^{3+} -based ICP with adenine and dipicolinic acid as ligands [60]. In this case, Hg^{2+} ion bound to adenine and interrupted the photoinduced electron transfer from adenine to dipicolinic acid, which initially quenched the energy transfer from the acid to Tb^{3+} ion. This effect caused an enhancement of the luminescence intensity after exposure to Hg^{2+} ion. In this case, the LOD was estimated to be 0.2 nmol L^{-1} , still much lower than the safety limit for drinking water.

For anion sensing, Zhang et al. reported Eu^{3+} -based ICP nanospheres which showed luminescence quenching after exposure to PO_4^{3-} in water [21]. The authors assigned the quenching mechanism to PO_4^{3-} coordinating with Eu^{3+} and thus weakening the interaction between Eu^{3+} and 1,4-benzenedicarboxylic ligand. The LOD was estimated to be 0.83 mmol L^{-1} , which is lower than the detection requirement of phosphate discharge criteria in aquatic environment ($\sim 6.4\text{--}320 \text{ mmol L}^{-1}$). Since the luminescent sensor was selective when exposed to other common substances present in water, it was tested with real water samples (tap water and river water). The results showed that PO_4^{3-} concentration could be effectively calculated in these samples through the Stern-Volmer equation.

As mentioned above in the characterization section, Yin et al. reported a white-light emitting ICP which could selectively detect a series of ionic analytes through change in the emission color [18]. The Ln-ICP was built from 5-boronoisophthalic acid and a mixture of Eu^{3+} , Tb^{3+} and Dy^{3+} precursors. EDX mapping showed that the three ions were evenly distributed in the ICP sphere, as can be seen in Fig. 8a. Depending on the analyte's preferred site of interaction, the luminescence was tuned in situ, meaning different emission colors could be observed (Fig. 8b).

Gao et al. reported the detection of the anthrax biomarker dipicolinic acid (DA) in aqueous solution using lanthanide-based ICPs as a smart ratiometric luminescent probe. The Ln^{3+} coordination polymer nanoparticles were constructed by cooperative self-assembly of Tb^{3+} and Eu^{3+} as metal centers and guanosine 5-monophosphate (GMP) as organic linker. When exposed to the DA, the Tb^{3+} -originated green luminescence was enhanced while Eu^{3+} red luminescence decreased, with sensitive ratiometric response and apparent visual luminescence color change. The coordination is stronger between DA and Tb^{3+} compared to Eu^{3+} , preventing the energy transfer from Tb^{3+} to Eu^{3+} ($\text{GMP} \rightarrow \text{Tb}^{3+} \rightarrow \text{Eu}^{3+}$) and exhibiting the antenna effect for Tb^{3+} induced by GMP. The luminescent nanoprobe can be successfully applied to visual real-time monitoring of the release of DA during the germination of *B. subtilis* spores, a harmless simulant of *B. anthracis* [61].

Other reported analytes for Ln-ICPs include: reactive oxygen species [62], hydrogen peroxide [63, 64], ethanol [45], cyclohexane and nitrobenzene [65], ciprofloxacin [43, 66], alkaline phosphatase [27, 41] and aminoacids [67].

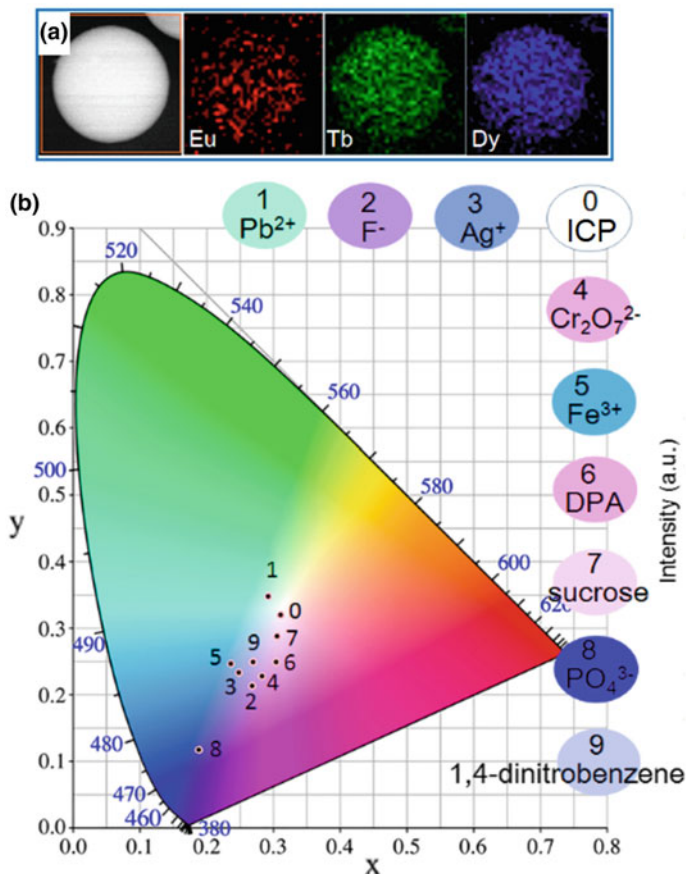


Fig. 8 **a** EDX elemental mapping of white-emitting Ln-ICPs; **b** CIE coordinates ($\lambda_{\text{ex}} = 275$ nm) for the response of Ln-ICPs to different anions, cations, sucrose, 1,4-dinitrobenzene, and dopamine (DPA). Adapted and reprinted with permission from [18]

5.2 Light-Emitting Devices

Unlike other spherical phosphor counterparts, like quantum dots, spherical Ln-ICPs have size-independent luminescence properties. The luminescence can also be tuned by adjusting the concentration of Ln³⁺ in the ICP structure. White-light emission can usually be achieved by combining red/green/blue (RGB) or yellow/blue (YB) emissive centers. While there are few examples for white-light emitting spherical Ln-ICPs, their potential utility in solid state lighting makes them topical and hence needs a mention [68]. Xu et al. reported Tb³⁺-based microspheres for tunable luminescence using 4,4',4''-benzene-1,3,5-triyl-tri-benzonate ligand. The authors took advantage of the blue emission from the ligand and green emission from Tb³⁺ and combined red emission by doping 0.5% (molar) of Eu³⁺, thus

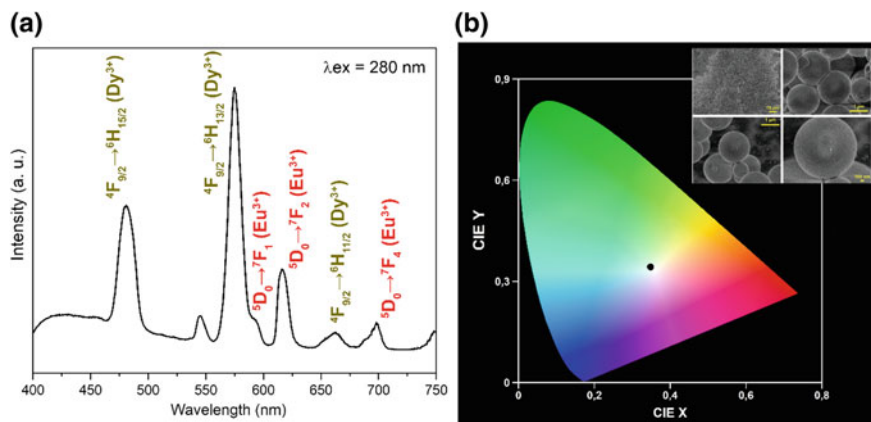


Fig. 9 **a** Emission spectrum of **Gd-M979** with the assigned intraconfigurational transitions of Eu^{3+} and Dy^{3+} ; **b** CIE diagram showing the (0.35, 0.34) coordinates calculated from the emission spectrum presented in (a), *inset*: SEM image of the **Gd-M979** sample [20]. Adapted and reprinted with permission from *The Royal Society of Chemistry*

achieving RGB white emission. Other emission colors could be obtained by adjusting the Eu^{3+} percentage. Zn-based ICP microspheres doped with Eu^{3+} and Tb^{3+} , reported by Ni et al. [40], used a similar approach. In this case, however, the lanthanide ions were occluded in the structure via post-synthetic modification.

Our group reported Tb^{3+} and Gd^{3+} based microspheres with pyrazole-3,5-dicarboxylic and malonic acids as ligands, using only water as solvent in a microwave-assisted synthesis [20]. The Tb^{3+} based ICP spheres can have their emission tuned by the addition of specific percentages of Eu^{3+} and Dy^{3+} in the synthesis, yielding microspheres with naked-eye visible green, yellow, orange and red emission under 280 nm excitation. White-light emission (CIE coordinates of 0.35, 0.34) was achieved by using a Gd^{3+} matrix (which acts as an optical dilutor since Gd^{3+} ion has no visible emissions) co-doped with 0.1% of Eu^{3+} and 2.0% of Dy^{3+} (sample **Gd-M979**). Dy^{3+} ion transition ${}^4F_{9/2} \rightarrow {}^6H_{15/2}$ peaked at 481 nm (blue) and ${}^4F_{9/2} \rightarrow {}^6H_{13/2}$ transition at 575 nm (yellow). Eu^{3+} ion characteristic red emission bands were used to drag the CIE coordinates to a warmer white color, as can be observed in Fig. 9.

5.3 Bio-related Applications

Besides sensing species in biological media, ICPs can find applications in drug delivery, bioimaging and as contrast agents for magnetic resonance imaging (MRI), taking advantage of the nanosized spherical particles [37, 69].

Drug delivery. In an active metal ion approach, Lin et al. reported a ICP constructed by the interaction between Tb^{3+} ion and a Pt-based ligand

(*c,c,t*-(diamminedichlorodisuccinato)Pt(IV)) for anti-cancer drug delivery [15]. To prevent the dissolution of the ICP particles in aqueous media, the authors coated the spheres with a shell of amorphous silica. The silica shell was then functionalized with angiogenic cancer cell receptors and tested *in vivo*. The results suggested that the material was internalized via receptor-mediated endocytosis, and once inside the cells, the ligand species released from the silica-coated ICPs could then be reduced to the active Pt(II) species by intracellular reductants that are present in high concentrations. Another approach involves the usage of drug-based linkers in the synthesis of ICPs. Che et al. prepared core-shell ICPs for delivery of carboxylate anti-cancer drugs. The spherical ICPs were synthesized using nontoxic, biocompatible and metabolizable microelements Zn^{2+} and Fe^{3+} as metal centers and different anticancer drugs (methotrexate, S-(N-p-chlorophenyl-N-hydroxycarbamoyl) glutathione and calcein) as bridging ligands. The particles were coated with 1,4-bis(imidazol-1-ylmethyl)benzene (BIX) linked to the Zn^{2+} and Fe^{3+} atoms, thus producing a pH-responsive shell. The mechanism of drug-delivery involves the cleavage of metal-BIX coordination bond with pH variations, leading to the exposure of the “drug-metal” ICP core into the surrounding environment, with subsequent release of the drug. The core-shell structure protected the drug core, improved the stability under physiological conditions, enabled pH-triggered drug release at the intended tissues and exhibited a higher cytotoxicity against HeLa cells than the free ICP core and free drug during *in vitro* cytotoxicity assays [70].

Bioimaging. The ICPs display potential as biomarkers and contrast enhancing agents for magnetic resonance imaging (MRI) [16]. Nishiyabu et al. synthesized ICP nanoparticles self-assembled from nucleotides (adenosine 5'-monophosphate, 5'-AMP) and lanthanide(III) ions. The particles were biocompatible, with structural diversity caused by the multiple functional groups from nucleobases and phosphate groups, which can serve as bidentate ligands. The ICPs self-assembled from 5'-AMP and Gd^{3+} was incorporated with perylene-3,4,9,10-tetracarboxylic acid fluorescent dye as guest molecule. The absorption and fluorescence peak maxima of the dye in nanoparticles were 477 and 500 nm, respectively. Figure 10a shows the fluorescence microscopy image of dye-doped 5'-AMP/ Gd^{3+} NPs added to HeLa cells. The authors then studied tissue localization of the dye-doped 5'-AMP/ Gd^{3+} nanoparticles *in vivo*. The fluorescence was observed only from the liver (see Fig. 10b), indicating that the nanoparticles were recognized by the hepatic reticuloendothelial system. Liver toxicity of 5'-AMP/ Gd^{3+} nanoparticles was also examined and the result demonstrated that they were nontoxic. The results demonstrated the potential of the ICP particles for biological applications, especially as imaging agents for liver. Being a Gd^{3+} -based material, the authors also tested the ICP nanoparticles as magnetic resonance imaging (MRI) contrast agents, because of their effect to accelerate spin-lattice relaxation (T_1). The leaching out of Gd^{3+} was estimated in HEPES buffer solutions for 1 week and just only 6.5–8.6 $\mu\text{mol L}^{-1}$ of free Gd^{3+} ions was present in the solution. In this case, the aqueous dispersions of 5'-AMP/ Gd^{3+} nanoparticles displayed higher contrast compared to $[\text{Gd}(\text{DTPA})(\text{H}_2\text{O})]^{2-}$ (Magnevist, DTPA: diethylenetriaminepentaacetic acid) commercially available contrast agent, as can be seen in Fig. 10c [71].

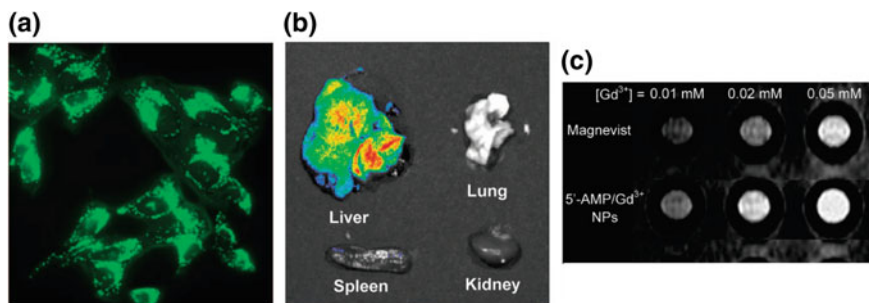


Fig. 10 **a** Fluorescence microscopy of dye-doped $5'$ -AMP/Gd $^{3+}$ NPs added to HeLa cells; **b** Fluorescent images of tissue samples (liver, spleen, lung and kidney) isolated from dye-doped $5'$ -AMP/Gd $^{3+}$ NPs-injected mice; **c** T $_1$ -weighted MR images of *Magnevist* and $5'$ -AMP/Gd $^{3+}$ NPs in 0.1 M HEPES buffer containing 50 μ g/mL of poly(sodium 4-styrene sulfonate) at pH 7.4. Adapted and reprinted with permission from [71]

5.4 Other Potential Applications

Templating. There are some reports on using spherical ICPs as templates (starting materials) to produce the corresponding metal oxides with the same spherical morphology after controlled atmosphere calcination [33, 34, 72–74]. The oxides obtained via this method can also achieve hollow structures by constructing an ICP shell on a silica core, using an etching process to remove the silica after the calcination [75].

Gas storage and separation. One of the first potential applications for MOFs was gas storage and separation due to high reported surface areas and permanent porosity. MOFs are suited for these applications since the high crystallinity yields very regular pore structures. Although ICPs' amorphous structures usually reduces their pore sizes and surface areas, two spherical Zn-based ICP particles have been reported as potential candidates for selective storage of H $_2$ [31, 32]. Using gas sorption isotherms of H $_2$, CO $_2$ and N $_2$, the authors demonstrated that the Zn-ICPs had higher affinity to H $_2$ due to its strong physisorption to metal centers and the presence of small pore channels with adequate size to capture this gas. Another Zn-based ICP was synthesized by Yang et al. with a fluorinated ligand which showed reversible photochromic behavior upon applying photostimuli in DMF solution and solid state [50]. The authors suggest that this property could provide a novel approach for the realization of light-triggered pore controlled ICPs, which have potential applications in the uptake and release of guests by using UV and visible light.

Microspheres for calibrating equipment. A potential and still not reported application for spherical ICPs is in the calibration of microscopes, in a similar way as organic polymer microspheres are used. For this kind of application, one still must control the homogeneity of size and shape of the ICP particles during the synthesis.

References

1. Batten, S.R., Champness, N.R.: Coordination polymers and metal-organic frameworks: materials by design. *Philos Trans A Math Phys Eng Sci* **375**, 20160032 (2017)
2. Yaghi, O.M., O'Keeffe, M., Ockwig, N.W., Chae, H.K., Eddaoudi, M., Kim, J.: Reticular synthesis and the design of new materials. *Nature* **423**, 705–714 (2003)
3. Li, H., Eddaoudi, M., O'Keeffe, M., Yaghi, O.M.: Design and synthesis of an exceptionally stable and highly porous metal-organic framework. *Nature* **402**, 276–279 (1999)
4. Batten, S.R., Champness, N.R., Chen, X.-M., Garcia-Martinez, J., Kitagawa, S., Öhrström, L., O'Keeffe, M., Paik Suh, M., Reedijk, J.: Terminology of metal-organic frameworks and coordination polymers (IUPAC Recommendations 2013). *Pure Appl. Chem.* **85**, 1715–1724 (2013)
5. Moghadam, P.Z., Li, A., Wiggin, S.B., Tao, A., Maloney, A.G.P., Wood, P.A., Ward, S.C., Fairen-Jimenez, D.: Development of a Cambridge structural database subset: a collection of metal-organic frameworks for past, present, and future. *Chem. Mater.* **29**, 2618–2625 (2017)
6. Kitagawa, S., Kitaura, R., Noro, S.I.: Functional porous coordination polymers. *Angew. Chem.-Int. Ed.* **43**, 2334–2375 (2004)
7. Batten, S.R., Champness, N.R., Chen, X.-M., Garcia-Martinez, J., Kitagawa, S., Öhrström, L., O'Keeffe, M., Suh, M.P., Reedijk, J.: Coordination polymers, metal-organic frameworks and the need for terminology guidelines. *CrystEngComm* **14**, 3001 (2012)
8. Eddaoudi, M., Moler, D.B., Li, H., Chen, B., Reineke, T.M., O'Keeffe, M., Yaghi, O.M.: Modular chemistry: secondary building units as a basis for the design of highly porous and robust metal-organic carboxylate frameworks. *Acc. Chem. Res.* **34**, 319–330 (2001)
9. Seoane, B., Castellanos, S., Dikhtiarenko, A., Kapteijn, F., Gascon, J.: Multi-scale crystal engineering of metal organic frameworks. *Coord. Chem. Rev.* **307**, 147–187 (2015)
10. Spokoyny, A.M., Kim, D., Sumrein, A., Mirkin, C.A.: Infinite coordination polymer nano- and microparticle structures. *Chem. Soc. Rev.* **38**, 1218 (2009)
11. Oh, M., Mirkin, C.A.: Chemically tailorable colloidal particles from infinite coordination polymers. *Nature* **438**, 651–654 (2005)
12. Mohammadikish, M., Ghanbari, S.: Preparation of monodispersed metal-based infinite coordination polymer nanostructures and their good capability for metal oxide preparation. *J. Solid State Chem.* **264**, 86–90 (2018)
13. Zhang, R.Z., Quan, S., Xia, M., Wang, Q., Zhang, W., Yang, J.M.: Effect of surface charge status of amorphous porous coordination polymer particles on the adsorption of organic dyes from an aqueous solution. *J. Colloid Interface Sci.* **525**, 54–61 (2018)
14. Jin, L.N., Liu, Q., Yang, Y., Fu, H.G., Sun, W.Y.: Large-scale preparation of indium-based infinite coordination polymer hierarchical nanostructures and their good capability for water treatment. *J. Colloid Interface Sci.* **426**, 1–8 (2014)
15. Rieter, W.J., Pott, K.M., Taylor, K.M.L., Lin, W.: Nanoscale coordination polymers for platinum-based anticancer drug delivery. *J. Am. Chem. Soc.* **130**, 11584–11585 (2008)
16. Liu, D., Huxford, R.C., Lin, W.: Phosphorescent nanoscale coordination polymers as contrast agents for optical imaging. *Angew. Chem.-Int. Ed.* **50**, 3696–3700 (2011)
17. D'Aquino, A.I., Kean, Z.S., Mirkin, C.A.: Infinite coordination polymer particles composed of stimuli-responsive coordination complex subunits. *Chem. Mater.* **29**, 10284–10288 (2017)
18. Wang, Y.M., Yang, Z.R., Xiao, L., Yin, X.B.: Lab-on-MOFs: color-coded multitarget fluorescence detection with white-light emitting metal-organic frameworks under single wavelength excitation. *Anal. Chem.* **90**, 5758–5763 (2018)
19. Kumar, P., Deep, A., Kim, K.-H., Brown, R.J.C.: Coordination polymers: opportunities and challenges for monitoring volatile organic compounds. *Prog. Polym. Sci.* **45**, 102–118 (2015)
20. Arroyos, G., Frem, R.C.G.: Rare earth phosphors based on spherical infinite coordination polymers. *New J. Chem.* **42**, 19070–19075 (2018)
21. Song, X., Ma, Y., Ge, X., Zhou, H., Wang, G., Zhang, H., Tang, X., Zhang, Y.: Europium-based infinite coordination polymer nanospheres as an effective fluorescence probe for phosphate sensing. *RSC Adv.* **7**, 8661–8669 (2017)

22. Zhong, S.-L., Xu, R., Zhang, L.-F., Qu, W.-G., Gao, G.-Q., Wu, X.-L., Xu, A.-W.: Terbium-based infinite coordination polymer hollow microspheres: preparation and white-light emission. *J. Mater. Chem.* **21**, 16574–16580 (2011)
23. Li, W.-Z., Zhou, Y., Liu, F., Li, Y., Xia, M.-J., Han, E.-H., Wang, T., Zhang, X., Fu, Y.: Fabrication of monodisperse flower-like coordination polymers (CP) microparticles by spray technique. *Nanomaterials* **7**, 237 (2017)
24. Bennett, T.D., Cheetham, A.K.: Amorphous metal-organic frameworks. *Acc. Chem. Res.* **47**, 1555–1562 (2014)
25. Deng, J., Wu, F., Yu, P., Mao, L.: On-site sensors based on infinite coordination polymer nanoparticles: recent progress and future challenge. *Appl. Mater. Today* **11**, 338–351 (2018)
26. Zhang, Z., Wu, Y., He, S., Xu, Y., Li, G., Ye, B.: Ratiometric fluorescence sensing of mercuric ion based on dye-doped lanthanide coordination polymer particles. *Anal. Chim. Acta* **1014**, 85–90 (2018)
27. Ou-Yang, J., Li, C.Y., Li, Y.F., Yang, B., Li, S.J.: An infinite coordination polymer nanoparticles-based near-infrared fluorescent probe with high photostability for endogenous alkaline phosphatase in vivo. *Sensor Actuat. B-Chem.* **255**, 3355–3363 (2018)
28. Wang, Y.M., Liu, W., Yin, X.B.: Self-limiting growth nanoscale coordination polymers for fluorescence and magnetic resonance dual-modality imaging. *Adv. Funct. Mater.* **26**, 8463–8470 (2016)
29. Zhang, Y., Guo, Y., Wu, S., Liang, H., Xu, H.: Photodegradable coordination polymer particles for light-controlled cargo release. *ACS Omega* **2**, 2536–2543 (2017)
30. Nouri, R., Abedi, S., Morsali, A.: A novel synthesis route for preparation of tetrazole-based infinite coordination polymers and their application as an efficient catalyst for Michael addition reactions. *J. Iran. Chem. Soc.* **14**, 1601–1612 (2017)
31. Jeon, Y.M., Armatas, G.S., Heo, J., Kanatzidis, M.G., Mirkin, C.A.: Amorphous infinite coordination polymer microparticles: a new class of selective hydrogen storage materials. *Adv. Mater.* **20**, 2105–2110 (2008)
32. Jeon, Y.M., Armatas, G.S., Kim, D., Kanatzidis, M.G., Mirkin, C.A.: Tröger's-base-derived infinite co-ordination polymer microparticles. *Small* **5**, 46–50 (2009)
33. Zhong, S., Jing, H., Li, Y., Yin, S., Zeng, C., Wang, L.: Coordination polymer submicrospheres: fast microwave synthesis and their conversion under different atmospheres. *Inorg. Chem.* **53**, 8278–8286 (2014)
34. Ma, D., Li, C., Wang, L., Liu, H., Zhong, S., Li, Y.: Preparation of RE₂O₂SO₄ (RE = La, Pr-Lu) microspheres from rare-earth-based infinite coordination polymers. *J. Nanopart. Res.* **19**, 341 (2017)
35. Paddock, S.W.: *Confocal Microscopy: Methods and Protocols*, 2nd edn., 381p. Springer Protocols, Hatfield (2014)
36. Zou, H., Wang, L., Zeng, C., Gao, X., Wang, Q., Zhong, S.: Rare-earth coordination polymer micro/nanomaterials: preparation, properties and applications. *Front. Mater. Sci.* **12**, 324–347 (2018)
37. Lin, W., Rieter, W.J., Taylor, K.M.L.: Modular synthesis of functional nanoscale coordination polymers. *Angew. Chem.-Int. Ed.* **48**, 650–658 (2009)
38. Sun, X., Dong, S., Wang, E.: Coordination-induced formation of submicrometer-scale, monodisperse, spherical colloids of organic-inorganic hybrid materials at room temperature. *J. Am. Chem. Soc.* **127**, 13102–13103 (2005)
39. Yang, M., Shen, Z., Chen, T., Bi, H., Yang, B., Xu, W.: Induced morphology control of Ln-asparagine coordination polymers from the macro to nanoscopic regime in polar solvent-water mixtures. *Dalton Trans.* **42**, 1174–1179 (2013)
40. Pan, H., Xu, S., Ni, Y.: Rare-earth post-modified Zn-based coordination polymer microspheres: Simple room-temperature preparation, fluorescent performances and application for detection of tryptophane. *Sensor Actuat. B-Chem.* **283**, 731–739 (2019)
41. Deng, J., Yu, P., Wang, Y., Mao, L.: Real-time ratiometric fluorescent assay for alkaline phosphatase activity with stimulus responsive infinite coordination polymer nanoparticles. *Anal. Chem.* **87**, 3080–3086 (2015)

42. Mohammadikish, M., Ahmadvand-Akradi, A.: Facile synthesis of novel zinc-based infinite coordination polymer nanoparticles. *Inorg. Chem. Commun.* **78**, 48–51 (2017)
43. Liu, B., Huang, Y., Shen, Q., Zhu, X., Hao, Y., Qu, P., Xu, M.: Turn-on fluorescence detection of ciprofloxacin in tablets based on lanthanide coordination polymer nanoparticles. *RSC Adv.* **6**, 100743–100747 (2016)
44. Jeon, Y.M., Heo, J., Mirkin, C.A.: Dynamic interconversion of amorphous microparticles and crystalline rods in salen-based homochiral infinite coordination polymers. *J. Am. Chem. Soc.* **129**, 7480–7481 (2007)
45. Deng, J., Shi, G., Zhou, T.: Colorimetric assay for on-the-spot alcoholic strength sensing in spirit samples based on dual-responsive lanthanide coordination polymer particles with ratiometric fluorescence. *Anal. Chim. Acta* **942**, 96–103 (2016)
46. Xiao, C., Xu, H., Zhong, S.: Au@Eu-based coordination polymers core-shell nanoparticles: photoluminescence and photothermal properties. *Mater. Lett.* **216**, 106–109 (2018)
47. Tao, P., Zeng, C.H., Zheng, K., Huang, C.Q., Zhong, S.L.: Uniform terbium coordination polymer microspheres: preparation and luminescence. *J. Inorg. Organomet. Polym. Mater.* **26**, 1087–1094 (2016)
48. Liu, R., Shuai, M., Xu, H., Zhong, S.: Uniform Gd-based coordination polymer hollow spheres: synthesis, formation mechanism and upconversion properties. *J. Inorg. Organomet. Polym. Mater.* **28**, 137–145 (2018)
49. Nie, Z.-W., Zeng, C.-H., Xie, G., Zhong, S.-L.: Uniform cerium-based coordination polymer microspheres: preparation and upconversion emission. *J. Nanosci. Nanotechnol.* **16**, 3705–3709 (2016)
50. Hu, X.G., Li, X., Yang, S.I.: Novel photochromic infinite coordination polymer particles derived from a diarylethene photoswitch. *Chem. Commun.* **51**, 10636–10639 (2015)
51. Chen, W., Li, S., Zeng, C.H., Zhong, S.: Eu-based coordination polymers micro-flowers: preparation and luminescence properties. *J. Inorg. Organomet. Polym. Mater.* **27**, 598–604 (2017)
52. Zhong, S., Ji, Y., Xie, Q., Wang, L., Li, Y., Jeong, J.H.: Coordination polymer nanospheres: preparation, upconversion properties and cytotoxicity study. *Mater. Lett.* **102–103**, 19–21 (2013)
53. Carné, A., Carbonell, C., Imaz, I., Maspoch, D.: Nanoscale metal–organic materials. *Chem. Soc. Rev.* **40**, 291–305 (2011)
54. Hu, D., Song, Y., Wang, L.: Nanoscale luminescent lanthanide-based metal–organic frameworks: properties, synthesis, and applications. *J. Nanoparticle Res.* **17**, 1–21 (2015)
55. Zhao, D., Wang, L., Li, Y., Zhang, L., Lv, Y., Zhong, S.: Uniform europium-based infinite coordination polymer submicrospheres: fast microwave synthesis and characterization. *Inorg. Chem. Commun.* **20**, 97–100 (2012)
56. Billinge, S.J.L.: The rise of the X-ray atomic pair distribution function method: a series of fortunate events. *Philos. Trans. R. Soc. A: Math. Phys. Eng. Sci.* **377**, 20180413 (2019)
57. Thommes, M., Kaneko, K., Neimark, A.V., Olivier, J.P., Rodriguez-Reinoso, F., Rouquerol, J., Sing, K.S.W.: Physisorption of gases, with special reference to the evaluation of surface area and pore size distribution (IUPAC Technical Report). *Pure Appl. Chem.* **87**, 1051–1069 (2015)
58. Zhang, X., Wang, W., Hu, Z., Wang, G., Uvdal, K.: Coordination polymers for energy transfer: Preparations, properties, sensing applications, and perspectives. *Coord. Chem. Rev.* **284**, 206–235 (2015)
59. Cho, W., Lee, H.J., Choi, S., Kim, Y., Oh, M.: Highly effective heterogeneous chemosensors of luminescent silica@coordination polymer core-shell micro-structures for metal ion sensing. *Sci Rep* **4**, 6518 (2014)
60. Tan, H., Liu, B., Chen, Y.: Lanthanide coordination polymer nanoparticles for sensing of mercury(II) by photoinduced electron transfer. *ACS Nano* **6**, 10505–10511 (2012)
61. Gao, N., Zhang, Y., Huang, P., Xiang, Z., Wu, F.Y., Mao, L.: Perturbing tandem energy transfer in luminescent heterobinuclear lanthanide coordination polymer nanoparticles enables real-time monitoring of release of the anthrax biomarker from bacterial spores. *Anal. Chem.* **90**, 7004–7011 (2018)

62. Wang, H.S., Bao, W.J., Bin, Ren S., Chen, M., Wang, K., Xia, X.H.: Fluorescent sulfur-tagged europium(III) coordination polymers for monitoring reactive oxygen species. *Anal. Chem.* **87**, 6828–6833 (2015)
63. Zeng, H.H., Qiu, W.B., Zhang, L., Liang, R.P., Qiu, J.D.: Lanthanide coordination polymer nanoparticles as an excellent artificial peroxidase for hydrogen peroxide detection. *Anal. Chem.* **88**, 6342–6348 (2016)
64. Tan, H., Ma, C., Li, Q., Wang, L., Xu, F., Chen, S., Song, Y.: Functionalized lanthanide coordination polymer nanoparticles for selective sensing of hydrogen peroxide in biological fluids. *Analyst* **139**, 5516–5522 (2014)
65. Hou, Y.-L., Xu, H., Cheng, R.-R., Zhao, B.: Controlled lanthanide–organic framework nanospheres as reversible and sensitive luminescent sensors for practical applications. *Chem. Commun.* **51**, 6769–6772 (2015)
66. Tan, H., Zhang, L., Ma, C., Song, Y., Xu, F., Chen, S., Wang, L.: Terbium-based coordination polymer nanoparticles for detection of ciprofloxacin in tablets and biological fluids. *ACS Appl. Mater. Interfaces* **5**, 11791–11796 (2013)
67. Zhang, Z., Wang, L., Li, G., Ye, B.: Lanthanide coordination polymer nanoparticles as a turn-on fluorescence sensing platform for simultaneous detection of histidine and cysteine. *Analyst* **142**, 1821–1826 (2017)
68. SeethaLekshmi, S., Ramya, A.R., Reddy, M.L.P., Varughese, S.: Lanthanide complex-derived white-light emitting solids: a survey on design strategies. *J. Photochem. Photobiol. C: Photochem. Rev.* **33**, 109–131 (2017)
69. Novio, F., Simmchen, J., Vázquez-Mera, N., Amorín-Ferré, L., Ruiz-Molina, D.: Coordination polymer nanoparticles in medicine. *Coord. Chem. Rev.* **257**, 2839–2847 (2013)
70. Xing, L., Cao, Y., Che, S.: Synthesis of core-shell coordination polymer nanoparticles (CPNs) for pH-responsive controlled drug release. *Chem. Commun.* **48**, 5995–5997 (2012)
71. Nishiyabu, R., Hashimoto, N., Cho, T., et al.: Nanoparticles of adaptive supramolecular networks self-assembled from nucleotides and lanthanide ions. *J. Am. Chem. Soc.* **131**, 2151–2158 (2009)
72. Liao, Y., Li, Y., Wang, L., Zhao, Y., Ma, D., Wang, B., Wan, Y., Zhong, S.: Multi-shelled ceria hollow spheres with a tunable shell number and thickness and their superior catalytic activity. *Dalton Trans.* **46**, 1634–1644 (2017)
73. Mohammadikish, M., Talebi, M.: Rapid production of acid-functionalized in fi nite coordination polymer nanoparticles and their calcination to mineral metal oxide. *Powder Technol.* **313**, 169–174 (2017)
74. Wei, H., Li, B., Du, Y., Dong, S., Wang, E.: Nucleobase-metal hybrid materials: preparation of submicrometer-scale, spherical colloidal particles of adenine-gold(III) via a supramolecular hierarchical self-assembly approach. *Chem. Mater.* **19**, 2987–2993 (2007)
75. Park, J.U., Lee, H.J., Cho, W., Jo, C., Oh, M.: Facile synthetic route for thickness and composition tunable hollow metal oxide spheres from silica-templated coordination polymers. *Adv. Mater.* **23**, 3161–3164 (2011)

Current Perspective on Synthesis, Properties, and Application of Graphitic Carbon Nitride Related-Compounds



F. M. Pinto and F. A. La Porta

Abstract Currently, graphitic carbon nitride (g-C₃N₄)-based materials are the centre of attention in chemistry and materials science because of their unique as well as fascinating properties, which are strongly desired for many technological applications. g-C₃N₄ is lamellar and composed of two-dimensional layers of carbon atoms naturally arranged in hexagonal networks. g-C₃N₄ is, therefore, analogous to graphene, but has nitrogen atoms bound through covalent bonds (sp²). This results in a stable, porous, heat-resistant polymeric semiconductor that is optically active under visible-light irradiation (and thus has excellent photocatalytic characteristics) as well as economically sustainable. The recent discovery of this new member of the graphene family is a crucial breakthrough, as there are only a few bi-dimensional organic solids. Hence, this chapter summarizes the current progress in the understanding of the synthesis and fundamental properties of g-C₃N₄-related materials.

Keywords Graphitic carbon nitride (g-C₃N₄) · Carbon materials · Layered structure · Triazine-based structures

1 Historical Perspective

Over the years, the research dedicated to the search for new advanced materials or the improvement of those already discovered has increased progressively and considerably, targeting the diverse applications in energy, environment, biomedicine, and technology [1]. Among the advanced materials, graphene has made a

F. M. Pinto

Engineering Department, Federal University of Lavras, Lavras, Brazil

e-mail: felipe.moreira@ufla.br

F. A. La Porta (✉)

Laboratory of Nanotechnology and Computational Chemistry (NanoQC),

Federal Technological University of Paraná, Londrina, Brazil

e-mail: felipelaporta@utfpr.edu.br

© Springer Nature Switzerland AG 2020

F. A. La Porta and C. A. Taft (eds.), *Emerging Research in Science and Engineering Based on Advanced Experimental and Computational Strategies*, Engineering Materials, https://doi.org/10.1007/978-3-030-31403-3_16

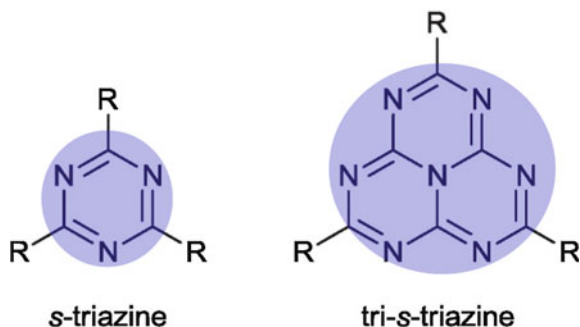
significant revolutionary impact because of its versatile chemical structure, which imparts extremely attractive and innovative properties, leading to its application in diverse fields such as touchscreen devices, the internet, prosthetics, and hydrogen cells as well as in the civil, automotive, aeronautics, and naval industries [1–8]. In addition, this emergent compound is promising for application in solar panels and lighting [9–11].

Graphene, which is the thinnest, lightest, and strongest material ever discovered, consists of a thin layer of carbon, in which the individual atoms are densely aligned, arranged in a hexagonal lattice [12]. It is estimated that 3 million layers of stacked graphene can fit in one million millimetres. Besides, graphene is a good conductor of heat and electricity, virtually transparent, flexible, elastic, durable, non-rusting, and has a low production cost [8–18]. In addition to graphene (two-dimensional (2D) carbon sheet), carbonaceous materials can also be arranged into other dimensional nanostructures such as stacked sheets (graphite), nanodiamonds, nanotubes, carbon quantum dots, nanohorns, or fullerenes [14, 15].

Graphene was first predicted in 1947 in the theoretical works of the Canadian researcher, Philip R. Wallace, during the investigation of the electronic structure properties of graphite [16]. However, it was the German chemist Boehm who named it ‘graphene’ in 1962 [17], and it was in 2004 that graphene was mechanically isolated from graphite by exfoliation while maintaining its structure and conductivity [19]. For this discovery, Geim (Russian-Dutch) and Novoselov (Russian-British) received the Nobel Prize in Physics in 2010 [20], which spurred an increase in graphene research owing to its invaluable application possibilities (in the same year, at least 3000 studies were published showing various new functionalities) and made it the centre of attention in the field of nanotechnology, until they were overcome, more recently, by hybrid perovskites.

Since then, there has been great encouragement in the study of other 2D nanomaterials [19–23]. The scientists at the University of Liverpool first produced graphitic carbon nitride ($g\text{-C}_3\text{N}_4$) crystals (initially called ‘triazine graphite carbon nitride’) [21], which were theoretically planned by the mid-1996 [22]. They were prepared from the dicyandiamide molecule by heating it in a quartz tube for 62 h at 600 °C, and the $g\text{-C}_3\text{N}_4$ flakes were removed by filtration [22, 23].

Fig. 1 Chemical structures of 1,3,5-triazine (*s*-triazine) and tri-*s*-triazine (*s*-heptazine) derivatives



Over the years, two structural models have been widely proposed to explain the geometry of $g\text{-C}_3\text{N}_4$, distinguished by the size of the nitrogen-linked aromatic fractions forming the 2D layers: one based on heptazine units (C_6N_7) and the other based on triazine units (C_3N_3) [24, 25], as shown in Fig. 1.

However, the first mention of heptazine compound in literature dates back to the 1830s, when Jöns Jacob Berzelius discovered the polymer after burning mercury (II) thiocyanate ($\text{Hg}(\text{SCN})_2$), which yielded a brown polymeric solid formed with the elimination of mercury sulphide and carbon disulphide in a reaction commonly known as the ‘Pharaoh’s serpent’ [26, 27]. This polymer is also known as poly (aminoimine) heptazine and consists of one-dimensional layers of ($\text{C}_6\text{N}(\text{NH}_2)_3$) monomers linked by NH bridges. The layers, in turn, are held together by intermolecular van der Waals forces. Edward Franklin studied the structure of this polymer in detail in 1922 and called it ‘carbon dioxide’ of the type C_3N_4 [28]. According to him, C_3N_4 was obtained by the numerous successive losses of ammonia through the heat treatment of melon ($\text{C}_2\text{N}_3\text{H}$). The substance was dubbed ‘melon’ by the German chemist Justus von Liebig, who extensively researched the compound and its analogues [29]. Other related compounds were soon discovered and researched, including melem ($\text{C}_6\text{N}_7(\text{NH}_2)_3$) and melam ($\text{C}_6\text{N}_{11}\text{H}_9$) [30].

These chemicals were so inert and so insoluble that deducing their structures at that time was difficult since the methods employed to characterize materials stemmed from reactionary characteristics. Particularly, in the 1920s, several structures were proposed for melon, including a series of tri-*s*-triazines [31, 32]. Then, in 1937, Linus Pauling performed crystallographic experiments, which revealed that the heptazine nucleus has a flat structure consisting of three fused *s*-triazine rings, as shown in Fig. 1 [33].

However, it was Nelson J. Leonard who first synthesized the major unsubstituted heptazine molecule, $\text{C}_6\text{N}_7\text{H}_3$, in the early 1980s and thoroughly characterized the molecule by crystallographic and spectroscopic methods as well as by theoretical calculations to study its fundamental properties [33, 34].

Although melem, melon, and the other related molecules have many industrial applications of interest such as in fireproof materials, not much attention was paid, until recently, to their technological potentials in the emergent fields [32, 33].

Kroke and his colleagues comprehensively studied trichlor-substituted tri-*s*-triazine and synthesized several other heptazine derivatives ideal building blocks for extended $g\text{-C}_3\text{N}_4$ mesh structures [23, 35, 36].

In the pursuit of C_3N_4 diamond, Komatsu and colleagues completely characterized melon and demonstrated that $g\text{-C}_3\text{N}_4$ structures are likely to take the form of bound heptazine [37–39]. His research group used a wide variety of tri-*s*-triazine derivatives, including the 2,5,8-tricarbodiimide-tris-*s*-triazine copper salt, which produced a diamond-like $g\text{-C}_3\text{N}_4$ structure [37–39]. On the other hand, Schnick and colleagues confirmed the melem structure and provided further evidence that $g\text{-C}_3\text{N}_4$ exists in the form of heptazine [40]. In Table 1, we summarize the findings in this field from the historical point of view.

Although the interest in compounds derived from heptazine fluctuated over time, it always permeated the minds of many scientists. For instance, what about

Table 1 Selected *s*-triazines and heptazines compounds and their year of discovery

R	<i>s</i> -Triazine	<i>s</i> -Heptazine	First reported/mentioned
NH ₂	Melamine	Melem	Liebig, 1834 [29] ^a
OH	Cyanuric acid	Cyamelic acid	Liebig, 1834 [29]
NCN ⁻	Tricyanomelamine	Melonates	Gmelin, 1835 [41]
Cl	Cyanuric chloride	Cyamelic chloride	Liebig, 1844 [42]
N ₃	Triazide triazine	Tri-azide tri- <i>s</i> -triazine	Pauling, 1937 [31]
H	Triazine	Tri- <i>s</i> -triazine	Hosmane, 1982 [34]

Adapted from [31]

^aAccording to Liebig, J. J. Berzelius first reported the reaction of Hg(SCN) that yields *s*-heptazine

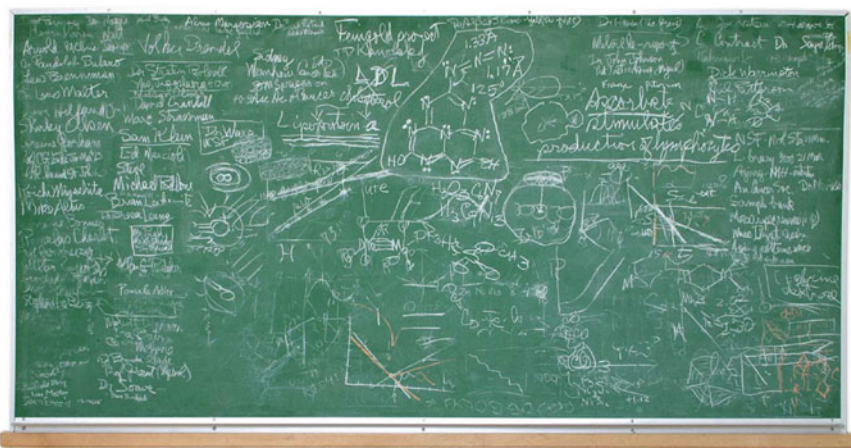


Fig. 2 Pauling's chalkboard with the representation drawing of a 'mystery molecule', as preserved in the OSU Libraries Special Collections. Reprinted from [43]

Pauling's mysterious heptazine with both hydroxyl groups and azide? Pauling intended it to be a potential spectroscopic marker for DNA binding. Pauling was so interested in the molecule that it was written on his chalkboard (Fig. 2) when he died on August 19, 1994.

2 Structure and Synthesis

We begin with the *g*-C₃N₄ molecule, which is one of the carbon nitride allotropes in the graphitic form [44]. The acronym comes precisely from this type of structure ('*g*' denotes graphitic) and from the proportions of the constituent atoms (e.g., carbon and nitrogen). Figure 3 shows that the incorporation of nitrogen into the azacycl-[3.3.3]azine structure, in principle, leads to an increase in thermal stability in this series of heteroaromatic systems [32]. More specifically, the compounds with a graphite structure are those that resemble graphite or its simplest form, graphene.

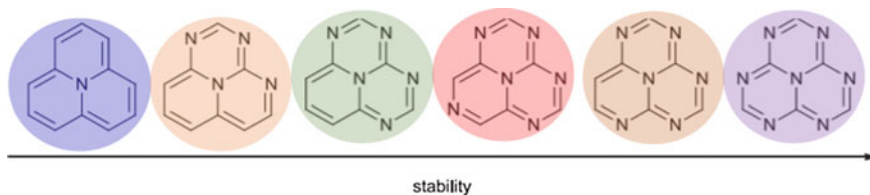


Fig. 3 Heteroaromatic azacycl-[3.3.3] azine-based compounds with alternating C and N atoms, from which well-known isoelectronic structures to the phenallen anion. Adapted from [32]

In the most common crystalline phase of this polymer, heptazine is joined to six other heptazines via three amine groups [31]. The monomeric unit of $g\text{-C}_3\text{N}_4$ is heptazine, also known as tri-*s*-triazine [45]. It consists of C_6N_7 , which is a planar triangular group of three fused triazine rings with three substituents at the vertices of the triangle [31, 44, 45].

In addition to the amine groupings, imine functional groups are present. As such, they are lamellar polymers made of fused ring sheets (similar to graphene) of high strength, high surface area, and potentially high electrical conductivity [31, 35, 36, 44].

In general, $g\text{-C}_3\text{N}_4$ is synthesized by the polycondensation of nitrogen-rich organic precursors such as melamine, cyanamide, dicyandiamide, urea, and thiourea [40, 44–47]. Although the precursor routes are initially distinct, at a given moment melamine is generated [23, 40–42, 47–51], from which the synthetic route follows the path shown in Fig. 4.

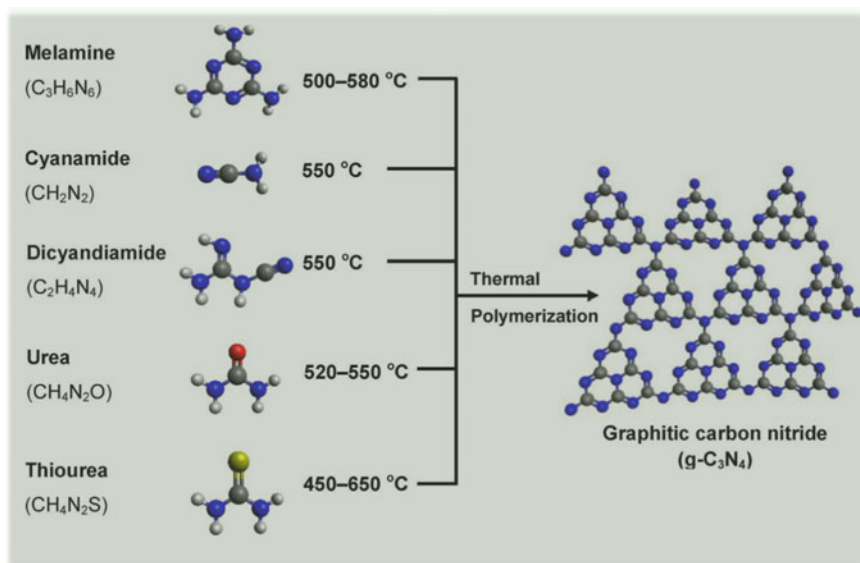


Fig. 4 Schematic of the formation of $g\text{-C}_3\text{N}_4$ compounds by thermal polymerization of different nitrogen-rich precursors. Adapted from [23]

Among the numerous allotropes of carbon nitrides, the best known are α - C_3N_4 , β - C_3N_4 , p - C_3N_4 , c - C_3N_4 , and g - C_3N_4 [44]. However, at room temperature, g - C_3N_4 is considered the most stable allotrope [44]. In principle, the g - C_3N_4 structure can be formed by two building blocks: triazine (C_3N_3) or heptazine (C_6N_7) [33]. Using the system formed by both the subunits is linked through a trigonal nitrogen atom (see Fig. 4), which is the most stable form of bond between the rings. However, theoretical studies show that the heptazine structure is energetically more favourable than the triazine structure [52].

The ideal structure of g - C_3N_4 consists only of C–N bonds with delocalized electrons in the π orbitals [48]. However, the materials obtained by the synthesis processes may contain small amounts of hydrogen present in the primary or secondary amines. In general, the presence of H atoms can indicate an incomplete precursor polymerization, which leads to the formation of structural defects [53–55]. Thus, a systematic exploration of the structural characteristics of the g - C_3N_4 system can provide key clues for elucidating their functional properties [48].

The presence of the conjugated π system in the heptazine rings, for example, imparts electronic properties that may be useful in its diverse catalytic applications [56, 57]. In principle, the H and N atoms in the g - C_3N_4 lattice impart outstanding surface-related properties, which is an interesting characteristic related to their chemical reactivity [57]. Such materials, however, require in-depth investigation for a better understanding of their nanoscale behaviours as well as revealing their huge potential for many emergent technological applications.

On the other hand, the solid-phase polycondensation method is the most commonly used method for the production of large amounts of g - C_3N_4 -based materials [23]. Particularly, g - C_3N_4 is synthesized from nitrogen-rich precursors via a combination of polyadditions and polycondensations by which the reagents are converted into melamine [58, 59]. The subsequent step, in general, is ammonia release and polymerization that leads to the formation of g - C_3N_4 [60, 61]. One of the main advantages of g - C_3N_4 -based materials is the absence of metals in their chemical structures; thus, they are non-toxic and compatible with diverse biological systems [48]. In addition, these advanced materials have high thermal stabilities, usually up to 600 °C, which may vary depending on the synthesis route and the polymerization degree. This process incurs high energy and time costs, and the physical and photocatalytic properties of the products are affected by a number of factors such as the reaction atmosphere, polycondensation time, and heating rate [23]. The g - C_3N_4 layers usually have negatively charged surfaces, which facilitate their dispersion in polar solvents [62]. Some notable examples of g - C_3N_4 synthesis from nitrogen-rich precursors are shown in Fig. 4.

3 Modifications to Synthesis

Using various synthetic strategies, g-C₃N₄ with numerous nanometre-scale morphologies have been widely prepared such as lamellae [63], fibres [64], tubes [65], points [66], template-supported morphologies [67], and highly porous structures [68].

Other synthesis strategies have been widely developed, such as microwave-assisted solid-phase synthesis [69], ionic liquid-assisted synthesis [70], and synthesis in a molten salt medium [71]. These strategies generally offer better products compared with that [72] prepared by the solid-phase synthesis method. However, given the wide use of classical synthesis, it is interesting to study the photocatalytic capacity of g-C₃N₄ obtained by this method.

Zhang and colleagues [73] investigated the synthesis of g-C₃N₄ using silica nanospheres as growth templates, which yielded a porous and ordered material, as shown in Fig. 5.

In another study, Zhang and colleagues [50] synthesized 2D g-C₃N₄ materials using SBA-15 silica as a support to produce g-C₃N₄ nanorods, as shown in Fig. 6.

Sun and colleagues [18] reported a synthesis strategy that involved the production of a g-C₃N₄ halo from cyanamide silica nanospheres, which under different synthesis and treatment conditions resulted in different shell sizes, as shown in Fig. 7. A similar strategy was followed by Zheng and colleagues [74] and the results are shown in Fig. 8.

The use of ordered mesoporous materials as templates has opened new opportunities for the synthesis of g-C₃N₄ materials with ordered periodic structures. This process can produce a wide variety of porous structures with large pore size distributions and well-defined and controlled morphologies in large-scale production

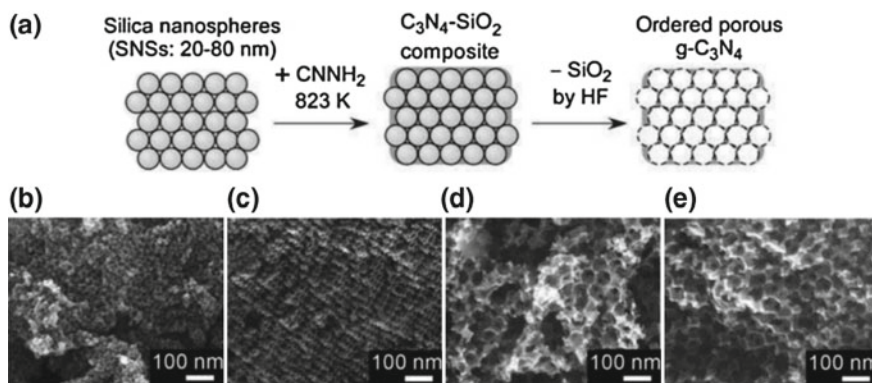


Fig. 5 a Illustration of the synthesis procedure for obtaining an ordered porous g-C₃N₄. SEM images of porous g-C₃N₄ synthesized using various silica spheres with diameters of **b** 20, **c** 30, **d** 50, and **e** 80 nm. Reprinted with permission from ref. [73]. Copyright 2011 John Wiley & Sons, Inc.

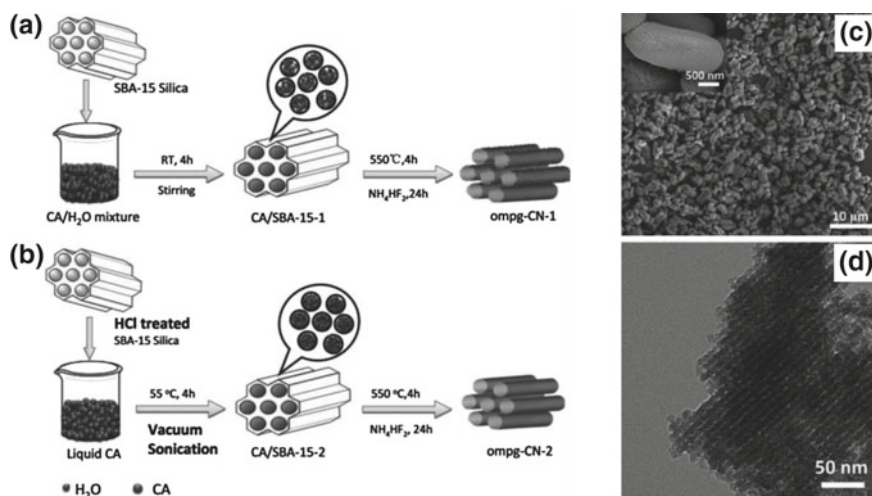


Fig. 6 Synthesis protocols of ordered mesoporous $g\text{-C}_3\text{N}_4$: **a** conventional approach and **b** novel approach involving acidification and a combined vacuum-sonication process. Typical **c** SEM and **d** TEM images of ompg-CN-2. CA and ompg-CN denote cyanamide and ordered mesoporous $g\text{-C}_3\text{N}_4$, respectively. Reprinted with permission from ref. [50]. Copyright 2013 John Wiley & Sons, Inc.

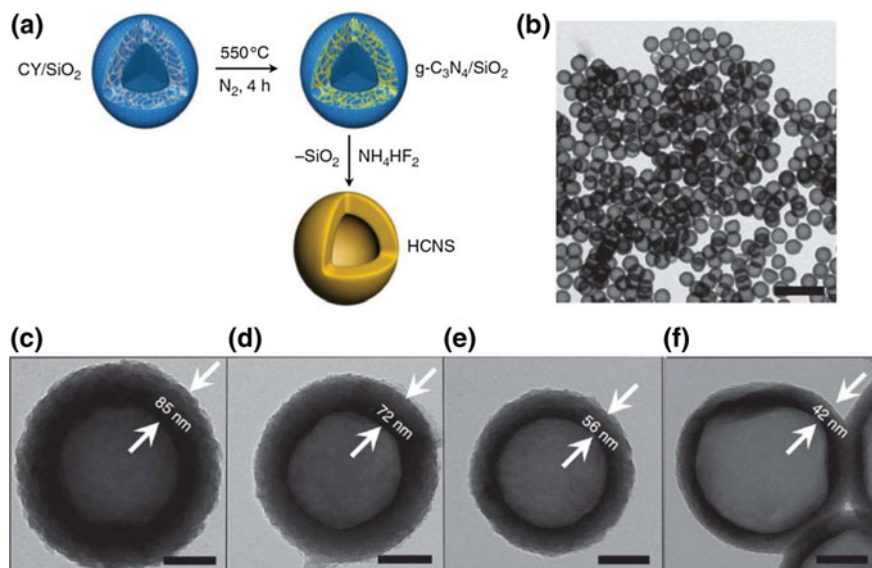


Fig. 7 **a** Synthesis strategy for hollow $g\text{-C}_3\text{N}_4$ nanospheres. CY denotes cyanamide. **b** TEM image of hollow $g\text{-C}_3\text{N}_4$ nanospheres. Scale bar is 1 μm . **c-f** TEM images of hollow $g\text{-C}_3\text{N}_4$ nanospheres with different shell thicknesses. Scale bar is 100 nm. Reprinted with permission from ref. [18]. Copyright 2012 Nature Publishing Group

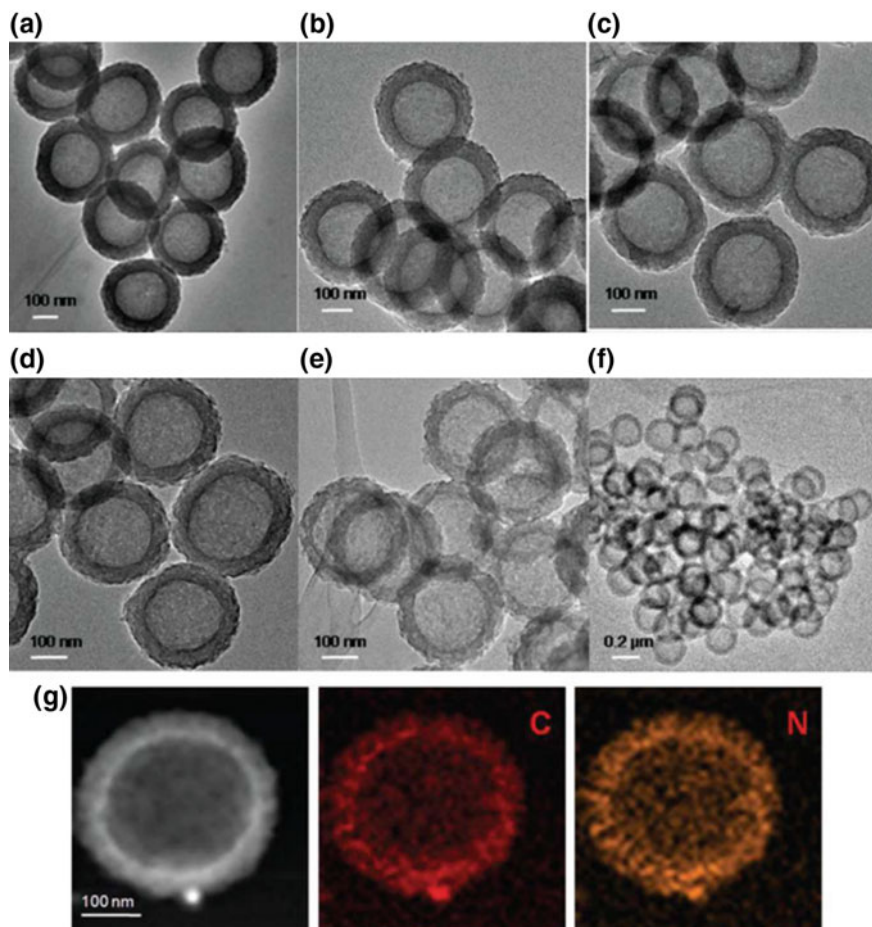


Fig. 8 a TEM images of hollow g-C₃N₄ nanospheres before post-annealing treatments. TEM images of hollow g-C₃N₄ nanospheres after post-annealing at temperatures of **b** 300, **c** 400, **d** 500, and **e**, **f** 550 °C. **g** EDX mapping images of hollow g-C₃N₄ nanospheres post-annealed at 550 °C. Reprinted with permission from ref. [74]. Copyright 2015 Royal Society of Chemistry

as well as various chemical functionalities to suit different applications [18, 50, 73–78]. In this process, g-C₃N₄ is formed around the template molecule, usually meso- and macroporous zeolites and silicas, through the formation of a physical bond between the template and precursor [75–84]. The different synthetic strategies and the resulting ordered mesoporous materials are shown in Figs. 9, 10, 11 and 12. Such studies are encouraged for the improvement and development of novel technologies of interest.

The research group of Prof. Menny Shalom of Ben-Gurion University of the Negev has been developing interesting g-C₃N₄ basement materials [79–82].

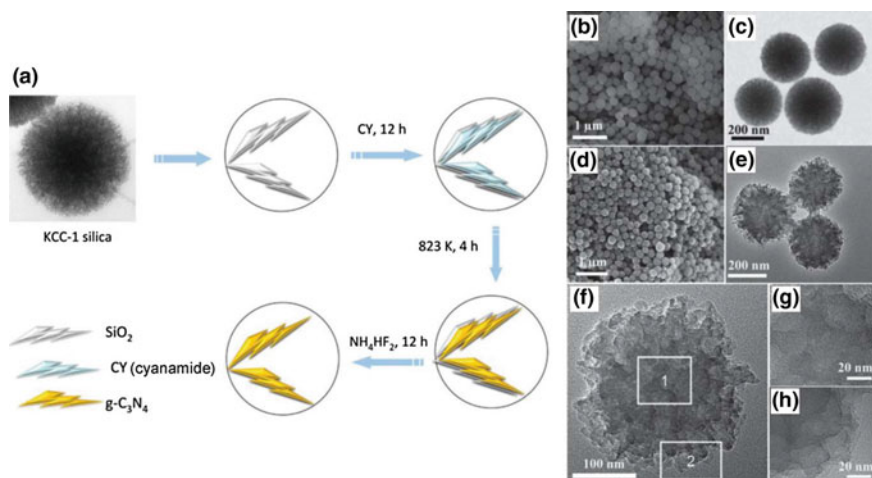


Fig. 9 a Synthesis of nanospherical $g\text{-C}_3\text{N}_4$ composed of nanosheets. **d–h** SEM and TEM images of **b, c** KCC-1 silica template and **d–h** nanospherical $g\text{-C}_3\text{N}_4$ composed of nanosheets. **g, h** Magnified images of areas indicated as 1 and 2 in panel (f), respectively. Reprinted with permission from ref. [75]. Copyright 2014 John Wiley & Sons, Inc.

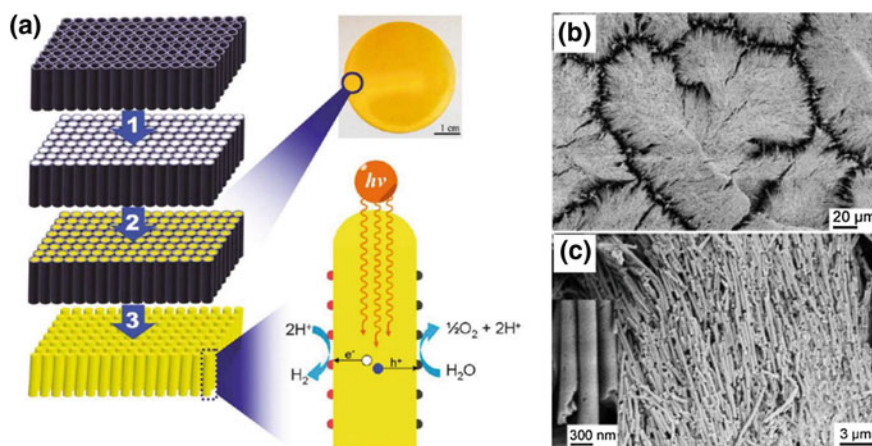


Fig. 10 a Synthesis of $g\text{-C}_3\text{N}_4$ nanorods in three steps: (1) Filling the anodic aluminium oxide (AAO) template (grey) with cyanamide (white), (2) heating the cyanamide/AAO under a N_2 environment, and (3) removal of the AAO template to yield $g\text{-C}_3\text{N}_4$ nanorods (yellow). **b, c** SEM images of $g\text{-C}_3\text{N}_4$ nanorods. The inset in (c) is the high-resolution SEM image of $g\text{-C}_3\text{N}_4$ nanorods. Reprinted with permission from ref. [76]. Copyright 2011 American Chemical Society

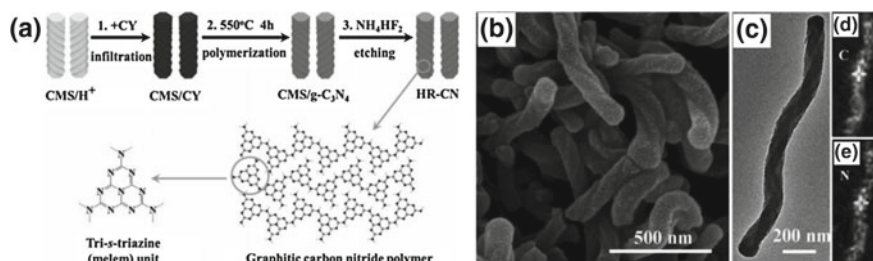


Fig. 11 **a** Synthesis method of helical $g\text{-C}_3\text{N}_4$ nanorods (denoted as HR-CN) using chiral CMS as the hard template and cyanamide (denoted as CY) as the precursor. **b** SEM and **c** TEM images of helical $g\text{-C}_3\text{N}_4$ nanorods. **d**, **e** Elemental mapping images of carbon (C) and nitrogen (N) elements in the helical $g\text{-C}_3\text{N}_4$ nanorods. Reprinted with permission from ref. [77]. Copyright 2014 John Wiley & Sons, Inc.

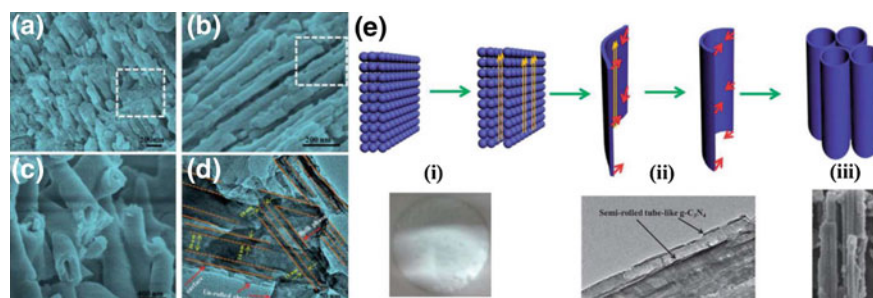


Fig. 12 SEM images of $g\text{-C}_3\text{N}_4$ nanotubes: **a** top view, **b** side view, and **c** surface morphology. **d** TEM image of $g\text{-C}_3\text{N}_4$ nanotubes developed at the surface and in the bulk phase, as shown by the dotted lines and squares. **e** Schematic of the formation of $g\text{-C}_3\text{N}_4$ nanotubes and the corresponding SEM and TEM images. Reprinted with permission from ref. [78]. Copyright 2014 Royal Society of Chemistry

An example of an interesting synthesis strategy is a 3D porous $g\text{-C}_3\text{N}_4$ synthesized by an easy and scalable NaCl-assisted ball milling method, as shown in Fig. 13.

4 Applications

4.1 Photoredox Applications for Artificial Photosynthesis (Water Splitting and Photofixation of CO_2)

Notably, $g\text{-C}_3\text{N}_4$ materials have many desired applications in the fields of photocatalysis, as it is a stable, low-cost polymeric semiconductor with an active band gap of ~ 2.7 eV in the visible range [40, 83–84]. It is widely used in the

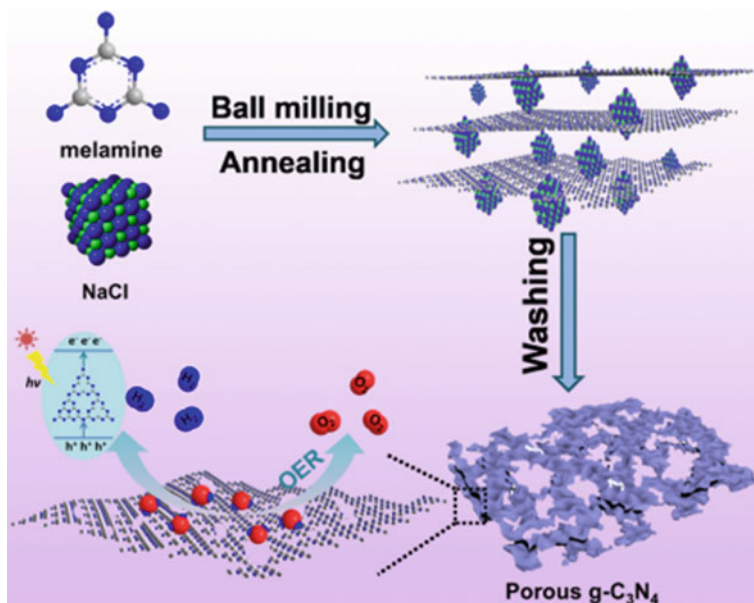


Fig. 13 Schematic representation of synthesis of 3D porous g-C₃N₄ by Menny's group. Reprinted with permission from ref. [79]. Copyright 2019 American Chemical Society

photocatalytic decomposition of water into H₂ and O₂, organic photosynthesis, pollutant degradation, and other applications [78, 79, 84].

As shown, the controlled heating of melamine leads to triazine ring condensation reactions forming a vast 2D network of linked heptazine units [31]. Thus, in addition to easy preparation and low cost, g-C₃N₄ stands out for being environmentally friendly and abundant as well as chemically and thermally stable [40]. Moreover, its structure is composed of bonded units of tri-s-triazine (heptazine, C₆N₇), which is rich in nitrogen groups (Lewis bases) and imparts interesting properties, enabling the insertion of transition metal ions by nanoparticle complexation or deposition, leading to a strategic position for the development of new heterogeneous catalytic systems in addition to evolution in the fields of biosensors, energy, adsorption, photocatalysis (visible photoabsorption), and fungicides [87–84].

Compared with other semiconductors exhibiting photocatalytic activity for oxidation reactions, g-C₃N₄ suffers from some intrinsic limitations because of its synthesis processes, such as a lower ASE and a high electron-gap pair recombination due to polymerization, defects, and poor crystallinity [40, 83, 84]. We believe that an in-depth knowledge of such changes may provide new chemical perspectives that will enable the elucidation of their fundamental properties at the nanoscale, which might be useful for promoting the emergence of new technologies.

Lei and colleagues [84] studied the doping of g-C₃N₄ with nitrogen-bound Pd 'pyridic' structures as they have excellent activity and selectivity for hydrogenation owing to the ease of hydrogen activation and hydrocarbon adsorption, especially at the atomically dispersed Pd sites. Furthermore, many authors have shown that such materials can decompose hydrogen peroxide (H₂O₂), leading to a known four-electron mechanism via sequential hydrogenation [84, 84]. Thus, the oxygen reduction reaction (ORR) mechanism of Pd_x/g-C₃N₄ (with x = 1–4) showed that x = 1 exhibited a higher activity because of a lower energy barrier (0.39 eV), while x = 2 and 3 were promising (energy barriers of 0.63 eV and 0.68 eV, respectively) and had lower values than that calculated for Pt (0.80 eV). On the other hand, x = 4 was found to be unfavourable for ORR, mainly because of its high-energy barrier (approximately 2.61 eV) [84].

Other researchers also explored g-C₃N₄ combinations with noble metals. Li et al. [84] investigated the photocatalytic activity of a platinum-doped efficient co-catalyst with high dispersion and stability, representing a new, highly efficient system for hydrogen evolution reactions. g-C₃N₄ was synthesized by the pyrolysis of urea and Pt-CN by the addition of H₂PtCl₆ in an aqueous dispersion of g-C₃N₄ to give 0.75 samples with 0.11, 0.16, and 0.38 mass% Pt (optimal content: 0.16%). Pt-NPs-CN samples were synthesized by adding H₂PtCl₆ to the g-C₃N₄ solution under Xe-lamp illumination. The dramatic improvement in photocatalytic performance was mainly because of the changes induced by the Pt atoms inserted into the g-C₃N₄ structure via the Pt-N/C bonds between the heptazine units and the metal [84].

Gao et al. [84] synthesized g-C₃N₄ from melamine and doped it with 34 wt% CuCl₂ (Cu-g-C₃N₄); the resulting materials exhibited a strong optical absorption in the visible region, which expanded to the near infrared region. Its efficiency was a priori verified in the photodegradation of methylene blue using H₂O₂ as an oxidizing agent. The material exhibited excellent photocatalytic activity in the dye degradation reaction under visible light as well as good stability, with more than 7-fold increase in its specific surface area after doping with the metal [84].

Xu and colleagues [84] doped g-C₃N₄ with Zn using dicyandiamide as the precursor and zinc halide (0.7, 1.4, 2.1, 2.8, and 3.5%) as the metal source, which resulted in a catalyst with high activity, stability, and reproducibility. They used the catalyst in the transesterification reaction of ethylene carbonate to dimethyl carbonate with CH₃OH. Despite the low surface area, the Zn-g-C₃N₄ catalysts demonstrated remarkably higher catalytic activity compared with the other carbon nitride mesoporous materials (doped with FeCl₃, CuCl₂, NiCl₂, and CoCl₂) under the same catalytic conditions, with higher conversion, selectivity, and yield [84].

Ge et al. [84] prepared g-C₃N₄ loaded with different amounts of Ag nanoparticles (in mass%) by the pyrolysis of melamine and AgNO₃, and determined their photocatalytic activities in methyl orange decomposition and the evolution of hydrogen under visible-light irradiation. The study showed that metallic silver (Ag⁰) was deposited on the polymeric structure, significantly increasing its performance, which can be attributed to the synergistic effect between the noble metal and g-C₃N₄ that promoted the efficient migration of photo-generated carriers [84].

4.2 *Environmental Decontamination*

Hydroxyl radicals can be generated using strong oxidizers such as ozone (O_3) and H_2O_2 , semiconductors materials (such as TiO_2 , WO_3 , ZnO , ZnS , Ag_3VO_4 , and Zn_2GeO_4), and ultraviolet (UV) irradiation [40, 98–84]. This results in the formation of oxygen-reacting organic radicals, which initiate a series of degradation reactions that can culminate in innocuous species, typically CO_2 and H_2O [40, 84].

Among all the advanced oxidation processes (AOPs) used, the Fenton reaction-type process (discovered by H. J. H. Fenton in 1890), which involves the addition of peroxide and iron, is one of the most frequently used because of the low initial investment cost and high degree of compound degradation [102–84]. Currently, Fenton's reagent is widely used to treat a wide variety of industrial wastes and chemicals that are highly hazardous to the environment (such as phenols, formaldehyde, and BTEX) as well as chemical wastes used in dyes, pesticides, wood preservatives, additive plastics, and rubber chemicals [102–84].

However, the Fenton reaction-type AOPs have the disadvantage of the formation of a bottom sludge that is rich in partially oxidized organic materials and metals, which lead to oxide and hydroxide formation [102–84]. This improperly isolated material can cause environmental damage due to an increased biochemical oxygen demand and the presence of heavy metals [104–84].

Diverse industrial sectors such as cosmetics, food, textiles, and paper employ dyes, which leach into watercourses and lead to environmental contamination since the effluents can be potentially toxic to aquatic life [102–84]. Furthermore, the dyes may prevent sunlight penetration, thereby decreasing the photosynthetic rate. Moreover, they generate dangerous compounds upon degradation, which prevent their removal by the conventional treatment methods [102–84].

Recently, $g-C_3N_4$ materials have found widespread use in photocatalytic oxidation and reduction reactions, including environmental applications such as the oxidative degradation of organic aqueous pollutants or gas-phase photolysis as a free-radical photoinitiator in polymerization, and the selective oxidation of alcohol or sulfonate functional groups [40, 84]. For instance, the production of photocatalytic hydrogen from aqueous systems has been demonstrated using $g-C_3N_4$ decorated with co-catalysts as an electrode, which is an innovative and promising system for hydrogen evolution photoelectrochemical reactions [95–84, 84]. Silica templates were used to produce mesoporous C_3N_4 products with large surface areas, which led to high photocatalytic activities [18, 71, 84]. The thermal or chemical exfoliation of bulk C_3N_4 produces colloidal nanoparticles that show better photocatalytic activities. The structural order in the stacking direction is usually of the order of a few nanometres and may vary according to different synthetic methods [84]. Such nanoscale changes create structural defects, which affect the physical and chemical properties of carbon nitride materials [40].

However, materials with a large number of stacked and condensed levels in their structure, called bulk, have several disadvantages such as a low photocatalytic efficiency, small surface area, and few active sites for interaction on their surfaces.

Diverse strategies have been widely employed to improve the performance of carbon nitrides as photocatalysts, such as structural modifications to increase the surface area and introduction of functionalization, doping with metals and non-metals to improve light absorption and obtain specific physicochemical properties, and the production of nanocomposites based on heterojunctions to intensify charge separation and accelerate photocatalytic processes [84]. Thus, carbon nitrides have become viable photocatalysts for various applications such as photocatalytic hydrogen production, CO₂ reduction, organic synthesis, contaminant degradation, and bioimaging [31, 40–69].

Wang et al. [84] produced an iron-doped g-C₃N₄ catalyst by calcining a mixture of melamine with polyvinylpyrrolidone and different amounts (0, 5, 10, 15, 20, and 25 g L⁻¹) of (Fe(NO₃)₃·9H₂O), and determined its activity in the degradation of methylene blue under visible-light irradiation. The maximum efficiency (85.2% degradation in 2 h) was obtained for the sample prepared with 4% Fe, which indicates that the presence of a metal in the structure increased the photocatalytic capacity by increasing the visible-light absorption capability, possibly by the donation of an additional electron to the system [84].

Although research on g-C₃N₄ is currently popular, it is not restricted to the synthesis of carbon nitride materials. Other properties of carbon nitride materials such as hardness, catalysis, and gas storage/sorption as well as the fabrication of organic semiconductors have gained significant research interests. Moreover, as observed from the publication data, progress in C/N chemistry continues, further increasing the interest in the additional properties of carbon nitrides. Hence, we believe that their synthesis and the understanding of their fundamental properties represent a great challenge for the development of next-generation advanced materials. We can therefore consider such systems a hot topic in the field of materials chemistry.

Acknowledgements The authors gratefully acknowledge the support from the Brazilian agencies CNPq (203012/2017–8), CAPES, FAPEMIG, and Fundação Araucária.

References

1. Longo, E., La Porta, F.A.: *Recent Advances in Complex Functional Materials*. Springer International Publishing, Cham (2017)
2. Pimenta, M.A., Geracitano, L.A., Fagan, S.B.: History and national initiatives of carbon nanotube and graphene research in Brazil. *Braz. J. Phys.* **49**(2), 288–300 (2019)
3. Sun, Z., Yan, Z., Yao, J., Beitler, E., Zhu, Y., Tour, J.M.: Growth of graphene from solid carbon sources. *Nature* **468**(7323), 549 (2010)
4. Koppens, F., Chang, D.: Garcia de Abajo, J.: Graphene plasmonics: a platform for strong light–matter interactions. *Nano Lett.* **11**(8), 3370–3377 (2011)
5. Yuan, Hu, López-Lorente, Ángela I., Mizaikoff, Boris: Graphene-based surface-enhanced vibrational spectroscopy: recent developments, challenges, and applications. *ACS Photonics* **6**(9), 2182–2197 (2019)

6. Du, J., Pei, S., Ma, L., Cheng, H.-M.: 25th anniversary article: carbon nanotube- and graphene-based transparent conductive films for optoelectronic devices. *Adv. Mater.* **26**, 1958–1991 (2014)
7. Yoo, E., Okata, T., Akita, T., Kohyama, M., Nakamura, J., Honma, I.: Enhanced electrocatalytic activity of Pt sub-nanoclusters on graphene nanosheet surface. *Nano Lett.* **9**, 2255–2259 (2009)
8. Xie, J.L., Guo, C.X., Li, C.M.: Construction of one-dimensional nanostructures on graphene for efficient energy conversion and storage. *Energy Environ. Sci.* **7**, 2559–2579 (2014)
9. Miao, X., Tongay, S., Petterson, M.K., Berke, K., Rinzler, A.G., Appleton, B.R., Hebard, A. F.: High efficiency graphene solar cells by chemical doping. *Nano Lett.* **12**(6), 2745–2750 (2012)
10. Wang, X., Zhi, L., Müllen, K.: Transparent, conductive graphene electrodes for dye-sensitized solar cells. *Nano Lett.* **8**(1), 323–332 (2008)
11. Cui, K., Maruyama, S.: Multifunctional graphene and carbon nanotube films for planar heterojunction solar cells. *Prog. Energy Combust. Sci.* **70**, 1–21 (2019)
12. Geim, A.K., Novoselov, K.S.: The rise of graphene. *Nat. Mater.* **6**(3), 183–191 (2007)
13. Lopes, L.C., da Silva, L.C., Vaz, B.G., Oliveira, A.R.M., Oliveira, M.M., Rocco, M.L.M., Orth, E.S., Zarkin, A.J.G.: Facile room temperature synthesis of large graphene sheets from simple molecules. *Chem. Sci.* **9**(37), 7297–7303 (2018)
14. Marinho, B., et al.: Electrical conductivity of compacts of graphene, multi-wall carbon nanotubes, carbon black, and graphite powder. *Powder Technol.* **221**, 351–358 (2012)
15. Georgakilas, V., Perman, J.A., Tucek, J., Zboril, R.: Broad family of carbon nanoallotropes: classification, chemistry, and applications of fullerenes, carbon dots, nanotubes, graphene, nanodiamonds, and combined superstructures. *Chem. Rev.* **115**, 4744–4822 (2015)
16. Wallace, P.R.: The band theory of graphite. *Phys. Rev. Lett.* **71**(9), 622 (1947)
17. Wirth-Lima, A.J., Silva, M.G., Sombra, A.S.B.: Comparisons of electrical and optical properties between graphene and silicene—a review. *Chin. Phys. B* **27**(2), 023201 (2018)
18. Sun, J., Zhang, J., Zhang, M., Antonietti, M., Fu, X., Wang, X.: Bioinspired hollow semiconductor nanospheres as photosynthetic nanoparticles. *Nat. Commun.* **3**, 1139 (2012)
19. Novoselov, K.S., et al.: Electric field effect in atomically thin carbon films. *Science* **306**, 666–669 (2004)
20. The Nobel Prize in Physics 2010. NobelPrize.org. Nobel Media AB 2019. Sat. 28 Sep 2019. <https://www.nobelprize.org/prizes/physics/2010/summary/>
21. Algara-Siller, G., et al.: Triazine-based graphitic carbon nitride: a two-dimensional semiconductor. *Angew. Chem. Int. Ed.* **53**, 7450–7455 (2014)
22. Teter, D.M., Hemley, R.J.: Low-compressibility carbon nitrides. *Science* **271**, 53–55 (1996)
23. Ong, W.-J., Tan, L.-L., Ng, Y.H., Yong, S.-T., Chai, S.-P.: Graphitic carbon nitride (g-C₃N₄)-based photocatalysts for artificial photosynthesis and environmental remediation: are we a step closer to achieving sustainability? *Chem. Rev.* **116**, 7159–7329 (2016)
24. Botari, T., et al.: Thermodynamic equilibria in carbon nitride photocatalyst materials and conditions for the existence of graphitic carbon nitride g-C₃N₄. *Chem. Mater.* **29**, 4445–4453 (2017)
25. Miller, T.S., et al.: Carbon nitrides: synthesis and characterization of a new class of functional materials. *Phys. Chem. Chem. Phys.* **19**, 15613–15638 (2017)
26. Irving, H.: A review concerning the intumescence of thiocyanates of Hg and similar compounds. *Sci. Prog.* **30**, 62–66 (1935)
27. Miller, T.S., et al.: Pharaoh's serpents: new insights into a classic carbon nitride material. *Z. Anorg. Allg. Chem.* **643**, 1572–1580 (2017)
28. Franklin, E.C.: The ammono carbonic acids. *J. Am. Chem. Soc.* **44**, 486–509 (1922)
29. Liebig, J.V.: Über einige Stickstoff-Verbindungen. *Ann. Pharm. (Lemgo, Ger.)* **10**, 10 (1834)
30. Lotsch, B.V., Schnick, W.: New light on an old story: formation of melam during thermal condensation of melamine. *Chem. Eur. J.* **13**, 4956–4968 (2007)

31. Schwarzer, A., Saplinova, T., Kroke, E.: Tri-s-triazines (s-heptazines)—from a “mystery molecule” to industrially relevant carbon nitride materials. *Coord. Chem. Rev.* **257**, 2032–2062 (2013)
32. Wilson, E.K.: Old molecules, new chemistry. *Chem. Eng. News* **82**(22), 34–35 (2004)
33. Pauling, L., Sturdivant, J.H.: The structure of cyameluric acid, hydromelonic acid and related substances. *Proc. Natl. Acad. Sci.* **23**, 615–620 (1937)
34. Hosmane, R.S., Rossman, M.A., Leonard, N.J.: Synthesis and structure of tri-s-triazine. *J. Am. Chem. Soc.* **104**, 5497–5499 (1982)
35. Kroke, E., Schwarz, M.: Novel group 14 nitrides. *Coord. Chem. Rev.* **248**, 493–532 (2004)
36. Kroke, E., Schwarz, M., Horath-bordon, E., Kroll, P., Norman, A.D.: Tri-s-triazine derivatives. Part I. From trichloro-tri-s-triazine to graphitic C_3N_4 structures. *New J. Chem.* **26**, 508–512 (2002).
37. Komatsu, T.: Prototype carbon nitrides similar to the symmetric triangular form of melon. *J. Mater. Chem.* **11**, 802–805 (2001)
38. Komatsu, T., Corporation, A.K.: Shock synthesis and characterization of new diamond-like carbon nitrides. *Phys. Chem. Chem. Phys.* **6**, 878–880 (2004)
39. Komatsu, T.: The first synthesis and characterization of cyameluric high polymers. *Macromol. Chem. Phys.* **202**, 19–25 (2001)
40. Ju, B., Irran, E., Kroll, P., Mu, H., Schnick, W.: Melem (2,5,8-Triamino-tri-s-triazine), an important intermediate during condensation of melamine rings to graphitic carbon nitride: synthesis, structure determination by X-ray powder diffractometry, solid-state NMR, and theoretical studies. *J. Am. Chem. Soc.* **125**, 10288–10300 (2003)
41. Gmelin, L.: Ueber einige Verbindungen des Melon's. *Ann. Der Pharm.* **15**, 252–258 (1835)
42. Liebig, J.: *Ann. Der Chem. Uns Pharm.* **50**, 337 (1844)
43. Courtesy Linus Pauling Papers, Special Collections & Archives Research Center, Oregon State University Libraries <http://scarc.library.oregonstate.edu/digitalresources/pauling/>
44. Naseri, A., Samadi, M., Pourjavadi, A., Moshfegh, A.Z., Ramakrishna, S.: Graphitic carbon nitride (g- C_3N_4)-based photocatalysts for solar hydrogen generation: recent advances and future development directions. *J. Mater. Chem.* **5**, 23406–23433 (2017)
45. Mishra, A., et al.: Graphitic carbon nitride (g- C_3N_4)-based metal-free photocatalysts for water splitting: a review. *Carbon* **149**, 693–721 (2019)
46. Wang, S., Li, C., Wang, T., Zhang, P., Li, A., Gong, J.: Controllable synthesis of nanotube-type graphitic C_3N_4 and their visible-light photocatalytic and fluorescent properties. *J. Mater. Chem. A* **2**, 2885–2890 (2014)
47. Cardozo Amorin, L.H., Suzuki, V., de Paula, N., Duarte, J.L., da Silva, M., Taft, C., La Porta, F.A.: Electronic, structural, optical, and photocatalytic properties of graphitic carbon nitride. *New J. Chem.* **43**(34), 13647–13653 (2019)
48. Wang, X., Maeda, K., Chen, X., Takanaabe, K., Domen, K., Hou, Y., Fu, X., Antonietti, M.: Polymer semiconductors for artificial photosynthesis: hydrogen evolution by mesoporous graphitic carbon nitride with visible light. *J. Am. Chem. Soc.* **131**(5), 1680–1681 (2009)
49. Bai, X., Yan, S., Wang, J., Wang, L., Jiang, W., Wu, S., Sun, C., Zhu, Y.: A simple and efficient strategy for the synthesis of a chemically tailored g- C_3N_4 material. *J. Mater. Chem. A* **2**, 17521–17529 (2014)
50. Zhang, Y., Liu, J., Wu, G., Chen, W.: Porous graphitic carbon nitride synthesized via direct polymerization of urea for efficient sunlight-driven photocatalytic hydrogen production. *Nanoscale* **4**, 5300–5303 (2012)
51. Zhang, G., Zhang, J., Zhang, M., Wang, X.: Polycondensation of thiourea into carbon nitride semiconductors as visible light photocatalysts. *J. Mater. Chem.* **22**, 8083–8091 (2012)
52. Melissen, S.T.A.G., Bahers, T.L., Steinmann, S.N., Sautet, P.: Relationship between carbon nitride structure and exciton binding energies: a DFT perspective. *J. Phys. Chem. C* **120**(43), 24542–24550 (2016)
53. Papailias, I., Giannakopoulou, T., Todorova, N., Demotikali, D., Vaimakis, T., Trapalis, C.: Effect of processing temperature on structure and photocatalytic properties of g- C_3N_4 . *Appl. Surf. Sci.* **358**, 278–286 (2015)

54. Jiang, T., Du, Y., Dong, M., Zhao, Q.: The facile synthesis and enhanced photocatalytic activity of a graphitic carbon nitride isotype heterojunction with ordered mesopores. *New J. Chem.* **43**, 10915–10925 (2019)
55. Jiménez-Calvo, P., Marchal, C., Cottineau, T., Caps, V., Keller, V.: Influence of the gas atmosphere during the synthesis of g-C₃N₄ for enhanced photocatalytic H₂ production from water on Au/g-C₃N₄ composites. *J. Mater. Chem. A* **7**, 14849–14863 (2019)
56. Bellamkonda, S., Shanmugam, R., Gangavarapu, R.R.: Extending the π -electron conjugation in 2D planar graphitic carbon nitride: efficient charge separation for overall water splitting. *J. Mater. Chem. A* **7**, 3757–3771 (2019)
57. Zhu, J., Xiao, P., Li, H., Carabineiro, S.A.: Graphitic carbon nitride: synthesis, properties, and applications in catalysis. *ACS Appl. Mater. Interfaces* **6**(19), 16449–16465 (2014)
58. Schaber, P.M., Colson, J., Higgins, S., Thielen, D., Anspach, B., Brauer, J.: Thermal decomposition (pyrolysis) of urea in an open reaction vessel. *Thermochim. Acta* **424**, 131–142 (2004)
59. Bernhard, A.M., Peitz, D., Elsener, M., Wokaun, A., Kröcher, O.: Hydrolysis and thermolysis of urea and its decomposition byproducts biuret, cyanuric acid and melamine over anatase TiO₂. *Appl. Catal. B Environ.* **115–116**, 129–137 (2012)
60. Xu, J., Wu, H.-T., Wang, X., Xue, B., Li, Y.-X., Cao, Y.: A new and environmentally benign precursor for the synthesis of mesoporous g-C₃N₄ with tunable surface area. *Phys. Chem. Chem. Phys.* **15**, 4510 (2013)
61. Liu, J., Zhang, T., Wang, Z., Dawson, G., Chen, W.: Simple pyrolysis of urea into graphitic carbon nitride with recyclable adsorption and photocatalytic activity. *J. Mater. Chem.* **21**, 14398–14401 (2011)
62. Ayán-Varela, M., Villar-Rodil, S., Paredes, J.I., Munuera, J.M., Pagán, A., Lozano-Pérez, A. A., Cenis, J.L., Martínez-Alonso, A., Tascón, J.M.D.: Investigating the dispersion behavior in solvents, biocompatibility, and use as support for highly efficient metal catalysts of exfoliated graphitic carbon nitride. *ACS Appl. Mater. Interfaces* **7**(43), 24032–24045 (2015)
63. Shi, L., Liang, T., Liang, L., Wang, F., Liu, M.: High temperature promoted synthesis of graphitic carbon nitride with porous structure and enhanced photocatalytic activity. *J. Porous Mater.* **22**, 1393–1399 (2015)
64. Tahir, M., Cao, C., Butt, F.K., Butt, M.S.: Large scale production of novel g-C₃N₄ micro strings with high surface area and versatile photodegradation ability. *Cryst. Eng. Comm.* **16**, 1825–1830 (2014)
65. Tahir, M., Mahmood, N., Zhu, J., Mahmood, A.: One dimensional graphitic carbon nitrides as effective metal-free oxygen reduction catalysts. *Sci. Rep.* **5**, 12389 (2015)
66. Zhang, S., Li, J., Zeng, M., Xu, J., Wang, X., Hu, W.: Polymer nanodots of graphitic carbon nitride as effective fluorescent probes for the detection of Fe³⁺ and Cu²⁺ ions. *Nanoscale* **6**, 4157–4162 (2014)
67. Yang, S., Feng, X., Wang, X., Müllen, K.: Graphene-based carbon nitride nanosheets as efficient metal-free electrocatalysts for oxygen reduction reactions. *Angew. Chem. Int. Ed. Engl.* **50**, 5339–5343 (2011)
68. Cadan, F.M.: Otimização Da Síntese de Nitreto de Carbono Grafítico e a Formação de Heteroestruturas Com Trióxido de Tungstênio. Universidade de São Paulo, 2017
69. Dai, H., Gao, X., Liu, E., Yang, Y., Hou, W., Kang, L., Fan, J., Hu, X.: Synthesis and characterization of graphitic carbon nitride sub-microspheres using microwave method under mild condition. *Diam. Relat. Mater.* **38**, 109–117 (2013)
70. Xu, L., Xia, J., Xu, H., Yin, S., Wang, K., Huang, L.: Reactable ionic liquid assisted solvothermal synthesis of graphite-like C₃N₄ hybridized α -Fe₂O₃ hollow microspheres with enhanced supercapacitive performance. *J. Power Sources* **245**, 866–874 (2014)
71. Bojdys, M.J., Müller, J., Antonietti, M., Thomas, A.: Ionothermal synthesis of crystalline, condensed, graphitic carbon nitride. *Chem. A Eur. J.* **14**, 8177–8182 (2008)
72. Wen, J., Xie, J., Chen, X., Li, X.: A review on g-C₃N₄-based photocatalysts. *Appl. Surf. Sci.* **391**, 72–123 (2017)

73. Zhang, J., Guo, F., Wang, X.: An optimized and general synthetic strategy for fabrication of polymeric carbon nitride nanoarchitectures. *Adv. Funct. Mater.* **23**, 3008–3014 (2013)
74. Zheng, D., Huang, C., Wang, X.: Post-annealing reinforced hollow carbon nitride nanospheres for hydrogen photosynthesis. *Nanoscale* **7**, 465–470 (2015)
75. Zhang, J., Zhang, M., Yang, C., Wang, X.: Nanospherical carbon nitride frameworks with sharp edges accelerating charge collection and separation at a soft photocatalytic interface. *Adv. Mater.* **26**, 4121–4126 (2014)
76. Li, X., Zhang, J., Chen, X., Fischer, A., Thomas, A., Antonietti, M., Wang, X.: Condensed graphitic carbon nitride nanorods by nanoconfinement: promotion of crystallinity on photocatalytic conversion. *Chem. Mater.* **23**, 4344–4348 (2011)
77. Zheng, Y., Lin, L., Ye, X., Guo, F., Wang, X.: Helical graphitic carbon nitrides with photocatalytic and optical activities. *Angew. Chem. Int. Ed. Engl.* **53**, 11926–11930 (2014)
78. Shengping Wang, C.L., Wang, T., Zhang, P., Li, A., Gong, J.: Controllable synthesis of nanotube-type graphitic C_3N_4 and their visible-light photocatalytic and fluorescent properties. *J. Mater. Chem. A* **2**, 2885–2890 (2014)
79. Qian, X., Meng, X., Sun, J., Jiang, L., Wang, Y., Zhang, J., Hu, X., Shalom, M., Zhu, J.: Salt-assisted synthesis of 3D porous g- C_3N_4 as a bifunctional photo- and electrocatalyst. *ACS Appl. Mater. Interfaces* **11**, 27226–27232 (2019)
80. Peng, G., Qin, J., Volokh, M., Liu, C., Shalom, M.: Graphene oxide in carbon nitride: from easily processed precursors to a composite material with enhanced photoelectrochemical activity and long-term stability. *J. Mater. Chem. A* **7**, 11718–11723 (2019)
81. Zheng, Y., Liu, J., Liang, J., Jaroniec, M., Qiao, S.Z.: Graphitic carbon nitride materials: controllable synthesis and applications in fuel cells and photocatalysis. *Energy Environ. Sci.* **5**, 6717–6731 (2012)
82. Volokh, M., Peng, G., Barrio, J., Shalom, M.: Carbon nitride materials for water splitting photoelectrochemical cells. *Angew. Chem. Int. Ed.* **58**, 6138–6151 (2019)
83. She, X., Wu, J., Xu, H., Mo, Z., Lian, J., Song, Y., Liu, L., Du, D., Li, H.: Enhancing charge density and steering charge unidirectional flow in 2D non-metallic semiconductor-CNTs-metal coupled photocatalyst for solar energy conversion. *Appl. Catal. B Environ.* **202**, 112–117 (2017)
84. Zhou, C., Shi, R., Shang, L., Wu, L.-Z., Tung, C.-H., Zhang, T.: Template-free large-scale synthesis of g- C_3N_4 microtubes for enhanced visible-light-driven photocatalytic H_2 production. *Nano Res.* **11**(6), 3462–3468 (2018)
85. Melissen, S., Le Bahers, T., Steinmann, S.N., Sautet, P.: Relationship between carbon nitride structure and exciton binding energies: A DFT perspective. *J. Phys. Chem. C* **119**, 25188–25196 (2015)
86. Wang, A., Wang, C., Fu, L., et al.: Recent advances of graphitic carbon nitride-based structures and applications in catalyst, sensing, imaging, and LEDs. *Nano-Micro Lett.* **9**, 47 (2017)
87. Del Poeta, M., Schell, W.A., Dykstra, C.C., Jones, S., Tidwell, R.R., Czarny, A., Bajic, M., Bajic, M., Kumar, A., Boykin, D., Perfect, J.R.: Structure-in vitro activity relationships of pentamidine analogues and dication-substituted bis-benzimidazoles as new antifungal agents. *Antimicrob. Agents Chem.* **42**, 2495 (1998)
88. Yu, S., Li, J., Zhang, Y., Li, M., Dong, F., Zhang, T., Huang, H.: Local spatial charge separation and proton activation induced by surface hydroxylation promoting photocatalytic hydrogen evolution of polymeric carbon nitride. *Nano Energy* **50**, 383–392 (2018)
89. Jia, Q., Zhang, S., Gao, Z., Yang, P., Gu, Q.: In situ growth of triazine–heptazine based carbon nitride film for efficient (photo) electrochemical performance. *Catal. Sci. Technol.* **9**, 425–435 (2019)
90. Bu, X., Li, J., Yang, S., Sun, J., Deng, Y., Yang, Y., Wang, G., Peng, Z., He, P., Wang, X., Ding, G., Yang, J., Xie, X.: Surface modification of C_3N_4 through oxygen-plasma treatment: a simple way toward excellent hydrophilicity. *ACS Appl. Mater. Interfaces* **8**, 31419–31425 (2016)

91. Wang, N., Wang, J., Hu, J., Lu, X., Sun, J., Shi, F., Liu, Z.H., Lei, Z., Jiang, R.: Design of Palladium-doped g-C₃N₄ for enhanced photocatalytic activity toward hydrogen evolution reaction. *ACS Appl. Energy Mater.* **1**, 2866–2873 (2018)
92. Cui, Y., Ding, Z., Liu, P., Antonietti, M., Fu, X., Wang, X.: Metal-free activation of H₂O₂ by g-C₃N₄ under visible light irradiation for the degradation of organic pollutants. *Phys. Chem. Chem. Phys.* **14**, 1455–1462 (2012)
93. Li, X., Bi, W., Zhang, L., Tao, S., Chu, W., Zhang, Q., Luo, Y.: Single-atom Pt as co-catalyst for enhanced photocatalytic H₂ evolution. *Adv. Mater.* **28**, 2427–2431 (2016)
94. Gao, J., Wang, Y., Zhou, S., Lin, W., Kong, Y.: A facile one-step synthesis of Fe-doped g-C₃N₄ nanosheets and their improved visible-light photocatalytic performance. *Chem. Cat. Chem.* **9**, 1708–1715 (2017)
95. Xu, J., Long, K., Wang, Y., Xue, B., Li, Y.: Fast and facile preparation of metal-doped g-C₃N₄ composites for catalytic synthesis of dimethyl carbonate. *Appl. Catal. A, Gen.* **496**, 1–8 (2015)
96. Wang, X., Maeda, K., Thomas, A., Takanabe, K., Xin, G., Carlsson, J.M., Domen, K., Antonietti, M.: A metal-free polymeric photocatalyst for hydrogen production from water under visible light. *Nat. Mater.* **8**, 76–80 (2008)
97. Suzuki, V., Amarin, L., Lima, N., Machado, E., Carvalho, P., Castro, S., Alves, C., Carli, A., Li, M.S., Longo, E., La Porta, F.D.A.: Characterization of the structural, photocatalytic and in vitro and in vivo anti-inflammatory properties of the Mn²⁺ doped Zn₂GeO₄ nanorods. *J. Mater. Chem. C* **7**, 8216–8225 (2019)
98. Wei, H., McMaster, W.A., Tan, J.Z., Cao, L., Chen, D., Caruso, R.A.: Mesoporous TiO₂/g-C₃N₄ microspheres with enhanced visible-light photocatalytic activity. *J. Phys. Chem. C* **121**, 22114–22122 (2017)
99. Sachs, M., Park, J.S., Pastor, E., Kafizas, A., Wilson, A.A., Francàs, L., Gul, S., Ling, M., Blackman, C., Yano, J., Walsh, A.: Effect of oxygen deficiency on the excited state kinetics of WO₃ and implications for photocatalysis. *Chem. Sci.* **10**(22), 5667–5677 (2019)
100. Kudo, A., Miseki, Y.: Heterogeneous photocatalyst materials for water splitting. *Chem. Soc. Rev.* **38**, 253–278 (2009)
101. Laine, D.F., Cheng, I.F.: The destruction of organic pollutants under mild reaction conditions: a review. *Microchem. J.* **85**, 183 (2007)
102. Oliveira, L.C.A., Ramalho, T.C., Souza, E.F., Guerreiro, M.C.: Catalytic properties of goethite prepared in the presence of Nb on oxidation reactions in water: computational and experimental studies. *Appl. Catal. B Environ.* **83**, 169 (2008)
103. Vorontsov, A.V.: Advancing Fenton and photo-Fenton water treatment through the catalyst design. *J. Hazard. Mater.* **372**, 103–112 (2019)
104. Walling, C.: Fenton's reagent revisited. *Acc. Chem. Res.* **84**, 125–131 (1975)
105. Hansson, H., Kaczala, F., Marques, M., Hogland, W.: Photo-Fenton and Fenton oxidation of recalcitrant industrial wastewater using nanoscale zero-valent iron. *Int. J. Photoenergy* Article ID 531076 ,11 (2012)
106. Ramos, P.H., La Porta, F.A., de Resende, E.C., Giacoppo, J.O.S., Guerreiro, M.C., Ramalho, T.C.: Fe-DPA as catalyst for oxidation of organic contaminants: evidence of homogeneous fenton process. *Z. Anorg. Allg. Chem.* **641**(5), 780–785 (2015)
107. Kumar, S., Karthikeyan, S., Lee, A.F.: g-C₃N₄-Based Nanomaterials for Visible Light-Driven Photocatalysis. *Catalysts* **8**(2), 74 (2018)
108. Gao, L., Cui, Y., Wang, J., Cavalli, A., Standing, A., Vu, T.T.T., Verheijen, M.A., Haverkort, J.E.M., Bakkers, E.P.A.M., Notten, P.H.L.: Photoelectrochemical hydrogen production on InP nanowire arrays with molybdenum sulfide electrocatalysts. *Nano Lett.* **14**, 3715–3719 (2014)
109. Wang, D., Sun, H., Luo, Q., Yang, X., Yin, R.: An efficient visible-light photocatalyst prepared from g-C₃N₄ and polyvinyl chloride. *Appl. Catal. B, Environ.* **156–157**, 323–330 (2014)

Chemical Modification of Polysaccharides and Applications in Strategic Areas



**Nívia do Nascimento Marques, Keila dos Santos Alves,
Rosângela Regia Lima Vidal, Ana Maria da Silva Maia,
Liszt Yeltsin Coutinho Madruga, Priscila Schroeder Curti
and Rosângela de Carvalho Balaban**

Abstract The synthesis of new polymeric materials from the monomers is an arduous task, which does not always achieve the desired success. A very promising alternative that grows each year is the chemical modification of existing polymers. In this case, the polymer is one of the reagents of well-known properties and, through conventional chemical reactions, new functional groups can be inserted into the polymer chain, leading to a wide diversity of properties and applications for the new materials obtained. However, for the chemical modification reaction to succeed, it is critical that the polymer has reactive functional groups that can be used in chemical reactions. Polysaccharides are renewable, biodegradable and abundant natural polymers throughout the planet Earth, which have, on average, three hydroxyls in each repeating unit. With these characteristics, they have been extensively used in reactions of chemical modification, to reach biodegradable products, renewable sources and with important physicochemical properties for the

N. do Nascimento Marques · L. Y. C. Madruga · R. de Carvalho Balaban (✉)
Universidade Federal do Rio Grande do Norte, Instituto de Química, Campus Universitário,
Lagoa Nova, Natal, Rio Grande do Norte CEP 59078-970, Brasil
e-mail: rosangelabalaban@hotmail.com

K. dos Santos Alves
Instituto Federal de Educação, Ciência e Tecnologia do Rio Grande do Norte, Natal-Central,
Av. Senador Salgado Filho, 1559, Natal, Rio Grande do Norte CEP 59015-000, Brasil

R. R. L. Vidal
Universidade Federal da Bahia, Instituto de Química, Departamento de Físico-química,
Rua Barão de Jeremoabo, 147, Campus universitário de Ondina, Salvador,
BA CEP 40170-115, Brasil

A. M. da Silva Maia
Universidade Federal de Tocantins, UFT, Campus Gurupi, Colegiado de Ciências agrárias e
biotecnológicas, Gurupi, Tocantins CEP 77402-970, Brasil

P. S. Curti
Universidade Tecnológica Federal do Paraná, UTFPR, Campus Londrina,
Departamento Acadêmico de Química, Avenida dos Pioneiros, 3131,
Londrina, Paraná CEP 86036-370, Brasil

industries. In this chapter, we will present different methodologies used in the synthesis of new materials from polysaccharides, as well as the study of their properties and technical feasibility of application in important sectors of the industry.

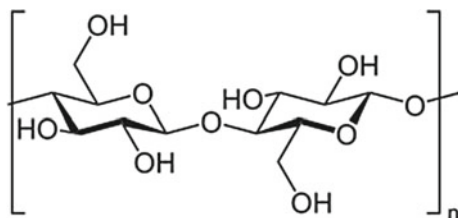
Keywords Polysaccharide • Chemical modification • Hydrocolloid

1 Cellulose

Cellulose is one of the most abundant biopolymers on Earth and highly important organic polymer [1, 2]. This biopolymer is found in higher plants, several marine animals, algae, fungi and bacteria [3]. The cellulose is considered the principal structural cell wall component of all major plants [4] and this polymer is present around 33% in plant, 50% in wood and 90% in cotton [5]. Besides, it owns many valuable properties, such as non-toxicity, renewability, biodegradability and can produce several derivatives by chemical modification [2], making this polymer attractive for using in several applications in the production of papers, paints, textiles, foods and pharmaceutical products [4].

Cellulose is a linear polymer of D-anhydroglucopyranose units (AGU) linked by β -(1 \rightarrow 4) glycosidic bonds between C-1 and C-4 of adjacent glucose moieties. Each AGU unit has three hydroxyl groups: a primary hydroxyl at C-6 and two secondary hydroxyls at C-2 and C-3 (Fig. 1). The average degree of polymerization (DP) as well as the polydispersity depend on the origin and the extraction method of the cellulose [5, 6]. This polymer is not soluble in water and in common organic solvents due to the intramolecular hydrogen bonding between the OH groups at C-2 and C-6 positions and the intermolecular hydrogen bonding between the OH groups at C-3 and C-6 positions. The presence of the strong intermolecular hydrogen bonding is the principal responsible for the insolubility of cellulose. Therefore, to dissolve this polymer it is necessary to break the intermolecular hydrogen bonds to gain access to the OH group at C-6 position. In addition, the intramolecular hydrogen bonds give the cellulose molecule greater rigidity and consequently high solution viscosity, high tendency to crystallize and ability to form fibrillar strands [5]. The insolubility of cellulose in water and in the most organic solvents represents a major obstacle for cellulose modification [7].

Fig. 1 Chemical structure of cellulose



1.1 Cellulose Derivatives, Some Properties and Potential Applications

Cellulose is submitted to chemical modification due to the reactivity of hydroxyl groups at C-2, C-3 and C-6 positions resulting in different cellulose derivatives [5]. Carboxymethylcellulose (CMC), which is one of the most important cellulose derivatives, presents a hydrophobic polysaccharide backbone and many hydrophilic carboxyl groups [8]. The carboxymethylation of cellulose [9] leads to a semi-flexible anionic polymer backbone based on β -(1 \rightarrow 4)-D-glucopyranose repeating units with hydroxyl groups partially substituted by carboxymethyl groups with average degree of substitution in the range 0.6–0.95 [10]. CMC is usually used as thickener or rheological modifier in food and oil industries, as well as in biomedical and pharmaceutical devices because it is biodegradable, nontoxic and inexpensive [8, 9, 11, 12]. The influence of carboxymethylcellulose on filtration control of water-based drilling fluids, in the presence of salt and calcium carbonate, was carefully evaluated by rheological measurements in the last years [12–14].

The effect of intra and/or intermolecular hydrophobic associations of modified carboxymethylcellulose, as a function of hydrophobic group content, polymer concentration, salt and temperature, has been evaluated through viscosity and light scattering measurements. In these studies, N, N-dihexylacrylamide [15], poly (N-isopropylacrylamide) (PNIPAM) [16–18] and Jeffamine[®] (the commercial name for methoxy poly(ethylene oxide/propylene oxide)-2-propylamine) [19], were used as hydrophobic moiety. The properties of all hydrophobically modified CMCs were compared to the precursor one, at high temperature and salinity, indicating promising performance of the modified CMC for application in improved oil recovery processes, in which is required enhanced viscosity in the conditions of oil reservoir (high temperature and high salinity).

Vidal et al. [15] evaluated the intra and intermolecular hydrophobic associations between carboxymethylcellulose chains modified with different amounts of N, N-dihexylacrylamide (1 to 6 mol%) in aqueous solutions (0.5 M NaCl, synthetic formation water and Milli-Q water), at different temperatures. The associating copolymers were obtained by inserting a low amount (1 to 6 mol%) of N, N-dihexylacrylamide onto the CMC chain through the micellar copolymerization method. The viscosity and dynamic light scattering results showed that the copolymer with 6 mol% hydrophobic group had the lowest values for intrinsic viscosity, average molar mass and hydrodynamic radius, indicating a strongly compact structure due to intramolecular hydrophobic associations. The authors also observed intermolecular hydrophobic interactions from rheological measurements of the copolymers with 1 and 3 mol% of N,N-dihexylacrylamide in synthetic formation water at high polymer concentrations (10 g/L) and high temperature (55 °C), concluding that the bridges formed between divalent cations and carboxyl groups were not sufficient to promote an increase in aggregate size.

Lima et al. [16] investigated the rheological behavior of physical blends between sodium carboxymethylcellulose (CMC) and PNIPAM for total polymer

concentrations of 2 and 6 g/L, and different CMC-PNIPAM percentage compositions (25–75, 50–50 and 75–25%) in aqueous solution as a function of temperature (25–40 °C). The PNIPAM was synthesized via free radical polymerization using potassium persulfate/*N,N,N',N'*-tetramethylethylenediamine (KPS/TEMED) redox pair as a free-radical initiator (10 and 2.5 mmol/L). The rheological behavior of pure polymers as a function of temperature was also analyzed for polymer concentration ranging from 0.5 to 6 g/L. The rheological results showed thermotolerant behavior for the physical blend containing 50% of CMC and 50% of PNIPAM in aqueous solution at 6 g/L, due to the increase of apparent viscosity with the temperature in the studied range. The authors attributed this behavior to the contributions of intermolecular hydrogen interactions and carboxylate groups along the CMC chain. They also observed increased apparent viscosities of physical blends at temperatures above 34.3 °C, due to the lower critical solution temperature (LCST) of PNIPAM chains, attributed to the hydrophobic contributions. Similar behavior was observed for the physical blend of 25% CMC and 75% PNIPAM in solution, with a total polymer concentration of 2 g/L. The authors concluded that the thermotolerant behavior observed in the CMC-PNIPAM physical blends depends on the total polymer concentration and the composition of the mixture.

Marques et al. [18] studied the synthesis reproducibility for PNIPAM-g-CMC obtained by precipitation polymerization method using potassium persulfate (KPS) as initiator with great mass ratio of NIPAM in the feed. This reproducibility was verified by spectroscopic and rheological properties. The authors also evaluated the thermal and rheological properties of PNIPAM based graft copolymers and compared with the precursor polymers and PNIPAM/CMC physical blend of the same chemical composition to that of copolymers. The results showed that the copolymers were successfully prepared and presented better stability than CMC and PNIPAM/CMC physical blends, attributed to the high content of PNIPAM in the copolymer. Besides, the PNIPAM-g-CMC showed a higher apparent viscosity than CMC/PNIPAM physical blend and PNIPAM, probably because of the grafts action as spacers. The authors also evaluated the rheological behavior of copolymers, physical blends and precursor polymers as a function of temperature (20–45 °C), at shear rate of 5 s^{-1} , in phosphate-buffered saline (PBS) with pH 7.2, for polymer concentration of 10 g/L. They observed that, for the PNIPAM and the physical blend, the apparent viscosity increases at association temperatures of 30.7 and 33.2 °C, respectively, attributed to the attractive interactions among the isopropyl groups of PNIPAM. The hydrophobic interactions were observed at higher temperature. For PNIPAM-g-CMC, it was observed the decrease of viscosity with the heating, and a discrete increase viscosity at 32.2 °C, indicating the start of hydrophobic interactions. After 33.8 °C, the apparent viscosity decreased again, due to the contraction of the network's aggregates. The authors concluded that the copolymer presented greater thermal stability with the increase of temperature and the chemical modification of CMC was confirmed by the spectroscopic and the rheological properties.

Marques et al. [17] evaluated the thermoassociative behavior of CMC-g-PNIPAM graft copolymers at low polymer concentrations (3 and 7 g/L) in water.

The amino terminated poly(*N*-isopropylacrylamide) (PNIPAM-NH₂) was synthesized by radical polymerization in deionized water using the redox pair potassium persulfate/2-aminoethanethiol hydrochloride (KPS/AET.HCl) in a glove box under N₂(g) atmosphere. The absence of oxygen was monitored during polymerization, in order to ensure that the PNIPAM-NH₂ molar mass would be controlled only by the amount of chain transfer agent. The CMC-g-PNIPAM graft copolymers were obtained in water using a water-soluble carbodiimide and *N*-hydroxysuccinimide as activators at 25 °C. The authors confirmed the chemical modification of CMC by coupling reaction with amino terminated PNIPAM by infrared spectroscopy together with TG/DTG analyses. The authors studied the side chain effect on the rheological behavior of three copolymers in water varying polymer concentration (3 and 7 g/L) and temperature (25 and 60 °C). No difference was observed between apparent viscosity for three copolymers with different side chains length of PNIPAM grafted on the CMC backbone, at polymer concentration of 3 g/L and at 25 °C. However, at 60 °C, some changes in viscosity were observed and attributed to the intramolecular hydrophobic interactions of PNIPAM above its LCST. At 60 °C and 7 g/L, some copolymers exhibited thermo-thickening behavior attributed to the intermolecular associations between the side chains that are favored by rising temperature. The researchers concluded that thermoassociative behavior in water for CMC-g-PNIPAM graft copolymers depend on the amount of chain transfer agent used for the PNIPAM-NH₂ synthesis.

Luz et al. [14] evaluated the influence of xanthan gum (XG) and carboxymethylcellulose (CMC) on filtration control of water-based drilling fluids at presence of salt (NaCl) in different concentrations (0.17, 0.34 and 0.51 M) and of calcite (calcium carbonate, CaCO₃) by rheological measurements. The authors also investigated the adsorption process of xanthan gum and CMC onto calcite particles surface, to make clear the polymer structural effects on the formation of filter cake. They prepared sixteen drilling fluids with the same xanthan gum concentration (4 g/L). All fluids presented an increase in the apparent viscosity and a reduction in the filtrate loss after addition of CMC. However, the best results were obtained when calcite was added. The fluids containing only XG as thickener did not control efficiently the fluid filtration loss even in the presence of calcite. An increase in the apparent viscosity and a significant decrease in the filtrate loss were observed when both CMC and calcite were added. The authors attributed this result to synergistic interactions between the polymers XG and CMC in the presence of calcite.

Pereira et al. [19] investigated the thermoassociative properties of graft copolymers (CMC-g-Jeffamine[®] M-1000 and CMC-g-Jeffamine[®] M-2070) and their resistance to a high salinity medium. Jeffamine[®] is the commercial name for methoxy poly(ethylene oxide/propylene oxide)-2-propylamine. It exhibits thermo-responsive properties, with an LCST that changes as a response to the difference in the ratio of propylene oxide (PO) and ethylene oxide (EO) repeat units in their structure. In this study, the authors employed Jeffamine samples with ethylene oxide:propylene oxide (EO:PO) ratios of 21:3 and 33:10. The graft copolymers were obtained by a coupling reaction between the -NH₂ terminal group from the polyetheramine and the -COO⁻ group in the carboxymethylcellulose repeat unit,

with addition of 1-ethyl-3-(3-dimethylaminopropyl) carbodiimide (EDC) and N-hydroxysuccinimide (NHS) as activators. The authors confirmed the synthesis of the graft copolymers by the emergence of the amide carbonyl band in the IR spectrum. They determined the value of the grafting degree of 9.52% for CMC-g-Jeffamine[®] M-1000 and 14.14% for CMC-g-Jeffamine[®] M-2070 from the ¹H NMR spectra for the graft copolymers. The effects of temperature on the associative behavior of graft copolymers in aqueous media were evaluated by UV-Vis spectroscopy, dynamic light scattering and rheological measurements. The researchers observed the decrease in transmittance for CMC-g-Jeffamine[®] M-2070 in 0.5 M K₂CO₃ and CMC-g-Jeffamine[®] M-1000 in 0.6 M K₂CO₃, at the cloud point temperature (CPT) of 39 °C and 43 °C, respectively, attributed to the association between hydrophobic groups with a rise in temperature, due to the salting out effect, which decreases polymer solubility in water. To observe turbidity at CMC-g-Jeffamine[®] M-1000, which has the higher hydrophilicity when compared to Jeffamine[®] M-2070, the authors added a larger amount of salt to solutions. From dynamic light scattering measurements, it was observed that the particle size increased with the temperature for both graft copolymers above CPT. This behavior was attributed to intermolecular associations. However, CMC-g-Jeffamine[®] M-1000 exhibited a greater hydrodynamic radius at 25 and 60 °C than CMC-g-Jeffamine[®] M-2070. The Jeffamine[®] M-1000 has higher hydrophilicity, resulting in greater interaction with water and increasing the volume occupied by macromolecules. The authors analyzed the apparent viscosity in 0.6 M K₂CO₃ for CMC-g-Jeffamine[®] M-1000 and carboxymethylcellulose, at 60 °C, and for CMC-g-Jeffamine[®] M-2070, at 40 °C. The two copolymer solutions were more viscous at low shear rates with more significant shear thinning behavior than CMC at 60 °C. The authors believe that this performance is due to the copolymers thermoassociative process, suggesting their applicability in enhanced oil recovery. The researchers concluded CMC-g-Jeffamine[®] M-1000 performed better with higher CPT, particles size, viscosity and thermothickening in salt solutions than CMC-g-Jeffamine[®] M-2070. Besides, this result qualifies this copolymer for industrial applications when an optimal viscosity range is required at high temperatures and salinity, such as in enhanced oil recovery.

Marques et al. [20] studied the synthesis of carboxymethylcellulose grafted with thermoresponsive polyetheramines Jeffamine[®] M-2070 (PEOPPO2070) and Jeffamine[®] M-600 (PEOPPO600) (ethylene oxide/propylene oxide = 33/10 and 1/9) prepared in water, at room temperature, by using a carbodiimide and N-hydroxysuccinimide as activators. The CMC-g-PEOPPO600 and CMC-g-PEOPPO2070 copolymers were characterized by ¹H NMR, IR spectroscopy and thermal analysis measurements. The authors confirmed the synthesis of the graft copolymers by the amide linkages formed through the reaction between -COO⁻ groups from CMC units and -NH₂ groups, and production of copolymers with 12 and 17% of grafting percentage for CMC-g-PEOPPO2070 and CMC-g-PEOPPO600, respectively. They also observed that graft copolymers were thermally more stable than their precursors. The weight-average molar mass (M_w), radius of gyration (R_g), and the second virial coefficient (A_2) for CMC and their graft copolymers were determined by static light scattering in 0.1 NaNO₃, at

25 °C, and the associative behavior of the graft copolymers as a function of temperature was studied through UV-Vis spectroscopy, dynamic light scattering and rheological measurements in different aqueous media. In the absence of salt, none of the graft copolymers showed cloud point temperature (TCP). However, the copolymers revealed a salt dependent-thermosensitive character. The higher the ionic strength the lower the TCP. The copolymers displayed thermo-thickening behavior when heated from 25 to 60 °C, above their TCP in 0.5 M K₂CO₃. The authors concluded that these graft copolymers with thermoresponsive behavior in saline media are attractive for using in harsh environments at enhanced oil recovery applications.

Fagundes et al. [13] studied the effect of carboxymethylcellulose on colloidal properties of calcite suspensions in drilling fluids by rheological properties, filtrate volume and zeta potential. All the drilling fluids evaluated had 4.3 g/L of xanthan gum, 8.5 g/L of CMC, 57 g/L of NaCl and 57 g/L of calcium carbonate, with average particle sizes of 7.64, 12.27 and 18.61 μm. The drilling fluids with more profitable properties (higher viscosities, lower filtrate loss and less negative zeta potential) were obtained for the formulations with smaller calcite particles with wide size distribution, and CMC with higher average molecular weight (M_w) and lower average degree of substitution (DS). The work showed the importance of effective interactions between CMC and calcite to improve drilling fluid properties.

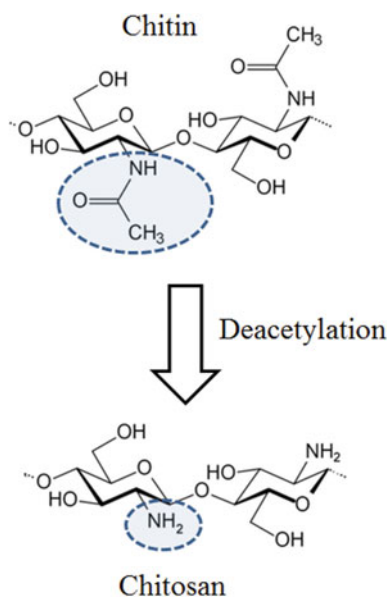
Madruga et al. [12] investigated the effect of the ionic strength of a number of salts and bases on the rheological properties and filtrate volume of Na-carboxymethylcellulose (CMC) and Na-kappa-carrageenan (KC) aqueous solutions and drilling fluids. The aqueous solutions of KC were less sensitive to the presence of cations than CMC solutions, at 25 and 55 °C. Both polymers showed lower solution viscosities with the increase of temperature. However, KC solutions had high viscosity even in the presence of salts. The monovalent ions in the drilling fluid interacted with the charged groups of CMC, reducing viscosity and increasing filtrate volume. In the case of KC, it was observed constant viscosity and filtrate volume, attributed to the double helix conformation adopted by this polymer. In the presence of bivalent ions, a decrease in the viscosity of CMC solutions and drilling fluids happened, as well as an increase in filtrate volume, because the bivalent cations form bridges between CMC chains, decreasing polymer solubility in water and consequently affecting filter cake permeability. However, no significant variation was observed in filtrate volume for the KC solutions and their drilling fluids, even with the addition of bivalent cations, attributed to the ordered helical structure for this polymer. For both polymers, when the pH increased above 12, it was observed a decrease in viscosity and an increase in filtrate volume, caused by the higher ionization of carboxylate and sulphate groups. The authors suggested cost-effective use of KC as a substitute for CMC in water-based drilling fluids during oil well operations.

2 Chitosan

The highlight of chitosan has grown significantly over the last several years, as it is commercially produced from renewable resources and has important structural and functional properties with a large variety of applications. Its precursor is chitin, an abundant biopolymer extracted mostly from crustaceans shell wastes. It is also found in the cell walls of some fungi and algae. Chitosan is a linear polysaccharide obtained mainly from the *N*-deacetylation of chitin. Its structure consists of $\beta(1 \rightarrow 4)$ linked 2-amino-2-deoxy-*D*-glucopyranose (*D*-glucosamine) and 2-acetamido-2-deoxy-*D*-glucopyranose (*N*-acetyl-*D*-glucosamine) units. However, the predominant repeating unit of chitosan is *D*-glucosamine, unlike its precursor, in which *N*-acetyl-*D*-glucosamine units prevail, as depicted in Fig. 2 [21–25].

In contrast to chitin, which is insoluble in water, chitosan is soluble only in acid aqueous solutions because of the protonation of the primary amino groups in *D*-glucosamine units. The cationic character and the solubility of chitosan in acidic aqueous medium, along with properties such as biocompatibility, biodegradability, non-toxicity and bioactivity have been considered of great importance for various—applications. In addition, the presence of groups such as amino $-\text{NH}_2$ and hydroxyl $-\text{OH}$ in the molecular structure allows many chemical modifications aiming to improve or impart new physicochemical properties to chitosan, which may expand the possibility of their application fields. Chitosan and its derivatives have been reference in several areas over the years such as the recovery of heavy metals, water

Fig. 2 Chemical structures of chitin and chitosan



treatment, the construction of structural matrices for food, cosmetic, agriculture, biomaterials and with great potential for biomedical and technological applications [24, 26–40].

One of the most important targets for increase the field of the technological and biomedical applications of chitosan-based biomaterials is the modification of chitosan structure with the aim of improving its solubility by the addition of hydrophilic functional groups. Another important focus is the development of chitosan derivatives with associative behavior in aqueous solutions and stimuli-responsive properties, this last one is frequently named as smart polymers [23, 27, 29, 41–44]. These materials undergo reversible changes in properties such as solubility, conformation, viscosity and particle size in response to external stimuli, such as alterations in temperature, pH, ionic strength, among others.

Considerable effort has been made to modify the molecular structure of chitosan and various chemically modified chitosan derivatives have been reported in the literature. They are usually carried out with typical chemical reactions involving the amine (at the C-2 position) or hydroxyl (at the C-3 and C-6 positions) functional groups in the chitosan. The amino group in the C-2 position is the important point of difference between chitosan and cellulose, where three hydroxyl groups of nearly equal reactivity are available. Owing to the greater reactivity of the amino groups, compared to hydroxyl groups, becomes easier and selective to obtain amino-derivatization of chitosan. However, in both cases the amino and hydroxyl groups are functionalized to obtain chitosan derivatives with important properties [29, 45].

The physicochemical properties of chitosan and its derivatives solutions are related to polymer-polymer interactions (intra- and inter-molecular) and polymer-solvent interactions. These relationships depend on the structural characteristics of the polymer and solution parameters, such as the degree of acetylation (DA: fraction of acetamide units on the chitosan backbone), charge density and its distribution along the polymeric chain, molecular weight, polymer concentration, temperature, dielectric constant of the solvent, pH of the solution, time and ionic strength. All these factors are very important to evaluate and to control the properties of chitosan in solution [21, 23, 28, 46–48].

Some examples of experimental approaches used to prepare chitosan derivatives with hydrophilic or/and hydrophobic functional groups in the chitosan polysaccharide chain are discussed, including its physicochemical properties and applications according to the recent literature.

2.1 Chitosan Derivatives, Some Properties and Potential Applications

Numerous methodologies and types of chemical reactions for chitosan modification are described in the literature. The properties and applications of chitosan derivatives also depend on the nature of functional groups added to the chitosan

backbone. Different reactions to increase the water solubility of chitosan are described, such as carboxymethylation, quaternization, alkylation, acylation and grafting onto chitosan [22, 24, 25, 28, 30, 31, 33, 49].

Considering only the functional groups present in the raw chitosan, without the addition of a new functional group to the polymer structure, the reacylation of amine groups has been used to improve the water solubility of chitosan. This is only achieved by deacetylated chitosan with DA around 50%, indicating reducing chain packing due to steric hindrances caused by acetyl groups [50–55]. Sogias and coauthors (2010) showed that occurs chemical disruption of chitosan crystallinity through partial reacylation caused by the addition of acetic anhydride.

Another way to synthesize water soluble chitosan is an important class named PEGylated-chitosans. Poly(ethylene glycol)—(PEG) and methoxy poly(ethylene glycol)—(mPEG) are hydrophilic polymers commonly grafted onto chitosan because of their biocompatible properties. Several studies have found that PEG-chitosan derivatives with nanoparticle-forming properties and solubility in a wide range of pH have a large potential as a drug delivery agent and biological activity suitable for pharmaceutical and biomedical applications. The activation of the hydroxyl group of PEG or mPEG with appropriate reagents allows the functionalization of amino and/or hydroxyl groups of chitosan [30, 56]. It is known that the solubility of mPEG-*g*-chitosan in water is effectively influenced by the degree of substitution (DS) with high molecular weight mPEG and DA of chitosan. Although mPEG graft onto chitosan improves water solubility, in general, the reaction methods used to obtain mPEG-*g*-chitosan are laborious. The difficult removal of reagents and catalyst dispersed in the final product, various reaction steps, slow purification processes and low degree of conversion of mPEG into mPEG-aldehyde are aspects that need to be overcome [29, 30, 54, 57].

The main challenge is to develop new methods that can be handled with simpler and more efficient processes and environmentally friendly to obtain chitosan derivatives. One-pot system and click reactions in polysaccharide modification are examples associated with this prospect [28, 29, 45]. The one-pot method to the chemistry reactions is defined as a process carried out in a single reaction vessel involving a series of distinct reactions to produce the desired product without isolating and purifying the intermediates after each step. Click reactions refers to chemical reactions which can be carried out under mild experimental conditions with high yielding, good selectivity, simple to perform and easy to remove solvents from reaction mixtures. The following Table 1 shows some references about the promising and versatile strategies to prepare chitosan derivatives with respect to one-pot method and click reactions.

According to literature, the strategy of grafting PEG onto chitosan is an important approach to expanding the applications of chitosan in different fields. However, its experimental methods still need development on an industrial scale [29]. Besides, a better understanding between chemical structures and controlling desired properties is still a challenging aspect for designing news materials [25, 28].

Considering the one-pot method, an interesting study is discussed in detail in text that follows. Also, the hydrodynamic properties of chitosan and derivatives in

Table 1 Examples of chitosan derivatives obtained by one-pot or click reactions method

Reaction method	Chitosan derivative	Main evaluated property	Desired application	Reference
One-pot/Click reactions	Chitosan/hyaluronic acid-based triple network hydrogel	Mechanical properties and cytotoxicity	Cartilage tissue engineering	[58]
One-pot	Chitosan-based supramolecular nanogels (Ad-SS-Ad/CD-CS)	pH/reduction dual-stimuli responsive controlled release/ cytotoxicity	Anticancer drug delivery system	[59]
One-pot	CMC/sewage sludge bio-adsorbent	Adsorption capacity and kinetics	Wastewater treatment	[60]
One-pot	Chitosan/PVA hydrogel nanofibers reinforced with HNT	Physical and mechanical properties/ cytotoxicity	Skin tissue regeneration	[61]
One-pot	Ag NPs/CMC chains onto the cotton fabric	Antibacterial activity and laundering durability	Preparation of antimicrobial cotton textiles	[62]
Click reaction	Chitosan grafted Hydroxyapatite Nanoparticles	water stability and cytotoxicity	Bone tissue engineering	[63]
Click reaction	Quaternized chitosan derivatives with 1,2,3-triazole as substituent with/ without Cl or Br	Water solubility and antifungal activity	Pesticide against some plant pathogenic fungi	[64]
Click reactions	Cationic chitosan derivatives with 1,2,3- triazole	Water solubility and antifungal/ antioxidant activities	Antifungal and antioxidant biomaterials	[65]
Click reaction	Furan–chitosan and bismaleimide cross–linker Hydrogels	Rheological behavior and swelling capacity and drug release	Stimuli–responsive drug carrier systems	[66]
Click reaction	Poly (thiolated chitosan-co-alkylated β -cyclodextrin) hydrogels	Physical and mechanical properties/drug release	Solid tumors treatment/drug release system	[67]

CMC carboxymethyl chitosan. PVA poly (vinyl alcohol). HNT halloysite nanotubes. Ag NPs/CMC silver nanoparticles/carboxymethyl chitosan. Ad-SS-Ad/CDCS disulfide bond embedded crosslinker/ β -cyclodextrin modified chitosan

aqueous solution as a function of varying pH, analyzed by Dynamic light scattering (DLS) measurements, are discussed. Chitosan was grafted with mPEG chains (molecular weight: M_w 2000 g/mol) as hydrophilic moieties and dodecyl aldehyde (C_{12} aldehyde) as hydrophobic moieties by reductive amination. This method may be performed in aqueous solution under very mild conditions at pH 4–6, room

temperature (25 °C) and homogeneous conditions to obtain randomly distributed substituents along the chitosan backbone. Chitosan derivatives were synthesized for study the effect of pH on the size of particles of polymers in aqueous solutions and evaluate the influence of hydrophilic and hydrophobic groups [68].

In this way, firstly, mPEG-terminal hydroxyl was converted into an aldehyde group by mild oxidation using acetic anhydride and anhydrous dimethyl sulfoxide (DMSO). The resulting reaction mixture without previous separation of the mPEG-aldehyde was used to modify chitosan, reaction between amino group of chitosan and aldehyde group, resulting in imine group, which was reduced to amine by addition of reducing agent, NaBH_4 . The polymer purification step is very important and influences the polymer properties. This procedure, at the end of the reaction, was carried out by pouring the reactional medium in acetone to precipitate the polymer and remove undesirable reactants. The precipitated polymer was separated, immediately dissolved in 0.5 M acetic acid solution, adjusted to pH 6, dialyzed against distilled water and freeze dried. Thus, chitosan (CH , $M_v = 4.5 \times 10^4$ g/mol and DA 19%) was chemically modified with grafting of mPEG by reductive amination and included concurrently the reacylation of amine groups of chitosan backbone, due to the presence of acetic anhydride in the reaction medium, while other amino groups remained free. The chemical modification of chitosan with mPEG and C_{12} aldehyde was carried out separately (CH-mPEG or CH- C_{12} aldehyde) and simultaneously (CH-mPEG- C_{12} aldehyde). CH-mPEG- C_{12} aldehyde was prepared likewise CH-mPEG, however, with simultaneous addition of dodecyl aldehyde/alcohol, leading to simultaneous reaction between dodecyl aldehyde and the chitosan amine groups. A reaction scheme for the preparation of chitosan derivatives is shown in Fig. 3.

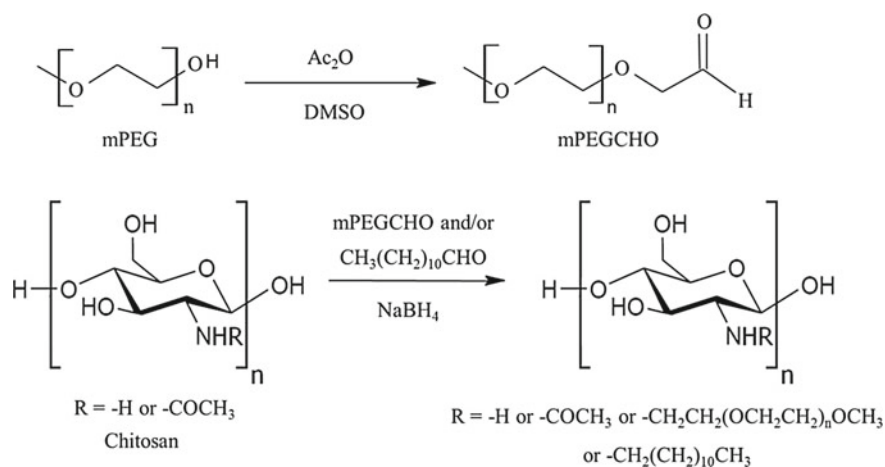


Fig. 3 Reaction scheme of chitosan derivatives by reductive amination

One of the advantages of the experimental method employed above is that the intermediates and reagents of reaction were only eliminated in the separation and purification process of the final product, avoiding the use of organic solvent and lost time, in contrast to the procedures frequently related to chitosan synthesis involving multiple steps.

Another benefit of the technique employed was to obtain modified chitosan with low degree of substitution (DS values for CH-mPEG and CH-mPEG-C₁₂ aldehyde were 2.4% and 3.5%, respectively) and water solubility in a wide range of pH. Despite of the fact that mPEG is biocompatible, it is not biodegradable. Therefore, a low degree of substitution is more appropriate, while that high degree of substitution of the amino groups on chitosan backbone could lead to lose of the physicochemical and biochemical properties of the precursor. Even low incorporation of hydrophilic and flexible mPEG chains onto chitosan backbone prevented interactions between the macromolecules, avoiding precipitation with increasing pH, in contrast to the precursor polymer, which precipitates above pH 6.5, as well as the hydrophobically modified chitosan (CH-C₁₂aldehyde—DS 10%).

In this study, DLS measurements were used to characterize the size of chitosan and its derivatives in aqueous solution, as well as the effect of pH on the stability and aggregation phenomenon in the dilute regime. The phenomenon of chitosan chain aggregation in aqueous solutions has been attributed primarily to three effects: (a) residual acetyl groups, (b) the deprotonation of amino groups and (c) polymer concentration. Also, news aspects that influence chitosan aggregation in aqueous solution have been addressed, such as procedures involved in the filtration of polymer solutions, considering different membrane types and porosity [48, 69–71].

Changes of solution pH alter the degree of ionization of the polymer, thereby affecting the charge density in a polyelectrolyte solution. Moreover, the charge density also depends on the distribution of fixed charges over the macromolecule, counterions and electrolytes added in solution. In the present case, at pH 3 and pH 6, populations of individual chains (hydrodynamic radius, $R_H = 24$ nm) and aggregates ($R_H = 478$ nm, pH 3 and $R_H = 151$ nm, pH 6) were well defined. At pH 5, the distribution curve of the chitosan particles showed a single population with a mean R_H value of 151 nm, attributed to the aggregates. However, individual chains may be hidden at pH 5 due to a wider particle distribution. In particular, the hydrodynamic radius of aggregates in the chitosan solution increases with the decreasing pH value of the solution. At pH 3, the chitosan chain is extended and its interaction with the counterions of the solvent may reduce the electrostatic repulsion between its positively charged chains and reduce the distance between its macromolecules, favoring the formation of aggregates through intermolecular interactions. This behavior can be explained by Manning's theory, which applies to polyelectrolyte solutions in the absence of salt and predicts the counterion condensation phenomenon. According to the model, polyelectrolytes can acquire a high charge density when dissolved in water. Thus, the electrostatic potential around the polyelectrolyte can affect the equilibrium of the counterions distribution in solution. On the other hand, when pH increases to 6, the charge density of protonated amino groups decreases. This contributes to reducing electrostatic repulsion and the

stiffness of the polyelectrolyte, leading to shrinkage of the polymer. Moreover, the reduction in the quality of the solvent also collaborates with this effect. These conditions favor the formation of aggregates that differ in size and nature from those found at pH 3, where larger aggregates are observed. This indicates that high charge density in the absence of salt may be a relevant factor in the formation of aggregates of chitosan molecules in solution. It is likely that the aggregates observed under these conditions are those identified by Chen et al. [70] for the aqueous solution of chitosan with low ionic strength ($I = 0.01$ M).

Chen et al. [70] studied the aggregation behavior of chitosan samples (DA 30 and 7.3%) in solutions with different salt concentrations (0.01–0.5 M) using DLS. In a solution with low ionic strength ($I = 0.01$ M), aggregates were evident regardless of the degree of acetylation and light scattering angle. According to the authors, aggregation at $I = 0.01$ M originates in a small number of species compared to the structure of the chitin present in solution. In this case, species above and protonated amino groups of chitosan may be asymmetrically distributed. Despite the presence of electrostatic repulsions, hydrogen bonds may be favored among species compared to chitin, thereby generating asymmetrical distribution between the groups in solution and favoring attractive interactions caused by dipolar variation in the solution. This would result in the aggregation of molecules with species similar to chitin in a different aggregation process from that found in solutions with high ionic strength ($I > 0.1$ M). The increase in ionic strength from 0.1 M and greater degree of acetylation contributed to increasing the hydrodynamic radius of chitosan in dilute solution. In a solution of average ionic strength ($I = 0.1$ M), the sample with the highest degree of acetylation only exhibited aggregates when the light scattering angle was reduced from 90° to 30° , whereas ionic strength had to be increased above 0.1 M in order to observe aggregates in the sample with the lowest degree of acetylation.

The mPEG side chain grafted onto chitosan contributed to an increase in the solubility of chitosan, with a simultaneous decrease in the stiffness of the polymer chain. In acid pH, the mPEG-g-chitosan chain exhibited a less extended conformation with aggregates smaller than those of chitosan. As pH increased, the charge density on the polymer backbone gradually decreased and the reduction in electrostatic repulsion reinforced the hydrogen bonding between CH-mPEG chains. The conformation of CH-mPEG becomes even more compressed owing to intra and intermolecular interactions favored by hydrogen bonds, resulting in smaller aggregates than in acid solution (hydrodynamic radius of aggregates $R_H = 190$ nm at pH 3, $R_H = 120$ nm at pH 5 and 6 and $R_H = 95$ nm at pH 9 and 11). The hydrogen bonds between the polymer chains and water molecules combined with smaller particle size contributed to further stabilization of polymer in neutral and basic solutions.

Hydrophobically modified chitosan (CH-C₁₂aldehyde) displays hydrophobic domains inherent to hydrophobic substituents and to chitosan itself, from acetyl groups. In general, grafting hydrophobic substituents onto chitosan increases its tendency to aggregate in aqueous solutions, similar to any other associative hydrophobic polyelectrolyte. In dilute solution, intramolecular aggregation

predominates when the number of associative groups in a polymer chain is sufficient to stabilize it; otherwise, intermolecular aggregation is favored [23]. The amount and length of hydrophobic constituents grafted onto chitosan influence aggregation behavior. Larger hydrophobic groups contribute significantly to aggregation of the polymer. An increase in the length of the substituent tends to generate larger aggregates when intermolecular interactions are favored, and smaller aggregates forming in a solution where intramolecular interactions predominate. Desbrières et al. [72] reported that from six carbon atoms onwards, there is a tendency to occur intermolecular aggregations since bulky species increase the steric hindrance and stiffness of the macromolecule. Nevertheless, length and degree of substitution should be considered together. In any case, the particle size is determined by the relationship between attractive forces through the hydrogen bonds and hydrophobic interactions that favor aggregation, and the electrostatic repulsions from the protonated amino groups [23].

In particular, at pH 3 and pH 5, the distribution curves of CH-C₁₂aldehyde particles exhibited populations with mean particle size attributed to individual chains ($R_H = 37$ nm, pH 3 and $R_H = 8,0$ nm, pH 5) and aggregates ($R_H = 478$ nm at pH 3 and $R_H = 95$ nm at pH 5). In addition, micrometer-sized aggregates were also observed. At pH 6, a wider distribution of particles was observed, with a mean hydrodynamic radius of 76 nm. The results indicate that particle size increases with the decrease in pH from 6 to 3, with aggregates five times larger observed at pH 3 which can be attributed to steric hindrance caused by the presence of *n*-dodecyl hydrophobic group. However, at pH 3 the aggregates are stables and when the pH of the solution is adjusted to 6.5, the attraction forces predominate causing precipitation. This behavior can be attributed to the combination of two effects: (i) Manning condensation, which reduces the electrostatic repulsion between polymer chains with extended conformation and (ii) the presence of hydrophobic groups containing 12 carbons, which favors the formation of intermolecular aggregates with a greater hydrodynamic volume than that of the chitosan chains containing acetyl groups. The results of DLS analyses for chitosan solutions and hydrophobic derivatives at pH 5.3 reported by Robles et al. [73] corroborate the data observed above. Mean hydrodynamic radius values of the hydrophobic derivatives in aqueous solution decreased when compared to chitosan (180 nm), becoming more accentuated with the increasing degree of substitution (DS) of *n*-dodecyl (155 nm, DS 5% and 125 nm, DS 50%) or *n*-octyl groups (130 nm, DS 5% and 70 nm, DS 50%) incorporated onto chitosan.

Hydrophilic and hydrophobic groups simultaneously incorporated onto chitosan were one way to avoid precipitation of chitosan above pH 6.5, at the same time, making it more hydrophobic. The values of R_H follow the trend of decreasing aggregate size with increasing pH (hydrodynamic radius of aggregates $R_H = 380$ nm at pH 3, $R_H = 120$ nm at pH 5, $R_H = 95$ nm at pH 6, $R_H = 76$ nm at pH 9 and $R_H = 60$ nm at pH 11). At pH 3, in particular, CH-mPEG-C₁₂aldehyde aggregates are larger than CH-mPEG aggregates due to the contribution of the 12-carbon hydrophobic group and smaller than CH and CH-C₁₂aldehyde aggregates, owing to the presence of the flexible mPEG chain. In basic pH, smaller

aggregates are observed when compared to CH-mPEG aggregates. These results suggest that the size of aggregates depends on the balance between charge density and the type of substituent grafted. Liu et al. [74] evaluated the aggregation process in aqueous solution of chitosan grafted with hydrophobic groups—polycaprolactone with molecular weight of 300 g/mol and hydrophilic groups—methoxy-poly(ethylene glycol) with molecular weight of 5000 g/mol. DLS results showed unimodal distribution attributed to aggregates with hydrodynamic diameters of approximately 200–400 nm. The aggregates decreased in size with the increase in pH and the degree of substituents inserted into chitosan but remained almost unaltered with the varying polymer concentration of the solution. The authors also found that the mPEG chains played an important role in the stability of the aggregates and that the size and stability of aggregates can be controlled by adjusting the ratio of hydrophobic and hydrophilic groups in the chitosan structure.

The introducing hydrophilic or hydrophobic groups to chitosan also may result in altering or improved mechanical and thermal properties. In general, the decrease in the viscosity of chitosan solutions with increasing shear rate is recognized as a shear thinning behavior. This effect is related to orientation of the polymer chains in the flow direction and disruption of the physical interactions between polymeric chains through the application of strains in the polymer solution as the shear rate increases. However, the physical interactions between the polymeric chains are capable of quickly reforming after the decreasing of shear rate due to molecular self-association process, showing that the hysteresis is present in the dynamic of these solutions. Moreover, the decrease in viscosity occurs also with the addition of electrolytes or increase pH in acid solutions due to the decrease of charge density.

Chitosan exhibits a partially crystalline structure with strong hydrogen bonds, which favor the intermolecular interactions resulting in high viscosity for the chitosan solutions. In particular, as opposed to that, grafting of mPEG segments onto the structure of chitosan can separate its chains through steric hindrance, resulting in a decrease of intermolecular interactions in acid pH and consequently decrease in viscosity. However, in basic pH solutions, up to 125 s^{-1} shear rates, the viscosities for the CH-mPEG solutions significantly increased and with a more pronounced shear thinning behavior when compared to performance in acid and neutral pH conditions, as well as for chitosan. This suggests an increase of the intermolecular interactions by hydrogen bonds and hydrophobic associations due to the decrease of solvent quality, which favors the polymer-polymer interactions increase, indicating the formation of stronger intermolecular aggregates. Indeed, chitosan hydrophobic segments favor intra/intermolecular aggregation when water soluble, thus they became with associative ability and viscosifying action such as hydrophobically modified polymers used as rheological modifiers (thickeners). Considering viscosity as a function of temperature (25–55 °C), in acid pH environment, the viscosity of polymers aqueous solutions (concentration at 10 g/L) decreased as temperature rose in concordance with greater thermal molecular agitation, which leads to reduced intermolecular interactions, thus decreasing the flow resistance. On the other hand, in basic medium, the viscosity of the CH-mPEG solutions was higher and maintained practically constant with the increase of temperature,

suggesting the formation of stronger intermolecular aggregates. In this case, when temperature increases, CH-mPEG chain undergoes dehydration. This process can be attributed to the break of hydrogen bonds, primarily between ether groups and water molecules, resulting in enhancement of intermolecular hydrophobic association.

Generally, responsive polymers to multiple stimuli are versatile materials. Tsao and coauthors (2015) showed that at 1.5 wt% mPEG-g-chitosan at 37 °C and at pH 4.0, the solution exists in a transparent sol state and at pH 7.5 and 8.5, the solution underwent a sol–gel transition, and became a stationary, non-flowing gel. PEG-chitosan hydrogels have many advantages compared with other synthetic derived because PEG is approved by the US Food and Drug Administration (FDA) for incorporation into a diversity of areas such as foods, cosmetics, pharmaceuticals and biomaterials.

From the point of view of responsive chitosan-based polymers, a more complete approach includes other synthetic segments and methods of preparation of chitosan derivatives. Marques et al. [43] described procedures and properties of temperature/pH dual-sensitive smart polymers focused on copolymers of chitosan with poly(N-isopropylacrylamide) (PNIPAM). An overview is presented of the concepts, behavior and applicability of these smart polymers, considering that many properties are universal and therefore can also be applied to other pH and temperature sensitive polymers. Some of the available methods involve free radical initiator graft copolymerization (“grafting from” method).

Marques et al. [75] obtained PNIPAM, poly(N-isopropylacrylamide)-chitosan (PNIPAM-CS), and poly(N-isopropylacrylamide)-chitosan-poly(acrylic acid) (PNIPAM-CS-PAA) by one-pot method, via free-radical precipitation copolymerization with potassium persulfate, using *N,N'*-methylenebisacrylamide as a crosslinking agent. The authors studied the stability and rheological behavior of polymer suspensions as a function of pH and temperature. They observed that the PNIPAM-CS particles showed higher stability in acid and neutral media and PNIPAM-CS-PAA particles were more stable in neutral and alkaline media. It is known that PNIPAM is a thermosensitive polymer which exhibits in aqueous solution a phase transition hydrophilic-hydrophobic type lower critical solution temperature (LCST) in approximately 32 °C. The incorporation of chitosan chains in crosslinked PNIPAM particles improved their stability in all pH ranges evaluated, which were also influenced by the temperature of the medium. Moreover, these dual-sensitive materials obtained allowed the particles stability to be adjusted, making phase separation faster or slower in order to adapt them to different environments depending on the desired application.

In technological applications such as the oil industry, the use of safe environmental polymers is increasingly required. Considering this approach [34, 35] published two recent articles, in which they prepared water-soluble carboxymethylchitosan (CMC) with great potential to be used as corrosion inhibitor for carbon steel in saline medium and as green scale inhibitor in oil wells. In the first study, CMC exhibited an excellent behavior as corrosion inhibitor in 3.5% NaCl medium, since the efficiency results were 85%, determined by the Tafel

curve's extrapolation at the maximum concentration studied (80 ppm). This performance was attributed to interactions of COOH, NH₂ and OH groups in the CMC with the metal surface. Another publication was about the study of visual compatibility and dynamic tube blocking test under the physicochemical conditions of oil wells in northeast of Brazil using CMC. The synthesis conditions allowed water-solubility in a large pH range evaluated (1–11). Carboxymethylchitosan acted as a scale inhibitor of CaCO₃ under synthetic brine medium, presenting a minimum inhibitor concentration of 170 ppm at 1000 psi and T = 70 °C. Moreover, CMC changed the CaCO₃ crystals morphology, preventing scale deposition. The CMC obtained showed the characteristics of an antiscaling product such as solubility in the medium, stability at the operating conditions and functional groups able to interact with the fouling ions.

The organic-inorganic hybrid materials have attracted a great interest in scientific and technological fields because of their versatility combine the advantages derived from both the organic and inorganic groups. In this context, Paixão et al. [37] prepared magnetic crosslinked chitosan microspheres with PNIPAM brushes to improve the hydrophobicity of the polymer system and to evaluate its efficiency in oily water treatment as a solid adsorbent. The oil removal efficiency of magnetic crosslinked chitosan microspheres (MCM) without and decorated with PNIPAM (MCM-PNIPAM) in reducing the organic phase in synthetic oily water was estimated by UV-vis absorption measurements. At 25 °C, temperature below the PNIPAM's LCST, this polymer doesn't present aggregation and the oil retention measured was around 85%, for both MCM and MCM-PNIPAM particles. However, at 40 °C, a temperature above the PNIPAM's LCST, the chains of this polymer shrink, forming aggregates. In this work, it was observed that this thermosensitive behavior of PNIPAM brushes improved the lipophilicity of magnetic crosslinked chitosan microspheres with oil removal efficiency around 97%. In this way, the addition of PNIPAM brushes (MCM-PNIPAM) contributed to an increase of 12% in the oil removal, compared to MCM.

In the same sense, Luz et al. [76] studied different synthesis methods for preparing chitosan-nanosilica hybrid materials aiming to apply in aqueous drilling fluids, especially in the control of fluid filtration at 25 °C (room temperature) and at 90 °C. From the characterization methods used (FTIR, TG-DTG, UV-vis), the authors confirmed the formation of chitosan-nanosilica hybrid materials in the three kind of procedure applied. From dynamic scattering light (DSL) and zeta potential techniques, it was verified that the effective diameter and the charge density on the hybrid materials surface were pH-sensitive. In acid medium (pH = 3), the effective diameter of chitosan-nanosilica hybrid particles increased, probably because of the presence of protonated amino groups in the chitosan chains, resulting in the formation of more hydrated and larger structures. On the other hand, in neutral pH (pH = 7), the zeta potential was negative, and the effective diameter of the hybrid materials decreased due to the deprotonation of amino groups of chitosan, resulting in the particles shrinkage. However, in alkaline medium (pH = 11), the zeta potential was negative, and the effective diameter of the hybrid materials increased again, because of the deprotonation of hydroxyl groups present in the silanol groups

and chitosan chains. The aqueous drilling fluids prepared using these hybrid materials presented a rise in apparent viscosity and decline in filtrate volume, especially at higher temperatures, like 90 °C. From these results, the authors conclude that the chitosan-nanosilica hybrid materials obtained from three different procedures may contribute to safer well-drilling operations and less damage to the permeability of the oil producing rock.

3 Starch

Starch is an abundant, renewable and biodegradable biomass produced as source of storage carbohydrate in plants. It is presented in most parts of higher plants, including leaves, stems, fruits, roots and sprouts, in the form of granules with diameters ranging from 1 to more than 100 μm , whereas the shape can be angular, oval, round, spherical or irregular, depending on its botanic origin. The main natural sources of commercial starch are corn, cassava, tapioca, wheat and potato [77–79].

Chemically, native starch (natural, unmodified starch) is composed of two types of polysaccharides, amylose and amylopectin, polymers of D-glucose, which together comprise 98–99% of the dry mass of starch. Other trace common components are lipids, proteins, minerals, phosphorous, enzymes, amino acids, and nucleic acids. Amylose is a mainly linear polymer with a molecular weight of 10^5 – 10^6 g/mol, constituted by anhydroglucose units linked by α -1,4 glycosidic bonds (99%), containing sparing α -1,6 branch points (\sim 1%). Amylopectin, on the other hand, has anhydroglucose units linked by α -1,4 glycosidic bonds with α -1,6 branching points every 20–30 glucose units and a higher molecular weight of 10^7 – 10^9 g/mol [80–82] (Fig. 4).

The amylose/amylopectin ratio impacts on the properties of starch and depends on many parameters, such as botanic source, growing climate conditions, geographic location for cultivation and soil. Typically, the amylose content in starch is of 20–25%, but waxy starch contains low or no amylose, whereas high-amylose starch contains more than 50% of amylose [83].

Physically, most native starches present a crystallinity of about 20–45%. The small branches in amylopectin and amylose chains can both form double helices, which results in the crystalline regions of starch, although in most starches this property is limited to amylopectin. However, amylose may contribute significantly to the crystallinity of high amylose starches. During gelatinization, the process of heating starch in the presence of water, the molecules of water diffuse into the granules, which then swells due to hydration, causing loss of crystallinity and leading to solubilization. However, during storage, retrogradation can occur, which is the reassociation in an ordered structure of the macromolecules, depending on parameters such as temperature, time and moisture content [77, 84, 85].

Starch is widely consumed in the native form, such as cereal grains and potatoes, as well as in food industry for thickening, texturizing, gelling and stabilizing effects. It has also been exploited in non-food applications, including cosmetics, detergents,

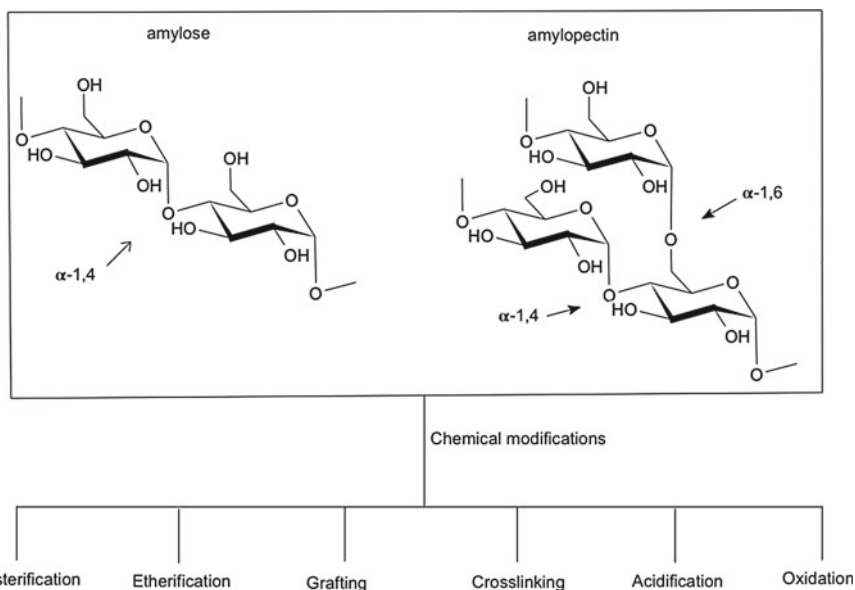


Fig. 4 Chemical structures of amylose and amylopectin and the common chemical reactions applied to achieve different functionalities

oil drilling, pharmaceuticals, plastics and textiles. However, some of its properties, such as its hydrophilic nature, lack of mechanical strength, retrogradation, low shear and low temperature resistance have encouraging the physical, enzymatic, genetic and chemical modification of starch [85, 86].

In particular, the presence of hydroxyl groups and ether linkages on the structures of amylose and amylopectin allows many chemical reactions, such as esterification, etherification, grafting, crosslinking, acidification and oxidation, each providing different properties, enlarging the possibility of applications (Fig. 4). Sometimes these reactions are combined to achieve the desired starch functionality [87, 88].

3.1 Starch Derivatives, Some Properties and Potential Applications

Esters of starch are commonly produced by the reaction of carboxylic acids or its derivatives with the many hydroxyl groups on amylose and amylose chains. Native starch is activated by an alkaline chemical, such as sodium hydroxide, to form alkoxides that attack the carbonyl group of the acid/acid derivative. Because there are three hydroxyl groups on each anhydroglucose unit, the degree of substitution (DS) can vary from 0 to 3. Starch esters with low DS (0.01–0.2) are soluble in cold

water. Starch esters with medium DS (0.3–1) are water-soluble, but not to the same extent as the low DS ones. High DS (2–3) starch esters are not soluble in water, but they are soluble in organic solvents. The DS depends on the botanical origin of native starch and on the specific reaction conditions [88, 89].

Starch esters with low DS are applied as films-forming, adherents, thickeners, stabilizers and encapsulation agents. The derivatives with high DS values are thermoplastic materials with improved mechanical properties, intended for replacing nonbiodegradable plastics. Highly hydrophobic starch esters have been solubilized on n-paraffin and employed as filtrate reducers on oil-based drilling muds [84, 89–91].

Starch esterified with octenyl succinic anhydride have led to derivatives with amphiphilic character, reduced gelatinization temperature, lower digestibility and higher swelling power, finding applications in food and pharmaceutical industry, mainly as emulsifier, encapsulating agent and fat replacer [86, 92, 93].

Etherification can produce cationic, anionic, amphoteric and non-ionic starch derivatives. It typically requires an alkaline catalyst to initiate the substitution of –OH to ether groups. In cationic starches, the positive ionic charges have been commonly produced by the introduction of amino, imino, ammonium, sulphonium, or phosphonium ending groups. The most important anionic starch is carboxymethyl starch. These ionic derivatives present better properties such as solubility in cold water, strong hydrophilicity and have found applications as flocculants in wastewater treatment [87, 94].

Amphoteric starches exhibit both anionic and cationic functional groups. Common anionic groups are phosphonate, phosphate, sulfonate, sulfate and carboxyl groups, while the cationic groups include quaternary ammonium and tertiary amino groups. They have found utility as flocculating agents in wastewater treatment, being used to remove cationic anionic impurities [87, 94].

Hydroxypropyl starch and hydroxyethyl starch are the most representative non-ionic starches. They are prepared by treatment of starch with propylene oxide and ethylene oxide, respectively, in the presence of a strong alkaline catalyst. Hydroxyethyl starch have received great attention due to their blood replacement therapy in surgery and intensive care medicine. The state of art of the hydroxypropylation of starch was recently explored by Fu et al. (2019). The bulky hydroxypropyl groups reduces hydrogen bonding among the macromolecules, which decreases the retrogradation of starch, leading to high temperature stable derivatives, as well as improves swelling and viscosity in water. This behavior renders applications as excipients in formulations that require improved shelf-life [88, 95].

Graft copolymerization is versatile way of combining the properties of the polymers involved. “Grafting from” and “grafting onto or to” are the two main approaches employed to obtain starch-grafted copolymers. In the grafting from route, the polymerization of monomers occurs from the initiation sites incorporated onto the polysaccharide backbone. Radical and ring opening polymerizations are the principal grafting from techniques employed on starch. The grafting onto route uses coupling reactions, such as click chemistry, between functional groups on the

polysaccharide backbone and reactive terminal groups of end-functional polymers [78, 81].

Two recent reviews present the state of starch-grafted copolymers and their applicability [81, 96]. The graft derivatives of starch have been studied as super-absorbents, flocculants and thickening agents. The size and spacing of the grafts influence their performance [96, 97].

Chemically crosslinked starch is produced by the reaction between hydroxyl groups of the polysaccharide chains with bifunctional or polyfunctional chemicals, linking one polymer chain to another. Some common crosslinking agents are phosphorus oxychloride, sodium tripolyphosphate, sodium trimetaphosphate and epichlorohydrin (most common crosslinking agent of polysaccharides). Crosslinked starch is resistant to high temperature, high shear and low pH environments. It is employed in food and non-food industry due to stabilizing, thickening and retrogradation resistance properties [78, 84, 87, 94].

Acid modification involves the use of acids such as HCl and H₂SO₄ to modify native starch below the gelatinization temperature. The acid performs random electrophilic attack on the oxygens of the glycosidic bonds, breaking the α -1,4 and α -1,6 links, thus reducing the molar mass of the polymeric chains, finding uses in many industries, such as paper, textile, food and pharmaceutical. For instance, acid hydrolysis of starch is applied to prepare glucose syrups, gum and candies [84, 87].

The acid attacks preferentially the amorphous regions of the granules at a high reaction rate and, in a subsequent stage, hydrolysis occurs at crystalline regions, at a slower rate. This process promotes an increase on the crystallinity of the granules. Under controlled conditions, the amorphous regions may be dissolved, leaving the rigid crystalline regions intact, producing platelet-like nanoscale highly crystalline residues. These nanocrystals present a highly reactive surface with plenty of hydroxyl groups, allowing the introduction of different surface functionalities [78, 80, 84].

The most commonly used oxidants of starch include hydrogen peroxide, per-acetic acid, potassium permanganate, sodium hypochlorite, chromic acid and nitrogen dioxide, which react under controlled temperature and pH. Generally, the commercial oxidation of starch employs sodium hypochlorite. During oxidation of starch, the hydroxyl groups of the D-glucose units are converted to carbonyl and then to carboxyl groups. Another chemical process involved is the oxidative cleavage of the glucosidic bonds (depolymerization) [78, 87, 88].

The oxidation of starch provides adhesivity, better stability and film formation, lower molar mass and lower viscosity. The presence of C=O groups considerably alters starch chemical binding with chemicals such as metals, amines and polyols, as well as with biological macromolecules, such as proteins. They can form hemiacetals and crosslinked derivatives with controllable swelling for hydrogels and can be applied for enzyme immobilization and on the delivery of macromolecules [78, 88].

4 Xanthan Gum

Xanthan gum is a water soluble heteropolysaccharide, whose mer has a complex structure made of five sugar residues. These residues are arranged as follows: two glucose residues in the main chain, joined by β -1,4 bonds. And a side group composed of a residue of glucuronic acid between two mannoses. The terminal mannose residue binds to the glucuronic acid residue by a β -1,4 bond. And it binds to the non-terminal mannose residue by a β -1,2 bond. The side group is alternately linked to a glucose residue in the main chain by a α -1,3 bond (Fig. 5). This polysaccharide is obtained through fermentative processes using bacteria of the genus *Xanthomonas*, with emphasis on *X. campestris*. Variations in strain and conditions used during fermentation influence the molar mass and degree of substitution of mannose residues, which may have an acetyl group at the *O*-6 position, and terminal mannose may also have a pyruvic acid residue attached to the *O*-4 and *O*-6 positions by a ketal bond. The degree of substitution of mannose residues affects the polysaccharide properties [98].

Xanthan gum is a bacterial exopolysaccharide and for its isolation, microorganisms are separated by centrifugation or filtration of the culture medium, followed by precipitation of the polymer by modification of the filtrate/supernatant pH and addition of non-solvents and salts. The glucuronic acid residue may be prepared as sodium, potassium or calcium salt. This residue and the pyruvate residue give the xanthan gum a polyanionic character [99]. It is soluble in hot or cold water and its chains may assume single helix, double helix or random conformations depending on the temperature and the ionic strength of the medium. Its rigid and water-ionizable structure gives it viscous properties even at low concentrations, and

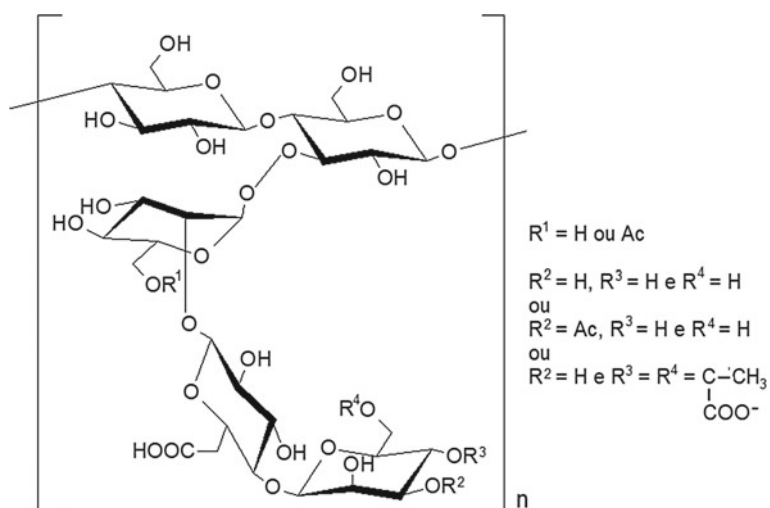


Fig. 5 Chemical structure of xanthan gum

makes it stable in a large pH range and resistant to heat degradation, making it widely applicable in the food, petroleum, beverage, drugs and cosmetics industries [100].

Modifying xanthan gum can increase its range of applications by giving it new properties, and there is much research on this topic. The main types of chemical modifications found for xanthan gum, obtaining copolymers with better properties than the original isolated polymers are: (i) direct grafting of vinyl polymers through the formation of free radicals by hydroxyl proton abstraction; (ii) introduction of new functional groups, increasing the number of copolymers that can be grafted to the polysaccharide and (iii) crosslinking.

Xanthan gum has excellent resistance to shear degradation, while polyacrylamide is widely used as a flocculant, but has low shear stability. Copolymerization of xanthan gum with polyacrylamides can be used to improve the properties of both polymers, as shown by Adhikary and Singh [101], who obtained free radical grafted copolymers using CAN. All copolymers had better flocculant property than the original xanthan gum and commercial partially hydrolyzed polyacrylamide-based flocculants.

Several modifications were made in order to improve the application of xanthan gum in the removal of pollutants, by improving its flocculant properties, as well as introducing new charges, which increases the adsorption of ionic compounds dispersed in aqueous medium. Modifications to employ the resulting copolymers in pharmaceutical forms also stand out. A prolonged release profile of hydrophilic drugs was observed with the modifications, which can be used to obtain formulations that reduce their frequency of administration. In addition to obtaining smart materials, which can be used to target active principles to specific tissues, which reduces the toxicity of formulations. These and other applications are described in the following sections.

4.1 Xanthan Gum Derivatives, Some Properties and Potential Applications

The main chemical modification of xanthan gum is the grafting of vinyl polymers onto its chain. This reaction can be done directly with xanthan gum and vinyl monomers, for example through free radical reactions [101–103], or through prior modification of xanthan gum by introducing reactive side groups [104] followed by grafting the vinyl chains [105]. The choice of graft form will depend on the desired properties. For example, in the latter case labile side groups can be introduced, which would facilitate the degradation of vinyl grafts, making biodegradation of the main chain easier after application of the copolymer.

Grafting of vinyl polymers onto xanthan gum can be done by the formation of free radicals in the reaction medium. These free radicals can react with the polysaccharide hydroxyls, generating macroradicals that react with the vinyl

monomers, initiating the graft polymerization process [103, 106]. This is a widely used method even today for its practicality and greener approach. One way traditionally described in the literature for free radical generation is the use of cerium ammonium nitrate (CAN), potassium persulphate (KPS) or ammonium persulphate (APS). Their decomposition to free radical generation can be catalyzed by heating, usually above 60 °C; using redox pairs, such as TEMED; or through microwave radiation (Table 2).

A mechanism for free radical synthesis has been suggested. In this, the free radicals formed by initiator decomposition abstract hydrogens at the O-6 position, forming radicals in the polysaccharide main chain, from which the vinyl monomer polymerization occurs [103, 109]. Several vinyl monomers were grafted onto xanthan gum from macroradical formation by hydroxyl radical abstraction and the synthesis conditions are summarized in Table 2.

Some drawbacks attributed to this type of reaction are homopolymer formation occurring parallel to the graft and the degradation of the polysaccharide main chain. The formation of homopolymers occurs due to the non-specificity of the initiator, which may react with the xanthan gum hydroxyls or directly with the vinyl monomers present in the reaction medium. The reaction of the initiator with the polysaccharide can trigger the decomposition of its main chain, reducing the molecular weight and affecting its viscosifying properties [102, 109].

The esterification of xanthan gum for the introduction of vinyl groups can be conducted in homogeneous or heterogeneous medium using various compounds as esterifying agents, for example acrylic acid, acryloyl chloride and maleic anhydride. The use of ester type bonds between the xanthan gum backbone and the vinyl polymer grafted chains is advantageous when the obtained copolymer is desired to have a faster degradation, since such bonding is more easily hydrolyzed in aqueous medium than the one formed by the addition reaction.

In the first case xanthan gum is dissolved in water and DEC (N'-[3-(dimethylaminopropyl)]-N-ethylcarbodiimide hydrochloride) can be used as activating agent, however this reaction usually leads to a low degree of substitution. In heterogeneous reactions, xanthan gum is dispersed in an organic solvent in which it has some swelling, for example DMF, in the presence of triethylamine. The use of organic solvents is necessary because the reactivity of water-soluble esterifying agents such as acrylic acid is low. In heterogeneous esterification, the higher the swelling of the xanthan gum chains, the greater the number of polymer chain functional groups accessible for the esterification reaction, which occurs predominantly in the primary hydroxyls (C6) and is positively affected by increasing the reaction time and temperature [104].

The obtained xanthan gum vinyl esters can be grafted with vinyl polymers to obtain copolymers, hydrogels and interpenetrating networks, for example [105]. Although degradation of the xanthan gum chain has not been evaluated, it is expected that this way of grafting vinyl polymers causes less or no polysaccharide degradation.

The introduction of reactive groups in xanthan gum was also explored to obtain precursors that allowed the formation of chemically cross-linked gels *in situ*. In this

Table 2 Examples of vinyl polymers grafted xanthan gum obtained by direct graft using free radicals

Vinyl polymer	Initiator	Activator	%G	%C	Main evaluated property	Desired application	References
PAAm	CAN	Not informed	–	–	Flocculation	Wastewater treatment	[101]
PAAm	CAN	Heating (60 °C)	63	57	Release kinetics	Adjuvant in tablets	[107]
PAAm	APS	Heating (80 °C)	–	–	Response to electrical stimulation	Transdermal drug delivery systems	[108]
PAAm	APS	Micro-wave	13–190	40–102	Release kinetics	Adjuvant in tablets	[107]
PAAm	KPS	TEMED	40	39–48	Grafting percentage and grafting efficiency	–	[102]
PAAm	KPS	Heating (60 °C)	40	31–39	Grafting percentage and grafting efficiency	–	[102]
PNVP	PMS	Thiourea	148–265	–	Release kinetics	Sustained drug release systems	[106]
PAA	APS	Heating (80 °C)	–	–	Adsorption	Wastewater treatment	[109]
PAA	APS	Micro-wave	484	–	Adsorption	Wastewater treatment	[110]
PDEAEMA	APS	Micro-wave	293	–	Adsorption	Wastewater treatment	[103]

PAAm polyacrylamide. *PNVP* poly(N-vinyl-2-pyrrolidone). *PAA* Poly(acrylic acid). *PDEAEMA* Poly(diethylamino ethyl methacrylate)

case the acrylate groups of the glucuronic acid and pyruvate residues were conjugated to dopamine. Dopamine side groups can be easily oxidized in the presence of horseradish peroxidase and H₂O₂, forming cross-links that can increase the stability of the formed gels. These hydrogels have been shown to be non-toxic and can be used in injectable systems for sustained drug delivery [111].

pH/redox responsiveness nanogels were obtained by cross-linking between the carboxyl groups of glucuronic acid residues from xanthan gum and the cystamine tetra-hydrazide (CTA) amino groups, aiming to obtain nanoparticles for targeted drug release at specific pH and redox potential sites such as those found in cancer cells. The nanogels obtained showed greater release of the chemotherapeutic agent doxorubicin in medium with pH 5 and presence of glutathione, a reducing agent found in high concentrations in cancer cells, than in medium with pH 7.4 and absence of glutathione [112].

5 Carrageenan

Carrageenans are natural sulfated polymers, linear and anionic heteropolysaccharides commercially obtained by red algae extraction. They are polysaccharides of high average molar mass ($4\text{--}6 \times 10^5 \text{ g mol}^{-1}$) and with high degree of polydispersion [113]. They consist of long linear chains of D-galactose and D-anhydrogalactose with ester sulfates with different degrees of sulfonation (between 15 and 40%) [114, 115]. There are three types of carrageenans commercially available: iota (ι), kappa (κ), and lambda (λ)—carrageenan. The difference between them is on 3 β -D-galactopyranose, 4-D-galactopyranose, or 4-3,6-anhydrogalactose bonds, respectively, as shown in Fig. 6. The iota and kappa carrageenans are gel formers, and the lambda-carrageenan is a thickener/viscosity supplier. Kappa carrageenan is the polysaccharide fraction with only one sulfate group per disaccharide repeat unit; iota-carrageenan has two sulfate groups, while lambda-carrageenan has three sulfate groups [113, 114]. Carrageenan has a structural role in the intercellular matrix of numerous *Rhodophyta* class seaweed species, where their amorphous structure promotes the flexibility required for the stress of wave and tidal movement [116].

Kappa-carrageenan (KC) has been proposed as a natural material for use in drilling fluids [12], as well as in regenerative medicine [117]. It can be used to develop edible films and coatings [118]. KC can also promote immunomodulatory and antitumor activities [119]. Carrageenan oligosaccharides and their differences are reported to play an important role as in vitro free radical scavengers and antioxidants as a signal of oxidative damage in living organisms, as well as presenting antitumor activity [120]. KC and Iota-carrageenan (IC) gels formed with potassium salt are reported in literature [121]. Electrolyte films based on IC are used in a green process to be applied in lithium batteries [122]. Commercial carrageenans have coagulant activity, where IC and lambda-carrageenan (LC) presented higher

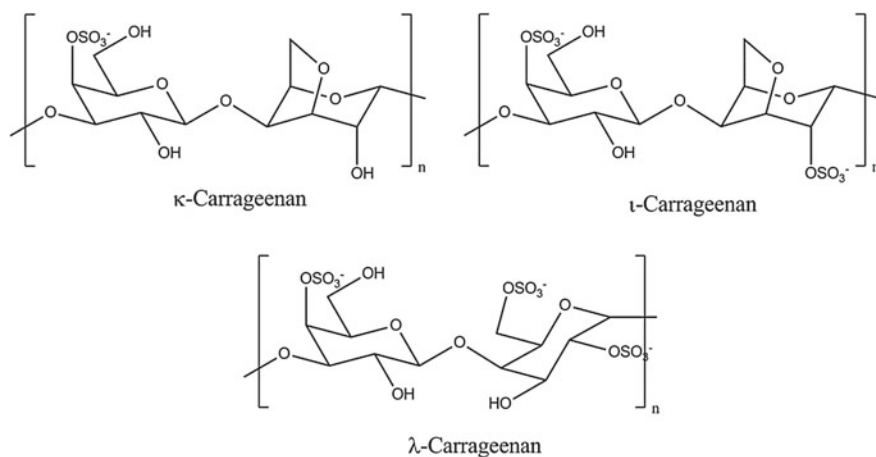


Fig. 6 Structures of commercial carrageenans

inflammatory potential than KC [123]. Encapsulated drugs were found to be released by an inexpensive and non-toxic mechanism using IC fibers [124]. Antiviral activity for herpesvirus type 1 and 3 has been reported for LC, as well as the use for adsorption of methylene blue dye in aqueous solutions [125–127]. The literature shows that carrageenans can be applied in the most different areas of industry as a sulfated natural polymer.

Chemical modifications of polysaccharides are important routes to achieve enhanced or new properties of a material that is biodegradable and mostly biocompatible. Hydroxyl groups are ubiquitous in polysaccharides structure and involved in most of the chemical modifications. The most usual functionalities are ester, ether, amide, amine and alkyl groups [128]. In this scenario, carrageenans make possible a giant number of modifications, properties and applications. Several chemical modifications have been proposed to modulate physicochemical properties of carrageenans. However, carrageenans from the *kappa*-family exhibit the higher reaction rates, in comparison to *iota* and *lambda*-carrageenans. It has been suggested that the presence of a sulfate group in C-2 of the α -galactose unit (present in *kappa*-carrageenan) accelerates slightly the reactions, and sulfate groups on C-2 of the β -unit (present in *lambda*-carrageenan) shows an increase in the reactions rate, suggesting that the presence of sulfate in that position slows down the reaction [129].

5.1 Carrageenan Derivatives, Some Properties and Potential Applications

Carboxymethylation of carrageenans is one of widely chemical modifications studied that lead to development of new polymers with different properties, due to its technical simplicity, low cost of chemical reagents, and modification of the ionic charge and structure of this polymer [130, 131]. The carboxymethylation of carrageenan occur by reaction of KC and monochloroacetic acid in alkaline media, by Williamson's ether synthesis procedure, via nucleophilic substitution [132]. Modification of carrageenan by the insertion of carboxyl groups leads to the possibility of attach other molecules to its backbone or increase the interaction with different materials, improving their properties and application [133]. Several are the reports on literature where carboxymethylated carrageenans are covalently attached to amine groups. Daniel-da-Silva et al. [133] modified chemically KC and IC by carboxymethylation and then covalently attached via amide bond to the surface of aminated silica-coated magnetite nanoparticles. These nanoparticles were used as recyclable sorbents for methylene blue dye removal, which improved the adsorption capacity due to high content of sulfonate groups that can interact electrostatically with dye molecules [133]. The same type of interaction was applied on the production of amphotericin B loaded carboxymethyl *iota*-carrageenan (CMIC) conjugated gelatin nanoparticles. Computational virtual screening studies were

employed for the selection of CMIC as a suitable excipient for amphotericin B and the nanoparticles conjugated with CMIC enabled macrophage targeting for the treatment of intracellular *C. glabrata* infections [134].

Carboxymethyl *kappa* and *iota* carrageenan (CMKC and CMIC, respectively) are frequently used due to their increased biological applications and improved electric conductivity. Fan et al. [135] prepared CMKC-collagen peptide via an imide-bond forming reaction between carboxyl groups in CMKC and amino groups in collagen peptide in the presence of 1-ethyl-(dimethylaminopropyl) carbodiimide and N-hydroxy sulfosuccinimide. The wound healing efficacy of collagen peptide derivatives were evaluated and results indicated that the derivatives were capable of providing suitable condition for granulation tissue formation without any adverse reaction for the body [135]. Also, nanoparticles of chitosan and CMIC proved to be suitable for the oral delivery of insulin and that they protect insulin from gastric and enzymatic degradation [131]. A series of biodegradable CMKC and CMIC based electrolytes films have been prepared by a solution casting technique with different ratios of lithium nitrate (LiNO_3) salts and were electrochemically stable up to 3.0 and 3.1 V, respectively [136]. CMIC films improved the conductivity to $\sim 10^{-3} \text{ S cm}^{-1}$ by salt addition in order to be applied in lithium ion battery [122]. Carboxymethylated carrageenan-based materials can be suitable for the development of solid bio-electrolytes for electrochemical and energy storage applications [137].

Modifying carrageenans by grafting a synthetic polymer can add new properties to the natural polymer, keeping most of its initial properties. These graft copolymers are usually prepared by radical polymerization of vinyl- or acryl-like monomers onto the polysaccharide and as it is usual in this type of reactions, an initiator is required [129]. Novel polyelectrolytes were obtained by grafting N-isopropylacrylamide (NIPAM) on the IC chain and it was observed that in spite of a low degree of grafting the polymer was highly thermosensitive [138]. Superabsorbent hydrogels from KC and nanocomposite hydrogels of KC are reported in literature through graft copolymerization method with acrylic acid. The reactions usually are carried out in aqueous solutions in the presence of N,N-methylene bis-acrylamide (MBA) as a crosslinker and ammonium persulfate (APS) as an initiator. Superabsorbent hydrogels exhibited a compact structure with fracture surface that indicated the presence of crosslinking density and spaces for water diffusion [139]. Nanocomposite hydrogels based on sepiolite clay were used to remove cationic crystal violet dye from water [140]. Some grafting reactions between mixtures of KC and IC with acrylamide are assisted by microwave irradiation in the presence of ammonium persulfate using ceric ammonium nitrate as the initiator. These reactions afforded a copolymer grafted at position C-2 of β -galactopyranosyl residues [141]. Also using microwave irradiation, in the presence of the water-soluble potassium persulfate initiator, KC grafted with poly (vinylpyrrolidone) hydrogels were formed and exhibited enhanced water-holding capacity despite weaker gel strength than that in the respective control polysaccharides [128, 142]. Suitable carriers for biomedical applications, such as drug release, were proposed as super paramagnetic iron oxide nanoparticles and

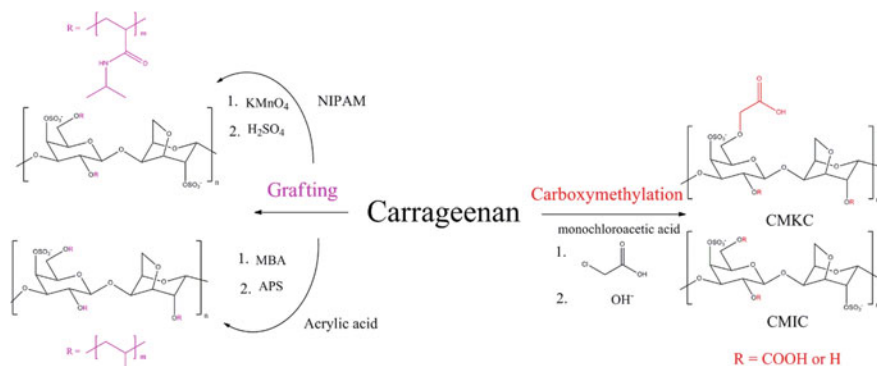


Fig. 7 Reactions of grafting and carboxymethylation of carrageenans

crosslinking of poly (acrylic acid) grafted onto KC, as nontoxic, temperature, and pH sensitive biomaterials [143]. Some reactions of grafting and carboxymethylation are shown in Fig. 7.

Oxidation is another reaction performed on carrageenans with the aim of adding negative charge. Complete oxidation of carrageenans allows the formation of carboxylic acid in the primary alcohol giving the polysaccharide a new negative charge [144]. In order to achieve regioselectivity in the oxidation reaction of the primary alcohols, 2,2,6,6-tetramethylpiperidine-1-oxyl (TEMPO) is used as a radical that selectively oxidizes primary alcohols [129]. With the increase of negative charges and addition to sulfate groups of the molecules, the oxidized carrageenans are widely proposed due to biological properties as antiviral, antibacterial and anticoagulant activity. KC, IC and LC were fully or partially oxidized at C-6 of the β -D-Galp units using TEMPO and tri-chloroisocyanuric acid in bicarbonate buffer, and the anticoagulant activity assays indicated that the introduction of the uronic acid in the carrageenan backbone increased the anticoagulant activity [145]. Also using TEMPO, in the presence of sodium hypochlorite and sodium bromide, full C-6 oxidation of KC and IC were assessed and rationalized through the application of molecular modeling. Partially oxidized carrageenans gave rise to products with a considerable increase in antiviral activity against Herpes virus 1 and 2 [146]. Another method, using hydrogen peroxide and copper sulfate redox system prepared KC with different oxidation levels. Oxidized KC could damage the bacterial cell wall and cytoplasmic membrane and suppress the growth of both Gram-positive and Gram-negative bacteria [144].

The addition of a positive charge is another modification performed to carrageenan. This modification allows generating amphoteric polysaccharides, as they keep the negative charge of the sulfate groups and the positive charge from the inserted group, and could have a variety of applications. The synthesis of cationic carrageenan can occur by reaction with 3-chloro-2-hydroxypropyltrimethyl ammonium chloride (CH-MPEG TAC) in alkaline solutions through the generation of the corresponding 2,3-epoxy reagent *in situ* [147]. Covis et al. [148] achieved the

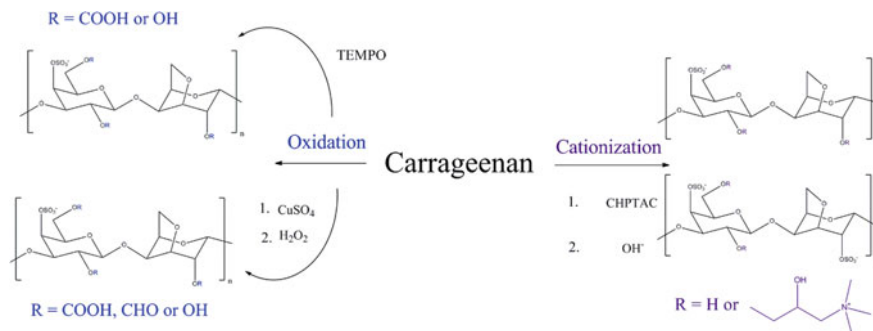


Fig. 8 Reactions of oxidation and cationization of carrageenans

production of cationized KC with a degree of substitution ranging from 0.13 to 0.75. The cationic moiety was linked to the polysaccharide by covalent link, especially ether bond [148]. However, the cationization of IC is reported as more difficult to happen, indicating as it was previously observed for agarose, that substitution starts preferentially on the 2-position of 3,6-anhydrogalactose residues and in iota-carrageenan this latter unit is sulfated [147]. LC was used in the synthesis of λ carrageenan calcium phosphate modified with dimethyl diallyl ammonium chloride and diallyl amine copolymer, which could be used as effective adsorbents of anionic dyes [149]. In summary, the cationized materials could be used as films for application in packaging and/or coating [147] and also as cationized hybrid materials for effective adsorption of acid dyes from wastewaters [149]. The scheme of reactions of oxidation and cationization is illustrated in Fig. 8.

Covalent crosslinking between polymeric chains can be obtained through irradiation, for different applications. Carboxymethyl derivatives of KC were cross-linked by gamma irradiation and demonstrated a significant increase in hemostatic capability, which suggest the potential of CMKC for development into hemostatic agents [150]. Irradiated carrageenan has also been tested as plant growth promoter and has been found to contain some antioxidant properties that increase with increasing dose and concentration. These radiation-degraded carrageenans exhibit growth-promoting activity on rice seedlings, bok-choi and mustard vegetables, and chrysanthemum tissue culture. Along with the degradation of carrageenans is its increase in reducing sugar, which provides its potential as antioxidant [151].

References

1. Klemm, D., Philipp, B., Heinze, T., et al.: Comprehensive cellulose chemistry. Fundam. Anal. Methods J. Am. Chem. Soc. **121**(37), 8677 (1999). <https://doi.org/10.1021/ja9857514>
2. France, K.J., Hoare, T., Cranston, E.D.: Review of hydrogels and aerogels containing nanocellulose. Chem. Mater. **29**, 4609–4631 (2017). <https://doi.org/10.1021/acs.chemmater.7b00531>

3. Jonas, R., Farah, L.F.: Production and application of microbial cellulose. *Polym. Degrad. Stabil.* **59**, 101–106 (1998). [https://doi.org/10.1016/S0141-3910\(97\)00197-3](https://doi.org/10.1016/S0141-3910(97)00197-3)
4. Richardson, S., Gorton, L.: Characterisation of the substituent distribution in starch and cellulose derivatives. *Anal. Chim. Acta* **497**, 27–65 (2003). <https://doi.org/10.1016/j.aca.2003.08.005>
5. Granström, M.: Cellulose derivatives: synthesis, properties and applications. Dissertation, University of Helsinki, Finland (2009). ISBN 978-952-10-5485-3
6. Klemm, D., Heublein, B., Fink, H.-P., et al.: Cellulose: fascinating biopolymer and sustainable raw material. *Angew. Chem. Int. Ed.* **44**, 3358–3393 (2005). <https://doi.org/10.1002/anie.200460587>
7. Heinze, T., Schwikal, K., Barthel, S.: Ionic liquids as reaction medium in cellulose functionalization. *Macromol. Biosci.* **5**, 520–525 (2005). <https://doi.org/10.1002/mabi.200500039>
8. Su, J.-F., Huang, Z., Yuan, X.-Y., et al.: Structure and properties of carboxymethyl cellulose/soy protein isolate blend edible films crosslinked by Maillard reactions. *Carbohydr. Polym.* **79**(1), 145–153 (2010). <https://doi.org/10.1016/j.carbpol.2009.07.035>
9. Greenway, T.M.: Water soluble derivatives and their commercial use. In: Gilbert, D.R. (ed.) *Cellulosic Polymers*, pp. 243–255. Hanser, New York (1994)
10. Oudhoff, K.A., Buijtenhuijs, FA(Ab), Wijnen, P.H., et al.: Determination of the degree of substitution and its distribution of carboxymethylcellulose by capillar zone electrophoresis. *Carbohydr. Res.* **339**, 917–1924 (2004). <https://doi.org/10.1016/j.carres.2004.06.008>
11. Arinaitwe, E., Pawlik, M.: Dilute solution properties of carboxymethyl celluloses of various molecular weights and degrees of substitution. *Carbohydr. Polym.* **99**, 423–431 (2014). <https://doi.org/10.1016/j.carbpol.2013.08.030>
12. Madruga, L.Y.C., da Câmara, P.C.F., Marques, N.N., et al.: Effect of ionic strength on solution and drilling fluid properties of ionic polysaccharides: a comparative study between Na-carboxymethylcellulose and Na-kappa-carrageenan responses. *J. Mol. Liq.* **266**, 870–879 (2018). <https://doi.org/10.1016/j.molliq.2018.07.016>
13. Fagundes, K.R.S., Luz, R.C.S., Fagundes, F.P., et al.: Effect of carboxymethylcellulose on colloidal properties of calcite suspensions in drilling fluids. *Polímeros* **28**(4), 373–379 (2018). <https://doi.org/10.1590/0104-1428.11817>
14. Luz, R.C.S., Fagundes, F.P., Balaban, R.C.: Water-based drilling fluids: the contribution of xanthan gum and carboxymethylcellulose on filtration control. *Chem. Pap.* **71**, 2365–2373 (2017). <https://doi.org/10.1007/s11696-017-0231-7>
15. Vidal, R.R.L., Balaban, R., Borsali, R.: Amphiphilic derivatives and carboxymethylcellulose: Evidence for intra- and intermolecular hydrophobic associations in aqueous solutions. *Polym. Eng. Sci.* **48**(10), 2011–2026 (2008). <https://doi.org/10.1002/pen.21180>
16. Lima, B.V., Vidal, R.R.L., Marques, N.N., et al.: Temperature-induced thickening of sodium carboxymethylcellulose and poly(N-isopropylacrylamide) physical blends in aqueous solution. *Polym. Bull.* **69**, 1093–1101 (2012). <https://doi.org/10.1007/s00289-012-0813-z>
17. Marques, N.N., Lima, B.L.B., Balaban, C.B.: Carboxymethylcellulose grafted to amino-terminated poly(N-isopropylacrylamide): preparation, characterization and evaluation of the thermoassociative behaviour at low concentrations. *Macromol. Symp.* **367**, 126–135 (2016). <https://doi.org/10.1002/masy.201600004>
18. Marques, N.N., Lima, B.V., Silveira, V.R., et al.: PNIPAM-based graft copolymers prepared using potassium persulfate as free-radical initiator: synthesis reproducibility. *Coll. Polym. Sci.* **294**, 981–991 (2016). <https://doi.org/10.1007/s00396-016-3854-2>
19. Pereira, B.H.A., Marques, N.N., Lima, B.L.B., et al.: Study of the thermoassociative process in carboxymethylcellulose derivatives. *J. Mol. Liq.* **272**, 1041–1047 (2018). <https://doi.org/10.1016/j.molliq.2018.10.126>
20. Marques, N.N., Balaban, R.C., Halila, S., et al.: Synthesis and characterization of carboxymethylcellulose grafted with thermoresponsive side chains of high LCST: the high temperature and high salinity self-assembly dependence. *Carbohydr. Polym.* **184**, 108–117 (2018). <https://doi.org/10.1016/j.carbpol.2017.12.053>

21. Domard, A.: A perspective on 30 years research on chitin and chitosan. *Carbohydr. Polym.* **84**(2), 696–703 (2011). <https://doi.org/10.1016/j.carbpol.2010.04.083>
22. Mourya, V.K., Inamdar, N.N.: Chitosan-modifications and applications: opportunities galore. *React. Funct. Polym.* **68**(6), 1013–1051 (2008). <https://doi.org/10.1016/j.reactfunctpolym.2008.03.002>
23. Philippova, O.E., Korchagina, E.V.: Chitosan and its hydrophobic derivatives: preparation and aggregation in dilute aqueous solutions. *Polym. Sci. Ser. A* **54**(7), 552–572 (2012). <https://doi.org/10.1134/S0965545X12060107>
24. Pillai, C.K.S., Paul, W., Sharma, C.P.: Chitin and chitosan polymers: chemistry, solubility and fiber formation. *Prog. Polym. Sci.* **34**(7), 641–678 (2009). <https://doi.org/10.1016/j.progpolymsci.2009.04.001>
25. Yadav, M., Goswami, P., Kunwar, P., et al.: Seafood waste: a source for preparation of commercially employable chitin/chitosan materials. *Bioresour. Bioprocess.* **6**(1), 1–20 (2019). <https://doi.org/10.1186/s40643-019-0243-y>
26. Alves, N.M., Mano, J.F.: Chitosan derivatives obtained by chemical modifications for biomedical and environmental applications. *Int. J. Biol. Macromol.* **43**(5), 401–414 (2008). <https://doi.org/10.1016/j.ijbiomac.2008.09.007>
27. Aranaz, I., Harris, R., Heras, A.: Chitosan Amphiphilic Derivatives. *Chem. Appl. Curr Org Chem* **14**(3), 308–330 (2010). <https://doi.org/10.2174/138527210790231919>
28. Argüelles-Monal, W.M., Lizardi-Mendoza, J., Fernández-Quiroz, D., et al.: Chitosan derivatives: introducing new functionalities with a controlled molecular architecture for innovative materials. *Polymers* **10**(3), 342 (2018). <https://doi.org/10.3390/polym10030342>
29. Campos, E.V.R., Oliveira, J.L., Fraceto, L.F.: Poly(ethylene glycol) and cyclodextrin-grafted chitosan: from methodologies to preparation and potential biotechnological applications. *Front Chem.* (2017). <https://doi.org/10.3389/fchem.2017.00093>
30. Casettari, L., Vllasaliu, D., Castagnino, E., et al.: PEGylated chitosan derivatives: synthesis, characterizations and pharmaceutical applications. *Prog. Polym. Sci.* **37**(5), 659–685 (2012). <https://doi.org/10.1016/j.progpolymsci.2011.10.001>
31. Kahya, N.: Water soluble chitosan derivatives and their biological activities: a review. *Polym. Sci.* **4**(2), 1–16 (2018). <https://doi.org/10.4172/2471-9935.100043>
32. Kumar, M.N.V.R.: A review of chitin and chitosan applications. *React. Funct. Polym.* **46**(1), 1–27 (2000). [https://doi.org/10.1016/S1381-5148\(00\)00038-9](https://doi.org/10.1016/S1381-5148(00)00038-9)
33. Kurita, K.: Controlled functionalization of the polysaccharide chitin. *Prog. Polym. Sci.* **26**(9), 1921–1971 (2001). [https://doi.org/10.1016/S0079-6700\(01\)00007-7](https://doi.org/10.1016/S0079-6700(01)00007-7)
34. Macedo, R.G.M.A., Marques, N.D.N., Paulucci, L.C.S., et al.: Water-soluble carboxymethylchitosan as green scale inhibitor in oil wells. *Carbohydr. Polym.* **215**, 137–142 (2019). <https://doi.org/10.1016/j.carbpol.2019.03.082>
35. Macedo, R.G.M.A., Marques, N.D.N., Tonholo, J., et al.: Water-soluble carboxymethylchitosan used as corrosion inhibitor for carbon steel in saline medium. *Carbohydr. Polym.* **205**, 371–376 (2019). <https://doi.org/10.1016/j.carbpol.2018.10.081>
36. Mohammed, M.A., Syeda, J.T.M., Wasan, K.M., et al.: An overview of chitosan nanoparticles and its application in non-parenteral drug delivery. *Pharmaceutics* **9**(4), 53 (2017). <https://doi.org/10.3390/pharmaceutics9040053>
37. Paixão, M.V.G., Luz, R.C.S., Balaban, R.C.: Thermoresponsive polymer brushes on magnetic chitosan microspheres: Synthesis, characterization and application in oily water of high salinity. *J. Mol. Liq.* (2019). <https://doi.org/10.1016/j.molliq.2019.04.069>
38. Rinaudo, M.: Chitin and chitosan: properties and applications. *Prog. Polym. Sci.* **31**(7), 603–632 (2006). <https://doi.org/10.1016/j.progpolymsci.2006.06.001>
39. Silva, H.S.R.C., Santos, K.S.C.R., Ferreira, E.I.: Quitosana: derivados hidrossolúveis, aplicações farmacêuticas e avanços. *Quím. Nova* **29**(4), 776–785 (2006). <https://doi.org/10.1590/S0100-40422006000400026>
40. Yadu, N.V.K., Raghvendra, K.M., Aswathy, V., et al.: Chitosan as promising materials for biomedical application: review. *Res. Dev. Material. Sci.* **2**(4), 170–185 (2017)

41. Alves, K.S., Vidal, R.R.L., Balaban, R.C.: Chitosan derivatives with thickening properties obtained by reductive alkylation. *Mater. Sci. Eng., C* **29**(2), 641–646 (2009). <https://doi.org/10.1016/j.msec.2008.11.008>
42. Du, H., Liu, M., Yang, X., et al.: The design of pH- sensitive chitosan- based formulations for gastrointestinal delivery. *Drug. Discov. Today* **20**(8), 1004–1011 (2015). <https://doi.org/10.1016/j.drudis.2015.03.002>
43. Marques, N.N., Maia, A.M.S., Balaban, R.C.: Development of dual-sensitive smart polymers by grafting chitosan with poly (*N*-isopropylacrylamide): an overview. *Polímeros* **25**(3), 237–246 (2015). <https://doi.org/10.1590/0104-1428.1744>
44. Tsao, C.T., Hsiao, M.H., Zhang, M.Y., et al.: Chitosan-PEG hydrogel with Sol-Gel transition triggerable by multiple external stimuli. *Macromol. Rapid Commun.* **36**(3), 332–338 (2015). <https://doi.org/10.1002/marc.201400586>
45. Wang, J., Wang, L., Yu, H., et al.: Recent progress on synthesis, property and application of modified chitosan: an overview. *Int. J. Biol. Macromol.* **88**(C), 333–344 (2016). <https://doi.org/10.1016/j.ijbiomac.2016.04.002>
46. Chiu, Y.-L., Chen, S.-C., Su, C.-J., et al.: pH-triggered injectable hydrogels prepared from aqueous *N*-palmitoyl chitosan: In vitro characteristics and in vivo biocompatibility. *Biomaterials* **30**(28), 4877–4888 (2009). <https://doi.org/10.1016/j.biomaterials.2009.05.052>
47. Kumirska, J., Weinhold, M., Thöming, J., et al.: Biomedical activity of chitin/chitosan based materials- influence of physicochemical properties apart from molecular weight and degree of *N*- acetylation. *Polymers* **3**(4), 1875–1901 (2011). <https://doi.org/10.3390/polym3041875>
48. Philippova, O.E., Korchagina, E.V., Volkov, E.V., et al.: Aggregation of some water-soluble derivatives of chitin in aqueous solutions: role of the degree of acetylation and effect of hydrogen bond breaker. *Carbohydr. Polym.* **87**(1), 687–694 (2012). <https://doi.org/10.1016/j.carbpol.2011.08.043>
49. Prashanth, K.V.H., Tharanathan, R.N.: Chitin/chitosan: modifications and their unlimited application potential—an overview. *Trends. Food Sci. Technol.* **18**(3), 117–131 (2007). <https://doi.org/10.1016/j.tifs.2006.10.022>
50. Kubota, N., Tatsumoto, N., Sano, T., et al.: A simple preparation of half *N*-acetylated chitosan highly soluble in water and aqueous organic solvents. *Carbohydr. Res.* **324**(4), 268–274 (2000). [https://doi.org/10.1016/S0008-6215\(99\)00263-3](https://doi.org/10.1016/S0008-6215(99)00263-3)
51. Lu, S., Song, X., Cao, D., et al.: Preparation of water-soluble chitosan. *J. Appl. Polym. Sci.* **91**(6), 3497–3503 (2004). <https://doi.org/10.1002/app.13537>
52. Qin, C., Li, H., Xiao, Q., et al.: Water-solubility of chitosan and its antimicrobial activity. *Carbohydr. Polym.* **63**(3), 367–374 (2006). <https://doi.org/10.1016/j.carbpol.2005.09.023>
53. Sogias, I.A., Khutoryanskiy, V.V., Williams, A.C.: Exploring the factors affecting the solubility of chitosan in water. *Macromol. Chem. Phys.* **211**(4), 426–433 (2010). <https://doi.org/10.1002/macp.200900385>
54. Sugimoto, M., Morimoto, M., Sashiwa, H., et al.: Preparation and characterization of water-soluble chitin and chitosan derivatives. *Carbohydr. Polym.* **36**(1), 49–59 (1998). [https://doi.org/10.1016/S0144-8617\(97\)00235-X](https://doi.org/10.1016/S0144-8617(97)00235-X)
55. Taghizadeh, S.M., Davari, G.: Preparation, characterization, and swelling behavior of *N*-acetylated and deacetylated chitosans. *Carbohydr. Polym.* **64**(1), 9–15 (2006). <https://doi.org/10.1016/j.carbpol.2005.10.037>
56. Abdel-Mohsen, A.M., Aly, A.S., Hrdina, R., et al.: Biomedical textiles through multifunctionalization of cotton fabrics using innovative methoxypolyethylene glycol-*N*-chitosan graft copolymer. *J. Polym. Environ.* **20**(1), 104–116 (2012). <https://doi.org/10.1007/s10924-011-0356-7>
57. Gorochovceva, N., Naderi, A., Dedinaite, A., et al.: Chitosan-*N*-poly(ethylene glycol) brush copolymers: Synthesis and adsorption on silica surface. *Eur. Polym. J.* **41**(11), 2653–2662 (2005). <https://doi.org/10.1016/j.eurpolymj.2005.05.021>
58. Engkagul, V., Sereemasun, A., Chirachanchai, S.: One pot preparation of chitosan/hyaluronic acid- based triple network hydrogel via in situ click reaction, metal coordination

- and polyion complexation in water. *Carbohydr. Polym.* **200**, 616–623 (2018). <https://doi.org/10.1016/j.carbpol.2018.07.090>
59. Li, J., Liu, P.: One-pot fabrication of pH/ reduction dual-stimuli responsive chitosan-based supramolecular nanogels for leakage- free tumor- specific DOX delivery with enhanced anti-cancer efficacy. *Carbohydr. Polym.* **201**, 583–590 (2018). <https://doi.org/10.1016/j.carbpol.2018.08.102>
 60. Ifthikar, J., Jiao, X., Ngambia, A., et al.: Facile one- pot synthesis of sustainable carboxymethyl chitosan—sewage sludge biochar for effective heavy metal chelation and regeneration. *Bioresour. Technol.* **262**, 22–31 (2018). <https://doi.org/10.1016/j.biortech.2018.04.053>
 61. Koosha, M., Raoufi, M., Moravvej, H.: One- pot reactive electrospinning of chitosan/ PVA hydrogel nanofibers reinforced by halloysite nanotubes with enhanced fibroblast cell attachment for skin tissue regeneration. *Colloids Surf. B Biointerfaces* **179**, 270–279 (2019). <https://doi.org/10.1016/j.colsurfb.2019.03.054>
 62. Xu, Q., Zheng, W., Duan, P., et al.: One-pot fabrication of durable antibacterial cotton fabric coated with silver nanoparticles via carboxymethyl chitosan as a binder and stabilizer. *Carbohydr. Polym.* **204**, 42–49 (2019). <https://doi.org/10.1016/j.carbpol.2018.09.089>
 63. Wei, J., Guo-Wang, P., Cui, L., et al.: Novel method to graft chitosan on the surface of hydroxyapatite nanoparticles via “Click” reaction. *Chem. Res. Chin. Univ.* **30**(6), 1063–1065 (2014). <https://doi.org/10.1007/s40242-014-4166-z>
 64. Li, Q., Tan, W., Zhang, C., et al.: Synthesis of water soluble chitosan derivatives with halogeno- 1,2,3- triazole and their antifungal activity. *Int. J. Biol. Macromol.* **91**, 623–629 (2016). <https://doi.org/10.1016/j.ijbiomac.2016.06.006>
 65. Tan, W., Zhang, J., Mi, Y., et al.: Synthesis, characterization, and evaluation of antifungal and antioxidant properties of cationic chitosan derivative via azide-alkyne click reaction. *Int. J. Biol. Macromol.* **120**(A), 318–324 (2018). <https://doi.org/10.1016/j.ijbiomac.2018.08.111>
 66. Guaresti, O., García-Astrain, C., Aguirresarobe, R.H., et al.: Synthesis of stimuli— responsive chitosan—based hydrogels by Diels—Alder cross—linking ‘click’ reaction as potential carriers for drug administration. *Carbohydr. Polym.* **183**, 278–286 (2018). <https://doi.org/10.1016/j.carbpol.2017.12.034>
 67. Yang, N., Wang, Y., Zhang, Q., et al.: In situ formation of poly (thiolated chitosan—co—alkylated β -cyclodextrin) hydrogels using click cross-linking for sustained drug release. *J. Mater. Sci.* **54**(2), 1677–1691 (2019). <https://doi.org/10.1007/s10853-018-2910-3>
 68. Alves, K.S.: Obtenção de polímeros graftizados de quitosana e estudo das propriedades físico-químicas para aplicação na indústria do petróleo. Thesis, Federal University of Rio Grande do Norte, Brazil (2013)
 69. Blagodatskikh, I., Bezrodnykh, E., Abramchuk, S., et al.: Short chain chitosan solutions: self-assembly and aggregates disruption effects. *J. Polym. Res.* **20**(2), 1–10 (2013). <https://doi.org/10.1007/s10965-013-0073-0>
 70. Chen, W., Hsu, C., Huang, J., et al.: Effect of the ionic strength of the media on the aggregation behaviors of high molecule weight chitosan. *J. Polym. Res.* **18**(6), 1385–1395 (2011). <https://doi.org/10.1007/s10965-010-9543-9>
 71. Popa-Nita, S., Alcouffe, P., Rochas, C., et al.: Continuum of structural organization from chitosan solutions to derived physical forms. *Biomacromol* **11**(1), 6–12 (2010). <https://doi.org/10.1021/bm9012138>
 72. Desbrières, J., Martinez, C., Rinaudo, M.: Hydrophobic derivatives of chitosan: characterization and rheological behaviour. *Int. J. Biol. Macromol.* **19**(1), 21–28 (1996). [https://doi.org/10.1016/0141-8130\(96\)01095-1](https://doi.org/10.1016/0141-8130(96)01095-1)
 73. Robles, E., Villar, E., Alatorre-Meda, M., et al.: Effects of the hydrophobization on chitosan—Insulin nanoparticles obtained by an alkylation reaction on chitosan. *J. Appl. Polym. Sci.* **129**(2), 822–834 (2013). <https://doi.org/10.1002/app.38870>
 74. Liu, L., Xu, X., Guo, S., et al.: Synthesis and self-assembly of chitosan-based copolymer with a pair of hydrophobic/hydrophilic grafts of polycaprolactone and poly(ethylene glycol). *Carbohydr. Polym.* **75**(3), 401–407 (2009). <https://doi.org/10.1016/j.carbpol.2008.07.038>

75. Marques, N.N., Curti, P.S., Maia, A.M.S., et al.: Temperature and pH effects on the stability and rheological behavior of the aqueous suspensions of smart polymers based on N-isopropylacrylamide, chitosan, and acrylic acid. *J. Appl. Polym. Sci.* **129**(1), 334–345 (2013). <https://doi.org/10.1002/app.38750>
76. Luz, R.C.S., Paixão, M.V.G., Balaban, R.C.: Nanosilica- chitosan hybrid materials: preparation, characterization and application in aqueous drilling fluids. *J. Mol. Liq.* **279**, 279–288 (2019). <https://doi.org/10.1016/j.molliq.2019.01.131>
77. Amagliani, L., O'Regan, J., Kelly, A.L., et al.: Chemistry, structure, functionality and applications of rice starch. *J. Cereal Sci.* **70**, 291–300 (2016). <https://doi.org/10.1016/j.jcs.2016.06.014>
78. Khlestkin, V.K., Peltek, S.E., Kolchanov, N.A.: Review of direct chemical and biochemical transformations of starch. *Carbohydr. Polym.* **181**, 460–476 (2018). <https://doi.org/10.1016/j.carbpol.2017.10.035>
79. Zia, F., Zia, K.M., Zuber, M., et al.: Starch based polyurethanes: a critical review updating recent literature. *Carbohydr. Polym.* **134**, 784–798 (2015). <https://doi.org/10.1016/j.carbpol.2015.08.034>
80. Dufresne, A.: Crystalline starch based nanoparticles. *Curr. Opin. Colloid Interface Sci.* **19** (5), 397–408 (2014). <https://doi.org/10.1016/j.cocis.2014.06.001>
81. Meimoun, J., Wiatz, V., Saint-Loup, R., et al.: Modification of starch by graft copolymerization. *Starch* (2018). <https://doi.org/10.1002/star.201600351>
82. Thakur, R., Pristijono, P., Scarlett, C.J., et al.: Starch-based films: major factors affecting their properties. *Int. J. Biol. Macromol.* **132**, 1079–1089 (2019). <https://doi.org/10.1016/j.ijbiomac.2019.03.190>
83. Basiak, E., Lenart, A., Debeaufort, F.: Effect of starch type on the physico-chemical properties of edible films. *Int. J. Biol. Macromol.* **98**, 348–356 (2017). <https://doi.org/10.1016/j.ijbiomac.2017.01.122>
84. Alcázar-Alay, S.C., Meireles, M.A.A.: Physicochemical properties, modifications and applications of starches from different botanical sources. *Food Sci. Technol.* **35**(2), 215–236 (2015). <https://doi.org/10.1590/1678-457X.6749>
85. Ogunsona, E., Ojogbo, E., Mekonnen, T.: Advanced material applications of starch and its derivatives. *Eur. Polym. J.* **108**, 570–581 (2018). <https://doi.org/10.1016/j.eurpolymj.2018.09.039>
86. Altuna, L., Herrera, M.L., Foresti, M.L.: Synthesis and characterization of Octenyl succinic anhydride modified starches for food applications. a review of recent literature. *Food Hydrocoll* **80**, 97–110 (2018). <https://doi.org/10.1016/j.foodhyd.2018.01.032>
87. Chen, Q., Yu, H., Wanf, L., et al.: Recent progress in chemical modification of starch and its applications. *RSC Adv.* **5**(83), 67459–67474 (2015). <https://doi.org/10.1039/C5RA10849G>
88. Masina, N., Choonara, Y.E., Kumar, P., et al.: A review of the chemical modification techniques of starch. *Carbohydr. Polym.* **157**, 1226–1236 (2017). <https://doi.org/10.1016/j.carbpol.2016.09.094>
89. Vanmarcke, A., Leroy, L., Stoclet, G., et al.: Influence of fatty chain length and starch composition on structure and properties of fully substituted fatty acid starch esters. *Carbohydr. Polym.* **164**, 249–257 (2017). <https://doi.org/10.1016/j.carbpol.2017.02.013>
90. Dias, F.T.G., Souza, R.R., Lucas, E.F.: Influence of modified starches composition on their performance as fluid loss additives in invert-emulsion drilling fluids. *Fuel* **140**, 711–716 (2015). <https://doi.org/10.1016/j.fuel.2014.09.074>
91. Marques, N.N., Garcia, C.S.N., Madruga, L.Y.C., et al.: Turning Industrial waste into a valuable bioproduct: starch from mango kernel derivative to oil industry mango starch derivative in oil industry. *J. Renew Mat.* **7**(2):139–152 (2019). <http://dx.doi.org/10.32604/jrm.2019.00040>
92. Li, S., Li, C., Yang, Y., et al.: Starch granules as pickering emulsifiers: role of octenylsuccinylation and particle size. *Food Chem.* **283**, 437–444 (2019). <https://doi.org/10.1016/j.foodchem.2019.01.020>

93. Zhu, F.: Starch based pickering emulsions: fabrication, properties, and applications. *Trends Food Sci. Technol.* **85**, 129–137 (2019). <https://doi.org/10.1016/j.tifs.2019.01.012>
94. Haroon, M., Wang, L., Yu, H., et al.: Chemical modification of starch and its application as an adsorbent material. *RSC Adv.* **6**(82), 78264–78285 (2016). <https://doi.org/10.1039/c6ra16795k>
95. Fu, Z., Zhang, L., Ren, M.-H., et al.: Developments in Hydroxypropylation of Starch: a review. *Starch* **71**(1–2) (2019). <http://dx.doi.org/10.1002/star.201800167>
96. Noordergraaf, I.W., Fourie, T.K., Raffa, P.: Free-radical graft polymerization onto starch as a tool to tune properties in relation to potential applications. a review. *Processes* **6**(4). (2018). <http://dx.doi.org/10.3390/pr6040031>
97. Kazeminejadfard, F., Hojjati, M.R.: Preparation of Superabsorbent Composite Based on Acrylic Acid-Hydroxypropyl Distarch Phosphate and Clinoptilolite for Agricultural Applications. *J. Appl. Polym. Sci.* **136**(16) (2019). <http://dx.doi.org/10.1002/app.47365>
98. Ahmad, N.H., Mustafa, S., Man, Y.B.C.: Microbial polysaccharides and their modification approaches: a review. *Int. J. Food Prop.* **18**, 332–347 (2015). <https://doi.org/10.1080/10942912.2012.693561>
99. Lachke, A.R.: Xanthan—a versatile gum. *Resonance* **9**, 25–33 (2004)
100. Petri, D.F.S.: Xanthan gum: a versatile biopolymer for biomedical and technological applications. *J. Appl. Polym. Sci.* (2015). <https://doi.org/10.1002/app.42035>
101. Adhikary, P., Singh, R.P.: Synthesis, characterization, and flocculation characteristics of hydrolyzed and unhydrolyzed polyacrylamide grafted xanthan gum. *J. Appl. Polym. Sci.* **94**, 1411–1419 (2004). <https://doi.org/10.1002/app.21040>
102. Maia, A.M.S., Silva, H.V.M., Curti, P.S., et al.: Study of the reaction of grafting acrylamide onto xanthan gum. *Carbohydr. Polym.* **90**, 778–783 (2012). <https://doi.org/10.1016/j.carbpol.2012.05.059>
103. Makhado, E., Pandey, S., Ramontja, J.: Microwave-assisted green synthesis of xanthan gum grafted diethylamino ethyl methacrylate: an efficient adsorption of hexavalent chromium. *Carbohydr. Polym.* (2019). <https://doi.org/10.1016/j.carbpol.2019.114989>
104. Hamcerencu, M., Desbrieres, J., Popa, M., et al.: New unsaturated derivatives of Xanthan gum: synthesis and characterization. *Polymer* **48**, 1921–1929 (2007). <https://doi.org/10.1016/j.polymer.2007.01.048>
105. Hamcerencu, M., Desbrieres, J., Popa, M., et al.: Stimuli-sensitive xanthan derivatives/N-isopropylacrylamide hydrogels: Influence of cross-linking agent on interpenetrating polymer network properties. *Biomacromol* **10**, 1911–1922 (2009). <https://doi.org/10.1021/bm900318g>
106. Kumar, A., Deepak, Sharma S., et al.: Synthesis of xanthan gum graft copolymer and its application for controlled release of highly water soluble Levofloxacin drug in aqueous medium. *Carbohydr. Polym.* **171**, 211–219 (2017). <https://doi.org/10.1016/j.carbpol.2017.05.010>
107. Kumar, A., Singh, K., Ahuja, M.: Xanthan-g-poly(acrylamide): Microwave-assisted synthesis, characterization and in vitro release behavior. *Carbohydr. Polym.* **76**, 261–267 (2009). <https://doi.org/10.1016/j.carbpol.2008.10.014>
108. Kulkarni, R.V., Sa, B.: Electroresponsive polyacrylamide-grafted-xanthan hydrogels for drug delivery. *J. Bioact. Compat. Polym.* **24**, 368–384 (2009). <https://doi.org/10.1177/0883911509104475>
109. Pal, A., Majumder, K., Bandyopadhyay, A.: Surfactant mediated synthesis of poly(acrylic acid) grafted xanthan gum and its efficient role in adsorption of soluble inorganic mercury from water. *Carbohydr. Polym.* **152**, 41–50 (2016). <https://doi.org/10.1016/j.carbpol.2016.06.064>
110. Makhado, E., Pandey, S., Nomngongo, P.N., et al.: Fast microwave-assisted green synthesis of xanthan gum grafted acrylic acid for enhanced methylene blue dye removal from aqueous solution. *Carbohydr. Polym.* **176**, 315–326 (2017). <https://doi.org/10.1016/j.carbpol.2017.08.093>

111. Liu, Z., Yao, P.: Injectable shear-thinning xanthan gum hydrogel reinforced by mussel-inspired secondary crosslinking. *RSC Adv.* **5**, 103292–103301 (2015). <https://doi.org/10.1039/C5RA17246B>
112. Zhang, L., Xu, J., Wen, Q., et al.: Preparation of xanthan gum nanogels and their pH/redox responsiveness in controlled release. *J Appl. Polym. Sci.* (2019). <https://doi.org/10.1002/app.47921>
113. Pelletier, E., Viebke, C., Meadows, J., et al.: Solution rheology of κ -carrageenan in the ordered and disordered conformations. *Biomacromol* **2**, 946–951 (2001). <https://doi.org/10.1021/bm010060c>
114. Almeida, N., Hirschi, S., Mueller, A., et al.: Viscoelastic properties of κ -carrageenan in saline solution. *J. Therm. Anal. Calorim.* **102**, 647–652 (2010). <https://doi.org/10.1007/s10973-010-0944-0>
115. de Morais, S.C., Cardoso, O.R., de Carvalho, Balaban R.: Thermal stability of water-soluble polymers in solution. *J. Mol. Liq.* **265**, 818–823 (2018). <https://doi.org/10.1016/j.molliq.2018.07.033>
116. Xu, J.B., Bartley, J.P., Johnson, R.A.: Preparation and characterization of alginate–carrageenan hydrogel films crosslinked using a water-soluble carbodiimide (WSC). *J. Memb. Sci.* **218**, 131–146 (2003). [https://doi.org/10.1016/S0376-7388\(03\)00165-0](https://doi.org/10.1016/S0376-7388(03)00165-0)
117. Popa, E.G., Gomes, M.E., Reis, R.L.: Cell delivery systems using alginate-carrageenan hydrogel beads and fibers for regenerative medicine applications. *Biomacromol* **12**, 3952–3961 (2011). <https://doi.org/10.1021/bm200965x>
118. Tavassoli-Kafrani, E., Shekarchizadeh, H., Masoudpour-Behabadi, M.: Development of edible films and coatings from alginates and carrageenans. *Carbohydr. Polym.* **137**, 360–374 (2016). <https://doi.org/10.1016/j.carbpol.2015.10.074>
119. Yuan, H., Song, J., Li, X., et al.: Immunomodulation and antitumor activity of κ -carrageenan oligosaccharides. *Cancer Lett.* **243**, 228–234 (2006). <https://doi.org/10.1016/j.canlet.2005.11.032>
120. Sun, T., Tao, H., Xie, J., et al.: Degradation and antioxidant activity of κ -carrageenans. *J. Appl. Polym. Sci.* **21**, 194–199 (2010). <https://doi.org/10.1002/app.31955>
121. Brenner, T., Tuvikene, R., Parker, A., et al.: Rheology and structure of mixed kappa-carrageenan/iota-carrageenan gels. *Food Hydrocoll* **39**, 272–279 (2014). <https://doi.org/10.1016/j.foodhyd.2014.01.024>
122. Jumaah, F.N., Mobarak, N.N., Ahmad, A., et al.: Derivative of iota-carrageenan as solid polymer electrolyte. *Ionics* **21**, 1311–1320 (2015). <https://doi.org/10.1007/s11581-014-1306-x>
123. Silva, F.R.F., Dore, C.M.P.G., Marques, C.T., et al.: Anticoagulant activity, paw edema and pleurisy induced carrageenan: action of major types of commercial carrageenans. *Carbohydr. Polym.* **79**, 26–33 (2010). <https://doi.org/10.1016/j.carbpol.2009.07.010>
124. Janaswamy, S., Gill, K.L., Campanella, O.H., et al.: Organized polysaccharide fibers as stable drug carriers. *Carbohydr. Polym.* **94**, 209–215 (2013). <https://doi.org/10.1016/j.carbpol.2013.01.008>
125. Agougui, H., Jabli, M., Majdoub, H.: Synthesis, characterization of hydroxyapatite-lambda carrageenan, and evaluation of its performance for the adsorption of methylene blue from aqueous suspension. *J. Appl. Polym. Sci.* **134**, 1–9 (2017). <https://doi.org/10.1002/app.45385>
126. Diogo, J.V., Novo, S.G., González, M.J., et al.: Antiviral activity of lambda-carrageenan prepared from red seaweed (*Gigartina skottsbergii*) against BoHV-1 and SuHV-1. *Res. Vet. Sci.* **98**, 142–144 (2015). <https://doi.org/10.1016/j.rvsc.2014.11.010>
127. Vissani, M.A., Galdo, N.S., Ciancia, M., et al.: Effects of lambda-carrageenan on equid herpesvirus 3 in vitro. *J. Equine Vet. Sci.* **S61–S62** (2016)
128. Chopin, N., Guillory, X., Weiss, P., et al.: Design polysaccharides of marine origin: chemical modifications to reach advanced versatile compounds. *Curr. Org. Chem.* **18**, 867–895 (2014). <https://doi.org/10.2174/138527281807140515152334>

129. Cosenza, V.A., Navarro, D.A., Stortz, C.A.: Chemical modification of carrageenans and application of the modified products. In: Pereira, L. (ed.) Carrageenans: sources and extraction methods. molecular structure, bioactive properties and health effects, pp. 189–227. Nova Science Publisher, New York (2016)
130. Dogsa, I., Tomšič, M., Orehek, J., et al.: Amorphous supramolecular structure of carboxymethyl cellulose in aqueous solution at different pH values as determined by rheology, small angle X-ray and light scattering. *Carbohydr. Polym.* **111**, 492–504 (2014). <https://doi.org/10.1016/j.carbpol.2014.04.020>
131. Sahoo, P., Leong, K.H., Nyamathulla, S., et al.: Optimization of pH-responsive carboxymethylated iota-carrageenan/chitosan nanoparticles for oral insulin delivery using response surface methodology. *React. Funct. Polym.* **119**, 145–155 (2017). <https://doi.org/10.1016/j.reactfunctpolym.2017.08.014>
132. Tranquilan-Aranilla, C., Nagasawa, N., Bayquen, A., et al.: Synthesis and characterization of carboxymethyl derivatives of kappa-carrageenan. *Carbohydr. Polym.* **87**, 1810–1816 (2012). <https://doi.org/10.1016/j.carbpol.2011.10.009>
133. Daniel-da-Silva, A.L., Salgueiro, A.M., Creaney, B., et al.: Carrageenan-grafted magnetite nanoparticles as recyclable sorbents for dye removal. *J. Nanoparticle Res.* **17**, 1–15 (2015). <https://doi.org/10.1007/s11051-015-3108-0>
134. Aparna, V., Melge, A.R., Rajan, V.K., et al.: Carboxymethylated ι-carrageenan conjugated amphotericin B loaded gelatin nanoparticles for treating intracellular *Candida glabrata* infections. *Int. J. Biol. Macromol.* **110**, 140–149 (2018). <https://doi.org/10.1016/j.ijbiomac.2017.11.126>
135. Fan, L., Tong, J., Tang, C., et al.: Preparation and characterization of carboxymethylated carrageenan modified with collagen peptides. *Int. J. Biol. Macromol.* **82**, 790–797 (2016). <https://doi.org/10.1016/j.ijbiomac.2015.10.063>
136. Mobarak, N.N., Jumaah, F.N., Ghani, M.A., et al.: Carboxymethyl carrageenan based biopolymer electrolytes. *Electrochim. Acta* **175**, 224–231 (2015). <https://doi.org/10.1016/j.electacta.2015.02.200>
137. Torres, F.G., Arroyo, J., Alvarez, R., et al.: Carboxymethyl κ/ι-hybrid carrageenan doped with NH4I as a template for solid bio-electrolytes development. *Mater. Chem. Phys.* **223**, 659–665 (2019). <https://doi.org/10.1016/j.matchemphys.2018.11.051>
138. Gawel, K., Karczewska, A., Bielska, D., et al.: A thermosensitive carrageenan-based polymer: synthesis, characterization and interactions with a cationic surfactant. *Carbohydr. Polym.* **96**, 211–217 (2013). <https://doi.org/10.1016/j.carbpol.2013.03.056>
139. Daud, J.M., Warzukni, N.S., Salim, R.M. et al.: Semi-refined κ-carrageenan: Part 1. Chemical modification of semi-refined κ-carrageenan via graft copolymerization method, optimization process and characterization of its superabsorbent hydrogel. *Orient. J. Chem.* **31**, 973–980 (2015). <http://dx.doi.org/10.13005/ojc/310243>
140. Mahdavinia, G.R., Asgari, A.: Synthesis of kappa-carrageenan-g-poly(acrylamide)/sepiolite nanocomposite hydrogels and adsorption of cationic dye. *Polym. Bull.* **70**, 2451–2470 (2013). <https://doi.org/10.1007/s00289-013-0966-4>
141. Arias, F., Mansilla, A., Matsuhiro, B., et al.: Carrageenans from nuclear phases of subantartic *Mazzaella laminarioides* (Gigartinales, Rhodophyta) and graft copolymerization of alkali-modified carrageenan with acrylamide. *J. Appl. Phycol.* **28**, 1275–1286 (2016). <https://doi.org/10.1007/s10811-015-0641-2>
142. Prasad, K., Mehta, G., Meena, R., et al.: Hydrogel-forming agar-graft-PVP and κ-carrageenan-graft-PVP Blends: rapid synthesis and characterization. *J. Appl. Polym. Sci.* **102**, 3654–3663 (2006). <https://doi.org/10.1002/app.24145>
143. Bardajee, G.R., Hooshyar, Z., Rastgo, F.: Kappa carrageenan-g-poly (acrylic acid)/SPION nanocomposite as a novel stimuli-sensitive drug delivery system. *Colloid Polym. Sci.* **291**, 2791–2803 (2013). <https://doi.org/10.1007/s00396-013-3018-6>
144. Zhu, M., Ge, L., Lyu, Y., et al.: Preparation, characterization and antibacterial activity of oxidized κ-carrageenan. *Carbohydr. Polym.* **174**, 1051–1058 (2017). <https://doi.org/10.1016/j.carbpol.2017.07.029>

145. dos Santos-Fidencio, G.C., Gonçalves, A.G., Nosedá, M.D., et al.: Effects of carboxyl group on the anticoagulant activity of oxidized carrageenans. *Carbohydr. Polym.* **214**, 286–293 (2019). <https://doi.org/10.1016/j.carbpol.2019.03.057>
146. Cosenza, V.A., Navarro, D.A., Pujol, C.A., et al.: Partial and total C-6 oxidation of gelling carrageenans. Modulation of the antiviral activity with the anionic character. *Carbohydr. Polym.* **128**, 199–206 (2015). <https://doi.org/10.1016/j.carbpol.2015.04.030>
147. Barahona, T., Prado, H.J., Bonelli, P.R., et al.: Cationization of kappa- and iota-carrageenan—Characterization and properties of amphoteric polysaccharides. *Carbohydr. Polym.* **126**, 70–77 (2015). <https://doi.org/10.1016/j.carbpol.2015.02.053>
148. Covis, R., Guegan, J.P., Jeftić, J., et al.: Structural and rheological properties of kappa (κ)-carrageenans covalently modified with cationic moieties. *J. Polym. Res.* (2016). <https://doi.org/10.1007/s10965-016-0971-z>
149. Sebeia, N., Jabli, M., Ghith, A.: [λ -Carrageenan-calcium phosphate] and [sodium alginate-calcium phosphate] modified with dimethyl diallyl ammonium chloride and diallylamin co-polymer as efficient adsorbents of anionic dyes. *Int. J. Biol. Macromol.* **126**, 641–652 (2019). <https://doi.org/10.1016/j.ijbiomac.2018.12.260>
150. Tranquilan-Aranilla, C., Barba, B.J.D., Vista, J.R.M., et al.: Hemostatic efficacy evaluation of radiation crosslinked carboxymethyl kappa-carrageenan and chitosan with varying degrees of substitution. *Radiat. Phys. Chem.* **124**, 124–129 (2016). <https://doi.org/10.1016/j.radphyschem.2016.02.003>
151. Abad, L.V., Aranilla, C.T., Relleve, L.S., et al.: Emerging applications of radiation-modified carrageenans. *Nucl. Instrum. Methods Phys. Res. Sect. B Beam. Interact. with Mater Atoms.* **336**, 167–172 (2014). <https://doi.org/10.1016/j.nimb.2014.07.005>

A TD-DFT Simulation on Organic Polymer: The Case of PEDOT



A. M. Andrade, A. Camilo Jr. and S. R. de Lazaro

Abstract Organic semiconductors (OS) are applied in many electronic devices, for instance, OLEDs. The main advantages of these materials are focused in flexibility, high possibilities for structural changes and synthesis. The chemical structure of OS is based on a polymeric chain formed by π conjugated bonds, which act as charge carriers for conductive and optical properties. One of the most investigated polymeric structure is Poly(3,4-ethylenedioxythiophene) (PEDOT) due to its planar molecular structure. To investigate the charge bulk influence formed by π conjugated bonds on excitation energy and band-gap of PEDOT were performed simulations in PM6, DFT and TD-DFT levels of theory. Consequently, Density of States (DOS) analysis showed an association between intermediary energy levels formed inside monomer band-gap and excitation energy profiles as essential factor to change electronic properties of PEDOT.

Keywords PEDOT · DFT · Conductive polymer · Excite state · Band-gap

Preface

The great contribution in the discovery of high conductivity in organic molecules happened in 1977 from scientific contribution of Shirakawa and co-authors researching the stability and electric conductivity at room temperature in thin films of Polyethylene. Until such research, the scientific literature showed chemical synthesis of covalent materials based on Sulfur and Bromide atoms with low performance for stability or conductivity; such compounds does not have Carbon atoms. The main contribution of these authors was point the high difference of electric conductivity between *cis*- and *trans*-Polyethylene molecular conformations proposing a connection between conductivity and molecular geometry of organic

A. M. Andrade · S. R. de Lazaro (✉)
Department of Chemistry, State University of Ponta Grossa,
Av. General Carlos Cavalcanti 4748, Ponta Grossa, Paraná, Brazil
e-mail: srlazaro@uepg.br

A. Camilo Jr.
Department of Physics, State University of Ponta Grossa,
Av. General Carlos Cavalcanti 4748, Ponta Grossa, Paraná, Brazil

compounds formed by Carbon atoms. After that, the researchers study deeper this effect showing that electric conductivity in such organic compounds is extremely dependent of the planarity localized among monomers of the polymeric chain. From a molecular point of view, such molecular planarity is caused by alternation between σ and π chemical bonds, more specifically, π delocalized electrons over all the polymeric structure possibility an electronic density more easily polarizable increasing the performance of electric or optical properties. Unfortunately, the industrial production of the conductive polymers based on Polyethylene is not favourable due to the high rigidity showed by material; one alternative is add dopant or lateral groups to polymer; however, such structural modifications modify the electrical property.

One solution developed as alternative to Polyethylene was finding other polymers with similar features, such as, Polythiophenes or Polyphenils but, the high structural disorder of these polymers has a high impact in the performance of the electronic devices from low electrical conductivity at order 100 S cm^{-1} . At beginning of 80s decade, organic polymers reach electric conductivity of $10,000 \text{ S cm}^{-1}$ and at the end of the same decade researchers initiated the search for organic molecules with similar properties to inorganic semiconductors finding a new class of conductive polymers, for instance, Polyaniline or Polypyrrol structures. Recently, conductive polymers are widely applied as charge carriers in solar cells, in the interaction with metals, carbon nanotubes and flexible electronic devices.

1 Introduction

1.1 Photovoltaic Devices

Nowadays, the need to produce alternative energy sources which can substitute fossil fuels is a worldwide challenge. Furthermore, policy efforts must be made to become the clean energy technologies competitive to cheaper energy sources, and its application in the society, especially for reducing global warming [1]. Since 1970, solar photovoltaic devices has been developed with objective to reach new low energy cost devices, but its application was limited by low energy conversion efficiency. During the last decades, solar energy conversion up to 30% was achieved in inorganic devices based on crystalline silicon devices; however, they are limited by high cost and short durability [2].

One way to avoid the high effective cost of solar cell devices is to replace silicon by organic semiconductors (OS) because its potential for roll-to-roll fabrication has more processable advantages mainly, high flexibility, easy to synthesize and endless possibilities on discovering new materials by organic structural modification, and capacity to be used in flexible substrates [3]. However, such OS also have the

problem of low efficiency at energy conversion [4]. Recently, studies with multiple organic solar cells called “sandwich” solar cells have shown to be good candidates to avoid the limited absorption spectra range [5, 6]. Furthermore, OS can be associated with inorganic semiconductors to produce flexible thin film devices with good charge transport properties [7]. The role of organic materials that can be used for application in solar cell devices is widespread in different organic classes, but the main characteristic found in all compounds is the π conjugation length allowing a high charge mobility between HOMO and LUMO orbitals [8, 9].

1.2 Charge Carriers in Organic Semiconductors

A possible structural classification for organic semiconductors is divided in two groups: (i) small molecules or oligomers, which are synthesized under vacuum condition; and (ii) polymers synthesized from aqueous condition. The difference between charge carriers materials is related to Solid State Chemistry concepts; type-*n* organic semiconductors are polymers that inject majority electrons or high electronic density as charge carriers while type-*p* organic semiconductors are featured majority as charge carriers using holes or low electronic density. Type-*n* materials show Fermi energy connected to electronic affinity whereas type-*p* materials, the Fermi energy is related to ionization energy of material.

The diffusion of charge carriers is an important effect for efficiency of organic devices; it acts from a local displacement of charge carriers in one preferential direction causing an electrical induction. The direction of diffusion is connected to charge carrier mobility, which dominates the charge carriers diffusion on layer of the organic semiconductor.

Organic polymeric materials used in solar cell devices must show high structure ordering of polymer bulk, once this molecular property contribute significantly for charge transport between High Occupied Molecular Orbital (HOMO) and Low Unoccupied Molecular Orbital (LUMO) frontiers orbitals spread in polymeric chain [8, 10, 11]. For better bulk formation efficiency, polymeric materials must show planar chain among monomers to produce charge carriers on polymeric chain [12]. Considering such property, the class of polythiophenes (PT) have attached attention, especially by experimental results in different synthesis routes [13, 14]. From many PT derivatives, Poly(3,4-ethylenedioxythiophene) (PEDOT) has been investigated since 1980, initially on BAYER laboratories, and it became an interesting candidate for application as OS, once PEDOT is easy to process in non-aqueous solvents, and it has excellent hole transport properties, allowing the application on different electronic devices, such as antistatic coatings, cathodes in capacitors, organic light emitting diodes (OLEDs), photovoltaic, and electrochromic films [15, 16].

PEDOT has been investigated to understand the contribution of π conjugate bonds on conductive and optical properties. Apperloo et al. [17] investigated the relation between monomeric units and ultraviolet absorption through experimental and semi-empirical results, but from this contribution there is no significant

theoretical contributions for a better understanding of the relation between molecular geometry, electronic structure and absorption spectra.

1.3 Density Functional Theory

The Density Functional Theory (DFT) has been widely used in molecular and solid simulations as for structure as for properties. Mainly, the low computational cost of the DFT regarding to Hartree-Fock (HF) methodologies has attract many researchers to DFT. It is important emphasizes that in DFT the electronic density (ρ) replaces to wave-function of the Schrödinger Equation, i.e., the focus to minimize the Energy of the system, extract information or properties is ρ and the electronic density is only dependent of distance r ; $\rho(r)$ The DFT shows that is possible a direct connection between Energy and $\rho(r)$ through the mathematical function denominated as functional; this function defines how from $\rho(r)$ is calculated the Energy. Another point, in HF formalism we have $4n$ variables (n is the number of electrons), while in DFT there is (x, y, z) variables to describe the electrons of system.

From Hohenberg-Kohn (HK) theorems is possible write that a molecular system in a ground state (ρ_0) has Total Energy (E_0) defined as summation among kinetic energy ($T[\rho_0]$), nucleus-electron attraction ($V_{ne}[\rho_0]$) and electron-electron repulsion ($V_{ee}[\rho_0]$). The development of the equations is complicated and posteriorly it was need introduce the approximation of non-iterative electrons moving under an effective potential (V_{eff}), such potential is independent of $r(r)$. This approximation is an alternative approach to reach the convergence criteria established by variational theorem and, consequently the exchange-correlation energy (E_{xc}) is obtained by derivation of E_{xc} regarding to $\rho(r)$. Furthermore, the more implication for DFT is know the analytical forms for all functional, mainly for E_{xc} term.

For a practical implementation of DFT formalism is used the correspondence with HF methodology. Then, the construction of Khon-Sham (KS) molecular orbitals (OM) is carry out from Linear Combination Atomic Orbitals (LCAO) approximation using basis sets. Any mathematical function can be used as a basis set since it satisfy the eigenvalue and eigenvectors equations. Unambiguously, basis sets are used to describe electrons in atoms to build the LCAO and MOs; there are two ways to represent such electrons: (i) all electrons or (ii) pseudopotential. The first case, the basis set describe all electrons of the atom, while in the second topic the core electrons are replaced by an electric potential reducing the number of electrons represented. The most popular mathematical functions used as basis sets are Gaussian functions.

The “heart” of DFT is the E_{xc} functional because it is the unique functional not knowledge and extremely important for properties in molecular systems. Since DFT equations were discovered another demand was initiated, such investigation is directed to find an analytical expression for E_{xc} functional. From this point, countless functional were developed trying contribute to this problem. During this

scientific search, which is held until today, it was found local and non-local functional been that non-functional functional were best succeeded; however, the results still were lowly representatives. At last two decades, the best functional are called as hybrid functional, in these functional the exchange term is replaced by exact term from HF methodology and it is allowed because of adiabatic connection. In the literature is possible search many functional used in several tests to determine for which molecular structures each functional is more representative; such situation shows the big difficult to find only one unique functional to solve the central problem in DFT, the E_{xc} functional.

1.4 Time-Dependent Density Functional Theory

The DFT has became one of theories more applied for molecules and materials in the last decades because of the exact definition of the E_{xc} term for a big amount of electrons. Moreover, one of the main limitations of the HK theorems is the no-description of time, for example, the simulation of electronic excitation from external field. To apply the DFT in such systems is need rewrite analogous forms for the HK theorems satisfying KS equations. The Runge and Gross (RG) researchers developed equations dependents of time for KS formalism. In these equations, RG found the exact electronic density dependent of time, $\rho(r, t)$, with external potential, $V(r, t)$, and the characteristic constant for systems dependents of time, $C(r, t)$; then, the researchers developed a wave-function as $\Psi(r, t)$. Interesting is that the $\Psi(r, t)$ is determined as dependent of electronic density:

$$\Psi(r, t) = \Psi[\rho(t)]e^{-i\alpha(t)} \quad (1)$$

$$\left(\frac{d}{dt}\right)\alpha(t) = C(t) \quad (2)$$

Applying Eq. 1 as tentative wave-function in Schrödinger Equation dependent of time only represented by Eqs. 3 and 4.

$$i = \frac{\partial}{\partial t} \Psi(r, t) = H(r, t) \Psi(r, t) \quad (3)$$

and the Hamiltonian (H) operator is defined as

$$H = T(r) + V_{e-e}(r) + V_{e-n}(r) + V(t) \quad (4)$$

where, $T(r)$, $V_{e-e}(r)$ and $V_{e-n}(r)$ are kinetic, electron repulsion and electron-nucleus repulsion operators; respectively. The external potential operator ($V(t)$) is dependent of time, it is important because inside of this term can be described all external potentials applied to system.

After exhaustive mathematical proceedings to prove RG theorem is concluded the existence of the connection between the external potential dependent of time ($V(t)$) and electronic density functional in ground state. Then, the next stage for RG was understand how the variational principle can be used in Eq. 3. The initial condition for wave-function is write in Eq. 5.

$$\Psi(r, t_0) = \Psi_0(t) \quad (5)$$

From this condition is found a wave-function for a quantum mechanic integral of action on a stationary point, $A[\rho]$, connected to $\rho(r, t)$. The $A[r]$ integral is divided in two parts: (i) independent of time called as universal part, it describes the number of electrons independently of time; (ii) dependent of time represented by an external potential ($v(r, t)$) dependent of time, Eq. 6.

$$v(r, t) = V_{e-n}(r) + V(r, t) \quad (6)$$

Equation 6 is an initial condition to develop KS equations dependent of time. Now, to describe the electronic density dependent of time is need know each monoelectronic orbital, Eq. 7.

$$i \frac{\partial}{\partial t} \phi_i(r, t) = \left(T(r) + v(r, t) + \int d^3 r' \frac{\rho(r', t)}{|r - r'|} + \frac{\delta A_{XC}[\rho]}{\delta \rho(r, t)} \right) \phi(r, t) \quad (7)$$

A_{XC} is knowledge as exchange-correlation term dependent of time and it is not defined analytically.

The first approximation carried out for A_{XC} term is denominated as Adiabatic Local Density Approximation (ALDA). In this proceeding is used an exchange-correlation term similar to E_{XC} independently of time considering that electronic density is low modified from time. Therefore, functional developed independent of time can be applied in the time formalism and the Time-Dependent Density Functional Theory (TD-DFT) is created. An example, the TD-DFT can be applied from an external electric field with long wavelength with a frequency (ω); one of most applications used is determine the absorption spectra from electronic excitation.

1.5 *Semi-empirical Methods*

Among the methods based on Quantum Mechanics used in the study of organic compounds, the main ones are the two implementations of the Hartree-Fock (HF) method, called **ab initio** methods and the *semi-empirical* methods. The ab initio calculation makes use of the molecular Hamiltonian and only uses experimental data of the values of the physical constants, and all integrals must be calculated. Its main disadvantage is the high computing time spent optimizing

medium and large molecules. The number of integrals to solve becomes very large and the computational cost is very expensive. To circumvent this disadvantage, an implementation known as semi-empirical methods was developed, which uses a simpler Hamiltonian, where 2-electron integrals have been replaced by parameters whose values are adjusted, based on experimental data or ab initio calculations. They provide good results for geometry and torsion barrier, with acceptable computational cost for the study of long oligomers, but the energies of the molecule tend to be overestimated.

Since the first implementations in the 1960s, several models have been presented, including MINDO, MNDO, ZINDO/S, AM1, PM3, PM5, RM1, PM6, PM7. ZINDO/S was specifically developed to simulate the optical absorption spectrum and the other to simulate the geometry and reproduction the molecular heat of formation.

2 Theoretical Methodology

2.1 *PM6 and DFT Electronic Structure*

3,4-ethylenedioxythiophene (EDOT) structures from monomer to decamer (1-EDOT to 10-EDOT) were optimized using PM6 [18] semi-empirical methodology available in Molecular Package 2012 (MOPAC2012) Program [19], where the gradient minimization was specified as 0.01 kcal mol⁻¹ applying Pulay and Camp [20] routines for SCF calculation. From optimized geometries, single-point calculation using GAMESS [21–23] was applied using B3LYP/6-31 + G(d, p) level of theory, with geometry gradient convergence tolerance of 1×10^{-6} Hartree, and SCF density convergence criteria set as 1×10^{-6} applying Pulay's [24] routine on SCF cycles. From single point calculations, orbital and gap energies and orbital densities were obtained. From 10-EDOT oligomers, the calculations showed a computational cost very high for molecular geometries.

2.2 *TD-DFT Single Excitation Calculations*

TD-DFT [25] was applied from 1-EDOT to 6-EDOT models to investigate single electronic excitations in gas phase with B3LYP/6-31 + G level for first 30 excited states for each EDOT molecular structure producing ultraviolet-visible (UV-vis) spectra for all molecular geometries of interest. The discussions are centered on comparison between theoretical and experimental UV-vis spectra results, the contribution of an orbital in particular for the excited state and how the oligomer size affect the UV-vis spectra. The normalized intensity (in a.u.) for theoretical UV-vis spectra is related to 170 nm peak as higher intensity peak.

3 Results and Discussion

3.1 Geometry Optimization

Optimized dihedral angles between monomers from 1-EDOT to 10-EDOT are shown in Table 1, they present good agreement for a planar polymeric chain. Other theoretical works showed similar results calculating a dihedral angle close to 180° among monomeric units [26, 27]. The choice for PM6 semi-empirical methodology was based on previously results [28, 29] comparing semi-empirical methodologies, where the best choice was PM6 producing polymeric planar configuration as expected for conductive polymers. These results show that is possible to simulate good geometries for conductive polymers applying semi-empirical methodology with much less computational cost comparing to Hartree-Fock (HF) or DFT methodologies, once the main objective of the semi-empirical calculations is produce a good start molecular geometry to investigate electronic property through theoretical methodologies.

3.2 DFT Single Point Energy Calculation

From good structural agreement produced by PM6 methodology for PEDOT oligomers geometry, a new electronic structure calculation was performed through DFT theory. The choice to produce molecular geometries by semi-empirical calculations, analyzing electronic structure through DFT theory was performed considering low computational cost to produce optimized geometries, and better electronic description, respectively [8, 25]. The more acceptable electronic mechanism in solid state theory is based on excitation of the electrons from Valence Band (VB) to Conduction Band (CB); an approximation for such mechanism is consider HOMO and LUMO orbitals as top of VB and bottom of CB.

Table 1 Mean dihedral angle (in degrees) between monomers from 1-EDOT to 10-EDOT from PM6 semi-empirical methodology

Structure	Mean dihedral angle ($^\circ$)
1-EDOT	–
2-EDOT	179.89
3-EDOT	179.61
4-EDOT	179.35
5-EDOT	179.19
6-EDOT	179.98
7-EDOT	179.06
8-EDOT	178.98
9-EDOT	179.07
10-EDOT	179.13

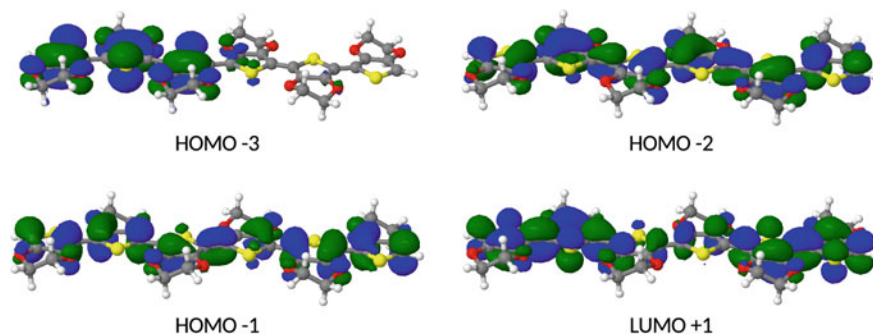


Fig. 1 Electronic densities obtained from 6-EDOT molecule for HOMO -3, HOMO -2, HOMO -1 and LUMO +1 molecular orbitals

This approximation is very useful and it reproduces with good agreement electronic results in conductive polymers, mainly, for big chain oligomers [30]. For 1-EDOT to 10-EDOT molecular structures were calculated HOMO and LUMO orbitals (Fig. 3), which are located over all oligomeric chain. It is possible to propose that HOMO-LUMO charge transport occurs between sulfur atoms and π conjugated bonds over the neighbor monomers. Once that these electrons are excited to LUMO orbital, they are available to perform the charge transfer through oligomeric chain [8, 31]. By the same theory, it is possible to confirm charge transport when LUMO orbital is continuously distributed all over molecule, providing a charge way on the material and, consequently, the conduction property toward oligomer [8]. In fact, good results for PEDOT conductivity [32] are explained by π conjugation length.

In general, from 2-EDOT the HOMO-LUMO representations show perpendicular direction between these orbitals, indicating that oligomer increasing causes increase of the number of π -conjugated bonds. From increase of monomeric units, π -conjugate bonds in HOMO orbitals are located in the polymeric central region of thiophene rings; however, these molecular densities are not connected indicating an insulate property. On the other hand, the π -conjugated bonds in LUMO orbitals are frontally oriented indicating a conductive property (Fig. 1).

3.3 Potential Energy Surface (PES) from DFT

The results for Potential Energy Surface (PES—Fig. 2) were calculated from DFT/B3LYP calculations and they show that growth oligomeric chain cause polymeric bulk formation inside chain producing a charge way at center of the oligomeric chain. This effect is only visualized from six monomeric units or 6-EDOT model, suggesting that from this structure is possible to estimate electronic properties with better precision. At same context, PES results provided information about why PEDOT produces better results for electronic conduction in large oligomeric size

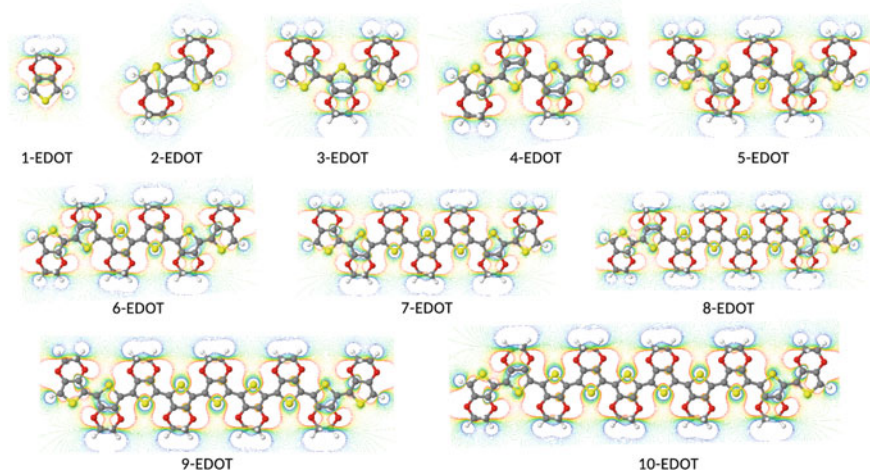


Fig. 2 Potential energy surface calculated from 1-EDOT to 10-EDOT models using DFT/B3LYP theory

than small oligomers with few monomeric units; for instance, from 1-EDOT to 5-EDOT the π -conjugate bonds are few and they do not feature a charge bulk distributed in all PEDOT molecular structure. However, between 6-EDOT to 8-EDOT structures there is the formation of a charge bulk always located between two monomers of chain border, such charge distribution indicate that monomers of chain border act as charge transfer barrier or chemical potential. This effect is wanted because the more chemical reactivity at long π -conjugate organic chain is localized at chain borders [33]. Then, conductive mechanism in PEDOT has two factors: (1) electronic excitation to promote the electronic mobility inside polymer and; (2) chemical potential is localized as charge transfer barrier between oligomeric units.

Another point, for PEDOT macrostructures is not observed intramolecular interaction becoming hard to perform charge transfer through π - π stacking interaction between neighbor oligomeric chains [8].

3.4 Density of States Analysis (DOS)

In semiconductors oxide, the analysis of Density of States (DOS) provide information about contributions of specific atoms for conduction (CB) and valence band (VB), especially on investigation of contributions on band gap energy formation. Similarly, for organic semiconductors, DOS provide information about how oligomeric size influence on CB and VB formations, being possible to understand the energy levels distribution (such as bulk formation and band-gap energy) from

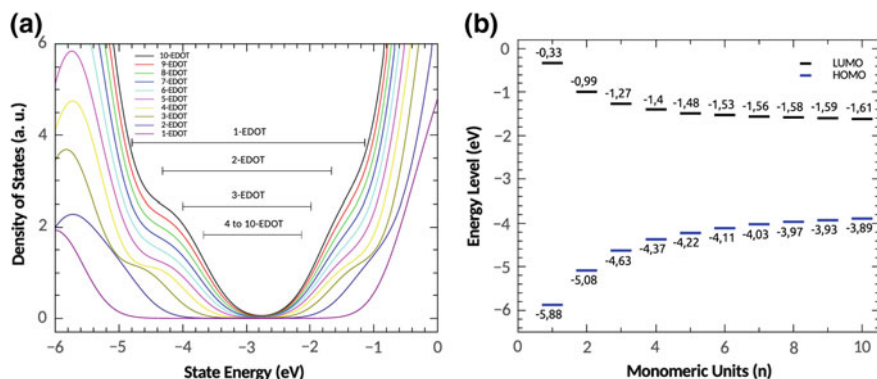


Fig. 3 **a** DOS expanded band-gap energy level and **b** HOMO-LUMO energy levels for 1-EDOT to 10-EDOT

increase monomeric units on the polymeric chain. DOS analysis performed from 1-EDOT to 10-EDOT oligomers showed low change on the shape of the VB and CB; however, how to explain the decrease of band-gap energy with increasing oligomeric size? Similarly, how to visualize bulk formation from electronic level on a polymeric system?

In general, there is no change of the band shape from increase monomeric units. Such result is expected because many energy levels are located at energies very close forming bands in agreement with Solid State Theory. However, the range localized between -5 and 0 eV is exactly an electronic region more specific for band-gap energy levels. Therefore, an analysis in details inside region (Fig. 3) presented an increase of energy levels amount in accordance with increase of monomeric units, indicating a bulk formation and decrease of band-gap. For small EDOT oligomers (1-EDOT to 5-EDOT) is possible to visualize the energy difference between HOMO and LUMO levels, from 5.56 eV to 2.74 eV; nevertheless, from 6-EDOT (where is produced polymeric bulk formation) to 10-EDOT is not possible to visualize a decrease of same order between HOMO and LUMO levels, becoming smaller the difference between these energy levels of 2.58 eV and 2.29 eV for 6-EDOT and 10-EDOT molecules; respectively. Furthermore, the contribution for reducing band-gap energy occurred as an increase of 1.98 eV on HOMO energy level (from -5.88 eV in 1-EDOT to -3.89 eV in 10-EDOT) and a decrease of LUMO energy level in order to 1.27 eV (from 0.33 eV in 1-EDOT to 1.60 eV in 10-EDOT).

DOS analysis showed an influence very commonly discussed in disordered semiconductors oxides, i.e. the introduction of new energy levels inside a band-gap initial; such effect is based on defects or impurities localize in crystalline structure [34]. Nevertheless, similar effect has been observed in the PEDOT polymeric structure; even, this polymer having a molecular organization different from disordered crystalline structure, the increase of monomer units cause introduction of energy levels from monomer band-gap. This change in the molecular structure of

polymer modify progressively its electronic and conductive properties; thus, became it progressively more conductive. Furthermore, these energy levels introduced inside monomer band-gap create the polymeric bulk and the π -conjugate bonds became each more available electrons for conductive mechanism inside polymeric structure. The monomers localized at polymer border are limitations for polymeric bulk acting as potential well. The quantum origin of this electronic effect is based on electron confinement or potential well [35]; the polymer chain act as space of electronic confinement modifying the energy levels and, consequently, the band-gap of polymer.

3.5 *TD-DFT Single Excitation*

TD-DFT calculations have gained attention of computational chemists to provide information about specific excitation of frontiers orbitals. This approach has produced good understanding for electron-hole transfers from simulations based on Theory Orbital Molecular (TOM); especially in organic semiconductors is possible to localize charge transport phenomena on molecular structure through calculated electronic density. Thus, single excitation TD-DFT simulations have represented in good agreement band-gap energy (E_g), Potential Electrostatic Surface (PES) and Density of States (DOS) results of the molecule [25]. However, for molecules more than 6-EDOT were observed a high computational cost, and it was not possible to perform these calculations. In particular, for 1-EDOT was observed that the lowest absorption energy connected to HOMO-LUMO absorption band shows different behavior compared with lowest energy absorption between 2-EDOT to 6-EDOT oligomers; such effect is due to absence of π -conjugate bonds located between two monomeric units. Single excitation in this discussion is a good agreement to foresee electronic spectra because it shows boundary effects very commonly found in computational chemistry. Band-Gap energy for PEDOT is experimentally estimate in 1.6 eV; such result is obtained through a broad band of highest absorption wavelength localized at UV-vis [30]. Our theoretical results (Fig. 4) suggest that this broad band is characterized by mixture of different PEDOT oligomer sizes. Each oligomer size, 1-EDOT to 6-EDOT, shows a single excitation very well featured; then, from a mixture different oligomers size is expected that electronic spectra is a broad band.

From oscillator strength analysis for 1-EDOT to 6-EDOT, the peak in 239 nm has higher value related to individual peaks for 1-EDOT (Table 2). Lorentzian convolution was applied to investigate excitation energy data. From 2-EDOT to 6-EDOT, oscillator strength of the lowest energy excitation has higher values if compared with all other calculated peak. With increase of monomeric units, energy difference between lowest energy peak and higher energy peak become more evident showing other important transitions from increase of the oligomeric chain. Thus, it is possible to consider HOMO-LUMO excitation with 99% (Table 2),

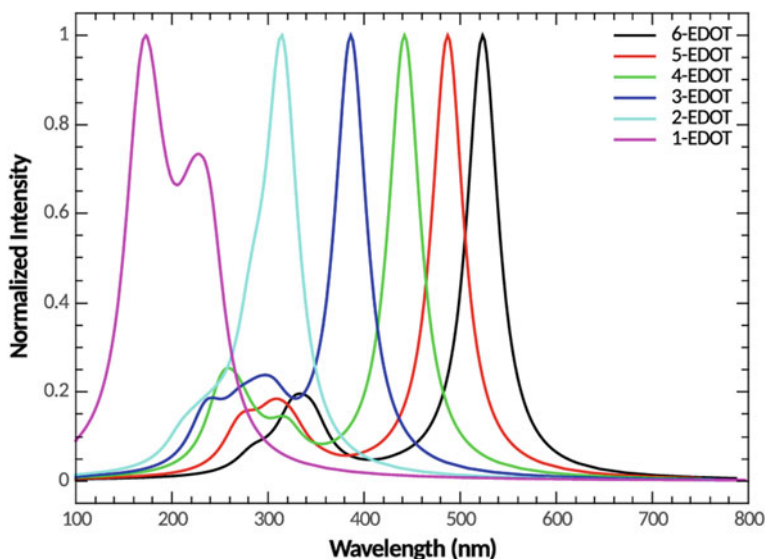


Fig. 4 TD-DFT results for single electronic excitation spectra from 1-EDOT to 6-EDOT molecules. Red shift is function of oligomer size

Table 2 Results for majority electronic transitions related to singlet excitation on different EDOT oligomers from TD-DFT calculations

Oligomers	Exc	f_{osc}	Main conf.	Contrib. (%)
1-EDOT	5.18	0.15	H \rightarrow L	92
	5.57	0.09	H - 1 \rightarrow L	93
2-EDOT	3.94	0.52	H \rightarrow L	98
	4.37	0.05	H - 2 \rightarrow L	51
			H - 1 \rightarrow L	43
	4.37	0.07	H - 1 \rightarrow L	51
		H - 2 \rightarrow L	43	
3-EDOT	3.21	0.88	H \rightarrow L	99
	4.06	0.07	H - 3 \rightarrow L	80
	5.26	0.05	H - 3 \rightarrow L + 1	63
4-EDOT	2.80	1.30	H \rightarrow L	99
	3.85	0.05	H - 2 \rightarrow L	44
	4.61	0.06	H - 1 \rightarrow L + 1	40
5-EDOT	2.55	1.70	H \rightarrow L	99
	3.78	0.07	H - 3 \rightarrow L	55
	3.98	0.08	H - 1 \rightarrow L + 1	50
	4.11	0.08	H - 1 \rightarrow L + 1	30
6-EDOT	2.37	2.08	H \rightarrow L	99
	3.58	0.19	H - 1 \rightarrow L + 1	34

Excitation Energy (Exc in eV), Oscillator Strength (f_{osc} in a. u.), HOMO = H and LUMO = L

the most important configuration for an electronic excitation state, mainly, because it is the majority among lowest energy electronic excitation.

Other contributions from TD-DFT calculations are results about higher energy excitation related to other important frontier orbitals, such as, HOMO -2 , HOMO -1 and LUMO $+1$ orbitals; which also contribute for excited states. For 1-EDOT molecule, the electronic excitation between HOMO -1 to LUMO orbitals represents 93% of the total contribution for excitation in 5.57 eV; whereas, for 2-EDOT molecule, the same electronic excitation has 4.37 eV. However, two oscillator strengths were produced with different contributions, 51% and 43% from HOMO -2 and HOMO -1 orbitals to LUMO orbital, respectively. Oscillator strengths associated to such electronic transitions were calculated as 0.05 a. u. and 0.07 a. u.; respectively. Nevertheless, these oscillator strengths have opposite signals suggesting that electronic excitation from both orbitals is possible. In the 4-EDOT oligomer, the excitation in 3.85 eV is connected to an electronic transition from HOMO -2 to LUMO representing 44% of the excitation total contribution; whereas, in 4.61 eV such total contribution is 40% of the excitation energy corresponding to HOMO -1 to LUMO $+1$ excitation. For 5-EDOT molecule, there is a HOMO -3 to LUMO excitation in 3.78 eV, correspondent to 55% of excitation energy and a HOMO -1 to LUMO $+1$ excitation is associated to two important excitation energies calculated in 3.98 and 4.11 eV. At last, 6-EDOT molecule shows an electronic transition between HOMO -1 and LUMO $+1$ orbitals with 34% of contribution for excitation energy in 3.58 eV. All these results suggest that HOMO and LUMO orbitals are the most important frontier orbitals because of the lowest energy excitation. However, HOMO -3 , HOMO -2 , HOMO -1 and LUMO $+1$ orbitals are also important to indicate charge transport alternatives. In fact, experimental results [36] present a second electronic excitation state more energetic than HOMO-LUMO excitation; nevertheless, it is not confirmed which molecular excitation state can produce such electronic absorption. Our TD-DFT single excitation calculations identify this electronic excitation state as several electronic transitions among HOMO -3 , HOMO -2 , HOMO -1 and LUMO $+1$ molecular orbitals; however, these electronic transitions are dependents of the oligomer size. Electronic densities obtained from 6-EDOT molecule (Fig. 1) are an example of how these molecular orbitals are important. Therefore, the amount and localization of energy levels are fundamentals to describe these electronic transitions of high energy. Such result is consequence of the introduction of energy levels inside band-gap in according to Theory of Bands for solid state [31].

3.6 *Band-Gap Energy Calculation*

Theoretical calculations through DFT methodology show higher values than experimental results for band-gap energy, especially for organic semiconductors [8]. For PEDOT, experimental results show an E_g value equal to 1.6 eV [30]; however, such result is obtained from molecular macrostructures formed by long

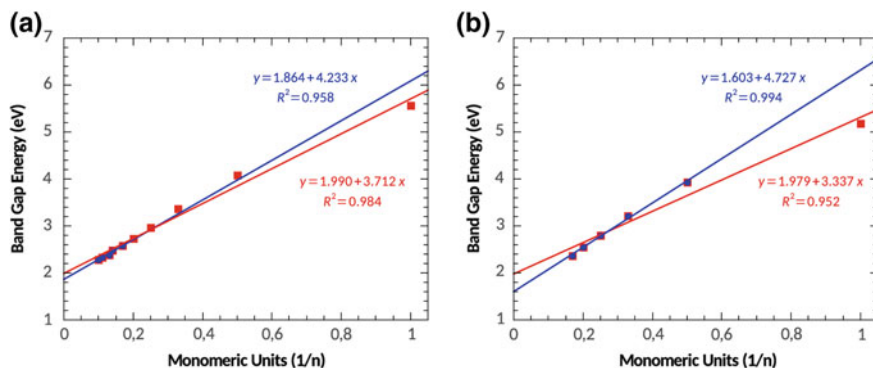


Fig. 5 **a** Analysis based on linear fitting for theoretical E_g from 1-EDOT to 10-EDOT (red line) and 6-EDOT to 10-EDOT (blue line) by DFT methodology. **b** Analysis based on linear fitting for theoretical E_g from 1-EDOT to 6-EDOT (red line) and 2-EDOT to 6-EDOT (blue line) by TD-DFT methodology

π -conjugate chain structures. Furthermore, quantum calculations are performed with small monomeric units or small oligomers because high computational cost to large systems through DFT methodology [8]. In fact, such DFT results underestimate E_g in relation to experimental results; nevertheless, E_g calculated at DFT/B3LYP level of theory has good agreement with experimental result [33]. Results obtained by DFT and TD-DFT levels of theory for 1-EDOT to 10-EDOT molecules and 1-EDOT to 6-EDOT molecules, respectively; are shown in Fig. 5, where monomeric units are represented as $1/n$ and n is the number of monomeric units. In general, the E_g energy reduces near to a constant value with tendency to experimental result.

From these results, we performed data extrapolations through linear fitting to estimate theoretical E_g considering an infinite polymeric chain, more specifically, when $1/n \rightarrow 0$. The difference between such extrapolations is based on which molecular structures and level of theory would be good candidates to calculate E_g . Then, for DFT simulations we use a linear fitting from 1-EDOT to 10-EDOT molecules and other linear fitting from 6-EDOT to 10-EDOT molecules (Fig. 5a), the results obtained were 1.99 eV and 1.84 eV; respectively. Therefore, the result more near of experimental result (1.6 eV) was linear fitting from 6-EDOT to 10-EDOT molecules. This result is important because indicates that energy levels of the frontier orbitals were better describes by models with charge bulk and π -conjugate bonds among monomeric units showing that exist a strong electronic influence from monomeric units localized at border of PEDOT.

TD-DFT results used for E_g data extrapolation (Fig. 5b) were obtained by maximum wavelengths estimated from 30 excited electronic states; such wavelengths are attribute to HOMO-LUMO electronic transition and they were changed for electromagnetic energy dimensioned as eV. Linear fitting showed in Fig. 5b were applied to these data showing that E_g values are different in relation to

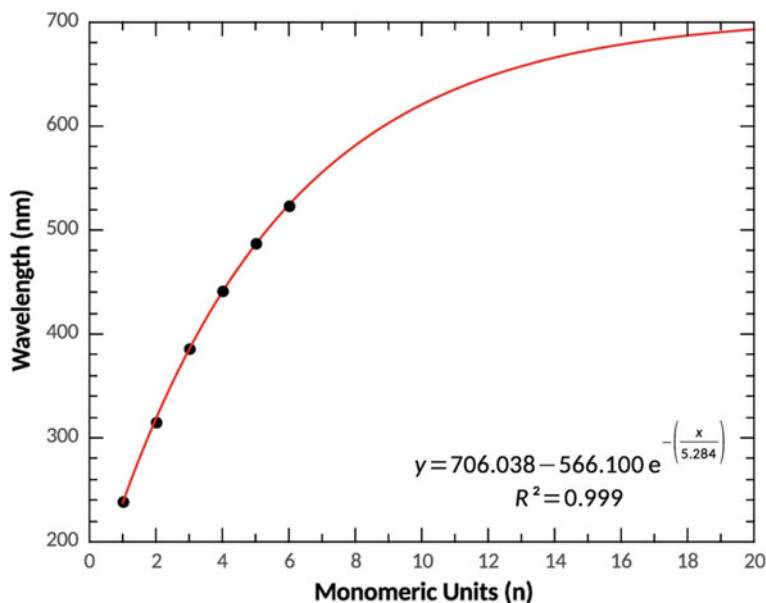


Fig. 6 Maximum wavelength absorption calculated for EDOT oligomers by TD-DFT calculation

1-EDOT molecule. Such difference is observed as E_g value of 1.97 eV was obtained from 1-EDOT to 6-EDOT models; whereas, another E_g result was estimated as 1.60 eV from 2-EDOT to 6-EDOT molecules. The main difference between DFT and TD-DFT levels of theory is centered in a wave-function more complete for TD-DFT because of single excitation simulated by 30 electronic states. Therefore, charge bulk and π -conjugate bonds among monomeric units were better describes by TD-DFT causing an exact extrapolation for theoretical E_g of PEDOT. Obviously, our theoretical investigation is limited only to PEDOT molecular structure, other conductive polymers need be simulated to evaluate such data extrapolation.

As discussed for HOMO and LUMO orbitals, the dependence of properties and oligomeric size also was verified for TD-DFT calculations, by results shown in **TD-DFT Sigle Excitation** section, where red shift is observed from 1-EDOT (239 nm) to 6-EDOT (523 nm), indicating that increase π conjugation bonds reduces the lowest energy absorption, favoring the generation of electron-hole pair in EDOT long chain oligomers. Once observed that data extrapolation by linear fitting in TD-DFT calculations provided good E_g values for EDOT models, it is possible to estimate the maximum absorption for an infinite PEDOT polymeric chain through plotting maximum absorption in function of monomeric units.

However, this data extrapolation was carried out from exponential fitting because in several studies is possible to find an exponential decrease of wavelength absorption as function of time [37, 38] or chemical composition [39, 40]. Then,

to extrapolate the result for theoretical maximum wavelength absorption was applied the $\lim_{x \rightarrow \infty} f(x)$, where $f(x)$ is equation obtained from exponential fitting. Such result is shown in Fig. 6 indicating a stabilization of maximum absorption in 706 nm, which agrees with experimental results [30] for PEDOT of a maximum value around 800 nm.

Experimental band shape suggest a mixture of different EDOT monomeric units, which is confirmed by our theoretical results, once red shift is observed for this polymer, discussed in **TD-DFT Single Excitation** section.

4 Conclusions

From optimized geometries with low computational cost by PM6 semi empirical methodology, electronic structure was better described from DFT calculations, showing a bulk formation from 6 monomeric units extending for longer polymeric chains. The same calculations provided information about frontier orbital location, showing polymeric central region the most important for charge transport property, where LUMO orbital extended for all over molecule, being possible to produce a charge distribution when anionic or cationic charges are injected. TD-DFT calculations clarify how band-gap energy decrease from increase monomeric units, showing π conjugation dependence between electronic and geometric structures. The relation between band-gap energy and HOMO-LUMO excitation energy was compared with experimental results, showing good agreement between such results. Projected DOS provided better understanding for changes in band-gap and UV-Vis spectra through insertion of energy levels inside band-gap monomer unit and these results showed a quantum confinement effect. Linear fitting used for data extrapolation from TD-DFT wavelength absorptions is a great result to calculate with great agreement the PEDOT band-gap.

Acknowledgements All authors thanks to Coordenação de Aperfeiçoamento de Pessoal de Nível Superior (CAPES), Fundação Araucária and State University of Ponta Grossa.

References

1. IEA and OECD: Solar Energy Perspectives (2011)
2. Kleider, J.P., Alvarez, J., Brézard-Oudot, A., Gueunier-Farret, M.E., Maslova, O.: Sol. Energy Mater. Sol. Cells **135**, 8–16 (2015)
3. Hedström, S., Persson, P.: J. Phys. Chem. C **116**, 26700–26706 (2012)
4. Constantinou, I., Lai, T.H., Zhao, D., Klump, E.D., Deininger, J.J., Lo, C.K., Reynolds, J.R.: ACS Appl. Mater. Interfaces. **7**, 4826–4832 (2015)
5. Lanzi, M., Salatelli, E., Benelli, T., Caretti, D., Giorgini, L., Di-Nicola, F.P.: J. Appl. Polym. Sci. **132**, n/a (2015)

6. Hermerschmidt, F., Kalogirou, A.S., Min, J., Zissimou, G.A., Tuladhar, S.M., Ameri, T., Faber, H., Itskos, G., Choulis, S.A., Anthopoulos, T.D., Bradley, D.D.C., Nelson, J., Brabec, C.J., Koutentis, P.A.: *J. Mater. Chem. C* **3**, 2358–2365 (2015)
7. Ràissi, M., Vignau, L., Cloutet, E., Ratier, B.: *Org. Electron.* **21**, 86–91 (2015)
8. Coropceanu, V., Cornil, J., da Silva Filho, D.A., Olivier, Y., Silbey, R., Bredas, J.L.: *Chem. Rev.* **107**, 926–952 (2007)
9. Facchetti, A.: *Chem. Mater.* **23**, 733–758 (2011)
10. Tu, G., Bilge, A., Adamczyk, S., Forster, M., Heiderhoff, R., Balk, L.J., Mühlbacher, D., Morana, M., Koppe, M., Scharber, M.C., Choulis, S.A., Brabec, C.J., Scherf, U.: *Macromol. Rapid Commun.* **28**, 1781–1785 (2007)
11. Dang, M.T., Hirsch, L., Wantz, G., Wuest, J.D.: *Chem. Rev.* **113**, 3734–3765 (2013)
12. Nikoofard, H., Gholami, M.: *C. R. Chim.* **17**, 1034–1040 (2014)
13. Wen, L., Jeong, D.C., Javid, A., Kim, S., Nam, J.D., Song, C., Han, J.G.: *Thin Solid Films* **587**, 66–70 (2015)
14. Das, S., Chatterjee, D.P., Ghosh, R., Nandi, A.K.: *RSC Adv.* **5**, 20160–20177 (2015)
15. Liu, J., Pathak, S., Stergiopoulos, T., Leijtens, T., Wojciechowski, K., Schumann, S., Kausch-Busies, N., Snaith, H.J.: *J. Phys. Chem. Lett.* **6**, 1666–1673 (2015)
16. Park, B., Pazoki, M., Aitola, K., Jeong, S., Johansson, E.M.J., Hagfeldt, A., Boschloo, G.: *ACS Appl. Mater. Interfaces.* **6**, 2074–2079 (2014)
17. Apperloo, J.J., Groenendaal, L.B., Verheyen, H., Jayakannan, M., Janssen, R.A.J., Dkhissi, A., Beljonne, D., Lazzaroni, R., Brédas, J.L.: *Chem. Eur. J.* **8**, 2384–2396 (2002)
18. Stewart, J.J.P.: *J. Mol. Model.* **13**, 1173–1213 (2007)
19. Stewart, J.: MOPAC2012, Stewart Computational Chemistry. Colorado Springs, CO, USA. <http://OpenMOPAC.net>
20. Camp, R.N., King, H.F.: *J. Chem. Phys.* **75**, 268–274 (1981)
21. Gordon, M.S., Schmidt, M.W.: In: In: Sloot, P.M.A., Abramson, D., Bogdanov, A.V., Gorbachev, Y.E., Dongarra, J.J., Zomaya, A.Y. (eds.) *Computational Science—ICCS 2003*, pp. 75–83. Springer, Berlin, Heidelberg (2003)
22. Gordon, M.S., Schmidt, M.W.: In: Dykstra, C., Frenking, G., Kim, K., Scuseria, G. (eds.) *Theory and Applications of Computational Chemistry*, pp. 1167–1189. Elsevier, Amsterdam (2005)
23. Schmidt, M.W., Baldrige, K.K., Boatz, J.A., Elbert, S.T., Gordon, M.S., Jensen, J.H., Koseki, S., Matsunaga, N., Nguyen, K.A., Su, S., Windus, T.L., Dupuis, M., Montgomery, J. A.: *J. Comput. Chem.* **14**, 1347–1363 (1993)
24. Pulay, P.: *J. Comput. Chem.* **3**, 556–560 (1982)
25. Elliott, P., Furche, F., Burke, K.: In: Lipkowitz, K.B., Cundari, T.R. (eds.) *Reviews in Computational Chemistry*, pp. 91–165. Wiley (2008)
26. Durães, J.A., da Silva Filho, D.A., Ceschin, A.M., Sales, M.J.A., Martins, J.B.L.: *J. Mol. Model.* **20**, 1–6 (2014)
27. Kaloni, T.P., Schreckenbach, G., Freund, M.S.: *J. Phys. Chem. C* **119**, 3979–3989 (2015)
28. Lee, K.H., Song, D.H., Park, B.J., Chin, I.J., Choi, H.J.: *Macromol. Theor. Simul.* **18**, 287–298 (2009)
29. Olasunkanmi, L.O., Ige, J., Ogunlusi, G.O., Olasunkanmi, L.O., Ige, J., Ogunlusi, G.O.: *J. Chem. J. Chem.* e640649 (2012–2013)
30. de Silva, K.M.N., Hwang, E., Serem, W.K., Fronczek, F.R., Garno, J.C., Nesterov, E.E.: *ACS Appl. Mater. Interfaces.* **4**, 5430–5441 (2012)
31. Harrison, W.A.: *Elementary electronic Structure*. World Scientific, Stanford University (2005)
32. Groenendaal, L., Jonas, F., Freitag, D., Pielartzik, H., Reynolds, J.R.: *Adv. Mater.* **12**, 481–494 (2000)
33. Yang, Y.L., Lee, Y.H., Lee, Y.P., Chiang, C.J., Shen, C., Wu, C.C., Ohta, Y., Yokozawa, T., Dai, C.A.: *Polym. Int.* **63**, 2068–2075 (2014)
34. Silbey, R.: In: Zyss, D.S.C. (eds.) *Nonlinear Optical Properties of Organic Molecules and Crystals*, pp. 3–20. Academic Press (1978)

35. Dkhissi, A., Beljonne, D., Lazzaroni, R., Louwet, F., Groenendaal, B.: *Theor. Chem. Acc.* **119**, 305–312 (2007)
36. Wasserberg, D., Meskers, S.C.J., Janssen, R.A.J., Mena-Osteritz, E., Bäuerle, P.: *J. Am. Chem. Soc.* **128**, 17007–17017 (2006)
37. López-Ruiz, N., Hernández-Bélanger, D., Carvajal, M.A., Capitán-Vallvey, L.F., Palma, A.J., Martínez-Olmos, A.: *Sens. Actuators B Chem.* **216**, 595–602 (2015)
38. Palmeira, T., Berberan-Santos, M.N.: *Chem. Phys.* **445**, 14–20 (2014)
39. Tsipis, A.C., Stalikas, A.V.: *J. Comput. Chem.* **36**, 1334–1347 (2015)
40. Yin, S.H., Liu, Y., Zhang, W., Guo, M.X., Song, P.: *J. Comput. Chem.* **31**, 2056–2062 (2010)

Magnetic Properties of Conducting Polymers



A. A. Correa, E. C. Pereira and A. J. A. de Oliveira

Abstract Modern society is dependent on different devices in which the fundamental behavior is deeply attached to the magnetic and electrical properties of the components used to build them. Until now, the development of new materials guarantees the improvement of the efficiency of these devices. However, new functionalized materials are necessary to the development of the next generation considering not only efficiency, but low environmental impact, durability, and low toxicity. One important concern is material weight and mild synthesis methods. In this sense, since the discovery of conducting polymers, in 1977, there are many and important applications of these materials. These compounds have as special properties the possibility to have their conductivity modulated between 10^{-6} up to 10^3 S cm^{-1} . Besides, most of them are redox materials, meaning they can be reversibly changed between the reduced (dielectric) and oxidized states (semiconductor). On the other hand, fundamental aspects of their behavior are still a challenge to researchers of many areas due to the very drastic changes associated with the redox behavior, such as conductivity, spectral absorbance, ionic intercalation, volume change, and more recently, magnetic properties. Specifically, this chapter presents a review about those works which have investigated the magnetic properties, its correlation with synthesis methods and redox behavior as well as the morphological effect. The concern of this chapter is to analyze the different magnetic phases present in conducting polymers, in particularly, antiferromagnetic, ferromagnetic phases observed at room temperature in some of these materials, which open many possibilities for different applications.

A. A. Correa

Materials Engineering Department, Federal University of São Carlos,
São Carlos, São Paulo, Brazil

E. C. Pereira

Chemistry Department, Federal University of São Carlos,
São Carlos, São Paulo, Brazil

A. J. A. de Oliveira (✉)

Physics Department, Federal University of São Carlos, São Carlos,
São Paulo, Brazil

e-mail: adilson@df.ufscar.br

© Springer Nature Switzerland AG 2020

F. A. La Porta and C. A. Taft (eds.), *Emerging Research in Science and Engineering Based on Advanced Experimental and Computational Strategies*, Engineering Materials, https://doi.org/10.1007/978-3-030-31403-3_19

Keywords Conducting polymer • Magnetic properties • Ferromagnetism • Diamagnetism • Paramagnetism

1 Introduction

Magnetic materials have always had different types of applications. From the invention of the compass, thousands of years ago, to the modern magnetic memories and spintronic devices, a large number of possibilities have emerged for the creation of new devices. In addition, the complexity involved in the different magnetic phenomena has also led to the advancement of new physical models to understanding the complexity of magnetic phases that matter presents.

On the other hand, since the discovery of conductive polymers [1, 2] in the 1970s, this type of material has attracted much interest due to its great technological potential and many complex physical phenomena. Due to the particular electronic behavior of these materials, described in analogy to inorganic semiconductor band theory [3, 4], many applications were possible. In conducting polymers, the charge transport is explained by the introduction of defect level inside the band gap [3, 4], which could be polarons and or bipolarons depending of the defect density. Polarons, which are spin $1/2$, can be formed by oxidation of the polymer chain by the removal of electrons, leading to the formation of a cation radical, which is balanced by the intercalation of an anion from the solution. This defect is also associated to a lattice distortion. The removal of a second electron of the whole system leads to the formation of a new polaron or, depending on how high is the defect density, to the formation of doubled charged bipolaron charge carrier, which is also associated with strong local lattice distortion. Thus, bipolarons are two electrons (zero spin and charge $2e$) coupled by a lattice vibration, and hence it is more stable than two polarons.

The conduction of electrons in these polymers occurs via the movement of these charge carriers along the polymer chain, rearranging single and double bonds in the conjugate system. The stability of the charge carriers is also associated with the presence of dopant ions to balance the charge and guarantee the electroneutrality. Then, the dopant species allows the stability of the energy levels to be introduced into the band gap, altering the polymer geometry network. As described above, in conducting polymers, the polaronic defect is created by the extra charge introduced in the doping (intercalation) process which leads to a deformation of the chain, consisting of a length change of the bond. In other words, breaking a double bond in the doping process introduces a positive charged defect and a dangling bond, which couple to produce the positive polaron. Fisher et al. [5] discussed the bipolaron stability with the introduction of the electron–electron interaction and concluded that the bipolaron stability has a lower energy than two polarons, although they also note that their calculations do not take into account doping ions. If, from a theoretical point of view, bipolarons seem to be a more stable defect than a polaron, many of the papers observed signatures of polaronic behavior from optical measurements [6, 7] and a Curie component of the magnetic susceptibility

due to localized magnetic moments observed in a variety of conducting polymers with different degrees of order and even at high doping levels [8, 9].

A possibility of ferromagnetic behavior in conductive polymers has been theoretically studied [3, 4, 10] and evidence of ferromagnetic interaction has been observed by different authors [11, 12]. An important concern in many papers is to guarantee the intrinsic character of the ferromagnetism. This behavior was investigated from different techniques as electron paramagnetic resonance (EPR) and magnetization measurements performed using a superconductor quantum interference device (SQUID) magnetometer. The high sensitivities of these techniques made it possible to check the intrinsic character of this ferromagnetic behavior.

2 Intrinsic Magnetic Behavior in Conducting Polymers

Experimentally, the magnetic properties of conductive polymers can be investigated mainly using two different techniques: EPR and magnetization measurements. EPR is high sensible and it is possible to investigate low energy modifications in the magnetic properties of the prepared polymers related to unpaired electrons. On the other hand, magnetization measurements observe the global response of magnetic moments in the samples. Thus, in this perspective, these two techniques provide complementary information.

In this sense, there are works in the literature where in situ EPR measurements were performed, that is, investigating the redox processes of polymer films in solution [13–15] or even the polymerization process [16]. Sun et al. [17], investigating thiophene derivatives, showed that the magnetic moments in these materials arise from the charge carriers presence in the polymer chains. Besides, the authors proposed that the charge transport occurs along C–C–C π bonds instead of C–S–C.

Nalwa et al. [8] described Curie-Weiss to Pauli paramagnetic behavior transition at 75 K in polypyrrole pellets and at 130 K in polythiophene pellets, both oxidized and doped with PF_6^- . This change of magnetic behavior was attributed to both electronic and morphological changes in the polymers. The spin susceptibility clearly changes from Curie to Pauli-like behavior in polypyrrole as the temperature is increases, while polythiophene only exhibits Curie behavior. From a different point of view, SQUID magnetization measurements also indicated the possibility of the coexistence of unpaired spins. Then, using this last technique, it points to the existence of paramagnetic species and paired spins in the conducting state. The temperature-dependent susceptibility demonstrates a dominant spin-coupling type of phenomenon, particularly in polypyrrole. The characteristic difference in the magnetic susceptibility of oxidized samples of polypyrrole and polythiophene may arise due to different physicochemical properties, such as, degree of conjugation, concentration of counteranions, degree of cross linking, and crystalline and morphological structures. The EPR studies show that polyheterocyclics are paramagnetic in their conducting state, and, to some extent, the intrinsic properties are influenced by the nature of the heteroatom in the conjugated polymer backbone.

Onoda et al. [10] showed that there is an increase in susceptibility with increasing the doping degree, followed by a decrease in this parameter, for doping level higher than 2.2 mol%. The authors explained their results proposing the conversion of polarons to bipolarons as the polymer oxidation is increased.

Pereira et al. [18] and Nascimento et al. [19] using EPR measurements, proposed a Peierls transition at 220 K for ClO_4^- poly-3-methylthiophene doped samples. The magnetic data were correlated also with differential scanning calorimetry data which indicates a phase transition at the same temperature. The EPR spectra for pressed pellets of ClO_4^- doped poly-3-methylthiophene measured after quenching the sample from ambient to 110 K, and rapidly heated to 223 K. The spectra were followed as function of the time and it is observed that the width of the EPR line broads with time. The authors proposed that the spectrum was composed of two superimposed process, with different widths, whose amplitudes had a significant change as the time is increased. The EPR spectra were fitted assuming two Lorentzian absorption lines with different widths and amplitudes. Although the linewidths remained the same, the amplitudes changed with time. For the narrow line we had found $\text{DH}_{1/2} = 7.65$ G and for the broad line $\text{DH}_{1/2} = 23.85$ G. An important observation in this work is that no time relaxation was observed, at this temperature, when the sample was slowly cooled from room temperature.

Nascimento et al. [20] revised the magnetic behavior the samples of poly(3-methylthiophene) partially doped with ClO_4^- prepared at room temperature. The basic assumption was that the magnetic moments were spin 1/2 polarons that can interact antiferromagnetically and/or ferromagnetically. In the small crystalline regions of the polymer, which were identified with the polymer portion that remained ferromagnetic at room temperature, the interaction gives rise to $S = 0$ and 1 bipolarons and the $S = 1$ triplet state was lower in energy. In the disordered region appeared bands of polarons ferromagnetically and antiferromagnetically coupled.

Barta et al. [21] observed magnetic phase transitions in poly(3-alkylthiophene) induced by FeCl_4^- dopant ions. Results obtained with magnetic susceptibility measurements showed that, at low temperatures, the polymer exhibited a paramagnetic phase transition when the dopant ion concentration is increased. According to the authors, the magnetic interaction observed is associated with an antiferromagnetic coupling between bipolarons and the doping ions.

Čík et al. [22] analyzed the influence of side chain on magnetic properties of poly(3-alkylthiophene) and observed that the structure of polymers studied affected the results, proposing that these properties could be dependent the crystalline portion of the polymer phase.

Genoud et al. [23] studied the effect of polypyrrol aging on the electronic properties using EPR and conductivity measurements. In the case of fresh chemical powder, it was observed a strong broadening of the EPR line, which was attributed to strong collisions of polarons against fixed iron paramagnetic centers. A linear relationship between EPR linewidth and macroscopic conductivity was interpreted in terms of a decrease of the mobility of polarons as a function of polymer ageing.

The authors proposed the existence of a metallic electronic state which is not the general case for conducting polymers.

Sersen et al. used magnetic susceptibility data to investigate the role of polaron in poly(3-dodecylthiophene) (PDDT) [24]. The authors submitted the samples to a thermal annealing at 450 K and cooled it to the glass transition temperature observing a strong spin-spin interaction. They concluded that the variation of antiferromagnetic behavior as a function of temperature is caused by a conversion of polarons into bipolarons.

Sanjai et al. [25] studied the magnetic properties in polyaniline doped with methane sulphonic acid and polyaniline-polyurethane blended samples, and observed the presence of Pauli and Curie susceptibility in both the samples.

Many studies were performed for investigation of magnetic behavior in pure polyaniline and its composites with different materials. Trivedi et al. [26] studied the ferromagnetism in polyaniline samples and claimed that the position of the self-trapped carriers were due to the non-coplanar orientation of the dopant and therefore a competition between ferromagnetic and antiferromagnetic yielded with a frustrated structure. The authors also proposed that the ferromagnetism is due to spin glass structure. The presence of inorganic ferromagnetic impurities was discarded by analysis of atomic absorption. Zaidi et al. [27] studied the magnetic behavior of the copolymer polyaniline and tetracyanoquinodimethane (TCNQ). This material has a critical temperature around 350 K. From X-ray diffraction, the authors show that PANI-TCNQ becomes more structurally ordered over time and this fact leads to an increase of the ferromagnetic contribution. Long et al. [28] studied the magnetic properties of polyaniline as a function of temperature and applied magnetic field and the authors observed that the magnetization and magnetic susceptibility of the sample depend on the applied magnetic field and the dopant concentration.

Kompan et al. [29] investigated the magnetic behavior of polyaniline and observed the possibility of to control the magnetic properties submitting them to chemical treatment. The highest oxidation state of polyaniline (pernigraniline) was characterized as a magnetically ordered state at room temperature. Variations in magnetic properties were observed to be related to the nature and structure of the polymer.

EPR data in pressed pellets of doped poly(3-methylthiophene) showed a single line that are split into a broad and a narrow-superimposed line below 225 K. Magnetic susceptibility measurements using SQUID magnetometer didn't reveal any special feature at this temperature. The authors attributed the broad line to the crystalline fraction of the polymer and the narrow line to the amorphous one [30]. Using Dyson theory, the same group investigates the electronic charge carriers in pressed pellets of poly(3-methylthiophene). The authors proposed that, for samples synthesized at 25 °C, the main defects are polarons, and, for samples prepared at 5 °C, bipolarons [31]. It is important to emphasize that, besides the electronic defects important differences in the chain length and even in the material morphology can be observed as the synthesis temperature is changed. Finally, the authors [32] showed the existence of room temperature charge-density-wave

(CDW) signatures using both DC and AC conductivity in pressed pellets samples. The values of the parameters obtained are consistent with a strong electron–phonon interaction as expected for quasi-one dimensional systems [33].

Electron paramagnetic resonance (EPR) experiments showed the distinct contributions of the disordered and crystalline regions at the metal–semiconductor transition temperature of poly(3-methylthiophene) [34]. As the level of disorder decreased, when small crystalline regions appeared, there was a tendency for the polarons to interact ferromagnetically. For more ordered regions or crystalline regions of larger sizes, there was a competition between localized ferromagnetic coupled polarons and delocalized ones, that is, between localization and delocalization. The semiconducting behavior of the disordered phase was observed, as well as the metallic behavior of the crystalline phase revealed by the increase in the conductivity with the decrease of the temperature [34].

One of the issues involving organic ferromagnetism was discussed by Dormann et al. [35] where the author gives arguments showing that for organic magnets high values of saturation magnetization, remanent magnetization and coercive field should not be expected. Rajca et al. [36] observed the magnetic properties of an organic p-conjugated polymer with a very large magnetic moment and magnetic order at low temperatures.

However, our group performed an extensive investigation of magnetic properties of pressed doped poly-3-methylthiophene and pellets using SQUID magnetometer, and proposed the existence of weak ferromagnetic at room temperature [37–39]. To discard the possibility of external contamination by ferromagnetic compounds Graphite Furnace Atomic Absorption Spectroscopy data have been measured and the results confirmed the absence of any contamination. The authors studied different synthesis conditions, the effect of the applied pressure on the samples and even the use of a different thiophene derivative, poly(3-hexylthiophene) [40]. The results show the existence of optimized conditions for sample preparation which are fundamental for the occurrence of room temperature ferromagnetic behavior. For example, the addition of a small amount of water (200 ppm) in the organic solvent used enhances the ferromagnetic properties due to changes of morphology of the samples. Magnetization as a function of applied magnetic field of poly(3-hexylthiophene) samples prepared with addition of 200 ppm of water in organic solvent and any addition of water. The authors observed that coercive field increases with addition of water due to changes morphology, as a consequence, of magnetic domains.

These effects are possibly related to termination reaction that water molecules promote in the chain growth process. Considering these facts, the polymerization was carried out in under controlled atmosphere. Then, this process has been conducted inside a dry box under an argon atmosphere but with the addition of small amount of water into the solvent used to synthesize the polymer. As described above, the addition of about 200 ppm of water during the synthesis leads to a high reproducible material with improved ferromagnetic properties [40].

Correa et al. [37] observed that the magnetization as a function of applied magnetic field at 300 K for poly(3-methylthiophene) samples synthesized

electrochemically and isostatically pressed at different values. Saturation magnetization (M_s) increases when increase pressure. In pressures of 250, 473 and 833 bar $M_s = 10^{-4}$ emu/g, 2×10^{-4} emu/g and 6.5×10^{-4} emu/g, respectively.

The remanent and saturation magnetization were dependent on the pressure used to synthesis of the pellets. The authors claimed that the results proposing that the increase in the pressure used leads to a connection among magnetic blocks inside the fibrils of the polymer, establishing a three-dimensional path for magnetic order.

Investigating poly(3-methylthiophene) pressed samples, our group identified different magnetic phases: diamagnetism, paramagnetism, ferromagnetism and antiferromagnetism, depending on the preparation conditions [38] and the amount of each is strongly dependent on the synthesis conditions as well as doping level and pressure used to prepare the pellets.

Finally, the effect of the doping level has been investigated [31, 37]. It was detected that for intermediary doping level, where the main charge carriers are polarons, results in the increase of the ferromagnetic phase amount in the samples.

Pereira et al. [38] investigated magnetization as a function of applied magnetic field for electrochemically synthesized poly(3-methylthiophene) sample at different temperatures. After the synthesis, the material was partially reduced to intermediary levels.

The authors observed that the remanent magnetization at 300 K and 5 K were 4.4×10^{-4} and 8.54×10^{-4} emu/g, respectively. The coercive fields were 85 and 170 Oe, respectively [38]. It was observed that besides ferromagnetic behavior the sample also presents diamagnetism and paramagnetism. The origin of different magnetic behavior observed in this sample is associated to fact that only a small amount of polarons contributed to stablish of ferromagnetic phase, as a consequence, a fraction of the sample is ferromagnetic, which hidden the observation of the classical ferromagnetic magnetization versus temperature curve.

The ferromagnetic behavior of poly(3-methylthiophene) sample was confirmed from thermoremanence measurements [39]. The sample was cooled from room temperature to 1.8 K without an applied field. At 1.8 K a magnetic field was applied for ten minutes and then removed. The measurements were performed with three different field-cooling conditions: $H = 500$ Oe (open circles), $H = 1000$ Oe (crosses), and $H = 5000$ Oe (squares). This experimental condition exhibits only ferromagnetic behavior. The magnetization dependence with temperature show that an increase in the magnetization with the increase of the magnetic field. Whereas for 500 Oe we could fit the data with a classical tridimensional $M(T) = M(0) - aT^{3/2}$ behavior, as the field was increased a change toward a lower exponent can clearly be observed. At $H = 5000$ Oe the data could be fitted with a bidimensional $M(T) = M(0) - bT$ behavior. The both fittings with different fields show that the critical temperature is approximately the same, around 815 K. The change of dimensionality with the increase of magnetic field indicates that the magnetic field is also responsible for localizing the magnetic moments, i.e., they are confined in a plane perpendicular to the applied field [39].

An important question always raised about the ferromagnetic behavior of organic compounds, particularly in conductive polymers, is whether their origin is

intrinsic. In addition to elemental analysis techniques, other experiments have shown that ferromagnetism emerges from the interaction of the polarons. De Paula et al. [40] shows the magnetization as a function of applied magnetic field at 300 K of poly(3-hexylthiophene) samples storage for a several months. In this case, can be easily seen that the saturation magnetization decreases with sample storage time. Samples stored for 4 weeks the M_s reduced to 35% of initial value [40]. If the ferromagnetic properties come from an external contamination by ferromagnetic compound these results were not expected.

Studying regioregular and regiorandomic samples of poly(3-hexylthiophene), Kahol et al. [41] observed an increase in the magnetic susceptibility of the samples as a function of the temperature. According to the authors, the increase in the magnetic susceptibility occurs by decoupling of the spins at high temperature.

de Paula et al. [42] studied the samples of ClO_4 -doped poly(3-hexylthiophene). The authors observed the presence of a ferromagnetic phase which is strongly dependent of the sample preparation conditions. Besides, the extension of reducing process, and the control of the charge carriers kind and density is another factor which affect the magnetic properties. In this case, once the electrochemical oxidation—reduction of the polymer of the reduction process, the Nernst potential of the material after a reduction step is a function of the defect density in the sample. The origin of the ferromagnetism was proposed to be associated with interactions between spin 1/2 polarons formed in the polymeric chain upon doping. Magnetization measurements (M) as a function of final reduction potential for different values of potentials after reduction show that the magnetization presents a maximum value for a sample with a final potential after reduction around 0.806 V. The authors claimed that this behavior occur due to polarons in the poly(3-hexylthiophene) chain and this condition was obtained controlling the concentration of polarons to limit the recombination into spinless bipolarons [42].

The ferromagnetic behavior in poly(thiophene)s also reported by other authors. Vandeleene et al. [43] investigated the magnetic properties of substituted poly(thiophene)s in their neutral state, and reported the influence of the nature of the substituent (alkyl, alkoxy, thioalkyl), the substitution pattern [head-to-tail (HT) versus head-to-head-tail-to-tail (HH-TT)], and the regioregularity on the magnetic properties. From EPR experiments was observed that poly(thiophene)s showed significant spin densities, which are governed by the nature of the substituent. The distance between the spins in the polymer chain was too large to allow spin coupling, and, therefore, these noninteracting spins are given rise to a typical Curie-Weiss paramagnetic behavior. SQUID magnetometry revealed the presence of superparamagnetic order at room temperature, while ferromagnetism was observed at 5 K [43].

Čík et al. [44] studied the magnetic properties of the synthesized poly(N-perfluorophenylpyrrole) using ZFC and FC magnetization curves and observed that, at low temperatures, the synthetic polymer has reached a ferromagnetic state. The synthesized polymer retained ferromagnetism even at 300 K. The anomalous magnetic behavior was explained in terms of spin–spin interaction of triplet polarons. Free polaron spins was stabilized on mutually interacting shorter

polypyrrole subunits. These magnetic states were caused by spin–spin interaction of polarons, which were present in the polymer. The existence of several polarons was confirmed by magnetic measurements as magnetic susceptibility as a function of temperature and relaxation phenomena on remanent magnetization.

3 Effects of Metals and Oxides in the Magnetic Behavior of Conducting Polymers

One of the main advantages that conductive polymers present is the capability to control their electrical conductivity over a wide range, allowing them to present themselves as insulating, semiconductor and even synthetic metals. On the other hand, magnetic particles when introduced into semiconductor materials allow interesting carrier bias effects, essential for spintronic applications. In this sense, the doping of particles or magnetic ions in conductive polymers opens up interesting possibilities for both fundamental and application research.

Marchesi et al. [45] studied the magnetic properties of polypyrrole doped with iron oxide. In this work, the incorporation of small amounts of iron oxide in the polypyrrole was made by the addition of FeCl_3 during the chemical synthesis of the polymer. A study of the magnetic properties of iron-free synthesized polypyrrol and iron-added polypyrrol was carried out. The addition of iron species showed an increase in the saturation magnetization twofold and in the ferromagnetic properties of polypyrrole, as expected.

Hatamie et al. [46] synthesized of dilute doped cobalt nanoparticles in emeraldine salt (ES) of polyaniline in the presence of dodecyl benzene sulfonic acid (DBSA) and p-toluene sulfonic acid (p-TSA) using a sonochemical-assisted-reduction approach. The authors studied the applied field dependent magnetization and showed that the sample exhibited hysteresis loop with a minimal doping of 3 wt% of Co nanoparticles and increased with the amount of Co nanoparticles in emeraldine salt due to dipolar interaction.

Taylan et al. [47] studied the magnetic properties of the conducting poly(vinyl chloride)/polyindole composites with different compositions. They observed of both polarons and bipolarons. Most of the composites were paramagnetic, which is expected as they contain unpaired electrons. Some composites were diamagnetic, and, the authors concluded the existence of bipolarons.

Umare et al. [48] prepared Fe_3O_4 nanoparticles by hydrolysis reaction of urea in ethylene glycol as solvent at 160 °C. The prepared Fe_3O_4 nanoparticles were incorporated into polyaniline (PANI) matrix during in situ chemical oxidative polymerization of aniline with different molar ratios of aniline. Saturation magnetizations of Fe_3O_4 , PANI/ Fe_3O_4 (19:1), and PANI/ Fe_3O_4 (9:1) are 27.5, 5.5 and 6.3 emu/g, respectively, indicating an increase of ferromagnetic interaction as more Fe_3O_4 is incorporated in PANI matrix as expected, whereas PANI was diamagnetic.

Suzuki et al. [49] reported the magnetic properties of regioregular poly(3-hexylthiophene)-capped Au nanoparticles (NPs) doped with iodine. The room-temperature magnetization curve of the undoped polythiophene-capped Au NPs exhibits a clear hysteresis behavior with a coercive force of 160 Oe. The results obtained showed that polythiophene capping could lead to spontaneous magnetic polarization in Au NPs, and the conductivity of the polymer capping does not affect the ferromagnetism of the Au nanoparticles.

Aydin et al. [50] synthesized the poly(3-thiophene acetic acid)/Fe₃O₄ nanocomposite. The polymer was synthesized by the precipitation of Fe₃O₄ in the presence of poly(3-thiophene acetic acid) (P3TAA). Through magnetization measurements was observed that P3TAA coated magnetite particles do not saturate at higher fields. There was no coercivity and remanence revealing superparamagnetic character.

Xie et al. [51] synthesized La-doped barium-ferrite/polythiophene (LB/PTh) composites by in situ chemical polymerization with ferric chloride (FeCl₃) as an initiator. The nanocomposite exhibited ferromagnetic behavior under applied magnetic field which is depended on the amount of Fe³⁺ concentration used.

Yano et al. [52] prepared polyaniline (PANI) coated electrode in the presence of chloranil (CHR). The measurements of the EPR spectra and the magnetic susceptibility of the samples revealed that the incorporation magnetized PANI. Although no ferromagnetic property was observed, it had an unusual paramagnetic property because the magnetic susceptibility was not inversely proportional to temperature. EPR spectra exhibited that the polaron species (cation radical species) were delocalized over the entire polymeric backbone of PANI. In a different work, Yano et al. [53] prepared the polyaniline (PANI) with the incorporation of the chloranil (CHR). The electrochemical behavior of PANI in the presence of CHR showed that the quinone electronically interacts with PANI. The quinone was incorporated into PANI during electrochemical oxidation. Measurements of EPR spectra and magnetic susceptibility indicated that the incorporation of the quinones magnetized PANI. Although PANI incorporating CHR showed no ferromagnetic properties, it did exhibit unusual paramagnetic properties.

Kim et al. [54] prepared the Fe₃O₄ nanoparticle-embedded poly(styrene)/poly(thiophene) core/shell composite particles (Fe₃O₄ NPs-PS/PTh) and were successfully fabricated via stepwise polymerizations. The composite particles exhibited superparamagnetic properties.

Zhao et al. [55] synthesized an electromagnetic composite using graphene (GN) nanosheets and polythiophene (PT) using in situ chemical polymerization. When the mass ratio of GN/PT was 0.4, the magnetic saturation value of the composites achieved 15.33 emu/g, and the conductivity reached 12.17×10^{-3} S/cm.

Singh et al. [56] investigated poly(3-methylthiophene) doped with different anions such as SnCl₅⁻ and SbCl₆⁻ prepared electrochemically in the presence of tetraalkylammonium salts. The authors attributed the variations in magnetic susceptibility to the variations in the unpaired spin concentration in the polymer chain units.

Nandapure et al. [57] synthesized nanocrystalline cobalt oxide (Co_3O_4) by sol-gel method using cobalt chloride as precursor. Conducting polyaniline-cobalt oxide ($\text{PANI}/\text{Co}_3\text{O}_4$) nanocomposites were synthesized by in situ polymerization of aniline (monomer) in the presence of as-synthesized nanocrystalline Co_3O_4 . Using magnetic measurements, the authors observed that pure Co_3O_4 is ferromagnetic in nature as expected. $\text{PANI}/\text{Co}_3\text{O}_4$ nanocomposites showed ferromagnetic with hysteresis loop area depending on concentration of Co_3O_4 in the PANI matrix.

Hosseini et al. [58] prepared polythiophene (PTh) nanofibers coated on $\text{MnFe}_2\text{O}_4/\text{Fe}_3\text{O}_4$ core-shell nanoparticles where MnFe_2O_4 is the magnetic core covered by Fe_3O_4 shell. The authors analyzed the changes in the magnetic and conductive properties after PTh coating. It was observed that the saturation magnetization and coercivity were lower for core-shell nanocomposites than for the MnFe_2O_4 core material. The saturation magnetization and coercivity decreased from 60.76 emu/g and 99.10 Oe for MnFe_2O_4 to 0.77 emu/g and 33.5 Oe, respectively, for $\text{MnFe}_2\text{O}_4/\text{Fe}_3\text{O}_4/\text{PTh}$.

Xie et al. [59] prepared chitosan-decorated ferrite-filled multi-walled carbon nanotubes (MWCNTs)/polythiophene composites using in situ chemical polymerization of thiophene in the presence of the chitosan decorated ferrite-filled MWCNTs. The chitosan-decorated ferrite-filled MWCNTs/polythiophene composites exhibited hysteresis loop behavior under an applied magnetic field, with saturation magnetization ($M_s = 0.18$ emu/g) and coercivity ($H_c = 312.5$ Oe). The magnetic parameters such as the high saturation magnetization and the small coercivity of the chitosan-decorated ferrite-filled MWCNTs/polythiophene composites are depended on the impedance matching of the ferrite and the MWCNTs.

Hosseini et al. [60] prepared nanofiber polythiophene layered on $\text{Ba}_x\text{Sr}_{1-x}\text{Fe}_{12}\text{O}_{19}/\text{Fe}_3\text{O}_4$ /polyacrylic acid core-shell structure. The saturation magnetization of nanoparticles decreases with increasing of polyacrylic acid and polythiophene content, while its conductivities increase with increasing of polythiophene content.

Hong et al. [61] prepared a hybrid material based on doped barium ferrite (BF)-titanium dioxide (TD) and multiwalled carbon nanotubes (MCNTs) coated by polythiophene (PTh) matrix. The magnetic properties of the samples were measured at room temperature and exhibited a clear hysteresis behavior. They demonstrate that the MCNTs content affected the magnetization of composites. A possible explanation was the presence of many delocalization electrons in the MCNTs structure, which were enable the formation of π - π conjugate structures between MCNTs and PTh.

Majumdar et al. [62] reported the observation of ferromagnetic ordering in π -conjugated polymeric semiconductors, namely regioregular poly (3-hexyl thiophene) (RRP3HT) and 1-(3-methoxycarbonyl)propyl-1-phenyl-[6, 6]-methanofullerene (PCBM), in temperature range from 5–300 K. Blending these two materials, the ferromagnetic ordering was suppressed by a huge paramagnetic signal. Particle induced X-ray emission spectroscopy indicated the presence of dilute magnetic impurities as residues from the synthesis process in the individual polymers. However the impurity signal was unable to explain the temperature dependence of

magnetization in these materials and the observed paramagnetism of the RRP3HT:PCBM blends.

Gulácsi et al. [63] studied the magnetic properties of conducting polymers within a one-dimensional periodic Anderson model in which stemming effects from electron–lattice interactions were explicitly included. The effective Hamiltonian derived via bosonization exhibited a ferromagnetic ground state in the intermediate coupling regime. For ferromagnetic polymers, the results showed that phononic contributions have insignificant effect on ferromagnetism. Gulácsi et al. [64], in another work, studied the influence of lattice vibrations on ferromagnetism in conducting polymers. The authors studied the ferromagnetic phase of conducting polymers analyzing phononic contributions using the periodic Anderson model (PAM).

Hosseini et al. [65] prepared magnetic and conductive graphite nanoflakes/ $\text{SrFe}_{12}\text{O}_{19}$ /polythiophene nanofiber-nanocomposites. It was found that the magnetization under applied magnetic field for the prepared composites exhibited a clear hysteretic behavior. It was found that saturated magnetization, remanent magnetization and coercive field for the nanocomposites exhibited a decrease with addition shell on the core.

Onoda et al. [66] presented results of in situ measurements of poly(3-phenylthiophene) during electrochemical *p*-type doping were discussed in terms of polaron and/or bipolaron models. It was considered that polarons are predominant at the lightly doped state, although only two additional optical transitions appeared below the interband transition.

Peymanfar et al. [67] prepared polymer-based multiphase magnetic nanocomposite $\text{SrAl}_{1.3}\text{Fe}_{10.7}\text{O}_{19}$ /MWCNT/PANi and this material was synthesized through a sonochemical method by in situ polymerization. Magnetic properties such as saturation magnetization (M_s), coercivity (H_c), and remanent magnetization (M_r) of nanocomposites $\text{SrAl}_{1.3}\text{Fe}_{10.7}\text{O}_{19}$, $\text{SrAl}_{1.3}\text{Fe}_{10.7}\text{O}_{19}$ /MWCNT and $\text{SrAl}_{1.3}\text{Fe}_{10.7}\text{O}_{19}$ /MWCNT/PANi were determined from the hysteresis curves at room temperature with applied fields up to 10 kOe. The saturation magnetization, remanent magnetization, and coercivity were dropped significantly by coating with the nonmagnetic MWCNT and PANi. Magnetic hysteresis loops of materials indicated the decrease in the magnetization of the as synthesized ternary nanocomposite. The authors observed diminution of saturation magnetization for $\text{SrAl}_{1.3}\text{Fe}_{10.7}\text{O}_{19}$ /MWCNT and was attributed to the decreased volume fraction of $\text{SrAl}_{1.3}\text{Fe}_{10.7}\text{O}_{19}$. The $\text{SrAl}_{1.3}\text{Fe}_{10.7}\text{O}_{19}$ surface defects were concealed by the deposition of PANi, thus causing the reduction of crystal anisotropy, which led to a decrease in coercivity.

Liu et al. [68] studied room temperature magnetic ordering for very small carbon dots (CDs), mat-like polyaniline nanofibers (Mat-PANI) and a composite of CDs@Mat-PANI containing 0.315 wt% CDs. It was observed the saturation magnetization enhancement in CDs@Mat-PANI and was attributed to electron transfer from Mat-PANI imine N-atoms to the encapsulated CDs.

Unver et al. [69] synthesized magnetite nanoparticles (Fe_3O_4 NPs) via reflux co-precipitation method and coated with various polymeric media of polypyrrole

(PPY), polyaniline (PANI), and polythiophene (PT) in the same experiment conditions. The superparamagnetic nature of composites was observed at room temperature.

Rouhi et al. [70] prepared the novel conductive nanocomposite by emulsion polymerization. Magnetite nanoparticles were synthesized via coprecipitation reaction. Then, poly (indole-co-thiophene) @Fe₃O₄ nanocomposite was prepared via emulsion copolymerization of indole and thiophene monomers using sodium dodecyl sulfate as an emulsifier and ammonium persulfate as an oxidant in the presence of Fe₃O₄ nanoparticles. The Fe₃O₄ nanoparticles showed saturation magnetization (M_s) of 65 emu/g, whereas the M_s values for Poly (In-co-T)@Fe₃O₄ (1:1) and Poly (In-co-T)@Fe₃O₄ (1:0.25) nanocomposites were 14 and 8 emu/g, respectively. Because the Poly (In-co-T) powder was not magnetic, the magnetic properties of the Poly (In-co-T)@Fe₃O₄ nanocomposites were attributed to the superparamagnetic properties of the Fe₃O₄ nanoparticles. The authors observed that, increasing of polymer content decrease the magnetic hysteresis loops of the nanocomposites.

Juybaria et al. [71] modified magnetite nanoparticles with polythiophene possessing core-shell structure and were prepared by two-step methods. At the first, a coprecipitating method was employed for the formation magnetite nanoparticles in an ammonia solution as precipitant system. Next, the thiophene monomers were adsorbed on the surface of Fe₃O₄ nanoparticles and were then embedded the Fe₃O₄ nanoparticles via oxidative polymerization using FeCl₃ as oxidant and H₂O₂ as redox catalyst in the solvent of acetonitrile. Magnetic properties were identified by vibrating sample magnetometer and revealed superparamagnetic behavior of Fe₃O₄/PTh nanocomposite. The results obtained showed that the polythiophene-coated magnetite had the saturation magnetization value lower than bare magnetite due to the coating layer on the magnetite surface in which the nonmagnetic domain cannot contribute to the overall magnetization.

Bai et al. [72] prepared attapulgite (ATP) into the system of ferrite composites. By sol-gel self-propagating combustion method, attapulgite/barium ferrite (ATP/BaFe₁₂O₁₉) was prepared, and then ternary composites of attapulgite/barium ferrite/polyaniline (ATP/BaFe₁₂O₁₉/PANI) were obtained by in situ oxidative polymerization of aniline on ATP/Ba Fe₁₂O₁₉ mixture. BaFe₁₂O₁₉ particles and all the composites behaved as a broad hysteresis loop at room temperature, indicating the ferromagnetic behavior of them. Due to the fact that ATP and PANI were non-magnetic the saturation magnetization, remanent magnetization and coercive fields values of ATP/BaFe₁₂O₁₉ composite and ATP/Ba Fe₁₂O₁₉/PANI composite were lower than those of pure BaFe₁₂O₁₉ powder. Generally, the coercivity of a material depends upon many factors, such as grain shape, morphology, structure, composition, magnetocrystalline anisotropy and magnetostriction.

Xi et al. [73] proposed a novel structured Janus nanoribbon array film. The flexible array film composed of ordered Janus nanoribbons was constructed by electrospinning using a purpose made co-axis//single-axis spinneret and an aluminum drum collection device, and simultaneously possesses anisotropical electrical conduction, superparamagnetism and fluorescence. Each one-dimensional

(1D) Janus nanoribbon was composed of a fluorescent–superparamagnetic bifunctional $[\text{Fe}_3\text{O}_4/\text{polymethylmethacrylate (PMMA)}]@[\text{Eu}(\text{BA})_3\text{phen}/\text{PMMA}]$ coaxial nanoribbon and conducting polyaniline (PANI)/PMMA nanoribbon. All of the Janus nanoribbons were aligned in the same aspect to generate a two-dimensional (2D) array film. The samples exhibited a superparamagnetic performance and the results demonstrated that the saturation magnetization of the $[\text{M}@\text{P}]/\text{C}$ JAF increased with more Fe_3O_4 NPs being introduced into the $\text{Fe}_3\text{O}_4/\text{PMMA}$ core, and this indicated that the superparamagnetism of the samples could be adjusted.

Singh et al. [74] prepared $\text{Fe}_3\text{O}_4/\text{Polythiophene (Fe}_3\text{O}_4/\text{PT)}$ hybrid nanocomposite by oxidative polymerization of thiophene over oleic acid-capped Fe_3O_4 nanoparticles. The zero coercivity and reversible hysteresis behavior indicated the superparamagnetic nature of $\text{Fe}_3\text{O}_4/\text{PT}$ nanocomposite at room temperature.

Tian et al. [75] used poly(methyl methacrylate) (PMMA) to manufacture Janus-structured fibers. $[\text{Fe}_3\text{O}_4/\text{PANI}/\text{PMMA}]||[\text{Eu}(\text{TTA})_3(\text{TPPO})_2/\text{PMMA}]$ with tri-functionality for anisotropic conduction, magnetism and fluorescence, were fabricated by a facile conjugate electrospinning technology with a rotating metal rod as a collecting device. Through magnetization measurements the introduction of more Fe_3O_4 NPs, caused an increase in the saturation magnetization of the Janus-structured microfibers array from 1.52 to 15.44 emu g^{-1} , showing that the Janus-structured microfibers array have adjustable magnetism.

Iqbal et al. [76] synthesized barium ferrite encapsulated polythiophene ($\text{BaFe}_{12}\text{O}_{19}/\text{PTh}$) nanocomposite. The sample exhibited excellent magnetic properties with a magnetic moment and coercivity of 25.78 emu/gm and 2.5 kOe, respectively. It was observed that the composites exhibit ferromagnetism, which further improves with the $\text{BaFe}_{12}\text{O}_{19}$ content in PTh.

4 Final Remarks

The evolution of the next generation of devices which will be used by the society is deeply related to the development of new materials for that task. Conducting polymers, their blends and composites are advanced materials with high modulable electronic, magnetic, and optical properties. Besides, they are low density, which makes easy their use in portable devices. As a consequence, the number of applications and devices they can be used is as well as large. The magnetic properties observed in this class of materials, as ferromagnetic phase, is well established to different authors using different techniques. From a fundamental point of view, the possibility of s and p conducting materials to present ferromagnetic behavior is definitively demonstrated, not only in conducting polymers, but also in other organic systems, like graphene. For sure, the possibility of low-level contamination is always a possibility during polymer preparation. To guarantee that ferromagnetic behavior is intrinsic, the existence of foreign elements must be below 50–10 ppb (about $5 \times 10^{-8} \text{ mol L}^{-1}$). Therefore, in each work, the demonstration of the

absence of any ferromagnetic external contamination must be performed. The use of Graphite Furnace Atomic Absorption Spectroscopy is a precise technique to this task once it can quantify element concentration as low as one part per trillion, i.e., 10^{-12} mol L⁻¹ which is far below the level contamination found in these samples.

In summary, since the discovery of conductive polymers in the 1970s and their applications to many electronic devices, such as mobile phones, high-resolution displays, and others, from the point of view of applications using magnetic properties, they are still very incipient. Advances in understanding the intrinsic magnetic phases of these polymers, as well as the effects due to the insertion of metallic particles and oxides, will allow new possibilities of applications, not only in the storage of information, but also in the development of organic spintronic devices. To achieve this goal, many fundamental studies still need to be done to fully understand the mechanisms associated with this interesting organic magnetism.

Acknowledgements The authors thank financial support from CNPq, CAPES and FAPESP (2013/07296-2).

References

1. Shirakawa, H., Louis, J., Macdiarmid, A.G., Chiang, C.K., Heeger, A.J.: Synthesis of electrically conducting organic polymers: halogen derivatives of polyacetylene, (CH)_x. *J. Chem. Soc. Chem. Comm.* **16**, 578–580 (1977)
2. Chiang, C.K., et al.: Electrical conductivity in doped polyacetylene. *Phys. Rev. Lett.* **39**, 1098–1101 (1977)
3. Fukutome, H., Takahashi, A., Ozaki, M.: Design of conjugated polymers with polaronic ferromagnetism. *Chem. Phys. Lett.* **133**(1), 34–38 (1987)
4. Bredas, J.L., Street, G.B.: Polarons, bipolarons, and solitons in conducting polymers. *Acc. Chem. Res.* **18**, 309–315 (1985)
5. Fisher, A.J., Hayes, W., Wallace, D.S.: *J. Phys. Condens. Matter* **1**, 5567 (1989)
6. Bertho, D., Jouanin, C., Lussert, J.M.: *Phys. Rev. B* **37**, 4039 (1988)
7. Wohlgenannt, M., Jiang, X.M., Vardeny, Z.V.: *Phys. Rev. B* **69**, R241204 (2004)
8. Nalwa, H.S.: Phase transitions in polypyrrole and polythiophene conducting polymers demonstrated by magnetic susceptibility measurements. *Phys. Rev. B* **39**, 5964–5974 (1989)
9. Mizoguchi, K., Kachi, N., Sakamoto, H., Kume, K., Yoshioka, K., Masubuchi, S., Kazama, S.: *Synth. Met.* **84**, 695 (1997)
10. Macedo, A.M.S., dos Santos, M.C., Coutinho-Filho, M.D., Macedo, C.A.: *Letters 6. Phys. Rev. Lett.* **74**, 1851–1854 (1995)
11. Yoshizawa, K., Tanaka, K., Yamabe, T., Yamauchi, J.: Ferromagnetic interaction in poly(m-aniline): electron spin resonance and magnetic susceptibility. *J. Chem. Phys.* **96**, 5516–5522 (1992)
12. Devine, J.N., Crayston, J.A., Walton, J.C.: Synthesis and design of potential polaronic ferromagnets. *Synth. Met.* **103**, 2294–2295 (1999)
13. Genies, E., Lapkowski, M.: Electrochemical in situ EPR evidence of twopolaron-bipolaron states in polyaniline. *J. Electroanal. Chem.* **236**, 199–208 (1987)
14. Kulszewicz-BajerAJER, I., et al.: Electrochemical spin response in polyalkylthiophenes and polydialkylbithiophenes. *Synth. Met.* **35**, 129–133 (1990)
15. Onoda, M., Nakayama, H., Morita, S., Yoshino, K.: Electronic properties of polythiophene derivatives. *Synth. Met.* **55**, 275–280 (1993)

16. Bacskai, J., Inzelt, G., Bartl, A., Dunsch, L., Paasch, G.: In situ electrochemical ESR investigations of the growth of one- and two-dimensional polypyrrole films. *Synth. Met.* **67**, 227–230 (1994)
17. Sun, Z.W., Frank, A.J.: Characterization of the intrachain charge-generation mechanism of electronically conductive poly (3-methylthiophene). *J. Chem. Phys.* **94**, 4600–4608 (1991)
18. Pereira, E., et al.: Thermal-history-dependent transition in pressed pellets of C104-doped poly (3-methylthiophene). *Phys. Rev. B* **50**, 3648–3651 (1994)
19. Nascimento, O.R., et al.: Kinetics of crystallization in conducting polymers observed from electron spin resonance. *J. Chem. Phys.* **109**, 8729–8730 (1998)
20. Nascimento, O.R., de Oliveira, A.J.A., Pereira, E.C., Correa, A.A., Walmsley, L.: The ferromagnetic behaviour of conducting polymers revisited. *J. Phys.: Condens. Matter* **20**, 035214–035221 (2008)
21. Barta, P., Niziol, S., Le Guennec, P., Pron, A.: Doping-induced magnetic phase transition in poly(3-alkylthiophenes). *Phys. Rev. B* **50**, 3016–3024 (1994)
22. Čík, G., Sersen, F., Dlhan, L., Szabo, L., Bartus, J.: Anomaly in magnetic properties of poly (3-alkylthiophene)s depending on alkyl chain length. *Synth. Met.* **75**, 43–48 (1995)
23. Genoud, F., Nechtscheina, M., Plancheb, M., Thieblemontb, J.: ESR and conductivity on polypyrrole: effect of ageing. *Synth. Met.* **69**, 339–340 (1995)
24. Sersen, F., Čík, G., Szabo, L., Dlhan, L.: Role of polarons in the antiferromagnetic behaviour of poly(3-dodecylthiophene). *Synth. Met.* **80**, 297–300 (1996)
25. Sanjai, B., Raghunathan, A., Natarajan, T.S., Rangarajan, G.: Charge transport and magnetic properties in polyaniline doped with methane sulphonic acid and polyaniline-polyurethane blend. *Phys. Rev. B* **55**, 734–744 (1997)
26. Trivedi, D.C.: Observation of ferromagnetism in polyaniline. *Synth. Met.* **121**, 1780 (2001)
27. Zaidi, N.A., Giblin, S.R., Terry, I., Monkman, A.P.: Room temperature magnetic order in an organic magnet derived from polyaniline. *Polymer (Guildf)*. **45**, 5683–5689 (2004)
28. Long, Y., et al.: Magnetic properties of conducting polymer nanostructures. *J. Phys. Chem. B* **110**, 23228–23233 (2006)
29. Kompan, M.E., Sapurina, I.Y., Babayan, V., Kazantseva, N.E.: Electrically conductive polyaniline—a molecular magnet with the possibility of chemically controlling the magnetic properties. *Phys. Solid State* **54**, 2400–2406 (2012)
30. Walmsley, L., et al.: Crystallization observed from the spin behavior in poly (3-methylthiophene). *Synth. Met.* **101**, 355 (1999)
31. Sercheli, M.S., et al.: Polarons, bipolarons, and crystallization in conducting polymers: an ESR study. *Phys. Status Solidi B Basic Res.* **220**, 631 (2000)
32. Souza, V.M., Walmsley, L., Correa, A.A., Pereira, E.C., Gobbi, A.L.: Evidence of room temperature charge-density wave behavior and glass-like states in pressed pellets of lightly doped poly (3-methyl thiophene). *Mol. Cryst. Liq. Cryst.* **374**, 119–124 (2002)
33. Souza, V.M., Walmsley, L., Correa, A.A., Pereira, E.C.: Field-dependent conductivity at low electric fields in pressed pellets of doped poly(3-methylthiophene): evidence of charge-density wave depinning. *Solid State Commun.* **126**, 141–145 (2003)
34. Kondo, J.M., et al.: Simultaneous observation of the magnetic and electric behavior in a correlated system near a metal-semiconductor transition: ESR in pellets of conducting polymers. *Phys. Rev. B* **80**, 014410–014416 (2009)
35. Dormann, E.: Magnetism in organic materials. *Synth. Met.* **71**, 1781–1784 (1995)
36. Rajca, A., Wongsriratanakul, J., Rajca, S.: Magnetic ordering in an organic. *Polymer* **294**, 1503–1506 (2001)
37. Correa, A.A., et al.: Weak ferromagnetism in poly(3-methylthiophene)(PMTh). *Synth. Met.* **121**, 1836–1837 (2001)
38. Pereira, E.C., et al.: Polaronic ferromagnetism in conducting polymers. *J. Magn. Magn. Mater.* **226**, 2023–2025 (2001)
39. Nascimento, O.R., et al.: Magnetic behavior of poly (3-methylthiophene): metamagnetism and room-temperature weak ferromagnetism. *Phys. Rev. B* **67**, 144422 (2003)

40. De Paula, F.R., Pereira, E.C., De Oliveira, A.J.A.: The influence of the morphology on the magnetic properties of poly (3-hexylthiophene). *J. Supercond. Nov. Magn.* **23**, 127–129 (2010)
41. Kahol, P.K., McCormick, B.J., Epstein, A.J., Pandey, S.S.: Effects of disorder on the magnetic state of poly(3-hexyl)thiophene. *Synth. Met.* **135–136**, 343–344 (2003)
42. de Paula, F.R., Walmsley, L., Pereira, E.C., de Oliveira, A.J.A.: Magnetic properties of poly (3-hexylthiophene). *J. Magn. Magn. Mater.* **320**, 193–195 (2008)
43. Vandeleene, S., et al.: Magnetic properties of substituted poly(thiophene)s in their neutral state. *Macromolecules* **43**, 2910–2915 (2010)
44. Čík, G., et al.: Ferromagnetism in poly(N-perfluorophenylpyrrole). *J. Magn. Magn. Mater.* **391**, 116–121 (2015)
45. Marchesi, L.F.Q.P., de Paula, F.R., de Oliveira, A.J.A., Pereira, E.C.: Magnetic properties of polypyrrole doped with iron. *Mol. Cryst. Liq. Cryst.* **522**, 1–6 (2010)
46. Hatamie, S., et al.: Cobalt nanoparticles doped emeraldine salt of polyaniline: a promising room temperature magnetic semiconductor. *J. Magn. Magn. Mater.* **322**, 3926–3931 (2010)
47. Taylan, N.B., Sari, B., Unal, H.I.: Preparation of conducting poly(vinyl chloride)/polyindole composites and freestanding films via chemical polymerization. *J. Polym. Sci. Part B Polym. Phys.* **48**, 1290–1298 (2010)
48. Umare, S.S., Shambharkar, B.H., Ningthoujam, R.S.: Synthesis and characterization of polyaniline-Fe₃O₄ nanocomposite: Electrical conductivity, magnetic, electrochemical studies. *Synth. Met.* **160**, 1815–1821 (2010)
49. Suzuki, K., et al.: Ferromagnetism of polythiophene-capped Au nanoparticles. *J. Appl. Phys.* **109**, 7–10 (2011)
50. Aydin, M., et al.: Synthesis, magnetic and electrical characteristics of poly(2-thiophen-3-yl-malonic acid)/Fe₃O₄ nanocomposite. *J. Alloys Compd.* **514**, 45–53 (2012)
51. Xie, Y., et al.: Preparation and electromagnetic properties of La-doped barium-ferrite/polythiophene composites. *Synth. Met.* **162**, 1643–1647 (2012)
52. Yano, J., et al.: Magnetization of conductive polymer polyaniline during the electro-oxidation in the presence of chloranil. *Mater. Lett.* **84**, 162–164 (2012)
53. Yano, J., Fukuoka, H., Kitani, A.: Electro-oxidation of polyaniline in the presence of electronic acceptors and the magnetic properties of the resulting polyaniline. *Thin Solid Films* **618**, 165–171 (2016)
54. Kim, Y.S., et al.: Multifunctional Fe₃O₄ nanoparticles-embedded poly(styrene)/poly(thiophene) core/shell composite particles. *Synth. Met.* **175**, 56–61 (2013)
55. Zhao, J., et al.: Preparation and characterization of an electromagnetic material: the graphene nanosheet/polythiophene composite. *Synth. Met.* **181**, 110–116 (2013)
56. Singh, D., Misra, R.A.: Electrochemical synthesis and properties of poly (3-methylthiophene) doped with pentachlorostannate anion. *Nov. Trends Electroorg. Synth.*, 153–154 (2013). https://doi.org/10.1007/978-4-431-65924-2_46
57. Nandapure, B., Kondawar, S., Salunkhe, M., Nandapure, A.: Nanostructure cobalt oxide reinforced conductive and magnetic polyaniline nanocomposites. *J. Compos. Mater.* **47**, 559–567 (2013)
58. Hosseini, S.H., Moghimi, A., Moloudi, M.: Magnetic, conductive, and microwave absorption properties of polythiophene nanofibers layered on MnFe₂O₄/Fe₃O₄ core-shell structures. *Mater. Sci. Semicond. Process.* **24**, 272–277 (2014)
59. Xie, Y., et al.: Preparation and electromagnetic properties of chitosan-decorated ferrite-filled multi-walled carbon nanotubes/polythiophene composites. *Compos. Sci. Technol.* **99**, 141–146 (2014)
60. Hosseini, S.H., Moloudi, M.: Preparation of nanofiber polythiophene layered on Ba_xSr_{1-x}Fe₁₂O₁₉/Fe₃O₄/polyacrylic acid core-shell structure and its microwave absorption investigation. *Appl. Phys. A Mater. Sci. Process.* **120**, 1165–1171 (2015)
61. Hong, X., et al.: A novel ternary hybrid electromagnetic wave-absorbing composite based on BaFe_{11.92}(LaNd)_{0.04}O₁₉-titanium dioxide/multiwalled carbon nanotubes/polythiophene. *Compos. Sci. Technol.* **117**, 215–224 (2015)

62. Majumdar, S., Lill, J., Rajander, J., Majumdar, H.: Observation of ferromagnetic ordering in conjugated polymers exhibiting OMAR effect. *Org. Electron.* **21**, 66–72 (2015)
63. Gulácsi, M., El-Mansy, M.A.M., Gulácsi, Z.: Electron-phonon interactions in conducting polymers. *Philos. Mag. Lett.* **96**, 67–75 (2016)
64. Gulácsi, M., Gulácsi, Z.: Emergence of ferromagnetism in conducting polymers in the presence of lattice vibrations. *Mod. Phys. Lett. B* **30**, 1650335 (2016)
65. Hosseini, S.H., Alamian, A., Mousavi, S.M.: Preparation of magnetic and conductive graphite nanoflakes/SrFe₁₂O₁₉/polythiophene nanofiber-nanocomposites and its radar absorbing application. *Fibers Polym.* **17**, 593–599 (2016)
66. Onoda, M., Nakayama, H., Morita, S., Yoshino, K.: Electrochemical doping properties and electronic states of poly (3-phenylthiophene). *J. Appl. Phys.* **73**, 2859 (2017)
67. Peymanfar, R., Javidan, A., Javanshir, S.: Preparation and investigation of structural, magnetic, and microwave absorption properties of aluminum-doped strontium ferrite/MWCNT/polyaniline nanocomposite at KU-band frequency. *J. Appl. Polym. Sci.* **134**(30), 45135 (2017)
68. Liu, J., et al.: Room-temperature magnetism in carbon dots and enhanced ferromagnetism in carbon dots-polyaniline nanocomposite. *Sci. Rep.* **7**, 1–7 (2017)
69. Unver, I.S., Durmus, Z.: Magnetic and microwave absorption properties of magnetite (Fe₃O₄) @conducting polymer (PANI, PPY, PT) composites. *IEEE Trans. Magn.* **53**(10), 1–8 (2017)
70. Rouhi, M., Mansour Lakouraj, M., Baghayeri, M., Hasantabar, V.: Novel conductive magnetic nanocomposite based on poly (indole-co-thiophene) as a hemoglobin diagnostic biosensor: synthesis, characterization and physical properties. *Int. J. Polym. Mater. Polym. Biomater.* **66**, 12–19 (2017)
71. Juybaria, F.E., Kamran-Pirzaman, A., Ghorbani, M.: Chemical modification of magnetite with polythiophene and characterization of formed core-shell nanocomposite. *Inorg. Nano-Metal Chem.* **47**, 121–126 (2017)
72. Bai, D., Feng, H., Chen, N., Tan, L., Qiu, J.: Synthesis, characterization and microwave characteristics of ATP/BaFe₁₂O₁₉/PANI ternary composites. *J. Magn. Mater.* **457**, 75–82 (2018)
73. Xi, X., et al.: Assembling exceptionally-structured Janus nanoribbons into a highly anisotropic electrically conductive array film that exhibits red fluorescence and superparamagnetism. *New J. Chem.* **42**, 18708–18716 (2018)
74. Singh, B., Doong, R.A., Chauhan, D.S., Dubey, A.K., Anshumali: Synthesis and characterization of Fe₃O₄/polythiophene hybrid nanocomposites for electroanalytical application. *Mater. Chem. Phys.* **205**, 462–469 (2018)
75. Tian, J., et al.: High pairing rate Janus-structured microfibers and array: high-efficiency conjugate electrospinning fabrication, structure analysis and co-instantaneous multifunctionality of anisotropic conduction, magnetism and enhanced red fluorescence. *RSC Adv.* **9**, 10679–10692 (2019)
76. Iqbal, S., Shah, J., Kotnala, R.K., Ahmad, S.: Highly efficient low cost EMI shielding by barium ferrite encapsulated polythiophene nanocomposite. *J. Alloys Compd.* **779**, 487–496 (2019)

Revised Fundamental Properties and Crystal Engineering of Spinel Ferrite Nanoparticles



Rafaella Casado Silva, Walmir Eno Pottker, Alane Stephanye A. Batista, Jefferson Ferraz Damasceno Felix Araujo and Felipe de Almeida La Porta

Abstract Extensive research on ferrite-based materials and their application in field of electronics is of great importance in near future. In the last decade, several experiments have been conducted for developing different forms of ferrite-based materials through controlling its size, composition, and morphology. Such studies indicate that the chemical and physical properties of these materials can in principle be manipulated based on the desired application and are highly relevant from the technological point of view. However, the relationship between the closed structure and the composition of these advanced nanoscale materials is still debatable. In this chapter, the chemical structure of spinel ferrite nanoparticles has been studied using crystal engineering. It is quite evident that the change in the morphology of its particles and in the degree of defects alter their magnetic, optical and catalytic properties significantly. This makes these materials suitable for use in electronic devices such as high-density recording media and as a medical guide.

Keywords Nanoparticles · Ferrites · Materials synthesis · Magnetic, optical and photocatalytic properties

1 Introduction

Great achievements in the study of advanced nanomaterials synthesis and its attractive functional properties has obtained a significant increase nowadays, mainly due to its multiple technological applications as, for example, in the electronic scope. Among these novel advanced materials, however, many strategies

R. C. Silva · W. E. Pottker · A. S. A. Batista · F. A. La Porta (✉)
NANOQC—Laboratory of Nanotechnology and Computational Chemistry,
Federal Technological University of Paraná UTFPR, Londrina, PR 86036-370, Brazil
e-mail: felipelaporta@utfpr.edu.br

J. F. D. F. Araujo
Physics Department, Pontifical Catholic University of Rio de Janeiro, Rio de Janeiro
22451-900, Brazil

© Springer Nature Switzerland AG 2020
F. A. La Porta and C. A. Taft (eds.), *Emerging Research in Science and Engineering Based on Advanced Experimental and Computational Strategies*,
Engineering Materials, https://doi.org/10.1007/978-3-030-31403-3_20

have been intensively developed to produce high-quality ferrite related-materials [1–8]. This likely is due to its surface effects (large surface volume) and also quantum confinement (size-dependent properties) that strongly affect its attractive nanoscale properties [1–5]. Particularly, it is important to note that the study of ferrite based materials is a notoriously field and hence has increased exponentially over the past few decades, as shown in Fig. 1, i.e., reflecting the importance given to this class of advanced materials, which have a huge potential of application in various areas (e.g., ranging from technological to biomedical field [1–17]).

On the basis of these considerations, it is well-known that ferrites based materials are usually formed from the reaction of an iron-rich precursor with any other metal forming divalent bonds. Thus, this refer compound has the formula MFe_xO_y where M can be Mg, Al, Ba, Mn, Cu, Ni, Co, Zn, Bi or the iron itself [1–10]. This versatile and unique class of nanocrystals can have different crystal structures, including spinel, hexagonal and also grenade [2]. In addition, these advanced materials are usually divided into five groups e.g. according to their magnetization and demagnetization capacity. From this perspective, for example, this way they can be usually divided into the soft, hard, square-loop, microwave and single crystal, as well. Yet, each group themselves, in particular, has a specific crystalline structure (like spinel, hexagonal or grenade), presenting a huge diversity of applications, which may, in theory, vary according to their crystallographic constitution [3].

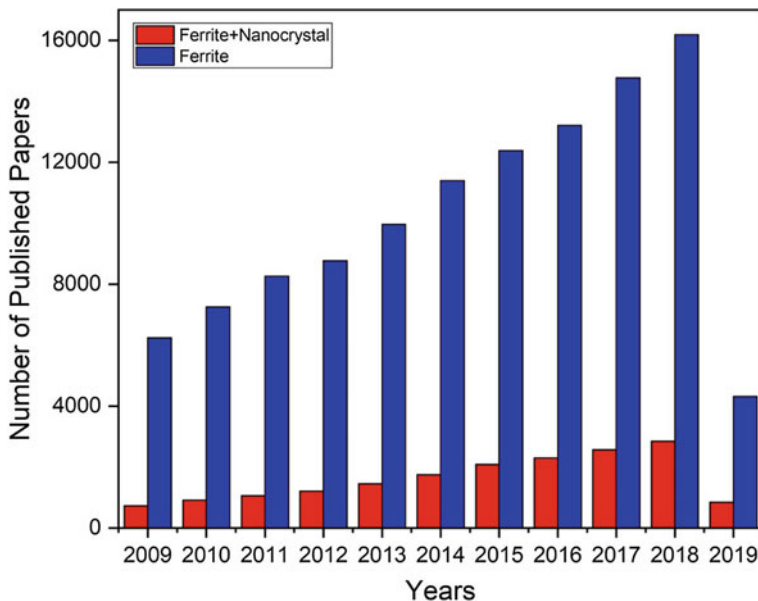


Fig. 1 Analysis of the importance of ferrite based materials from 2010 to 2019 by the Scopus database based on the keywords Ferritas and Nanocrystals (August 27, 2019)

Hence, as mentioned above, in view of the magnetic susceptibility and magnetic permeability are important parameters widely used to describe as well as classify the magnetic behavior of these advanced materials. Of course, in some cases, such as in diamagnetic materials, the corresponding susceptibility is as low and negative as the permeability [4]. In other cases, however, the relationship between the magnetization and the applied field is not linear, so magnetic susceptibility varies according to magnetic field intensity, i.e., resulting in magnetic susceptibility and permeability with high values, such as in the case of ferromagnetic materials [4]. As expected from the former, there is a strong interaction between spins; thus, a high number of spins tend to become aligned in the same direction [4, 5]. Even at room temperature, the alignment is so strong that thermal vibrations cannot destroy this kind of material. Interestingly, the total magnetic field (the field applied to the material plus the induced field) in this material can be 103 or 104 times the applied field [4, 5].

In ferrimagnetic materials, are known that the atoms have permanent dipole moments, which interact to each other, causing antiparallel and unequal alignment [6–10]. Thus, in the presence of an external magnetic field, they become aligned in the direction of the applied field, showing high and positive values of magnetic susceptibility ($10^{-2} < \chi < 10^6$), e.g., in the case of Fe_2O_3 ferrite [9, 10]. Also, the results shown that magnetic permeability makes them possible to be applied to devices, such as antennas, and their resistance to electricity is usually desirable in transformer cores to reduce secondary currents. Moreover, is known that some ferrites absorb microwave energy in one direction so that they can in principle be suitably used in microwave waveguides [2].

The huge importance of ferrite based materials is fundamentally related to their excellent magnetic and dielectric properties. Thus, in this perspective, this advanced material can widely be applied to magnetic recording media and magnetic fluid for information storage and/or retrieval, catalysts, magnetically guided drug delivery, magnetic resonance imaging, sensors, pigments, and so on [11–16]. In addition to these applications, ferrite-related materials can also be used as a permanent magnetic material for high-density recording media [5, 12, 13], insulators, circulators, high-quality filters, and many magnetic optical devices [14–16].

Herein, we have focused on the chemical insights based on crystal engineering of spinel ferrite nanoparticles, in order to elucidate their fundamental properties. This chapter is organized as follows: the Sect. 2 will discuss the normal and inverse spinel-like structure that ferrite can assume. In Sect. 3 the main methods of obtaining will be addressed, being hydrothermal (CH and MH), co-precipitation (CP) and sol-gel (SG) and how the ferrite can be characterized. Section 4 discusses the influence of morphology on the magnetic, optical and catalytic responses of nanocrystalline ferrite. Finally, in Sect. 5, we will show the influence of doping on the same properties discussed in Sect. 4.

2 The Crystalline Structure of Ferrite

The spinel-like ferrites structure, whose general formula is MFe_2O_4 , can be found in normal or inverted form [17]. In normal spinel ferrite, all divalent cations M^{2+} are present at tetrahedral sites and trivalent cations (Fe^{3+}) at octahedral sites [17–19]. A notable example of normal spinel-type ferrite (see structure shown in Fig. 2) is of zinc ferrite ($ZnFe_2O_4$). On the other hand, in the case of inverse spinel ferrite, the divalent cations occupy octahedral sites and trivalent cations are equally distributed between both tetrahedral and octahedral sites [17]. One compound with this type of structure is nickel ferrite ($NiFe_2O_4$). Its crystalline structure (see Fig. 2) is strictly composed of octahedral tetrahedral $[FeO_4]$ and $[FeO_6]$ clusters, while the Ni^{2+} ion is found only in $[NiO_6]$ octahedral clusters [18, 19].

However, it is well known that the method of preparing ferrites may in principle alter the degree of inversion of the crystal structure [17–21]. For example, Thomas et al. report that some preparation methods, such as sol-gel, cause changes in the magnetic behavior of $ZnFe_2O_4$ [20, 21]. This means that most of the chemical and physical properties of nanoparticles strongly depend on the distribution of cations in the lattice.

3 Method of Preparation and Characterization

3.1 Preparation Methods

It additionally is known that the physical and chemical behavior of nanocrystals depends on the synthesis process used [22]. Among the various methods available for the preparation of nanocrystalline ferrite, with more or less defects, the most popular including hydrothermal [23], sol-gel [24] and co-precipitation [25], and therefore will be the focus of this chapter.

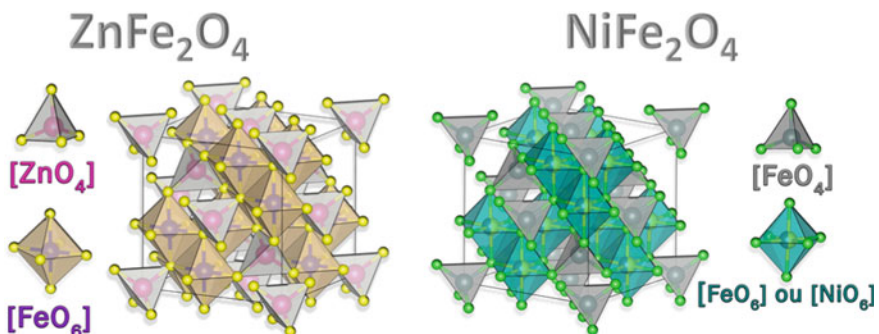


Fig. 2 Crystalline structure of $ZnFe_2O_4$ (normal spinel) and $NiFe_2O_4$ (inverse spinel) with space group $Fd3m$

In the conventional hydrothermal (CH) method, in particular, there are many strategies to control the growth conditions [23, 26–29]. In general, this approach is designed to exploit the solubility of the vast majority of inorganic substances in the water at elevated temperatures and pressures followed by crystallization of the material dissolved in the fluid [23, 26–29]. At high temperatures, as is well-known, the properties of reagents, including their solubility and reactivity, also change. Therefore, these changes provide more parameters for producing different morphologies as well as metastable phases, for instance, which are not possible at low temperatures. Thus, this approach has widely been for the production (scalable) of diverse target ferrites with highly pure and crystalline. In this perspective, one of the advantages of this method is the control of particle size, morphology and other physical characteristics by adjustments in reaction temperature, time, additives and other factors [23, 26–28].

Thus, for this strategy, the control of physical characteristics of target nanocrystals is strongly dependent on CH conditions used (e.g., parameters like water pressure, pH conditions, concentration, temperature, reaction time and nature of precursors) [23, 26–29]. In this method, the solvent is not limited to water and may include other polar or non-polar solvents, one of which is benzene, in which case the process is more appropriately called solvothermal synthesis [29]. Here the fundamental principle is the same.

For instance, Wang et al. [30] were responsible for developing a unified approach for the synthesis of a wide variety of nanocrystals with different chemical properties and low dispersion. The strategy cited by these authors is based on a general mechanism of phase transfer and separation that occurs at the interfaces of the liquid, solid and soluble phases present during CH synthesis [30]. As an example, in view that both Fe_3O_4 (magnetite) and CoFe_2O_4 (cobalt ferrite) can be prepared by the described method with uniform sizes of about 9 and 12 nm, respectively [30]. In addition, monodisperse, hydrophilic and monocrystalline ferrite beads were also synthesized by hydrothermal reduction [31–42]. In relation to other traditional processes, usually is well-known that the hydrothermal growth of a huge diversity of target materials lead to a better crystallinity of product of interest [32]. However, in recent years, there have widely been reports that CH preparation techniques have been replaced by the microwave-assisted hydrothermal (MH) method, as this new synthetic route provides rapid and uniform heating, that speeds up the process allowing obtaining advanced materials in extremely short times [32–41]. We also believe this methodology (due to its simplicity and excellent control of the growth conditions) to be dominant in the preparation of a variety of new advanced materials in the future.

Another method that has received great attention in preparing of ferrites based materials, is the self-combustion sol-gel (SG) method comprises an exothermic and thermally induced anionic oxirreduction reaction of xerogel, which is obtained by the oxidizing agent (aqueous solution containing the desired metal salts) and the reducing agent (organic complexing) [11]. Nitrate salts are widely used as they are an oxidizing source of low temperature and water-soluble NO_3^- for synthesis [43].

In particular, the volume of gases released during xerogel combustion and the loss of mass during the process allows the formation of ferrite nanopowders and furthermore may in principle prevent in some cases the formation of agglomerates [44, 45]. As is well-known, during the combustion process, in particular, the transformation of crystalline ferrite into the xerogel occurs from the heat generated by the chemical reaction [46]. Hence, the temperature of the flame during combustion may range from 600 to 1350 °C, respectively. It additionally is known that the physical characteristics of the product obtained by this strategy depend on the type of complexant, solution pH value, atmospheric environment, heat source and reaction conditions [11, 43–49]. The advantages of using SG are in principle based on good chemical homogeneity, a highly crystalline and pure product, fine particle size, in addition to easy control of stoichiometry of target material [47–49]. Finally, taking this into consideration, the SG method is mainly used in the production of complex metal oxides, inorganic, temperature-maintained hybrid materials and thermodynamically unfavorable or metastable materials [50].

On the other hand, the co-precipitation (CP) method is a low-cost technique as well as one of the most industrially used for manufacturing a variety of advanced materials on a large scale. In a CP synthesis, the precipitates may be hydroxides, carbonates or oxalates, all of which may be thermally decomposed into the corresponding oxides [25, 51–53]. Also, from a practical standpoint, the precipitation can be performed electrolytically or chemically. However, the particle size is not small and monodisperse enough for specific applications such as media application registration [25]. This is because the reaction control is only kinetic and thermodynamic parameters [51].

Fundamentally, the first stage of co-precipitation occurs nucleation (formation of primary nuclei). In spite of surface tension and the action of electrostatic forces act on the formation of precipitating submicrometric crystals. Then the precipitate is separated from the liquid and washed (with organic solvent or water) to remove by-products that are weakly bound to the surface of the powders. By-products, in turn, can also be eliminated during the drying process [54].

In the second stage, through calcination, occurs the crystallization of the material in which leads to the disappearance and/or formation of desired phases. This step also involving eliminates by-products still present in the powders as-prepared. It additionally is at this stage that the material acquires some characteristics of the electrical, magnetic and crystallographic properties of the product. Finally, after calcination, the powder is often compacted and sintered. In sintering occurs the densification of the powders that have been compacted, thus varying the shape and size of the particles and pores [55, 56]. As disadvantage of chemical co-precipitation, in particular, the product is, in turn, susceptible to changes in solution conditions during batch preparation. There is also the formation of unwanted, which in turn is difficult to remove from final products. However, in the case of electrolyte co-precipitation, there are no such disadvantages, hence, providing good control and a high degree of purity occur [53].

3.2 Physical Characterization

A large variety of suitable preparation methods for the design of crystalline materials with different sizes and shapes has been widely reported in the literature [11, 22–53]. Hence, the exotic chemical behavior of these advanced materials can, in theory, be revealed from the investigation in-depth of their microstructure.

A NiFe_2O_4 sample was prepared using the MH method. As shown in Fig. 3 (a), the XRD pattern revealed the formation of a single-phase cubic face-centered (fcc) structure with high crystallinity [57]. In this case, all the reflections of the planes, which can be seen below, are in accordance with the JCPDS standard, card no. 86-2267. The absence of the secondary phase indicates that the NiFe_2O_4 nanoparticles have high purity. Hence, the average crystal size was calculated to be 8.9 nm approximately, and the grid parameter value (a, b and c) was calculated to be 8.33 Å. These values are closer to the data that have been reported in the literature [59].

Fig. 3 (b) depicts the TEM images. It was observed that the average particle size of the prepared sample was about 20 nm and the surface area was calculated to be

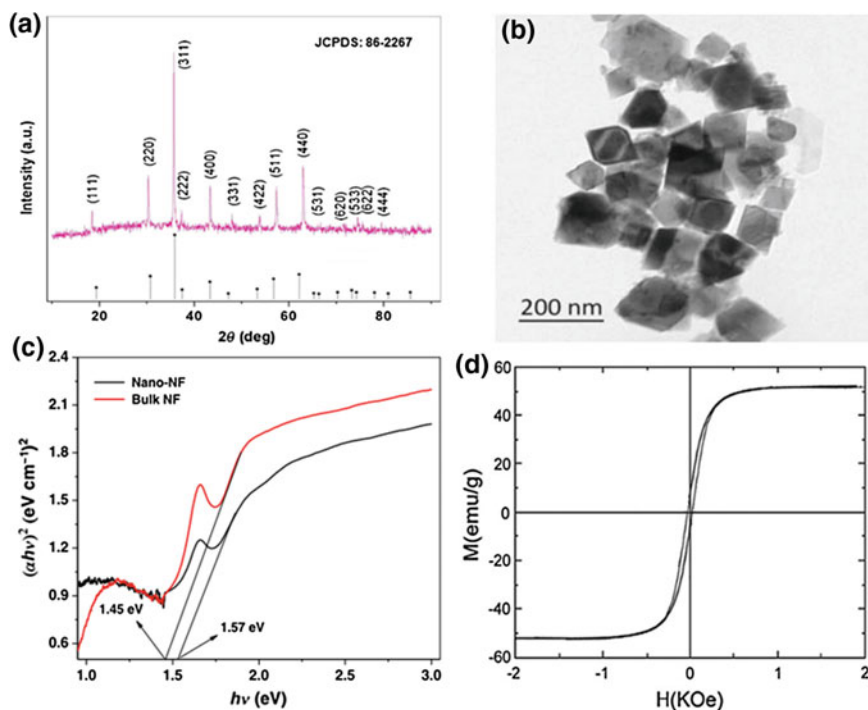


Fig. 3 a XRD pattern, b TEM images, c diffuse reflectance spectrum (adapted from Ref. [57]) and d magnetization hysteresis (± 2.0 kOe) at room temperature of different NiFe_2O_4 samples synthesized through MH (adapted from Ref. [58])

$55.7 \text{ m}^2 \text{ g}^{-1}$ approximately. A value of 170 nm was reported by Wang et al. [60] by using the solvent solution technique at $180 \text{ }^\circ\text{C}$ for 48 h. However, the value obtained above is much lesser than the reported value. Surface area (S) is an important physical property of nanomaterials because of their grain size. Also, the magnetic response of ferrite-based materials are highly sensitive to exposed surface (with respect to its area and chemical structure) [61]. In minute magnetic particles, the direction of magnetization can be altered through thermal agitation, which reflects its superparamagnetic property [62, 63]. These systems exhibit properties that are analogous to paramagnetic systems, but with a higher magnetic moment [64].

When the dimension of the magnetic material is reduced to a critical size, it leads to decrease in its domain region [65, 66]. As a result, a monodomain is formed, which leads to spontaneous magnetization within the particle [67]. The magnetic material remains magnetized in one direction only, leading to the formation of an immense magnetic moment. It is also observed that the coercivity reaches its optimum value as the size of the magnetic particle comes closer to critical diameter [68].

In case of particles whose diameter is lesser than the critical diameter, the magnetic moment is strongly influenced by thermal fluctuation, spontaneously demagnetizes the particle set and the coercivity becomes zero [63, 69, 70]. These particles are known as superparamagnetic particles [63]. It is observed that superparamagnetic particles have a mean diameter that lies in the nanometer region and monodisperse in nature.

The optical band gap generated by the samples that are synthesized using the MH method can be evaluated through diffuse reflectance spectrum. The results obtained were compared to that of NiFe_2O_4 in bulk quantity and the measurements were made ranging from 200 nm to 1500 nm. As seen in Fig. 3 (c), the nano- NiFe_2O_4 (nano-NF) particles exhibited a band gap value of 1.57 eV approximately, which is greater than 1.45 eV exhibited by NiFe_2O_4 in bulk quantity.

Huo et al. [58] studied the magnetic properties of NiFe_2O_4 , which was synthesized through hydrothermal reaction at $180 \text{ }^\circ\text{C}$ for 10 h. Fig. 4 (a) depicts the typical hysteresis loop formed by a soft magnetic material with saturation

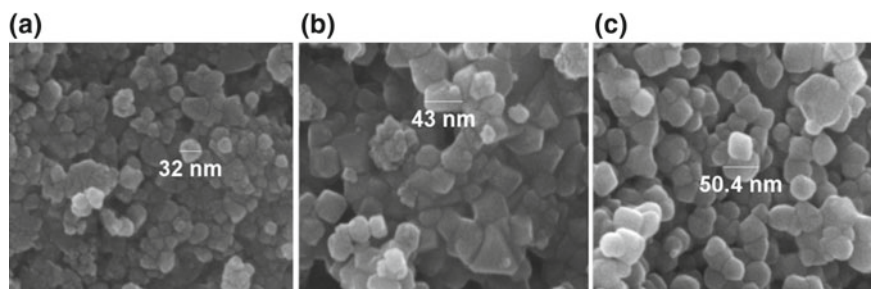


Fig. 4 Typical SEM images for cobalt ferrite synthesized at temperatures of **a** $75 \text{ }^\circ\text{C}$. **b** $85 \text{ }^\circ\text{C}$ and **c** $95 \text{ }^\circ\text{C}$. Adapted from Ref. [71]

magnetization (M_s) of 53.6 emu/g and coercivity of about 68 Oe. The reported value of 56 emu/g for the bulk sample [48], was consistent with the values that were determined by other studies reported in the literature [72]. It is observed that the value of M_s increases with the improvement in the crystallinity of material. Thus, higher M_s and lower coercivity results from high crystallinity and uniform morphology, respectively [73].

4 Effects of Morphology on the Magnetic, Photocatalytic and Optical Properties of Spinel Ferrite

As mentioned earlier, magnetic nanoparticles have promising applications, mainly as catalysts and magnetic data storage. However, for much of their applications, is need the control of their morphology, size, chemical composition, monodispersity, as well as, the degree of the structural defects in the sample, since their physico-chemical properties strongly depend on these parameters [74]. Therefore, in this section, changes in synthesis such as reaction time, reagent concentration and temperature will be discussed with base on their magnetic, optical and photocatalytic responses.

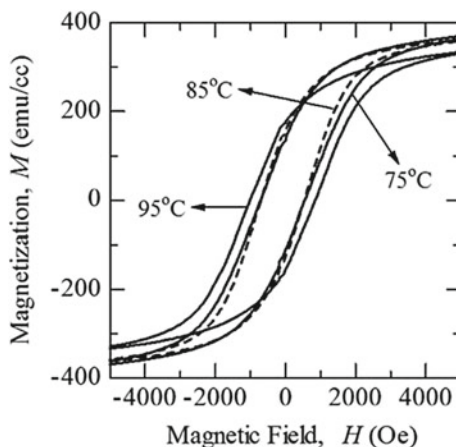
El Maalam et al. [75] proposed that the synthesis of $ZnFe_2O_4$ crystals using the CP method is beneficial as it allows good stoichiometric control and produces ultrafine particles for a short duration at low temperature. In this study, the concentration of reagents and their reaction time are responsible for disorderliness seen in cation (Zn^{2+} and Fe^{3+} ions) which are distribution in both the tetrahedral and the octahedral sites. This disorderliness is responsible for the significant variation of magnetic properties of $ZnFe_2O_4$ crystals [75]. It is also observed that the synthesized sample with high inversion degree exhibits higher magnetization values. The cation distribution between sites A and B can be increased if the reaction is maintained for a fixed interval of time.

The magnetic property of the nanocrystalline ferrites is also influenced by the temperature at which the sample is synthesized. Hutamaningtyas et al. [71] proposed that the synthesis of cobalt ferrite ($CoFe_2O_4$) at the temperatures of 75 °C, 85 °C and 95 °C, respectively, showed changes in the absorption range which was closer to 590 cm^{-1} using the CP method. The changes in the absorption range were due to an increase in the synthesis temperature. The effect of temperature was further studied by analyzing the high peaks generated by the sample using XRD. The analysis revealed that an increase in temperature led to an increase in the relative intensity of peaks generated by the samples as seen in the XRD patterns, and gave a better understanding of the structure of the crystal. As seen in Fig. 4, the size of the $CoFe_2O_4$ crystallites increases with increase in temperature. It was observed that as the size of the grain increases, it becomes homogeneous thus forming peaks with high intensity as seen in the XRD pattern.

Fig. 5 depicts the hysteresis curves formed by CoFe_2O_4 crystals at 75 °C and 85 °C, respectively. It was found that the magnetic properties of CoFe_2O_4 crystals did not show significant difference at both temperatures. An increase in the synthesis temperature leads to changes in the coercive field, the remanence magnetization (M_r) and the saturation magnetization (M_s) of CoFe_2O_4 crystals. The coercive field at the temperature of 75 °C, 85 °C and 95 °C was calculated to be 618 Oe, 625 Oe, and 923 Oe, respectively. The change in the coercive field indicates that the synthesis temperature came closer to the CoFe_2O_4 nanoparticle grains, thus, making it feasible to produce particle with large grain size. In case of CoFe_2O_4 crystals, when the crystallite size is lesser than 70 nm, a single domains is observed [76]; however, recent studies indicate that a similar domain has been observed with crystalline size of 45 nm as well [77]. CoFe_2O_4 samples exhibit a high coercive field at different temperatures due to fixation of the magnetic domains at the interface [78]. It is also observed that the value of M_r increases with an increase in the temperature due to change in the coupling of randomly oriented nanograins [79]. The hysteresis curve also shows that the value of M_s decreases with increase in the synthesis temperature. This phenomenon arises as the tetrahedral sites are not only occupied by Fe^{3+} , but are shared with Co^{2+} ions. A decrease in the value of M_s indicates that Fe^{3+} and Co^{2+} cations were replaced and redistributed in the octahedral sites. The octahedral sites are predominantly occupied by the Co^{2+} cations, which leads to the reduction in the total magnetic moment, thus, reducing the value of M_s [19, 52–54].

Qiu et al. [80], synthesized ZnFe_2O_4 films using the SG method at the temperatures of 350 °C, 400 °C, 450 °C and 500 °C, respectively, to analyze the effect of morphology on the catalytic properties of ferrites. This films is used to decompose methyl orange using the radiation from a xenon lamp. In Fig. 6, it can be seen that the rate of degradation of the dye varied on basis of the calcination temperature. The maximum variation was observed at the temperature of 450 °C. Hence, it can be concluded that the quantum effect is responsible for the

Fig. 5 Typical hysteresis curves for cobalt ferrite nanoparticles synthesized at temperatures of 75, 85 and 95 °C. Adapted from Ref. [71]



negative semiconductor valence band and for a positive valence range. This leads to an increase in the oxidation and reduction reactivity which further helps in improving the catalytic activity of the ferrites [80].

The interfacial effect produces more defects owing to the recombination of the center of electrons and holes, which could, in theory, decrease its catalytic activity. At the time of growth of granules on a film, both the quantum and interfacial effects decrease. The interfacial effect is optimum at temperatures below 450 °C [80]. Above this temperature, the quantum effect becomes dominant. Thus, the clash between these two effects leads to the change in the photocatalytic reactivity flexion of ZnFe_2O_4 film [80].

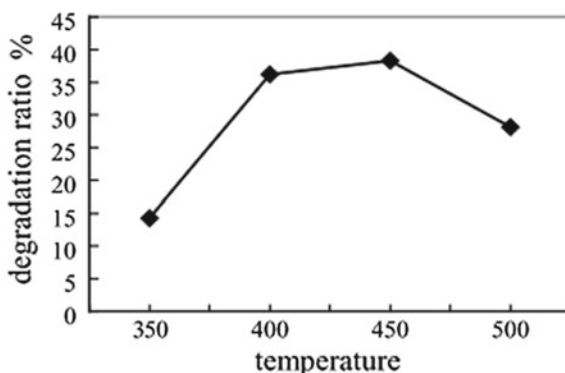
Sapna et al. [81] proposed the synthesis of ZnFe_2O_4 through spherical morphology (ZFS), stems (ZFR) and flowers (ZFF) using the MH technique. Fig. 7a–c depicts the various morphologies that are formed. During the process of hydrothermal synthesis, the precursors and the solvents create an uneven growth of crystals in different directions. The process of nucleation and rate of growth further leads to the formation of different morphologies [82]. Table 1 shows the morphology and dimensions obtained for each sample.

To assess the relevance between morphology and bandgap (E_g), the authors used UV-Vis spectroscopy. Figure 7d shows the optical absorption of the samples in the 200 to 800 nm wavelength range. Figure 7e–g show the graph $(\alpha h\nu)^2$ versus $h\nu$ for ZFS, ZFR, and ZFF, respectively [81]. By the graph analysis, the E_g values found were 4 eV for ZFS, 2.86 eV for ZFR and 3.47 eV for ZFF [81]. All samples had higher E_g compared to bulk ZnFe_2O_4 (1.9 eV) reported in the literature [83].

5 Effects of Doping on the Magnetic, Photocatalytic and Optical Properties of Spinel Ferrite

The effect of the substitutional doping of the host matrices causes noticeable changes in their fundamental properties [84–95]. In this perspective, the preference of the dopant site (tetrahedral or octahedral) can easily be determined from

Fig. 6 Relationship between degradation rate and calcination temperature of the film. Adapted from Ref. [80]



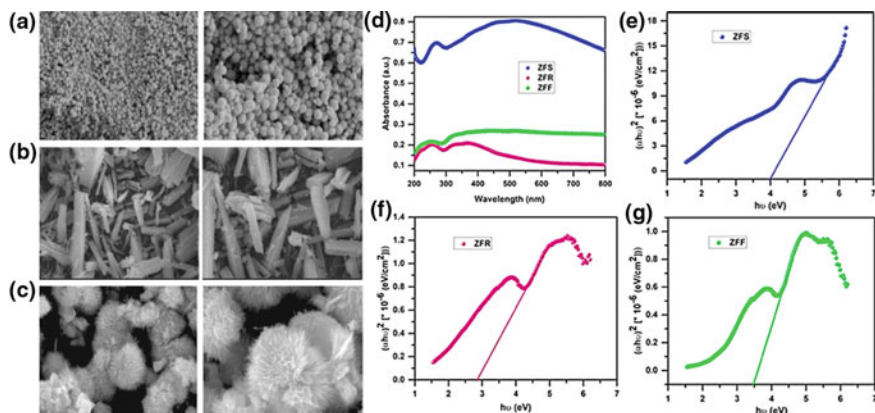


Fig. 7 a FESEM image ZFS. b FESEM image ZFR. c FESEM image ZFF. d Optical absorption of ZFS, ZFR and ZFF samples. e E_g ZFS. f E_g ZFR and g E_g ZFF. Adapted from Ref. [81]

Table 1 Morphology and dimensions of MH synthesized ZFS, ZFR and ZFF samples

Sample	Morphology	Dimensions
ZFS	Nanospheres	100–150 nm
ZFR	Nanobaster	5–8 μm
ZFF	Flower (3D)	3–6 μm

spectroscopic studies [19]. Yet, the difference in ionic radius during the doping of host matrix, in particular, may induce a strain in the lattice, that can in principle be verified by XRD along with the purity of the formed phase in this case [85].

On the other hand, Zhang et al. [86] studied the synthesis of Co-doped Mn-Zn ferrite, which is prepared using the CP method. A magnetic field of -600 to 600 Oe was applied to the doped Mn-Zn ferrite at room temperature to study the changes in their magnetic properties. The hysteresis loops representing the changes in the magnetic property of doped ferrites is shown in Fig. 8a. All the tested samples exhibit superparamagnetic properties without loss of hysteresis when under the influence of low magnetic field indicating zero coercivity [86]. In Fig. 8b, it can be seen that the value of M_s increases with an increase in the content of Co, and it reaches the maximum value of approximately 73 emu/g. The value further decreases as the content of Co increases. Overall, this variation can be described in terms of redistribution of cations and the moment-exchange interactions at sites A and B in a spinel network. In the crystalline structure of a Mn-Zn ferrite, the Mn^{2+} and Zn^{2+} ions occupy the A sites, whereas the Co^{2+} and Fe^{2+} cations occupy the B sites, and the Fe^{3+} ions randomly occupy both the sites [87, 88]. When the concentration of the dopant exceeds 1.0 at.%, the value of M_s decreases for the prepared samples. This, suggests that the Co^{2+} ions have entered the B site and pushed the Fe^{3+} ions to A sites, as described in the literature [89, 90].

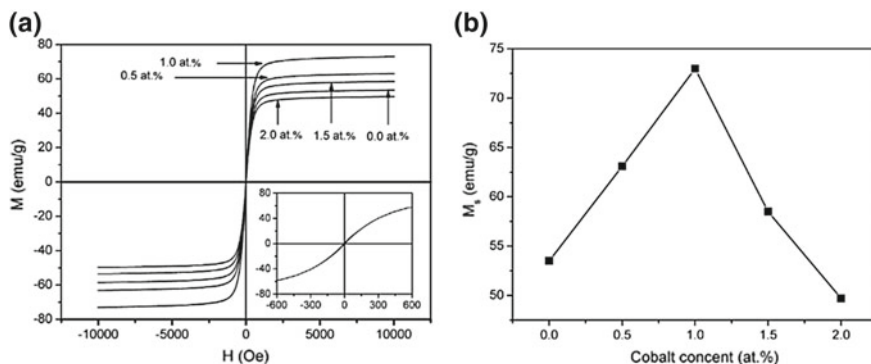


Fig. 8 **a** Hysteresis loops of the Co-doped Mn-Zn ferrites, calcined at 1150 °C. The inset shows the hysteresis loop of the ferrite particles with 1.0 at.% Co in magnetic fields ranging from –600 to 600 Oe and **b** variation of the saturation magnetization M_s with Co content at room temperature. Adapted from Ref. [86]

Previous studies on doped nanocrystalline ferrites show that these have a potential for use in the field of photocatalytic applications. For instance, Naik et al. [91] conducted a study on NiFe_2O_4 using Al^{3+} doped self-combustion SG which was found to be an effective photocatalyst for degradation of rose bengal (RB), malachite green (MG), alizarin red (AZ), methylene blue (MB) and titan yellow (TY) under visible light. The results [91] show an increase in the doping activity of $\text{NiAl}_x\text{Fe}_{2-x}\text{O}_4$ ($x = 0.0, 0.1, 0.3, 0.5$ and 0.7) (NAF NPs) to 63% when x is 0 and to 99.8% when x is 0.5 in 150 min as shown in Fig. 9. Thus, it could be concluded that an increase in the concentration of Al^{3+} increases the efficiency of photo-bleaching of the RB dye [91].

From the kinetic study of photocatalytic degradation, it was observed that the velocity constant (k) of the sample where $\text{NiAl}_{0.5}\text{Fe}_{1.5}\text{O}_4$ was $4.03 \times 10^{-2} \text{ min}^{-1}$ when degraded the RB dye, while the pure material has a constant of about $0.62 \times 10^{-2} \text{ min}^{-1}$ under visible light illumination [91]. These results are summarized in Table 2. From the data obtained it was concluded that doping with Al^{3+} for $x = 0.5$ is the amount ideal, resulting in a more efficient separation of photoinduced pairs [91–95]. Hence, above the ideal limit ($x = 0.5$) was observed that the catalytic activity decreased. This likely is because when the Al^{3+} concentration reaches its ideal limit, the spatial charge regions become narrower and the surface barrier higher [93–95].

Melo et al. [96] have also synthesized $\text{Co}_{1-x}\text{Ni}_x\text{Fe}_2\text{O}_4$ ($0 \leq x \leq 1$) by MH method. They analyzed the effect of doping on the optical properties of $\text{Co}_{1-x}\text{Ni}_x\text{Fe}_2\text{O}_4$ powders, as shown in Fig. 10. According to Brus's model [97],

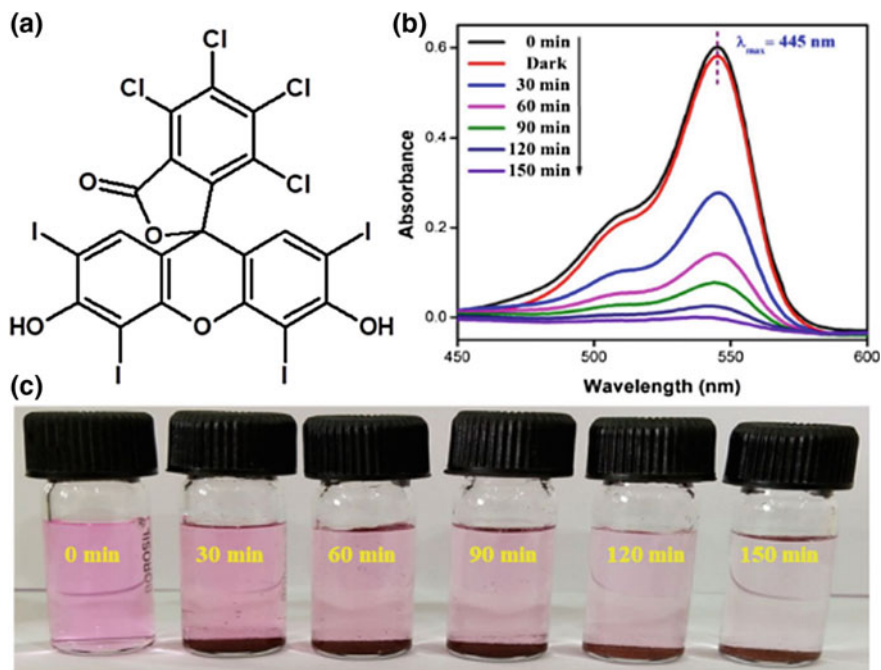


Fig. 9 a Chemical structure of RB dye. b UV-Vis absorbance spectra of RB dye during degradation and c digital picture of decolorization of RB dye by NAF NPs obtained at different times. Adapted from Ref. [91]

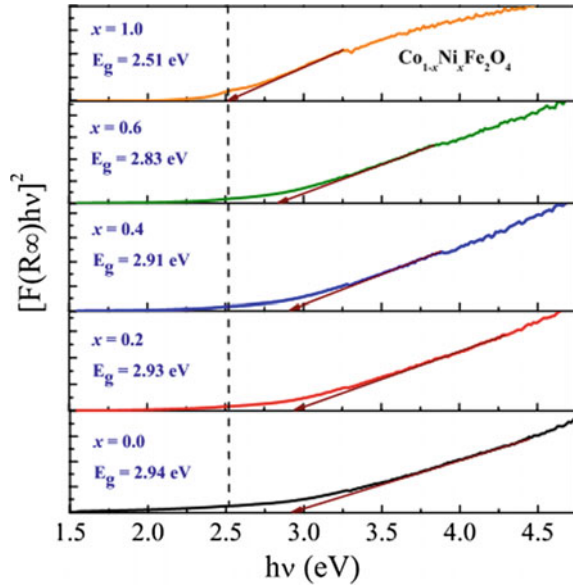
Table 2 Photocatalytic degradation (%), the velocity constant (k), time and temperature for RB dye NAF NPs

Composition	Degradation (%)	$k \times 10^{-2} \text{ min}^{-1}$	Time (min)	Temperature ($^{\circ}\text{C}$)
NiFe_2O_4	63	0.62	150	27
$\text{NiAl}_{0.1}\text{Fe}_{1.9}\text{O}_4$	80	1.02	150	27
$\text{NiAl}_{0.3}\text{Fe}_{1.7}\text{O}_4$	91	1.57	150	27
$\text{NiAl}_{0.5}\text{Fe}_{1.5}\text{O}_4$	99.8	4.03	150	27
$\text{NiAl}_{0.7}\text{Fe}_{1.3}\text{O}_4$	95	2.03	150	27

Adapted from Ref. [66]

the alteration in the band gap (E_g) values may arise mainly from the difference in particle size as-prepared. Thus, the E_g value found for pure CoFe_2O_4 (in film form) was higher than reported in the literature, ~ 2.50 eV [98] and ~ 2.70 eV [99].

Fig. 10 E_g values obtained for $\text{Co}_{1-x}\text{Ni}_x\text{Fe}_2\text{O}_4$, $x = 0.0$; $x = 0.2$; $x = 0.4$; $x = 0.6$ and $x = 1$. Adapted from Ref. [96]



6 Conclusion

Direct chemical insights into materials design can be acquired from the correlation of spectroscopic properties (at the short-, medium- and long-range) with theoretical calculations of a diverse range of advanced crystalline materials. From the chosen method of preparation (e.g., CH, MH, SG, and CP), it was possible to observe that similar compounds presented different characteristics, leading to a significant change in their chemical nanoscale response.

It is noteworthy that obtaining different morphologies could in principle be considered a well-reasoned strategy for provided new advanced materials with tuned properties. Thus, such alterations could allow the emergence of applications out of the conventional for these advanced materials. Therefore, it is extremely important to focus studies on the most advantageous ways to obtain ferrite based materials by analyzing the preparation methods already reported. Improving synthetic routes and making them more energy efficient is one of the future challenges that need further research. These combined efforts, in turn, enable the emergence of new technologies.

References

1. Naseri, M.G., Saion, E.B., Ahangar, H.A., Hashim, M., Shaari, A.H.: Simple preparation and characterization of nickel ferrite nanocrystals by a thermal treatment method. *Powder Technol.* **212**(1), 80–88 (2011)
2. Editors of Encyclopaedia Britannica: Ferrite—Iron Oxide Compound [Online]. Available: <https://www.britannica.com/science/ferrite-iron-oxide-compound>
3. Joy, D.C.: Chemical analysis of ferrites. *Talanta Rev.* **30**, 299–315 (1983)
4. Chen, C.H.: *Magnetism and Metallurgy of Solt Magnetic Materials*. Courier Dover Publications (1986)
5. Cullity, B.D.: *Introduction to Magnetic Materials*. Addison-Wesley, MA (1972)
6. Griffiths, D.J.: *Introduction to Electrodynamics*, 3rd edn. N. J. Prentice Hall, Upper Saddle River (1999)
7. Jiles, D.: *Introduction to Magnetism and Magnetic Materials* (1991)
8. Moskowitz, B.M.: *Hitchhiker Guide to Magnetism*, 3rd edn. (2006)
9. Sinnecker, J., Grossinger, R., Turtelli, R.S., Exel, G., Greifeneder, G., Kuss, C.: *J. Magn. Magn. Mater.*, 194 (1994)
10. Hsu, C., McGuire, T.R.: *Magnetism and Magnetic Materials*. Academic Press, New York (1968)
11. Airimioaei, M., et al.: Synthesis and functional properties of the $\text{Ni}_{1-x}\text{Mn}_x\text{Fe}_2\text{O}_4$ ferrites. *J. Alloys Compd.* **509**(31), 8065–8072 (2011)
12. González-Carreño, T., Morales, M.P., Serna, C.J.: Barium ferrite nanoparticles prepared directly by aerosol pyrolysis. *Mater. Lett.* **43**(3), 97–101 (2000)
13. Bate, G.: Magnetic recording materials since 1975. *J. Magn. Magn. Mater.* **100**(1–3), 413–424 (1991)
14. Joseyphus, R.J., Narayanasamy, A., Nigam, A.K., Krishnan, R.: Effect of mechanical milling on the magnetic properties of garnets. *J. Magn. Magn. Mater.* **296**(1), 57–64 (2006)
15. Garskaite, E., et al.: On the synthesis and characterization of iron-containing garnets ($\text{Y}_3\text{Fe}_5\text{O}_{12}$, YIG and $\text{Fe}_3\text{Al}_5\text{O}_{12}$, IAG). *Chem. Phys.* **323**(2–3), 204–210 (2006)
16. Niaz Akhtar, M., et al.: $\text{Y}_3\text{Fe}_5\text{O}_{12}$ nanoparticulate garnet ferrites: comprehensive study on the synthesis and characterization fabricated by various routes. *J. Magn. Magn. Mater.* **368**, 393–400 (2014)
17. Andersen, H.L., Saura-Múzquiz, M., Granados-Miralles, C., Canévet, E., Lock, N., Christensen, M.: Crystalline and magnetic structure-property relationship in spinel ferrite nanoparticles. *Nanoscale* **10**(31), 14902–14914 (2018)
18. Lazarević, Z.Ž., et al.: Nanodimensional spinel NiFe_2O_4 and ZnFe_2O_4 ferrites prepared by soft mechanochemical synthesis. *J. Appl. Phys.* **113**(18), 0–11 (2013)
19. Smit, J.: *Ferrites: Physical Properties of Ferrimagnetic Oxides in Relation to Their Technical Application* (1959)
20. Zhang, Y., Shi, Q., Schliesser, J., Woodfield, B.F., Nan, Z.: Magnetic and thermodynamic properties of nanosized Zn ferrite with normal spinel structure synthesized using a facile method. *Inorg. Chem.* **53**(19), 10463–10470 (2014)
21. Thomas, J.J., Shinde, A.B., Krishna, P.S.R., Kalarikkal, N.: Temperature dependent neutron diffraction and Mössbauer studies in zinc ferrite nanoparticles. *Mater. Res. Bull.* **48**(4), 1506–1511 (2013)
22. Pottker, W.E., et al.: Influence of order-disorder effects on the magnetic and optical properties of NiFe_2O_4 nanoparticles. *Ceram. Int.* **44**(14), 17290–17297 (2018)
23. Chen, D., Chen, D., Jiao, X., Zhao, Y., He, M.: Hydrothermal synthesis and characterization of octahedral nickel ferrite particles. *Powder Technol.* **133**(1–3), 247–250 (2003)
24. Sutka, A., Mezinskas, G.: Sol-gel auto-combustion synthesis of spinel-type ferrite nanomaterials. *Front. Mater. Sci.* **6**(2), 128–141 (2012)

25. Hessian, M.M., Rashad, M.M., El-Barawy, K.: Controlling the composition and magnetic properties of strontium hexaferrite synthesized by co-precipitation method. *J. Magn. Magn. Mater.* **320**(3–4), 336–343 (2008)
26. Chen, D., Jiao, X., Cheng, G.: Hydrothermal synthesis of zinc oxide powders with different morphologies. *Solid State Commun.* **113**(6), 363–366 (1999)
27. Sapieszko, R.S., Matijevic, E.: Preparation of well defined colloidal particles by thermal decomposition of metal chelates—2. Cobalt and nickel. *Corrosion* **36**(10), 522–530 (1980)
28. Dell’Agli, G.M.G.: Hydrothermal synthesis of ZrO_2 - Y_2O_3 solid solutions at low temperature. *J. Eur. Ceram. Soc.* **20**, 139–145 (2000)
29. Burda, C., Chen, X., Narayanan, R., El-sayed, M.A.: *Chemistry and Properties of Nanocrystals of Different Shapes* (2005)
30. Wang, X., Zhuang, J., Peng, Q., Li, Y.: A general strategy for nanocrystal synthesis. *Nature* **437**(7055), 121–124 (2005)
31. Lu, A.H., Salabas, E.L., Schüth, F.: Magnetic nanoparticles: synthesis, protection, functionalization, and application. *Angew. Chem. Int. Ed.* **46**(8), 1222–1244 (2007)
32. Wang, J.: Prepare highly crystalline $NiFe_2O_4$ nanoparticles with improved magnetic properties. *Mater. Sci. Eng. B Solid-State Mater. Adv. Technol.* **127**(1), 81–84 (2006)
33. Xie, H., Shen, D., Wang, X., Shen, G.: Microwave hydrothermal synthesis and visible-light photocatalytic activity of γ - Bi_2MoO_6 nanoplates. *Mater. Chem. Phys.* **110**(2–3), 332–336 (2008)
34. Verma, S., Joy, P.A., Kholam, Y.B., Potdar, H.S., Deshpande, S.B.: Synthesis of nanosized $MgFe_2O_4$ powders by microwave hydrothermal method. *Mater. Lett.* **58**(6), 1092–1095 (2004)
35. Kim, C.K., Lee, J.H., Katoh, S., Murakami, R., Yoshimura, M.: Synthesis of Co-, Co-Zn and Ni-Zn ferrite powders by the microwave-hydrothermal method. *Mater. Res. Bull.* **36**(12), 2241–2250 (2001)
36. Kholam, Y.: Microwave hydrothermal preparation of submicron-sized spherical magnetite (Fe_3O_4) powders. *Mater. Lett.* **56**(October), 571–577 (2002)
37. Bensebaa, F., Zavaliche, F., L’Ecuyer, P., Cochrane, R.W., Veres, T.: Microwave synthesis and characterization of Co-ferrite nanoparticles. *J. Colloid Interface Sci.* **277**(1), 104–110 (2004)
38. Kumada, N.K.N., Komarneni, S.: Microwave hydrothermal synthesis of ABi_2O_6 ($A = Mg, Zn$). *Mater. Lett.* **33**(9), 1411–1414 (1998)
39. Kholam, Y.B., Deshpande, S.B., Khanna, P.K., Joy, P.A., Potdar, H.S.: Microwave-accelerated hydrothermal synthesis of blue white phosphor: Sr_2CeO_4 . *Mater. Lett.* **58**(20), 2521–2524 (2004)
40. Abothu, I.R., Liu, S.F., Komarneni, S., Li, Q.H.: Processing of $Pb(Zr_{0.52}Ti_{0.48})O_3$ (PZT) ceramics from microwave and conventional hydrothermal powders. *Mater. Res. Bull.* **34**(9), 1411–1419 (1999)
41. Vadivel Murugan, A., Sonawane, R.S., Kale, B.B., Apte, S.K., Kulkarni, A.V.: Microwave-solvothermal synthesis of nanocrystalline cadmium sulfide. *Mater. Chem. Phys.* **71**(1), 98–102 (2001)
42. Kholam, Y.B., Deshpande, A.S., Patil, A.J., Potdar, H.S., Deshpande, S.B., Date, S.K.: Synthesis of yttria stabilized cubic zirconia (YSZ) powders by microwave-hydrothermal route. *Mater. Chem. Phys.* **71**(3), 235–241 (2001)
43. Selvan, R.K., Augustin, C.O., Berchmans, L.J., Saraswathi, R.: Combustion synthesis of $CuFe_2O_4$. *Mater. Res. Bull.* **38**(1), 41–54 (2003)
44. Sertkol, M., Köseoğlu, Y., Baykal, A., Kavas, H., Toprak, M.S.: Synthesis and magnetic characterization of $Zn_{0.7}Ni_{0.3}Fe_2O_4$ nanoparticles via microwave-assisted combustion route. *J. Magn. Magn. Mater.* **322**(7), 866–871 (2010)
45. Yu, L., Cao, S., Liu, Y., Wang, J., Jing, C., Zhang, J.: Thermal and structural analysis on the nanocrystalline $NiCuZn$ ferrite synthesis in different atmospheres. *J. Magn. Magn. Mater.* **301**(1), 100–106 (2006)

46. Wu, K.H., Ting, T.H., Li, M.C., Ho, W.D.: Sol-gel auto-combustion synthesis of SiO₂-doped NiZn ferrite by using various fuels. *J. Magn. Magn. Mater.* **298**(1), 25–32 (2006)
47. Costa, A.C.F.M., Morelli, M.R., Kiminami, R.H.G.A.: Microstructure and magnetic properties of Ni_{1-x}Zn_xFe₂O₄ synthesized by combustion reaction. *J. Mater. Sci.* **42**(3), 779–783 (2007)
48. George, M., Mary John, A., Nair, S.S., Joy, P.A., Anantharaman, M.R.: Finite size effects on the structural and magnetic properties of sol-gel synthesized NiFe₂O₄ powders. *J. Magn. Magn. Mater.* **302**(1), 190–195 (2006)
49. Mukasyan, A.S., Epstein, P., Dinka, P.: Solution combustion synthesis of nanomaterials solution combustion synthesis of nanomaterials. *Proc. Combust. Inst.* **31**(Jan 2007), 1789–1795 (2016)
50. Cao, G.: *Nanostructures & Nanomaterials*, 2nd edn. Imperial College Press, University of Washington, USA (2004)
51. Masip, E.M.: Síntesis electroquímica de nanopartículas de ferrita de cobalto, caracterización y aplicaciones biomédicas. *Dissertação*, p. 220 (2015)
52. Goldman, A.: *Modern Ferrite Technology*, 2nd edn. Springer, Pittsburgh, PA, USA (2006)
53. Snelling, E.C.: *Soft Ferrites: Properties and Applications*, 1^a edn. Iliffe (1969)
54. Buschow, K.H.J. (ed.) *Handbook of Magnetic Materials*, p. 542. Van der Waals-Zeeman Institute University of Amsterdam; Elsevier, Netherlands (2006)
55. Sivakumar, N., Narayanasamy, A., Shinoda, K., Chinnasamy, C.N., Jeyadevan, B., Greneche, J.M.: Electrical and magnetic properties of chemically derived nanocrystalline cobalt ferrite. *J. Appl. Phys.* **102**(1), 013916 (2007)
56. Shiau, F.-S., Fang, T.-T., Leu, T.-H.: Effect of particle-size distribution on the microstructural evolution in the intermediate stage of sintering. *J. Am. Ceram. Soc.* **80**(2), 286–290 (2005)
57. Naidu, K.C.B., Madhuri, W.: Hydrothermal synthesis of NiFe₂O₄ nano-particles: structural, morphological, optical, electrical and magnetic properties. *Bull. Mater. Sci.* **40**(2), 417–425 (2017)
58. Huo, J., Wei, M.: Characterization and magnetic properties of nanocrystalline nickel ferrite synthesized by hydrothermal method. *Mater. Lett.* **63**(13–14), 1183–1184 (2009)
59. Moradmard, H., Farjami Shayesteh, S., Tohidi, P., Abbas, Z., Khaleghi, M.: Structural, magnetic and dielectric properties of magnesium doped nickel ferrite nanoparticles. *J. Alloys Compd.* **650**, 116–122 (2015)
60. Wang, J., Ren, F., Yi, R., Yan, A., Qiu, G., Liu, X.: Solvothermal synthesis and magnetic properties of size-controlled nickel ferrite nanoparticles. *J. Alloys Compd.* **479**(1–2), 791–796 (2009)
61. Hamdeh, H.H., Mahmoud, M.H., Elshahawy, A.M., Makhlof, Salah A.: Synthesis of highly ordered 30 nm NiFe₂O₄ particles by the microwave-combustion method. *J. Magn. Magn. Mater.* **369**, 55–61 (2014)
62. Issa, B., Obaidat, I.M., Albiss, B.A., Haik, Y.: Magnetic nanoparticles: Surface effects and properties related to biomedicine applications. *Int. J. Mol. Sci.* **14**(11), 21266–21305 (2013)
63. Bean, C.P., Livingston, J.D.: Superparamagnetism. *J. Appl. Phys.* **30**(4), S120–S129 (1959)
64. Kotnala, R.K., Shah, J.: *Ferrite Materials: Nano to Spintronics Regime*, vol. 23. Elsevier (2015)
65. Zhang, M., et al.: Size effects on magnetic properties of Ni_{0.5}Zn_{0.5}Fe₂O₄ prepared by sol-gel method. *Adv. Mater. Sci. Eng.* **044317**(2010), 3–11 (2016)
66. Liu, C., Zhang, Z.J.: Size-dependent superparamagnetic properties of Mn spinel ferrite nanoparticles synthesized from reverse micelles. *Chem. Mater.* **13**(6), 2092–2096 (2001)
67. Sechovský, V.: Magnetism in solids: general introduction. *Encycl. Mater. Sci. Technol.*, 5018–5032 (2001)
68. Cullity, B.D.: Fine particles and thin films. In: *Introduction to Magnetic Materials*, p. 385. Addison-Wesley, Ed. London (1972)
69. Rikken, R.S.M., Nolte, R.J.M., Maan, J.C., Van Hest, J.C.M., Wilson, D.A., Christianen, P.C.M.: Manipulation of micro- and nanostructure motion with magnetic fields. *Soft Matter* **10**(9), 1295–1308 (2014)

70. Li, L., et al.: Superparamagnetic iron oxide nanoparticles as MRI contrast agents for non-invasive stem cell labeling and tracking. *Theranostics* **3**(8), 595–615 (2013)
71. Hutamaningtyas, E., Utari, Suharyana, Purnama, B., Wijayanta, A.T.: Effects of the synthesis temperature on the crystalline structure and the magnetic properties of cobalt ferrite nanoparticles prepared via coprecipitation. *J. Korean Phys. Soc.* **69**(4), 584–588 (2016)
72. Šepelák, V., Schultze, D., Krumeich, F., Steinike, U., Becker, K.D.: Mechanically induced cation redistribution in magnesium ferrite and its thermal stability. *Solid State Ionics* **141–142**, 677–682 (2001)
73. Maensiri, S., Masingboon, C., Boonchom, B., Seraphin, S.: A simple route to synthesize nickel ferrite (NiFe₂O₄) nanoparticles using egg white. *Scr. Mater.* **56**(9), 797–800 (2007)
74. Lu, L.T., et al.: Synthesis of magnetic cobalt ferrite nanoparticles with controlled morphology, monodispersity and composition: the influence of solvent, surfactant, reductant and synthetic conditions. *Nanoscale* **7**(46), 19596–19610 (2015)
75. El Maalam, K., et al.: The effects of synthesis conditions on the magnetic properties of zinc ferrite spinel nanoparticles. *J. Phys. Conf. Ser.* **758**(1), 012008 (2016)
76. Berkowitz, A.E., Schuele, W.J.: Magnetic properties of some ferrite micropowders. *J. Appl. Phys.* **30**(4), S134–S135 (1959)
77. Maaz, K., Mumtaz, A., Hasanain, S.K., Ceylan, A.: Synthesis and magnetic properties of cobalt ferrite (CoFe₂O₄) nanoparticles prepared by wet chemical route. *J. Magn. Magn. Mater.* **308**(2), 289–295 (2007)
78. Lima, A.C., et al.: The effect of Sr²⁺ on the structure and magnetic properties of nanocrystalline cobalt ferrite. *Mater. Lett.* **145**, 56–58 (2015)
79. Skomski, R.: *Simple Models of Magnetism*. New York (2008)
80. Qiu, J., Wang, C., Gu, M.: Photocatalytic properties and optical absorption of zinc ferrite nanometer films. *Mater. Sci. Eng. B Solid State Mater. Adv. Technol.* **112**(1), 1–4 (2004)
81. Sapna, Budhiraja, N., Kumar, V., Singh, S.K.: Shape-controlled synthesis of superparamagnetic ZnFe₂O₄ hierarchical structures and their comparative structural, optical and magnetic properties. *Ceram. Int.* **45**(1), 1067–1076 (2019)
82. Cao, Y., Qin, H., Niu, X., Jia, D.: Simple solid-state chemical synthesis and gas-sensing properties of spinel ferrite materials with different morphologies. *Ceram. Int.* **42**(9), 10697–10703 (2016)
83. Singh, A., Singh, A., Singh, S., Tandon, P., Yadav, B.C., Yadav, R.R.: Synthesis, characterization and performance of zinc ferrite nanorods for room temperature sensing applications. *J. Alloys Compd.* **618**, 475–483 (2015)
84. Spaldin, N.: *Magnetic Material: Fundamentals and Device Applications* (2003)
85. Aakash, A., Chowdhury, R., Das, D., Mukherjee, S.: Effect of doping of manganese ions on the structural and magnetic properties of nickel ferrite. *Ceram. Int.* **42**(6), 7742–7747 (2016)
86. Zhang, C.F., Zhong, X.C., Yu, H.Y., Liu, Z.W., Zeng, D.C.: Effects of cobalt doping on the microstructure and magnetic properties of Mn-Zn ferrites prepared by the co-precipitation method. *Phys. B Condens. Matter* **404**(16), 2327–2331 (2009)
87. Feng, J., Guo, L.Q., Xu, X., Qi, S.Y., Zhang, M.L.: Hydrothermal synthesis and characterization of Mn_{1-x}Zn_xFe₂O₄ nanoparticles. *Phys. B Condens. Matter* **394**(1), 100–103 (2007)
88. Justin Joseyphus, R., Narayanasamy, A., Shinoda, K., Jeyadevan, B., Tohji, K.: Synthesis and magnetic properties of the size-controlled Mn-Zn ferrite nanoparticles by oxidation method. *J. Phys. Chem. Solids* **67**(7), 1510–1517 (2006)
89. Singh, A.K., Singh, A.K., Goel, T.C., Mendiratta, R.G.: High performance Ni-substituted Mn-Zn ferrites processed by soft chemical technique. *J. Magn. Magn. Mater.* **281**(2–3), 276–280 (2004)
90. Singh, A.K., Goel, T.C., Mendiratta, R.G., Thakur, O.P., Prakash, C.: Magnetic properties of Mn-substituted Ni-Zn ferrites. *J. Appl. Phys.* **92**(7), 3872–3876 (2002)
91. Naik, M.M., Naik, H.S.B., Nagaraju, G., Vinuth, M., Vinu, K., Rashmi, S.K.: Effect of aluminium doping on structural, optical, photocatalytic and antibacterial activity on nickel

- ferrite nanoparticles by sol-gel auto-combustion method. *J. Mater. Sci.: Mater. Electron.* **29** (23), 20395–20414 (2018)
92. Lassoued, A., Lassoued, M.S., Dkhil, B., Ammar, S., Gadri, A.: Photocatalytic degradation of methyl orange dye by NiFe₂O₄ nanoparticles under visible irradiation: effect of varying the synthesis temperature. *J. Mater. Sci.: Mater. Electron.* **29**(9), 7057–7067 (2018)
 93. Jesudoss, S.K., et al.: Studies on the efficient dual performance of Mn_{1-x}Ni_xFe₂O₄ spinel nanoparticles in photodegradation and antibacterial activity. *J. Photochem. Photobiol. B Biol.* **165**, 121–132 (2016)
 94. Rashmi, S.K., Naik, H.S.B., Jayadevappa, H., Sudhamani, C.N., Patil, S.B., Naik, M.M.: Influence of Sm³⁺ ions on structural, optical and solar light driven photocatalytic activity of spinel MnFe₂O₄ nanoparticles. *J. Solid State Chem.* **255**(June), 178–192 (2017)
 95. Murashkina, A.A., Murzin, P.D., Rudakova, A.V., Ryabchuk, V.K., Emeline, A.V., Bahnemann, D.W.: Influence of the dopant concentration on the photocatalytic activity: Al-doped TiO₂. *J. Phys. Chem. C* **119**(44), 24695–24703 (2015)
 96. Melo, R.S., Banerjee, P., Franco, A.: Hydrothermal synthesis of nickel doped cobalt ferrite nanoparticles: optical and magnetic properties. *J. Mater. Sci.: Mater. Electron.* **29**(17), 14657–14667 (2018)
 97. Brus, L.E.: Electron-electron and electron-hole interactions in small semiconductor crystal-lites: the size dependence of the lowest excited electronic state. *J. Chem. Phys.* **80**(9), 4403–4409 (1984)
 98. Ravindra, A.V., Padhan, P., Prellier, W.: Electronic structure and optical band gap of CoFe₂O₄ thin films. *Appl. Phys. Lett.* **101**(16), 1–5 (2012)
 99. Holinsworth, B.S., et al.: Chemical tuning of the optical band gap in spinel ferrites: CoFe₂O₄ vs NiFe₂O₄. *Appl. Phys. Lett.* **103**(8), 2–6 (2013)